



Editorial

Announcing: Organic Electronics Letters

Organic Electronics is pleased to announce the addition of a new section dedicated to brief and very timely communications of exceptional importance to the organic electronics community. This new "Letters" section guarantees rapid (within four weeks) turn-around of papers during the review process. Once accepted, the paper will be published on-line under a special "Letters" heading and will appear in the next print issue available. All Letters submissions will be handled by Stephen Forrest, who has been assigned as the Letters special section editor.

Authors interested in submitting papers to Organic Electronics Letters should follow these guidelines:

1. All submissions must have content that is new and timely and not previously published in any form. The content should be of broad interest to the readership of Organic Electronics. The Letters Editor has the discretion to move those submitted papers not deemed to fulfill these criteria to the Regular Papers section of the journal.
2. Papers should be no longer than 4 journal pages in length (approximately 2500 words or

less, total; normal one column figures occupy approximately 300 words of journal space and should be included in the total word count).

3. Papers intended for publication in the Letters section should be clearly noted as such in the transmittal letter to the Editor. We recommend (optional) that a list of at least 5 potential referees for the paper be included in the transmittal letter to minimize time spent in the editorial office. All other procedures followed for full length submissions to Organic Electronics should also be followed for Letters submissions.

We hope that you find Organic Electronics Letters to be a useful addition to the journal and we look forward to your support.

Donal Bradley
Stephen Forrest
Josef Salbeck
Kazuhiko Seki

Editors

Available online 2 March 2005



Theoretical analysis on light-extraction efficiency of organic light-emitting diodes using FDTD and mode-expansion methods

Alongkarn Chutinan *, Kuniaki Ishihara, Takashi Asano, Masayuki Fujita, Susumu Noda *

*Department of Electronic Science and Engineering, Kyoto University, Kyotodaigaku-katsura, Nishikyo-ku, Kyoto 615-8510, Japan
CREST, Japan Science and Technology Corporation, Japan*

Received 5 February 2004; received in revised form 25 November 2004; accepted 4 December 2004

Available online 21 December 2004

Abstract

We report a theoretical analysis on light-extraction efficiency of the organic light-emitting diodes. We utilize both a numerical method such as the finite-difference time-domain method and an analytic method such as the mode-expansion method. The results of both methods are compared to confirm the accuracy of the results. It is found that even though the refractive index contrast between the indium-tin-oxide (ITO) anode and the glass substrate is as small as 0.5, more than 40% of emitted light power is trapped in the ITO layer.

© 2004 Elsevier B.V. All rights reserved.

PACS: 78.20.Bh

Keywords: Organic light-emitting diode; FDTD; Mode-expansion method

1. Introduction

Organic light-emitting diodes (OLEDs) have attracted much attention due to their strong poten-

tials for flat panel display applications. However, the low light-extraction efficiency of OLEDs still remains an important issue and poses a significant challenge for researchers to develop schemes that improve the light coupling efficiency [1]. In order to do so, it is necessary to fully understand the coupling of emitted light to the surrounding materials and free space. The issue regarding the light-extraction efficiency of the OLEDs has been investigated theoretically or experimentally in

* Corresponding authors. Tel.: +416 978 5207; fax: +416 978 2537 (A. Chutinan); tel.: +81 75 383 2315/2319; fax: +81 75 383 2317/2320 (S. Noda).

E-mail addresses: chutinan@physics.utoronto.ca (A. Chutinan), snoda@kuee.kyoto-u.ac.jp (S. Noda).

various articles [2–6]. In the theoretical analyses reported, a number of models ranging from the classical ray optics [2] to the combined classical and quantum mechanical microcavity [3] are utilized. However, a non-trivial discrepancy can be seen among different articles. In this paper, we report a light-extraction efficiency analysis of the OLED where both the numerical method such as the finite-difference time-domain (FDTD) method and the analytic method such as the mode-expansion method are used. The results of FDTD are compared with those of the mode-expansion method to confirm the accuracy of the results.

2. Calculation of light-extraction efficiency by 3D FDTD

Fig. 1 shows a schematic of the OLED structure studied here. The structure consists of a metal cathode, a tris-(9-hydroxyquinoline) aluminum (Alq_3 , refractive index $n_1 = 1.7$), a poly-(*N*-vinylcarbazole) (PVK, $n_2 = 1.67$), an indium-tin-oxide (ITO, $n_3 = 2.0$) anode and a glass substrate ($n_4 = 1.5$). Here, we assumed that the light is emitted from the excitons, which are created at the interface of the Alq_3 and PVK layers. The emitted light can be categorized into three modes: the waveguide modes that are trapped inside the organic and ITO layer, the glass modes that escape the ITO layer but are trapped in the glass substrate by total internal reflection at the interface of glass

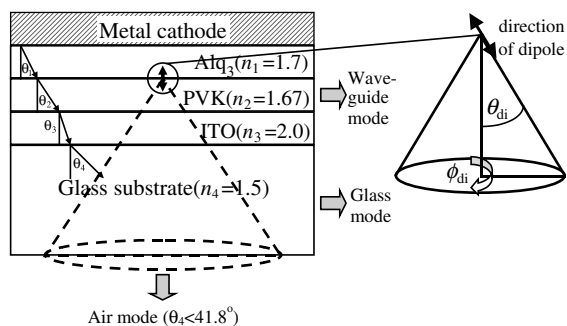


Fig. 1. Schematic depicting the OLED structure and computational model. The structure consists of four layers, i.e., Alq_3 , PVK, ITO and the glass substrate. The dipole is placed at the Alq_3 /PVK interface and can align in arbitrary direction described by angles ϕ_{di} and θ_{di} .

and air, and the air modes that escape the glass substrate to air.

First, we explain the calculation by the three-dimensional (3D) FDTD method [7]. The above-described OLED structure is modeled inside the FDTD computational domain. The metal cathode is modeled as a perfect electric conductor and the absorption loss is not considered here. The substrate is modeled as a very thick layer of glass and is terminated by the Mur's secondary absorbing boundary condition [8], which allows electromagnetic waves to propagate out of the computational domain without being reflected back into the computational domain. This is equivalent to that the glass substrate is assumed to be infinitely thick. The spatial and temporal resolution of our FDTD calculation are 10 nm and 0.33 fs, respectively. The size of computational domain is $9800 \times 9800 \times 1000$ nm, where the last dimension refers to the direction perpendicular to the OLED layers. As shown in Fig. 1, the power of the waveguide mode is determined by simply calculating the power that flows along the Alq_3 /PVK/ITO waveguide. The power transmission from glass to air is treated by ray optics [4], i.e., the light that propagates inside the glass substrate with an angle less than the critical angle of glass/air (41.8°) is considered as the air mode and the light that propagates inside the glass substrate with an angle larger than 41.8° is considered as the glass mode. A dipole is placed at the Alq_3 /PVK interface and excited by a continuous wave with the wavelength $\lambda = 524$ nm. The emitted powers are obtained after the FDTD simulations have reached steady states. In our calculations, 7000 time steps were iterated. Since the direction of dipole can be arbitrary, the results must be averaged over all dipole directions. This can be expressed by the following equation:

$$\bar{p} = \frac{\int_0^{\pi/2} \int_0^{2\pi} p(\theta_{\text{di}}, \phi_{\text{di}}) \sin(\theta_{\text{di}}) d\theta_{\text{di}} d\phi_{\text{di}}}{\int_0^{\pi/2} \int_0^{2\pi} \sin(\theta_{\text{di}}) d\theta_{\text{di}} d\phi_{\text{di}}}, \quad (1)$$

where $p(\theta_{\text{di}}, \phi_{\text{di}})$ is the power of the waveguide mode, the glass mode, or the air mode as a function of the dipole direction θ_{di} and ϕ_{di} .

Since the OLED structure is uniform in the in-plane direction, $p(\theta_{\text{di}}, \phi_{\text{di}})$ is uniform along the angle ϕ_{di} or $p(\theta_{\text{di}}, \phi_{\text{di}}) = p(\theta_{\text{di}})$. Thus, the averaging becomes only for the θ_{di} direction. We calculate by 3D FDTD the dipole power for each mode for various θ_{di} and find that the power $p(\theta_{\text{di}})$ can be perfectly described by the equation

$$p(\theta_{\text{di}}) = p(0^\circ)\cos^2(\theta_{\text{di}}) + p(90^\circ)\sin^2(\theta_{\text{di}}). \quad (2)$$

This agrees well with the theoretical prediction by the mode-expansion method. By substituting Eq. (2) into Eq. (1), we finally obtain

$$\bar{p} = \frac{1}{3}p(0^\circ) + \frac{2}{3}p(90^\circ). \quad (3)$$

Eq. (3) implies that we only need to calculate for two different cases, $\theta_{\text{di}} = 0^\circ$ and $\theta_{\text{di}} = 90^\circ$, to obtain the average powers. We calculate the power of the waveguide mode, glass mode and air mode by FDTD for the following cases: the thickness of Alq₃ and PVK layers is 80, 40 nm, respectively, and the thickness of the ITO layer is varied from 10 to 300 nm. The results are shown by circles in Fig. 2. Fig. 2 shows the ratio of the emission rate of each mode to the total emission rate. Note that the absolute values of the total emission rates vary among the different structural parameters. We also calculate the emission rate for the case that the thickness of PVK layer is 40 nm, the thickness of

the ITO layer is 150 nm, and the thickness of Alq₃ layer is varied from 10 to 300 nm. The results are shown in Fig. 3.

We note here that in the FDTD calculation, it was difficult to separate the radiation modes with radiation angle θ_{rad} near 90° from the waveguide modes since both propagate along the same direction. We have used a large computational domain to separate the radiation modes with $\theta_{\text{rad}} < \sim 80^\circ$ from the waveguide modes. This is adequate for most of the cases where the peaks in radiation patterns fall at the angle smaller than 80° . However, at some structural parameters where the radiation mode is emitted at the angle near 90° , non-negligible errors can occur. To illustrate this point, we show in Fig. 4(a) and (b) the electric field patterns emitted from the dipole for the different cases, $\theta_{\text{di}} = 0^\circ$ and $\theta_{\text{di}} = 90^\circ$, respectively. The thickness of Alq₃ layer, PVK layer and ITO layer are 80, 40 and 150, respectively. In both Fig. 4(a) and (b), only the components parallel to the dipole are shown. That is, in Fig. 4(a), only the components of electric field that are perpendicular to the OLED layer are shown. In Fig. 4(b) only the parallel components are shown. This is justified since those components shown are the strongest components in each case. As clearly visible, for $\theta_{\text{di}} = 0^\circ$, the emitted power mostly couples to the

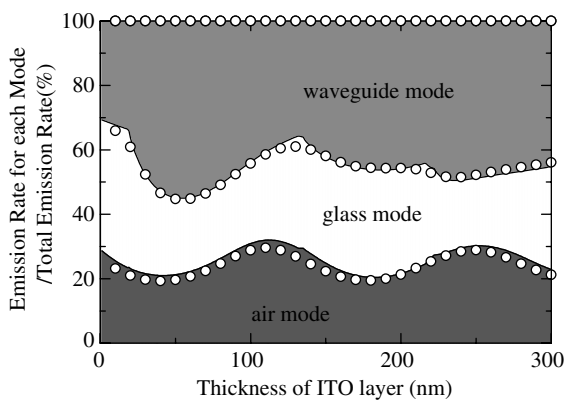


Fig. 2. Ratio of the emission rate of air modes, glass modes, and waveguide modes to the total emission rate as a function of the thickness of ITO layer. The thickness of the Alq₃ and PVK layer is 80 and 40 nm, respectively. The solid lines and circles are calculated by the mode-expansion method and the FDTD, respectively.

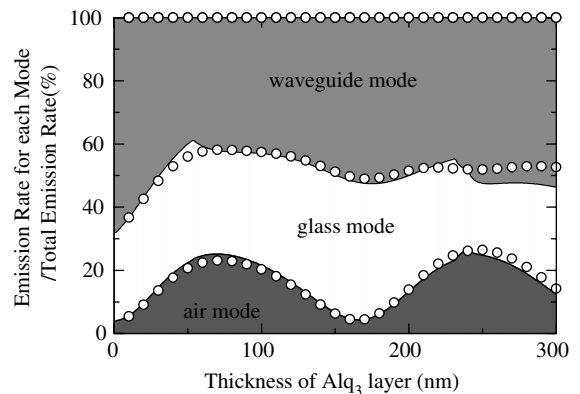


Fig. 3. Ratio of the emission rate of air modes, glass modes, and waveguide modes to the total emission rate as a function of the thickness of Alq₃ layer. The thickness of the PVK and ITO layer is 40 and 150 nm, respectively. The solid lines and circles are calculated by the mode-expansion method and the FDTD, respectively.

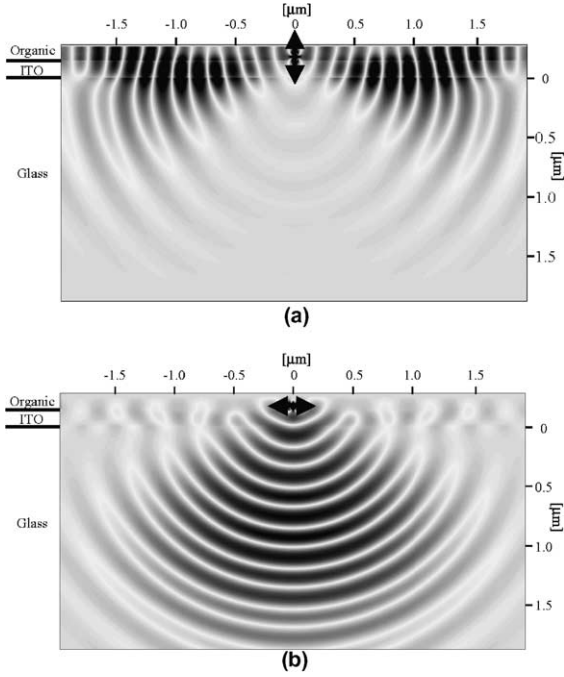


Fig. 4. Electric field patterns emitted from dipoles with different orientations. (a) $\theta_{\text{di}} = 0^\circ$, only the components of electric field that are perpendicular to the OLED layer are shown. (b) $\theta_{\text{di}} = 90^\circ$, only the parallel components are shown. The thickness of Alq₃ layer, PVK layer and ITO layer are 80, 40 and 150, respectively. The arrows show the direction of dipole.

waveguide mode and partially couples to the radiation modes with large radiation angles. It is especially difficult in these cases to accurately separate the waveguide modes from the radiation modes. In contrast, for $\theta_{\text{di}} = 90^\circ$, the coupling of the emitted power to the waveguide modes and the radiation modes with large radiation angles is insignificant. Thus, the power emitted in the radiation can be determined more accurately. This will be discussed again in the next section from the mode-expansion method point of view. It is expected that separation of the radiation modes and waveguide modes by spatial filtering would improve the accuracy for FDTD.

3. Mode-expansion method

We describe the mode-expansion method for our OLED structure. The power emitted into each

mode or the spontaneous emission rate for each mode γ is given by

$$\gamma = \gamma_0 \cdot \frac{3\pi^2 \omega_0}{k^3} \cdot \sum_{\mu} |\hat{\mathbf{d}} \cdot \vec{\mathbf{E}}_{\mu}(\vec{\mathbf{x}}')|^2 \delta(\omega_{\mu} - \omega_0), \quad (4)$$

where γ_0 is the spontaneous emission rate in free space, $\hat{\mathbf{d}}$ is the dipole moment, $\vec{\mathbf{E}}_{\mu}(\vec{\mathbf{x}}')$ is the normalized electric field at the position of dipole, ω_0 is the angular frequency of dipole, k is the wave vector and \sum_{μ} is the summation over all wave vectors for each mode [9].

The normalization equation for electric field is given as

$$\int \varepsilon(\vec{\mathbf{x}}) \vec{\mathbf{E}}_{\nu}^*(\vec{\mathbf{x}}) \cdot \vec{\mathbf{E}}_{\mu}(\vec{\mathbf{x}}) d\mathbf{r} = \delta_{\mu\nu}. \quad (5)$$

The summation over all wave vectors leads to the term of density of state $\rho(\omega)$. Therefore, Eq. (4) can be rewritten as

$$\gamma = \gamma_0 \cdot \frac{3\pi^2 \omega_0}{k^3} \cdot \int |\hat{\mathbf{d}} \cdot \vec{\mathbf{E}}_{\mu}(\vec{\mathbf{x}}')|^2 \delta(\omega_{\mu} - \omega_0) \rho(\omega) d\omega. \quad (6)$$

First, we consider the radiation modes. The radiation eigenmodes can be described as a function of an incident angle θ for a layered structure. The density of state is also a function of θ and can be written as $\rho = \sin(\theta)$. Here, as the same as FDTD, we also consider that the glass substrate is infinitely thick. Thus, the radiation mode here refers to the mode that propagates inside the glass substrate. This is equivalent to the sum of glass modes and air modes. We use the transfer matrix formalism to solve for the eigenmodes. For S-polarized plane waves incident on an m -layers structure with an incident angle θ_m , the electric field inside each layer can be described as follows:

$$\mathbf{E}_i = (0, 0, E_{zi}), \quad i = 1 \dots m, \quad (7)$$

where the subscript i describe the i th layer (see Fig. 1).

$$E_{zi}(y) = A_i \exp\{-j\kappa_i(y - y_i)\} + B_i \exp\{j\kappa_i(y - y_i)\}, \quad (8)$$

$$\kappa_i = k_0 n_i \cos(\theta_i), \quad n_i \sin(\theta_i) = n_m \sin(\theta_m). \quad (9)$$

Assuming $A_1 = 1$, the perfect electric conductor condition at the cathode surface gives $B_1 = -A_1 = -1$. By using Eqs. (7)–(9) and considering the continuity of the field at each interface, the coefficient for the glass layer (A_4) can be easily found. We let $U_S = |A_4|$.

Next, we consider coupling between the S-polarized waves and a dipole. It is found that the S-polarized waves couple to the 90° dipole but not the 0° dipole. Following Eq. (6) in [10] and using Eq. (6) in this paper, the emission rate of the 90° dipole to the S-polarized radiation mode can be written as

$$\begin{aligned} \gamma_{90S} &= \frac{3\pi^2}{4\pi^3} \gamma_0 \cdot \int_0^{2\pi} \sin(\phi)^2 d\phi \\ &\quad \times \int_{-\pi/2}^{\pi/2} \sin^2(k_0 \cdot n_1 \cdot \cos(\theta_1) \cdot dp) \\ &\quad \left/ \left(n_4^2 \cdot U_S^2(\theta_4) \right) \cdot n_4^3 \cdot \sin(\theta_4) d\theta_4 \right. \\ &= \frac{3}{2} \gamma_0 \int_0^{\pi/2} \sin^2(k_0 \cdot n_1 \cdot \cos(\theta_1) \cdot dp) \\ &\quad \left/ \left(n_4^2 \cdot U_S^2(\theta_4) \right) \cdot n_4^3 \cdot \sin(\theta_4) d\theta_4, \right. \quad (10) \end{aligned}$$

where dp is the dipole position (within the Alq_3 layer) and the term $n_4^3 \cdot \sin(\theta_4)$ corresponds to the density of state for bulk glass. The emission rate into the air mode and the glass mode can be calculated by simply changing the range of integration to (0–41.8°) and (41.8–90°), respectively.

For P-polarized waves, it is found that they couple to both 0° dipole and 90° dipole. Again, following Eq. (7) in [10], the emission rate into P-polarized modes for the 90° dipole is

$$\begin{aligned} \gamma_{90P} &= \frac{3\pi^2}{4\pi^3} \gamma_0 \cdot \int_0^{2\pi} \cos(\phi)^2 d\phi \\ &\quad \times \int_{-\pi/2}^{\pi/2} \sin^2(k_0 \cdot n_1 \cdot \cos(\theta_1) \cdot dp) \\ &\quad \left/ \left(n_1^2 \cdot U_P(\theta_4)^2 \right) \cdot \cos^2(\theta_1) \cdot n_4^3 \cdot \sin(\theta_4) d\theta_4 \right. \\ &= \frac{3}{2} \gamma_0 \int_0^{\pi/2} \sin^2(k_0 \cdot n_1 \cdot \cos(\theta_1) \cdot dp) \\ &\quad \left/ \left(n_1^2 \cdot U_P(\theta_4)^2 \right) \cdot \cos^2(\theta_1) \cdot n_4^3 \cdot \sin(\theta_4) d\theta_4, \right. \quad (11) \end{aligned}$$

where U_P is $|A_4|$ for the case of P-polarized waves. Similarly, following Eq. (11) in [10], the emission rate into P-polarized modes for the 0° dipole is

$$\begin{aligned} \gamma_{0P} &= \frac{3\pi^2}{4\pi^3} \gamma_0 \cdot \int_0^{2\pi} d\phi \\ &\quad \times \int_{-\pi/2}^{\pi/2} \cos^2(k_0 \cdot n_1 \cdot \cos(\theta_1) \cdot dp) \\ &\quad \left/ \left(n_1^2 \cdot U_P(\theta_4)^2 \right) \cdot \sin^2(\theta_1) \cdot n_4^3 \cdot \sin(\theta_4) d\theta_4 \right. \\ &= 3\gamma_0 \int_0^{\pi/2} \cos^2(k_0 \cdot n_1 \cdot \cos(\theta_1) \cdot dp) \\ &\quad \left/ \left(n_1^2 \cdot U_P(\theta_4)^2 \right) \cdot \sin^2(\theta_1) \cdot n_4^3 \cdot \sin(\theta_4) d\theta_4. \right. \quad (12) \end{aligned}$$

The average emission rate for the radiation mode can be found using Eq. (3) as

$$\bar{\gamma}_{\text{rad}} = \frac{1}{3} \gamma_{0P} + \frac{2}{3} (\gamma_{90P} + \gamma_{90S}). \quad (13)$$

Second, we consider the waveguide mode. The waveguide eigenmodes are also calculated by the transfer matrix formalism. For the case of the waveguide mode, the density of state becomes a function of the phase index and group index of the waveguide mode. Using Eq. (6), we obtain the emission rate for the 0° dipole, which couples only to the TM waveguide modes.

$$\begin{aligned} \gamma_{\text{WG0}} &= \gamma_0 \cdot \frac{3}{4} \cdot \lambda \\ &\quad \times \left\{ \sum_m n_{\text{phase}}^{\text{TM}}(m) \cdot n_{\text{group}}^{\text{TM}}(m) \cdot \left| \vec{\mathbf{E}}_{ym}(\vec{\mathbf{x}}') \right|^2 \right\}, \quad (14) \end{aligned}$$

where m describes the m th order TM mode, $n_{\text{phase}}^{\text{TM}}$ and $n_{\text{group}}^{\text{TM}}$ are the phase index and the group index of the TM waveguide mode, respectively. Similarly, for the 90° dipole, which couples to both the TM and TE modes, the emission rate can be found as follows:

$$\begin{aligned} \gamma_{\text{WG90}} &= \gamma_0 \cdot \frac{3}{8} \cdot \lambda \\ &\quad \times \left\{ \sum_m n_{\text{phase}}^{\text{TM}}(m) \cdot n_{\text{group}}^{\text{TM}}(m) \cdot \left| \vec{\mathbf{E}}_{xm}(\vec{\mathbf{x}}') \right|^2 \right. \\ &\quad \left. + \sum_l n_{\text{phase}}^{\text{TE}}(l) \cdot n_{\text{group}}^{\text{TE}}(l) \cdot \left| \vec{\mathbf{E}}_{zl}(\vec{\mathbf{x}}') \right|^2 \right\}, \quad (15) \end{aligned}$$

where l describe the l th order TE mode, $n_{\text{phase}}^{\text{TE}}$ and $n_{\text{group}}^{\text{TE}}$ are the phase index and the group index of the TE waveguide mode, respectively.

The results for the mode-expansion mode are shown by the solid line in Fig. 2 and 3. An excellent agreement between FDTD and the mode-expansion method can be seen in both figures. Thus, the accuracy of our calculation is confirmed.

We can see in both Figs. 2 and 3 that the emission rate into the waveguide modes change abruptly at some positions as we increase the thickness of the ITO layer or the Alq₃ layer. These correspond to the change in the number of waveguide modes as the thickness of the ITO or Alq₃ layers increases. For example, in Fig. 2, the 1st order TE mode starts to appear at ITO thickness = 20 nm and the 2nd order TM mode appears at ITO thickness = 136 nm. Similarly, in Fig. 3, the 2nd order TE mode starts to appear at Alq₃ thickness = 56 nm and the 2nd order TM mode appears at Alq₃ thickness = 241 nm. In total, we may conclude that ~25% of light emitted can escape to air, ~32% is trapped in the glass substrate, and ~43% is trapped in the Alq₃/PVK/ITO layer.

The mode-expansion method provides detailed descriptions of light emission from the OLED, for example, the radiation pattern. We show in Fig. 5 the modal strength (intensity) as a function of propagation angle in the glass substrate for two cases with different thickness of the ITO layer. The thickness of the Alq₃ and PVK is 80 and 40 nm, respectively. The solid and dashed lines show the modal strength of the S-polarized and the P-polarized mode, respectively. First, Fig. 5(a) shows the modal strength for the case that the ITO layer is 50 nm. Fig. 5(b) show the same plot for ITO layer = 130 nm. It is seen that while the modal strength in Fig. 5(a) shows only small values for the large angle (>80°), the modal strength for the P-pol with a large angle in Fig. 5(b) is non-negligible. These values become even more significant when we calculate the emission rate, which is the integral of the modal strength multiplied by the density of state $\sin(\theta)$ over the angle θ . These emitted powers at the large angle must be measured correctly. However, as discussed in the previous section, there is difficulty in distinguishing the radiation mode with a large angle from the waveguide

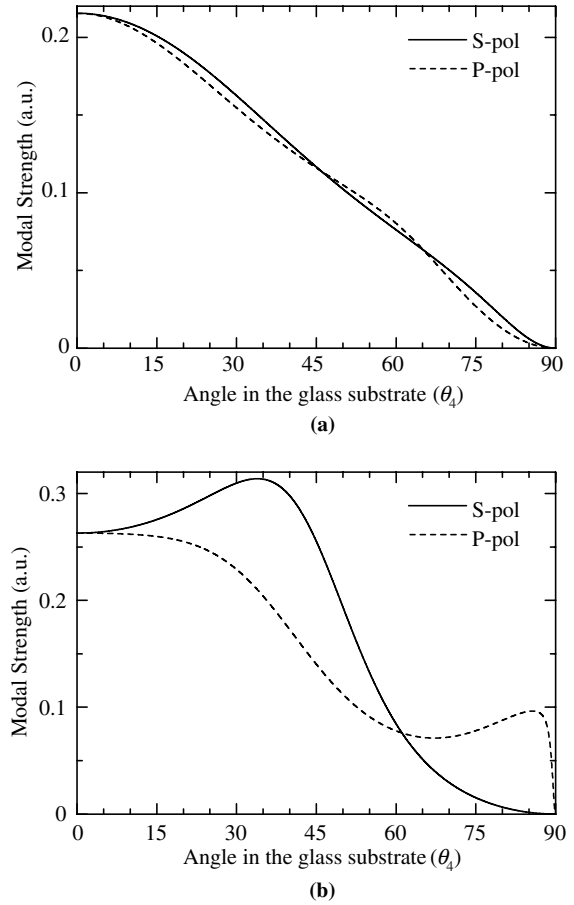


Fig. 5. Modal strength (intensity) of the radiation mode as a function of angle. The solid and dashed lines show modal strength of the S-polarized and P-polarized mode, respectively. The thickness of the Alq₃ and PVK layers is 80 and 40 nm, respectively. The thickness of the ITO layer is (a) 50 nm, (b) 130 nm.

mode in the calculation by FDTD and this leads to non-negligible errors in the FDTD results. In contrast, for the case in Fig. 5(a), the above-described problem in FDTD results in only negligible errors. This explains why the FDTD results are slightly different from those of the mode-expansion method at some particular structural parameters. Note that the emission rate for the air mode is not affected by the above argument since the air mode contains only the mode with angle <41.8°. The small discrepancy between the FDTD and the mode-expansion method for the air mode may

mainly come from the insufficient resolution of the FDTD grid in defining the light cone with angle = 41.8° .

4. Conclusion

In summary, we have presented a theoretical analysis on light-extraction efficiency of the OLED using the FDTD and the mode-expansion method. An excellent agreement between the results of both methods was found, and thus confirmed the accuracy of our calculation. It has been found that even though the index contrast between the ITO layer and the glass substrate was as small as 0.5, more than 40% of emitted light power was trapped in the ITO layer.

In light of this analysis, we believe the FDTD method can be used as a powerful analytical tool for complex OLED designs since the method is applicable to virtually any type of structures, including one that is too complex to study by analytical methods. This makes the FDTD method very advantageous over analytic approaches. Furthermore, the FDTD method may be combined with the mode-expansion method to provide a novel and even more powerful analytical tool (that takes advantages of both methods) for the recently proposed microstructured OLED, for example, the OLED with photonic crystals [11,12].

Acknowledgements

This work is partly supported by a grant-in-aid for creative scientific research from the Ministry of Education, Culture, Sports, Science and Technology of Japan and the Kyoto University comprehensive innovation alliance.

References

- [1] S.R. Forrest, *Org. Electron.* 4 (2003) 45.
- [2] G. Gu, D.Z. Garbuzov, P.E. Burrows, S. Venkatesh, S.R. Forrest, *Opt. Lett.* 22 (1997) 396.
- [3] M.-H. Lu, J.C. Sturm, *J. Appl. Phys.* 91 (2002) 595.
- [4] J.S. Kim, P.K.H. Ho, N.C. Greenham, R.H. Friend, *J. Appl. Phys.* 88 (2000) 1073.
- [5] M. Ikai, S. Tokito, Y. Sakamoto, T. Suzuki, Y. Taga, *Appl. Phys. Lett.* 79 (2001) 156.
- [6] C. Adachi, M.A. Baldo, M.E. Thompson, S.R. Forrest, *J. Appl. Phys.* 90 (2001) 5048.
- [7] K.S. Yee, *IEEE Trans. Antennas Propagat.* AP-14 (1966) 302.
- [8] G. Mur, *IEEE Trans. Electromagn. Compat.* EMC-23 (1981) 377.
- [9] E.A. Hinds, in: P.R. Berman (Ed.), *Cavity Quantum Electrodynamics*, Academic, New York, 1994.
- [10] D. Meschede, W. Jhe, E.A. Hinds, *Phys. Rev. A* 41 (1990) 1587.
- [11] M. Fujita, T. Ueno, T. Asano, S. Noda, H. Ohhata, T. Tsuji, H. Nakada, N. Shimoji, *Electron. Lett.* 39 (2003).
- [12] Y.J. Lee, S.H. Kim, J. Huh, G.H. Kim, Y.H. Lee, S.H. Cho, Y.C. Kim, Y.R. Do, *Appl. Phys. Lett.* 82 (2003) 3779.



Relationship between the ionization and oxidation potentials of molecular organic semiconductors

Brian W. D'Andrade^a, Shubhashish Datta^a, Stephen R. Forrest^{a,*},
Peter Djurovich^b, Eugene Polikarpov^b, Mark E. Thompson^b

^a Department of Electrical Engineering, EQUAD B301, Princeton University, Princeton, NJ 08544, United States

^b Department of Chemistry, University of Southern California, Los Angeles, CA 90089, United States

Received 28 July 2004; received in revised form 11 January 2005; accepted 22 January 2005

Available online 17 March 2005

Abstract

A relationship between the energy of the highest occupied molecular orbital (HOMO) and the oxidation potential of molecular organic semiconductors is presented. Approximating molecules as dipoles consisting of a positively charged ion core surrounded by an electron cloud, the HOMO energy (E_{HOMO}) is calculated as that required to separate these opposite charges in a neutral organic thin film. Furthermore, an analysis of image charge forces on spherical molecules positioned near a conductive plane formed by the electrode in an electrochemical cell is shown to explain the observed linear relationship between E_{HOMO} and the oxidation potential. The E_{HOMO} 's of a number of organic semiconductors commonly employed in thin film electronic devices were determined by ultraviolet photoemission spectroscopy, and compared to the relative oxidation potential (V_{CV}) measured using pulsed cyclic voltammetry, leading to the relationship $E_{\text{HOMO}} = -(1.4 \pm 0.1) \times (qV_{\text{CV}}) - (4.6 \pm 0.08) \text{ eV}$, consistent with theoretical predictions.

© 2005 Elsevier B.V. All rights reserved.

PACS: 73.20.-r; 82.45.Wx; 71.20.Rv; 78.40.Me

Keywords: Electrochemistry; Photoelectron spectroscopy; Organic thin film; Dipole

1. Introduction

Knowledge of charge carrier energy levels in organic thin films is essential for the understanding

and design of organic devices [1]. For example, an organic light emitting device (OLED) usually consists of several layers of various stacked organic thin films [2], and offsets in the energies between layers act as potential energy barriers to the flow of charge and molecular excited states (or excitons). The highest occupied molecular orbital (HOMO) and lowest unoccupied molecular orbital

* Corresponding author. Tel.: +1 609 258 4532; fax: +1 609 258 7272.

E-mail address: forrest@princeton.edu (S.R. Forrest).

(LUMO) energy are used to describe isolated molecules. Energy levels in solid-state organic films, bonded by weak intermolecular interactions, can be derived from these orbital energies. For convenience, we will refer to the derived energy levels in the solid-state as the HOMO and LUMO.

Two conventional methods to ascertain HOMO energies (E_{HOMO}) are ultraviolet photoemission spectroscopy (UPS) [3] and cyclic voltammetry (CV) [4,5]. UPS experiments determine the ionization energy (E_i) of a molecule on the surface of a thin film, where $E_i = -E_{\text{HOMO}}$ [6]. Solution-based CV experiments determine the relative molecular oxidation potentials (V_{CV}), which are indirectly related to E_i . It is therefore desirable to determine E_{HOMO} from UPS data; however, the high cost and complexity of UPS systems tends to favor the use of CV in many laboratories.

In this paper, we explore the relationship between E_{HOMO} determined from UPS of organic thin films, and V_{CV} as determined from cyclic voltammetry. Previous studies [7–9] consider solid and solution state solvation effects to approximately describe this relationship. In this work, the relationship is explained using a simple electrostatic model that takes into account the additional effect of image charges, thereby allowing for an accurate and *quantitative* comparison between these independently measured quantities for a broad range of molecules of interest in organic electronics.

A description of the individual techniques along with their relative strengths and weaknesses is given in Section 2. A quantitative theory of the relationship between E_{HOMO} and V_{CV} as measured by UPS and CV, respectively, is developed in Section 3, and experimental procedures are given in Section 4. Results and discussion of the analysis are in Section 5, and conclusions are provided in Section 6.

2. Ultraviolet photoemission spectroscopy and cyclic voltammetry

In UPS, ultraviolet light is incident on a thin film sample, ejecting electrons from its surface. The kinetic energy of the electron varies according

to its molecular orbital, and the sum of the absolute value of the electron kinetic energy and its orbital potential energy is equal to the photon energy. An electron from the HOMO has the highest kinetic energy [10,11].

A typical organic thin film UPS spectrum of the metallic–organic phosphor *fac*-tris(2-phenylpyridine)iridium [Ir(ppy)₃] due to illumination from the 21.22 eV He I α line is shown in Fig. 1. The HOMO position relative to the vacuum level is estimated by linearly extrapolating the low binding energy side of the spectrum to the zero intensity baseline, corresponding to the intersection of the pair of lines shown. Similarly, the intersection of the lines at high binding energy provides an estimate of the lowest energy electrons. The difference between the two energies is the maximum of the kinetic energy, E_{kin} , of the emitted HOMO electrons at the sample surface, whereby E_{HOMO} is calculated from $E_{\text{kin}} - 21.22$ eV.

In CV, the organic material is dissolved in a solvent containing an electrolyte, a reference solute, and the working, counter and reference electrodes. Voltage is swept across the electrodes, inducing a current. To avoid resistive drops and internal polarization, the voltage measured is that of the

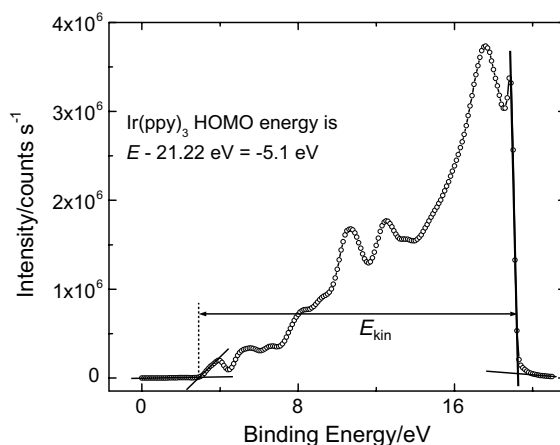


Fig. 1. UPS spectrum of an Ir(ppy)₃ thin film grown on Ag and biased at -3 V. The ionization energy is determined by linearly extrapolating the high and low energy slopes of the spectrum to the spectral baseline, using the four lines shown. The energy separation, E_{kin} , between these two points is subtracted from the photon energy of 21.22 eV to determine the HOMO energy.

working electrode relative to the reference electrode. The sample is oxidized to the +1 state (corresponding to a singly ionized molecule) upon contact with the working electrode, at the voltage corresponding to the average of the anodic and cathodic peak currents. This voltage is related to the energy of the HOMO [5], since only the electron from this orbital is involved in the oxidation process.

An example of a cyclic voltammogram of $\text{Ir}(\text{ppy})_3$ is given in Fig. 2. The reversible oxidation peaks of the reference and sample have positive potential values, and V_{CV} is the difference between the potentials at which the reference solute and samples are oxidized. Also shown are the negative potentials at which the sample is reversibly reduced to its -1 and -2 states.

In cyclic voltammetry, consideration must be given to the effects of the solvent, the electrolyte, the electrodes, and the reversibility of the redox reaction of the sample. The acquisition of an accurate value of V_{CV} requires that the solvent resist oxidation. Furthermore, the electrolyte and electrodes also must not react with the sample, and oxidation of the samples must be reversible, result-

ing in closed current–voltage loops. The potential measured for a reversible redox reaction in a cyclic voltammetry experiment is however a good estimate for the thermodynamic standard oxidation potential with an error on the order of millivolts [12]. In UPS measurements, materials must have a low room temperature vapor pressure to be compatible with the ultrahigh vacuum (UHV) ($\sim 10^{-9}$ Torr) environment, and the films must be chemically and morphologically stable under ultraviolet radiation. Also, inaccuracies in measuring E_{HOMO} can occur from charging of the film and the surrounding UHV apparatus.

The UPS system used in our experiments has a resolution of 150 meV, whereas redox potentials in CV are determined to within 50 meV. UPS measurements made using synchrotron radiation sources can have higher resolutions (~ 20 meV), but their cost is often prohibitive for routine measurements. For CV, the resolution is determined by the error in the voltmeter, the stability of the power source, and the sweep rate; the oxidation reaction must occur on a time scale that is short compared to the voltage cycle time. Neither method probes the bulk ionization energy introducing additional potential measurement uncertainties. As noted previously, UPS only explores the energetics of surface and near-surface electronic states, and CV measures the potential energy of electron orbitals of molecules suspended in an electrolytic environment.

3. Analytical comparison between UPS and CV measurements

We now consider image charge effects between a dipolar molecule suspended in an electrolyte near a conducting, metallic electrode that results in a simple, quantitative relationship between UPS and CV measurements. This effect ignores the details of other solvation effects, the metal workfunction [13,14], details of the molecular frontier orbitals, and the explicit role of the electrolyte [15,16], that have been previously identified as playing a role in the energies from these two techniques. These other factors that contribute to the relationship between the two measurements are simply grouped

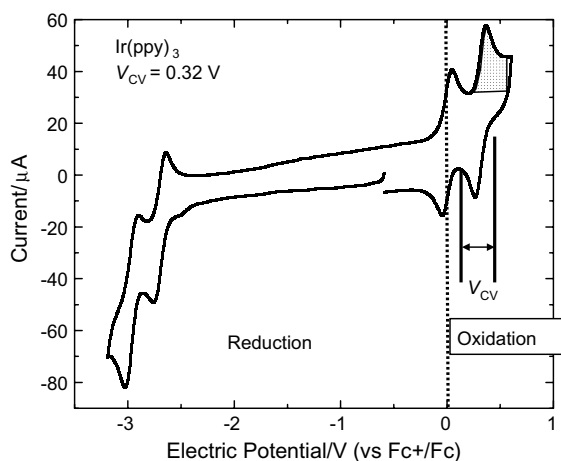


Fig. 2. Example of a pulsed cyclic voltammogram for $\text{Ir}(\text{ppy})_3$. Voltages for the sample and reference solute are recorded as the center voltage between the peak for the oxidation of the sample and the peak for the reduction of the oxidized sample, as shown. V_{CV} is determined from the difference between the oxidation potentials shown.

together and expressed in the form of a ratio of effective dielectric constants. Hence, while the electrostatic model provides an excellent fit to the observed trends, it does not strive to explain the detailed effects nor the physical origins of these other contributions, but rather assumes that their contribution is accounted for in the details of the macroscopic dielectric constant of the electrolytic solution.

Molecular oxidation is studied in UPS by considering the energy required to singly ionize a molecule on the surface of a film of relative dielectric constant, ϵ_{film} . We approximate a molecule as a positive ion core surrounded by an electron cloud with an effective radius, r . The oxidative potential measured by UPS is therefore given by the Coulomb energy:

$$U_{\text{UPS}} = E_{\text{HOMO}} = -\frac{1}{4\pi\epsilon_0\epsilon_{\text{film}}} \cdot \frac{q^2}{r}. \quad (1)$$

Here, q is the electron charge, and ϵ_0 is the permittivity of vacuum.

Image charge effects have been shown to reduce the HOMO energy levels relative to the vacuum level for thin monolayers in UPS experiments [6], and they can be used to explain the relationship between the work function and ionization energy of metals [17]. In CV measurements, molecules are in contact with a conductive electrode, so the dipole arising from image charges of the molecular ion core and the electrons should also play a significant role. Additionally, the molecules are dissolved in a dielectric solution; hence, the solvation effect is also an important consideration [18,19]. With the inclusion of the conducting, planar electrode, the equipotential surface around the positive molecular core can be approximated as a sphere whose center is displaced from the electrode due to the image, thereby reducing the total potential energy. To estimate E_i as measured by CV, we approximate the molecule as having an electron occupying an equipotential sphere of effective radius, r , with a positive core at a distance, d , from the conducting electrode, as shown in the inset, Fig. 3. The molecular dipole induces its image in the electrode. This results in an apparent offset of the core charge ($+q$) by a distance, Δ , as shown. Equating the potential of a conducting surface at

the points nearest and farthest from the electrode, the molecular potential as measured by its oxidative voltage is

$$\begin{aligned} V_{\text{OX}} &= V_{\text{CV}} + V_{\text{REF}} \\ &= \frac{q}{4\pi\epsilon_0\epsilon_{\text{CV}}} \left[\frac{1}{r - \Delta} - \frac{1}{2d - r + \Delta} \right] \\ &= \frac{q}{4\pi\epsilon_0\epsilon_{\text{CV}}} \left[\frac{1}{r + \Delta} - \frac{1}{2d + r + \Delta} \right], \end{aligned} \quad (2)$$

where V_{REF} is the oxidation potential of the reference solute used in cyclic voltammetry, and ϵ_{CV} is the effective dielectric constant near the electrode, which is a function of both the dielectric constant of the solvent, ϵ_{Sol} , and the screening from the electrolyte. The shift between the core and the center of the electron cloud is then given by the positive real root of the following cubic equation:

$$\Delta^3 + (4d + r)\Delta^2 + (4d^2 - r^2)\Delta - r^3 = 0. \quad (3)$$

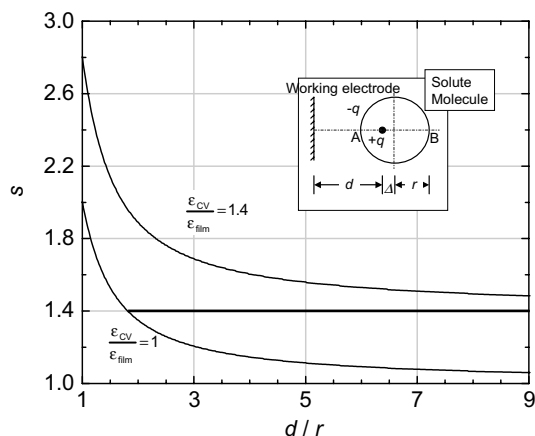


Fig. 3. The rate of change in the HOMO energy of a molecule relative to its oxidation energy ($s = (1/q)|dE_{\text{UPS}}/dV_{\text{CV}}|$), versus the distance from the conductor normalized to the radius of the molecule, d/r , for two extreme cases where either the image charge effect or the solvation effect is solely responsible for the difference in energy levels measured using UPS and CV. The bold line corresponds to possible situations involving both the effects that are consistent with the experimental fit in Fig. 4. *Inset*: Schematic diagram showing an equipotential “molecular sphere” of radius, r , having a charge $-q$, and a $+q$ point charge inside it. Here, Δ is the distance between the center of the sphere and the positive charge which is offset due to induced image charges in the metal electrode.

Comparing Eqs. (1) and (2),

$$V_{CV} = -\frac{E_{HOMO}}{qs} - V_{REF},$$

where

$$s = \frac{\epsilon_{CV}}{\epsilon_{film}} f(r, d)$$

and

$$f(r, d) = \frac{1}{r} \left[\frac{1}{r + \Delta} - \frac{1}{2d + r + \Delta} \right]^{-1}.$$

Generally, ϵ_{CV} is greater than ϵ_{film} due to solvation effects. The slope, s , of a plot of E_{HOMO} versus V_{CV} is then the product of the ratio of permittivities and the image charge factor, $f(r, d)$. The y -intercept of the plot is determined by the reference solute used in the CV measurement. A plot of s as a function of d/r is given in Fig. 3 for two values of the ratio of permittivities. Hence, Eq. (4) provides a quantitative relationship between V_{CV} measured by cyclic voltammetry, and the ionization energy of the molecules under study.

4. Experimental

Silicon substrates used for UPS measurements were oxidized for 5 min in 4:1 $H_2SO_4:H_2O_2$, etched for 2 min in dilute HF, and blown dry with pure nitrogen. The substrates were fastened to copper substrate holders with copper clips, then loaded into the ultrahigh vacuum system.

A 50 nm thick Ag film was deposited onto the substrate and substrate holder, with electrical connection between these surfaces made via the copper clips. Furthermore, the Ag film was used to establish the Fermi energy in the organic film, assuming they are aligned in equilibrium. After Ag deposition, the substrate is transferred under UHV to the organic deposition system [20].

Prior to film growth, organic materials, purified by train sublimation [21], were outgassed and loaded into the growth chamber with a base pressure of 5×10^{-9} Torr. The deposited films were 10 nm thick, and were transferred from the growth chamber into the UPS analysis chamber under UHV. The contact potential between the sample

and the detector limits the collection of low kinetic energy electrons. Hence, the thin film substrates were biased at either -3 V or -4 V to overcome this potential barrier.

The oxidation potentials of the sample molecules listed in Table 1, dissolved in dimethylformamide, acetonitrile, and dichloromethane (see Table 2 for their relative dielectric constants at room temperature [22]), were obtained versus a ferrocene/ferrocenium reference solute using differential pulse voltammetry, and using tetrabutylammonium hexafluorophosphate as the electrolyte. The solutions contained only micro-molar concentrations of the sample solutes to prevent shifts in oxidation potential due to concentration effects [5], and the voltage between the working and counter electrodes was swept at a scan rate of 100 mV/s. The working electrode was 0.2 cm in diameter by 1.5 cm long.

Only materials that could be reversibly oxidized (i.e. resulting in closed CV loops) were considered. In the context of electrochemistry, a reversible redox reaction is one where an electrogenerated intermediate is stable in the timeframe of the experiment. The reversible intermediate should have a half-life $> 10^{-2} \times (\text{scan rate})^{-1}$, where the scan rate is measured in V/s [23]. Neither aluminum tris(quinoline-8-olate) (Alq_3) nor aluminum(III) bis(2-methyl-8-quinolinato)4-phenylphenolate (BALq) undergo reversible oxidation. The potential given for these molecules is the irreversible anodic peak potential, the first peak of the CV trace. However, an irreversible peak potential may correspond to within 100 mV of the reversible oxidation potential if the species generated by a reversible electron-transfer process is consumed by a rapid, chemical follow-up reaction [24]. This may occur for both Alq_3 and BALq in the CV measurements.

5. Results and discussion

Both UPS and electrochemical methods have been used to determine the HOMO energies of materials incorporated into organic electronic devices. Only the UPS measurement provides a direct measure of the HOMO energy of a given compound in the solid-state. Electrochemical methods

Table 1
List of molecules studied and their associated oxidation and ionization energies

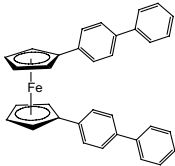
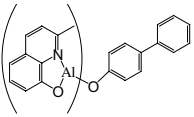
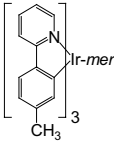
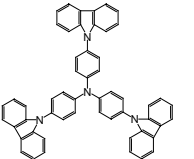
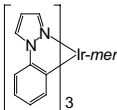
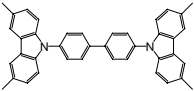
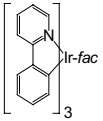
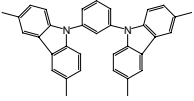
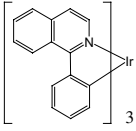
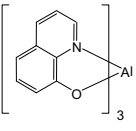
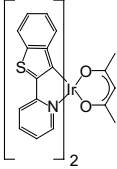
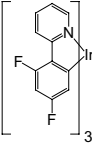
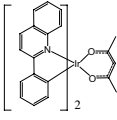
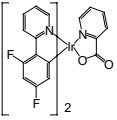
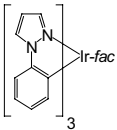
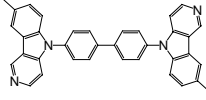
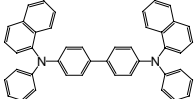
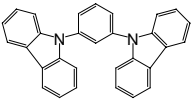
Electric potential/V (versus Fc/Fc ⁺ in DMF)	E_i /eV	Structural formula	Electric potential/V (versus Fc/Fc ⁺ in DMF)	E_i /eV	Structural formula
0.00	-4.76		0.68	-5.52	
0.18	-4.85		0.69	-5.71	
0.28	-5.11		0.72	-5.76	
0.31	-5.10		0.74	-5.61	
0.32	-5.07		0.75	-5.65	
0.36	-4.99		0.78	-5.68	
0.37	-5.07		0.89	-5.91	
0.38	-5.03		0.92	-5.99	
0.38	-5.30		1.00	-5.98	

Table 1 (continued)

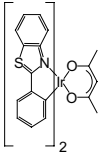
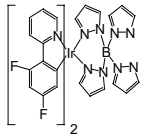
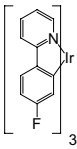
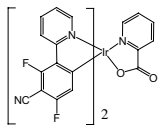
Electric potential/V (versus Fc/Fc ⁺ in DMF)	E_i /eV	Structural formula	Electric potential/V (versus Fc/Fc ⁺ in DMF)	E_i /eV	Structural formula
0.56	-5.33		1.08	-6.08	
0.56	-5.50		1.23	-6.36	

Table 2
Linear fits of E_{HOMO} versus V_{CV} for different solvents

	Dielectric constant at 300 K	s	V_{REF}
Dimethylformamide (DMF)	38.3	1.4 ± 0.2	3.2 ± 0.6
Acetonitrile (ACN)	37.5	1.4 ± 0.2	3.2 ± 0.7
Dichloromethane (CH ₂ Cl ₂)	9.1	1.2 ± 0.1	3.9 ± 0.5

require the use of a reference compound with measured oxidation potential (V_{CV}) and E_i values. Comparison of the oxidation potentials for the reference sample and unknown sample has been used to estimate the difference in E_i values for the two materials. The most common reference compound for such measurements is ferrocene, due to its highly reversible oxidation and the stability of both neutral and cationic forms in a wide range of solvents. The assumptions in this electrochemical method are that there is a one-to-one correspondence between shifts in oxidation potential and E_i and that the reference compound has well defined V_{CV} and E_i values, as shown previously for metal-free phthalocyanines [7]. We will show below that the one-to-one correspondence between shifts in V_{CV} and E_i is not valid. Additionally, the ferrocene reference solute commonly used in electrochemical studies does not have a well defined solid-state E_i value. The commonly used E_i value for ferrocene (4.8 eV) was inferred from theoretical electrochemical studies [25–27], which estimated the work function for a standard hydrogen electrode (SHE) as 4.6 V, and $V_{\text{CV}} = 0.2$ V versus SHE [28].

One reason for the difficulty in performing UPS measurements of a ferrocene thin film is the high volatility of the material, so cold substrate holders are required in a UHV environment [29]. The adiabatic ionization energy of ferrocene in the gas phase is reported to be 6.72 eV [30], and Ritsko et al. [29] have previously measured the thin film E_i of ferrocene to be 5.4 eV; however, that work provides no information on how the thin film is biased to avoid contact potential effects that occur in the experimental setup. The error caused by the contact potential is typically removed by applying a -3 V, relative to ground, bias to the sample, as is done in this study [3]. Without biasing the sample, the value of E_i is unreliable and could be larger than a value determined when the sample is biased. Thus, the experimental results obtained by Ritsko et al. on the solid-state samples of ferrocene are inconsistent with the results presented here, due to experimental considerations.

The volatility of ferrocene is substantially decreased by adding a biphenyl group to each of the cyclopentadienyl rings of the ferrocene molecule. The HOMO energy for this ferrocene derivative is 4.76 eV. The biphenyl substitution does not affect the oxidation potential of ferrocene, so the value determined here is a good estimate for the HOMO energy of ferrocene itself. Our measured E_i matches that previously estimated from electrochemical methods, supporting the use of this value for the ferrocene reference sample.

The E_{HOMO} of several representative electronic materials from families of organometallic

complexes [31–35], triarylaminines [36], and carbazoles [37] are plotted versus V_{CV} in Fig. 4. The molecular structural formulae, V_{CV} and E_{HOMO} of this family of molecules are listed in Table 1. There is a linear relationship between the two measurements, best fit by the single solid line, following

$$E_{HOMO} = -(1.4 \pm 0.1) \times (qV_{CV}) - (4.6 \pm 0.08) \text{ eV}, \quad (4)$$

with a linear regression correlation coefficient of 0.978.

In Fig. 3, s is plotted versus normalized distance of the solute molecules from the conductor, d/r , for two extreme conditions. For $\epsilon_{CV}/\epsilon_{film} = 1$, the discrepancy between the energy levels is solely due to image charge effects. In this case, it is assumed that monolayers of solute are formed on the surface of the electrode such that the immediate neighborhood of the solute molecules in CV differs from that of UPS only by the presence of the conducting electrode, thereby making the dielectric constants the same in both situations. Assuming close packing of spherical molecules next to the

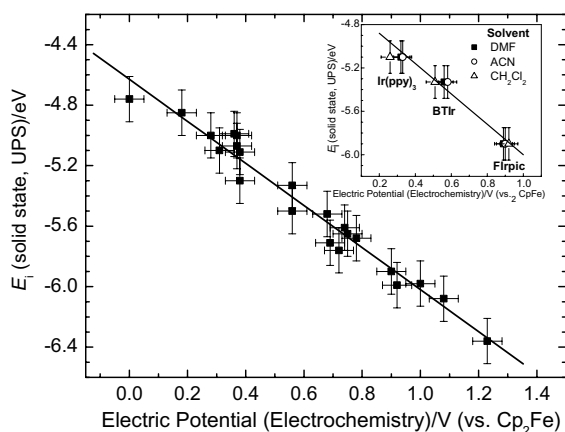


Fig. 4. HOMO energies (E_{HOMO}) determined using UPS versus relative oxidation potentials (V_{CV}) for several types of molecules: iridium and aluminum chelates, triarylaminines and carbazoles using dimethylformamide (DMF) as solvent and a ferrocene/ferrrocenium reference. The solid line is a best fit to the data following $E_{HOMO} = -(1.4 \pm 0.1)qV_{CV} - (4.6 \pm 0.08) \text{ eV}$. Inset: E_{HOMO} versus V_{CV} for the solvents DMF, acetonitrile (ACN) and dichloromethane (CH_2Cl_2) with a ferrocene/ferrrocenium reference sample. The solid line is the fit obtained with DMF as solvent.

working electrode, $d/r = 1.8 \pm 0.2$ (i.e. the value at $s = 1.4$) corresponds to 3.5 ± 0.7 monolayers. From the area under the second positive peak of the CV measurement (see shaded area in Fig. 2), we infer that $(4.5 \pm 0.5) \times 10^{14}$ molecules are oxidized per voltage scan with a voltage sweep rate of 100 mV/s. Given that the area of the working electrode is 0.94 cm^2 , and that each monolayer consists of $(1.4 \pm 0.4) \times 10^{14}$ molecules, we find that $r = 0.44 \pm 0.07 \text{ nm}$. Based on space-filling model calculations of Alq_3 , $\text{Ir}(\text{ppy})_3$, 4,4'-bis[*N*-(1-naphthyl)-*N*-phenyl-amino]biphenyl (NPD), and *N,N'*-dicarbazolyl-3,5-benzene (mCP), the volumes of these molecules are 0.540 nm^3 , 0.520 nm^3 , 0.645 nm^3 , and 0.438 nm^3 , respectively, corresponding to radii of 0.5 nm, 0.5 nm, 0.54 nm, and 0.47 nm, respectively, in agreement with the estimated value of $r = (0.44 \pm 0.07) \text{ nm}$.

For the case of $\epsilon_{CV}/\epsilon_{film} = 1.4$, the discrepancy between the energy levels is entirely due to the solvation effect. Hence, $f(r, d) \rightarrow 1$ as $d/r \rightarrow \infty$. In fact, for the cases studied here, $1 < \epsilon_{CV}/\epsilon_{film} < 1.4$, both solvation and image charges should be considered (Fig. 3, bold line).

Cyclic voltammetry data for three molecules were taken using two other solvents, acetonitrile (ACN) and dichloromethane with ferrocene/ferrrocenium as the reference sample in all cases. The V_{CV} for several molecules in these solvents are plotted against E_{HOMO} in the inset of Fig. 4, along with the fit obtained earlier with dimethylformamide (DMF) as the solvent. The fits for the individual solvents and their dielectric constants at room temperature are given in Table 2. The dielectric constants of dimethylformamide and acetonitrile are almost identical, and thus the oxidation potentials obtained are also similar. Although dichloromethane has a dielectric constant that is four times less than the other solvents, the change in s is only 15%, which is within experimental error. This suggests that the image charge effect has a more significant contribution to the slope than the solvation effect. Nevertheless, in all cases the fits are linear and are quantitatively consistent with the analysis in Section 2.

This model is based on molecules being spherical; a simplification that allows for an analytical expression of the image charge factor. In this case,

only d/r , along with the ratio of dielectric constants of the film to the solvent are required to accurately determine the HOMO energy from V_{CV} . Consideration of more complicated molecular shapes leading to higher order multipoles would involve other parameters such as molecular orientation with respect to the conductor. However, the accuracy afforded by such complications is insufficient to change the value inferred from the image charge factor. A detailed molecular orbital calculation to determine the energy levels of different redox states of the molecule would provide a better physical understanding of the dependence of the effective dielectric constant, ϵ_{CV} , on the dielectric constant of the solvent, ϵ_{Sol} , while taking into account the screening effects due to the supporting electrolyte. Nevertheless, the simplicity of the model presented here, along with the analysis of an extreme case of identical dielectric constants assumed in the UPS and CV experiments, is sufficient to conclude that the image charge factor, along with solvation effects, are all that are necessary to derive a quantitative relationship between the CV and UPS methods.

6. Conclusion

We have shown that a linear relationship exists between the HOMO energy found using UPS and the oxidation potential found from CV. This relationship is explained by a combination of solvation and image charge effects. The latter is quantified by approximating a molecule as a positive ion core surrounded by an electron cloud with an effective radius, r , inducing image charge in the conductive working electrode, and polarization of the electrolyte. We find that the two spectroscopic techniques are quantitatively related by $E_{HOMO} = -(1.4 \pm 0.1) qV_{CV} - (4.6 \pm 0.08) \text{ eV}$ for a wide range of organic electronic materials, where E_{HOMO} is directly measured from the UPS spectrum.

Acknowledgements

The authors are grateful to Prof. Antoine Kahn and Dr. Jason Brooks for helpful discussions. We

also thank Universal Display Corp. for partial support of this work.

References

- [1] S.T. Lee, Y.M. Wang, X.Y. Hou, C.W. Tang, *Appl. Phys. Lett.* 74 (1999) 670.
- [2] R.J. Holmes, B.W. D'Andrade, S.R. Forrest, X. Ren, J. Li, M.E. Thompson, *Appl. Phys. Lett.* 83 (2003) 3818.
- [3] A. Rajagopal, C.I. Wu, A. Kahn, *J. Appl. Phys.* 83 (1998) 2649.
- [4] J. Goodisman, *Electrochemistry: Theoretical Foundations, Quantum and Statistical Mechanics, Thermodynamics, The Solid State*, Wiley, New York, 1987.
- [5] D.T. Sawyer, A. Sobkowiak, J. Julian, L. Roberts, *Electrochemistry for Chemists*, first ed., John Wiley & Sons, New York, 1995.
- [6] E.V. Tsiper, Z.G. Soos, W. Gao, A. Kahn, *Chem. Phys. Lett.* 360 (2002) 47.
- [7] R.O. Loutfy, Y.C. Cheng, *J. Chem. Phys.* 73 (1980) 2902.
- [8] N. Sato, G. Saito, H. Inokuchi, *Chem. Phys.* 76 (1983) 79.
- [9] K. Seki, *Mol. Cryst. Liq. Cryst.* 171 (1989) 255.
- [10] H. Ishii, K. Sugiyama, E. Ito, K. Seki, *Adv. Mater.* 11 (1999) 605.
- [11] D. Cahen, A. Kahn, *Adv. Mater.* 15 (2003) 271.
- [12] A.J. Bard, L.R. Faulkner, *Electrochemical Methods. Fundamentals and Applications*, Wiley, New York, 1980.
- [13] J.O.M. Bockris, S.D. Argade, *J. Chem. Phys.* 49 (1968) 5133.
- [14] W.N. Hansen, D.M. Kolb, *J. Electroanal. Chem.* 100 (1979) 493.
- [15] A. Frumkin, B. Damaskin, *J. Electroanal. Chem.* 79 (1977) 259.
- [16] R. Gomer, G. Tryson, *J. Chem. Phys.* 66 (1977) 4413.
- [17] E. Chen, W.E. Wentworth, J.A. Ayala, *J. Chem. Phys.* 67 (1977) 2642.
- [18] D.E. Richardson, *Inorg. Chem.* 29 (1990) 3213.
- [19] M.F. Ryan, J.R. Eyster, D.E. Richardson, *J. Am. Chem. Soc.* 114 (1992) 8611.
- [20] Kurt J. Lesker, Pittsburgh, PA 15268.
- [21] S.R. Forrest, *Chem. Rev.* 97 (1997) 1793.
- [22] T.J. Bruno, P.D.N. Svoronos, *CRC Handbook of Basic Tables for Chemical Analysis*, CRC Press, Boca Raton, FL, 1989, p. 89.
- [23] L. Nadjo, J.-M. Savéant, *J. Electroanal. Chem.* 48 (1973) 113.
- [24] J.O. Howell, J.M. Goncalves, C. Amatore, L. Klasinc, R.M. Wightman, J.K. Kochi, *J. Am. Chem. Soc.* 106 (1984) 3968.
- [25] S. Trasatti, *Pure Appl. Chem.* 58 (1986) 955.
- [26] J. Pommerehne, H. Vestweber, W. Guss, R.F. Mahrt, H. Bassler, M. Porsch, J. Daub, *Adv. Mater.* 7 (1995) 551.
- [27] C.J. Bloom, C.M. Elliott, P.G. Schroeder, C.B. France, B.A. Parkinson, *J. Am. Chem. Soc.* 123 (2001) 9436.
- [28] H.M. Koepp, H. Wendt, H. Strehlow, *Z. Electrochem.* 64 (1960) 483.

- [29] J.J. Ritsko, P. Nielsen, J.S. Miller, *J. Chem. Phys.* 67 (1977) 687.
- [30] J.W. Rabalais, L.O. Werme, T. Bergmark, L. Karlsson, M. Hussain, K. Siegbahn, *J. Chem. Phys.* 57 (1972) 1185.
- [31] J.F. Ambrose, L.L. Carpenter, R.F. Nelson, *J. Electrochem. Soc.* 122 (1975) 876.
- [32] C.H. Chen, J.M. Shi, *Coord. Chem. Rev.* 171 (1998) 161.
- [33] S. Lamansky, P. Djurovich, D. Murphy, F. Abdel-Razzaq, R. Kwong, I. Tsyba, M. Bortz, B. Mui, R. Bau, M.E. Thompson, *Inorg. Chem.* 40 (2001) 1704.
- [34] S. Lamansky, P.I. Djurovich, F. Abdel-Razzaq, S. Garon, D.L. Murphy, M.E. Thompson, *J. Appl. Phys.* 92 (2002) 1570.
- [35] A.B. Tamayo, B.D. Alleyne, P.I. Djurovich, S. Lamansky, I. Tsyba, N.N. Ho, R. Bau, M.E. Thompson, *J. Am. Chem. Soc.* 125 (2003) 7377.
- [36] B.E. Koene, D.E. Loy, M.E. Thompson, *Chem. Mater.* 10 (1998) 2235.
- [37] K.R.J. Thomas, J.T. Lin, Y.T. Tao, C.W. Ko, *J. Am. Chem. Soc.* 123 (2001) 9404.



Study and comparison of conducting polymer hole injection layers in light emitting devices

C. Tengstedt ^{a,*}, A. Crispin ^b, C.-H. Hsu ^c, C. Zhang ^d, I.D. Parker ^d,
W.R. Salaneck ^b, M. Fahlman ^a

^a Department of Science and Technology, Linköping University, SE-601 74 Norrköping, Sweden

^b Department of Physics, Linköping University, SE-581 83 Linköping, Sweden

^c Dupont Displays, The Experimental Station, Wilmington, DE 19880, USA

^d Dupont Displays, Santa Barbara, CA 93117, USA

Received 3 August 2004; received in revised form 18 November 2004; accepted 5 February 2005

Available online 17 March 2005

Abstract

A set of polyaniline- and poly(3,4-ethylene dioxythiophene)-based materials were studied as hole injection layers in polymer light emitting devices. The choice of polymeric counterion/dopant poly(styrenesulfonic acid), and poly(acrylamido-2-methyl-1-propanesulfonic acid), and poly(acrylamide) blended with polyaniline/poly(acrylamido-2-methyl-1-propanesulfonic acid) was found to influence both work function and film morphology, which in turn affects device performance. The work functions of the polymer films spanned the range of over 1 eV and the surface region of the films were found to be low in conducting polymer content compared to the bulk. This was particularly the case of the polyaniline/poly(acrylamido-2-methyl-1-propanesulfonic acid) blended with poly(acrylamide) which showed device efficiency equal to that of the poly(3,4-ethylene dioxythiophene)–poly(styrenesulfonic acid) reference. The turn on voltage, however, was significantly larger, likely due to the insulating poly(acrylamide)-rich surface region of the polyaniline/poly(acrylamido-2-methyl-1-propanesulfonic acid)/poly(acrylamide) film. The polymer blend of polyaniline/poly(styrenesulfonic acid) yielded the highest work function (5.5 ± 0.1 eV).

© 2005 Elsevier B.V. All rights reserved.

PACS: 71.20.Rv; 68.47.Mn

Keywords: Polyaniline; PEDOT; Poly(acrylamido-2-methyl-1-propanesulfonic acid); Poly(styrenesulfonic acid); Poly(acrylamide); Photoelectron spectroscopy

* Corresponding author. Tel.: +46 13 282471; fax: +46 13 288969.

E-mail address: carte@ifm.liu.se (C. Tengstedt).

1. Introduction

There is a steady growth in the field of conjugated polymers with numerous applications [1–10]. However, the biggest application so far, polymer light emitting diodes (PLEDs), is still working on fundamental issues such as degradation upon running of the devices [11–13]. It is known today that device efficiency and lifetime can be enhanced by adding extra layers between the electrodes and the active materials. For the anode contact, so-called buffer materials, typically conducting polymers such as poly(3,4-ethylene dioxothiophene) (PEDOT) and polyaniline (PAni) systems, are deposited as interfacial layers between the anode and the electroluminescent polymer (ELP) [14–20]. On the cathode side, thin alkali halide layers between the ELP and the electrode can be used to improve device performance [21–23]. Good band alignment between the contacts and the ELP is essential for device performance [24] and by introducing a contacting material that modifies the electrode work function, better band alignment can be obtained. The most popular buffer layer material for the anode side is poly(3,4-ethylene dioxothiophene)–poly(styrenesulfonic acid), PEDOT–PSSA [25]. PEDOT–PSSA is in many ways an ideal hole injection layer (HIL) for polymer LEDs. A PEDOT–PSSA film has a high work function [26], acts as a metal in terms of band alignment at interfaces [26], is transparent, has a high conductivity for a polymer and serves as buffer material for ions and oxygen that can diffuse from the anode [18,27]. PEDOT–PSSA is however acidic by nature, due to the acidic counter ions in PSSA. This leads to etching of the anode electrode, giving rise to unwanted “free” metallic ions released from the anode into the devices. Furthermore, PEDOT–PSSA suffers from UV- and electron-induced degradation [28,29] and overoxidation can lead to permanent transition into insulating states of the polymer system [30]. Hence, there are still reasons to either improve PEDOT–PSSA or find other, more suitable materials for HILs in PLEDs. PAni is one such candidate given its superior stability, and PAni–PSSA has been reported to be more effective under certain conditions [20]. In this paper, different polymeric coun-

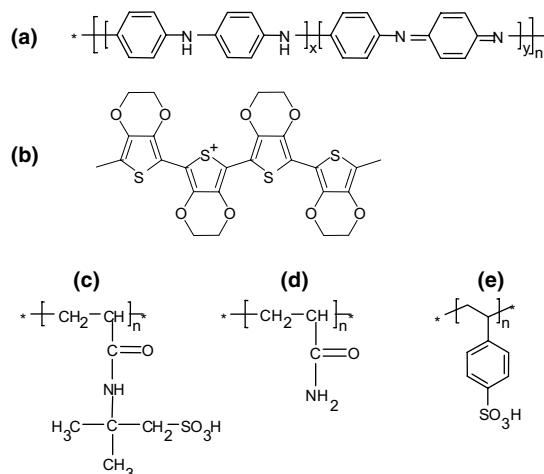


Fig. 1. Chemical structure of (a) (emeraldine base) polyaniline, (b) poly(3,4-ethylenedioxy-thiophene), (c) poly(acrylamido-2-methyl-1-propanesulfonic acid), (d) polyacrylamide and (e) polystyrenesulfonic acid.

ter ions are used for PEDOT and PAni and the counter ion induced effects on the electronic and morphological properties of the resulting films are studied. The specific systems are: PAni doped with poly(styrenesulfonic acid) (PSSA), poly(acrylamido-2-methyl-1-propanesulfonic acid) (PAA-MPSA), and PAni–PAA-MPSA blended with insulator polyacrylamide (PAM), and PEDOT where PAA-MPSA is used as counter ion. Results from photoelectron spectroscopy study and UV–Vis–NIR optical absorption are presented describing changes in work function, stoichiometry and thermal stability depending on polymeric counter ion. The suitability of the materials as HILs in PLEDs also was tested and compared to PEDOT–PSSA by fabricating PLEDs and obtaining IV-characteristics and luminescence efficiency. The chemical structures of the materials are depicted in Fig. 1.

2. Experimental

2.1. Synthesis and material

Composition and characterization of each material either synthesized in Dupont or obtained from outside are described below:

2.1.1. *PAni-PAAMPSA*

PAAMPSA-doped (protonated) polyaniline was made by oxidative polymerization of aniline. Amount of aniline and PAAMPSA in molar ratio of 1 to 1 was added with water in a glass reactor to form 2.8% (w/w) reagent concentration. PAAMPSA is a water-soluble polymeric acid having a weight-averaged molecular weight of 2 million. The solution, while being stirred, was added slowly with a 20%(w/w) ammonium persulfate (APS), an oxidant, water solution slowly to cause aniline to polymerize oxidatively. The amount of APS is 0.4 in molar ratio to aniline or PAAMPSA. The reaction mixture turned green in about 20 min and polymerization was allowed to proceed for about a couple of hours. The green color is attributed to protonation, or called doping, of polyaniline emeraldine base formed in polymerization of aniline in the presence of PAAMPSA. The electrically conductive PAni/PAAMPSA exists as dispersed particles in the water. The polymer was then precipitated with acetone and subsequently washed with acetone to purify the polymer. It was then dried in a vacuum oven for storage. Thermal gravimetric analysis (TGA) shows that the polymer exhibits a small amount of weight loss as soon as heated above room temperature due to evaporation of absorbed water and then stabilizes at higher temperature, but starts to show decomposition at the temperature above about 190° in nitrogen. The dried polymer powder sample was re-dispersed in de-ionized water at 1.0% by weight and subsequently agitated with a mechanical grinder to break up aggregates for reducing particle size of PAni/PAAMPSA. The formed dispersion usually contains PAni/PAAMPSA particles having less than 0.1 µm.

2.1.2. *PAni-PAAMPSA-PAM*

Aqueous PAni-PAAMPSA-PAM dispersion was made as follows: Portion of the 1.0% PAni-PAAMPSA dispersion was diluted to 0.8% (by weight) first before mixed with an equal amount of 1.6% (by weight) PAM in water. PAM purchased from PolySciences Inc. is a water-soluble and electrically insulating polymer having molecular weight of 5–6 millions. Addition of PAM, which is compatible with PAni-PAAMPSA was

to reduce conductivity of buffer layer in the devices for preventing cross-talk between pixels in passive matrix displays. The mixture in the dispersion was then agitated mechanically to break up aggregates to form reduced particle size. A small sample of the dispersion was dried and analyzed for weight loss. TGA shows that the polymer exhibits a small amount of weight loss as soon as heated above room temperature due to evaporation of absorbed water and then stabilizes at higher temperature, but starts to show decomposition at the temperature above 190° in nitrogen atmosphere.

2.1.3. *PAni-PSSA*

Polyaniline doped (protonated) by poly(styrenesulfonic acid), PSSA, was provided as a ~3.7% dispersion by weight in water by Covion GmbH in Frankfurt, Germany. A small sample of the dispersion was dried and then analyzed for weight loss. TGA shows that the polymer exhibits a small amount of weight loss as soon as heated above room temperature due to evaporation of absorbed water. However, it does not show any additional weight loss even up to 200° in nitrogen atmosphere.

2.1.4. *PEDOT-PAAMPSA*

Aqueous PEDOT-PAAMPSA dispersion was made by oxidative polymerization of Baytron-M in the presence of PAAMPSA. Baytron-M purchased from H.C. Starck in Germany is 3,4-dioxyethylenethiophene monomer. Amount of PAAMPSA and sodium persulfate, an oxidant, in a molar ratio of about 0.4 was placed in a glass reactor containing deionized water and a small amount of ferric sulfate as a catalyst. PAAMPSA as a 15.0 wt.% in water was purchased from Aldrich. It has weigh-averaged molecular weight of 2 million. The mixture was stirred with a stirring paddle powered by an air-driven overhead stirrer while Baytron-M® in a molar ratio of 0.36 to PAAMPSA was added. The polymerization was allowed to proceed for 24 h at about 22 °C. During the time, the polymerization changed from a clear liquid to a dark color liquid, which is PEDOT/PAAMPSA dispersion in water. The dark color is due to partially oxidized poly(3,4-dioxyethylenethiophene) backbone in which the positive

charges were balanced by part of PAAMPSA anions. The aqueous PEDOT/PAAMPSA was further treated with Lewatit[®] S100 and Lewatit[®] MP62 WS ion-exchange resins, both from Bayer GmbH, to remove impurities. Final solid% of the dispersion was about 1.2%. A small sample of the dispersion was dried and then analyzed for weight loss. TGA shows that the polymer exhibits a small amount of weight loss as soon as heated above room temperature due to evaporation of absorbed water. However, it does not show any additional weight loss even up to 200° in nitrogen atmosphere.

2.1.5. PEDOT–PSSA

Aqueous PEDOT–PSSA dispersion was purchased from H.C. Starck in a trade name of Baytron-P CH8000. It consists of about 2.6% PEDOT–PSSA in which positive charges in the partially positively charged poly(3,4-dioxyethylenethiophene) backbone were balanced by part of PSSA anions. A small sample of the dispersion was dried and then analyzed for weight loss. TGA shows that the polymer exhibits a small amount of weight loss as soon as heated above room temperature due to evaporation of absorbed water. However, it does not show any additional weight loss even up to 200 °C in nitrogen atmosphere.

2.2. Device fabrication

2.2.1. General procedure

A general procedure for making polymeric light emitting diodes (PLEDs) is described as follows. All PLEDs were fabricated at Dupont Displays in Santa Barbara, California and have the following configuration: ITO(anode)/HIL(buffer layer)/light emitting polymer(LEP)/Ba(EIL)/Aluminum(cathode). The glass/ITO substrates (30 mm × 30 mm) having ITO thickness of 100–150 nm and conductivity 20 Ω/sq were patterned to create 15 m × 20 mm light emitting area. The ITO was then cleaned in mild organic solvents (alcohols) followed by drying and storage in a 70 °C oven and subsequently treated with UV/ozone before use. The different conducting polymer dispersions were spin-coated in air at a spin

speed between 1000 and 2500 rpm on to ITO to form HIL (hole injection layer) layer, or so-called buffer layer. The electrical lead areas were then wiped cleaned with damp swabs before baked at the baking conditions specified hereunder in section “film specifications” together with conductivities. Nominal thickness of the HIL is also specified in the “film specifications” section. Immediately after spin coating, the samples were transferred to dry-box while still hot to avoid reabsorption of water). The HIL containing layer pieces were then top-coated with Covion’s PDY131, a super yellow emitter, using 0.5% (w/w) solution in toluene. PDY131 is substituted-poly(*p*-phenylene-vinylene). The spin speed was ~1500 rpm until films completely dry, in a dry box with moisture and O₂ content <1 ppm and nominal thickness of the layer was 70 nm. No subsequent heat treatment was performed. Electrical contact areas were then wiped clean with toluene. The HIL and LEP containing substrates were then masked and placed in a vacuum chamber. After pumping to a base pressure of 2×10^{-7} Torr, a layer of Barium to a thickness of 3 nm to function as an electron injection layer and subsequently a layer of Aluminum to a thickness of 400 nm to function as cathode. The chamber was then vented and the devices were then encapsulated using a glass lid and an UV curable epoxy. Such encapsulation has proven to be effective for air exposure of >6 months. These devices were then measured for current/voltage, and brightness for calculation of device efficiency shown in Table 1.

2.2.2. Film specifications

In the case for spin-coated PANi–PAAMPSA, films at thicknesses of about 60 nm were prepared for device fabrication. Before the top coating with the light emitting polymer solution, the films were baked at 90 °C in nitrogen for 30 min in order to remove moisture. The conductivity of the baked films was in the range of 10^{-3} S/cm. The spin-coated PANi–PAAMPSA–PAM films were prepared such that the film thicknesses were about 160 nm and then baked at 200 °C for 4 min in nitrogen. The baking conditions were chosen to remove moisture prior to top coating with a light emitting polymer solution and to maximize device

Table 1
Work function of the materials as measured by UPS

Material	Thermal treatment	Work functions (± 0.1) [eV]
PAni-PAAMPSA	As prepared	4.8
	90 °C, 30 min in vacuum	4.8
	30 min at 90 °C followed by 4 min at 200 °C in vacuum	4.8
PAni-PAAMPSA-PAM	As prepared	5.2
	90 °C, 30 min in vacuum	5.1
	30 min at 90 °C followed by 4 min at 200 °C in vacuum	5.3
PAni-PSSA	As prepared	5.4
	90 °C, 30 min in either vacuum, argon or in nitrogen	5.5 (Vac); 5.2 (Ar); 4.6 (N ₂)
	30 min at 90 °C followed by 4 min at 200 °C in vacuum	5.6
PEDOT-PAAMPSA	As prepared	4.2
	90 °C, 30 min vacuum	4.6
	30 min at 90 °C followed by 4 min at 200 °C in vacuum	4.6
PEDOT-PSSA (ref.)	As prepared	5.3
	90 °C, 30 min nitrogen	5.0
	200 °C, 4 min in air	5.3

performance. The conductivity of the baked spin-coated films was in the range of 10^{-5} S/cm. Spin-coated films of PAni-PSSA with conductivity in the range of 10^{-5} S/cm after baked at 90 °C for 30 min in nitrogen or 200 °C for 5 min in air were prepared. The latter baking conditions were also used prior to top coating with a light emitting polymer solution for making light emitting diodes. Film thickness of the material in the light emitting diodes was about 160 nm. The conductivity of spin-coated films of PEDOT-PAAMPSA is in the range of 10^{-7} S/cm after baked at 90 °C for 30 min in nitrogen. The baking conditions were also used prior to top coating with a light emitting polymer solution for making light emitting diodes. Film thickness of the material in light emitting diodes was about 100 nm. Spin-coated and heat treated films of PEDOT-PSSA had conductivity in the range of 10^{-5} S/cm after baked at 90 °C for 30 min in nitrogen or 200 °C for 5 min in air. The latter baking conditions were used for device fabrication, prior to top coating with a light emitting polymer solution. Film thickness of the material in light emitting diodes was about 160 nm.

2.3. Material analysis

Photoelectron spectroscopy and UV-Vis-NIR optical absorption was used in order to study sur-

face and bulk electronic properties, respectively. The photoelectron spectroscopy was carried out using an ultra high vacuum system at a base pressure of 10^{-10} mbar equipped with a Scienta[®] ESCA 200 with a hemispherical electron energy analyzer. Both a monochromatized Al(K α)-source, at $h\nu = 1486.6$ eV and a synchrotron radiation source at MAX-lab, see <http://www.maxlab.lu.se>, was used for the X-ray photoelectron spectroscopy, XPS, measurements and a monochromatized He I and He II source was used for the ultraviolet photoelectron spectroscopy, UPS, measurements. The resolution of the analyzer was such that the full width at half maximum of the Au(4f7/2) core level was 0.65 eV. A Perkin-Elmer Lambda 9 UV-Vis-NIR spectrometer was used for the absorption measurements. The materials studied were all obtained from DuPont[®] Displays. The substrates used for the photoelectron spectroscopy studies were ITO, gold and silicon. Quartz and ITO were used as substrates in the UV-Vis-NIR absorption studies. Each substrate was cleaned in acetone, isopropanol and ozone, 5 min for each step, before spin casting the aqueous polymer dispersions onto the substrate using the same speed as for device fabrication. In order to remove the excess water after spin casting, different heating procedures were used, depending on the dispersion, trying to mimic device

fabrication procedure. In the PANi–PAAMPSA and the PANi–PAAMPSA–PAM cases, the heating procedures were: not heated (reference), samples heated during 30 min at 90 °C in vacuum, sample heated at both 90 °C, 30 min followed by 4 min at 200 °C in vacuum and sample heated at 200 °C for 30 min or in nitrogen. For PANi–PSSA, the heating procedures were: not heated (reference), heated at 90 °C for 30 min in either nitrogen, argon (in a “glove bag”) or in vacuum, sample heated at 90 °C for 30 min vacuum followed by 4 min at 200 °C in vacuum and heated 4 min at 200 °C in air. In the PEDOT–PAAMPSA case, the heating procedures were: as prepared, heated in vacuum and 90 °C for 30 min followed by 4 min 200 °C in vacuum. For purposes of reference, Baytron-P PEDOT–PSSA was studied as well, and the results are included in the tables but are not discussed in any detail, as spectroscopy data is readily available in literature [31,32]. The heating procedure for PEDOT–PSSA was: as prepared, heated at 90 °C for 30 min in nitrogen or heated at 200 °C during 4 min in air. All samples used for the photoelectron spectroscopy studies were introduced not more than 5 min after heating into a load lock system of the vacuum equipment and was pumped down to $P < 10^{-6}$ mbar within 30 min. The samples prepared for absorptions studies were measured right after preparation and the measurements were performed in air.

3. Results and discussion

3.1. PANi–PAAMPSA

The XPS-derived stoichiometry of the PANi–PAAMPSA films suggests a PAAMPSA rich surface. The atomic concentrations of C, O, N, S for the pristine PANi–PAAMPSA films are identical to that of pure PAAMPSA within the error margins of the technique. For the films heated at 200 °C, there is a decrease of the S and O content, suggesting diffusion of some PANi to the surface region (~ 60 Å) or heating-induced decomposition of the PAAMPSA with loss of SO_3^- units, as have been seen for PSSA [31]. The C(1s) core level spectrum (not shown) features the high binding energy peak

expected of the carbonyl groups of PAAMPSA, also suggesting a PAAMPSA overlayer.

In Fig. 2 the N(1s) core level spectra for PANi–PAAMPSA and PAAMPSA films are compared for each type of heat treatment. Note that the N(1s) core level spectrum of PAAMPSA contains two features, yet the chemical structure of PAAMPSA depicted in Fig. 1 contains only one type of nitrogen, C_2NH , which produces the peak at ~ 399.8 eV. The second peak at ~ 401.6 eV originates from C_2NH that has been changed into C_2NH_2^+ by accepting a proton from a $\text{SO}_3^- \text{H}^+$ group on the PAAMPSA, i.e., so-called protonation. (The shift towards higher binding energy is a consequence of the added positive charge on the nitrogen due to the protonation.) The shape and binding energy positions of the N(1s) core level features of PANi–PAAMPSA and PAAMPSA are identical for the as-prepared samples and differ only slightly when heat treated samples are compared, further strengthening the argument for the proposed formation of a PAAMPSA-rich surface region in the films. The small differences in the N(1s) spectra upon heating may be due to ordering effects in the film, i.e., diffusion of PANi to the surface, since the broadening towards lower binding energy is consistent with the binding energy for PANi nitrogen (amine ~ 399.9 eV, imine ~ 398.6 eV) [33]. The possibility of sample damage upon heating occur-

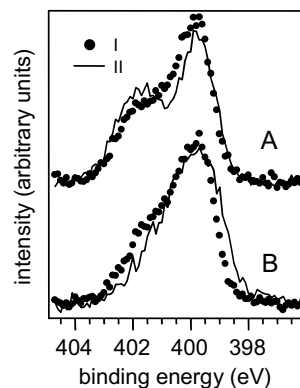


Fig. 2. XPS N(1s) core level spectra, normalized to the binding energy of saturated C(1s) at 285 eV, of PAAMPSA (dots, I) and PANi–PAAMPSA (solid line, II), (A) heated 90 °C, 30 min in vacuum, and (B) heated 200 °C, 30 min in nitrogen.

ring as well cannot be ruled out based on the N(1s) spectra, however since all XPS spectra show great similarities, both in shape and binding energy, a PAAMPSA-rich region of the surface more or less independent of heating procedure is suggested. However, given the similarities between PAAMPSA and protonated polyaniline core level features (fully protonated PANi lacks imine nitrogen), the valence band structure was measured by means of UPS using He II light. The valence electronic structures of protonated PANi (emeraldine salt), a conductor, and PAAMPSA, an insulator, are vastly different so UPS is a more sensitive technique for deciding which material is present. UPS is however more surface sensitive, 10–20 Å for He II light compared to the 60 Å probed by XPS, and hence the material composition at the absolute surface is obtained. The He II valence band spectra of PAAMPSA and PANi–PAAMPSA, shown in Fig. 3, display great similarities between spectrum of pure PAAMPSA and the PANi–PAAMPSA films, which again indicates a PAAMPSA-rich surface. There is no PANi feature appearing in the spectra, even for the 200 °C heated films, suggesting that if some PANi chains do diffuse into the surface region, they do not reach the actual surface (the XPS probe depth is ~ 3 times that of UPS).

Together, the XPS and UPS results make a strong argument that the surface region (up to

~ 60 Å) of the PANi–PAAMPSA films consists mainly of PAAMPSA, regardless of heating procedure. In order to study the homogeneity within the PAAMPSA-rich over-layer, photon energy dependent depth profiling [32,34] were performed at the MAX synchrotron radiation facility. The spectra (not shown) indicated a homogeneous mixture within the probing depth of XPS.

Due to the limited probing depth of photoelectron spectrometry, optical absorption experiments were also carried out in order to study the bulk properties of the films. Indeed, due to (nitrogen containing) over-layer of PAAMPSA, it is not possible to establish the degree of doping for the polyaniline simply by resolving the nitrogen core level spectra. However a qualitative estimate of the doping level can be established from the absorption spectra (see Fig. 4). Absorption bands at 2.8 eV (~ 440 nm) and 1.5 eV (800 nm) are characteristic of p-doped (protonated) PANi [35,36]. The rather narrow peak around 1.5 eV is due to localized charge carriers, polarons, typical for the compact coil conformation of protonated PANi [37]. Both spectra have a small absorption tail towards higher wavelengths (lower energies). A small or no absorption tail indicates localized charge carriers, the extension of the absorption tail is an indicator of the localization of the charge carriers in the protonated PANi [37].

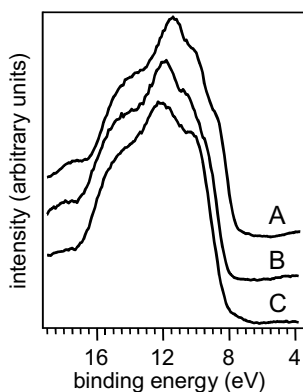


Fig. 3. He II spectra of PAAMPSA and heat-treated PANi–PAAMPSA, plotted versus the vacuum level. The different spectra shows (A) as prepared PAAMPSA, (B) PANi–PAAMPSA heat treated at 90 °C, 30 min in vacuum, (C) PANi–PAAMPSA heat treated at 200 °C, 30 min in nitrogen.

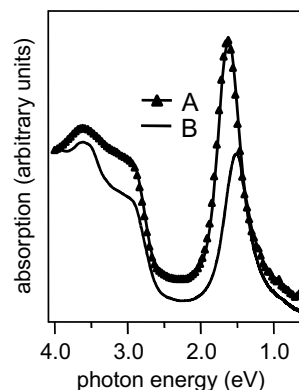


Fig. 4. UV-Vis-NIR spectra of (A) PANi PAAMPSA heated 90 °C, 30 min in vacuum and (B) PANi PAAMPSA heated 200 °C, 30 min in nitrogen.

3.2. PANi-PAAMPSA-PAM

The mixture PANi-PAAMPSA-PAM system differs from the PANi-PAAMPSA material. The XPS-derived stoichiometry suggest surface region containing a blend of PAM and PAAMPSA, with an excess of PAM. Due to the similar elemental composition of the components, no quantitative conclusions can safely be drawn. Energy dependent depth profiling (not shown) indicates that the blend is homogeneous over the probe depth (~ 60 Å), however.

The XPS core-level spectra of N(1s) PAM and PANi-PAAMPSA-PAM films are plotted in Fig. 5 for each type of heat treatment. The shape of the spectra is clearly different from those of pure PAAMPSA and PANi-PAAMPSA as expected from the stoichiometry results. The PANi-PAAMPSA-PAM spectra are PAM-like in that they show a main feature located at ~ 400 eV from the C₂NH nitrogen of PAM (and PAAMPSA). The spectra show broadening of the main peak upon the heat treatment. The broadening on the low binding energy side of the peak cannot result from reorganization of the film since none of the blend components have features at ~ 398 eV in the N(1s) spectrum. It is worth noting that the low binding energy side increases significantly for the 200 °C heating and the stoichiometry changes, showing loss of S and O (as for the heated PANi-

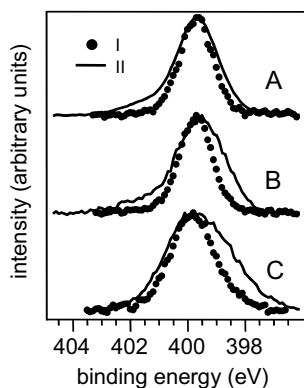


Fig. 5. XPS of N(1s) core level, normalized to the binding energy of saturated C(1s) at 285 eV, of samples PAM (dots, I) and PANi-PAAMPSA-PAM (solid line, II), the samples were heated as (A) as prepared, (B) samples heated 90 °C, 30 min in vacuum and (C) samples heated 200 °C, 30 min nitrogen.

PAAMPSA films). Pure PAM films also show a broadening of the main peak at ~ 400 eV upon heat treatment, though not as significant as in the PANi-PAAMPSA-PAM case. New nitrogen compounds through modification of both PAM and PAAMPSA could explain the broadening seen in the N(1s) spectrum. Hence we propose that the heat treatment modify both the PAM and PAAMPSA chains, most significant for the 200 °C treatment, with new chemical species forming from the modified components.

In order to more clearly establish the composition of the topmost surface layer, UPS spectra of PANi-PAAMPSA-PAM films (not shown) were obtained. The spectra are almost identical to that of pure PAM, suggesting that the topmost layer of the films consists of PAM (almost) exclusively. XPS valence band spectra (Fig. 6) were also obtained for PAM, PAAMPSA and PANi-PAAMPSA-PAM films. Using X-rays, the probe depth is increased as mentioned earlier, here to about ~ 80 Å due to the increased kinetic energy of the emitted electrons. Since the valence electronic structures for the three components are quite different, the XPS valence band spectrum can be used to better determine the blend composition in this extended surface region (~ 80 Å). The XPS valence band spectra show great similarities between the valence bands of PAM and PANi-PAAMPSA-PAM i.e., strengthening the proposed model of a PAM-rich surface region in the PANi-PAAMPSA-PAM films.

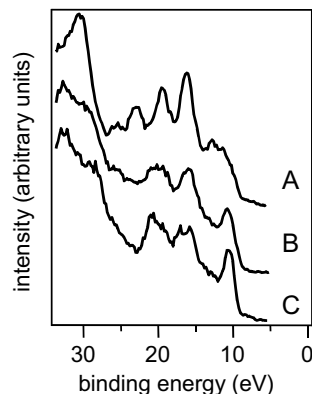


Fig. 6. XPS valence band spectra, aligned to the vacuum level. The spectra originate from as prepared: (A) PAAMPSA, (B) PANi-PAAMPSA-PAM and (C) PAM.

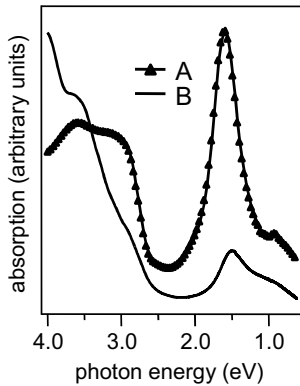


Fig. 7. UV-Vis-NIR spectra of (A) PANi-PAAMPSA-PAM heated 90 °C, 30 min in vacuum and (B) PANi-PAAMPSA-PAM heated 200 °C, 30 min in nitrogen.

The absorption spectra of PANi-PAAMPSA-PAM, depicted in Fig. 7, show a strong feature at 1.5 eV (localized polaronic charge carrier states) for the 90 °C heated films. Like for the PANi-PAAMPSA material, there is no strong tail into the IR that would indicate delocalized charge carriers and a highly conductive film. The 200 °C heat treatment introduces significant changes in the absorption spectrum. The intensity of the 1.5 eV peak is decreased relative to the higher energy absorption features. If a localized to delocalized charge carrier transformation occurred (typically by morphology changes in the film), the decrease in the 1.5 eV peak would be accompanied by an increased tail into the IR [37]. This is not evident in our spectra, however, as the tail retains the same decreasing slope into the IR as for the 90 °C films. Thermal de-protonation of the PANi also can be ruled out, as a emeraldine salt to emeraldine base transition would move the 1.5 eV peak to 2.0 eV and broaden it [37], which is not seen in the spectra. We hence speculate that the drop of intensity may be due to chemical modification/degradation of the PANi due to reaction with thermally degraded PAM, PAAMPSA or species thereof.

3.3. PANi-PSSA

The stoichiometry of the studied films indicates a PSSA-rich surface containing of about eight PSSA monomer units per PANi monomer unit

(see Fig. 1). The C(1s) core level features (not shown) of PANi and PSSA overlap each other and form one broad peak centered at around 285.0 eV. The N(1s) core level spectrum does not contain any contribution from PSSA and can thus be used to determine the level of protonation in the PANi. The N(1s) spectrum of pristine PANi-PSSA (see Fig. 8) is fitted using three peaks representing protonated amine $-\text{NH}_2^+$ (~ 402.7 eV), protonated imine $-\text{NH}^+$ (401.6 eV) and amine $-\text{NH}-$ (400.2 eV). The combined relative intensity of the protonated imine and protonated amine features, i.e., the doping level, was found to be about 60% (see Fig. 8). The doping level, as estimated from the N(1s) spectra remained $\sim 60\%$ upon 90 °C and 200 °C heat treatments (not shown), nor where there a loss of sulfur signal, thus indicating that the PANi-PSSA is stable at these temperatures.

The PANi-PSSA was sensitive to prolonged heating in nitrogen atmosphere, however, unlike the cases where argon atmosphere or vacuum was used. It earlier has been shown that the sulfonic acid of PSSA in PEDOT-PSSA can catch NH_3 impurities in the N_2 gas (or air) when in the presence of water leading to PSSA $-\text{NH}_4^+$ [32]. Similar modifications were seen in the S(2p) core level spectrum for PANi-PSSA (not shown). Hence, unless the N_2 gas is ultra pure, it should not be viewed as an inert atmosphere for PANi-PSSA.

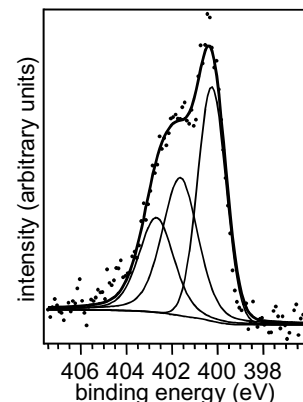


Fig. 8. Deconvolution of the N(1s) core level spectrum of as prepared PANi-PSSA. The spectra are normalized to the binding energy of saturated C(1s) at 285 eV.

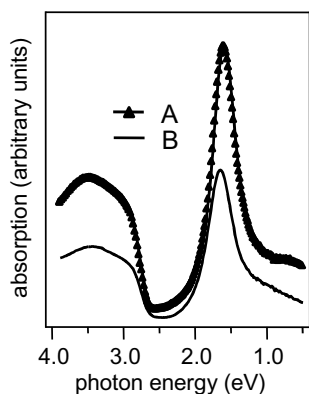


Fig. 9. UV-Vis-NIR spectra of PANi-PSSA: (A) heated 90 °C, 30 min in argon, (B) heated 200 °C, 4 min in air.

The optical absorption spectrum of PANi-PSSA (see Fig. 9) does not change upon heating except for an overall reduction of intensity. The relative intensities of the various absorption features are retained, indicating that the bulk of the film (like the surface region) does not undergo degradation upon heat treatment. As for the other PANi-materials in this study, we do not see the tail into the IR that would indicate delocalized charge carriers and a strong absorption peak at ~ 1.5 eV representing localized polarons is present in the spectra for both heat treatments.

3.4. PEDOT-PAAMPSA

Stoichiometric data from the XPS core level spectra suggests a surface region of (insulating) PAAMPSA. The C(1s) spectrum (not shown) is identical to that of pure PAAMPSA. Furthermore, the S(2p) spectrum has the spin split doublet at ~ 168 eV derived from the $\text{SO}_3^- \text{H}^+$ sulfur of the PAAMPSA. PEDOT sulfur has a spin split doublet at ~ 164 eV [31,32] but no feature appears in that region for the PEDOT-PAAMPSA films. This indicates that the atomic concentration of PEDOT sulfur is significantly less than 1% and that the PEDOT to PAAMPSA ratio in the surface region can at the most be $\sim 1:10$. Hence, the surface region is significantly PEDOT-poorer than that of films from PEDOT-PSSA dispersions [32].

The N(1s) feature is quite different from that of pure PAAMPSA, however. The N(1s) spectrum of

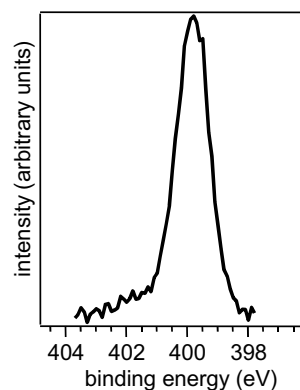


Fig. 10. N(1s) core level spectrum of as prepared PEDOT-PAAMPSA, normalized to the binding energy of saturated C(1s) at 285 eV.

pure PAAMPSA shows two clearly different features, due to self-protonation, as described earlier. In contrast, the N(1s) spectra of PEDOT-PAAMPSA (see Fig. 10) only have one feature, centered at 399.8 eV, i.e., C_2NH . Hence, no self-protonation occurs for the PAAMPSA in these films. The reason for the difference to the PANi-PFESA case, where self protonation did occur is not yet understood, though the great differences in synthesis and chemical environment are likely the explanation.

3.5. Device performance

The work functions of the materials studied are given in Table 1. The difference between the work function of a hole injection layer (HIL) and the electro-luminescent polymer's (ELP) valence band (ionization potential) determines the barrier towards hole injection [38] and the ionization potential of the used ELP was measured by UPS to be 5.4 eV (± 0.1 eV). Ideally, one would like to have a HIL work function larger than the ELP ionization potential, which would reduce the barrier to zero. Hence, a high work function of the HIL is generally preferred as this should improve device performance. The films yielding the highest work function, as measured by UPS, were PANi-PSSA, 5.5 ± 0.1 eV depending of heat treatment. Prolonged heating in nitrogen atmosphere dramatically reduces the work function, however, to

4.6 eV. Hence, as mentioned above, nitrogen should not be viewed as an inert atmosphere for PANi–PSSA films unless ultra pure. PANi–PAAMPSA–PAM films also had high work function, 5.2 ± 0.1 eV depending on heat treatment. PANi–PAAMPSA and PEDOT–PAAMPSA had significantly lower values, the highest values are 4.8 eV and 4.6 eV, respectively, depending on heat treatment.

Turn on voltages and efficiencies of devices made using these HIL materials are given in Table 2, with devices fabricated using standard PEDOT–PSSA as the HIL included as reference. The material that produced devices with the highest efficiency, 8 cd/A, was PANi–PAAMPSA–PAM. However, this HIL also yielded devices with the highest turn on voltage, 4.6 V. PANi–PSSA has the second highest efficiency together with a rather low turn on voltage, 3.4 eV. In the cases of PANi–PAAMPSA and PEDOT–PAAMPSA, systems producing devices with rather low turn on voltage, 3.3 V and 3.5 V, respectively, the efficiencies are however in the lower range of the compared materials. In comparison, the PEDOT–PSSA based devices had an efficiency equal to the best value of the HILs (PANi–PAAMPSA–PAM), but a significantly lower turn on voltage, 3.4 V compared to 4.6 V.

The device results are surprising since the work function of the HIL materials does not seem to play the significant role for determining the turn on voltage as one might assume. One explanation could be that it is the electron injection that is the limiting step and the turn on voltage should hence be independent of the HIL layer given that the same cathode and ELP material was used in all de-

vices. Indeed, the turn on voltage is fairly constant for the PANi–PSSA, PANi–PAAMPSA and PEDOT–PAAMPSA devices, suggesting that for those HILs the hole injection is more efficient than the electron injection and hence independent of the HILs, despite the large differences in work function, close to 1 eV between PANi–PSSA and PEDOT–PAAMPSA. The large turn on voltage for PANi–PAAMPSA–PAM compared to the other systems (including PEDOT–PSSA) needs a separate explanation, however. Here, the comparatively thick, insulating, PAM-rich surface region may play a role as an insulating blocking layer slowing down the hole injection into the ELP and preventing the electrons from reaching the anode, thus shifting the recombination and light producing region to the interface between the ELP and the HIL (see Fig. 11). The ionization potential of the PANi–PAAMPSA–PAM surface region is 8.3 eV as measured by UPS, yielding a large barrier for hole injection into an ELP, where the ionization potentials are typically less than

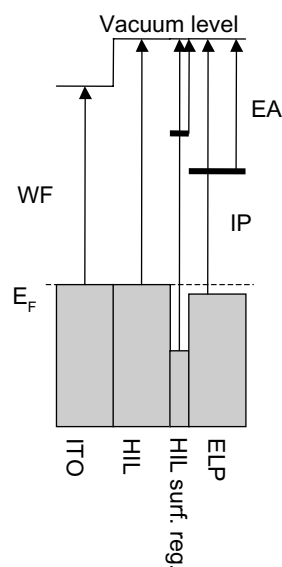


Fig. 11. Schematic picture of the anode side of a PLED where the PAM-rich, insulating surface region of the PANi–PAAMPSA–PAM HIL serves as an electron- and hole-blocking barrier. The work function (WF), electron affinity (EA) and ionization potential (IP) of the materials are depicted with arrows.

Table 2

Device data, turn on voltage [V] and efficiency (light output per ampere) [cd/A] obtained at 200 cd/m²

Material	Volt [V]	Eff. [cd/A]	Baking condition
PAni–PAAMPSA	3.3	7.5	90 °C/N ₂ /30 min
PAni–PAAMPSA–PAM	4.6	8	200 °C/N ₂ /4 min
PAni–PSSA	3.4	7.8	200 °C/air/5 min
PEDOT–PAAMPSA	3.5	7	90 °C/N ₂ /30 min
PEDOT–PSSA (ref.)	3.4	8	200 °C/air/5 min

6 eV. Besides reducing exciton quenching due to image potentials on the electrodes, such a blocking layer of suitable thickness may also balance the charge injection, increasing efficiency at the expense of turn on voltage.

4. Summary and conclusions

A number of PANi and PEDOT based HIL materials were studied to determine the influence of polymeric counter ion on the material properties and performance in PLEDs. In all of the PANi and PEDOT systems, the chemical composition in the surface region of the films was different from that of the bulk, with the surface region being low in conducting polymer content. The choice of polymeric counter ion(s) affects both thickness and conducting polymer content, with the PAAMPSA–PAM system providing the thickest surface regions with the lowest PANi concentration. We demonstrate that the work function of PANi and PEDOT can be tuned over a large range (0.7 and 1.1 eV, respectively) by using different polymeric counter ions. The work function of PANi can be tuned from 4.8 eV (PANi–PAAMPSA) to 5.5 eV (PANi–PSSA), and the work function of PEDOT can be tuned from 4.2 eV (PEDOT–PAAMPSA) to 5.3 eV (PEDOT–PSSA). PSSA yields the highest work function for both systems. PANi–PAAMPSA–PAM and PEDOT–PSSA produce the highest efficiency for the PLEDs studied, but the PANi–PAAMPSA–PAM gives a significantly higher turn on voltage for the PLEDs, which we ascribe to the relatively thick insulating PAM-rich surface region. No strong correlation between work function of the HILs and device efficiency is seen, indicating that for the particular PLEDs, hole injection/current is not the limiting factor.

Acknowledgements

The authors acknowledge financial support from DuPont Displays. Research in Norrköping is also supported by the Swedish Research Council (VR); by the Swedish Foundation for Strategic Research funded Center for Organic Electronics,

COE@COIN, and Center for Advanced Molecular Materials, CAMM; by the Center for Nanotechnology (CeNano) at Linköping University; by the Carl Tryggers Foundation and by RTN-LAMINATE (EU project number 00135).

References

- [1] C.S. Lee et al., *Synth. Met.* 135–136 (2003) 13.
- [2] F. Jonas, J.T. Morrison, *Synth. Met.* 85 (1997) 1397.
- [3] X. Yongyao et al., *J. Electrochem. Soc.* 147 (2000) 2050.
- [4] Y. Yang, A.J. Heeger, *Nature* 372 (1994) 344.
- [5] J.H. Shim et al., *Thin Solid Films* 441 (2003) 284.
- [6] Q. Pei et al., *Synth. Met.* 85 (1997) 1229.
- [7] M. Fahlman, S. Jasty, A.J. Epstein, *Synth. Met.* 85 (1997) 1323.
- [8] S.K. Dhawan et al., *Sens. Actuators, B* 40 (1997) 99.
- [9] D. Cottevieille et al., *Synth. Met.* 101 (1999) 703.
- [10] J. Isaksson et al., *Adv. Mater.* 16 (2004) 316.
- [11] K.Z. Xing et al., *Adv. Mat.* 9 (1997) 1027.
- [12] L.-M. Do et al., *Synth. Met.* 111–112 (2000) 249.
- [13] W. Bijnens et al., *Synth. Met.* 96 (1998) 87.
- [14] B. Werner et al., PANi as a hole injection layer for OLEDs and PLEDs, in: *Organic Light-Emitting Materials and Devices VI*, SPIE-Int. Soc. Opt. Eng., 2003.
- [15] M.J. Cazeza et al., *Synth. Met.* 98 (1998) 45.
- [16] Y. Yang, A.J. Heeger, *Appl. Phys. Lett.* 64 (1994) 1245.
- [17] S. Karg et al., *Synth. Met.* 80 (1996) 111.
- [18] J.C. Carter et al., *Appl. Phys. Lett.* 71 (1997) 34.
- [19] A.C. Arias et al., *Synth. Met.* 102 (1999) 953.
- [20] R.W.T. Higgins, N.A. Zaidi, A.P. Monkman, *Adv. Funct. Mater.* 11 (2001) 407.
- [21] L.S. Hung, C.W. Tang, M.G. Mason, *Appl. Phys. Lett.* 70 (1997) 152.
- [22] T.M. Brown et al., *Appl. Phys. Lett.* 77 (2000) 3096.
- [23] P. Piromreun et al., *Appl. Phys. Lett.* 77 (2000) 2403.
- [24] H. Ishii et al., *J. Lumin.* 87–89 (2000) 61.
- [25] L. Groenendaal et al., *Adv. Mater.* 12 (2000) 481.
- [26] T. Kugler et al., *Chem. Phys. Lett.* 310 (1999) 391.
- [27] M.P. de Jong, L.J. van IJendoorn, M.J.A. de Voigt, *Appl. Phys. Lett.* 77 (2000) 2255.
- [28] A.W. Denier van der Gon, J. Birgerson, M. Fahlman, W.R. Salaneck, *Org. Electron.* 3 (2002) 111.
- [29] X. Crispin et al., *J. Polym. Sci., Part B: Polym. Phys.* 41 (2003) 2561.
- [30] H.J. Ahonen, J. Lukkari, J. Kankare, *Macromolecules* 33 (2000) 6787.
- [31] G. Greczynski, T. Kugler, W.R. Salaneck, *Thin Solid Films* 354 (1999) 129.
- [32] S.K.M. Jönsson et al., *Synth. Met.* 139 (2003) 1.
- [33] M. Fahlman et al., Iron-polyaniline interfaces: Implications for corrosion protection, in: P. Zarras, J.D. Stenger-Smith, Y. Wei (Eds.), *Electroactive Polymers for Corrosion Control*, ACS Symposium Series 843, 2003.

- [34] G. Greczynski et al., *J. Electron Spectrosc. Relat. Phenom.* 121 (2001) 1.
- [35] Y. Geng et al., *Synth. Met.* 84 (1997) 81.
- [36] I. Kulszewicz-Bajer et al., *Synth. Met.* 114 (2000) 125.
- [37] W. Zheng et al., *Synth. Met.* 84 (1997) 63.
- [38] G. Greczynski, M. Fahlman, W.R. Salaneck, *Chem. Phys. Lett.* 321 (2000) 379.



The interplay between the optical and electronic properties of light-emitting-diode applicable conjugated polymer blends and their phase-separated morphology

Monika Voigt, John Chappell, Thom Rowson, Ashley Cadby, Mark Geoghegan, Richard A.L. Jones, David G. Lidzey *

Department of Physics and Astronomy, Hicks Building, The University of Sheffield, Hicks Building, Hounsfield Road, Sheffield S3 7RH, United Kingdom

Received 6 August 2004; received in revised form 14 December 2004; accepted 2 February 2005
Available online 14 March 2005

Abstract

We have investigated a series of different blends of the device applicable conjugated polymers poly(9,9-dioctylfluorene) [F8] and poly(9,9-dioctylfluorene-*alt*-benzothiadiazole) [F8BT]. Scanning force microscopy indicates that blend films of F8 and F8BT spin-cast from toluene have more coarsely structured phase-separated domains, whereas films cast from chloroform are much more finely structured. This conclusion is confirmed using photoluminescence (PL) measurements, where we show that the degree of energy transfer from F8 to F8BT can be used as a measure of de-mixing in the blend. We have investigated different F8:F8BT blend films as the active semiconductor in light emitting diodes (LEDs). We find that the electroluminescence (EL) efficiency of the LED is a strong function of the relative composition of the blend, with highest efficiency occurring in blends of 95:5 F8:F8BT. In this particular polymer system, the morphological structure of the blend appears less important in determining LED efficiency than does the blend composition.

© 2005 Elsevier B.V. All rights reserved.

1. Introduction

Blends of conjugated polymers have become increasingly important as the active charge trans-

porting and emissive material in opto-electronic devices [1–3]. This is because the majority of conjugated polymers tend to preferentially transport one type of charge carrier (electrons or holes) and therefore blending different polymers together can be used to create a device-applicable material having improved electronic properties [4]. This approach has been used by a number of different

* Corresponding author. Tel.: +44 114 222 3501; fax: +44 114 272 8079.

E-mail address: d.g.lidzey@sheffield.ac.uk (D.G. Lidzey).

groups to create efficient polymeric light emitting diodes (LEDs) [5–11]. For an excellent overview of the use of polymer blends in LEDs, (in particular those based on polyfluorenes), the reader is directed to a recent comprehensive review [12].

In many cases, polymer blend thin films are not homogeneous. This is because the solution-based process used to cast the film often permits the polymers to undergo de-mixing (phase-separation) before the film eventually vitrifies [13]. This occurs as the large molecular weight of many polymeric materials results in an insufficient entropy gain to generate a negative free energy of mixing. Control over the characteristic length-scale of phase separation can be achieved by control over the kinetics of polymer de-mixing. A widely studied route to achieve this is by solvent quenching. In solvent quenching, the polymers are dissolved in a common solvent and form a homogenous solution. On spin-casting, a phase-separated thin-film is formed when the solvent evaporates to leave the vitrified polymers. A slowly evaporating solvent is expected to give the film more time to develop larger phase-separated regions. Lower vapour pressure solvents can thus be used to create phase-separated films having reduced characteristic length-scales. Alternative approaches to reduce the phase-separation quench-time are to use lower molecular weight polymers, higher temperatures [2] and faster spin-speeds [14]. By adjusting these parameters, the length-scale of phase-separation can be varied from nanometres to microns. In addition to this lateral phase-separation, the broken symmetry imposed by the surface and interface of a thin film can also lead to phase-separation normal to the plane of the film; a process termed ‘self-stratification’ or ‘vertical-segregation’. Whilst phase-separation in both ‘classical’ [13,15] and conjugated [16–20] polymer blend films formed by spin-casting has been well studied, the effect of such phase-separation on the electronic properties of the blend film when used as the active semiconductor in an optoelectronic device is presently an area of active ongoing research [1–3,21,22].

In this paper, we discuss the morphology of a blend of two conjugated polymers, and discuss the role of the blend morphology on their photolu-

minescence (PL) and electroluminescence (EL) properties. The polymers we have used are poly(9,9-dioctylfluorene) [F8] and poly(9,9-dioctylfluorene-*alt*-benzothiadiazole) [F8BT]. Previous studies of these polymers in devices have concentrated on blends of between 5% and 25% F8BT blended into F8, with blends of 5% F8BT in F8 shown to have good performance in LEDs [5,6,23]. Here, we explore the optical, electronic and structural properties of thin-film blends of F8 and F8BT containing a wide range of relative F8BT concentrations, spin-cast from two different solvents: chloroform and toluene. Scanning force microscopy shows that the characteristic length-scale of phase-separation is significantly greater when the blend is spin-coated from toluene compared to when a more volatile solvent is used such as chloroform. Due to the overlap of the PL emission of F8 with the absorption of F8BT, exciton transfer can occur from F8 to F8BT via Förster transfer (dipole–dipole coupling) [24,25]. This transfer process appears partially hindered in films cast from toluene, as such films are strongly phase-separated and undergo surface-stratification, forming a thin (~ 10 nm) surface-rich layer of F8. We have previously argued that photogenerated excitons can become ‘localised’ in this surface-layer [18]. The absence of such a F8 surface layer in films cast from chloroform is accompanied by a more intimate mix between F8 and F8BT, and in these films we measure almost complete energy transfer. We have fabricated LEDs using various F8:F8BT blends as the active semiconducting medium and find that efficiency and performance of devices is found to be a stronger function of the blend composition rather than film morphology.

2. Experimental methods

The chemical structures of the polymers F8 and F8BT are shown in Fig. 1. F8 is a blue-fluorescent polymer that has a large non-dispersive hole mobility ($4 \times 10^{-4} \text{ cm}^{-2} \text{ V}^{-1} \text{ s}^{-1}$ as measured by time-of-flight at an applied field of 0.5 MV cm^{-1} [26]). F8BT is a green fluorescent polymer that has a large but dispersive electron mobility (with the fastest carriers having an effective mobility of

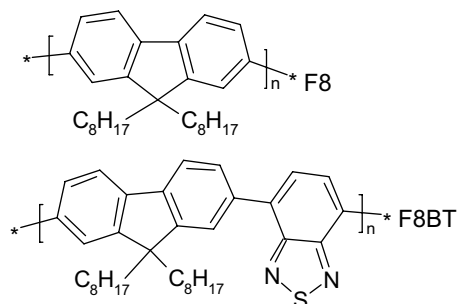


Fig. 1. The chemical structures of F8 and F8BT.

$\sim 10^{-3} \text{ cm}^{-2} \text{ V}^{-1} \text{ s}^{-1}$ also at 0.5 MV cm^{-1}). Time-of-flight measurements have identified F8BT as either having a very low hole-mobility [4,27], or having a hole mobility equal to that of the electron mobility (both being $\sim 10^{-3} \text{ cm}^2 \text{ V}^{-1} \text{ s}^{-1}$) [28]. The difference between these observations was explained on the basis of the F8BT hole mobility being dependent on the exact physical characteristics of the polymer (e.g. molecular mass and polydispersity) [28]. At present we have no specific information regarding the hole-mobility of the F8BT material that we have studied, however our results are consistent with it conducting only electrons.

Polymer blend films were created by firstly mixing F8 and F8BT together in a common solvent (chloroform or toluene), and then spin-casting. In all cases, we refer to the composition of the blend in terms of the mass of F8BT compared to the total combined mass of F8 and F8BT (expressed as a percentage). Such F8:F8BT polymer blends were used as the active semiconductor in an LED. The LED substrate consisted of an ITO anode coated with a 70 nm thick poly(3,4-ethylene-dioxythiophene)/poly(styrene-sulfonic acid) (PEDOT-PSS) film. The PEDOT-PSS was supplied by HC Starck Ltd, (product code Baytron P VP CH8000). An F8BT:F8 blend was then spin-coated onto the PEDOT:PSS film with a relative F8BT concentration ranging from 1% to 90%. For completeness, films were also cast from pure F8 and pure F8BT. In all cases, the coating speed was adjusted between 3000 and 6000 rpm to create a polymer-blend film whose thickness was in the range of 95 to 110 nm. A cathode was then ther-

mally evaporated onto the blend film, consisting of a 300 nm calcium layer capped with 100 nm of aluminium. Devices were evaluated by measuring their current–voltage–luminance characteristics. The EL emission spectra were measured using an 1/8th m spectrograph coupled to a CCD camera.

To study the continuous wave PL emission from the polymer blend films, a 405 nm GaN laser was used as an excitation source. The laser was shone on to the surface of the film and the emission was measured using a CCD spectrograph. We have also characterised the emission from the film by both exciting and recording the PL through the glass-substrate. As the absorption coefficient of F8 at the laser wavelength is almost an order of magnitude greater than that of F8BT, it indicates that the majority (>90%) of the primary excitations (singlet-excitons) are photo-generated on F8 molecules. Blend films were also characterised using a scanning force microscope operating in tapping mode. In all cases, measurements were made on blend films spin-cast on PEDOT:PSS coated ITO.

3. Structural characterisation of F8:F8BT blends

SFM images of F8BT:F8 blends spin-cast from toluene having relative F8BT concentrations of 5%, 25%, 50% and 90% are shown in Fig. 2(a), (b), (c) and (d) respectively. Films cast from chloroform, corresponding to relative F8BT concentrations of 5%, 25%, 50% and 90% are shown in Fig. 2(e), (f), (g) and (h) respectively. For films cast from toluene, it can be seen that the topography of the 5% F8BT blend (Fig. 2(a)) is the smoothest, having a surface characterised by apparently structure-less domains, with a peak-to-peak roughness (determined from a line-scan) of approximately $\pm 8 \text{ nm}$ and a lateral size of $\sim 20 \text{ nm}$. Note however that the surface structure observed here is significantly more textured than that observed in a pure F8 film spin-cast from toluene [29]. This indicates that the presence of even a relatively low fraction of F8BT results in a modification to the film structure. It can be seen that the 25% F8BT blend film cast from toluene (Fig. 2(b)) has a significantly more textured surface, with a roughness of

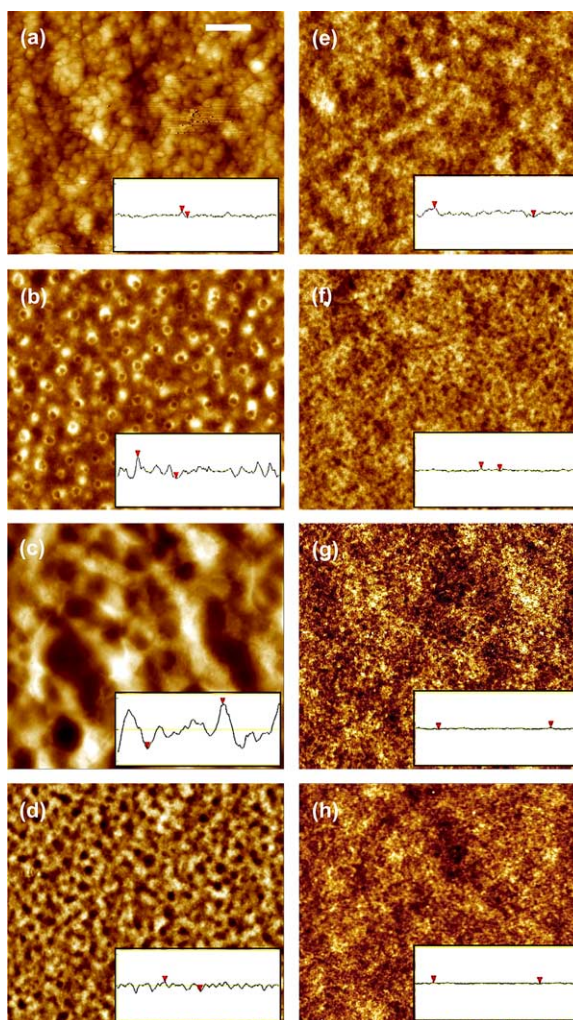


Fig. 2. Topographic SFM image of F8:F8BT blends, having a relative concentration of (a) 5% F8BT, (b) 25% F8BT, (c) 50% F8BT, (d) 90% F8BT spin-cast from toluene and (e) 5% F8BT, (f) 25% F8BT, (g) 50% F8BT and (h) 90% F8BT spin-cast from chloroform. The scale bar is 1 μm for all images. The inset in each image shows a line-scan taken across the image. Here, the arrows indicate the maximum roughness which is (a) 8 nm, (b) 30 nm, (c) 60 nm, (d) 13 nm, (e) 4 nm, (f) 3 nm, (g) 3 nm and (h) 3 nm.

± 30 nm. Here, ring-like structures are observed having an average diameter of ~ 250 nm. When the same blend is spin-coated from xylene, a similar surface morphology is also observed [6]. Whilst we cannot presently identify the composition of such ring-like structures, it is possible that they are formed by the collapse of solvent droplets that became trapped within one of the phases of the blend during spin-casting. Due to the higher solubility of F8 in toluene compared to F8BT, it

is possible that these structures contain a significant fraction of F8.

In a 50% F8BT blend cast from toluene, we find the coarsest phase-separation, with an interpenetrating network formed. Here, the surface roughness is approximately ± 60 nm, with the phase-separated domains having an average lateral length-scale of 1–2 μm . Fig. 2(d) shows a 90% F8BT blend film cast from toluene. This film is characterised by a pitted surface having a rough-

ness ± 13 nm and a characteristic length-scale of ~ 300 nm. Using scanning near field transmission measurements, we have previously studied 50% F8BT blends, and found that the raised network observed in Fig. 2(c) is rich in F8BT, whilst the lower-lying domains are rich in F8 [18]. We also confirmed earlier measurements [5,19,20] that there is a significant degree of mixing in both phases, and that neither phase should be considered as being ‘pure’. This mixing between the polymers in the two phase separated domains is also likely to occur at the other F8:F8BT concentrations studied here.

In blends spin-cast from chloroform (see Fig. 2(e)–(h)) we observe much finer length-scale surface features. The surface roughness of the films is lower than those cast from toluene; for example, the 25% F8BT blend (Fig. 2(f)) has a surface roughness of 3 nm with a typical lateral length-scale of ~ 50 –100 nm. It is not clear whether the surface structures we observe in chloroform cast blends are related to different phase-separated domains, or whether they simply result from fluctuations in film thickness. It is possible (although unlikely) that no phase-separation occurs in chloroform cast films, as the volatile nature of the solvent may present very little opportunity for de-mixing to occur before the film vitrifies. In general, we find that blend films cast from chloroform are very much more homogeneous than are films cast from toluene. This results from the fact that chloroform is a much more volatile solvent, and thus the time available for the system to undergo phase-separation during spin-casting is significantly reduced.

We have previously used ion-beam depth profiling experiments to study surface stratification in blends of F8 and F8BT [18]. This technique can be used to determine the depth dependent composition of a deuterium-labelled component in a thin film [30]. We have previously shown that a 10 nm thick surface rich layer of deuterated-F8 (d-F8) is present in 50:50 F8:F8BT blends cast from toluene, and that this layer runs continuously over the entire surface of the film. Such surface wetting layers appear to be quite common in other polyfluorene blends [9,21]. Our subsequent measurements [31] demonstrate that an enriched d-F8 surface

layer exists for a wide range of F8BT:F8 concentrations when the film is cast from toluene, however this surface layer is almost completely absent in blends spin-cast from chloroform.

4. Photoluminescence from F8:F8BT blends

Fig. 3(a) shows the normalized PL emission measured from a thin film of the polymers F8 and F8BT, and from blend films of F8BT and F8 spin-cast from chloroform. Data are presented for blends having relative F8BT concentrations of 1%, 5% and 50%. Here, laser excitation was incident on the top surface of the polymer-blend film. The emission from F8 peaks at 430 nm, and has a clearly defined vibronic progression. The emission from F8BT peaks at 535 nm and is essentially featureless apart from a shoulder at 575 nm.

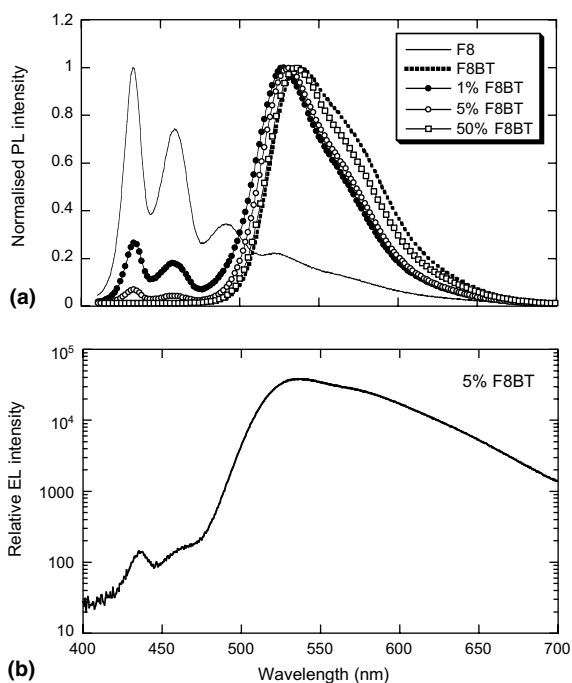


Fig. 3. Part (a) above shows the PL emission from a thin film of F8 and F8BT. PL emission is also shown for F8:F8BT blend films containing 1%, 5% and 50% F8BT. In all cases, the films were spin-cast from chloroform. Part (b) shows (on a logarithmic scale) the EL emission from an LED containing a blend film of 5% F8BT / 95% F8 spin-cast from chloroform.

In the blend films there appears to be a gradual blue-shift in the short-wavelength edge of the F8BT as its concentration in the blend is reduced. This spectral-shift most likely occurs due to reduced self-absorption. This is because there is a relatively large overlap between emission and absorption of F8BT around 500 nm (i.e. $\alpha = 27,000 \text{ cm}^{-1}$ at 500 nm), and as the F8BT is diluted into F8 this self-absorption drops significantly (as F8 is effectively transparent at wavelengths above 450 nm). This reduction in self-absorption results in a relative enhancement in the PL emission from the short-wavelength side of the F8BT emission band, resulting in a blue-shift of emission. From the spectra shown in Fig. 3(a), it can also be seen that there is a progressive reduction in emission intensity around 575 nm as the relative F8BT concentration is reduced. Whilst we cannot conclusively account for this change, it is possible that it originates from a reconfiguration of the F8BT molecular conformation, resulting in a change in the Huang-Rhys parameter. We note however that red-shifted and broadened features observed in PL are often assigned to inter-chain interactions resulting from the formation of excimers. Interchain states such as excimers and exciplexes have a weak coupling to the ground state, resulting in a relatively reduced fluorescence emission rate. To investigate whether excimer emission contributes to the spectral broadening observed in the F8BT PL spectrum, we have measured its fluorescence decay lifetime in thin-film form. We find that the F8BT fluorescence emission is characterised by a mono-exponential decay, having a lifetime of 1.6 ns at 550 nm, which lengthens to 2 ns at 650 nm. Compared to many conjugated polymers this is a relatively long fluorescence decay lifetime. However F8BT has been shown to have a high fluorescence quantum yield of up to 80% [32]. This indicates that non-radiative channels that compete with fluorescence emission (and therefore shorten the observed decay lifetime) appear to be relatively suppressed. Significantly, we do not detect any decay components having decay lifetimes in the range of 10's of ns, indicating that excimer emission is not a dominant decay channel in these particular F8BT films.

It can be seen that all the blend spectra shown in Fig. 3(a) are dominated by the emission from F8BT. However there remains a significant fraction of the F8 emission from the 5% and 1% F8BT containing films. We can quantify the degree of energy transfer between F8 and F8BT by calculating the relative intensity of the 'residual' F8 emission (I_{F8}) [obtained by integrating the blend emission spectrum between 410 and 475 nm], compared to the total combined F8 and F8BT emission (I_{TOTAL}) [obtained by integrating between 410 and 700 nm]. This is expressed using the parameter ε , where $\varepsilon = I_{\text{F8}} / I_{\text{TOTAL}}$. Fig. 4 plots ε determined for different blend films as a function of the relative F8BT concentration, spin-cast from either toluene or chloroform. We find that for both blends cast from toluene and chloroform, ε is virtually independent on whether the film was excited with the laser incident on the surface or through the substrate. For films cast from toluene, it can be seen that ε remains almost constant between 0.05 and 0.1. However for films cast from chloroform, ε decreases very rapidly as the F8BT concentration is increased. This degree of mixing between the F8 and F8BT is likely to be strongly dependent on the specific molecular weights of the polymers used. Thus exciton transfer may well be more (or less) efficient in the same nominal F8/F8BT blend depending on the exact source of the polymers that are used.

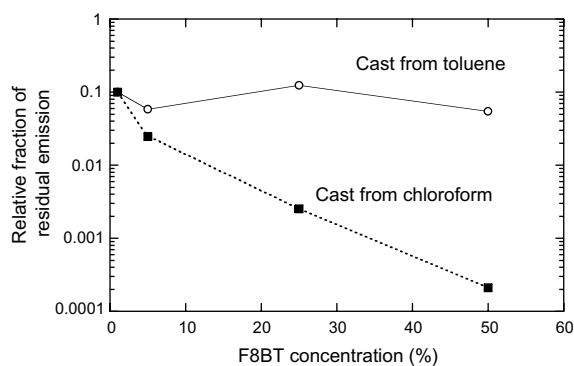


Fig. 4. The fractional emission of residual F8 fluorescence compared to the total fluorescence emission as a function of the relative F8BT concentration. Data are shown for blends cast from both toluene and chloroform. Note that the fluorescence was generated following laser excitation into the F8 component of the blend.

We have previously argued [18] that the PL emission properties of F8:F8BT blends are dominated by the presence of the F8-rich surface layer. In this model, we proposed that the majority of the residual F8 emission in such blends came from excitons that had been photo-generated on F8 molecules in the F8-rich surface layer, but did not diffuse into the ‘bulk’ of the film and undergo Förster-transfer to F8BT. We believe that the results presented here support this idea, as we find that in films cast from toluene (which have a F8-rich surface layer at all F8BT concentrations), there is always a significant fraction of excitons that recombine on F8 without undergoing transfer to F8BT. However in films cast from chloroform, this F8-rich surface layer is absent, with energy transfer from F8 to the F8BT ‘acceptor’ molecules being a strong function of the relative F8BT concentration.

It is interesting to note however, that the F8-rich surface layer on the toluene-cast films does not cause any significant asymmetry in the intensity of residual emission, dependent on whether the film was excited with the laser incident on the surface or through the substrate. There are a number of possible explanations for this observation: First, as the polymer films studied are optically thin, combined with the fact that the F8BT molecules have an absorption coefficient at the excitation wavelength that is an order of magnitude lower than that of F8, it is possible that a sub-phase rich in F8BT will be largely transparent to the excitation laser. In this case, the F8 surface-layer might absorb an equal amount of laser-radiation whether it is excited through the substrate or through the top air-surface interface. Second, it is also probable that some of the residual F8 emission is generated within the bulk of the film. This would necessarily imply that there is a degree of nanoscale de-mixing between F8 and F8BT even within the different phase-separated domains.

5. Electroluminescence from F8:F8BT blends

Fig. 3(b) shows the EL emission spectra (plotted on a logarithmic scale) recorded from LEDs based on a 5% F8BT blend spin-cast from

chloroform. It can be seen that in direct contrast to the PL emission, the residual F8 emission is now very strongly suppressed. For example, a 5% F8BT blend cast from chloroform is characterised by a ratio of residual F8 emission fraction determined from the EL spectra to be $\epsilon_{\text{EL}} = 0.002$. This compares with a measurement of the residual emission following photoexcitation from the same blend of $\epsilon_{\text{PL}} = 0.06$ (i.e. ~ 30 times greater). As our SFM and ion-beam measurements indicate that blend films cast from chloroform are relatively homogeneous, we assume that the local composition of the blend from where the PL is generated (which is in general closer to the film surface) is similar to where EL is generated (which is assumed to be somewhere within the ‘bulk’ of the film).

The significant absence of the residual F8 emission from the EL emission spectra suggests that excitons are primarily created on F8BT molecules following the injection of electrons and holes into the device. This could either occur by the direct recombination of an electron and a hole on an F8BT molecule, or by the intermediate formation of a geminate electron–hole pair, where an electron resides on an F8BT molecule and a hole on a F8 molecule. An exciton would then be created on the F8BT molecule following charge transfer of the hole. This latter process would require electron injection and transport to preferentially occur via F8BT molecules, with hole injection and transport to occur via F8. Such a picture has been used to explain the operation of other polyfluorene copolymer blends that incorporate F8BT [10].

The electron affinity of F8BT (as measured by cyclic voltametry [CV]) is relatively large compared to that of F8 (being 3.0 and 2.12 eV respectively [34]). F8 is also known to be strongly electron trapping. Thus it is likely that electron injection and transport will occur primarily via F8BT. The ionization potential of F8 and F8BT are very similar—both being approximately 5.8 to 5.9 eV [33] (as measured by CV). Therefore hole injection into both F8 and F8BT molecules is possible. Whether holes are principally transported by F8 or by F8BT is therefore determined by their relative hole-mobility. F8 is known to have a relatively large, non-dispersive hole mobility [26].

The mobility of holes in F8BT is dependent on the particular source of the polymer; early reports indicated that holes are strongly trapped in F8BT [4,27]. More recent work on F8BT has suggested that electrons and holes have a similar mobility [28]. To explain this difference it was suggested that this increase in hole-transport occurred due to improved control over the chemical synthesis [28], with effects of molecular weight and polydispersity being highlighted. It has also been demonstrated that the mobility of carriers in conjugated polymers is highly dependent on the processing history of the polymer, with effects such as thermal annealing [28] and the alignment of polymer chains [35] all being important contributory factors. It is therefore likely that the effective mobility of charges of either polarity in a polymer blend will be strongly dependent on the detailed nanostructure of the blend. This suggests that a simple extrapolation of electronic properties (such as mobility) measured in a 'pure' film may not a good predictor of the actual mobility of the same material when it is incorporated into a blend.

Fig. 5(a) shows the EL efficiency (in cd A^{-1}) measured at 10 V for LEDs having their active polymer blend layer cast either from toluene or chloroform. It can be seen for both types of LED, the EL efficiency initially rises as the F8BT concentration increases and then reaches its maximum value at around 5% F8BT. However as the F8BT concentration is increased further, the EL efficiency then falls for both types of LED. The highest efficiency EL emission (4.15 cd A^{-1}) was emitted from LEDs based on 5% F8BT spin-cast from toluene, which reach a brightness of $\sim 1000 \text{ cd m}^{-2}$ at 10 V. Although the EL efficiency of 5% F8BT devices is less than previous reports of F8 / F8BT blend LEDs having the same composition (which reported efficiencies of up to 8.5 cd/A) [23], we note that research by the Dow Chemical Corporation on this system has also identified 5% F8BT blends as having the best performance in LEDs.

Fig. 5(b) shows the LED turn-on voltage, arbitrarily defined as the voltage required to achieve an LED brightness of 10 cd m^{-2} . Here, it can be seen that the turn on-voltage for LEDs cast from toluene are (at low F8BT concentrations) lower than

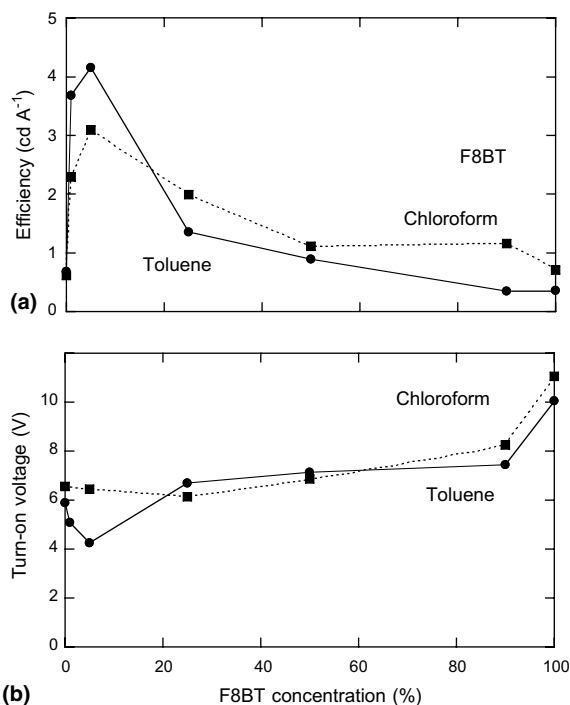


Fig. 5. The electronic properties of LEDs based on blends of F8 and F8BT as a function of F8BT concentration. Part (a) shows the device EL efficiency (in cd A^{-1}) measured at 10 V. Part (b) shows the LED turn-on voltage, arbitrarily defined as the voltage required to achieve an LED brightness of 10 cd m^{-2} .

those cast from chloroform. In both cases, the turn on voltage is approximately equal for F8BT concentrations $\geq 25\%$, and increases significantly for F8BT concentrations $\geq 90\%$. It can also be seen that for blend films containing more than 5% F8BT, LEDs with their active layer cast from chloroform have rather higher EL efficiency than those cast from toluene.

In general, the efficiency of organic LEDs is dependent on the relative balance between electron and hole currents in the active semiconductor layer. The relative balance between the electron and hole currents within an LED are functions of the relative mobility of electrons and holes and also the ease by which they are injected into the device. Previous work [5] has shown that F8BT forms an ohmic contact with a calcium cathode, whilst F8 forms a blocking contact with a PEDOT:PSS anode. Therefore the relative ease by which electrons can be injected into F8BT

compared to holes into F8 suggests that the blend will become dominated by electron transport above some critical F8BT concentration. Our results confirm this, and we find that small ($\sim 5\%$) amounts of F8BT doped into F8 significantly improve the efficiency of EL emission by presumably improving electron-injection and electron transport in the device. However this improvement in device efficiency is quickly reversed once the F8BT concentration exceeds 5%, as the injection and transport of electrons becomes more efficient than that of holes, leading to imbalanced charge fluxes within the device and thus reduced exciton generation efficiency.

It can be seen that LEDs based on 100% F8BT have the lowest EL efficiency and the highest turn-on voltage of all devices studied. Such high turn-on voltages suggest that charge is being trapped within the LED. If we assume that the particular F8BT material that we are using is characterised by a low hole-mobility, then such trapped charge is most likely to be electrons that have accumulated at the interface with the PEDOT:PSS layer which is believed to be an electron-blocking material. The build-up of electrons at the anode interface in LEDs composed of a blend of 95% F8/5% F8BT has previously been identified using electromodulation spectroscopy [36,37]. As the injection of carriers is known to be mobility dependent [38], a low hole mobility in F8BT would also result in a low hole density within the active layer, thus accounting for the poor EL efficiency of the 100% F8BT LEDs.

The role of the enriched F8 surface layer in modifying LED efficiency is not presently understood. As demonstrated in Fig. 5(a), LEDs having this surface layer (i.e. those cast from toluene) have a higher EL efficiency at F8BT concentrations $\leq 5\%$, but lower EL efficiency for F8BT concentrations $> 5\%$. If (as we propose above) electrons dominate the charge flow through the LED for F8BT concentrations $> 5\%$, it suggests that there is a sufficient concentration of F8BT molecules in the F8-rich surface layer to not significantly impede electron injection. It is possible however such a F8 rich surface layer might actually improve the injection of electrons into the device. We note that a recent study [39] has shown

that it is possible to gain significant improvements in the efficiency of a polymeric LED by inserting a thin (10 nm) layer of an insulating (saturated) polymer between the interface of the conjugated polymer and the cathode. Here, it was argued that the presence of a low dielectric constant layer reduced the effective barrier for electron injection into the conjugated polymer. Whether the F8 rich surface-layer fulfils a similar role is unknown.

Our results indicate that at F8BT concentrations $> 5\%$, LEDs having fine-scale phase separation (i.e. those cast from chloroform) have slightly higher EL efficiencies than those in which the film appears coarsely structured (cast from toluene). It has been shown that such strong phase-separation can be used to good effect in photovoltaic devices based on polyfluorene blends [3]. Here it was found that the external quantum efficiency of the device scaled linearly with the interfacial area of the phase-separated domains, implying that charge pairs generated close to an interface could diffuse to a preferential rich-phase and thus find a direct percolation path to the collection electrode. In F8BT/F8 blends cast from toluene, we tentatively suggest that this relatively coarse phase-separation also leads to spatially separated electron and hole leakage-currents, thereby reducing the exciton generation efficiency. However it is clear that the relative difference in the efficiency between LEDs cast from toluene and chloroform is relatively small, confirming that neither of the blend-phases should be considered as pure, effectively reducing the probability of charge carriers of either sign transversing the entire thickness of the device without undergoing recombination with a charge carrier of opposite polarity. This indicates that in this particular blend, the degree of phase-separation is less important in determining device efficiency than is the overall composition of the blend.

6. Summary

We find that F8:F8BT blend films spin-cast from chloroform appear relatively homogeneous and well-mixed, whereas films cast from toluene undergo coarse phase-separation at F8BT

concentrations >5%. Films cast from toluene are also characterised by an F8-rich surface layer that is absent in films cast from chloroform. Through PL emission measurements, we found that a fraction of the excitons photo-generated in strongly demixed films are unable to undergo energy transfer to F8BT and result in the residual F8 emission observed in the PL spectra. Blend films cast from chloroform are more finely mixed and do not have an F8-rich surface layer. In such finely mixed blends, exciton transfer from F8 to F8BT is virtually complete at low (~5%) F8BT concentrations.

F8:F8BT blends were used as the active layer in LEDs. We find that devices based on high concentrations of F8BT have poor EL efficiency, an effect that we ascribe to the device charge-flow being dominated by electron injection and transport. We find in general that the overall composition of the blend has a more profound impact on LED efficiency than does the degree of polymer mixing.

Acknowledgements

We thank Robert Fletcher and Jim O'Brien at The Dow Chemical Company for the gift of the F8 and F8BT polymers and Alasdair Campbell for useful comments made during the preparation of the manuscript. We thank Linda Swanson and Ramune Rutkaite for the fluorescence lifetime measurements on F8BT. We gratefully acknowledge the UK Engineering and Physical Science Research Council for support of this work through grants GR/R26658/01 (Polymer blend semiconductor devices: the interplay of polymer physics and semiconductor physics), GR/R68279101 (DISPLAY) and GR/S58331 (Time-resolved scanning near-field optical microscopy of device applicable polymer blends). This work was performed as part of the Nanoscale Science and Technology M.Sc. course run jointly between the Universities of Sheffield and Leeds.

References

- [1] P.F. van Hutten, V.V. Krasnikov, G. Hadziioannou, in: W.R. Salaneck, K. Seki, A. Khan, J.J. Pireaux (Eds.), *Conjugated Polymer and Molecular Interfaces*, Marcel Dekker Inc., New York, Basel, 2001.
- [2] J.J.M. Halls, A.C. Arias, J.D. Mackenzie, W. Wu, M. Inbasekaran, E.P. Woo, R.H. Friend, *Adv. Mater.* 12 (7) (2000) 498–502.
- [3] H.J. Snaith, A.C. Arias, A.C. Morteani, C. Silva, R.H. Friend, *Nano Letters* 2 (12) (2002) 1353–1357.
- [4] A.J. Campbell, H. Antoniadis, T. Virgili, D.G. Lidzey, X. Wang, D.D.C. Bradley, in: Z.H. Kafafi (Ed.), *Proceedings of SPIE*, 4464, 2002, pp. 211–222.
- [5] J. Morgado, R.H. Friend, F. Cacialli, *Appl. Phys. Lett.* 80 (2002) 2436.
- [6] J. Morgado, E. Moons, R.H. Friend, F. Cacialli, *Adv. Mater.* 13 (2001) 810.
- [7] A. Charas, J. Morgado, J.M.G. Martinho, A. Fedorov, L. Alcácer, F. Cacialli, *J. Mater. Chem.* 12 (2002) 3523–3527.
- [8] J. Liu, Y. Shi, Y. Yang, *Appl. Phys. Lett.* 79 (5) (2001) 578–580.
- [9] N. Corcoran, A.C. Arias, J.S. Kim, J.D. MacKenzie, R.H. Friend, *Appl. Phys. Lett.* 82 (2) (2003) 299–301.
- [10] A.C. Morteani, A.S. Dhoot, J.S. Kim, C. Silva, N.C. Greenham, C. Murphy, E. Moons, S. Ciná, J.H. Burroughes, R.H. Friend, *Adv. Mater.* 15 (20) (2003) 1708–1712.
- [11] F. Hide, C.Y. Yang, A.J. Heeger, *Synth. Met.* 85 (1997) 1355–1356.
- [12] E. Moons, *J. Phys.: Condens. Matter* 14 (2002) 12235.
- [13] S. Walheim, M. Böltau, U. Steiner, G. Krausch, in: R.W. Richards, S.K. Peace (Eds.), *Polymer Surfaces and Interfaces III*, John Wiley and Sons Ltd., 1999.
- [14] K. Dalnoki-Veress, J.A. Forrest, J.R. Stevens, J.R. Dutcher, *Physica A* 239 (1997) 87–94.
- [15] M. Geoghegan, G. Krausch, *Prog. Polym. Sci.* 28 (2003) 261–302.
- [16] C.M. Ramsdale, I.C. Bache, J.D. MacKenzie, D.S. Thomas, A.C. Arias, A.M. Donald, R.H. Friend, N.C. Greenham, *Physica E* 14 (2002) 268–271.
- [17] J. Chappell, D.G. Lidzey, *J. Microsc.* 209 (3) (2003) 188–193.
- [18] J. Chappell, D.G. Lidzey, P.C. Jukes, A.M. Higgins, R.L. Thompson, S. O'Connor, I. Grizzi, R. Fletcher, J. O'Brien, M. Geoghegan, R.A.L. Jones, *Nature Materials* 2 (2003) 616–621.
- [19] R. Stevenson, R.G. Milner, D. Richards, A.C. Arias, J.D. Mackenzie, J.J.M. Halls, R.H. Friend, D.-J. Kang, M. Blamire, *J. Microsc.* 202 (2) (2001) 433–438.
- [20] R. Stevenson, R. Riehn, R.G. Milner, D. Richards, E. Moons, D.-J. Kang, M. Blamire, J. Morgado, F. Cacialli, *Appl. Phys. Lett.* 79 (6) (2001) 833–835.
- [21] A.C. Arias, J.D. MacKenzie, R. Stevenson, J.J.M. Halls, M. Inbasekaran, E.P. Woo, D. Richards, R.H. Friend, *Macromol.* 34 (2001) 6005–6013.
- [22] A.C. Arias, N. Corcoran, M. Banach, R.H. Friend, J.D. MacKenzie, W.T.S. Huck, *Appl. Phys. Lett.* 80 (10) (2002) 1695–1697.
- [23] C.I. Wilkinson, D.G. Lidzey, L.C. Palilis, R.B. Fletcher, S.J. Martin, X.H. Wang, D.D.C. Bradley, *Appl. Phys. Lett.* 79 (2) (2001) 171–173.

- [24] A.R. Buckley, M.D. Rahn, J. Hill, J. Cabanillas-Gonzalez, A.M. Fox, D.D.C. Bradley, *Chem. Phys. Lett.* 339 (2001) 331.
- [25] J. Hill, S.Y. Heriot, O. Worsfold, T.H. Richardson, A.M. Fox, D.D.C. Bradley, *Synth. Met.* 139 (3) (2003) 787–790.
- [26] M. Redecker, D.D.C. Bradley, M. Inbasekaran, E.P. Woo, *Appl. Phys. Lett.* 73 (1998) 1565–1567.
- [27] A.J. Campbell, D.D.C. Bradley, H. Antoniadis, *Appl. Phys. Lett.* 79 (14) (2001) 2133–2135.
- [28] T. Kreouzis, D.D.C. Bradley, A.J. Campbell, *Proc. SPIE* 5214 (2004) 141–149.
- [29] M. Ariu, D.G. Lidzey, M. Lavrentiev, D.D.C. Bradley, M. Jandke, P. Stroehriegel, *Synth. Met.* 116 (1–3) (2001) 217–221.
- [30] M. Geoghegan, in: R.W. Richards, S.K. Peace (Eds.), *Polymer Surfaces and Interfaces III*, John Wiley & Sons Ltd., Chichester, 1999, pp. 43–73.
- [31] A.M. Higgins, S.J. Martin, R.L. Thompson, M. Voigt, D.G. Lidzey, R.A.L. Jones, M. Geoghegan, *J. Phys.: Condens. Matter* 17 (2005) 1319.
- [32] A.C. Morteani, P. Sreearunothai, L.M. Herz, R.H. Friend, C. Silva, *Phys. Rev. Lett.* 92 (24) (2004) 247402.
- [33] R.B. Fletcher, Dow Chemical Company, private communication.
- [34] S. Janietz, D.D.C. Bradley, M. Grell, C. Giebeler, M. Inbasekaran, E.P. Woo, *Appl. Phys. Lett.* 73 (17) (1998) 2453–2455.
- [35] H. Sirringhaus, R.J. Wilson, R.H. Friend, M. Inbasekaran, W. Wu, E.P. Woo, M. Grell, D.D.C. Bradley, *Appl. Phys. Lett.* 77 (3) (2000) 406–408.
- [36] P.A. Lane, J.C. deMello, R.B. Fletcher, M. Bernius, *Appl. Phys. Lett.* 83 (17) (2003) 3611–3613.
- [37] P.J. Brewer, P.A. Lane, A.J. deMello, D.D.C. Bradley, J.C. deMello, *Adv. Funct. Mater.* 14 (6) (2004) 562–570.
- [38] Y. Shen, M.W. Klein, D.B. Jacobs, J.C. Scott, G. Malliaras, *Phys. Rev. Lett.* 86 (17) (2001) 3867–3870.
- [39] J.H. Park, O.O. Park, J.-W. Yu, J.K. Kim, Y.C. Kim, *Appl. Phys. Lett.* 84 (10) (2004) 1783–1785.



Impact of electrode contamination on the α -NPD/Au hole injection barrier

A. Wan, J. Hwang, F. Amy, A. Kahn *

Department of Electrical Engineering, Engineering Quadrangle, Princeton University, Princeton, NJ 08544, USA

Received 3 January 2005; received in revised form 15 February 2005; accepted 22 February 2005
Available online 19 March 2005

Abstract

This paper addresses the effects of ambient exposure of a polycrystalline Au electrode prior to making contact with the hole-transport material *N,N'*-diphenyl-*N,N'*-bis (1-naphthyl)-1,1'-biphenyl-4,4'-diamine (α -NPD). Ultraviolet photoemission spectroscopy (UPS) and current–voltage (*I–V*) measurements are used to investigate the resulting hole barrier and charge injection characteristics. UPS measurements show that the hole barrier with the contaminated low work function Au electrode is reduced by 0.4–0.6 eV with respect to the barrier with the clean high work function Au electrode. The corresponding interface dipoles are 0.3 eV for the former and 1.3 eV for the latter. *I–V* measurements confirm this unexpected change in barrier. These results are accounted for using the induced density of interface state model, and considering the role of the contamination layer in reducing the direct interaction between metal and molecules.

© 2005 Elsevier B.V. All rights reserved.

1. Introduction

Standard processing of organic light emitting diodes (OLEDs) and other organic devices often involve exposure of electrode surfaces and organic interfaces to controlled atmosphere (e.g. N₂) or ambient conditions. The adsorption of gas molecules can have a significant impact on the properties of organic materials, e.g. via doping [1], and of

devices, e.g. via changes in energy barriers at exposed metal–organic (MO) [2] or organic–organic interfaces. Much work has been done to characterize MO interfaces of small molecule [3,5–10,12,14] and polymer based devices [3,4,8,11], prepared under ultra-high vacuum (UHV) conditions (base pressure $\sim 10^{-9}$ – 10^{-11} Torr), high vacuum (HV) conditions (base pressure $\sim 10^{-6}$ – 10^{-8} Torr), or in controlled or even ambient atmospheres [1,2,13]. Yet, relatively few studies have focused on the impact of contamination from ambient exposure on the interface electronic structure, i.e., the energy level alignment, in organic devices

* Corresponding author. Tel.: +1 609 258 4642; fax: +1 609 258 6279.

E-mail address: kahn@princeton.edu (A. Kahn).

[1,2,13]. Most metal–organic interfaces prepared and measured under ultra-clean UHV conditions depart from the traditional Scottky–Mott picture and exhibit a significant interface dipole [5–8]. On the other hand, sample preparation at higher pressures (i.e. bell-jar evaporation at base pressure 10^{-6} Torr) or measurements at higher pressures generally lead to different results than those obtained in UHV [1,2]. This infers that charge injection barriers between organics and metals can be significantly modified by the presence of contamination layers [13].

The interface between Au and the hole-transport material *N,N'*-diphenyl-*N,N'*-bis (1-naphthyl)-1,1'-biphenyl-4,4'-diamine (α -NPD) used in OLEDs (Fig. 1) serves here as a model system for studying barriers built under “practical” (i.e., ambient or N_2) conditions. Au is a relatively inert material with high work function (~ 5.3 eV for a clean polycrystalline Au surface), making it a good candidate for studying the effect of contamination of the electrode without significant oxidation and other reactive chemistry. The transport gap and ionization energy (IE) of α -NPD are ~ 4 eV and 5.5 eV, respectively [5,16,17]. Hole injection barriers at metal– α -NPD interfaces are generally in excess of 1 eV, even with high work function electrodes like Au and indium tin oxide (ITO) [16–18], leading to devices that are injection limited even at high field [15]. This situation can be partly remedied using interface layers such as copper phthalocyanine (CuPc) [17] and poly(3,4-ethylenedioxythiophene)/poly(styrene sulfonate) (PEDOT-PSS) [18,19] to reduce the hole barrier.

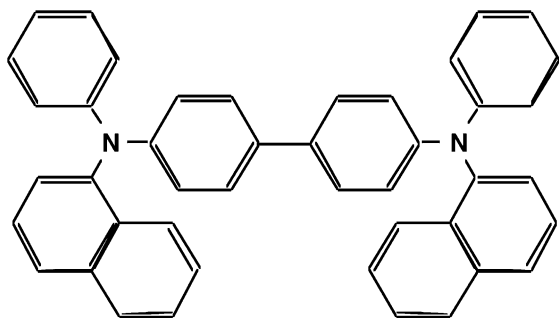


Fig. 1. Chemical structure of the *N,N'*-diphenyl-*N,N'*-bis (1-naphthyl)-1,1'-biphenyl-4,4'-diamine (α -NPD) molecule.

The former introduces an intermediate energy level between the electrode Fermi level and the α -NPD highest occupied molecular orbital (HOMO) level [17]. The latter is a high work function doped polymer (~ 5.1 eV) [18,19]. Typical of organic–organic heterojunctions, the interface dipole between PEDOT-PSS and α -NPD is small, leading to a relatively small energy difference between the PEDOT-PSS Fermi level and the α -NPD HOMO, i.e. a small hole injection barrier. In the present work, we re-examine the formation of the Au– α -NPD interface on a Au surface contaminated by ambient exposure. The paradoxical result is that, although the contaminated Au surface has a lower work function than the clean Au surface, it actually forms a lower hole barrier with α -NPD and is a more efficient hole injector.

2. Experimental

The Au substrates were made by thermal evaporation of Au(800 Å) on Ti(100 Å) on p + –Si(100). The Au surface was cleaned ex situ with a 1 minute degreasing step in acetone and a 1 minute rinse in methanol. The substrates were then introduced into the UHV chamber (base pressure $\sim 2 \times 10^{-10}$ Torr) via a fast load-lock, and either (i) transferred directly to the UHV organic deposition chamber (referred to as “contaminated” Au) or (ii) sputtered clean with 1 keV Ar^+ followed by Au deposition in UHV at room temperature using a Knudsen cell at a rate of ~ 0.5 Å/s (referred to as “clean” Au). In each case, the Au surface composition was determined by Auger electron spectroscopy (AES) and X-ray photoemission spectroscopy (XPS). The substrates were then transferred in situ to the UHV organic deposition chamber (base pressure 1×10^{-9} Torr) where α -NPD was vapor deposited. Thin α -NPD films were incrementally deposited at low rates (~ 0.2 Å/s) for valence state analysis by ultraviolet photoemission spectroscopy (UPS) using a He discharge lamp. The experimental resolution of UPS was 0.15 eV. For each Au surface and α -NPD film, the work function was determined from the positions of the Fermi level measured from the Au Fermi step, and of the vacuum level measured

from the tangent line extrapolation of the onset of the secondary electron peak. For in situ I - V measurements, devices were made by evaporating α -NPD at higher rates (~ 1 – 2 Å/s) to achieve thicknesses more suitable for the measurement (1500 Å), followed by evaporation of a clean top contact Au of 200 Å through a shadow mask.

3. Results and discussion

3.1. Au substrate contamination and work function

AES and UPS spectra taken on clean and contaminated Au substrates are shown in Figs. 2 and 3, respectively. The primary contaminants on the contaminated Au samples are carbon-containing species and trace amounts of O. The C coverage determined by AES and XPS is 0.5–1 monolayer (ML). No contaminant is detected on the clean Au samples, and both valence 5f features and Fermi step are much better defined on these surfaces. The work function of clean Au determined by UPS, is 5.4 ± 0.1 eV, whereas the work function of contaminated Au is 4.7 ± 0.1 eV. Note that significant variations of the work function of contam-

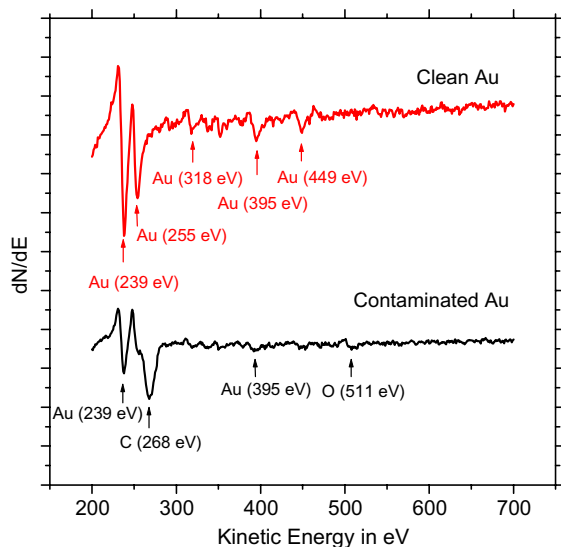


Fig. 2. AES spectra taken from clean Au and contaminated Au. Contaminants on Au consist primarily of C with trace amounts of O.

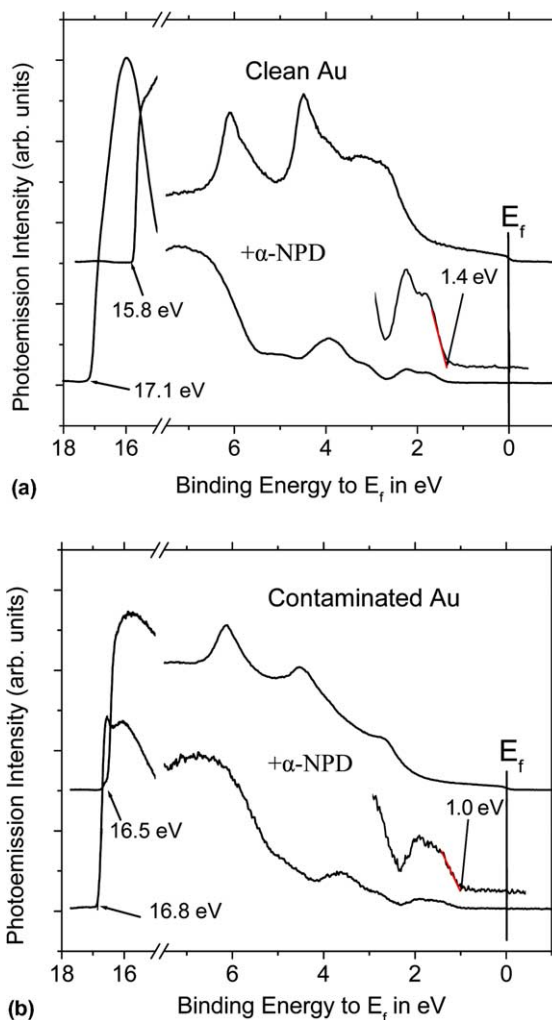


Fig. 3. UPS He I (21.22 eV) spectra of (a) clean Au and clean Au with 50 Å α -NPD, (b) contaminated Au and contaminated Au with 50 Å α -NPD.

inated Au samples are observed, with values ranging from 4.7 eV to 5.1 eV, whereas the work function of clean Au varies only between 5.3 eV and 5.4 eV.

3.2. Au/ α -NPD interface

The UPS spectra of α -NPD films deposited on clean and contaminated Au substrates are shown in Fig. 3(a,b). The lower binding energy region exhibits the characteristic doublet of the HOMO

and HOMO-1 levels [20]. The HOMO level is localized mostly on the lone pairs of the nitrogen atoms and on the para carbon atoms of the two benzene rings in the biphenyl core, and the HOMO-1 level is centered on the lone pairs of the nitrogen atoms [21]. For each interface, the dipole between substrate and organic film is determined by the shift in vacuum level (seen as the shift of the photoemission onset on the left of each panel in Fig. 3), and the hole injection barrier is defined as the energy difference between the low binding energy edge of the HOMO feature and the Fermi level. For clean Au, the interface dipole is 1.3 ± 0.1 eV and the hole injection barrier is 1.4 ± 0.1 eV (Fig. 4(a)). The ionization energy (IE) of the organic film determined for 50 Å α -NPD, is 5.5 ± 0.1 eV, in good agreement with previously reported values [5,16,17]. In comparison, the dipole at the interface with contaminated Au is only 0.3 ± 0.1 eV and the hole barrier is 1.0 ± 0.1 eV (Fig. 4(b)). The IE, measured again on a 50 Å film, is 5.4 ± 0.1 eV, nearly identical to the first value. No change in the position of the α -NPD vacuum level as a function of thicknesses (10–100 Å) is observed in either case, indicating the absence of significant band bending in this thickness range. Some variation in the hole injection barrier is observed as a function of the initial work function of the contaminated Au. Indeed, “contamination” is a poorly controlled state of the surface and contaminated Au work functions as high as 5.1 ± 0.1 eV were observed. Similarly, charge injection barriers as low as 0.7–0.8 eV were

obtained, although the value reported above is more representative of the series of experiments performed in this work.

3.3. In situ I - V measurements

The I - V characteristics measured in situ on devices grown on clean and contaminated Au substrates are shown in Fig. 5. For each substrate, the currents injected from the bottom contact (the substrate) and from the top contact (the evaporated Au pad) are measured as a function of bias. We make here the well grounded approximation that these devices are hole-only devices and that the measured current is predominantly, if not exclusively, a hole current. The reason is 2-fold. First, α -NPD is a hole-transport material with presumably very small electron mobility. Second, the single-particle gap of α -NPD is 4.0 eV [5,16,17]. Given the hole barriers reported above, the electron injection barriers are 2.6 eV and 3.0 eV for clean and contaminated Au, respectively, much larger than the corresponding hole barriers.

The devices grown on clean Au give symmetric I - V characteristics, i.e. equal top-injected and bottom-injected hole currents, over six orders of magnitude of current density (Fig. 5(a)). This, in itself, is an interesting observation, given the expected difference in morphology between interfaces formed by evaporating the organic material on the metal and those formed by reverse deposition sequence. Similar observations have been made for a number of metal–organic–metal structures

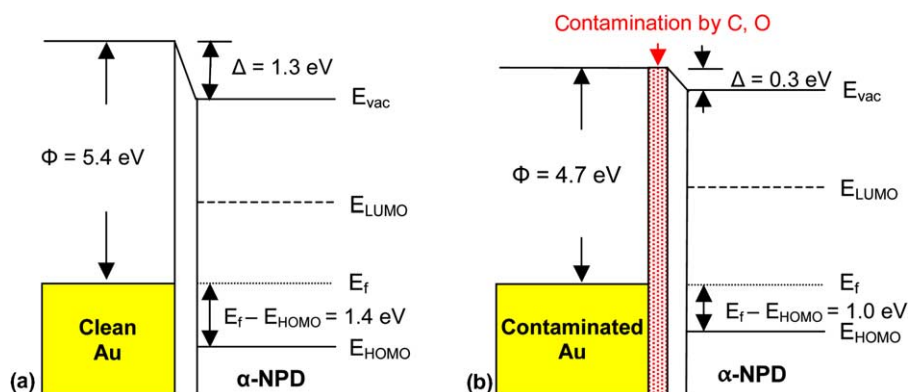


Fig. 4. Energy level alignment deduced from Fig. 3 for (a) α -NPD/clean Au and (b) α -NPD/contaminated Au.

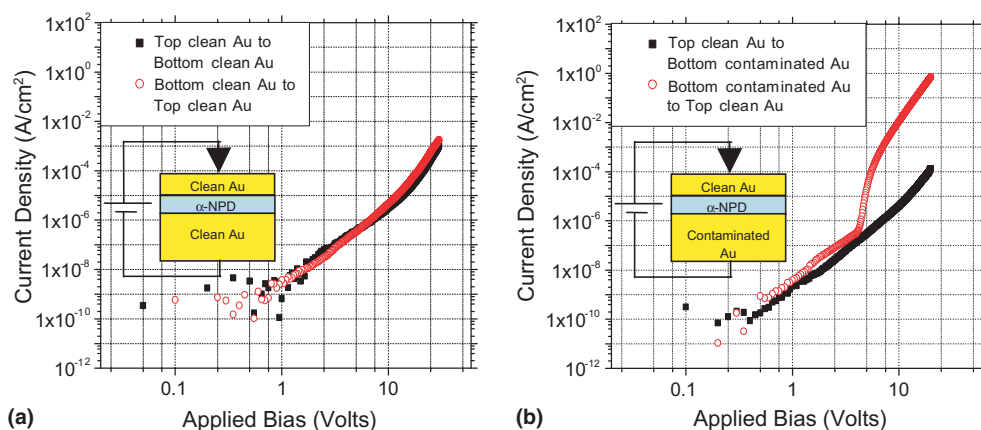


Fig. 5. I - V measurements for (a) 200 Å clean Au/1500 Å α -NPD/clean Au substrate, and (b) 200 Å clean Au/1500 Å α -NPD/contaminated Au substrate.

[19,21]. The devices grown on contaminated Au have asymmetric I - V characteristics. The current injected from the bottom contaminated Au is several orders of magnitude larger than the current injected from the top clean contact above 5 V (Fig. 5(b)). The current injected from the top clean Au contact in Fig. 5(b) is also in very good agreement with the current injected from the top and bottom clean contact in Fig. 5(a), suggesting that the α -NPD films grown on clean and contaminated Au substrates have similar morphologies. Any significant change in the overall structure of the film would lead to significant changes in the I - V characteristics. The difference in hole injection is therefore mostly due to the difference in barrier measured by UPS.

3.4. Discussion

Even though the Schottky–Mott limit is rarely, if ever, achieved at metal–semiconductor interfaces, a high work function metal is expected to, and generally does, produce a lower hole injection barrier than a low work function metal. This is true of metal–organic interfaces as well [5]. In the present case, however, the contaminated Au substrate with lower work function actually produces a lower hole injection barrier than the clean Au substrate. To understand this effect, one must examine the interaction at the MO interface and the role that contamination plays in modifying this

interaction. Since we do not observe measurable band bending in the organic film, doping of the organic material originating from the contamination [1] does not play a significant role. On the other hand, contamination is likely to play a dominant role at the level of the intimate molecule–metal interaction, and to affect directly the formation of the interface dipole and the alignment of the molecular levels with respect to the metal Fermi level.

A metal–semiconductor interface dipole results from a charge exchange defined by the position of the metal Fermi level relative to the semiconductor (valence, conduction and gap) states. In turns, gap states at the semiconductor interface result from a variety of interface interactions, such as bonding and/or chemical reaction or from the physical proximity of the continuum of metallic states to the semiconductor energy gap [22]. The position of the metal Fermi level relative to the charge neutrality level (CNL) of this induced density of states determines the amount and sign of charge transfer to these gap states, and contributes therefore to the interface dipole [23,24]. Finally, another mechanism of interface vacuum level shift is the compression of the metal surface electronic tail by adsorbed molecules, which leads to the apparent formation of a dipole [18,25,26].

In the present case, the contamination layer on the Au surface partially suppresses the density of electrons that normally tails into the vacuum at

the Au surface, and reduces the work function of the surface. By the same token, this contamination layer reduces the impact of the first layer of α -NPD molecules on that electronic tail. The vacuum level shift, or interface dipole, measured after deposition of the first molecular layer of the organic material is therefore smaller than for the clean Au interface (0.3 eV vs 1.3 eV). This mechanism, however, does not explain the change in molecular level position and interface barrier, e.g., E_F -HOMO. Strong chemical bonding is also unlikely for α -NPD on clean as well as on contaminated Au.

The decrease in interface hole barrier between clean and contaminated Au corresponds to a change in the anchoring of the molecular levels with respect to the metal Fermi level. The mechanism that forced the Fermi level in a specific position of the α -NPD gap and induced a dipole has been weakened or eliminated, letting the interface evolve closer to a non-interactive interface, the limit of which is known as the Schottky–Mott limit. The chemical interaction is weak, even on the clean Au substrate, and it is difficult to rationalize the change based on interface bonding. We turn therefore to the concept of charge exchange defined by the occupation of an induced density of interface states (IDIS) [23,24]. The continuum of metallic states in close proximity with the organic semiconductor induces a density of gap states, i.e. the IDIS, at the organic interface. The interface energetics of the MO interface is defined by the metal work function, i.e. the position of the Fermi level, by the position of the charge neutrality level (CNL) of the IDIS, and by the density of states around the CNL. The degree to which E_F and CNL ultimately align depends on the initial difference between the two levels, i.e. the metal work function minus the CNL referenced to the vacuum level, and on the density of states around the CNL.

For the clean Au– α -NPD interface, the initial metal work function is 5.4 eV and the CNL position is \sim 4.2 eV below the vacuum level (or 1.3 eV above the HOMO edge) [24]. As the Fermi level is initially below the CNL of the organic film, the IDIS model predicts an alignment via electron transfer from the organic molecules to the metal,

resulting in an interface vacuum level shift downward from the metal to the organic, as observed in the experiment (Figs. 3 and 4). The experimental position of the Fermi level at the Au– α -NPD interface, determined by UPS, is 1.4 eV above the HOMO edge, which is fairly close to the CNL. It is important to emphasize here that the density of induced gap states around the CNL determines how the system responds to a difference between metal work function and CNL, and how closely E_F ultimately aligns with the CNL. This concept, developed almost two decades ago for inorganic semiconductor–metal interfaces, [27] was recently applied to several MO interfaces and produced the proper quantitative trends in barrier heights vs metal work function [23,24].

The contamination layer at the Au surface prevents the intimate molecule–metal interaction that dominates the clean interface. The simple intuitive chemical picture of such an effect is that the energy levels of the interface molecules are less strongly anchored with respect to the metal. Within the IDIS model, the less intimate contact between molecule and substrate substantially reduces the density of states around the CNL. A recent calculation shows that the density of states around the CNL for a monolayer of PTCDA (perylene-tetracarboxylic dianhydride) molecules lying flat on a Au(111) surface is reduced by a factor of three (down to $0.5 \times 10^{14} \text{ eV}^{-1} \text{ cm}^{-2}$) when the distance between the molecule and the metal surface is increased from 2.8 Å to 3.5 Å [23]. This reduction leads to a weaker pinning of the Fermi level around the CNL and, consequently, to an interface energetics closer to vacuum level alignment (Fig. 4(b)). In the present case, even though the work function of the Au surface is significantly reduced by the contamination (4.7 eV instead of 5.4 eV), the dipole is reduced by a greater amount (1.3 eV for clean Au to 0.3 eV for contaminated Au), resulting in a lower hole injection barrier.

The barrier lowering is consistent with the observed increase by four orders of magnitude in the injected hole current (Fig. 5). Interestingly, a similar increase had been observed at the Au– α -NPD interface when the interface region of the organic film is p-doped with \sim 0.5% F₄-TCNQ [28]. In that case, the current increase is due hole

tunneling through the narrow space charge region, leading to a bulk limited, rather than an injection limited current. In the present case, the current increase is due to the actual lowering of the barrier, as a result of the Au surface contamination. Since there is no significant band bending in the organic film due to the contamination, the similar current increase suggests that the barrier in the contaminated Au device is low enough for the current at high field to no longer be limited by charge injection. While the hole current in the α -NPD devices grown on clean Au is injection limited, the current in the α -NPD devices grown on contaminated Au is limited by bulk transport [28].

As a final note, we stress again that this study compares two interfaces formed on the surface of a same metal, clean surface vs contaminated surface, and explains the observed change in interface energetics in terms of a contamination-induced change in the interface interaction. The conclusions are valid for Au and are presumably applicable to other metals forming non-reactive interfaces with molecular films. These conclusions, however, do not imply that a low work function metal, like Mg or Al, should produce a smaller hole barrier than a high work function metal like Au or Pd. All the studies of dependence of barrier height on the work function of the clean metal show normal behavior, i.e., decrease of the MO hole barrier with increasing metal work function [6–8,29,5]. Furthermore, these conclusions are consistent with results obtained by manipulation of the electrode work function to decrease the interface hole barrier, e.g. via adsorption of a dipolar molecular interlayer on a metal surface [30] or ozone treatment on ITO surfaces [31,32]. In the former case, the molecular interlayer decouples the organic film from the metal surface, much like the contamination layer on the Au surface in the present study, and leads to near vacuum level alignment across the interface and lower hole injection barrier. In the latter case, the electrode material, ITO, exhibits near-metallic conductivity but does not have the continuum of states of a metal, which, on a clean metal surface, is responsible for creating the interface-induced gap states and pinning the Fermi level near the organic CNL. ITO–organic interfaces follow more closely vacuum level

alignment, and respond better to a manipulation of the ITO work function.

4. Summary

Thin films of α -NPD were grown on clean and contaminated Au substrates. The interface energetics measured via UPS and the I – V characteristics show that the hole injection barrier is significantly lower for the low work function electrode (contaminated Au) than for the high work function electrode (clean Au). The result is contrary to conventional wisdom, according to which the higher work function metal should produce a lower hole injection barrier. This is rationalized with a model of interface-induced gap states. The density of states around the charge neutrality level at the clean Au– α -NPD interface leads to a final position of the metal Fermi level 1.4 eV above the organic HOMO, with corresponding charge transfer and interface dipole. The reduction of the induced density of states caused by a physical decoupling of the molecules from the metal surface at the contaminated interface allows the Fermi level to move further away from the CNL and reduces the charge transfer. These results can be used to explain the discrepancies reported in the literature on the relative performances of Au electrodes for hole injection into organic films prepared in high vacuum vs lower vacuum or ambient conditions.

Acknowledgements

This work was supported by the Princeton MRSEC of the National Science Foundation (DMR-0213706) and by a grant from the NSF (DMR-0408589).

References

- [1] Q. Zhou, R.D. Gould, *Thin Solid Films* 317 (1998) 432.
- [2] Y. Shen, A. Hosseini, M.H. Wong, G.G. Malliaras, *Chem. Phys. Chem.* 5 (2004) 16–25.
- [3] L. Yan, Y.L. Gao, *Thin Solid Films* 417 (2002) 101.

- [4] P.F. van Hutten, V.V. Krasnikov, G. Hadziioannou, *Synth. Met.* 122 (2001) 83.
- [5] A. Kahn, N. Koch, W. Gao, *J. Polym. Sci., Polym. Phys.* 41 (2003) 2529.
- [6] H. Ishii, K. Seki, *IEEE Trans. Electron Dev.* 44 (1997) 1295.
- [7] I.G. Hill, A. Rajagopal, A. Kahn, Y. Hu, *Appl. Phys. Lett.* 73 (1998) 662.
- [8] W.R. Salaneck, K. Seki, A. Kahn, J.-J. Pireaux (Eds.), *Conjugated Polymer and Molecular Interfaces*, Dekker, 2002.
- [9] L. Yan, N.J. Watkins, S. Zorba, Y.L. Gao, C.W. Tang, *Appl. Phys. Lett.* 81 (2002) 2752.
- [10] H. Peisert, M. Knupfer, J. Fink, *Appl. Phys. Lett.* 81 (2002) 2400.
- [11] T. Kubota, S. Yokoyama, T. Nakahama, S. Mashiko, Y. Noguchi, Y. Majima, M. Iwamoto, *Thin Solid Films* 393 (2001) 379.
- [12] A.J. Mäkinen, I.G. Hill, T. Noda, Y. Shirota, Z.H. Kafafi, *Appl. Phys. Lett.* 78 (2001) 670.
- [13] C. Shen, I.G. Hill, A. Kahn, *Adv. Mater.* 11 (1999) 1523.
- [14] Y. Kurosaka, N. Tada, Y. Ohmori, K. Yoshino, *Synth. Met.* 102 (1999) 1101.
- [15] J.C. Scott, G.G. Malliaras, *Chem. Phys. Lett.* 299 (1999) 115.
- [16] I.G. Hill, A. Kahn, *J. Appl. Phys.* 84 (1998) 5583.
- [17] I.G. Hill, A. Kahn, *J. Appl. Phys.* 86 (1999) 2116.
- [18] N. Koch, J. Ghijsen, A. Elschner, R.L. Johnson, J.-J. Pireaux, J. Schwarz, A. Kahn, *Appl. Phys. Lett.* 82 (2003) 70.
- [19] N. Koch, A. Elschner, J. Schwartz, A. Kahn, *Appl. Phys. Lett.* 82 (2003) 2281.
- [20] I.G. Hill, A. Kahn, J. Cornill, D.A. dos Santos, J.L. Brédas, *Chem. Phys. Lett.* 17 (2000) 444.
- [21] C. Shen, A. Kahn, J. Schwartz, *J. Appl. Phys.* 89 (2001) 449.
- [22] C. Shen, I.G. Hill, A. Kahn, J. Schwartz, *J. Am. Chem. Soc.* 122 (2000) 5391.
- [23] H. Vazquez, R. Oszwaldowski, P. Pou, J. Ortega, R. Perez, F. Flores, A. Kahn, *Europhys. Lett.* 65 (2004) 802.
- [24] H. Vazquez, F. Flores, R. Oszwaldowski, J. Ortega, R. Perez, A. Kahn, *Appl. Surf. Sci.* 234 (2004) 107.
- [25] H. Ishii, K. Sugiyama, E. Ito, K. Seki, *Adv. Mater.* 11 (1999) 605.
- [26] X. Crispin, V. Geskin, A. Crispin, J. Cornil, R. Lazzaroni, W.R. Salaneck, J.-L. Bredas, *J. Am. Chem. Soc.* 124 (2002) 8131.
- [27] F. Flores, C. Tejedor, *J. Phys. C* 20 (1987) 145.
- [28] W. Gao, A. Kahn, *J. Appl. Phys.* 94 (2003) 359.
- [29] C. Shen, A. Kahn, I.G. Hill, in: W.R. Salaneck, K. Seki, A. Kahn, J.-J. Pireaux (Eds.), *Conjugated Polymer and Molecular Interfaces*, Marcel Dekker, Inc., 2001, pp. 351–400.
- [30] I. Campbell, J.D. Kress, R.L. Martin, D.L. Smith, N.N. Barashkov, J.P. Ferraris, *Appl. Phys. Lett.* 71 (1997) 3528.
- [31] C.C. Wu, C.I. Wu, J.C. Sturm, A. Kahn, *Appl. Phys. Lett.* 70 (1997) 1348.
- [32] D.J. Markiewicz, I.G. Hill, A. Kahn, J. Schwartz, *J. Appl. Phys.* 87 (2000) 572.



Ultraviolet photoelectron spectroscopy of nanocrystalline TiO₂ films sensitized with (2,2'-bipyridyl)ruthenium(II) dyes for photovoltaic applications

Julie H. Snook^a, Lynne A. Samuelson^a, Jayant Kumar^b,
Young-Gi Kim^{c,1}, James E. Whitten^{c,*}

^a Natick Soldier Center, US Army Research, Development, and Engineering Command, Natick, MA 01760, USA

^b Department of Physics and Center for Advanced Materials, University of Massachusetts Lowell, Lowell, MA 01854, USA

^c Department of Chemistry and Center for Advanced Materials, University of Massachusetts Lowell, Lowell, MA 01854, USA

Received 5 January 2005; received in revised form 1 March 2005; accepted 2 March 2005

Available online 24 March 2005

Abstract

Ultraviolet photoelectron spectroscopy (UPS) has been used to determine the highest occupied molecular orbital (HOMO) energy levels of a series of related 2,2'-bipyridyl-substituted ruthenium dyes utilized in the fabrication of photovoltaic devices. UPS analysis of nanocrystalline TiO₂ thin films sensitized with a monolayer of *cis*-dithiocyanato-*N,N*-bis-(2,2'-bipyridyl-4,4'-dicarboxylic acid)-ruthenium(II), commonly referred to as "N3", indicates that the HOMO is located 5.47 eV below the vacuum level. Combination of the UPS results with measurement of the bandgap of the dye by UV–Vis absorbance spectroscopy yields an estimated lowest unoccupied molecular orbital (LUMO) energy of 3.93 eV below the vacuum level. Similar analyses have been performed for the related dyes, (5-amino-1,10-phenanthroline)bis-(2,2'-bipyridyl-4,4'-dicarboxylic acid)-ruthenium(II), (1,10-phenanthroline)bis-(2,2'-bipyridyl-4,4'-dicarboxylic acid)-ruthenium(II), and (5-amino-1,10-phenanthroline)bis-(2,2'-bipyridine)-ruthenium(II); giving values of 3.35, 3.08, and 3.43 eV, respectively, for the positions of the LUMOs below the vacuum level. These results indicate that the LUMO of N3 has better overlap with the conduction band of TiO₂ located 3.70 eV below the vacuum level, and this may at least partially be responsible for its outstanding photovoltaic performance.

© 2005 Elsevier B.V. All rights reserved.

PACS: 79.60.Fr

Keywords: Electronic structure; Photoemission; Photovoltaics

* Corresponding author. Tel.: +978 934 3666.

E-mail address: james_whitten@uml.edu (J.E. Whitten).

¹ Current address: Chemistry Department, University of Florida, Gainesville, FL 32611, USA.

1. Introduction

A variety of organic photovoltaic materials are presently being explored toward the goal of developing high efficiency, high surface area, low cost, lightweight alternatives to traditional silicon-based solar cells. Materials being investigated include conjugated polymers [1–4] and oligomers [5], solution processible blends [6–8] and co-evaporated films [9] of conjugated polymers or oligomers and fullerene, and fullerene derivatives [10,11]. One of the most promising technologies, originally developed by Grätzel and coworkers [12–14], consists of dye-sensitized solar cells (DSSCs) that use nanocrystalline titanium dioxide as an electrode. A variety of dyes have been used, and efficiencies of over 10% have been reported for systems utilizing the most well-studied dye, *cis*-dithiocyanato-*N,N*-bis(2,2'-bipyridyl-4,4'-dicarboxylic acid)-ruthenium(II), commonly referred to as N3 [14,15].

The mode of charge generation and transport in DSSCs is as follows [12–14,16]: 1. The dye sensitizer absorbs visible light, exciting an electron from the highest occupied molecular orbital (HOMO) into the lowest unoccupied molecular orbital (LUMO); 2. The excited electron is transferred to the conduction band of the semiconductor where it travels to a conducting glass electrode; 3. The electron flows through an external circuit and load to the counter electrode; 4. The electron reduces the oxidant (typically I_3^-) present in the electrolyte; 5. The reductant (typically I^-) in the electrolyte regenerates the ground-state, neutral dye molecule, thus completing the circuit. To ensure fast and efficient electron injection, the energy of the dye LUMO must be higher than that of the TiO_2 conduction band edge. To regenerate the neutral dye molecule and complete the circuit, the energy of the dye HOMO must lie below the oxidation potential of the redox mediator. An understanding of the relative positions of the energy levels involved at the dye–semiconductor interface is useful for explaining and/or predicting the efficiency of electron transfer from the excited dye to the semiconductor.

Because of its surface sensitivity, photoelectron spectroscopy (PES) is ideal for studying the electronic states of a surface. The valence electron

levels of a surface can be investigated using ultraviolet photoelectron spectroscopy (UPS) or PES with synchrotron radiation (SRPES). A fundamental issue in the study of solid interfaces is the energy level alignment of the species forming the interface. Extensive investigation of organic semiconductor–metal interfaces has revealed that the commonly held assumption of vacuum level alignment is not always valid [17]. Much less work has been performed on interfaces comprised of discrete organic molecules and inorganic semiconductors.

Several groups have begun to use UPS and SRPES to study the dye–semiconductor interfaces found in DSSCs [18–24], and important information related to interfacial chemistry and physics related to device performance has been realized from these studies. Of course, it should be noted that in addition to the degree of overlap of the dye and nanocrystalline semiconductor electronic energy levels, other factors also affect overall efficiencies of dye-sensitized solar cells. These include the rate of electron transfer from the dye to the semiconductor and the overlap of energy levels between the dye and the redox couple in the electrolyte [22]. The presence of competing energy-wasting pathways, such as back transfer from titania to the dye may also affect efficiencies [25].

In the present work, we have used UPS to probe the interface between nanocrystalline TiO_2 and four related ruthenium dyes, including N3. Nanocrystalline TiO_2 is preferable to a smooth titanium dioxide surface owing to its higher effective surface area [26–29]. In addition to N3, the dyes used in this study are the complex cations (5-amino-1,10-phenanthroline)bis-(2,2'-bipyridyl-4,4'-dicarboxylic acid)-ruthenium(II), (Ru1); (1,10-phenanthroline)bis-(2,2'-bipyridyl-4,4'-dicarboxylic acid)-ruthenium(II), (Ru2); and (5-amino-1,10-phenanthroline)bis-(2,2'-bipyridine)-ruthenium(II), (Ru3). The dyes Ru1 and Ru2 are isolated as chloride salts, and Ru3 is isolated as the hexafluorophosphate salt. The molecular structures of the dyes are shown in Fig. 1. We report and compare the HOMO energy levels of the dyes and the valence band edge of TiO_2 as determined by UPS, and the reproducibility of the measurements is discussed. The results are compared with values for the oxidation potentials of the dyes as measured

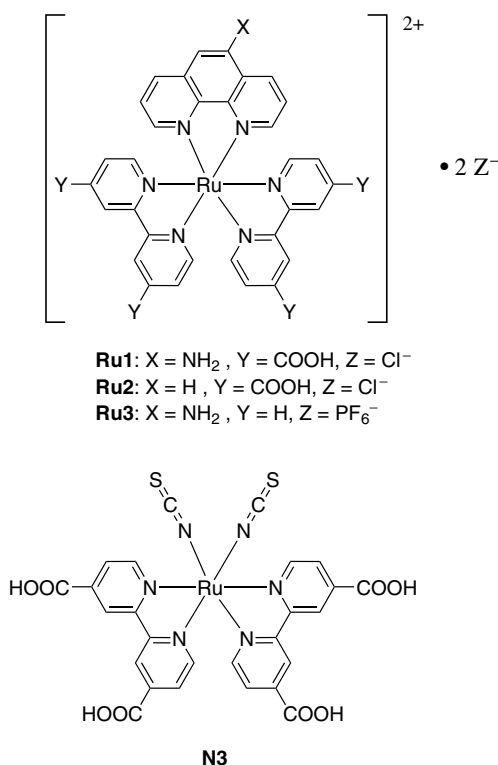


Fig. 1. Chemical structures of the dyes studied: (5-amino-1, 10-phenanthroline)bis-(2,2'-bipyridyl-4,4'-dicarboxylic acid)-ruthenium(II) (Ru1); (1,10-phenanthroline)bis-(2,2'-bipyridyl-4,4'-dicarboxylic acid)-ruthenium(II) (Ru2); (5-amino-1, 10-phenanthroline)bis-(2,2'-bipyridine)-ruthenium(II) (Ru3); *cis*-dithiocyanato-*N,N*-bis-(2,2'-bipyridyl-4,4'-dicarboxylic acid)-ruthenium(II) (N3).

by cyclic voltammetry. The HOMO energy level results are combined with the UV–Vis absorption spectra of the dyes to estimate the dye LUMO energy levels. Comparison of the dye energy levels with the TiO₂ band edges indicates that the LUMO of N3 is more closely aligned to the TiO₂ conduction band edge (CBE) than the other three dyes investigated.

2. Experimental

2.1. Sample preparation

The ruthenium-based dyes used for this study were synthesized under argon and with the exclu-

sion of light. The dyes designated as N3, Ru2, and Ru3 were synthesized as described in the literature [15,30,31]. The dye Ru1 was synthesized by dissolving 149 mg of *cis*-dichlorobis(2,2'-bipyridyl-4,4'-dicarboxylic acid)-ruthenium(II) (prepared as reported previously in [15]) and 42 mg of 5-amino-1,10-phenanthroline (Polyscience) in 15 ml of dimethylformamide and refluxing for 6 h. After cooling, a dark red powder was removed by filtration and dried under vacuum at room temperature for 3 days to obtain Ru1 in 43% yield.

Films of nanocrystalline TiO₂ on SnO₂:F-coated glass substrates (TEC 15, sheet resistance 15 Ω/square) were prepared in a manner similar to that described previously and referred to as “Method B” by Nazeeruddin et al. [15]. In this work, the TiO₂ colloid was spread onto the substrate via spin-coating. The coated plates were sintered in air at 450–500 °C for 30–60 min. For UPS studies, the film area was approximately 1 cm². The TiO₂ films were sensitized by immersing the plates in 0.5 mM ethanol solutions (for Ru1, Ru2, and N3) and 0.5 mM acetone solutions (for Ru3) for up to 48 h. The resulting colored films were typically rinsed with solvent to remove dye not chemisorbed on the TiO₂ surface. Some samples of Ru1, Ru2, and Ru3 were prepared without rinsing to determine the effects of rinsing on the UP spectra. All samples were dried under flowing argon. Silver paint (Electron Microscopy Sciences) was used to adhere the sample to a metal stub compatible with the photoelectron spectrometer, and the edges of the sample surface were connected electrically to the stub via silver paint.

2.2. UPS measurements

The ultraviolet photoelectron spectroscopy studies were performed in a VG ESCALAB photoelectron spectrometer having a base pressure of $\approx 2 \times 10^{-9}$ mbar. The excitation source was a He I lamp ($h\nu = 21.22$ eV), and the samples were biased with a battery at -6.34 V, relative to ground, during the measurements in order to be able to measure the low kinetic energy portion of the spectrum. Typically, ten scans were acquired and averaged for each spectrum, and eight different spectra (with the UV light hitting slightly

different regions of the surface) were acquired per sample.

2.3. UV–Vis absorption measurements

Solid-state UV–Vis absorption spectra of the dyes adsorbed onto TiO₂ films were measured on a Perkin-Elmer Lambda9 spectrophotometer using an unsensitized TiO₂ film as the reference sample.

3. Results and discussion

As acquired, the spectra are referenced to the Fermi level of the electron energy analyzer. For an interface between an organic dye molecule and an inorganic semiconductor through which no dark current should flow, we assume vacuum level alignment of the dyes and TiO₂. Conversion

of the spectra to the solid-state scale relative to the vacuum level is achieved by setting the low kinetic energy photoelectron onset to an ionization energy of -21.22 eV. By this procedure, the vacuum level corresponds to an ionization energy of 0 eV. The low ionization energy region of the normalized, averaged UP spectra of unsensitized TiO₂ and the dye/TiO₂ films are shown in Fig. 2. We expect the UP spectrum of a TiO₂ film sensitized with a dye monolayer to mainly reflect the density of states for the dye. The inelastic mean free path of the photoelectrons is only ≈ 5 angstroms, and the height of an N3 molecule projected from the TiO₂ surface is comparable to this distance [14,32]. Thus, assuming a monolayer of dye is adsorbed onto the TiO₂ surface, the electrons from TiO₂ will not contribute substantially to the UP spectra. For each dye, a small peak corresponding to the HOMO (or combination of high-lying occu-

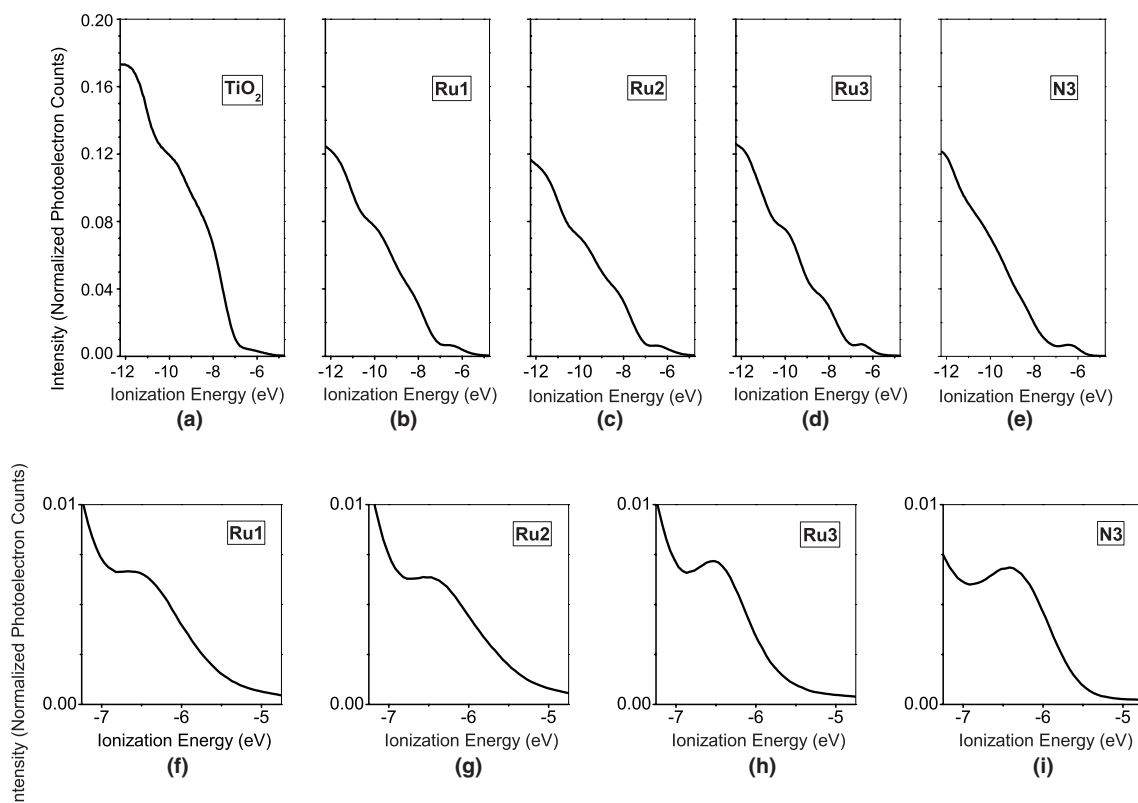


Fig. 2. Normalized, averaged UP spectra of TiO₂ and dyes adsorbed onto TiO₂. The intensity maximum near the vacuum level cutoff is set to one. Spectra (a)–(e) have the same ordinate and abscissa ranges. Spectra (f)–(i) are expanded from spectra (b)–(e), respectively.

pied molecular orbitals) is apparent at the low energy side of the spectrum. The peak is more distinct, and its onset steeper for the N3 and Ru3 dye/TiO₂ films, than for the Ru1 and Ru2 films. A similar peak is not observed in the spectra of bare TiO₂. The TiO₂ and N3/TiO₂ spectra obtained are consistent with reported results [19,22].

We obtained the HOMO energy level of each dye relative to the vacuum level by estimating the onset of the spectrum at low ionization energy. To consistently analyze each spectrum, the energy level of the HOMO was calculated by linear extrapolation of the tangent line through the inflection point of the low ionization energy side of the HOMO peak to the *x*-intercept. A similar analysis was performed to determine the energy of the valence band edge of TiO₂. The mean HOMO energy levels for the four dyes are listed in Table 1. The means and associated standard deviations for the individual samples of each dye are plotted in Fig. 3. Similar results were obtained

Table 1

UPS results: HOMO energy levels of dyes with standard deviations^{a,b}

Dye	Number of spectra	HOMO energy level (eV)
Ru1	40	-5.355 ± 0.166
Ru2	48	-5.213 ± 0.203
Ru3	48	-5.597 ± 0.075
N3	56	-5.472 ± 0.047

^a Valence band edge of TiO₂ (15 spectra) is -6.938 ± 0.076 eV.

^b From Ref. [34], the redox potential for the I^-/I_3^- mediator relative to vacuum level is -4.85 eV.

for each N3 sample despite sensitization times ranging from 30 min to 24 h. Although the precision of the HOMO energy level result obtained for N3 was within the resolution of the experiment (estimated to be 0.05 eV), the results for the other dyes were less reproducible. The variation in results is seen among different samples of the same dye, and to a lesser degree among the eight spectra acquired for a given sample. Also, one sample of

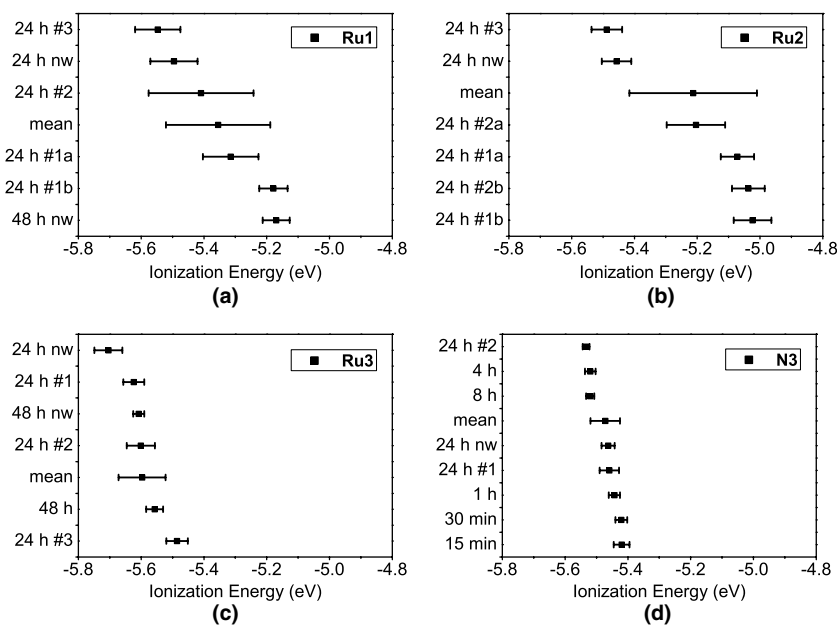


Fig. 3. Mean values for HOMO energy levels determined from the eight spectra collected for each dye sample: (a) Ru1; (b) Ru2; (c) Ru3; (d) N3. For ease of comparison, all plots are displayed with the same abscissa range. Standard deviations are represented by error bars. The mean value for all of the samples of a given dye is also displayed. Samples are identified by sensitization time. Also, sequence number is specified if multiple samples prepared using the same sensitization time were studied. Samples that were analyzed twice are identified with a letter as part of the sequence number (a for the first analysis, b for the second). The experiments in which the samples were not washed are designated by “nw”.

Ru1 and two samples of Ru2 were stored in a desiccator and re-analyzed ten days after the initial spectra acquisition. Within the error of the measurements, no difference due to storage was observed. The results from the second acquisition are included in the averages presented. The inability to more precisely determine the HOMO energy levels may be related to the HOMO peak shape for the Ru1 and Ru2 dyes. Our method for determining the peak onset may be less reliable for the less distinct and more gradually inclining peaks. Also, comparison of the middle sections of the spectra reveal that the densities of states for the Ru1 and Ru2 dyes have a similar shape to that of bare TiO₂, particularly at ionization energies of 9.8 and 11.5 eV (Fig. 4). The shape of the Ru3 dye spectra also resembles that of TiO₂. In contrast, the N3 spectra have a unique peak structure. The similarity may be coincidental, or it may suggest that a complete dye monolayer on TiO₂ is not formed by the other dyes.

To determine if complete dye coverage was not being achieved upon sensitization for 24 h, the sensitization times for Ru1, Ru2, and Ru3 were increased to 48 h. However, the shapes of the spectra and the calculated energy level results were not

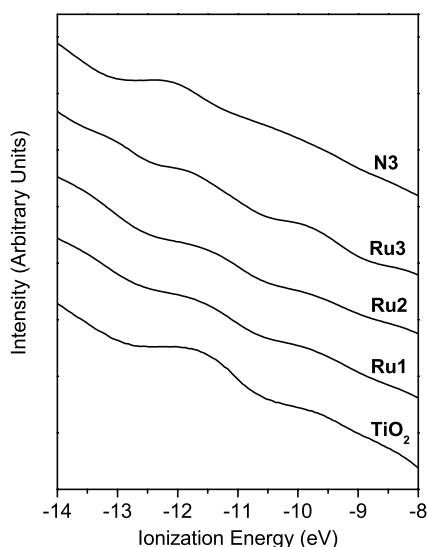


Fig. 4. Middle regions of the normalized, averaged UPS spectra of TiO₂ and dyes adsorbed on TiO₂. Spectra are vertically offset for clarity.

significantly different from those obtained from sensitization for 24 h. Considering the structures of the dyes, it is reasonable to envision that the dyes with two bipyridyl ligands and one 1,10-phenanthroline ligand would be more sterically hindered than N3 with its two isothiocyanate ligands instead of 1,10-phenanthroline. Thus, it is possible that the maximum amount of dye that can be adsorbed onto the TiO₂ surface will leave spots of exposed TiO₂ that contribute photoelectrons to the spectra. In an attempt to fill in the bare spots with dye molecules not chemisorbed onto TiO₂, the solvent washing step was omitted after sensitization for 24 h and 48 h. Again, no significant difference was observed, and the results were averaged with those of the previous samples. The approach was taken further with the Ru1/TiO₂ system in which after sensitization for 24 h, excess dye solution was added to two samples (1 drop every 30 min for a total of 10 or 20 drops) and allowed to dry. Both samples exhibited a moderate amount of charging, manifested by some spikiness in the spectra. Conversion of the spectra to the solid-state scale and determination of the HOMO energy levels can still be achieved as described above. The results were not significantly different than previously determined, although these results were not included in the final average.

HOMO energy levels of dyes may be estimated from their oxidation potentials, as determined by cyclic voltammetry (CV) [15,33,34]. CV measurements on Ru1, Ru2 and Ru3 have recently been performed [35], and Table 2 presents a comparison of the UPS and CV conclusions. The results of the two techniques may differ because of solvation effects on the dye in CV analysis. While it would be interesting to perform CV measurements of dye films, it should be noted that only a monolayer of dye is adsorbed on the TiO₂ substrate, and such measurements would only be directly relevant if they were of films adsorbed on TiO₂. For CV analysis, this is problematic due to the semiconducting nature of the titanium dioxide.

The UPS result for N3 correlates well with the CV solution data from the literature, as shown in the table. In particular, it is significant that the HOMO energy level obtained from UPS most closely matches the oxidation potential for the doubly

Table 2

Comparison of HOMO energy levels as determined by UPS with oxidation potentials determined by cyclic voltammetry

Dye	HOMO from UPS (eV)	E_{ox} from CV (V)	E_{ox} on solid-state scale (eV) ^a
Ru1	−5.36	1.60	−6.30
Ru2	−5.21	1.66	−6.36
Ru3	−5.60	1.55	−6.25
N3	−5.47	0.85 ^b 0.57 ^c	−5.59 −5.31 −5.45 ^d

^a Where $E_{\text{SS}} = -(E_{\text{SCE}} + 4.74)$ or $E_{\text{SS}} = -(E_{\text{Ag/AgCl}} + 4.70)$.

^b Ref. [15], where N3 is fully protonated; reference cell is SCE.

^c Ref. [33] where N3 is fully deprotonated; reference cell is SCE.

^d Ref. [34] where this value is cited as E_{ox} of doubly deprotonated N3.

deprotonated N3 (N719 in [34]) since the dye has been shown to bind to TiO_2 films with two carboxylate groups [14,36]. The UPS results for the other dyes do not match the previously obtained CV results as closely. Certainly, if the UPS results were affected by incomplete dye coverage of TiO_2 , then matching would not be expected. It may be that the HOMO for each of the other ruthenium dyes undergoes a greater change in distribution and energy upon binding to TiO_2 than does that of N3. However, the UV–Vis absorption spectra of the dye/ TiO_2 films (Fig. 5) show that the absorbance maxima for Ru1, Ru2 and Ru3 are red-shifted less than 5 nm relative to the solution spectra. The absorbance maximum for N3 is red-shifted nearly 10 nm relative to solution [15]. This suggests either that the HOMO changes less for Ru1, Ru2 or Ru3 than for N3 upon adsorption, or that each HOMO–LUMO pair changes in such a way as to keep the band gap similar to that of the dye in solution.

The UV–Vis absorption data can be combined with the UPS results to obtain the energy and density of states of the populated vibrational levels of the LUMO. The ground vibrational state of the LUMO is estimated by adding the energy at the approximate onset of the absorption curve to the HOMO as determined by UPS. The actual HOMO–LUMO band gap is slightly larger than the optical gap because the latter accounts for the electron–hole interaction in the excited dye

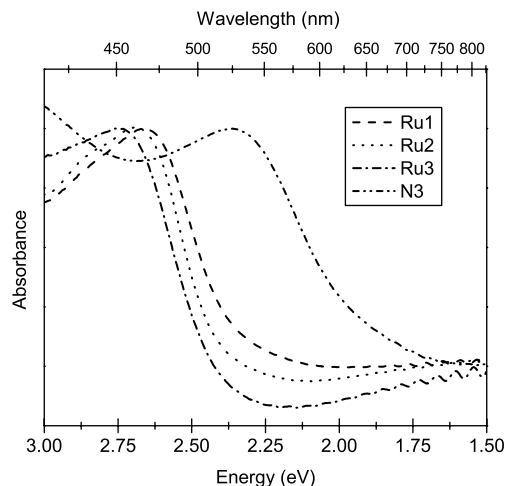


Fig. 5. Solid-state UV–Vis spectra of dyes adsorbed on TiO_2 . The absorbance maxima are slightly red-shifted relative to solution spectra. The apparent increase in absorbance at lower energy is a result of light scattering by the solid film.

[17,37,38]. The optical absorbance maximum is also noted since it has been demonstrated that electrons in vibrationally excited states can be injected into the conduction band of a semiconductor [34]. The conduction band edge (CBE) of TiO_2 is estimated by adding the known band gap of 3.2 eV [13] to the valence band edge (VBE) as determined by UPS. The relative positions of the dye frontier orbitals and the TiO_2 bands are depicted in Fig. 6. Based upon our UPS results, the LUMOs of all the dyes lie above the TiO_2 CBE, with N3 having the lowest enthalpic driving force for electron injection. In Table 3, the LUMOs of the dyes as determined using our UPS results are compared to the LUMOs determined using the CV data cited in Table 2. If the HOMO energy level values as estimated by CV are more accurate than the UPS results, then the ground vibrational states of the LUMOs for Ru1, Ru2 and Ru3 are lower in energy than the TiO_2 CBE and the absorption maxima at approximately the same energy as the TiO_2 CBE. In this situation, a large proportion of electronically excited electrons in Ru1, Ru2 and Ru3 would not have the driving force required for injection into TiO_2 .

Recent measurements of the photovoltaic efficiencies of devices comprised of Ru1, Ru2 and

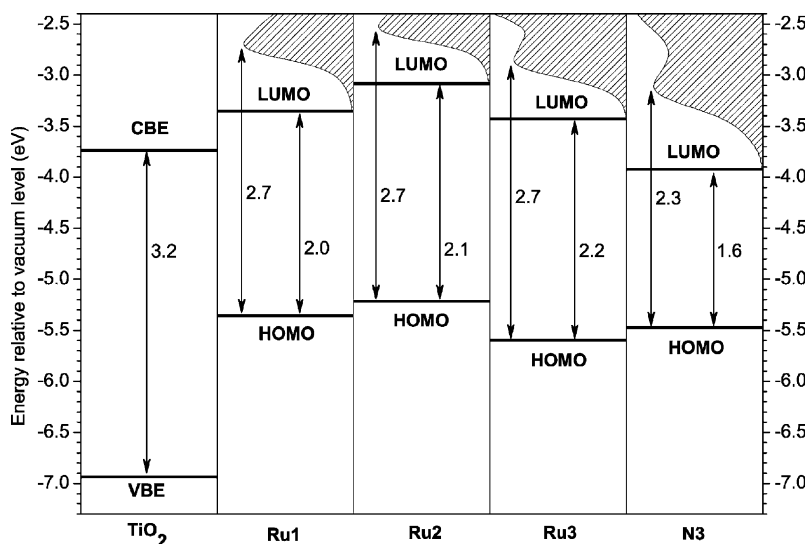


Fig. 6. Comparison of the positions of the dye frontier orbitals with the band edges of TiO_2 . The shaded areas correspond to the UV–Vis spectra of the dyes which have been positioned on the vacuum level scale by adding the energy at maximum absorbance (i.e. 2.3 eV for N3, cf. Fig. 5) to the HOMO energy level as determined by UPS. The ground vibrational states of the dye LUMOs are estimated from the approximate absorption onset. The band gap energies are indicated.

Table 3

Comparison of the estimated dye LUMO energy levels as determined by UV–Vis absorbance, and UPS or CV measurements as reported in Table 2^a

Dye	UPS results		CV results	
	LUMO (eV)	Absorbance maximum ^b (eV)	LUMO (eV)	Absorbance maximum ^b (eV)
Ru1	−3.35	−2.70	−4.29	−3.64
Ru2	−3.08	−2.53	−4.23	−3.68
Ru3	−3.43	−2.86	−4.08	−3.51
N3	−3.93	−3.12	−3.91	−3.10

^a Conduction band edge of TiO_2 is -3.74 eV.

^b The energy corresponding to maximum optical absorbance is added to the LUMO energy to obtain the energy of the most populated vibrational excited state on the solid-state scale.

Ru3 are 2.1, 2.6 and 0.9%, respectively [35]. Devices comprised of N3 with certified efficiencies of over 10% are clearly superior [14,15]. Other factors may have more significant effects on device efficiency than the relative location of the LUMOs above the TiO_2 CBE. For example, the poor efficiency of the Ru3 device was expected owing to the lack of carboxylate groups on the dye with which to chemically bind to the TiO_2 . The most significant advantage N3 has over the other dyes is its absorbance over a larger part of the solar

spectrum, particularly in the red and near-IR regions (recall Fig. 5). In addition, modeling results indicate that the distributions of the HOMO and LUMO over the N3 molecule are ideal for electron injection into TiO_2 and subsequent reduction of the dye cation by the redox mediator: the HOMO is predominantly distributed over the ruthenium center and thiocyanate ligands, whereas the LUMO is distributed over the bipyridyl ligands [14,39]. Also, the possible incomplete monolayer coverage of the phenanthroline-substituted dyes

onto TiO₂ (as suggested by the lack of precision in the UPS results) may contribute to the poorer efficiencies of devices made with these dyes.

4. Conclusions

We have established that UPS can be used to reproducibly determine the energy of the HOMO of N3 adsorbed onto TiO₂. The agreement between the HOMO energy levels of N3 as determined by UPS and CV suggests that alignment of the vacuum levels of N3 and TiO₂ is valid. The poorer precision of the UPS results for the other ruthenium dyes may be an indication that the dyes do not adsorb onto TiO₂ as consistently or completely as does N3. The lack of agreement between the UPS and CV results for each of the three dyes may also be evidence of incomplete dye coverage on TiO₂. More work should be done to determine how CV measurements of dye solutions correlate with solid-state UPS analyses. This work gives further evidence of the close alignment between the N3 LUMO and TiO₂ CBE, which is a critical characteristic of an efficient dye-sensitized solar cell. In the case of the other ruthenium dyes investigated, the relatively poor alignment of the dye LUMO energy levels with the TiO₂ conduction band is likely a contributing factor to their lower photovoltaic efficiencies.

Acknowledgements

This research was performed while one of the authors (J.H.S.) held a National Research Council Research Associateship Award at Natick Soldier Center. The authors thank Xin Liu for help with spectra acquisition, Yanping Wang for help with sample preparation, and Dr. Ravi Mosurkal for helpful discussions. This work was supported by US Army RDECOM, Natick Soldier Center.

References

- [1] K.M. Coakley, M.D. McGehee, *Chem. Mater.* 16 (2004) 4533.
- [2] Y.G. Kim, J. Walker, L.A. Samuelson, J. Kumar, *Nano Lett.* 3 (2003) 523.
- [3] M. Kaneko, K. Takayama, S.S. Pandey, W. Takashima, T. Endo, M. Rikukawa, K. Kaneto, *Synth. Met.* 121 (2001) 1537.
- [4] P.A. van Hal, M.P.T. Christiaans, M.W. Wienk, J.M. Kroon, R.A.J. Janssen, *J. Phys. Chem. B* 103 (1999) 4352.
- [5] G.K.R. Sanadeera, P.V.V. Jayaweera, V.P.S. Perera, K. Tennakone, *Solar Energy* 73 (2002) 103.
- [6] N. Camaioni, L. Garlaschelli, A. Geri, M. Maggini, G. Possamai, G. Ridolfi, *J. Mater. Chem.* 12 (2002) 2065.
- [7] N.S. Sariciftci, *Curr. Opin. Solid State Mater. Sci.* 4 (1999) 373.
- [8] M.C. Scharber, C. Winder, H. Neugebauer, N.S. Sariciftci, *Synth. Met.* 141 (2004) 109.
- [9] S.C. Veenstra, G.G. Malliaras, H.J. Brouwer, F.J. Esselink, V.V. Krasnikov, P.F. van Hutten, J. Wildeman, H.T. Jonkman, G.A. Sawatzky, G. Hadziioannou, *Synth. Met.* 84 (1997) 971.
- [10] J.-F. Nierengarten, T. Gu, G. Hadziioannou, D. Tsamouras, V. Krasnikov, *Helvet. Chim. Acta* 87 (2004) 2948.
- [11] Z. Zhu, S. Hadjikyriacou, D. Waller, R. Gaudiana, *J. Macromol. Sci. Pure Appl. Chem.* A41 (2004) 1467.
- [12] B. O'Regan, M. Grätzel, *Nature* 353 (1991) 737.
- [13] A. Hagfeldt, M. Grätzel, *Chem. Rev.* 95 (1995) 49.
- [14] A. Hagfeldt, M. Grätzel, *Acc. Chem. Res.* 33 (2000) 269.
- [15] M.K. Nazeeruddin, A. Kay, I. Rodicio, R. Humphry-Baker, E. Müller, P. Liska, N. Vlachopoulos, M. Grätzel, *J. Am. Chem. Soc.* 115 (1993) 6382.
- [16] D. Cahen, G. Hodes, M. Grätzel, J.F. Guillemoles, I. Riess, *J. Phys. Chem. B* 104 (2000) 2053.
- [17] (a) H. Ishii, K. Seki, Energy level alignment at organic-metal interfaces, in: W.R. Salaneck, K. Seki, A. Kahn, J.J. Pireaux (Eds.), *Conjugated Polymer and Molecular Interfaces*, Marcel Dekker, New York, 2002, pp. 293–349, see also references therein; (b) C. Shen, A. Kahn, I. Hill, Organic molecular interfaces: Investigations of electronic structure, chemistry, and carrier injection properties, in: W.R. Salaneck, K. Seki, A. Kahn, J.J. Pireaux (Eds.), *Conjugated Polymer and Molecular Interfaces*, Marcel Dekker, New York, 2002, pp. 351–400, see also references therein.
- [18] (a) H. Rensmo, S. Södergren, L. Patthey, K. Westermark, L. Vayssieres, O. Kohle, P.A. Brühwiler, A. Hagfeldt, H. Siegbahn, *Chem. Phys. Lett.* 274 (1997) 51.
- [19] K. Westermark, A. Henningsson, H. Rensmo, S. Södergren, H. Siegbahn, A. Hagfeldt, *Chem. Phys.* 285 (2002) 157.
- [20] K. Westermark, H. Rensmo, H. Siegbahn, K. Keis, A. Hagfeldt, L. Ojamäe, P. Persson, *J. Phys. Chem. B* 106 (2002) 10102.
- [21] K. Westermark, H. Rensmo, A.C. Lees, J.G. Vos, H. Siegbahn, *J. Phys. Chem. B* 106 (2002) 10108.
- [22] G. Liu, W. Jaegermann, J. He, V. Sundström, L. Sun, *J. Phys. Chem. B* 106 (2002) 5814.
- [23] G. Liu, A. Klein, A. Thissen, W. Jaegermann, *Surf. Sci.* 539 (2003) 37.

- [24] T. Ma, K. Inoue, H. Noma, K. Yao, E. Abe, *J. Mater. Sci. Lett.* 21 (2002) 1013.
- [25] R. Gaudiana, S. Hadjikyriacou, J. He, D. Waller, Z. Zhu, *J. Macromol. Sci., Pure Appl. Chem. A* 40 (2003) 1295.
- [26] J. Desilvestro, M. Grätzel, L. Kavan, J. Moser, J. Augustynski, *J. Am. Chem. Soc.* 107 (1985) 2988.
- [27] N. Vlachopoulos, P. Liska, J. Augustynski, M. Grätzel, *J. Am. Chem. Soc.* 110 (1988) 1216.
- [28] L. Kavan, M. Grätzel, S.E. Gilbert, C. Klemenz, H.J. Scheel, *J. Am. Chem. Soc.* 118 (1996) 6716.
- [29] C.J. Barbé, F. Arendse, P. Comte, M. Jirousek, F. Lenzmann, V. Shklover, M. Grätzel, *J. Am. Ceram. Soc.* 80 (1997) 3157.
- [30] B. Ullrich, S. Seeger, J. Wolfrum, *Proc. SPIE-Int. Soc. Opt. Eng.* 2629 (1996) 88.
- [31] C.D. Ellis, L.D. Margerum, R.W. Murray, T.J. Meyer, *Inorg. Chem.* 22 (1983) 1283.
- [32] V. Shklover, Yu.E. Ovchinnikov, L.S. Braginsky, S.M. Zakeeruddin, M. Grätzel, *Chem. Mater.* 10 (1998) 2533.
- [33] M.K. Nazeeruddin, S.M. Zakeeruddin, R. Humphry-Baker, M. Jirousek, P. Liska, N. Vlachopoulos, V. Shklover, C.-H. Fischer, M. Grätzel, *Inorg. Chem.* 38 (1999) 6298.
- [34] F. Lenzmann, J. Krueger, S. Burnside, K. Brooks, M. Grätzel, D. Gal, S. Rühle, D. Cahen, *J. Phys. Chem. B* 105 (2001) 6347.
- [35] Y.-G. Kim, L.A. Samuelson, J. Kumar, to be published.
- [36] K.S. Finnie, J.R. Bartlett, J.L.J. Woolfrey, *Langmuir* 14 (1998) 2744.
- [37] K. Seki, T. Tani, H. Ishii, *Thin Solid Films* 273 (1996) 220.
- [38] I.G. Hill, A. Rajagopal, A. Kahn, Y. Hu, *Appl. Phys. Lett.* 73 (1998) 662.
- [39] H. Rensmo, S. Lunell, H. Siegbahn, *J. Photochem. Photobiol. A* 114 (1998) 117.



The influence of the optoelectronic properties of poly(3-alkylthiophenes) on the device parameters in flexible polymer solar cells

Maher Al-Ibrahim^a, H.-Klaus Roth^a, M. Schroedner^a, Alexander Konkin^a,
Uladzimir Zhokhavets^b, Gerhard Gobsch^b, Peter Scharff^b, Steffi Sensfuss^{a,*}

^a Department of Functional Polymer Systems, TITK Institute, Breitscheidstrasse 97, D-07407 Rudolstadt, Germany

^b TU Ilmenau, Institute for Physics, Weimarer Strasse 32, D-98684 Ilmenau, Germany

Received 25 February 2004; received in revised form 18 November 2004; accepted 22 February 2005

Available online 28 March 2005

Abstract

In this report regioregular poly(3-alkylthiophenes) (P3ATs) (P3HT: poly(3-hexylthiophene), P3OT: poly(3-octylthiophene), P3DDT: poly(3-dodecylthiophene) were studied regarding their optical and electrochemical properties and used as electron donors in polymer solar cells. The optical band gap energy for the three polymers amounts to 1.92 eV. With longer side chain length their electrochemical band gaps are slightly increased, whereas the absorption coefficient undergoes a systematic decrease. The absorption spectra of the pristine P3ATs exhibit a distinctive blue shift of the π - π^* interband transition upon mixing with PCBM 1:3 (as prepared films; P3HT: \sim 45 nm, P3OT: \sim 85 nm, P3DDT: \sim 50 nm). Films based on composites of the three polymers with PCBM ([6,6]-phenyl-C61-butyric acid methyl ester) show a distinctive photoluminescence quenching effect. At 77 K two types of light-induced electron spin resonance (ESR) signals were identified, one of polaron ($P^{\bullet+}$) on the polymer chain and one of $PCBM^{\bullet-}$ radical anion, which detect the photoinduced charge generation and charge transfer in P3AT/PCBM composites.

Photovoltaic devices were prepared on flexible PET-ITO foils on ambient conditions using P3HT/PCBM (1:3 wt.%) with $\eta_{AM1.5} = 1.54\%$, P3OT/PCBM (1:3 wt.%) with $\eta_{AM1.5} = 1.1\%$ and P3DDT/PCBM (1:3 wt.%) with $\eta_{AM1.5} = 0.59\%$ (A : 0.25 cm², $P_{IN} = 100$ mW/cm²). The serial and parallel resistance increases within the series P3HT:PCBM < P3OT:PCBM < P3DDT:PCBM cells, therefore the short-circuit current decreases and the open-circuit voltage increases in this order.

© 2005 Elsevier B.V. All rights reserved.

* Corresponding author. Tel.: +49 3672 379556; fax: +49 3672 379379.
E-mail address: sensfuss@titk.de (S. Sensfuss).

PACS: 73.50.Pz; 76.30.Pk; 78.40.Me; 78.66.Sq

Keywords: Polymer solar cells; Cyclic voltammetry; Poly(3-alkylthiophenes); Photoluminescence; Absorption coefficient; Light-induced electron spin resonance spectroscopy (LESR)

1. Introduction

Plastic electronics based on organic semiconductors is a very promising technology to enter the low-cost low-performance segment of the electronic market. Polymer solar cells, which typically use conjugated polymers as electron donors and n-conducting organic materials as electron acceptors, can be processed from solution or dispersion. That offers a very important technological potential for low-cost fabrication of large-area solar cells using high-volume processes like reel-to-reel technologies. The discovery of ultrafast charge transfer in p-conducting polymer/fullerene composites by Sariciftci in 1992 [1] represents a decisive milestone in the field of polymer solar cells. It has to be pointed out, that especially the high asymmetry between forward and back polymer-fullerene electron transfer rate, that covers nine orders of magnitude [2], allows blending of donor and acceptor components to prepare solar cell architectures possessing only one photoactive composite layer instead of donor monolayers or donor-acceptor bilayers. At present, an external AM1.5 power conversion efficiency of 2.5% with MDMO-PPV/PCBM (1:4 wt.%, active area: 7.5 mm², $P_{IN} = 80 \text{ mW/cm}^2$, mismatch factor $m = 0.753$) [3] and 3.5% with P3HT/PCBM (active area: 5–8 mm², $P_{IN} = 80 \text{ mW/cm}^2$) [4] is state of the art. Recently, a solar cell based on MDMO-PPV:PCBM-C71 ([6,6]-phenyl-C71-butyric acid methyl ester) was reported with an external AM1.5 power conversion efficiency of 3% ($P_{IN} = 100 \text{ mW/cm}^2$, active area: 10 mm² [5]). All these cells were processed on rigid glass substrates. As long as polymer solar cells require rigid glass substrates, they will offer only limited advantages compared with silicon. Therefore our approach is the exclusive use of flexible substrates. We reported about large-area polymer solar cells based on MDMO-PPV/PCBM (1:3 wt.%), P3OT/C₆₀

(1:3 wt.%), P3HT/PCBM (1:3 wt.%) and phenylene-ethynylene/phenylene-vinylene hybrid polymers/PCBM (1:3 wt.%) fabricated on flexible ITO (indium tin oxide) coated polyester foils [6–10].

Beside a suitable relative LUMO_{donor}–LUMO_{acceptor} position, the necessary avoidance of a ground state D–A doping and well adapted ohmic contacts to the asymmetrical electrodes, the solubility of donor as well as acceptor material plays an important role for organic cells based on D–A composites. Both the morphology [3] and the optimal thickness of the photoactive layer are crucial factors for obtaining a high current from such devices.

Conjugated polymers frequently used in polymer solar cells are derivatives of poly(phenylene vinylenes) (e.g. MDMO-PPV or MEH-PPV) and the regioregular poly(3-alkylthiophenes) (P3ATs). Poly(3-alkylthiophenes) (P3ATs) have been found to be an outstanding class of polymers possessing good solubility, processability, environmental stability, electroactivity, and other interesting properties [11,12]. Regioregular P3ATs are superior to regiorandom P3ATs concerning the degree of intermolecular order and their electronic properties arising from it [11,13].

Cyclic voltammetry (CV) is a well-tried method for the determination of oxidation and reduction potentials of various polymers, which allows calculation of their HOMO/LUMO levels [14]. These values give valuable information, which donor material can or should preferably be combined with which acceptor for a promising fabrication of polymer photovoltaic devices.

The comparison of the photoluminescence (PL) of an donor with that of the D/A composite provides an important, but also simple method to detect the charge transfer (CT), which is indicated by the quenching effect of the composite [1].

For studying the charge transport mechanisms in conducting polymers and in polymer/acceptor

composites, light-induced electron spin resonance spectroscopy (LESR) was found to be a useful tool. These processes play a central role in the photophysics of polymer solar cells [6,15].

It is the objective of this report to show the influence of the alkyl side chain length of regioregular poly(3-hexylthiophene) P3HT, poly(3-octylthiophene) P3OT and poly(3-dodecylthiophene) P3DDT on the electrochemical and optical properties as well as on the parameters of corresponding photovoltaic devices. C₆₀-fullerene, [6,6]-phenyl-C61-butyric acid methyl ester (PCBM) and bismorpholino-C₆₀-fullerene (BM-C₆₀) were applied as acceptor. The following preliminary investigations were carried out: determination of absorption coefficients, seeking for photoluminescence quenching of the P3ATs induced by the appropriate acceptor when blending both materials, detection of charge transfer in P3AT/fullerene composites by light-induced spin resonance technique (LESR) and estimation of the position of valence (HOMO) and conducting band (LUMO) using cyclic voltammetry. The latter allows to predict the energy band diagram for appropriate photovoltaic devices and facilitates the materials choice.

Photovoltaic devices based on P3ATs as electron donor and [6,6]-PCBM were fabricated on flexible ITO polyester foils and characterised

applying AM1.5 conditions. The device area amounts to 0.25 cm², the cells were prepared and handled without any protection against oxygen and air humidity.

2. Experimental techniques

Regioregular poly(3-hexylthiophene) P3HT, poly(3-octylthiophene) P3OT and poly(3-dodecylthiophene) P3DDT were purchased from Aldrich and used as received. C₆₀-fullerene (98%) was also purchased from Aldrich. [6,6]-Phenyl-C61-butyric acid methyl ester (PCBM) was synthesised in the laboratory of the Hummelen group at University of Groningen and bismorpholino-C₆₀-fullerene (BM-C₆₀) was prepared in the group of Prof. Scharff/Technical University of Ilmenau/Germany. The chemical structures of the applied materials are given in Fig. 1.

Cyclic voltammetry (CV) experiments were carried out in a three-electrode cell consisting of a platinum working electrode, a platinum counter electrode and a Ag/AgCl reference electrode using a sweep rate of 10–15 mV/s (Solartron potentiostat 1285). The fullerenes were dissolved in a mixture of *o*-dichlorobenzene (*o*-DCB)/acetonitrile (4:1 w/w) (anhydrous, Aldrich/stored over mole sieve, Fluka) containing 0.1 m tetra-*n*-butyl ammonium

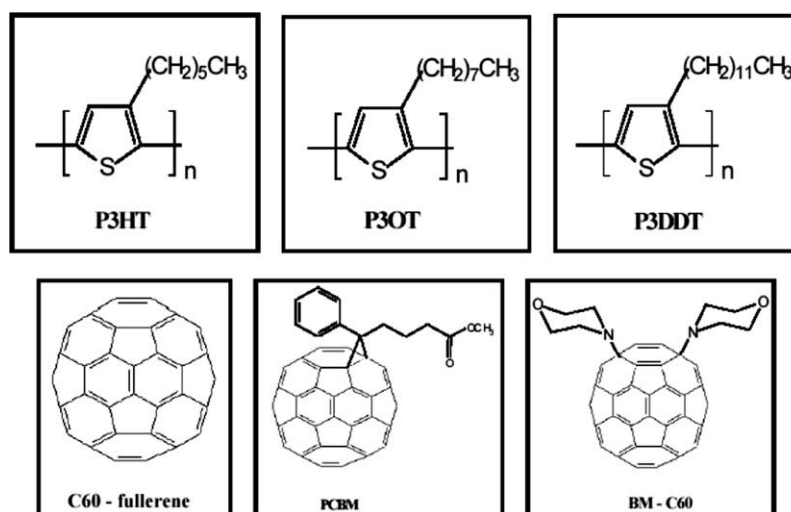


Fig. 1. Chemical structures for the investigated P3ATs and of the used fullerenes.

hexafluorophosphate (Fluka/electrochemical grade) in order to produce solutions with a concentration of 3×10^{-4} mol/l. The polymers were measured in form of films, prepared by placing solutions onto the platinum electrode and allowing these films to dry for 25 min at 40 °C. The supporting electrolyte was 0.1 M Bu_4NPF_6 dissolved in dry acetonitrile (over mole sieve, Fluka). Before carrying out the measurements nitrogen was passed through all solutions to replace traces of oxygen.

The optical absorption coefficients were obtained from the analysis of ellipsometric spectra measured with a Woollam VSAE[®] variable angle spectroscopic ellipsometer with rotating analyser. The optical absorption spectra of pristine polymers were recorded using spin-coated films on Si-wafers. E_g^{opt} is the onset of the low energy optical absorption edge from UV–VIS spectra measured in form of films.

The photoluminescence (PL) spectra were measured by exciting the samples with the 459 nm line of an Ar^+ laser at 80 K. The emission was detected with a cooled Yobin Yvon CCD camera combined with a Spex 1404 0.85 m double-grating monochromator.

The ESR experiments were carried out using a BRUKER X-band spectrometer ELEXSYS E500 at 77 K. Photolysis was performed with ILA 120-1 Ar^+ laser operating at $\lambda = 488$ nm.

For photovoltaic device preparation the substrates (polyester foil coated with 100 nm indium tin oxide ITO, surface resistance of 60 Ω /square) were cleaned in an ultrasonic bath filled with a methanol/isopropanol-mixture. The size of the substrates was 5 cm \times 5 cm. After drying the substrate a thin layer (\sim 100 nm) of PEDOT:PSS (poly(3,4-ethylenedioxythiophene)–poly(styrene-

sulfonate) (Baytron P, Bayer AG/Germany) was spin-coated and dried. Subsequently, the photoactive layer was prepared by spin coating P3HT/PCBM (1:3 weight ratio), P3OT/PCBM (1:3 weight ratio) or P3DDT/PCBM (1:3 weight ratio) solutions in 1,2,4-trimethylbenzene on the top of the PEDOT:PSS layer. The thickness of the photoactive layers was typically in the range of 100–150 nm. The aluminium cathode was thermally deposited (\sim 80 nm) through a shadow mask, which define a device area of 0.25 cm².

I/V curves were recorded with a Keithley SMU 2400 Source Meter by illuminating the cells from the ITO side with 100 mW/cm² white light from a Steuernagel solar simulator to realise AM1.5 conditions. All cells were prepared and measured on ambient conditions.

3. Results and discussion

3.1. HOMO/LUMO determination by cyclic voltammetry

Electrochemical data can give valuable information regarding intrinsic materials stability and allow the estimation of the relative position of HOMO/LUMO levels of materials investigated. The knowledge of these values is required for compiling suitable donor–acceptor pairs.

Table 1 shows the onset and the peak values for oxidation and reduction potentials determined vs. Ag/AgCl.

The reduction values of C₆₀, PCBM and BM-C₆₀ show distinctive differences. C₆₀ (–0.53 V) appears to be a more effective electron acceptor than PCBM (–0.61 V). BM-C₆₀ shows a clearly lower

Table 1

Cyclic voltammetry data, HOMO and LUMO levels and E_g^{CV} of different donor and acceptor materials

Material	E_p^{ox} vs. Ag/AgCl (V)	$E_{\text{onset}}^{\text{ox}}$ vs. Ag/AgCl (V)	HOMO (eV)	E_p^{red} vs. Ag/AgCl (V)	$E_{\text{onset}}^{\text{red}}$ vs. Ag/AgCl (V)	LUMO (eV)	E_g^{CV} (eV)
C ₆₀	+1.80	+1.72	–6.03	–0.53	–0.49	–3.82	2.21
PCBM	+1.75	+1.61	–5.90	–0.61	–0.57	–3.73	2.17
BM-C ₆₀	+1.88	+1.61	–5.92	–0.89	–0.81	–3.50	2.42
P3HT	+1.12	+0.82	–5.20	–1.15	–0.85	–3.53	1.67
P3OT	+1.25	+0.87	–5.25	–1.10	–0.83	–3.55	1.70
P3DDT	+1.30	+0.91	–5.29	–1.04	–0.83	–3.55	1.74

electron affinity (-0.89 V) in comparison to PCBM and C_{60} . This may be explained by the nucleophilic character of the attached morpholine moieties.

As it can be recognized from Table 1, the oxidation potential of the P3ATs is directly proportional to the chain length, whereas the reduction potential shows an inverse dependence. This is due to the fact, that the density of π -electrons and charges is increasing as the length of the side chain decreases, caused by better π -stacking and improved interchain coupling [16], that enhances the donor character and favours oxidation. Additionally, it is conceivable that longer alkyl chains generate a type of shielding effect hampering the electron donation.

According to the empirical equation relation $E^{\text{HOMO/LUMO}} = [-\exp(E_{\text{onset}} \text{ (vs. Ag/AgCl)} - E_{\text{onset}} \text{ (Fc/Fc+ vs. Ag/AgCl)}) - 4.8 \text{ eV}$ [17,18] including the ferrocene value -4.8 eV (with respect to the vacuum level, which is defined as being zero), the HOMO/LUMO levels can be estimated from the $E_{1/2}^{\text{ox}}/E_{1/2}^{\text{red}}$ values, that have been obtained from measurements in solution (fullerenes). For the performed film measurements (polymers) the $E_{\text{onset}}^{\text{ox}}$ and $E_{\text{onset}}^{\text{red}}$ values serve to the calculation of the corresponding HOMO and LUMO.

The LUMO of C_{60} (-3.82 eV) is lower in energy than that of PCBM (-3.73 eV) and of BM- C_{60} (-3.50 eV), which means that the acceptor strength of C_{60} is higher than that of PCBM and BM- C_{60} .

The HOMO of P3HT is slightly higher in energy than that of the HOMOs of P3OT and of P3DDT. These values are in accordance with the literature for P3OT [14], for P3HT [19,20] and for P3DDT [20]. The LUMO of the three polythiophenes are almost at the same energetic level. Up till now reliable information regarding the LUMO levels of such P3ATs estimated from cyclic voltammetry data are still uncertain. Fig. 2 exhibits the resulting energy band diagram in relation to the work function of indium tin oxide (ITO) and aluminium (Al), which are usually applied as electrodes in polymer solar cells.

The HOMO of all three polymers is distinctively higher in energy than that of C_{60} , PCBM and BM- C_{60} . Nevertheless, the relative positions

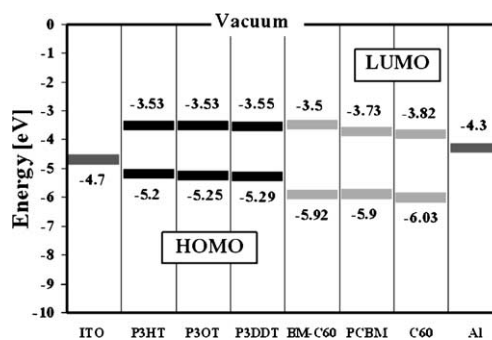


Fig. 2. Energy band diagram with HOMO/LUMO levels of the donor polymers P3HT, P3OT and P3DDT and the fullerene acceptors estimated from cyclic voltammogramic data in relation to the work function of the common electrode materials ITO and Al.

Table 2
Optical data of P3ATs determined from ellipsometric data

Material	λ_{max} [nm]	Absorption coefficient at λ_{max} (cm^{-1})	$E_{\text{g}}^{\text{opt}}$ (eV)
P3HT	500 (2.48)	1.75×10^5	1.92
P3OT	512 (2.42)	1.38×10^5	1.92
P3DDT	515 (2.41)	1.12×10^5	1.93

of the donor LUMO and the acceptor LUMO are important for the intended charge transfer. As shown in Fig. 2, the differences between the LUMOs of P3HT, P3OT or P3DDT and the LUMOs of C_{60} or PCBM are in the range of 0.2–0.3 eV, respectively. It seems that these differences are sufficiently high in order to enable an unrestricted and directed charge transfer, as it will be described in the following. Regardless of, we found the position of LUMO of BM- C_{60} at nearly the same level like that of P3HT, P3OT, P3DDT, consequently a selective charge transfer into this fullerene material becomes uncertain or impossible. Although $\Delta\text{LUMO}_{\text{D-A}}$ data obtained from cyclic voltammetric measurements do not represent absolute values, they should be suitable to compare materials if applying identical experimental conditions.

The electrochemical gap of all investigated polymers is clearly lower than the optical gap, which was determined from the absorption edges of UV–VIS spectra in solid state (see Tables 1 and 2). Although the effect of discrepancy between

E_g^{opt} and E_g^{CV} has already been reported in several references [21–23], a comprehensive discussion is still lacking.

3.2. Optical properties of poly(3-alkylthiophenes)

Materials with high absorption coefficients are necessary for the application in polymer solar cells. This is due to the requirement, that the film thickness of the photoactive layer should normally not exceed some hundreds of nanometers (typical are 100–300 nm). This limitation is determined by the much lower charge carrier mobility and the distinctively shorter exciton diffusion length of these carriers in semiconducting polymers compared with inorganic semiconductors.

Fig. 3 shows the absorption spectra of films made from the three poly(3-alkylthiophenes). The absorption maximum (λ_{max}) of P3HT, P3OT and P3DDT can be observed at 500 nm (2.48 eV), 512 nm (2.42 eV) and 515 nm (2.41 eV), respectively. These λ_{max} -values when correlated with the energy of π - π^* interband transition indicate a more pronounced planarity of the backbone chains for P3DDT than for P3HT [24]. This is due to the fact that longer side groups restrict the number of possible conformations, that two adjacent thiophene rings can form by rotating around their shared C–C-bond.

With decreasing length of the side chain the absorption coefficient increases for the investigated polymers in the following graduation: P3DDT < P3OT < P3HT (Table 2). In accordance to the

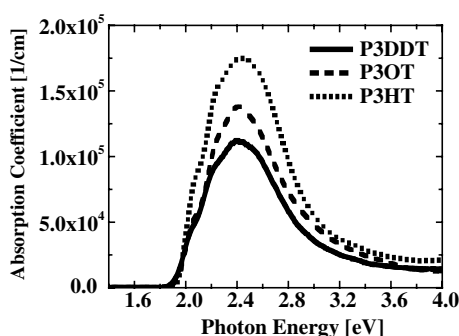


Fig. 3. Absorption spectra for P3HT, P3OT and P3DDT thin films.

literature [14,25–27] the optical gap was found to be approximately 1.92 eV for all three polythiophenes and does not depend on the side chain length.

The absorption spectra of pristine P3HT, P3OT and P3DDT show distinctive changes upon blending the polymers with PCBM. The peak wave length of the π - π^* interband transition of the P3ATs is shifted towards shorter wave length and especially in the case of P3DDT the spectrum becomes less structured [7,9]. However, the position of the three fullerene bands (at 220, 270, 340 nm) and the both longer-wave absorption bands of P3ATs (at \sim 555 and \sim 605 nm) as well as the optical band edges remain nearly uninfluenced. This feature and the fact that no additional absorption band appears is an indication that these changes are not generated by ground state doping of the polythiophenes by PCBM. The π - π^* interband transition blue shift is increased with the fullerene content and amounts to \sim 45 nm for P3HT:PCBM (1:3) and \sim 50 nm for P3DDT:PCBM (1:3) composite films (as prepared), respectively. Differently from that solid films based on P3OT:PCBM (1:3) composites exhibit a higher blue shift of \sim 85 nm. Accordingly, the composite films differ significantly in their optical appearance: the P3HT:PCBM (1:3) and P3DDT:PCBM (1:3) films looks more red-brown, whereas the P3OT:PCBM (1:3) film appears orange-brown. (The colours of the pristine P3HT, P3OT and P3DDT as prepared films are violet, red-brown and rubin-red, respectively.) The same spectral behaviour has already been reported in [28] for regioregular P3HT/fullerene and P3OT/fullerene composites and by Morita et al. [29] for regiorandom P3HT/ C_{60} and poly(3-octadecylthiophene)/ C_{60} blends. It may be possibly assigned to disruption of the interchain packaging by a high PCBM concentration and/or conformational changes of the polythiophene chains. The detected higher shift for P3OT upon mixing with PCBM (1:3) compared to P3HT and P3DDT may be due to differences in the molecular weights of the three polythiophenes [30] or is a special feature of the applied solvent (1,2,4-trimethylbenzene) inducing unfavourable chain conformations and/or a disadvantageous interchain packaging. This

shift is reduced after annealing but remains higher for P3OT:PCBM than for analogous films based on the other two polymers (these results will be given in a future report).

3.3. Detection of charge transfer by photoluminescence quenching and ESR experiments

The strong photoluminescence (PL) of conjugated polymers accompanied by its quenching in the presence of C₆₀-fullerene or its derivatives indicates the charge transfer from polymer to fullerene [1].

Films made from composites of P3HT/PCBM (1:3 wt.%) [9] and P3OT/PCBM (1:2 wt.%) [7] show a distinctive photoluminescence quenching effect.

Fig. 4 exhibits the PL spectra of P3DDT and blends of P3DDT with three different fullerenes. In contradiction to the blends consisting of P3DDT/C₆₀ and P3DDT/PCBM (1:1 wt.%), the photoluminescence quenching of P3DDT/BM-C₆₀ (1:1 wt.%) composite film is significantly reduced. This could be due to an energetic problem caused by the relative LUMO_{P3DDT}/LUMO_{BM-C₆₀} position and would be in agreement with the cyclic voltammetry data for this D–A combination (see Fig. 2).

The effective charge separation in the systems P3HT:PCBM (1:2 wt.%), P3OT:PCBM (1:2 wt.%), P3DDT:PCBM (1:2 wt.%) has been established by two LESR signals (light-induced

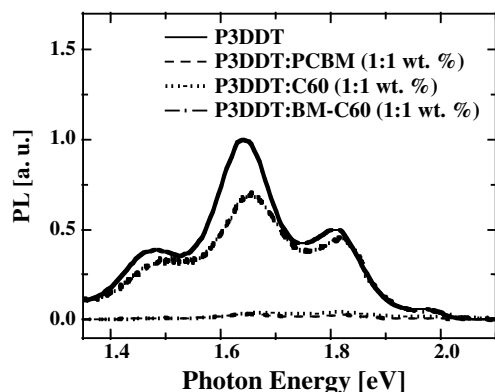


Fig. 4. Film photoluminescence spectra of P3DDT and blends of P3DDT with different fullerenes (1:1 wt.%).

electron spin resonance spectroscopy). They can be assigned to positive polarons (P⁺) on polymer chain with g -factor $g_{\text{iso}} \approx 2.0022$ and to radical anions of PCBM with $g_{\text{iso}} \approx 1.9995$ [6,15,31] (Figs. 5–7). P3HT:PCBM (1:2) and P3OT:PCBM (1:2) composite films show a strong P⁺ ESR signal without light excitation (Figs. 5 and 6), that may be caused by traces of impurities or the effect of

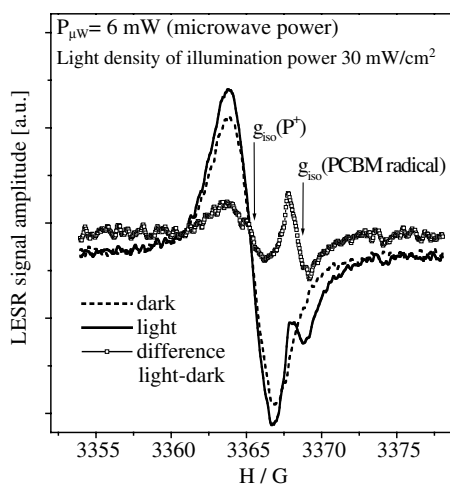


Fig. 5. Dark, light and difference ESR spectra of P3HT:PCBM (1:2 wt.%, measured in form of a film, Ar⁺ laser with λ : 488 nm, T : 77 K).

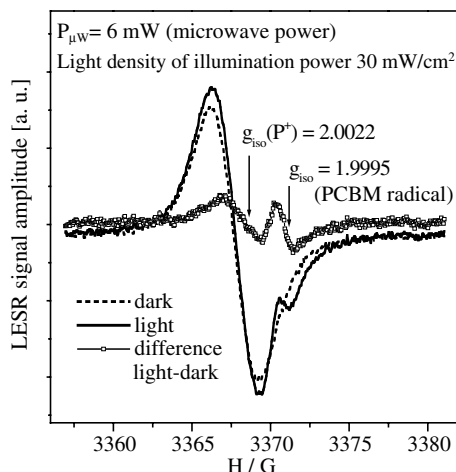


Fig. 6. Dark, light and difference ESR spectra of P3OT:PCBM (1:2 wt.%, measured in form of a film, Ar⁺ laser with λ : 488 nm, T : 77 K).

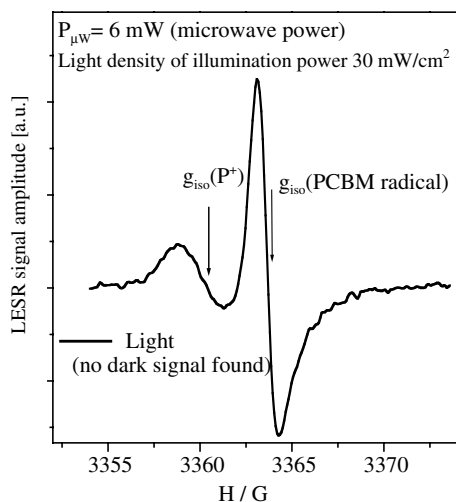


Fig. 7. Light-induced ESR spectrum of P3DDT:PCBM (1:2 wt.%, measured in form of a film, Ar⁺ laser with λ : 488 nm, T : 77 K).

entrapped oxygen. Despite the fact, that previous investigations using P3DDT/C₆₀ [6,7] with another batch of P3DDT could prove the existence of a dark signal, P3DDT/PCBM (1:2 wt.%) does not yield any signal without being exposed to radiation (Fig. 7).

Dark ESR and light-induced ESR spectra (Ar⁺ laser operating at $\lambda = 488$ nm) for films of P3HT:PCBM and P3OT:PCBM are depicted in Figs. 5 and 6, respectively. After starting light exposition the amplitude of the polaron signal increases as the time proceeds and a signal to be assigned to the high-field component (PCBM radical anion) starts to appear additionally. Hence, the distinctive spectroscopic features between spectra taken during radiation and in the dark, respectively, clearly indicate the charge separation process of the investigated composites (Figs. 5 and 6). Applying the same conditions the signal amplitude ratio of P3DDT/PCBM (1:2 wt.%) films (Fig. 7) appears to be changed compared to Figs. 5 and 6 (the PCBM⁻ signal amplitude is distinctively higher in intensity than the polaron signal). Contrary to the P3ATs/PCBM composites no ESR signal could be detected in P3DDT/BM-C₆₀ films. This is in accordance with the results from photoluminescence measurements (see Fig. 4) and

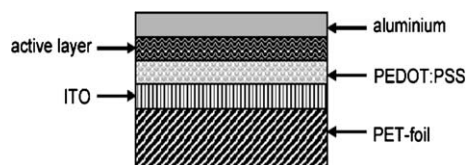


Fig. 8. Cross-section of the typical device configuration of prepared flexible polymer solar cells.

HOMO/LUMO determinations (see Fig. 2). Dynamic parameters obtained by the line width analysis and the saturation effects for all three systems will be published elsewhere.

3.4. Flexible photovoltaic devices based on P3AT/PCBM

The photovoltaic devices consist of four layers as shown in Fig. 8. A flexible polyester foil coated with indium tin oxide (ITO) is used as substrate (the device area amounts to 0.25 cm², 16 cells were fabricate at one 5 × 5 cm substrate). All cells were prepared and measured on ambient conditions illuminated with white light of a Steuernagel solar simulator AM1.5 ($P_{IN} = 100$ mW/cm²).

Fig. 9 shows the current–voltage characteristics of the solar cell based on P3HT/PCBM (1:3 wt.%) in the dark and on AM1.5 conditions with light intensity of 100 mW/cm² at room temperature [9,32]. This device exhibits a rectification of forward and backward current in the dark at ± 2 V

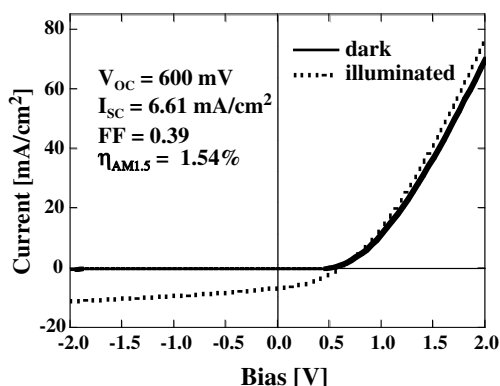


Fig. 9. I – V characteristics of a PET foil/ITO/PEDOT-PSS/P3HT:PCBM (1:3 wt.%) / Al cell ($A = 0.25$ cm²) in the dark and under illumination with white light ($P_{IN} = 100$ mW/cm²).

of 5×10^{-3} . The cell has an open-circuit voltage (V_{OC}) of 600 mV, a short-circuit current (I_{SC}) of 6.61 mA/cm^2 and a calculated fill factor (FF) of 0.39. The overall efficiency for this polymer solar cell is 1.54%.

The described non-post-treated devices may most likely be compared with that published in [4]. When comparing both as produced P3HT:PCBM cells it became obvious, that besides others the substrate material will determine the cell performance in an extent that cannot be neglected. The application of different materials and characterisation methods complicate comparisons of flexible solar cells [33–35].

The authors in [4] were able to reach further improvement of the device performance by a post-production treatment that includes annealing or simultaneous annealing and applying an external electric field. A detailed investigation how such methods will influence cell parameters is still in progress and will be published separately.

V_{OC} of the cell in the present report (600 mV) is higher than that of the as produced cell (300 mV) in [4] as well as that of the device treated subsequently (550 mV, annealing followed by applying an external voltage [4]). Despite using the same photoactive materials and the same electrodes this effect is obvious. It may be due to differences in the PEDOT:PSS layer or higher shunts [36] caused by the influence of film preparation conditions. Differences in the blend morphology resulting from the choice of solvent or from varying the donor/acceptor ratios can lead to differences in the open-circuit voltage [37]. I_{SC} (6.61 mA/cm^2) is higher than that of the untreated cell (2.5 mA/cm^2) but still lower than for the annealed cell in [4] (7.5 mA/cm^2) or for the post-production treated cell (8.5 mA/cm^2). Nevertheless, I_{SC} is essentially determined by the applied D/A ratio (influencing the absorption and the mobility [38]), the used solvent [37,39], the resulting film morphology and the nanodomain size as well as by the realised charge carrier mobility [38,39]. Of course, the surface resistance of the used ITO substrates (ITO-PET foils: $60 \Omega/\text{square}$, compared with ITO glass in [4]: $15 \Omega/\text{square}$) is not to be neglected. FF of the presented cell (0.39, the device area is factor 3–5 higher) is approximately the same of the compared

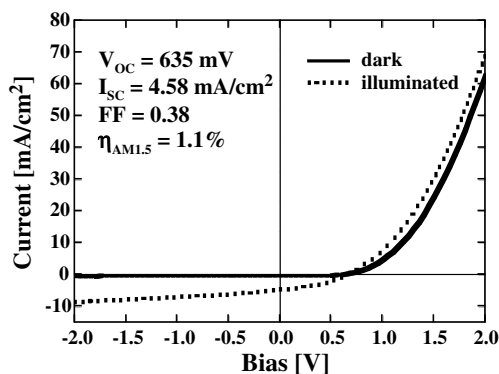


Fig. 10. I - V characteristics of a PET foil/ITO/PEDOT-PSS/P3OT:PCBM (1:3 wt.)/Al cell ($A = 0.25 \text{ cm}^2$) in the dark and under illumination with white light ($P_{IN} = 100 \text{ mW/cm}^2$).

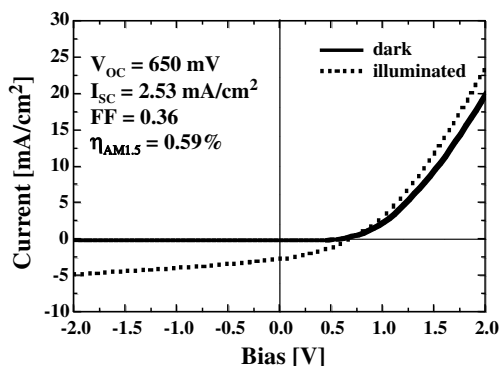


Fig. 11. I - V characteristics of a PET foil/ITO/PEDOT-PSS/P3DDT:PCBM (1:3 wt.)/Al cell ($A = 0.25 \text{ cm}^2$) in the dark and under illumination with white light ($P_{IN} = 100 \text{ mW/cm}^2$).

Table 3

Photovoltaic performance parameters of the cells depicted in Figs. 9–11 on AM1.5 conditions

Active layer	V_{OC} (mV)	I_{SC} (mA/cm^2)	FF	$\eta_{e(AM1.5)}$ (%)
P3HT/PCBM	600	6.61	0.39	1.54
P3OT/PCBM	635	4.58	0.38	1.10
P3DDT/PCBM	650	2.53	0.36	0.59

cell (0.4) but clearly lower than the annealed (0.57) and the post-production treated cell (0.6) in [4]. In the consequence, the overall efficiency for our cell (1.54%) is higher than the cell in [4] without annealing (0.4%) but still lower than it is after heating (2.5%) and upon post-production treatment (3.5%).

Figs. 10 and 11 show the current–voltage characteristics of the solar cell based on P3OT/PCBM (1:3 wt.%) and P3DDT/PCBM (1:3 wt.%) in the dark and on AM1.5 conditions applying a light intensity of 100 mW/cm² at room temperature.

Table 3 summarises the photovoltaic performance parameters of the cells depicted in Figs. 9–11 on AM1.5 conditions.

The open-circuit voltage of the three cells mentioned above increases in the graduation P3HT (600 mV) < P3OT (635 mV) < P3DDT (650 mV). Different acceptors (fullerenes) have been investigated in combination with the same donor [21], where the authors found, that the open-circuit voltage depends on the acceptor strength of the fullerenes applied. This result fully does support the assumption, that the open-circuit voltage of a donor–acceptor bulk-heterojunction cell is directly related to the energy difference between the HOMO level of the donor and the LUMO level of the acceptor component. In agreement with this result and the realisable trend comparing E_p^{ox} , E_{onset}^{ox} of P3HT, P3OT, P3DDT (see Table 1) a possible explanation could be that the relatively small differences in the HOMO levels of the three polythiophenes slightly affect their donor strength and this corresponds with the energy difference between HOMO level of the donor polymers and LUMO level of PCBM.

The cell based on P3HT possesses a higher short-circuit current (6.61 mA/cm²) than the cells based on P3OT (4.58 mA/cm²) and P3DDT (2.53 mA/cm²). Regioregular head-to-tail P3HT is well known for a high degree of intermolecular order leading to high charge carrier mobilities ($\mu_{hole} \sim 0.1 \text{ cm}^2 \text{ V}^{-1} \text{ s}^{-1}$ [40], $\mu_{hole} \sim 0.2 \text{ cm}^2 \text{ V}^{-1} \text{ s}^{-1}$ [41] measured in form of field effect transistor (FET) geometries). The hole mobilities for P3OT ($\mu_{hole} \sim 0.01\text{--}0.001 \text{ cm}^2 \text{ V}^{-1} \text{ s}^{-1}$, $\mu_{hole} \sim 0.001 \text{ cm}^2 \text{ V}^{-1} \text{ s}^{-1}$ [42] determined in form of FET geometries) and for P3DDT ($\mu_{hole} \sim 0.002\text{--}0.005 \text{ cm}^2 \text{ V}^{-1} \text{ s}^{-1}$ [43] measured in form of FET geometries) were described to be lower. Assuming the same de-

gree of regioregularity as well as of polymerisation degree for all three P3ATs, the hole mobility should increase as the length of the side chains decreases due to their contribution to the degree of intermolecular order and chain packaging density. Additionally, the potential barrier of P3OT/ITO is slightly higher than that of P3HT/ITO and somewhat lower than that of P3DDT/ITO (see Fig. 2 and Table 1). This is much more anticipated by the E_p^{ox} -value when comparing P3HT–P3OT–P3DDT, than it is expressed by the differences in HOMO levels that are based on the E_{onset}^{ox} . Thus the hole injection from the HOMO of the polymers into ITO becomes less restricted in the case of P3HT compared to the other two polythiophenes. P3HT shows a higher absorption coefficient than P3OT and P3DDT (see Fig. 3). Its $\pi\text{--}\pi^*$ interband transition blue shift upon mixing with PCBM (1:3) amounts only to $\sim 45 \text{ nm}$ remaining the well-resolved vibrational structure of the pristine P3HT absorption (in solid state). The latter points on the fact that most of the chains should be well planarised giving more extended π -conjugation [30] than e.g. in the case of P3OT and P3DDT. P3OT exhibits the highest blue shift of $\pi\text{--}\pi^*$ interband transition ($\sim 85 \text{ nm}$) upon addition of PCBM, hence it is able to absorb less photons than the other two polymers, which should decrease the current of the cell. After blending with PCBM the P3DDT shows the most distinctive loss of the fine structure resolution in UV–VIS absorption indicating on a disturbance of the planarisation of the P3DDT chains and/or a disruption of the interchain packaging [44] by the PCBM molecules. Possibly this effect compensates the worse absorption of P3OT:PCBM (1:3) compared with P3DDT:PCBM (1:3) (see Section 3.2) leading to the lowest I_{SC} for the P3DDT:PCBM cell.

The cells based on P3HT:PCBM and P3OT:PCBM have approximately the same fill factor (0.39 and 0.38, respectively). A disturbed or less ordered morphology of the photoactive layer and the higher serial resistance may be the reason for the slightly lower fill factor (0.36) found for devices based on P3DDT:PCBM with respect to the values of P3HT and P3OT. Therefore the external AM1.5 power conversion is found to be higher for

¹ From OFET characteristics recorded in our laboratory the hole mobility of regioregular poly(3-octylthiophene) was calculated to $\sim 0.01\text{--}0.001 \text{ cm}^2 \text{ V}^{-1} \text{ s}^{-1}$.

the cell based on P3HT (1.54%) than for the P3OT (1.1%) and P3DDT (0.59%) devices.

According to the single diode model described in [45,46] the serial resistance (R_s) of the cells based on P3HT amounts to $4.5 \Omega \text{ cm}^2$, $11 \Omega \text{ cm}^2$ for P3OT and $39 \Omega \text{ cm}^2$ for P3DDT device. This is in agreement with the literature data given for the hole mobilities for the regioregular P3ATs (given above) decreasing from P3HT to P3DDT as well as the lowest injection barrier at the P3AT/ITO interface in the case of P3HT. Besides from the mobility the lifetime of charge carriers is important because the product of both determines the distance that charge carriers can drift under a certain electric field [47]. Nevertheless, the serial resistance adds all contributions from bulk transport, from interface transfer and from transport through the contacts [38]. The parallel resistance (R_p) of the cell based on P3HT is $246 \Omega \text{ cm}^2$, $303 \Omega \text{ cm}^2$ for P3OT and $1000 \Omega \text{ cm}^2$ for P3DDT device. A decreasing R_p may be caused by shorts due to pinholes (P3DDT:PCBM layers possess a less uniform morphology related to P3HT:PCBM films), a faster charge carrier recombination or a significant bulk conductivity. The latter is supported by the detected dark polaron signals in the ESR spectra for P3HT:PCBM and P3OT:PCBM films (Fig. 5 or Fig. 6) differently from P3DDT:PCBM layers (Fig. 7) indicating a higher doping level for P3HT and P3OT due to impurities in the pristine polymers. Nevertheless, the different photovoltaic parameters of the cells based on P3HT, P3OT and P3DDT may be explained in accordance with the values of their resistances. A lower R_p results in a steeper slope of I - V curve in the third quadrant and may reduce V_{OC} . An increasing R_s diminishes the slope in the first quadrant of I - V characteristics and decreases FF and I_{SC} , respectively. The cell based on P3HT has the lowest serial resistance and the lowest parallel resistance. For this reason it shows the highest current and the lowest voltage. The cell based on P3DDT has the highest serial resistance and the highest parallel resistance. Consequently, it yields the lowest current and the highest voltage. The cell based on P3OT is a compromise between both borderline cases. These results are in agreement with the analysis of the influence of the resistance

values on the photovoltaic parameters of organic solar cells as described in [36].

4. Summary

The HOMO and LUMO levels of regioregular P3HT, P3OT, P3DDT as well as of C_{60} , PCBM and BM- C_{60} were estimated from cyclic voltammetry data. The values of the poly(3-alkylthiophenes) (P3ATs) slightly depend on the length of the alkyl side chain, whereas the energy of the HOMO and the absorption coefficients of the three P3ATs are inversely proportional to this length. The absorption spectra of pristine P3HT, P3OT and P3DDT show distinctive changes upon blending the polymers with PCBM. The peak wave length of the π - π^* interband transition of the P3ATs is shifted towards shorter wave length, whereas the position of the three fullerene bands as well as the optical band edges remain nearly uninfluenced. The π - π^* interband transition blue shift amounts to $\sim 45 \text{ nm}$ for P3HT:PCBM (1:3), $\sim 85 \text{ nm}$ for P3OT:PCBM (1:3) $\sim 50 \text{ nm}$ for P3DDT:PCBM (1:3) (as prepared films). The detected higher shift for P3OT:PCBM (1:3) may be due to differences in the molecular weights of the three polythiophenes or is a special feature of the applied solvent inducing unfavourable chain conformations and/or a disadvantageous interchain packaging.

Induced D-A charge transfer processes in P3AT/PCBM composites were detected by photoluminescence quenching after blending with PCBM and the polaron ($P^{\cdot+}$ on polymer chain) as well as the PCBM radical anion could be assigned to signals found in light-induced electron spin resonance (LESr) spectra.

According to the results obtained, it can be concluded, that an energetic difference of only $\sim 0.2 \text{ eV}$ between the LUMO of P3HT, P3OT or P3DDT and the LUMO of PCBM seems to be sufficient to ensure a directed D-A charge transfer. On the other hand the position of BM- C_{60} was found on nearly the same level like that of P3HT, P3OT, P3DDT, which is in agreement with the PL quenching result (only partially) and the ESR measurements (no signal detected) for P3DDT/BM- C_{60} .

Large-area flexible polymer solar cells (16 cells of 25 mm² on 5 × 5 cm PET foil substrates) based on P3HT:PCBM (1:3 wt.%), P3OT:PCBM (1:3 wt.%) and P3DDT:PCBM (1:3 wt.%) were fabricated still without any post-production treatment and characterised (AM1.5) at ambient conditions. The devices show V_{OC} values between 600 and 650 mV. V_{OC} systematically increases in the order P3HT:PCBM < P3OT:PCBM < P3DDT:PCBM cells, which is probably due to the slightly lower HOMO levels of P3DDT and P3OT compared with P3HT. Although the differences are apparently insignificant, the observed influence on V_{OC} is based on and averaged from a large number individual experiments.

I_{SC} of the P3HT:PCBM cell (6.61 mA/cm²) is higher than that of P3OT:PCBM (4.58 A/cm²) and P3DDT:PCBM device (2.53 mA/cm²). These values are determined by a higher absorption coefficient of the pristine polymer, by the lowest blue shift of the π - π^* interband transition upon blending with PCBM, by an increased hole mobility and by a lower energy transition barrier for holes undergoing transfer from the HOMO level into ITO anode regarding P3HT against P3OT and P3DDT. All three materials do also possess fill factors having the same order of magnitude. Within the series of material compositions P3HT/PCBM < P3OT/PCBM < P3DDT/PCBM the serial and parallel resistance as well as the open-circuit voltage increases, whereas the short-circuit current decreases. The device parameters are fully reproducible on the same conditions.

Acknowledgements

We wish to thank our colleagues Dr. T. Schulze and Prof. H.-K. Roth for the helpful discussions. Financial support from the German Ministries BMWI (project no. 347/01) and BMBF (project no. 01SF0119) is gratefully acknowledged.

References

- [1] N.S. Sariciftci, L. Smilowitz, A.I. Heeger, F. Wudl, *Science* 258 (1992) 1474.
- [2] C.J. Brabec, G. Zerza, G. Cerullo, S. De Silvestri, S. Luzzati, J.C. Hummelen, N.S. Sariciftci, *Chem. Phys. Lett.* 340 (2001) 232.
- [3] C.J. Brabec, N.S. Sariciftci, J.C. Hummelen, *Adv. Funct. Mater.* 11 (2001) 15.
- [4] F. Padinger, R.S. Rittberger, N.S. Sariciftci, *Adv. Funct. Mater.* 11 (13) (2003) 1.
- [5] M.M. Wienk, J.M. Kroon, J.H. Verhees, J. Knol, J.C. Hummelen, P.A. van Hal, R.A.J. Janssen, *Angew. Chem. Int. Ed.* 42 (2003) 3371.
- [6] S. Sensfuss, A. Konkin, H.-K. Roth, M. Al-Ibrahim, U. Zhokhavets, G. Gobsch, V.I. Krinichnyi, G.A. Nazmutdinova, E. Klemm, *Synth. Met.* 137 (1–3) (2003) 1433.
- [7] S. Sensfuss, M. Al-Ibrahim, A. Konkin, G. Nazmutdinova, U. Zhokhavets, G. Gobsch, D.A.M. Egbe, E. Klemm, H.-K. Roth, in: *Int. Sympos. on Opt. Sci. and Techn., SPIE's 48th Annual Meeting*, 3–8.08.2003, Proceedings, vol. 5215, 2003, p. 129.
- [8] M. Al-Ibrahim, H.-K. Roth, S. Sensfuss, *Appl. Phys. Lett.* 85 (9) (2004) 1481.
- [9] M. Al-Ibrahim, H.-K. Roth, U. Zhokhavets, G. Gobsch, S. Sensfuss, *Sol. Energy Mater. Sol. Cells* 85 (1) (2004) 13.
- [10] M. Al-Ibrahim, A. Konkin, H.-K. Roth, D.A.M. Egbe, E. Klemm, U. Zhokhavets, G. Gobsch, S. Sensfuss, *Thin Solid Films* 474/1–2 (2005) 201–210.
- [11] T.-A. Chen, X. Wu, R.D. Rieke, *J. Am. Chem. Soc.* 117 (1995) 233.
- [12] H. Xie, S. O'Dwyer, J. Corish, D.A. Morton-Blake, *Synth. Met.* 122 (2001) 287.
- [13] N. Camaioni, M. Catellani, S. Luzzati, A. Martelli, A. Miglioni, *Synth. Met.* 125 (2002) 313.
- [14] T. Ahn, B. Choi, S.H. Ahn, S.H. Han, H. Lee, *Synth. Met.* 117 (2001) 219.
- [15] V. Dyakonov, G. Zoriniats, M. Scharber, C.J. Brabec, R.A.J. Janssen, J.C. Hummelen, N.S. Sariciftci, *Phys. Rev.* 59 (1999) 8019.
- [16] A. Heeger, P. Smith, *Conjugated Polymers*, Bredas and Silbey, Kluwer Academic Publishers, Netherlands, 1991, pp. 142–210.
- [17] Y. Liu, M.S. Liu, A.K.-Y. Jen, *Acta Polymer.* 50 (1999) 105.
- [18] S.-W. Hwang, Y. Chen, *Macromolecules* 3 (2001) 2981.
- [19] D. Chirvase, Z. Chigvare, M. Knipper, J. Parisi, V. Dyakonov, J.C. Hummelen, *Synth. Met.* 138 (2003) 299.
- [20] K. Takahashi, K. Tsuji, K. Imoto, T. Yamaguchi, T. Komura, K. Murata, *Synth. Met.* 130 (2002) 177.
- [21] C.J. Brabec, A. Cravino, D. Meissner, N.S. Sariciftci, T. Fromherz, M.T. Rispens, L. Sanchez, J.C. Hummelen, *Adv. Funct. Mater.* 11 (5) (2001) 374.
- [22] R. Cervini, X.-C. Li, G.W. Spencer, A.B. Holmes, S.C. Morath, R.H. Friend, *Synth. Met.* 84 (1997) 359.
- [23] B. Liu, W.-L. Yu, Y.-H. Lai, W. Huang, *Chem. Mater.* 13 (2001) 1984.
- [24] X. Qiao, X. Wang, Z. Mo, *Synth. Met.* 118 (2001) 89.
- [25] G. Dicker, T.J. Savenije, B.-H. Huisman, D.M. de Leeuw, M.P. de Haas, J.M. Warman, *Synth. Met.* 137 (2003) 863.

- [26] J.J. Apperloo, R.A.J. Janssen, M.M. Nielsen, K. Bechgaard, *Adv. Mater.* 12 (2000) 1594.
- [27] W.R. Salaneck, I. Lundström, B. Ranby (Eds.), *Conjugated Polymers and Related Materials Proceedings of the Eighty-first Nobel Symposium*, Oxford University Press, 1993, p. 290.
- [28] N. Camaioni, L. Garlaschelli, A. Geri, M. Maggini, G. Possamai, G. Ridolfi, *J. Mater. Chem.* 12 (2002) 2065.
- [29] S. Morita, S. Kiyomatsu, A.A. Zakhidov, K. Yoshino, *J. Phys.: Condens. Matter* 5 (1993) L103.
- [30] A. Zen, J. Pflaum, S. Hirschmann, W. Zhuang, F. Jaiser, U. Asawapirom, J.P. Rabe, U. Scherf, D. Neher, *Adv. Funct. Mater.* 14 (8) (2004) 757.
- [31] V. Dyakonov, I. Riedel, C. Deibel, J. Parisi, C.J. Brabec, N.S. Sariciftci, J.C. Hummelen, *Mater. Res. Soc. Sympos. Proc.* 665 (2001) C7.1.1.
- [32] M. Al-Ibrahim, S. Sensfuss, J. Uziel, G. Ecke, O. Ambacher, *Sol. Energy Mater. Sol. Cells* 85 (2) (2004) 277.
- [33] D. Gebeyehu, C.J. Brabec, F. Padinger, T. Fromherz, J.C. Hummelen, D. Badt, H. Schindler, N.S. Sariciftci, *Synth. Met.* 118 (2001) 1–9.
- [34] C.J. Brabec, F. Padinger, J.C. Hummelen, R.A.J. Janssen, N.S. Sariciftci, *Synth. Met.* 102 (1999) 861.
- [35] C.J. Brabec, F. Padinger, V. Dyakonov, J.C. Hummelen, R.A.J. Janssen, N.S. Sariciftci, *AIP Conf. Proc.* 442 (1998) 519.
- [36] K. Petrisch, PhD Thesis, Technische Universität Graz, Austria, 2000.
- [37] J. Liu, Y. Shi, Y. Yang, *Adv. Funct. Mater.* 11 (6) (2001) 420.
- [38] H. Hoppe, N.S. Sariciftci, *J. Mater. Res.* 19 (2004) 1924.
- [39] M.T. Rispens, A. Meetsma, R. Rittberger, C.J. Brabec, N.S. Sariciftci, J.C. Hummelen, *Chem. Commun.* 17 (2003) 2116.
- [40] H. Siringhaus, P.J. Brown, R.H. Friend, M.M. Nielsen, K. Bechgaard, B.M.W. Langefeld-Voss, A.J.H. Spiering, R.A.J. Janssen, E.W. Meijer, P. Herwig, D.M. de Leeuw, *Nature* 401 (1999) 685.
- [41] A. Ullmann, J. Ficker, W. Fix, H. Rost, W. Clemens, I. McCulloch, M. Giles, *Mater. Res. Soc. Sympos. Proc.* 665 (2001) C7.5.
- [42] M. Plötner, T. Wegener, S. Richter, S. Howitz, W.-J. Fischer, in: *EMRS Spring Meeting 2004, Strasbourg, 24–28.05.2004, Symposium F, F/PII.19*.
- [43] S. Scheinert, G. Paasch, M. Schrödner, H.-K. Roth, S. Sensfuss, Th. Doll, *J. Appl. Phys.* 92 (1) (2002) 330.
- [44] P.J. Brown, D.S. Thomas, A. Köhler, J. Wilson, J.-S. Kim, C. Ramsdale, H. Siringhaus, R.H. Friend, *Phys. Rev. B* 67 (2003) 064203.
- [45] C.J. Brabec, A. Cravino, G. Zerza, N.S. Sariciftci, R. Kiebooms, D. Vanderzande, J.C. Hummelen, *J. Phys. Chem. B* 105 (2001) 1528.
- [46] C. Winder, Diploma Thesis, University Linz, 2001.
- [47] P. Schilinsky, C. Waldauf, J. Hauch, C.J. Brabec, *J. Appl. Phys.* 95 (2004) 2816.



PMMA–Ta₂O₅ bilayer gate dielectric for low operating voltage organic FETs

A.-L. Deman, J. Tardy *

CNRS and Ecole Centrale de Lyon Laboratoire d'Electronique, Optoélectronique et Microsystèmes (LEOM), UMR 5512, 36 avenue Guy de Collongue, 69134 Ecully cedex, France

Received 1 April 2004; received in revised form 3 March 2005; accepted 3 March 2005

Available online 2 April 2005

Abstract

This paper reports on a study on pentacene field effect transistors (OFETs) with a gate dielectric made of a bilayer PMMA/Ta₂O₅ where PMMA (poly(methyl methacrylate)) is spin-coated on top of an evaporated layer of Ta₂O₅. A comparison with devices with only Ta₂O₅ is presented. These latter exhibit very low operating voltage associated to the high dielectric constant of this oxide but also show some surface trapping and gate leakage. These two drawbacks can be overcome by depositing a PMMA layer on Ta₂O₅. With such a bilayer gate dielectric, gate leakage current is considerably reduced and the quality of the interface between pentacene and PMMA was much improved compared to that with Ta₂O₅ as evidenced from the much higher output drain current. The influence of PMMA thickness in the range 15–250 nm is presented. OFETs with field effect mobility, on/off current ratio, and sub-threshold slope of respectively 0.4 cm² V⁻¹ s⁻¹, 3 × 10⁵ and 1.2 V/decade were obtained.

© 2005 Elsevier B.V. All rights reserved.

PACS: 71.20.Rv; 72.80.Le; 73.40.Qv; 73.61.Ph; 77.84.Jd

Keywords: OFET; High-*K* dielectric; Pentacene; Ta₂O₅; PMMA

1. Introduction

This last decade, organic field effect transistors have gained much interest mainly due to their potential applications in what is commonly called

large area electronics. These include driving circuits for future all-organic OLEDs flat panel displays [1], plastic RF–ID circuits [2], gas sensors [3], chemical species sensors [4]. The continuous improvement in the quality of organic semiconductors, their compatibility with plastic substrates [5,6], and their low cost and low temperature process make them good candidates for all these applications. Nevertheless OFETs performances

* Corresponding author. Tel.: +33 4 72 18 60 65; fax: +33 4 78 43 35 93.

E-mail address: jacques.tardy@ec-lyon.fr (J. Tardy).

do not rely only on the semiconductor material quality as intrinsic mobility. OFETs are working in accumulation regime and most of the modulated charge lies within the first 10 nm. That does mean that the interface properties between the semiconductor and the gate dielectric are of tremendous importance on the field effect mobility. Improvement of the gate dielectric material and of its interface with the organic semiconductor would be highly beneficial to the performances of OFETs. Roughness [7], density of surface traps [8], dielectric constant [9] are crucial parameters. Among inorganic dielectrics, the most often used was SiO₂ grown on highly doped Si gate. However its weak dielectric constant ($\epsilon = 3.9$) remains a serious limitation for low power and nomad applications since operating voltage largely above 50 V are necessary for sufficient charge injection in the channel. Replacement with silicon nitride does not lead to significant improvement [7]. High-*K* materials such as Al₂O₃ [9,10] and Ta₂O₅ [11,12] were also proposed for gate oxide in OFETs. This latter reference reports on an investigation on the influence of electric field and temperature on mobility of pentacene transistors with Ta₂O₅ grown by anodic oxidation on plastic substrates. The mobility and on/off ratio obtained in this study are competitive with typical results for this materials combination ($0.36 \text{ cm}^2 \text{ V}^{-1} \text{ s}^{-1}$ and 10^4 , respectively). It is commonly observed that the operating voltage was noticeably reduced with Ta₂O₅, but this dielectric remains somewhat leaky. Other studies proposed to realise all-organic transistors with the use of polymer dielectrics as polyvinyl phenol (PVP) based polymers [13,14] or PMMA [15,16]. One major advantage of organic–organic interface is the noninteracting nature of this interface in most cases [17]. That means an abrupt interface without reactive interlayer or dipoles as observed in metal/organic interfaces [18]. The organic/oxide interface is also highly dependent on the surface preparation of the oxide as the numerous studies on the influence of ITO surface treatment on OLEDs performances shown in the past [19]. In spite of the potential improvement of device operation with organic/organic interface, organic dielectrics also show the drawback of a small dielectric constant. In order

to reconcile the respective advantages of an high-*K* oxide for low operating voltage and polymer dielectric for a better interface with the organic semiconductor, a bilayer gate dielectric consisting of a Ta₂O₅ film covered with a PMMA film is reported in this study.

2. Experimental

Ta₂O₅ (purchased from Cerac Inc.) was deposited by e-beam evaporation in presence of an oxygen partial pressure (8×10^{-5} – 2×10^{-4} mbar) on highly doped Si substrate kept at room temperature. The deposition rate and the film thickness were respectively 5 Å/s and 120 nm. Some films have been annealed at 600 °C for 1 h in O₂ atmosphere. For the bilayer gate dielectric, a solution of PMMA in anisole was spin-coated onto the Ta₂O₅ and allowed to dry at 120 °C for 1 min. The thickness of PMMA after drying is in the range 18–250 nm for a solution in the concentration range 10–40 g/l. Then a 80 nm thick pentacene film was deposited by thermal evaporation at a rate of 0.7 Å/s on the substrate maintained at 70 °C. The pentacene (purchased from Aldrich) was used as received without any further purification. The devices were completed by the evaporation of interdigitated Au top contact source and drain electrodes through a shadow mask. The channel length was 100 μm and the developed width was $19 \times 1000 \mu\text{m}$. Fig. 1 gives the schematic structure of the two FETs processed with, respectively, Ta₂O₅ and PMMA/Ta₂O₅ gate dielectrics.

Capacitance structures were also processed to determine the dielectric characteristics. On Ta₂O₅, Al electrodes were patterned by lithography with various capacitance areas in the range 1×10^{-4} – $36 \times 10^{-4} \text{ cm}^2$. In the case of PMMA, Al electrodes were evaporated through a shadow mask and the capacitance area was $5 \times 10^{-3} \text{ cm}^2$. *C*–*V* measurements were carried out at RT with a HP 4284 LCR meter at 1 MHz. Current–voltage characteristics of Al/PMMA/Ta₂O₅/Si p⁺⁺ structures were recorded with a HP 4145 parameters analyser and the leakage current through the insulator was determined at a field of 0.2 MV/cm when only Ta₂O₅ was used and at 0.5 MV/cm for

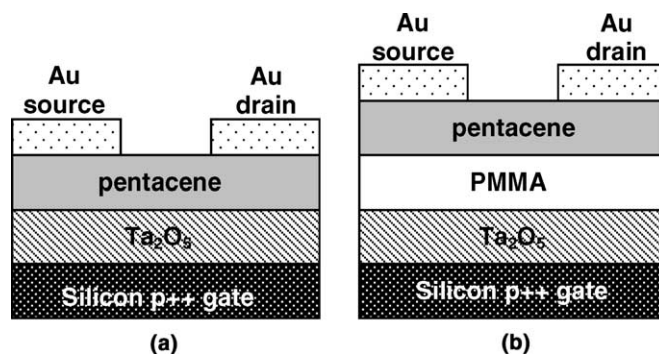


Fig. 1. Schematic structure of the OFET with Ta₂O₅ (a) and PMMA/Ta₂O₅ (b) gate dielectrics.

PMMA/Ta₂O₅ bilayers. Transistors were characterised in air at room temperature by using two Keithley 2400 Source-Meter units under Labview[®] environment. No degradation of the devices was observed during characterisation. Between two characterisation runs, the OFETs were kept under vacuum in order to obtain reproducible results. Too long a time spent in atmosphere (over a few days) leads to continuously degraded performances due to the humidity sensitivity of pentacene.

3. Results and discussion

3.1. Electrical properties of evaporated Ta₂O₅

It is well known that the performances of a MOSFET strongly rely on the structural and electronic qualities of the gate insulator. Ta₂O₅ deposited by reactive evaporation at room temperature may contain several defects which could degrade the electrical characteristics of the OFET: multiphase material, local variation of composition, inhomogeneity, roughness, bulk and surface traps. We then investigated different deposition conditions by varying the oxygen pressure, the substrate temperature during the evaporation and post-deposition annealing in oxygen or nitrogen atmosphere at temperatures in the range 150–600 °C. Best results were obtained with an oxygen partial pressure of 2×10^{-4} Torr. Some Ta₂O₅ depositions were carried out with the substrate at 150 °C. These films did not reveal any change compared

with those deposited by thermal evaporation on room temperature substrates. The dielectric constant of 120 nm thick Ta₂O₅ films is $\epsilon_r \cong 18$. Some films however exhibited an unexplained dielectric constant greater than 30. Thinner films (80 nm) show $\epsilon_r \cong 21$ –22, and were also much less leaky than thicker films.

The leakage current I_L at an electric field of 0.2 MV/cm through the Ta₂O₅ film was assessed from I – V characteristics of Al/Ta₂O₅/Si n⁺⁺ structures. This field corresponds to 2.4 V for a 120 nm thick film which is a typical operating voltage for OFET with Ta₂O₅ gate oxide (see below). Nonannealed films usually exhibit I_L as high as 10–200 $\mu\text{A}/\text{cm}^2$ depending on the area of the device. On contrary, devices annealed at 600 °C show a very low leakage current down to 0.2–2 $\mu\text{A}/\text{cm}^2$. This strong decrease is attributed to the growth of a SiO₂ layer at the interface between Si and Ta₂O₅ upon annealing consecutively to Ta₂O₅ dissociation and Si oxidation. Considering the SiO₂ and the Ta₂O₅ capacitances in series with respective dielectric constant $\epsilon_r = 3.9$ and $\epsilon_r = 22$ or 30, and an effective constant after annealing of $\epsilon_r = 18$, we can evaluate that the thickness of the SiO₂ film grown at the interface is between 4.7 nm and 12 nm. This SiO₂ interface layer helps in improving the gate leakage current in OFET.

3.2. OFET with only Ta₂O₅ gate oxide

Fig. 2 shows the characteristics $I_D(V_D)$ and $\sqrt{I_D}(V_G)$ of two devices which only differ by the fact that Ta₂O₅ (120 nm) has not been annealed

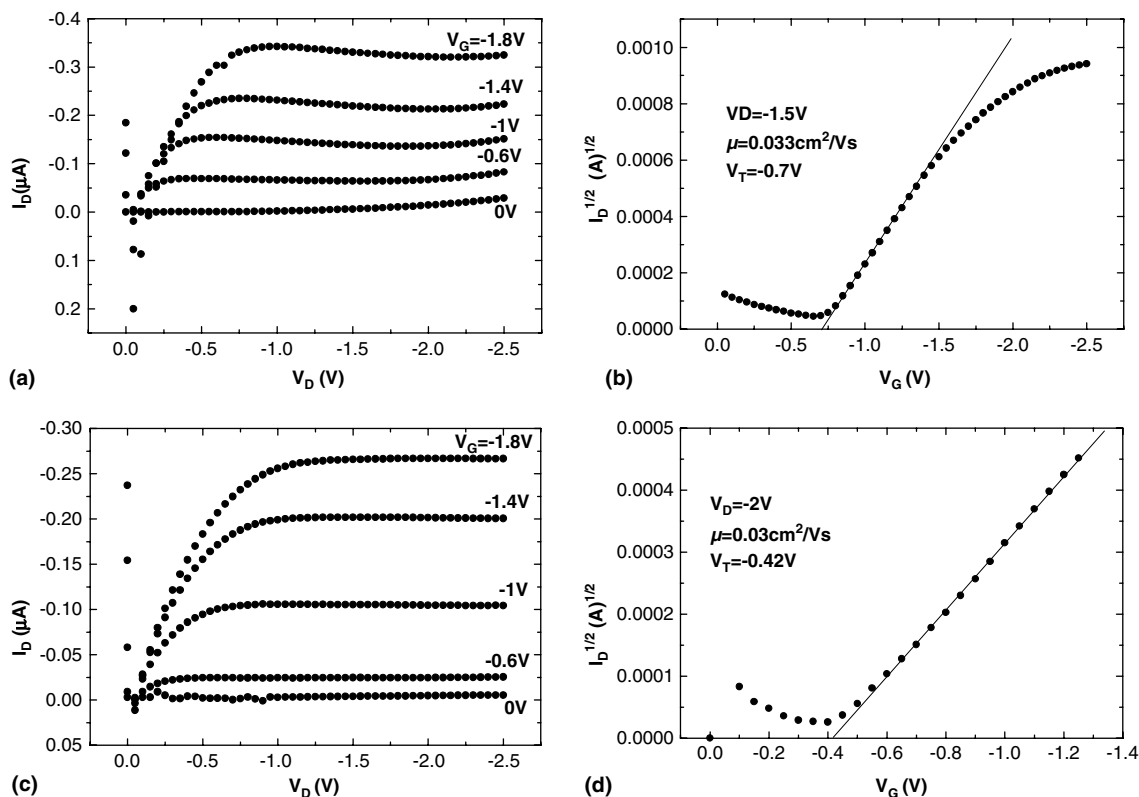


Fig. 2. Output and transfer characteristics of OFETs with 120 nm Ta_2O_5 as gate dielectric either nonannealed ((a) and (b)) or annealed at 600 °C for 1 h in O_2 ((c) and (d)).

after deposition (Fig. 2(a) and (b)) or has been annealed at 600 °C in oxygen for 1 h (Fig. 2(c) and (d)). We can first point out the very low operating voltage of these devices as compared with more conventional devices on SiO_2 . The output characteristics for nonannealed (NA) Ta_2O_5 show a rather high positive current at low V_D (Fig. 2(a)). When Ta_2O_5 was annealed this current is much lower (Fig. 2(c)). The increase of leakage current with the gate voltage bears out the assignment to a drain-to-gate current through the gate insulator. Leakage lowering after Ta_2O_5 annealing bears out the results reported in the preceding section on reduced leakage through Ta_2O_5 attributed to SiO_2 formation at the interface between Ta_2O_5 and Si gate upon annealing. In a similar way, a beneficial influence of a thin SiO_2 film (3–17 nm) deposited

on TiO_2 was recently reported [20]. Improved field effect mobility, on/off ratio and gate leakage current of poly(3-hexylthiophene) FET was observed. The saturation current on NA- Ta_2O_5 is not constant. This could be due to trapping of injected holes which are released at a high V_D . This effect has not been observed for heat treated Ta_2O_5 where we can expect that annealing helps in removing surface states induced by dangling bonds. The smaller threshold voltage for annealed Ta_2O_5 ($V_T = -0.4$ V instead of $V_T = -0.7$ V for NA- Ta_2O_5) as well as a higher on/off ratio bear out this hypothesis. The mobility remains about $3\text{--}4 \times 10^{-2} \text{ cm}^2 \text{ V}^{-1} \text{ s}^{-1}$ independently of Ta_2O_5 annealing. This value is quite similar to that observed with $\text{Al}_2\text{O}_{3-x}$ gate oxide [5]. Nevertheless it should be mentioned that the on/off ratio we

obtained remains comparatively low. In work to be published elsewhere, we will report on a strong influence of the Ta₂O₅ thickness on the OFET performance. For example, a 80 nm instead of a 120 nm thick Ta₂O₅ leads to sharply improved performances of OFET since the mobility μ and

the on/off ratio are observed to increase to $0.15 \text{ cm}^2 \text{ V}^{-1} \text{ s}^{-1}$ and 1.2×10^3 respectively, whereas the leakage current is even slightly lower than for the current devices. This suggests that the microstructure of Ta₂O₅ is dependent on the thickness.

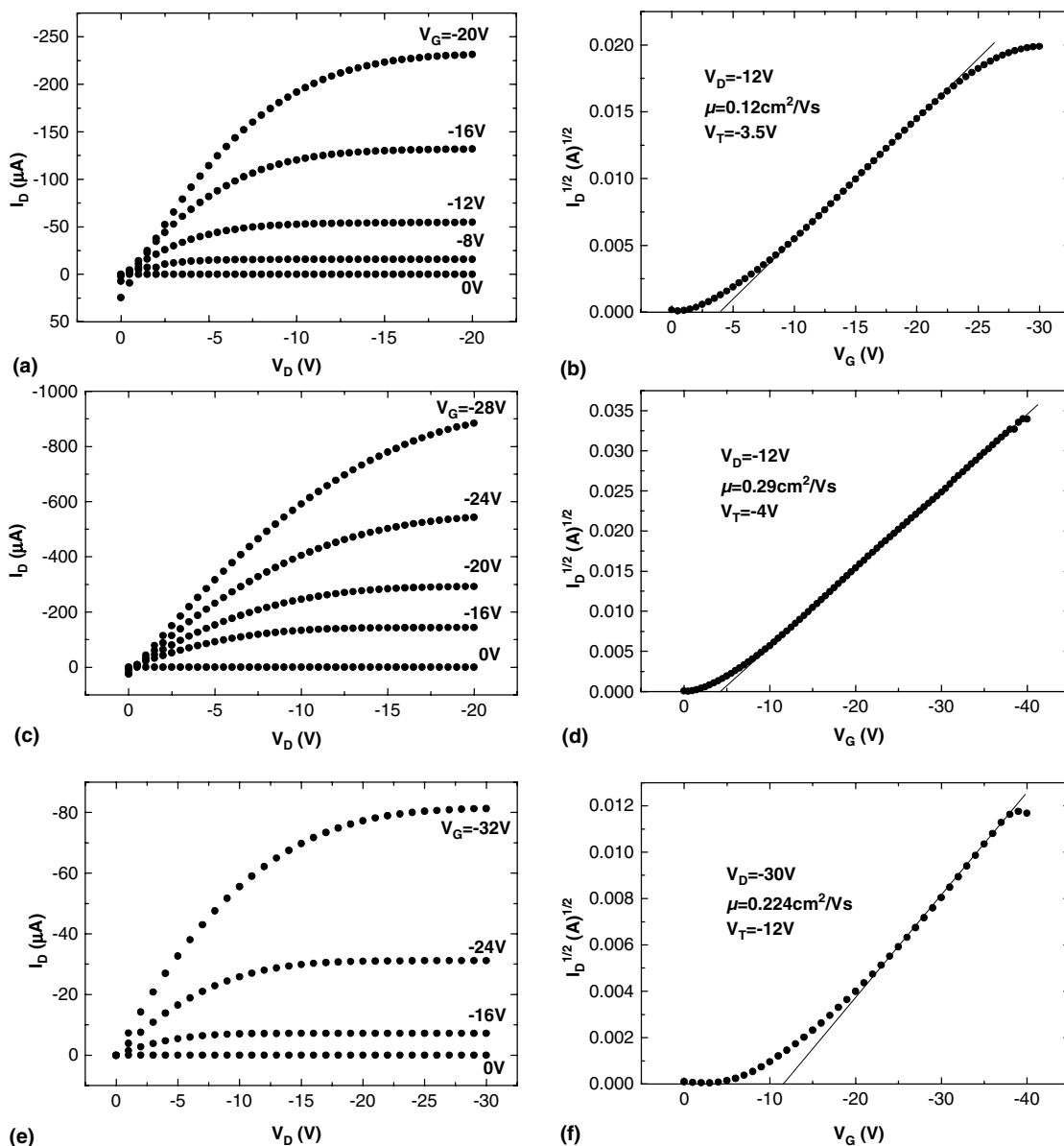


Fig. 3. Output and transfer characteristics of OFETs with PMMA/Ta₂O₅ as bilayer gate dielectric. PMMA thickness is 15 nm ((a) and (b)), 37.5 nm ((c) and (d)) and 250 nm ((e) and (f)). Ta₂O₅ thickness is 120 nm.

Table 1

Dielectric characteristics of Ta₂O₅ and performances of OFETs with Ta₂O₅ and PMMA/Ta₂O₅ gate dielectric: operating voltage, mobility, threshold voltage, and sub-threshold swing

Nature of the dielectric	Ta ₂ O ₅ non annealed	Ta ₂ O ₅ annealed 600 °C in O ₂	Annealed Ta ₂ O ₅ + 15 nm PMMA	Annealed Ta ₂ O ₅ + 37.5 nm PMMA	Annealed Ta ₂ O ₅ + 250 nm PMMA
Gate capacitance (nF/cm ²)	229	125	74	39	8.5
Leakage current (μA/cm ²)	20–100 @ 0.2 MV/cm	1–2 @ 0.2 MV/cm	0.14 @ 0.5 MV/cm	0.09 @ 0.5 MV/cm	2–16 @ 0.5 MV/cm
Operating voltage (V)	0 to –2	0 to –2	0 to –20	0 to –28	0 to –32
Mobility (cm ² V ⁻¹ s ⁻¹)	3.6 × 10 ⁻²	3 × 10 ⁻²	0.12	0.29	0.25
Threshold voltage (V)	–0.7	–0.4	–3.5	–4	–12
Sub-threshold swing (V/dec)	0.5	0.44	1.04	1.2	1.25
On/off ratio	67	170	4.3 × 10 ⁴	2.7 × 10 ⁵	1 × 10 ⁵

3.3. Devices with PMMA/Ta₂O₅ bilayer gate dielectric

Fig. 3 reports the electrical characteristics for three devices with a gate dielectric made of 120 nm Ta₂O₅ with spun on layers of PMMA with thicknesses of 15, 37.5 and 250 nm. We first observe a strong increase of the drain current compared to what obtained with Ta₂O₅ only. In comparison to devices with only Ta₂O₅, the operating voltage increases to 20–30 V due to the low dielectric constant of the PMMA layer which reduces the equivalent gate capacitance. From the transfer characteristics, the measured threshold voltage is about –4 V for the two thinnest PMMA layers and V_T increases up to –12 V for the 250 nm thick PMMA. The major improvement brought by PMMA is the strong increase of field effect mobility which reach 0.3 cm² V⁻¹ s⁻¹ for 37.5 nm PMMA. The highest μ_{FE} obtained was 0.4 cm² V⁻¹ s⁻¹ with pentacene used as purchased without any further purification and devices characterised in air. The on/off ratio also increases with PMMA and reaches 2.7 × 10⁵ for 37.5 nm PMMA. The sub-threshold swing remains about constant between 1 V/dec and 1.2 V/dec at $V_D = -12$ V.

We also observe that the gate leakage dramatically decreases upon deposition of PMMA since very low leakage is observed for the thinnest two PMMA films. The higher leakage for thick PMMA (250 nm) is attributed to insufficient curing after deposition. For this thickness, annealing for a much longer period is necessary to eliminate

all traces of solvents. The well separated characteristics at low drain voltage in the linear regime indicate a rather small contact resistance. All these data point to the beneficial influence of a thin PMMA film on Ta₂O₅ on device performances. Improvement is to be associated with a pentacene/PMMA interface of much better quality than the pentacene/Ta₂O₅ interface in terms of electronic states but also in terms of roughness. Table 1 summarises the data reported in the paper.

4. Conclusions

In this paper we reported a new gate dielectric for OFETs made of a PMMA/Ta₂O₅ bilayer. This dielectric design combines the respective advantages of the two materials, say, the high dielectric constant of Ta₂O₅ and an improved PMMA/pentacene interface. Devices with operating voltages in the range 0–2.5 V were obtained with Ta₂O₅ dielectric constant ($\epsilon_r \cong 20$). Devices showing a high mobility, a high on/off ratio and very low leakage current were obtained with PMMA spun on Ta₂O₅. Optimum PMMA thickness was found to be about 37 nm but beneficial effect was already achieved with PMMA layers as thin as 15 nm. It should be mentioned that all the process can be carried out at near room temperature. Work is currently in progress towards a better characterisation of the electrical and structural properties of pentacene/PMMA interface and on improved Ta₂O₅ bulk and surface properties.

Acknowledgements

This study benefited from a financial support of French Research Ministry under the program Nanosciences 2003. The technical assistance of P. Cremillieu is warmly acknowledged.

References

- [1] H. Sirringhaus, N. Tessler, R.H. Friend, *Synth. Met.* 102 (1999) 857.
- [2] P.F. Baude, D.A. Ender, M.A. Haase, T.W. Kelly, D.V. Muyres, S.D. Theiss, *Appl. Phys. Lett.* 82 (2003) 3964.
- [3] B. Crone, A. Dodabalapur, A. Gelperin, L. Torsi, H.E. Katz, A.J. Lovinger, Z. Bao, *Appl. Phys. Lett.* 78 (2001) 2229.
- [4] C. Bartic, A. Campitelli, S. Borghs, *Appl. Phys. Lett.* 82 (2003) 475.
- [5] J.H. Lee, S.H. Kim, G.H. Kim, S.C. Lim, H. Lee, J. Jang, T. Zyung, *Synth. Met.* 139 (2003) 445.
- [6] A. Bonfiglio, F. Mameli, O. Sanna, *Appl. Phys. Lett.* 82 (2003) 3550.
- [7] D. Knipp, R.A. Street, A.R. Völkel, *Appl. Phys. Lett.* 82 (2003) 3907.
- [8] For a general discussion on interface traps, see: S.M. Sze, *Physics of Semiconductor Devices*, Wiley, New York, 1981.
- [9] L.A. Majewski, M. Grell, S.D. Ogier, J. Veres, *Organic Electronics* 4 (2003) 27.
- [10] J. Lee, J.H. Kim, S. Im, *Appl. Phys. Lett.* 83 (2003) 2689.
- [11] C. Bartic, H. jansen, A. Campitelli, S. Borghs, *Organic Electronics* 3 (2002) 65.
- [12] Y. Iino, Y. Inoue, Y. Fujisaki, H. Sato, M. Kawakita, S. Tokito, H. Kikuchi, *Jpn. J. Appl. Phys.* 42, Part 1 299 (2003).
- [13] H. Klauk, M. Halik, U. Zschieschang, G. Schmid, W. Radik, W. Weber, *J. Appl. Phys.* 92 (2002) 5259.
- [14] H. Sirringhaus, R.J. Wilson, R.H. Friend, M. Ibasekaran, W. Wu, E.P. Woo, M. Grell, D.D.C. Bradley, *Appl. Phys. Lett.* 77 (2000) 406.
- [15] R. Bourguiba, F. Garnier, G. Horowitz, R. Hajlaoui, P. Delannoy, M. Hajlaoui, H. Bouchriha, *Eur. Phys. J. Appl. Phys.* 14 (2001) 121.
- [16] S. Uemura, M. Yshida, S. Hoshino, T. Kodzasa, T. Katama, *Thin Solid Films* 438/439 (2003) 378.
- [17] A. Rajagopal, C.I. Wu, A. Khan, *J. Appl. Phys.* 83 (1998) 2649.
- [18] I.G. Hill, A. Kahn, *J. Appl. Phys.* 84 (1998) 5583.
- [19] For a recent review on OLEDs materials and devices, see L.S. Hung, C.H. Chen, *Mater. Sci. Eng. Rep.* 39 (2002) 143.
- [20] G. Wang, D. Moses, A.J. Heeger, H.-M. Zhang, M. Narasimhan, R.E. Demaray, *J. Appl. Phys.* 95 (2004) 316.



Polarization at the gold/pentacene interface

F. Amy*, C. Chan, A. Kahn

Department of Electrical Engineering, Princeton University, E-quad room c434, Princeton, NJ 08544, USA

Received 8 February 2005; received in revised form 7 March 2005; accepted 10 March 2005

Available online 7 April 2005

Abstract

Direct and inverse photoemission spectroscopy are used to investigate the electronic polarization $P = P^+ + P^-$ induced by the pentacene anion and cation at the Au/pentacene interface. Based on the spectroscopic measurements and on previously published calculations, we determine that the total polarization at the metal interface is approximately 0.67 eV larger than at the surface of the pentacene film, leading to a corresponding decrease of the interface transport gap. This reduced interface gap leads to hole and electron injection barriers of 0.47 eV and 1.17 eV, respectively.

© 2005 Elsevier B.V. All rights reserved.

1. Introduction

Organic semiconductors have major potential applications in the fields of light emitting diodes, thin film transistors and photovoltaic cells. These devices comprise multiple layers of organic materials and contacts for electron and hole injection or extraction. Metal–organic and organic–organic interfaces are therefore of paramount importance for small molecule and polymer devices alike, and have received considerable attention in the past decade [1–4]. The most widely accepted conclusion of these interface studies is that

metal–organic contacts generally do not follow the Schottky–Mott model and exhibit large dipole barriers [1,2,5,6]. The origins of these dipoles ranges from charge transfer with [7] or without [6] interface chemistry, to reduction of the metal work function by the organic layer [1] and occupation of the metal-induced density of interface states in the gap of the organic material [8,9]. Beyond the mechanisms of dipole and barrier formation, however, subtle issues are also likely to have a significant impact on charge carrier injection. Polarization and gap narrowing at the metal/organic interface is one of these issues, and is the focus of the present study.

Organic solids of π -conjugated molecules are characterized by weak intermolecular (van der Waals) bonds and small intermolecular wave

* Corresponding author. Tel.: +1 609 258 3582; fax: +1 609 258 6279.

E-mail address: famy@princeton.edu (F. Amy).

function overlap. Charge carriers are localized and modeled as molecular anions (electrons) and cations (holes) embedded in a matrix of neutral molecules. The electronic polarization of the dielectric medium by the central charge, which results in the formation of a polaron, is a major effect with an energy scale larger than intermolecular transfer integrals. Charge transport occurs via thermally activated polaron hopping.

Among many organic semiconductors considered for field-effect transistors, pentacene has drawn the most attention and has been used as a relatively high-mobility hole transport material [10–12]. This is due to two factors. First, pentacene films with good morphology and molecular ordering can be obtained by evaporation on suitably treated dielectric surfaces [13]. Second, the relaxation energy of the pentacene molecular ion is smaller by a factor of at least two than in other commonly used hole transport materials [14]. The result is a small polaron binding energy, which, added to relatively good molecular ordering, gives a mobility of the order of $1 \text{ cm}^2/\text{V s}$. Yet, the benefit of this performance is best realized if charge carrier injection is not a significant limitation in the device. The energetics of pentacene/metal interfaces used in devices are therefore of prime importance.

Several phenomena contribute to polarization and reorganization of molecular levels upon occupation of a molecule by an excess charge: (i) electronic polarization of the surrounding molecules, which accounts for most of the screening of the central charge; (ii) molecular relaxation, which accounts for conformational changes of the molecular ion due to the charge; and (iii) lattice relaxation, which accounts for the response of the structure of the molecular film to the presence of the central charge. The molecular relaxation ($\sim 100 \text{ meV}$) and lattice relaxation ($\sim 10 \text{ meV}$) are small compared to the electronic polarization component ($\geq 1 \text{ eV}$) [14–16]. Because of the low dielectric constant of organic materials ($\epsilon \sim 3$), the electronic polarization has a significant impact on the energy level of the transport states.

Like in inorganic semiconductors, the transport gap E_t , or single-particle gap, of the molecular film is the energy difference between the electron trans-

port state and the hole transport state (Fig. 1), and is the minimum energy necessary to create an uncorrelated electron-hole pair infinitely separated in the bulk of the material. It is equal to the difference between the adiabatic ionization energy (I) and electron affinity (A) of the single (gas-phase) molecule reduced by the sum P of the energies of electronic polarization and lattice relaxation (the molecular relaxation is already included in $I - A$). Since the electronic polarization is a long range Coulomb interaction and the polarization cloud extends over several molecular lattice constants, P and E_t are affected by the proximity of a surface or interface. Because of image charges in the metal, P is larger at the metal–organic interface than in the bulk of the material. On the other hand, P is smaller at the free surface of the organic film since vacuum is not polarizable [17]. Therefore E_t is expected to be smaller at the metal interface and larger at the free surface [18,19].

This work focuses on polarization and narrowing of the transport gap at the Au/pentacene interface. Direct and inverse photoemission spectroscopies are used to measure the energy of the highest occupied and lowest unoccupied molecular orbitals (HOMO, LUMO) of pentacene as a function of film thickness. HOMO and LUMO levels represent the hole and electron transport levels, respectively. The analysis of these levels as a function of film thickness provides a measure

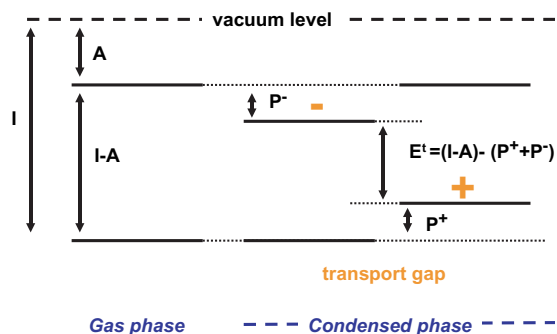


Fig. 1. Adiabatic ionization energy (I) and electron affinity (A) of the gas-phase molecule (left); transport gap and levels of the relaxed molecular ions in the condensed phase, including polarization energies P^+ and P^- for holes and electrons, respectively (right).

of interface polarization and transport gap narrowing.

2. Experiments

Measurements were performed on pentacene films thermally evaporated on Au from a solid source. Deposition and spectroscopy measurements were performed in ultra high vacuum (UHV). Ultra-violet photoemission spectroscopy (UPS) was done using the He I (21.22 eV) line of a discharge lamp, with a total resolution of 150 meV. Inverse photoemission spectroscopy (IPES) was performed in the isochromat mode using a photon detector [20] centered at a fixed energy of 9.2 eV, with a total resolution of 450 meV. The UPS and IPES energy scales were aligned by measuring the position of the Fermi level on a freshly evaporated Au film. The position of the vacuum level, E_{vac} was measured for each surface using the onset of photoemission [21].

The substrates were Si(100) wafers coated with 50 Å of Ti and 1200 Å of Au. The organic films were prepared by incremental deposition of pentacene at rates of about 0.5–1 Å/s on the room temperature substrate covered by a freshly deposited Au layer. The samples were studied with UPS first and IPES second. In order to prevent degradation of the organic film during IPES, the beam current density was limited to 10^{-6} A/cm². No charging or degradation of the organic layer was detected with either technique.

3. Results and discussion

A composite of UPS and IPES spectra of a 75 Å pentacene film on polycrystalline Au is displayed in Fig. 2. The UPS spectrum (negative energies) maps the density of filled states whereas the IPES part (positive energies) maps the density of empty states. The energy scale is relative to the position of the Fermi level E_F measured on Au. Under the assumption of thermodynamic equilibrium, the position of E_F is taken as constant across the film. E_{vac} is at 4.49 eV above E_F in this particular case.

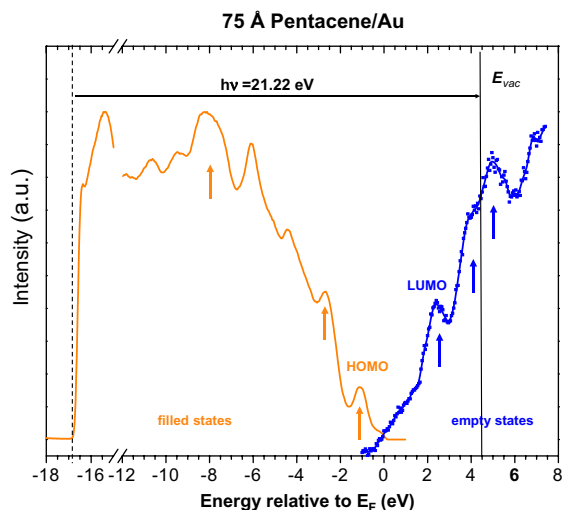


Fig. 2. Composite UPS/IPES spectrum of the filled and empty states recorded from a 75 Å thick film of pentacene deposited on Au. Energy scales are aligned by measuring the Fermi level position with UPS and IPES on a clean Au substrate. Arrows indicate pentacene molecular energy levels. E_{vac} is at 4.49 eV above Fermi level.

Characteristic features of the pentacene levels, including the HOMO and LUMO levels, are outlined by arrows in Fig. 2. UPS and IPES probe the hole state (molecular cation) and electron state (molecular anion) of the organic film, respectively. Once the molecule is charged (by electron removal in UPS, or electron addition in IPES), the major contribution to polarization is the fast response of the electronic charge density of the surrounding molecules, which occurs in $\sim 10^{-16}$ s. UPS and IPES electrons have a kinetic energy typically between 5 and 15 eV and travel over molecular distances of 10–15 Å in $1-5 \times 10^{-15}$ s. The electronic component of the polarization (1–1.5 eV) is therefore included in both UPS and IPES spectra and these techniques measure the energy of the nearly fully relaxed positive or negative polaron, respectively. The molecular relaxation occurs on a time scale of 10^{-15} – 10^{-14} s [22], and may or may not be included in these measurements. However, that contribution to polarization energy is smaller (~ 100 meV) than the electronic component, particularly in the case of pentacene [14]. The lattice relaxation component is too slow ($\sim 10^{-13}$ s) to be accounted for with either UPS or IPES, but

only contributes a few tens of meV to the total polarization energy [16]. This is considerably smaller than the energy resolution of the measurement techniques, and is neglected here.

The UPS spectrum of the 75 Å thick pentacene film (Fig. 2) exhibits a Fermi step and other features related to the Au substrate, indicating three-dimensional growth and/or pinholes in the organic film under the deposition conditions given above [13].

The position of the centroid of the HOMO and LUMO peaks measured with respect to E_{vac} is plotted in Fig. 3 as a function of film thickness. As the pentacene thickness increases, both peaks shift away from the Fermi level, while the position of E_{vac} does not change significantly. Given the surface sensitivity of the measurements (5–10 Å), the measured energy levels correspond to molecular ions *at the surface of the film*. The 0.54 eV increase between the gap of the thin film ΔE^{ml} and the gap of the thick film ΔE^s (Fig. 3) corresponds to a decrease in electronic polarization at the surface of the film with increasing distance from the Au interface. The increase in the gap is limited to the first 5–10 nm. This result is consistent with the ~ 0.45 eV increase observed for PTCDA on Au and Ag [19]. It is also consistent with results obtained for naphthalenetetracarboxylic dianhydride (NTCDA), which show an increase between

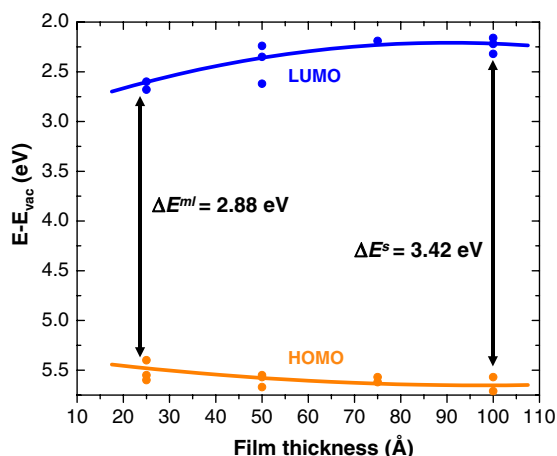


Fig. 3. Measured energy position of the HOMO (bottom) and LUMO (top) peak with respect to the vacuum level as a function of the pentacene film thickness.

the 4 Å film gap (ΔE^{ml}) and the 64 Å film gap (ΔE^s) (Fig. 4). In the NTCDA case, the 4 Å HOMO peak is weak, its position is difficult to determine accurately, and the change in polarization energy is measured from a deeper level (labeled M on Fig. 4). The 0.21 eV shift of M from thin to thick film is indicative of the decrease in hole polarization energy P^+ . The 64 Å spectrum gives a 5.32 eV energy separation between M and the HOMO peak. Assuming that this energy separation is the same for the 4 Å thin film, one finds that the gap increase from $\Delta E^{ml} = 5.61$ eV for the 4 Å film to $\Delta E^s = 5.94$ eV for the 64 Å film.

The decrease in ionization energy and increase in electron affinity near the metal interface reflects the extra polarization due to the image charge for ions located within a small distance of the substrate (Fig. 5(a) and (b)). The polarization decreases until the film thickness is such that the contribution from the metal substrate becomes negligible. The effect depends quantitatively on the organic material and on the substrate. The dielectric function of the organic film, the morphology of the interface and the structure of the organic film are all important parameters. Interestingly, in the case of pentacene on Au, the change in polarization energy seems to be smaller for holes than for electrons, i.e. $P^+ < P^-$. More symmetric values of P^+ and P^- or even an opposite relation,

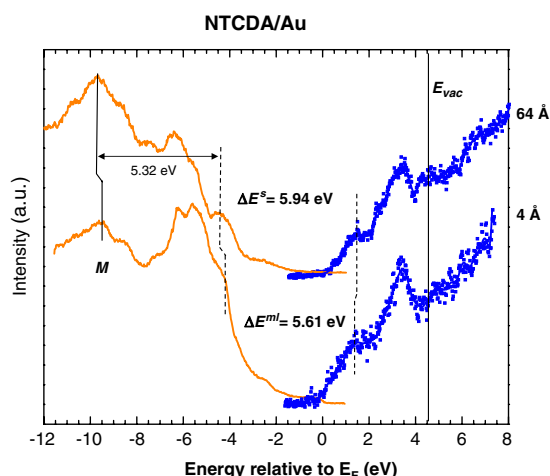


Fig. 4. Composite UPS/IPES NTCDA spectrum of the filled and empty states as a function of film thickness.

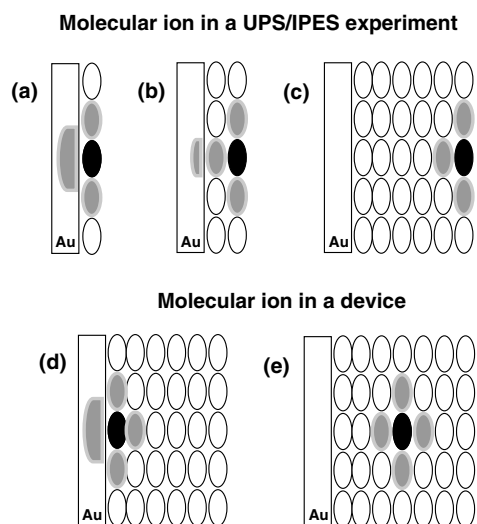


Fig. 5. Molecular ion in films of various thicknesses. Open molecules are neutral; grey molecules are nearest neighbor polarized molecules. Black molecules are ionized by the excess charge. Cases (a)–(c) are representative of UPS/IPES measurements on thin vs. thick films, while cases (d) and (e) correspond to charge injection in a device.

have been reported [15,23], and we cannot rule out that part of the observed difference (≤ 0.1 eV) is due to a slight charging effect during IPES measurement on the thicker films. Negative charging of the surface would result in an increase of the shift of the LUMO peak away from the Fermi level, artificially increasing the effect interpreted as a decrease in polarization energy. If this was the case, however, it would only affect measurements on the thicker films.

The analysis of the HOMO peak of the 100 Å thick film shows that its full-width-at-half-maximum is 15% smaller than that of the 25 Å thick film. The width of the LUMO varies as well, but the experimental broadening in the IPES measurement precludes convincing analysis. The width of the UPS peak is in part due to random disorder, and non-equivalent molecular sites within the film. The pentacene molecules lay flat on the Au substrate in the interface layer, and adopt a more vertical orientation in subsequent layers [24]. Because of the three-dimensional growth, of structural disorder in the film and of increased polarization at the interface, a wider HOMO peak is expected

for thin films that include both flat and vertical molecules. Thicker films appear more homogeneous since the probed region includes mostly vertically oriented molecules. The HOMO and LUMO peaks are Gaussian distributions of states and the position of the centroid of the peak is assumed to be representative of the energy levels of a single molecule [22]. Thus the distance between the centroid of the HOMO and LUMO peak measured by UPS and IPES is representative of the transport gap *at the surface of the film*. Vibrational excitation in UPS and IPES tends to shift both measured HOMO and LUMO away from the Fermi level [22] and a correction of about 100 meV is applied to the position of each peak [19], reducing the surface transport gap E_t^s by 200 meV with respect to the energy difference ΔE between the measured HOMO and LUMO centroids ($E_t^s = \Delta E - 200$ meV).

The energy of the transport states and the transport gap at the metal/organic interface, i.e. E_t^i , are important for carrier injection. To extract their value from the UPS and IPES measurements, the polarization energy at the metal/pentacene interface must be understood. However, although the pentacene film is grown incrementally in our experiment, access to the real interface polarization is not straightforward. UPS and IPES are sensitive to the polarization at the surface of the film only. If the film is thick and includes a realistic interface, surface sensitivity of the techniques limits the measurements to the film surface and precludes access to the interface polarization (Fig. 5(c)). If, on the other hand, the film is thin, e.g. one or two molecular layers (Fig. 5(a) and (b)), polarization can be measured but the system is not representative of a real interface buried under a thick film. Indeed, the polarization energy in the organic layer at the interface between the metal and a thick organic film (Fig. 5(d)) should be larger than that measured for a monolayer thick film on the metal surface. The difference is the additional polarization energy provided by the top molecular layers. For a crystalline pentacene film on Au, Tsiper et al. have calculated that the increase in polarization energy between a single molecular layer and the interface molecular layer of a thick film on Au is 130 meV [23]. Thus the

pentacene transport gap relevant to a device at the Au interface is ~ 30 meV smaller than the value measured for the monolayer film, i.e. $E_t^i = (\Delta E^{ml} - 200 \text{ meV}) - 130 \text{ meV} = 2.54 \text{ eV}$. Interestingly, Tsiper et al. also show that the polarization induced by a charge in the bulk of a thick pentacene film (Fig. 5(e)) is basically equivalent to the polarization induced in a single monolayer on the Au substrate. Although the pentacene film studied here is far from perfectly crystalline, the results of the calculation can be used as a good approximation to evaluate the bulk transport gap: $E_t = E_t^{ml} = \Delta E^{ml} - 200 \text{ meV} = 2.68 \text{ eV}$. This value is in good agreement with the results of electro-absorption [25,26] ($E_t = 2.78$ to 2.85 eV) and calculations [23] ($E_t = 2.74 \text{ eV}$).

For crystalline pentacene on Au, calculations [23] show that the decrease in total polarization energy from the surface of the monolayer to the surface of the thick film is 227 meV . Similar calculations done for PTCDA on Au lead to 400 meV [19]. The difference stems from the fact that the pentacene molecule has lower relaxation energy and is less polarizable than PTCDA. In addition, the crystalline structure of the films considered in these calculations are different, with the PTCDA molecules lying flat on the Au substrate [19] and the pentacene molecules in a tilted stand-up position [23]. In pentacene films obtained by thermal evaporation on Au substrate, the interface molecules are flat on the metal surface and progressively stand up in subsequent layers [24]. A molecular ion lying flat on the metal surface is closer to its image charge than it would be in a tilted configuration, and thus induces a stronger polarization. The observation of a larger decrease in surface polarization (540 meV) as compared to the calculation (227 meV) between the 25 \AA and the 100 \AA thick films may therefore be due to the difference between observed and assumed orientation of the interface molecules.

The charge injection barriers for both electrons and holes can be determined more precisely by spectroscopy with the knowledge of the difference between surface and interface polarization. The interface HOMO and LUMO levels derive from the UPS and IPES measurements corrected for interface polarization. With the deposition of the

first few Angstroms of pentacene, the vacuum level of the Au substrate (work function $W_f = 5.05 \text{ eV}$) shifts down by 0.6 eV , indicative of an interface dipole Δ_{dip} (Fig. 6). The positions of the HOMO and LUMO relative to the Fermi level are measured at the surface of the film, and the analysis of the surface vs. interface polarization presented above is used to deduce their positions at the interface. Fig. 6 shows a schematic of the interface energetics. The centroid of the HOMO and LUMO peaks are at 0.85 eV and 1.69 eV below and above E_F , respectively. For injection purposes, it is useful to specify the position of the onset of the filled and empty frontier orbitals, defined by linear extrapolation of the leading edge of the HOMO and LUMO peaks. Based on the UPS and IPES measurements corrected for surface vs. interface polarization and experimental resolution, the electron and hole injection barriers, arbitrarily defined as the energy difference between E_F and the HOMO and LUMO onsets, are $\Phi_h = 0.47 \text{ eV}$ and $\Phi_e = 1.17 \text{ eV}$, respectively. The polarization energy E_t is 2.68 eV .

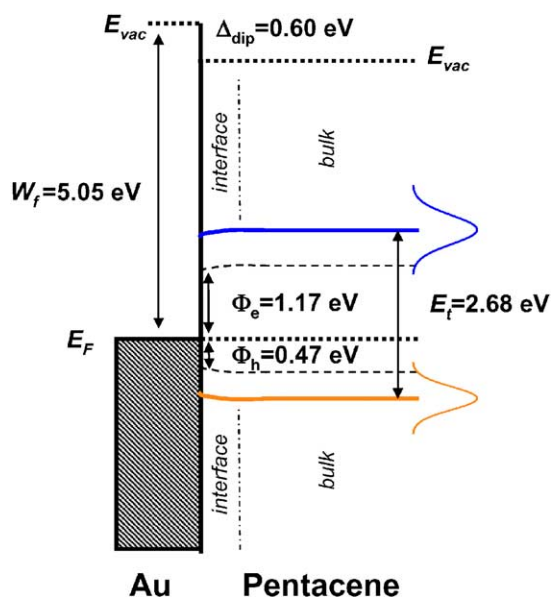


Fig. 6. Energy level of the pentacene/Au interface derived from this UPS/IPES study. Given the measured 5.05 eV Au substrate work function (W_f), charge injection barrier for holes (Φ_h) and for electrons (Φ_e) are respectively 0.47 eV and 1.17 eV . The positive interface dipole (Δ_{dip}) is 0.6 eV and the bulk transport gap (E_t) is 2.68 eV .

at the metal organic interface affects the transport gap and reduces the charge injection barriers with respect to previously reported Au/pentacene barriers, for which polarization had been neglected ($\Phi_h = 0.85$ eV and $\Phi_e = 1.35$ eV) [27]. The concept of energy stabilization by additional polarization should apply to all metal/semiconductor interfaces for which polaronic transport is important, and should be accounted for in device contact modeling.

4. Summary

The energetics of the Au/pentacene interface were characterized with combined direct and inverse photoemission spectroscopies. A 0.6 eV positive dipole (down shift of E_{vac} from Au into pentacene) is measured at the interface. The combination of previously published calculation and PES and IPES measurements as a function of pentacene thickness shows a stronger polarization at the metal interface, which translates into a 0.67 eV reduction in the interface transport gap with respect to the surface gap. Hole and electron injection barriers are estimated to be 0.47 eV and 1.17 eV respectively. Similar results obtained on NTCDA/Au or PTCDA/Au [22] confirm the point that the stabilization of energy levels by polarization is an effect that needs to be taken into account for device modeling, since it has a significant impact on charge injection barriers.

Acknowledgements

This work was supported in part by the National Science Foundation (DMR-0408589) and the New Jersey Center for Organic Optoelectronics.

References

- [1] H. Ishii, K. Sugiyama, E. Ito, K. Seki, *Adv. Mater.* 11 (8) (1999) 605.
- [2] A. Kahn, N. Koch, W. Gao, *J. Polym. Sci. Part B: Polym. Phys.* 41 (2003) 2529.
- [3] W.R. Salaneck, K. Seki, A. Kahn, J.J. Pireaux (Eds.), *Conjugated Polymer and Molecular Interfaces: Science and Technology for Photonic and Optoelectronic Applications*, Marcel Dekker, New York, 2002.
- [4] Y. Shen, A.R. Hosseini, M.H. Wong, G.G. Malliaras, *Chem. Phys. Chem.* 5 (2004) 16.
- [5] H. Ishii, K. Seki, *IEEE Trans. Electron Dev.* 44 (8) (1997) 1295.
- [6] I.G. Hill, A. Rajagopal, A. Kahn, *Appl. Phys. Lett.* 73 (5) (1998) 662.
- [7] C. Shen, A. Kahn, J. Schwartz, *J. Appl. Phys.* 89 (1) (2001) 449.
- [8] H. Vazquez, F. Flores, R. Oszwaldowski, J. Ortega, R. Perez, A. Kahn, *Appl. Surf. Sci.* 234 (2004) 107.
- [9] H. Vazquez, R. Oszwaldowski, P. Pou, J. Ortega, R. Perez, F. Flores, A. Kahn, *Europhys. Lett.* 65 (6) (2004) 802.
- [10] C.D. Dimitrakopoulos, S. Purushothaman, J. Kymissis, A. Callegari, J.M. Shaw, *Science* 283 (5403) (1999) 822.
- [11] H. Klauk, M. Halik, U. Zscheischang, G. Schmid, W. Radlik, *J. Appl. Phys.* 92 (9) (2002) 5259.
- [12] T.W. Kelley, L.D. Boardman, T.D. Dunbar, D.V. Muyres, M.J. Pellerite, T.P. Smith, *J. Phys. Chem. B* 2003 (107) (2003) 5877.
- [13] R. Ruiz, D. Choudhary, B. Nickel, T. Toccoli, K.C. Chang, A.C. Mayer, P. Clancy, J.M. Blakely, R.L. Headrick, S. Iannotta, G.G. Malliaras, *Chem. Mater.* 16 (2004) 4497.
- [14] N.E. Gruhn, D.A. Filho, T.G. Bill, M. Malagoli, A. Kahn, J.L. Brédas, *J. Am. Chem. Soc.* 124 (2002) 7918.
- [15] N. Sato, H. Inokuchi, E.A. Silinsh, *Chem. Phys.* 115 (1987) 269.
- [16] E.A. Silinsh, V. Capek, *Organic Molecular Crystals: Interaction, Localization, and Transport Phenomena*, AIP press, New York, 1994.
- [17] W.R. Salaneck, *Phys. Rev. Lett.* 40 (1) (1978) 60.
- [18] I.G. Hill, A.J. Mäkinen, Z.H. Kafafi, *J. Appl. Phys.* 88 (2) (2000) 889.
- [19] E.V. Tsiper, Z.G. Soos, W. Gao, A. Kahn, *Chem. Phys. Lett.* 360 (2002) 47.
- [20] C.I. Wu, Y. Hirose, H. Sirringhaus, A. Kahn, *Chem. Phys. Lett.* 272 (1997) 43.
- [21] D. Cahen, A. Kahn, *Adv. Mater.* 15 (4) (2003) 271.
- [22] I.G. Hill, A. Kahn, Z.G. Soos, R.A. Pascal, *Chem. Phys. Lett.* 327 (2000) 181.
- [23] E.V. Tsiper, Z.G. Soos, *Phys. Rev. B* 68 (2003) 085301.
- [24] G. Beernink, T. Strunskus, G. Witte, Ch. Woll, *Appl. Phys. Lett.* 85 (3) (2004) 398.
- [25] P.J. Bounds, W. Siebrand, I. Eisenstein, R.W. Munn, P. Petelenz, *Chem. Phys.* (1985).
- [26] P. Petelenz, M. Slawik, K. Yokoi, M.Z. Zgierski, *J. Chem. Phys.* 105 (11) (1996) 4427.
- [27] N. Koch, J. Ghijsen, A. Elschner, R.L. Johnson, J.J. Pireaux, J. Schwarz, A. Kahn, *Appl. Phys. Lett.* 82 (1) (2003) 70.



The effect of doping iodine on organic light-emitting diode

S.F. Chen, Y.K. Fang *, S.C. Hou, C.Y. Lin, C.S. Lin, W.R. Chang, T.H. Chou

*VLSI Technology Laboratory, Institute of Microelectronics, Department of Electrical Engineering,
National Cheng Kung University, No. 1, University Road, P.O. Box 7-200, Tainan, Taiwan*

Received 26 August 2004; received in revised form 2 November 2004; accepted 11 March 2005

Available online 7 April 2005

Abstract

The performances of organic light-emitting diodes (OLEDs) with the configuration Al/Alq₃ (Aluminum Tris-(8-hydroxyquinoline))/TPD(N,N'-diphenyl-N,N'-bis-(3-methylphenyl)-1,1'-bipheny-4,4'-diamine)/ITO have been significantly improved by doping iodine (I₂) on both Alq₃ and TPD layers. The luminance is promoted from 2800 cd/m² without doping to 8000 cd/m² with I₂ doping under bias 10 V. Additionally, the driving voltage (@100 cd/m²) was reduced from 7.5 V without doping to 5.2 V with I₂ doping. We attribute the promotions to the reduction of the electron and hole injection energy barrier at Al/Alq₃ and TPD/ITO interfaces and the expansion of trap energy states beneath the LUMO of Alq₃ generated by I₂ doping. The mechanism is illustrated comprehensively with a schematic energy diagram model and nicely supported with photoluminescence (PL), electroluminescence (EL) spectra and other experimental results.

© 2005 Elsevier B.V. All rights reserved.

Keywords: Organic light-emitting diodes (OLEDs); Turn on voltage; Driving voltage; Photoluminescence (PL); Electroluminescence (EL)

1. Introduction

Organic light emitting diodes (OLED) have been widely applied on cell phone display, liquid-crystal-display and television for the advantages of low power dissipation, wider vision angle, high

luminescence, shorter response time and simplified fabrication [1]. In the past, the technologies to improve the performances, such as electroluminescence efficiency and driving voltage, have been concentrated on lowering barrier height on metal contact [1,2], using high luminescence organic materials [1,3–7] and buffer layer or inter-layers [8–12]. Even these technologies could enhance the performance of OLED, however they also complicate the fabrication process or need some special doping materials [13]. Therefore, there are still

* Corresponding author. Tel.: +886 6 2080398; fax: +886 6 2345482.

E-mail address: ykfang@eembox.ee.ncku.edu.tw (Y.K. Fang).

needed the simpler methods or more common doping materials.

In general, for the bi-layer OLED as shown in the inset of Fig. 1, Al/Alq₃ (Aluminum Tris-(8-hydroxyquinoline))/TPD(N,N'-diphenyl-N,N'-bis-(3-methylphenyl)-1,1'-bipheny-4,4'-diamine)/ITO is adopted to study for its simple structure, where Alq₃ and TPD are electron transport layer (ETL) and hole transport layer (HTL), respectively [14]. To reduce the driving voltage, the common approach is to lower the barrier at Al/Alq₃ interface, for the barrier of Al/Alq₃ contact is larger than the barrier of TPD/ITO [15] and the current is controlled by electrons injection into Alq₃ [16]. In other word, lowering Al/Alq₃ barrier is more effective than lowering the TPD/ITO barrier [17–19]. On the other hand, it has been evidenced that the incorporation of iodine (I₂) on organic material could increase the conductivity [20]. Hence, in this study, we lowered Al/Alq₃ barrier with doping iodine on ETL and improve the output luminance by doping iodine (I₂) on both ETL and HTL layer simultaneously. The doped I₂ molecules on ETL layer generate traps states beneath the lowest unoccupied molecular orbital (LUMO) of Alq₃ [15,21], thus expanding the excited band of LUMO and lowering the Al/Alq₃ barrier for electron to inject. Compared to the reported methods [1–12], the technique possesses the advantage of low cost, convenience and be compatible to the current OLEDs fabrication process. Furthermore,

a schematic energy diagram model has been employed to illustrate the improving mechanism comprehensively.

2. Device design, fabrication and measurement

The bi-layer OLEDs samples with the configuration of Al/Alq₃/TPD/ITO, as schematically described in the inset of Fig. 1, were prepared in the glass substrates pre-coated by indium tin oxide (ITO) with sheet resistance $R_s \leq 10 \Omega/\text{square}$ and work function of 4.9 eV. After ultrasonic cleaning in H₂O–H₂O₂–NH₃OH solution, the substrates were taken into a stain steel chamber which then be evacuated to 1×10^{-5} Torr to deposit TPD as HTL. The thickness of TPD layers is 500 Å. Next, Alq₃ with thickness of 500 Å as ETL and Al with thickness of 1500 Å as cathode were evaporated sequentially in the chamber with 1×10^{-5} Torr. In this work, OLED samples were doped I₂ by evaporation of Alq₃ on ETL with various weight ratios I₂ powder (i.e. Alq₃/I₂ = 1/1, 1/10) and on HTL by evaporation of TPD with weight ratio of 10/1 I₂ powder (i.e. TPD/I₂ = 1/10) respectively. On the other hand, HP4156 and TOPCON BMP were used to measure the electrical characteristics and output luminance, respectively. Additionally, the photoluminescence (PL) and electroluminescence (EL) were measured with Fluorolog-3 Fluorescence on device samples.

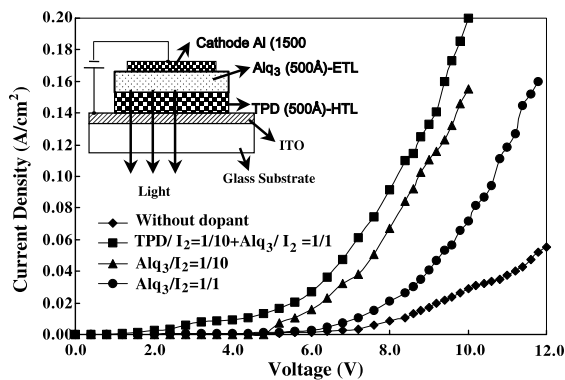


Fig. 1. The J/V curves of bi-layer OLEDs with Alq₃ or both Alq₃ and TPD simultaneously doped with doping different I₂ in weight ratio. The inset presents schematic structure diagram of OLEDs.

3. Results and discussion

Fig. 1 gives the measured current density–voltage (J/V) curves with various weight ratios as parameter. With doping I₂ (i.e. Alq₃/I₂ = 1/1), the current densities of OLED are improved in comparison to that without doping especially under large bias. Also, the improvement is enhanced with increase of dopant weight ratio, i.e., Alq₃/I₂ = 1/10 is better than Alq₃/I₂ = 1/1. For example, the current density with Alq₃/I₂ = 1/10 doping increases to 67 mA/cm² and 155 mA/cm² from 9 mA/cm² and 29 mA/cm² for OLED without dopant under 8 V and 10 V biases, respectively. We attribute the increase of current density to the lowering of

injection barrier on Alq₃/Al interface. The I₂ doping generates the additional traps thus expanding the trap states beneath the LUMO of Alq₃ and will be explained in detail later (Fig. 3). The increased injection of electrons therefore promotes the output luminance as shown in Fig. 2, the measured output luminance as a function of bias with I₂ weight ratio as parameter. For example, with Alq₃/I₂ = 1/1 doping, the luminance is promoted to 4100 cd/m² from 2800 cd/m² without doping under 10 V bias.

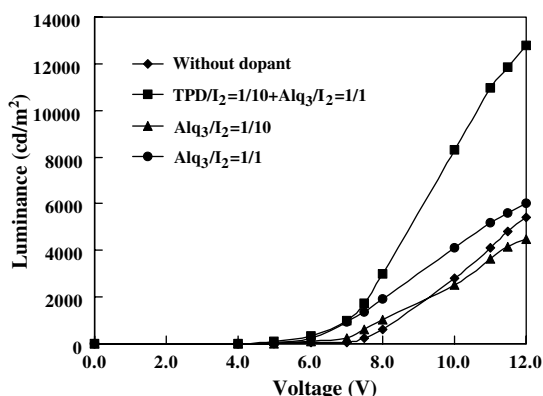


Fig. 2. The output luminance of OLEDs as a function of bias voltage with Alq₃ or both Alq₃ and TPD simultaneously doped with doping different I₂ in weight ratio as parameter.

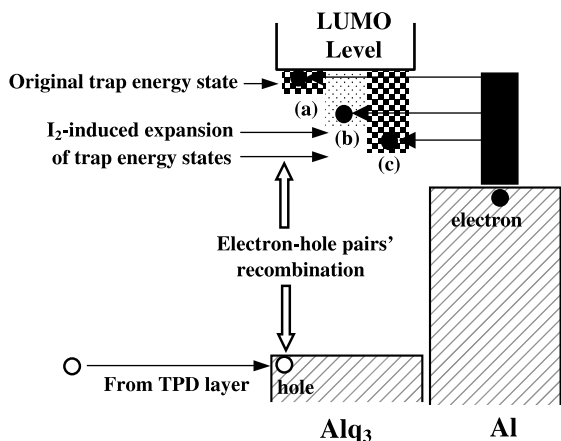
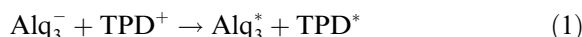
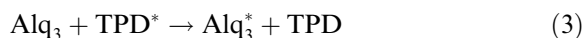
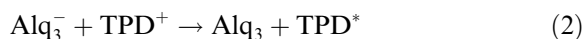


Fig. 3. The energy diagram of bi-layer OLEDs. The reduction of energy barrier at interface of Alq₃/Al with I₂ doping and different trap states beneath LUMO of Alq₃ expanded with doping different I₂ in weight ratio are denoted: (a) for original states, (b) for expanded states of Alq₃/I₂ = 1/10 doped, (c) for expanded states of Alq₃/I₂ = 1/1 doped.

However, contrary to the *J/V* curve, the luminance degrades to 2500 cd/m² under 10 V bias with Alq₃/I₂ = 1/10 doping. For a first glance, the heavier I₂ doping caused quenching of radical Alq₃⁻ is supposed to response this luminance degradation under heavier I₂ doping. It is well known, the luminance of OLED is come from the radiative decay of excited state Alq₃ [14], i.e. Alq₃^{*}. And, the Alq₃^{*} is formed through following two mechanisms [14]; one is direct excitation of Alq₃ by the reaction between a radical anion of Alq₃⁻ and radical cation of TPD⁺:



The other involves the excitation of TPD by the reaction of the two charge carriers as:



However, the doping of I₂ in Alq₃ also generates Alq₃⁺ and I₃⁻ [20] and the Alq₃⁺ could quench the generation of Alq₃⁻ [22] thus reducing the luminance. Similar results were found in organic rubrene doped Alq₃. In which, the reaction products could act as a quencher of Alq₃ excitons [3]. Furthermore, the degradation of luminance and current efficiency caused by the quenching effect is more serious for heavier I₂ doping as summarized in Table 1. Additionally, the driving voltage can be reduced with doping I₂. For example, as listed in Table 1, the driving voltage of Alq₃/I₂ = 1/1 doping is reduced to 5.3 V in comparison to 6.0 V with Alq₃/I₂ = 1/10 doping and to 7.5 V without dopant. The reason is quite clear, since the driving voltage has been defined as a voltage achieving luminance of 100 cd/m² [18], therefore the quenching effect induced luminance degradation in heavier I₂ doping OLED also results in the less reduction of driving voltage. Moreover, it has been found that the trap states can be generated efficiently and expanded with dopant quantity for OLEDs with Alq₃ doped by nitrogen from the measurement of the turn-on voltage and driving voltage [15]. Therefore, we propose a model with the energy band as illustrated in Fig. 3 to explain the improvement mechanism in driving voltage. For more clearly, we denote the trap energy states

Table 1

The summary of driving voltages, luminance and EL current efficiency of the OLED with doping different I_2 in weight ratio

	Without dopant	$Alq_3/I_2 = 1/1$	$Alq_3/I_2 = 1/10$	$TPD/I_2 = 1/10 + Alq_3/I_2 = 1/1$
V_D (V) ^a	7.5	5.3	6.0	5.2
L (cd/m ²)@8 V	600	1900	1100	3000
L (cd/m ²)@10 V	2800	4100	2500	8000
γ (cd/A) ^b @8 V	6.7	8.5	1.6	3.8
γ (cd/A)@10 V	9.6	5.3	1.6	4.0

^a V_D : Driving voltage @100 cd/m².^b γ : EL current efficiency [24].

under LUMO of Alq_3 as (a) original state without doping, and the (b) and (c) represent for bands of state expanded by the doping of I_2 with weight ratios of $Alq_3/I_2 = 1/1$ and $Alq_3/I_2 = 1/10$, respectively. As the trap states below the LUMO are expanded thus in turn lower the barrier for electron to jump from Al. The lowering of barrier then causes a great injection of electron and leads the increase of luminance and reduction in driving voltage.

The model stated above is nicely supported with the measured photoluminescence (PL) and electroluminescence (EL) (in the inset) spectra as presented in Fig. 4. Compared to without doping, the λ_{peak} , peak of wave length of PL and EL with doping I_2 are shifted from 511 nm and 518 nm to 519 nm and 525 nm, respectively. The red shift of λ_{peak} means the shrinkage of effect band gap in

Alq_3 thus in good agreement with experimentally results of reduction in driving voltage and larger luminance for lowering the electron injection energy barrier with I_2 doping [23].

Based on the above discussions, it is concluded a slight I_2 doping could only promote the luminance, but does not improve current density obviously. Therefore, we tried to promote the total current density by adding the doping of I_2 in TPD simultaneously. According to the experimental results, we found by incorporating I_2 in TPD ($TPD/I_2 = 1/10$) and Alq_3 ($Alq_3/I_2 = 1/1$) simultaneously, the improvement in both current density (see line with squares in Fig. 1) and luminance (see line with squares in Fig. 2) are very significantly and even better than doping Alq_3/I_2 only ($Alq_3/I_2 = 1/10$ or $Alq_3/I_2 = 1/1$). For example, the improvement in luminance is up to 160% and 200%, in comparison to the one with $Alq_3/I_2 = 1/1$ doping only, under bias 8 V and 10 V, respectively, while the promotion in current density is more than 434% and 277%. On the other hand, in comparison to the without doping, with $I_2/Alq_3 = 1/1 + I_2/TPD = 1/10$ doping, the driving voltage can be lowered from 7.5 V to 5.2 V; the current density raised to 200 mA/cm² from 29 mA/cm² under 10 V bias; the luminance is dramatically raised from 2800 cd/m² to 8000 cd/m². The exact mechanism is not clear now. However, at the first glance, we suppose the barrier of TPD/ITO interface could be lowered just the same as the interface of Alq_3/Al with I_2 doping. The lowering of energy barrier both in Alq_3/Al and ITO/TPD interfaces enhances the injection of electrons and holes thus promoting the both current density and luminance. However, it still needs some more experiments to build a clear model.

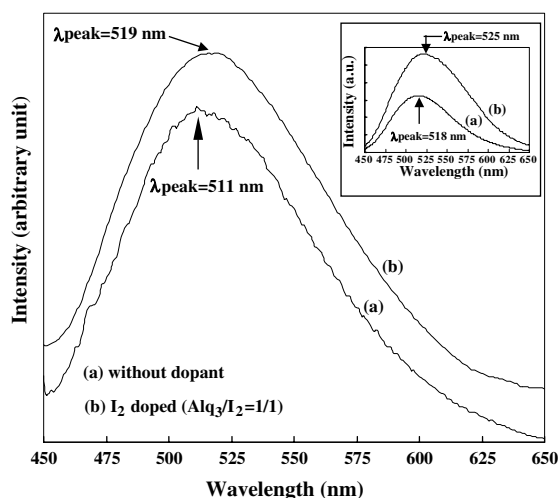


Fig. 4. The PL and EL (the inset) spectrum of the OLED devices with $Alq_3/I_2 = 1/1$ doping and without I_2 doping.

4. Conclusion

The effect of doping TPD and Alq₃ with various I₂ weight ratios have been studied in detail. In comparison to without doping, with doping of iodine in both Alq₃ and TPD (I₂/Alq₃ = 1/1 + I₂/TPD = 1/10), the driving voltage can be lowered from 7.5 V to 5.2 V; the current density raised to 200 mA/cm² from 29 mA/cm² under 10 V bias and the luminance dramatically raised from 2800 cd/m² to 8000 cd/m². The significant improvement is attributed to the reduction of both electron and hole energy barriers at Al/Alq₃ and TPD/ITO interfaces caused by I₂ doping, respectively. The operation mechanism has been illustrated comprehensively with energy schematic diagram and nicely supported by the measured PL and EL spectrum. Therefore, the developed technology is an effective method to reduce driving voltage and increase luminance of OLEDs.

Acknowledgements

This work was supported by the National Science Council of the Republic of China with the contrast of NSC-93-2215-E-006-005.

References

- [1] X. Jiang, Appl. Phys. Lett. 83 (2003) 1875.
- [2] J. Lee, Y. Park, Appl. Phys. Lett. 82 (2003) 173.
- [3] G. Sakamoto, C. Adachi, T. Koyama, Y. Taniguchi, C.D. Merrit, H. Murta, Z.H. Kafafi, Appl. Phys. Lett. 75 (1999) 766.
- [4] J. Kalinowski, L.C. Picciolo, H. Murata, Z.H. Kafafi, J. Appl. Phys. 89 (2001) 1866.
- [5] H. Murata, C.D. Merritt, Z.H. Kafafi, Appl. Phys. Lett. 75 (1999) 3252.
- [6] H. Mattoussi, H. Murata, C.D. Merrit, Y. Iizumi, J. Kido, Z.H. Kafafi, J. Appl. Phys. 86 (1999) 2642.
- [7] B.W. D'Andre, M.A. Baldo, C. Adachi, J. Brooks, Appl. Phys. Lett. 79 (2001) 1045.
- [8] Y. Shao, Y. Yang, Appl. Phys. Lett. 83 (2003) 2453.
- [9] W. Reib, H. Riel, P.F. Seidler, H. Vestweber, Synthetic Metals 99 (2003) 213.
- [10] C.O. Poon, F.L. Wong, S.W. Tong, R.Q. Zhang, C.S. Lee, S.T. Lee, Appl. Phys. Lett. 83 (2003) 1038.
- [11] Y. Qiu, Y. Gao, L. Wang, P. Wei, L. Duan, D. Zhang, G. Dong, Appl. Phys. Lett. 81 (2002) 3540.
- [12] A.B. Chwang, R.C. Kwong, J.J. Brown, Appl. Phys. Lett. 79 (2002) 725.
- [13] W.J. Lee, Y.K. Fang, H.C. Chiang, S.F. Chen, W.R. Chang, C.Y. Lin, T.Y. Lin, J.J. Ho, Solid-State Electron. 47 (2003) 1127.
- [14] S. Miyata, H.S. Nalwa, Organic Electroluminescent Materials and Devices, Gordon and Breach Publishers, 1997.
- [15] W.J. Lee, Y.K. Fang, H.C. Chiang, S.F. Chen, W.R. Chang, C.Y. Lin, T.Y. Lin, W.D. Wang, S.C. Hou, J.J. Ho, Solid-State Electron. 47 (2003) 927.
- [16] P.E. Burrows, S.R. Forrest, Appl. Phys. Lett. 64 (1994) 2285.
- [17] J. Blochwitz, M. Pfeiffer, T. Fritz, K. Leo, Appl. Phys. Lett. 73 (1998) 729.
- [18] X. Zhou, M. Pfeiffer, J. Blochwitz, A. Werner, A. Nollau, T. Fritz, K. Leo, Appl. Phys. Lett. 78 (2001) 410.
- [19] C. Gansorig, A. Fujihira, Appl. Phys. 77 (1996) 4211.
- [20] <http://www.nobel.se/chemistry/laureates/2000/chemadv.pdf>.
- [21] P.E. Burrows, Z. Shen, V. Bulovic, D.M. McCarty, S.R. Forrest, J.A. Cronin, J. Appl. Phys. 79 (1996) 7991.
- [22] R.H. Young, C.W. Tang, A.P. Marchetti, Appl. Phys. Lett. 80 (2002) 874.
- [23] F. Huang, A.G. MacDiarmid, Appl. Phys. Lett. 71 (1997) 2415.
- [24] C. Qiu, H. Chen, IEEE Trans. Electron Dev. 48 (2001) 2131.



Effect of the alkali metal content on the electronic properties of PEDOT:PSS

C.H.L. Weijtens^{a,*}, V. van Elsbergen^a, M.M. de Kok^b, S.H.P.M. de Winter^b

^a Philips Research Laboratories Aachen, Weissshausstrasse 2, 52066 Aachen, Germany

^b Philips Research Laboratories Eindhoven, Prof. Holstlaan 4, 5656 AA Eindhoven, The Netherlands

Received 6 October 2004; received in revised form 26 November 2004; accepted 6 February 2005

Available online 7 April 2005

Abstract

The effect of the sodium and cesium ion surface concentration on the electronic properties of spin-coated poly(3,4-ethylenedioxythiophene)-poly(styrenesulfonic acid) films, known as PEDOT:PSS, has been studied by means of ultra-violet and X-ray photoelectron spectroscopy. The sodium and cesium concentration in the film has been varied by the addition of NaOH or CsOH to the PEDOT:PSS dispersion. Hydrogen ions of the acid PSSH are exchanged for sodium or cesium ions, resulting in the salt PSSNa or PSSCs without changing the oxidation state of PEDOT, i.e., without doping/dedoping the material.

The work function changes from 5.1 to 4.0 eV with increasing alkali surface concentration. The ionization potential remains constant at 5.0 eV above 1 at% alkali metal content and coincides with the work function below 1 at%. Thus, the material changes from a semiconductor-like to a metal-like state.

© 2005 Elsevier B.V. All rights reserved.

PACS: 73.20.r; 79.60.Fr

Keywords: Cesium; Ionization potential; Sodium; PEDOT:PSS; Photoelectron spectroscopy; Work function

1. Introduction

Recently, emissive flat panel displays based on organic light-emitting diodes (OLEDs) are indus-

trialized. Two types of OLEDs exist: small-molecule OLEDs using evaporable small molecules in the active light-emitting stack [1] and polymer-based OLEDs (PLEDs) [2]. The later type consists basically of a light-emitting semiconducting conjugated polymer film sandwiched between two electrodes. The cathode generally is composed of a low-work-function metal (Ba, Ca) with an aluminum film on top to reduce the resistance and to

* Corresponding author. Tel.: +49 241 6003 373; fax: +49 241 6003 483.

E-mail address: christ.weijtens@philips.com (C.H.L. Weijtens).

protect the electron-injecting metal. The anode is normally made up of an ITO film spin-coated with a layer of poly(3,4-ethylenedioxythiophene):poly(styrenesulfonic acid) (PEDOT:PSS) [3]. Insertion of the PEDOT:PSS layer significantly improved device stability, reduced the amount of catastrophic short-circuits and resulted in an anode with a work function independent of the substrate handling procedure [4,5]. The molecular structure of PEDOT:PSS, a hole-conducting polymer, is illustrated in Fig. 1.

PEDOT has in its oxidized form good hole conductivity but is as such unstable in water. The polyelectrolyte PSS acts as charge-compensating counter-ion to stabilize the p-doped conducting polymer and forms a processable water-borne dispersion with PEDOT. Normally, excess of PSS is added which remains present in the spin-coated film as poly(styrenesulfonic acid) (PSSH) or as its sodium salt (PSSNa) [6]. Commercial PEDOT:PSS dispersions generally have a low Na^+ content of less than 400 ppm with respect to the dispersion [7]. It is, however, possible to exchange the protons by addition of NaOH to the dispersion.

A recent publication [8] has discussed the effect of the pH of the PEDOT:PSS dispersion on the device performance of PLEDs, focusing on the range pH 1.6–9. Raman spectroscopy indicated deformation of the PEDOT chain and formation of polaron states at high pH resulting in a reduction of charge localization along the PEDOT backbone.

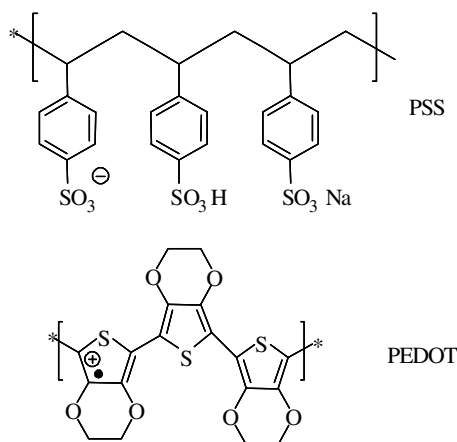


Fig. 1. Molecular structure of PSS and PEDOT.

Despite the larger charge localization, the electrical conductivity was only reduced by a factor of 3, as it is in PLED-grade PEDOT:PSS limited by hopping between PEDOT chains and not by the intrinsic hole mobility along the PEDOT backbone. de Kok et al. [8] ascribed the decrease in device efficiency and lifetime with increasing pH to an increasing hole-injection barrier height.

The hole-injection properties of the anode are one of the important issues determining the PLED performance. The hole-injection barrier towards PEDOT:PSS is determined by the work function and the ionization potential of PEDOT:PSS. Several articles [9,10] describe the adjustment of the work function of PEDOT:PSS by chemical doping or dedoping through the addition of oxidizing or reducing agents or by an electrochemical treatment. For instance, de Jong et al. [9] have increased the work function of a trimer version of PEDOT by chemical doping from ~ 4.2 eV for the neutral trimer to ~ 5.0 eV for the oxidized trimer, while Petr et al. [10] have varied the work function of PEDOT:PSS electrochemically between 5.3 eV and 4.7 eV.

In the present article, we will discuss in greater detail the effect of the alkali metal content, which correlates with the pH of the dispersion, on the electronic properties of PEDOT:PSS films, as measured by ultraviolet and X-ray photoelectron spectroscopy (UPS and XPS). We will show that the work function cannot only be modified by oxidation or reduction as described in the literature [9,10], but also without changing the oxidation state of the material through the exchange of protons by alkali metal ions, i.e., through an acid to salt conversion. We will also show that PEDOT:PSS turns from a semiconductor-like to a metal-like state at an alkali metal content below about 1 at%, i.e., at a pH below about 1.6, a region not considered in the previous paper [8].

2. Experimental

Samples have been prepared by spin-coating aqueous Baytron® P AI4083 and CH8000 dispersions with a solid content of 2.8 wt%, a PEDOT:PSS weight ratio of 1:6 and 1:20 and a

(film) conductivity of 10^{-3} S/cm and 10^{-5} S/cm [7] on Au-coated Si. Occasionally, ITO-coated glass substrates have been applied, but no significant effects of the substrate have been observed. The pH of the dispersion was modified using 1.0 M NaOH (p.a. from Merck) or a 50 wt% CsOH solution in water (from Aldrich). The sodium and cesium content in the coating and the pH of the dispersion are therefore correlated and cannot be considered separately in the present study, see Fig. 2. At low pH the alkali metal content is a more discriminating measure, while the pH is more discriminating at high pH. After spinning, the samples were heated for 5 min at 150 °C in an argon-filled glove box. A portable fast-entry air lock system was used to transport the samples under vacuum to the surface science set-up.

XPS and UPS measurements were performed in a multi-chamber VG Microlab 300 A ESCA system with a base pressure in the 10^{-8} Pa range. The analysis chamber was equipped with an X-ray source with a Mg/Al double anode for XPS and a differentially pumped, windowless discharge lamp for UPS. Energy distribution curves of photo-emitted electrons were measured with a concentric hemispherical analyzer. The UPS spectra were recorded using He-I radiation and for XPS Al(K_{α}) radiation was used.

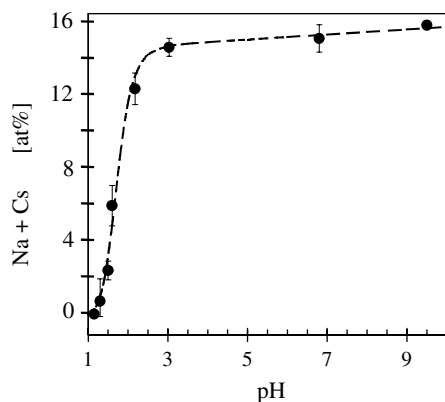


Fig. 2. Measured Na + Cs surface concentration versus pH. The Na and Cs concentration has been determined by XPS except at <1% where it is set equal to the concentration in the dispersion. The line is added as a guide to the eye.

The Na and Cs surface concentration has been determined by XPS except at the lowest concentrations (<1 at%), in which case the alkali concentration in the dispersion (referenced to its solid content) has been used. The ionization energy I was calculated from the energetic difference in the UPS spectrum between the onset of secondary electron emission and the high-energy cut-off at the highest occupied molecular orbital (HOMO). The work function Φ was derived from the onset of secondary electron emission in combination with the known position of the Fermi energy. The PEDOT:PSS conductivity is sufficient to prevent charging.

3. Results

Fig. 3(a) shows the S(2p) XPS core level spectra obtained from PEDOT:PSS films with a nominal 1:20 weight ratio but with different Na contents. The spin-orbit split S(2p) doublet has an energy difference of 1.2 eV and an intensity ratio of 2:1. The intensity ratio (except for the PEDOT-related contributions [11]) and the energy difference of the S(2p) doublet were fixed during deconvolution. In contrast to Greczynski [11] no asymmetric tail was added in the deconvolution of the PEDOT contributions, as these were small in all investigated samples. Three different compounds are discerned. The pair at 169.1 eV and 170.3 eV (labeled 3) is ascribed to PSSH and is not observed in the Na-rich sample. The pair at 168.6 eV/169.8 eV is related to PSSNa (labeled 2) and is not present in the Na-deficient sample. In the middle spectrum both pairs are present and also a minor contribution of the PEDOT-related peaks (labeled 1) is observable around 165 eV.

Fig. 3(b) shows the O(1s) XPS spectra of the same samples. PSSH has two contributions (labeled 3) to the O(1s) spectrum, a large one at 532.4 eV originating from oxygen double-bonded to sulfur and a smaller one at 533.5 eV from hydroxyl-oxygen. The area ratio and separation have been fixed during deconvolution to 2:1 and 1.1 eV, respectively. The hydroxyl peak is broadened due to the formation of hydrogen bonds [11]. PSSNa has a single contribution at 532.1 eV (labeled 2)

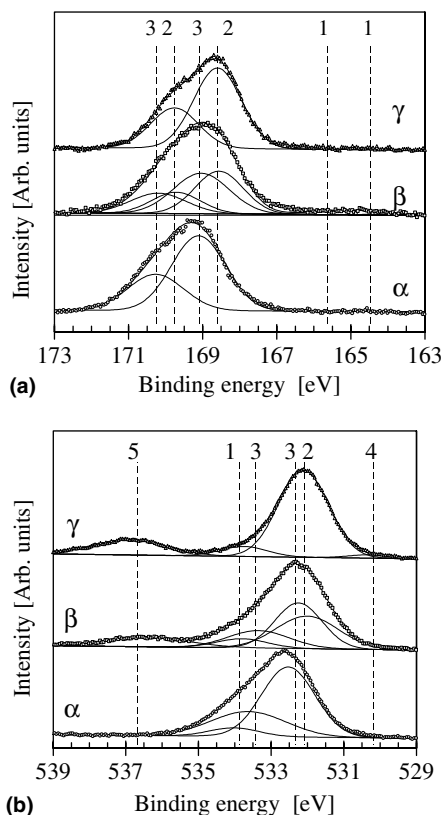


Fig. 3. S(2p) (a) and O(1s) (b) core level spectra of three PEDOT:PSS films with different amounts of Na: 0.1 at% (α), 5.6 at% (β) and 14.1 at% (γ). All films have a nominal PEDOT:PSS weight ratio of 1:20. The symbols indicate experimental results, while the solid curves indicate the deconvoluted contributions. The numbers indicate: 1: S or O from PEDOT, 2: S or O from PSSNa, 3: S or O from PSSH, 4: O from NaOH and 5: Na(KLL) Auger line.

and PEDOT has a peak at 534.0 eV (labeled 1). Finally, a Na Auger line is observed around 537 eV (labeled 5) and at the highest Na contents a small contribution near 530 eV (labeled 4) can be resolved, which is ascribed to oxygen in NaOH. The occurrence of the last contribution indicates that the transition from the acid form of PSS into its sodium salt is completed and some excess NaOH remains present.

In Fig. 4 the S(2p) and the O(1s) spectra are compared for PEDOT:PSS films obtained from dispersions with NaOH or CsOH added. The total amount of alkali metal is similar in both films. Both films have a nominal PEDOT:PSS weight

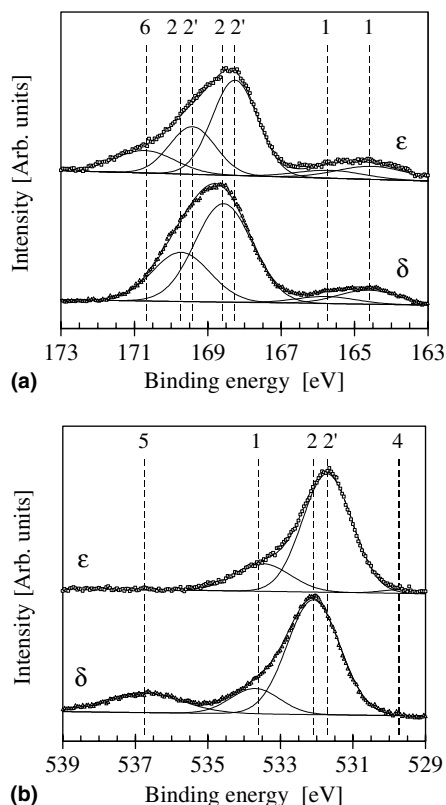


Fig. 4. S(2p) (a) and O(1s) (b) core level spectra of two PEDOT:PSS films containing either 12.8 at% Na (δ) or 10.7 at% Cs and 0.7 at% Na (ϵ). Both films have a nominal PEDOT:PSS weight ratio of 1:6. The same conventions are applied as in Fig. 3 except for 4: O from NaOH or CsOH and 6: Cs(4p_{1/2}). The PSS-related contributions are slightly shifted in the Cs-containing sample compared to the Na-containing samples; this is indicated by an accent.

ratio of 1:6 resulting in larger PEDOT-related contributions than in the spectra of Fig. 3. Compared to Fig. 3, a new contribution is observed around 170.5 eV in the deconvoluted S(2p) spectrum of the Cs-containing film, which is ascribed to Cs(4p_{1/2}) and is labeled 6. The Cs(4p_{3/2}) contribution is located just outside the depicted range. The positions of the PSSCs-related contributions are shifted to a lower binding energy than those of PSSNa.

The C(1s) spectrum (not shown) consists of a single peak with a shoulder at the high binding energy side that is ascribed to C bound to either oxygen or sulfate.

Fig. 5 shows the position of the PEDOT- and PSS-related contributions as a function of the sum of the Na and the Cs surface concentration. All Cs samples contained also some Na ($\sim 1\%$) in the surface layer as the PEDOT:PSS dispersions to which Cs was added were not completely Na-free. The peak positions, except of the PEDOT-related S(2p) doublet, do not change with the alkali metal content except near 0 at%. The PSSH-re-

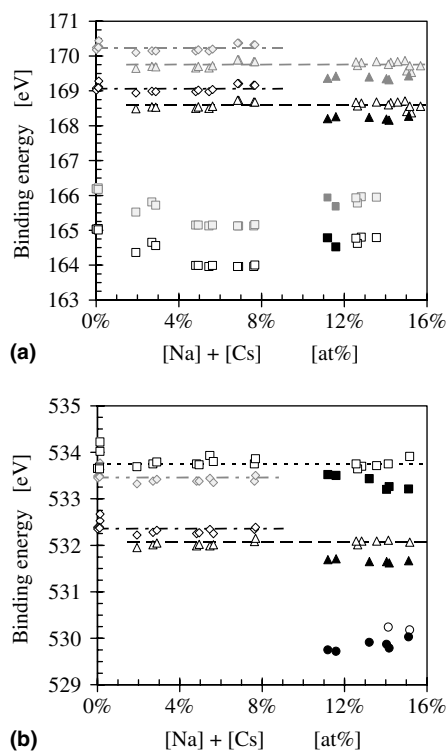


Fig. 5. Position of the S(2p) (a) and O(1s) (b) lines as a function of the alkali metal surface concentration. Squares indicate PEDOT related features (i.e., label 1 in Figs. 3 and 4), triangles PSS-Na and PSSCs related features (label 2), diamonds PSSH related features (label 3) and circles indicate NaOH or CsOH related features (label 4). In (a) the black symbols indicate the $2p_{3/2}$ component of the S(2p) doublet, while the grey symbols indicate the $2p_{1/2}$ component. The black diamonds in (b) refer to double-bonded oxygen and the grey diamonds to hydroxyl oxygen in PSSH. Open symbols indicate samples with Na as alkali metal while closed symbols refer to samples with Cs as main alkali metal. The Na and Cs concentration has been determined by XPS except at $<1\%$ where it is set equal to the concentration in the dispersion. The lines are added as guides to the eye.

lated peaks remain visible until about 8 at%, the PSSNa related peaks are visible above about 2 at% and beyond 11 at% hydroxide-related peaks can be discerned. The PSS-related S(2p) and O(1s) peaks are shifted to 0.4 eV lower binding energy for the Cs-containing samples compared to the Na-samples. The lower electronegativity of Cs compared to Na will result in a higher electron density on the sulfate group and thus in lower binding energies.

Fig. 6 shows the UPS spectra of the same samples as in Figs. 3 and 4. PSS-related features dominate the spectra except in the region near the Fermi edge. The dominance is caused by the combination of the nominal PEDOT:PSS ratio and the surface segregation of PSS. PSS species give, however, no signal in the binding energy range between 2 and 0 eV and the weak feet shown in the insets have to be ascribed to PEDOT as has

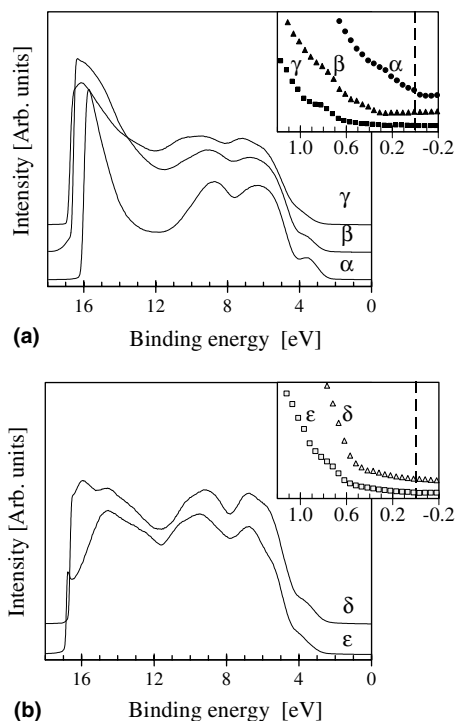


Fig. 6. UPS spectra of PEDOT:PSS films spun on Au-coated Si. The insets show a $1000\times$ expanded view near the Fermi level. (a) Effect of the Na content, (b) Cs versus Na. The same samples have been measured as in Figs. 3 and 4. The vertical offset in the insets is different from that in the main figures.

been indicated earlier by Greczynski [6]. The position of the onset of the feet depends on the Na and Cs content.

Fig. 7 shows the variation of ionization potential and work function with Na + Cs content (a) or pH of the applied dispersion (b). No significant difference is observed between Na and Cs containing films, between films prepared from 1:6 or 1:20 PEDOT:PSS dispersions, or between films on an Au-coated Si or an ITO-coated glass substrate.

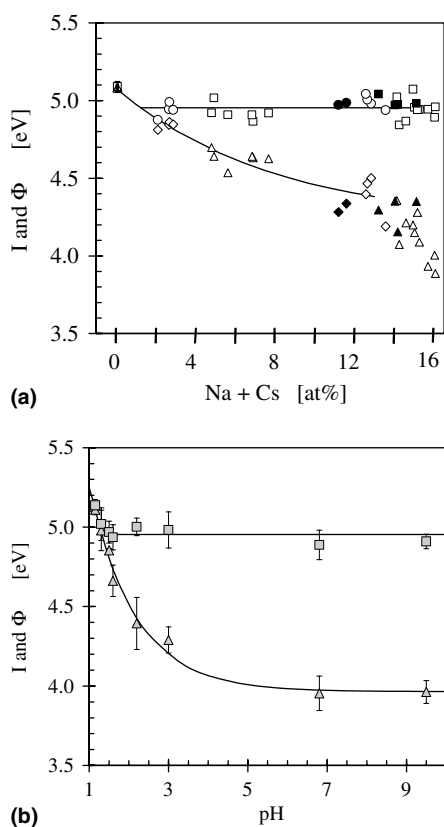


Fig. 7. Ionization potential (squares, circles) and work function (triangle, diamonds) as a function of the alkali metal surface concentration (a) and of the pH of the applied dispersion (b). The open symbols indicate samples with Na as alkali metal while the closed symbols refer to samples with Cs as main alkali metal. The squares and triangles refer to films prepared from 1:20 PEDOT:PSS dispersions while in the case of the circles and the diamonds a 1:6 dispersion was applied. No discrimination between the samples is made in (b). The lines are added as guide to the eye.

The ionization potential is not affected by the alkali metal content above about 1 at% or by the pH above pH 1.5 and equals 4.96 ± 0.07 eV. The work function strongly decreases with increasing Na and Cs content. The HOMO and the Fermi level are well separated.

Above about 12 at% (or pH 2.5) a large scatter in the work function is observed in Fig. 7(a). At these alkali metal concentrations the PEDOT:PSS dispersion behaves no longer as a buffer and minor variations in the hydroxide addition will strongly affect the pH of the dispersion, see Fig. 2. In this case, the pH will be a more discriminating measure than the alkali metal content as determined by XPS. Indeed, Fig. 7(b) shows in this range less scatter and indicates that the work function saturates at high pH around 3.98 ± 0.08 eV.

The work function crosses the $I = 4.96$ eV line when the alkali metal concentration is reduced below about 1%. The ionization potential coincides with the work function. The Fermi level has crossed the top of the valence band and the HOMO level coincides with the Fermi level and no longer with the top of the valence band. Thus, the material has turned from a semiconducting state to a metallic one.

4. Discussion

A good match is obtained between our results, shown in Figs. 5 and 7, and literature [6–9,11–13]. The measured shift from PSSNa to PSSH, 0.5 eV and 0.4 eV for the $S(2p_{3/2})$ and the $O(1s)$ line, respectively, matches well with the values of Greczynski [6,11]. Also the separation between the $O(1s)$ line of PEDOT and PSSNa (1.7 eV) corresponds with that of Greczynski. The separation for the $S(2p_{3/2})$ line varies with sodium and cesium content. Greczynski et al. obtained a separation of 3.9 eV for the $S(2p_{3/2})$ line for a film with a PSSNa:PSSH ratio of 1.4:1 and a PEDOT:PSS ratio of 1:3.5 corresponding to approximately 3.5–4 at% Na, which fits well with the estimated value at this concentration as estimated from Fig. 5.

Three regions can be discerned in Figs. 5 and 7: ~ 0 at%, ~ 2 –8 at%, and $> \sim 11$ at% Na + Cs. Fig. 8 shows schematically the energy level dia-

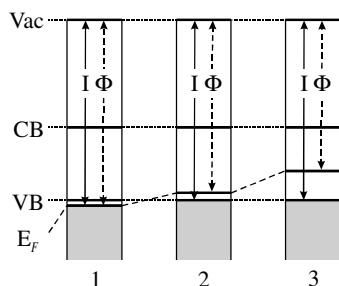


Fig. 8. Energy level diagram for the three regions discerned in the text: ~ 0 at%, ~ 2 –8 at% and $> \sim 11$ at% Na + Cs. I , Φ , E_F , Vac, CB and VB indicate respectively the ionization potential, the work function, the Fermi level, the vacuum level, the conduction and the valence band edge. The grey blocks indicate occupied levels, the HOMO level is located at the top of the grey blocks. For clarity, the vacuum levels of the three diagrams are aligned. In the spectra, the Fermi levels are aligned and the other levels shift.

gram for each region. The grey blocks indicate occupied states, thus the HOMO level is located at the top of the grey blocks.

In the first region, ~ 0 at% Na + Cs, the ionization potential and the work function coincide. The Fermi level is located inside the valence band. The observed work function is similar to the ones published for sodium-deficient, oxidized PEDOT: 5.0 eV for the oxidized trimer version of PEDOT [9], 5.3 eV for electrochemically oxidized PEDOT [10]. Only PEDOT and PSSH related features are observed in the S(2p) and O(1s) XPS spectra.

In the second region, ~ 2 –8 at%, PSSH is gradually replaced by PSSNa (or PSSCs). The ionization potential is constant while the work function decreases. The Fermi level has crossed the top of the valence band and the HOMO level is fixed at the top of the valence band and no longer coincides with the Fermi level. The material has turned from a metal-like state to a semiconducting-like state.

Although commercial PEDOT:PSS generally has a low Na^+ content, the Na concentration of the investigated samples is seldom given in literature. Greczynski et al. [6] obtained a work function of 4.7 eV for a film with approximately 3.5–4 at% Na. Petr et al. [10] reported a work function of 5.1 eV for a PEDOT:PSS film with one sodium atom per four sulfur atoms, which corresponds

to about 2–2.5 at% Na. The film was (partly) electrochemically reduced resulting in a work function of 4.7 eV. Koch et al. [12] have reported a value between 4.80 and 5.15 eV ascribing the variations to changes in the surface composition without further specifying the composition.

In the third region, $> \sim 11$ at%, only PSSNa, PSSCs, PEDOT, and hydroxide related contributions are discerned. This indicates the acid to salt transition is completed around 8–11 at% in good agreement with the 10% derived from the titration curve shown in [8] and the theoretically estimated value of 8 at%. PSS^- is exchanged by OH^- as counter charge to PEDOT^+ , but PEDOT remains oxidized.

The positive charge of PEDOT^+ in PEDOT:PSS is not localized on a single monomer unit, but is delocalized over several rings. The positive charge on one particular PEDOT unit depends on its distance to the counter-ions [6]. Exchange of PSS^- by OH^- will lead to larger charge localization in PEDOT. The larger S(2p) binding energy of PEDOT sulfur indicates indeed a shift of the positive charge towards sulfur and larger charge localization in PEDOT.

Also Raman spectroscopy has shown diminishing charge delocalization along the PEDOT chain with increasing alkali metal content [8]. We could not confirm with UPS the presence of the PEDOT-related polaron states observed in Raman spectra, probably due to the low intensity of PEDOT-related signals in the UPS spectra.

The work function in the third region is comparable with that published for undoped PEDOT: 4.0–4.2 eV [9,13]. The 1 eV difference between the ionization potential and work function will result in a significant hole-injection barrier and will thus hamper efficient operation of PLEDs at high pH as was reported in an earlier publication [8]. The UPS measurements confirm the proposed increase in the hole-injection barrier height with increasing pH.

Exchanging Na^+ by Cs^+ reduces the binding energy of the PSS-related S(2p) and O(1s) lines due to the lower electronegativity of Cs compared to Na. The exchange does not affect PEDOT-related features including the ionization potential as the PEDOT and the PSS system are now in first order

decoupled and Na and Cs are not bound to PEDOT.

Comparing finally the amount of PEDOT and PSS shows a discrepancy between the bulk and the surface. A PEDOT:PSS weight ratio of 1:6 corresponds with a molar ratio of 1:4.3. XPS analysis indicated, however, an average molar ratio of 1:6.4 at the surface. The PEDOT:PSS ratio could not be determined accurately by XPS for films with a 1:20 PEDOT:PSS weight ratio (i.e., a molar ratio of 1:14.3) but appears to be in the order of 1:23. Thus, the surface is PEDOT-depleted (or PSS-enriched); only about 2/3 of the expected amount of PEDOT is observed. Greczynski et al. [6,11] have reported larger PEDOT-depletion at the surface but applied a dispersion with a 1:1.2 molar ratio. XPS did not show evidence of an effect of the Na/Cs concentration on the PEDOT-PSS segregation or of substantial Na/Cs surface segregation.

To summarize, we have shown that changing the alkali metal content in the film can modify the work function of spin-coated PEDOT:PSS films. In contrast to other publications, this is accomplished by adjusting the pH of the PEDOT:PSS dispersion with NaOH or CsOH without changing the oxidation state of the material, i.e., the material is neither doped nor dedoped. A transition is observed between a metal-like state with the Fermi level inside the valence band and a semi-conducting-like state with the Fermi level above the valence band. Therefore, PEDOT:PSS films with a low Na and Cs content, i.e., prepared from

a low pH dispersion, will have a low hole-injection barrier.

References

- [1] C.W. Tang, S.A. Van Slyke, *Appl. Phys. Lett.* 51 (1987) 913.
- [2] J.H. Burroughes, D.D.C. Bradley, A.R. Brown, R.N. Marks, K. Mackay, R.H. Friend, P.L. Burn, A.B. Holmes, *Nature* 347 (1990) 539.
- [3] G. Heywang, F. Jonas, *Adv. Mater.* 4 (1992) 116.
- [4] A. Berntsen, Y. Croonen, C.T.H.F. Liedenbaum, H. Schoo, R.-J. Visser, J. Vleggaar, P. van de Weijer, *Opt. Mater.* 9 (1998) 12.
- [5] T. Kugler, W.R. Salaneck, H. Rost, A.B. Holmes, *Chem. Phys. Lett.* 310 (1999) 391.
- [6] G. Greczynski, Th. Kugler, M. Keil, W. Osikowicz, M. Fahlman, W.R. Salaneck, *J. Electron Spectrosc. Relat. Phenom.* 121 (2001) 1.
- [7] Commercial information from H.C. Starck can be found at www.hcstarck.com.
- [8] M.M. de Kok, M. Buechel, S.I.E. Vulto, P. van de Weijer, E.A. Meulenkamp, S.H.P.M. de Winter, A.J.G. Mank, H.J.M. Vorstenbosch, C.H.L. Weijtens, V. van Elsbergen, *Phys. Stat. Sol. (A)* 201 (2004) 1342.
- [9] M.P. de Jong, A.W. Denier van der Gon, X. Crispin, W. Osikowicz, W.R. Salaneck, L. Groenendaal, *J. Chem. Phys.* 118 (2003) 6495.
- [10] A. Petr, F. Zhang, H. Peisert, M. Knupfer, L. Dunsch, *Chem. Phys. Lett.* 385 (2004) 140.
- [11] G. Greczynski, Th. Kugler, W.R. Salaneck, *Thin Solid Films* 354 (1999) 129.
- [12] N. Koch, A. Kahn, J. Ghijsen, J. Pieaux, J. Schwartz, R.L. Johson, A. Elschner, *Appl. Phys. Lett.* 82 (2003) 70.
- [13] K.Z. Xing, M. Fahlman, X.W. Chen, O. Inganäs, W.R. Salaneck, *Synth. Metals* 89 (1997) 161.



High-mobility *n*-channel organic field-effect transistors based on epitaxially grown C₆₀ films

Th.B. Singh^{a,*}, N. Marjanović^a, G.J. Matt^a, S. Günes^a, N.S. Sariciftci^a,
A. Montaigne Ramil^b, A. Andreev^b, H. Sitter^b, R. Schwödauer^c, S. Bauer^c

^a *Linz Institute for Organic Solar Cells (LIOS), Physical Chemistry, Johannes Kepler University Linz, Altenbergerstrasse 69, Linz A-4040, Austria*

^b *Institute of Semiconductor and Solid State Physics, Johannes Kepler University Linz, Linz A-4040, Austria*

^c *Soft Matter Physics, Johannes Kepler University Linz, Linz A-4040, Austria*

Received 18 November 2004; received in revised form 9 March 2005; accepted 11 March 2005

Available online 19 April 2005

Abstract

We present C₆₀-based *n*-channel organic field-effect transistors with mobility in the range of 0.4–1 cm²V⁻¹s⁻¹. A solution-processed organic dielectric divinyltetramethyldisiloxane-bis(benzocyclobutene) (BCB) was used as a gate dielectric and C₆₀ films were grown on top by hot wall epitaxy. Devices characterised in inert atmosphere conditions show high stability with an on/off ratio >10⁴. The determined mobility values are nearly gate voltage independent.

© 2005 Elsevier B.V. All rights reserved.

1. Introduction

Organic thin-film electronics developed to a promising technology in the last two decades with demonstrated prototypes of organic thin film transistors, organic integrated circuits for radio frequency identification tags (RFID-tags) [1,2] and active matrix displays [3]. Organic field effect transistors (OFETs) have also been fabricated in arrays to drive electro-phoretic display pixels [4].

The performance of the individual transistors limits the switching speed in an integrated circuit, which can be roughly estimated by the ratio of mobility and channel length of the transistor [3]. To obtain higher switching speed, the search for higher mobility materials is therefore important along with the effort to downscale the transistor geometry.

Among all the various p-type organic semiconductors, pentacene in thin film form has been reported as promising material because of its mobility of 1.5 cm²V⁻¹s⁻¹ [5a]. Organic single crystals such as rubrene have shown mobilities as high as 15 cm²V⁻¹s⁻¹ [5b]. On the other hand,

* Corresponding author. Tel.: +43 732 2468 8767; fax: +43 732 2468 8770.

E-mail address: birendra.singh@jku.at (Th.B. Singh).

very few organic semiconductors are n-type, viz., fullerenes, [6,7] fluorinated phthalocyanines, [8] naphthalenes and N-substituted naphthalene 1,4,5,8-tetracarboxylic diimide [9] or N,N'-dialkyl-3,4,9,10-perylene tetracarboxylic diimide (PTCDI, PTCDI-C₅ [10] and PTCDI-C₈H, correspondingly) with a highest obtained mobility of $0.6 \text{ cm}^2 \text{ V}^{-1} \text{ s}^{-1}$ [11]. Most of these results are achieved by growing the semiconductor on surface treated or untreated SiO₂ or Al₂O₃. Although the van der Waals type interactions between organic molecules and inorganic substrates are rather weak, the crystallographic phases, the orientation, and the morphology of the resulting organic semiconductor films critically depend on the interface and growth kinetics. In this paper, we present results on OFETs fabricated using hot wall epitaxy (HWE) grown C₆₀ films on top of an organic insulator. HWE, working close to thermodynamical

equilibrium is well known [12] as appropriate technique to grow highly ordered organic thin films, including C₆₀ films [13]. The relatively smooth surface of the organic insulating film interfaced with a highly ordered HWE grown C₆₀ film resulted in mobilities of $0.4\text{--}1 \text{ cm}^2 \text{ V}^{-1} \text{ s}^{-1}$ and an on/off ratio $>10^4$. The obtained mobility is found to be nearly gate voltage independent with a normalised subthreshold slope of $8 \text{ V nF/decade cm}^2$. Furthermore, the field effect mobility has been found to be thermally activated with an activation energy of $\sim 100 \text{ meV}$ within the temperature range of 90–300 K.

2. Experimental

A scheme of the device geometry is shown in Fig. 1(a). The device fabrication starts with etching

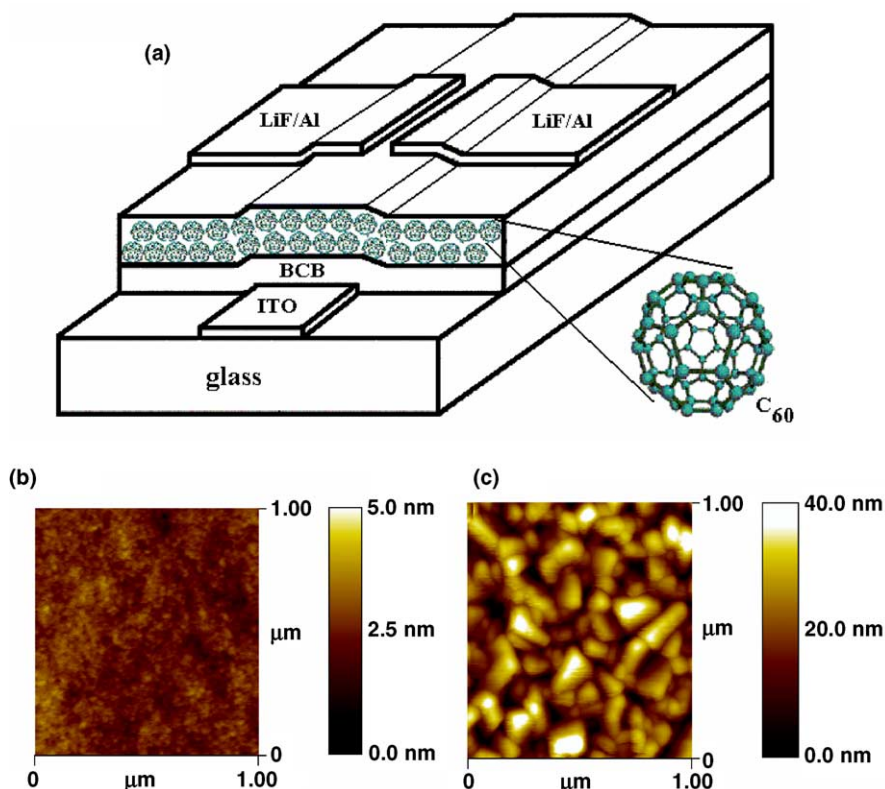


Fig. 1. (a) Scheme of the staggered *n*-channel OFET device structure; (b) AFM image of the BCB dielectric surface; (c) AFM image of the C₆₀ surface in the channel region of the fabricated OFET.

the indium tin oxide (ITO) on the glass substrate. After patterning the ITO and cleaning in an ultrasonic bath, a BCB layer is spin coated at 1500 rpm resulting in a 2 μm thick film. BCB was used as received from Dow Chemicals and curing was done according to the standard procedure [14]. BCB is an excellent dielectric material with a rather low dielectric constant $\epsilon_{\text{BCB}} = 2.6$ and a small, nearly temperature independent thermal expansion coefficient [15]. A 300 nm thick C_{60} film was grown by HWE on top of the dielectric at a substrate temperature of 130 $^{\circ}\text{C}$. The top source and drain electrodes, (LiF/Al 0.6/60 nm) were evaporated under vacuum (2×10^{-6} mbar) through a shadow mask. LiF/Al is expected to form ohmic contacts on fullerenes [16]. The channel length, L of the device is 35 μm and the channel width is $W = 1.4$ mm, which results in a W/L ratio of ≈ 40 . From the measurement of the BCB film thickness, $d = 2$ μm and the dielectric constant of BCB, $\epsilon_{\text{BCB}} = 2.6$, a dielectric capacitance $C_{\text{BCB}} = 1.2$ nF/cm² was calculated. In our devices we have a d/L ratio ≈ 0.05 acceptable not to screen the gate field by the source drain contacts. Device transportation from the HWE chamber to the glove box and further electrical characterisation (using Keithley 236 and Keithley 2400 instruments) were carried out under argon environment. The surface morphology and thickness of the dielectric was determined with a Digital Instrument 3100 atomic force microscope (AFM) and a Dektak surface profilometer respectively. Device characterisation at various temperatures was performed in a He flow cryostat (Cryo Industries) using a Lakeshore 331 as temperature controller.

3. Results and discussion

As shown in Fig. 1(b), the dielectric layer showed a very smooth surface with a roughness < 5 nm. This enables us to grow the semiconductor (C_{60}) with a very good control of the film morphology (Fig. 1(c)). A recent study shows that the first couple of monolayers next to the dielectric dominates the charge transport in organic semiconductor layers [17].

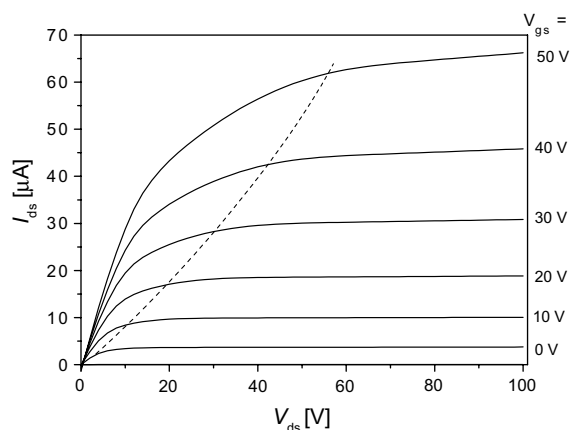


Fig. 2. $I_{\text{ds}}(V_{\text{ds}})$ curve of the OFET in the accumulation mode. The dotted line is a guide for the eye for saturated I_{ds} . The data shown here are taken in ascending V_{gs} mode with an integration time of 1 s.

Fig. 2 shows the transistor characteristics of a device with a well saturated curve occurring pinch off at a drain source voltage $V_{\text{ds}} \geq V_{\text{gs}}$ (gate voltage). From the slope at $V_{\text{ds}} = 0$ V of the curve at $V_{\text{gs}} = 0$ V, we estimated a conductivity of 5×10^{-6} S cm⁻¹. For the same device (see Fig. 3) we measured the transfer characteristics. The data presented in Fig. 3 hold for $V_{\text{ds}} = 60$ V. One can

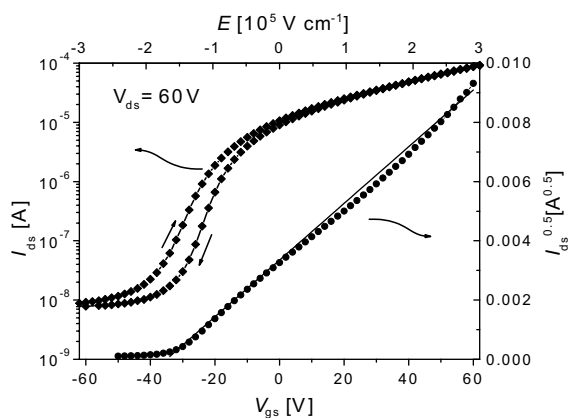


Fig. 3. Semilogarithmic plot of I_{ds} vs. V_{gs} (left scale) and plot of $I_{\text{ds}}^{0.5}$ vs V_{gs} (right scale) for the same C_{60} OFET as in Fig. 2. The full line shows a fit to the data (return curve) using Eq. (1) from which a field-effect mobility $\mu = 0.63$ cm²/Vs is obtained. Each measurement was carried out with an integration time of 1 s.

see that the transistor turns on at an onset voltage of $V_t = -35$ V without significant hysteresis and the drain–source current I_{ds} increases quadratically. The device shows an on/off ratio $> 10^4$ which is calculated as the ratio of I_{ds} at $V_{gs} = 60$ V and I_{ds} at $V_{gs} = V_t$. We have observed consistently the effect of having large drain–source current even when $V_{gs} = 0$ V. This effect is minimized when the dielectric layer is preheated at high temperature prior to the deposition of the active layer. This effect is proposed to be due to the presence of unintentional dopants at the interface of the untreated dielectric. Interfacial effects seem to play a major role in organic electronics devices [18]. From $V_t = -(qn_0d_sC_{BCB}) + V_{fb}$, [19] where $V_{fb} = 0.1$ V [16] is the flat band potential (which accounts for the work function difference between the semiconductor and the gate electrode without considering fixed charges at the dielectric and at the interface), d_s is the thickness of the semiconductor, q is the elementary charge and C_{BCB} is the capacitance of the gate dielectric, we were able to estimate the density of free carriers at equilibrium n_0 . This yields a relatively high electron density of $\sim 10^{17}$ cm $^{-3}$.

As shown in Fig. 3, from the fit to the data using equation [20]:

$$I_{ds} = \frac{\mu WC_{BCD}}{2L} (V_{gs} - V_t)^2 \quad (1)$$

we extract a field effect mobility of 0.63 cm 2 V $^{-1}$ s $^{-1}$ in the saturation regime for $V_{ds} = 60$ V (note the fitting line used for the mobility extraction fits the data over a wide range of V_{gs}). However, for calculating the field effect mobility, the contact resistance of LiF/Al and C $_{60}$ is not taken into account by assuming that the contact resistance is fairly low. Our studies of the dependence of the field effect mobility on the metal work function in soluble methanofullerene based OFETs have shown a highest obtained mobility μ of 0.2 cm 2 V $^{-1}$ s $^{-1}$ with LiF/Al as drain–source electrode. Use of higher work function metal electrodes viz. Cr, Au, etc. in these OFETs leads to slightly reduced mobilities presumably due to large contact resistance [18]. Similarly we have also observed a slight decrease in the field effect mobility in C $_{60}$ OFETs with higher work function electrodes (not shown here). The

device performance and the mobility strongly depends on the choice of the dielectric layer mainly due to the different surface energies of dielectric layers. The sharp turn on of I_{ds} is a measure of the quality of the dielectric/semiconductor interface which is defined by the normalized subthreshold slope, $S = C_{BCB}dV_{gs}/d(\log I_{ds})$ [5]. As usually observed in organic FETs, a subthreshold slope of 8 VnF/decadecm 2 obtained by us is very high which can be reduced by reducing the thickness of the dielectric layer. We presume, the most important factor in achieving this high mobility OFET is the combination of a smooth organic dielectric surface with a highly ordered C $_{60}$ film grown by HWE [13]. It can be mentioned here that very few studies have been done so far on growing highly ordered organic thin films on top of organic dielectrics partly due to low glass transition temperatures and unwanted hysteresis. Use of BCB among other organic dielectrics is based on the fact that it provides devices with a small hysteresis. In addition BCB is a high glass transition temperature polymer, an additional advantage for optimizing the film growth conditions at high substrate temperatures. Previous reports on C $_{60}$ FETs grown on SiO $_2$ have shown highest obtained mobilities of 0.5 cm 2 V $^{-1}$ s $^{-1}$ [6e].

We further analysed the validity of Eq. (1) for different V_{ds} via local approximation assuming V_{gs} independent of μ :

$$\mu = \frac{2L}{WC_{BCD}} \left(\frac{\partial \sqrt{I_{ds}}}{\partial V_{gs}} \right)^2 \quad (2)$$

The mobility as a function of V_{gs} was determined assuming Eq. (2), which is valid in the saturation regime, at $V_{ds} = 60$ V. As shown in Fig. 4 the mobility is found to be almost constant for $V_{ds} \geq 123V_{gs}$ with values as high as 1 cm 2 /Vs at $V_{gs}, V_{ds} = 60$ V. These mobilities are comparable with the electron mobility determined by photocurrent measurements [21] or time of flight experiment on single crystalline C $_{60}$ [22]. Further we carried out measurements at very large V_{gs} (up to 100 V) and very large V_{ds} (up to 100 V) where we observed a non-linear transport which leads to a trap filled limited (TFL) regime [23]. We have observed a drastic increase in the device perfor-

mance and its field-effect mobility in the devices when the dielectric layer is cleaned by preheating in situ at temperatures above 250 °C which normally occurs during the epitaxial growth of thin films [23]. The values shown here are an average of at least fifty different devices fabricated under identical conditions with a narrow statistical distribution in the obtained mobility. We also calculated the transconductance, $g = (\partial V_{gs}/\partial I_{ds})$ [20] of these devices and plotted the channel resistance g^{-1} vs. V_{gs} in Fig. 4. We observed a g in the range of 3–10 μS which is again a relatively high value for an n-type organic semiconductor.

Loading of the devices in a cryostat for low temperature studies was done by carefully loading the devices inside the glove box environment. Such an arrangement is in general needed in order not to degrade the device performance which normally occurs in n -channel OFETs during transportation. C_{60} OFETs exhibit a temperature dependent mobility with an Arrhenius behaviour as shown in Fig. 5. The activation energy obtained is ~ 100 meV. This activation energy may be influenced by several parameters including a temperature dependent contact resistance. An activation energy of the same order is also found in soluble methanofullerene based OFETs while it is difficult to state what really causes the activation energy in these devices [18].

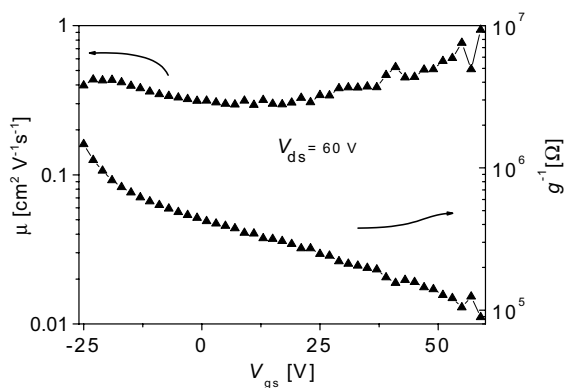


Fig. 4. Effective FET mobility (left scale) obtained from the channel transconductance after Eq. (2) showing a step-wise dependence on V_{gs} with a nearly constant μ over a large range of V_{gs} in the saturated regime ($V_{ds} = 60$ V). Channel resistance $1/g$ (right scale) as a function of V_{gs} .

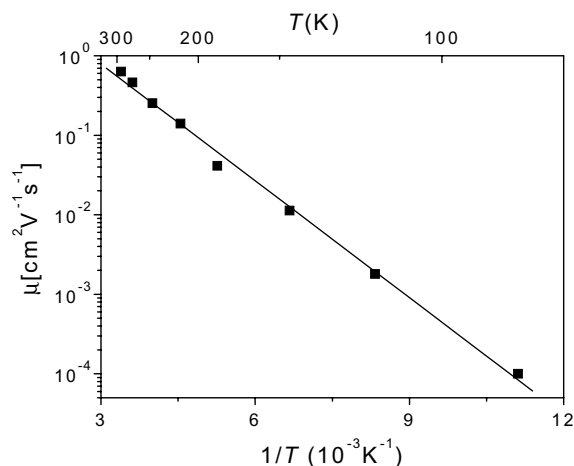


Fig. 5. Arrhenius plot of the temperature dependent mobility of C_{60} BCB OFETs.

4. Conclusions

In conclusion, we have demonstrated an n -channel OFET with an electron mobility of $0.4\text{--}1\text{ cm}^2\text{V}^{-1}\text{s}^{-1}$ along with an on/off ratio $>10^4$ using a solution based organic dielectric BCB film in combination with HWE grown C_{60} films. The obtained mobility is nearly gate voltage independent.

Acknowledgements

Special thanks are to Michael Auinger and Philipp Stadler for technical help. This work was performed within the Christian Doppler Society's dedicated laboratory on Plastic Solar Cells funded by the Christian Doppler Society and Konarka Austria GesmbH. Furthermore, we acknowledge financial support from the Austrian Foundation for the Advancement of Scientific Research (FWF P15155, P15627 and P15629).

References

- [1] (a) Two most recent review articles, W. Clemens, W. Fix, J. Ficker, A. Knobloch, A. Ullmann, J. Mater. Res. 19 (2004) 1963;

- (b) G. Horowitz, J. Mater. Res. 19 (2004) 1946, and references therein.
- [2] B. Crone, A. Dodabalapur, Y.-Y. Lin, R.W. Filas, Z. Bao, A. Laduca, R. Sarpeshkar, H.E. Katz, W. Li, Nature 403 (2000) 521.
- [3] H.E.A. Huitema, G.H. Gelinck, J.B.P.H. van der Putten, K.E. Kuijk, C.M. Hart, E. Cantatore, P.T. Herwig, A.J.J.M. van Breemen, D.M. de Leeuw, Nature 414 (2001) 599.
- [4] J.A. Rogers, Z. Bao, K. Baldwin, A. Dodabalapur, B. Crone, V.R. Raju, V. Kuck, H.E. Katz, K. Amundson, J. Ewing, P. Drzaic, Proc. Natl. Acad. Sci. 98 (2001) 4835.
- [5] (a) Y.-Y. Lin, D.J. Gundlach, S.F. Nelson, T.N. Jackson, IEEE Electr. Dev. Lett. 18 (1997) 606;
(b) V.C. Sundar, J. Zaumseil, V. Podzorov, E. Menard, R.L. Willett, T. Someya, M.E. Gershenson, J.A. Rogers, Science 303 (2004) 1644.
- [6] (a) J. Kastner, J. Paloheimo, H. Kuzmany, in: H. Kuzmany, M. Mehring, J. Fink (Eds.), Electronic Properties of High- T_c Superconductors, Springer Series in Solid State Sciences, 1993;
(b) R.C. Haddon, A.S. Perel, R.C. Morris, T.T.M. Palstra, A.F. Hebard, Appl. Phys. Lett. 67 (1995) 121;
(c) R.C. Haddon, J. Am. Chem. Soc. 118 (1996) 3041;
(d) K. Horiuchi, K. Nakada, S. Uchino, S. Hashii, A. Hashimoto, N. Aoki, Y. Ochiai, M. Shimizu, Appl. Phys. Lett. 81 (2002) 1911;
(e) S. Kobayashi, T. Takenobu, S. Mori, A. Fujiwara, Y. Iwasa, Appl. Phys. Lett. 82 (2003) 4581;
(f) S. Kaboyashi, S. Mori, S. Lida, H. Ando, T. Takenobu, Y. Taguchi, A. Fujiwara, A. Taninaka, H. Shinohara, Y. Iwasa, J. Am. Chem. Soc. 125 (2003) 8116.
- [7] (a) K. Shibata, Y. Kubozono, T. Kanabara, T. Hosokawa, T. Hosokawa, A. Fuziwara, Y. Ito, H. Shinohara, Appl. Phys. Lett. 84 (2004) 2572;
(b) T. Kanabara, K. Shibata, S. Fujiki, Y. Kubozono, S. Kashino, Y. Kubozono, S. Kashino, T. Urisu, M. Sakai, A. Fujiwara, R. Kumashiro, K. Tanigaki, Chem. Phys. Lett. 379 (2003) 223.
- [8] Z. Bao, A.J. Lovinger, J. Brown, J. Am. Chem. Soc. 120 (1998) 207.
- [9] H.E. Katz, J. Johnson, A.J. Lovinger, W. Li, J. Am. Chem. Soc. 122 (2000) 7787.
- [10] R.J. Chesterfield, J.C. McKeen, Ch.R. Newman, C.D. Frisbie, P.C. Ewbank, K.R. Mann, L.L. Miller, J. Appl. Phys. 95 (2004) 6396.
- [11] P.R.L. Malenfant, C.D. Dimitrakopoulos, J.D. Gelorme, L.L. Kosbar, T.O. Graham, Appl. Phys. Lett. 80 (2002) 2517.
- [12] A. Andreev, G. Matt, C.J. Brabec, H. Sitter, D. Badt, H. Seyringer, N.S. Sariciftci, Adv. Mater. 12 (2000) 629.
- [13] D. Stifter, H. Sitter, Appl. Phys. Lett. 66 (1995) 679.
- [14] L.-L. Chua, P.K.H. Ho, H. Sirringhaus, R.H. Friend, Appl. Phys. Lett. 84 (2004) 3400.
- [15] R. Schwödiauer, G.S. Neugschwandtner, S. Bauer-Gogonea, S. Bauer, W. Wirges, Appl. Phys. Lett. 75 (1999) 3998.
- [16] (a) V.D. Mihaileti, J.K.J. van Duren, P.W.M. Blom, J.C. Hummelen, R.A.J. Janssen, J.M. Kroon, M.T. Rispens, W.J.H. Verhees, M.M. Wienk, Adv. Funct. Mater. 13 (2003) 43;
(b) G.J. Matt, N.S. Sariciftci, T. Fromherz, Appl. Phys. Lett. 84 (2004) 1570;
(c) C.J. Brabec, A. Cravino, D. Meissner, N.S. Sariciftci, T. Fromherz, M.T. Rispens, L. Sanchez, J.C. Hummelen, Adv. Funct. Mater. 11 (2001) 374.
- [17] F. Dinelli, M. Murgia, P. Levy, M. Cavallini, F. Biscarini, D.M. de Leeuw, Phys. Rev. Lett. 92 (2004) 116802.
- [18] Th.B. Singh, N. Marjanović, Ph. Stadler, M. Auinger, G.J. Matt, S. Günes, N.S. Sariciftci, R. Schwödiauer, S. Bauer, J. Appl. Phys. 97 (2005) 083714.
- [19] G. Horowitz, R. Hajlaoui, F. Kouki, Eur. Phys. J. AP 1 (1998) 361.
- [20] S.M. Sze, Physics of Semiconductor Devices, Wiley, New York, 1981;
M. Shur, M. Hack, J. Appl. Phys. 55 (1984) 3831.
- [21] D. Sarkar, N.J. Halas, Solid State Commun. 90 (1994) 261.
- [22] E. Frankevich, Y. Maruyama, H. Ogata, Chem. Phys. Lett. 214 (1993) 39.
- [23] Th. B. Singh, N. Marjanović, G.J. Matt, S. Günes, Ph. Stadler, M. Auinger, N.S. Sariciftci, R. Schwödiauer, S. Bauer, A. Montaigne Ramil, A. Andreev, H. Sitter, submitted.



Efficient organic light-emitting device from exciplex emission between 4,4',4''-tris[3-methylphenyl(phenyl)amino]triphenylamine and 2,2',2''-(1,3,5-benzenetriyl)tris-[1-phenyl-1H-benzimidazole]

Shufen Chen, Zhijun Wu, Yi Zhao, Chuannan Li, Jingying Hou, Shiyong Liu *

National Laboratory Optoelectronics, Jilin University, Changchun 130023, PR China

Received 14 July 2004; received in revised form 17 November 2004; accepted 8 March 2005

Available online 7 April 2005

Abstract

A new-type exciplex emission was obtained employing hole-transporting material 4,4,4''-tris[3-methylphenyl(phenyl)amino]triphenylamine (m-MTDATA) doped in the electron-transporting material 2,2,2''-(1,3,5-benzenetriyl)tris-[1-phenyl-1H-benzimidazole] (TPBI) with structures of ITO/m-MTDATA (45 nm)/NPB (5 nm)/m-MTDATA:TPBI ((10 nm, molecular weight ratio were 3:1, 1:1 and 1:3)/TPBI (25 nm)/Alq₃ (15 nm)/LiF (0.5 nm)/Al. For comparison, a device with exciplex emission generated at the interface between a hole-transporting material m-MTDATA and an electron-transporting material TPBI with a structure ITO/m-MTDATA (45 nm)/NPB (5 nm)/m-MTDATA (5 nm)/TPBI (30 nm)/Alq₃ (15 nm)/LiF (0.5 nm)/Al was also fabricated. The maximum efficiencies of the doped-devices reached 3.8 lm/W (at 4 V with a luminance of 145.7 cd/m²), 3.2 lm/W (at 4 V with a luminance of 132 cd/m²) and 4.6 lm/W (at 4 V with a luminance of 170.5 cd/m²) with different molecular weight ratio (MWR) 3:1, 1:1 and 1:3, respectively, comparing to that of the none-doped device of 1.8 lm/W (at 4 V with a luminance of 49.6 cd/m²). At such a low voltage, exciplex emission was major for all the devices above. Only yellow emission was obtained in none-doped structure and the maximum luminance reached 2555 cd/m² at 12 V. Commission International de L'Eclairage coordinate (1931, CIE) in this structure changed from (0.397, 0.532) to (0.311, 0.413) with voltage from 4 to 16 V. In doped devices, a yellow emission was obtained at a low bias voltage and then turned into white emission with increasing of voltage for stronger blue emission from m-MTDATA due to the sufficient charge trapping from TPBI to m-MTDATA. The CIE coordinates were (0.406, 0.533), (0.409, 0.533) and (0.427, 0.536) at 4 V for MWR 3:1, 1:1 and 1:3, respectively. At 8, 8, 12 V, white emission were obtained with CIE coordinates (0.320, 0.400), (0.311, 0.384), (0.319, 0.401) for MWR 3:1, 1:1, 1:3 and turned into (0.264, 0.303), (0.246, 0.275), (0.302, 0.363) when

* Corresponding author. Tel.: +86 431 8941670; fax: +86 431 5168270.
E-mail address: syliu@mail.jlu.edu.cn (S. Liu).

voltage increased to 16 V. The maximum luminance was 3810 (at 14 V), 4210 (at 12 V) and 4583 cd/m^2 (at 12 V) for MWR 3:1, 1:1 and 1:3, respectively.

© 2005 Elsevier B.V. All rights reserved.

1. Introduction

Recently, a number of papers have showed electroluminescence (EL) spectra of organic light-emitting devices (OLEDs) differ substantially from the photoluminescence (PL) spectra of their component materials. The EL spectra shows often up as red-shifted broad bands which have been mostly assigned as emission from exciplexes formed at organic solid interface between hole-transporting layer (HTL) and electron-transporting layer (ETL) molecules [1–8]. Exciplexes are formed by interaction of an excited electron donor(acceptor) molecule $D^*(A^*)$ with its unexcited counterpart $A(D)$, they could be observed in PL spectra of D–A combined systems.

Here, we report a new-type exciplex emission by doping hole-transporting material m-MTDATA into electron-transporting material TPBI. For comparison, the exciplex emission generated at the interface m-MTDATA/TPBI is also studied. The chemical structures of materials we used, experimental preparation and measurement will be described in detail as below.

2. Experiments

Fig. 1 shows the chemical structures of m-MTDATA, TPBI and two other organic materials 4,4-bis[N-(1-naphthyl-1-)-N-phenyl-amino]-biphenyl (NPB) and tris-(8-hydroxyquinoline) aluminum (Alq_3). m-MTDATA (hole-injection layer), NPB (hole-transporting layer), TPBI (electron-transporting layer) and Alq_3 (electron-injection and electron-transporting layer) were deposited by resistively heated quartz boats onto cleaned glass substrates precoated with transparent, conductive indium-tin oxide (sheet resistance is $30 \Omega/\text{square}$ and thickness is 120 nm). Before deposition, the ITO-coated glass substrates were cleaned by scrubbing and sonication in acetone, ethanol,

deionized water sequentially and then dried in an oven at 120°C . The deposition was in a high vacuum about 10^{-4} – 10^{-5} Pa and at a rate of 0.1–0.3 nm/s. The layer thickness of deposited material was monitored in situ using an oscillating quartz thickness monitor. At last, a LiF buffer layer and Aluminum (Al) were deposited onto the organic films at a background pressure of 10^{-4} Pa. A PR650 spectra scan spectrometer and Keithley model 2400 programmable voltage–current source were used to measure luminance–current density–voltage characteristics and EL spectra. The PL spectra and absorption (ABS) spectra were measured by a RF-5301PC spectrofluorophotometer (Xe lamp as excitation light source in a range of 220–750 nm) and UV-1700 ultraviolet visible spectrophotometer (halogen lamp and deuterium lamp as two beam light source in a range of 190–1100 nm), respectively. 100 nm-thick organic solid films were deposited onto quartz substrates to obtain PL spectra and ABS spectra. All measurements were conducted at room temperature in ambient environment.

3. Results and discussions

The device structures are listed as follows:

- (a) ITO/m-MTDATA (45 nm)/NPB (5 nm)/m-MTDATA (5 nm)/TPBI (30 nm)/ Alq_3 (15 nm)/LiF (0.5 nm)/Al.
- (b,c,d) ITO/m-MTDATA (45 nm)/NPB (5 nm)/m-MTDATA:TPBI (x , 10 nm)/TPBI (25 nm)/ Alq_3 (15 nm)/LiF (0.5 nm)/Al $x = 3:1$ (b), $1:1$ (c), $1:3$ (d). Here, x is molecular weight ratio (MWR) of m-MTDATA and TPBI.
- (e) ITO/m-MTDATA (45 nm)/NPB (5 nm)/m-MTDATA: Alq_3 (3:1, 10 nm)/ Alq_3 (40 nm)/LiF (0.5 nm)/Al.

Fig. 2(a) shows the EL spectra of the device (a) at 4 V and 13 V. There are four emissive peaks of

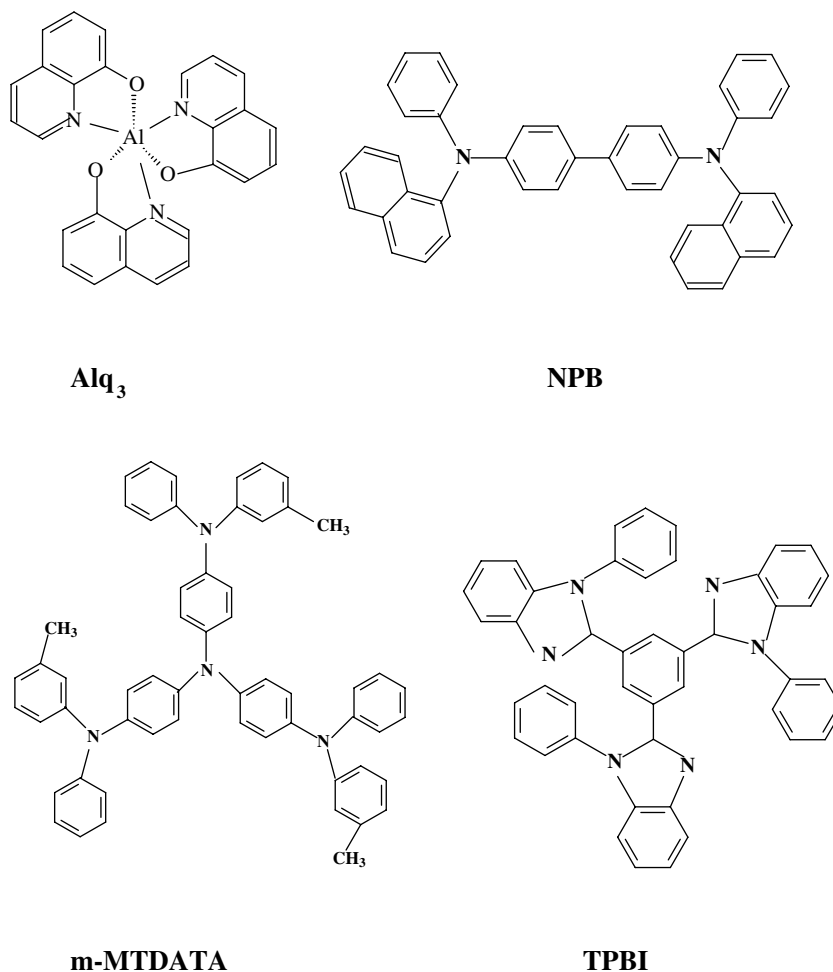


Fig. 1. Chemical structures of materials we used.

436, 528, 556, 592 nm and a weak long wavelength band (about 600–750 nm) in the EL spectra. 436 nm-peak and 528 nm-peak are resulted from emission of m-MTDATA and Alq₃, respectively. Both 556 and 592 nm-peak come from exciplex emission. The weak long wavelength band is considered as recombination and emission from trapping of h–e heteropairs at the interface m-MTDATA/TPBI. We can explain the results above as follows. The emission peak of 528 nm is attributed to emission of Alq₃ because the 528 nm-peak becomes stronger comparing to other component emission as driving voltage increases. If 528 nm-peak comes from exciplex emission,

comparing to other component emission, the peak would become weaker as increase of voltage [10,11]. And another explanation from energy band theory will be discussed later. The small shoulder of 436 nm is owing to emission of m-MTDATA. From Fig. 2(b), there is a small overlap between ABS spectra of m-MTDATA and PL spectra of TPBI, so Förster energy transfer processes from TPBI to m-MTDATA is minor and charge trapping process is dominant which leads to emission of m-MTDATA. Because charge trapping occurs only at the interface of m-MTDATA and TPBI in device (a) and it is typically limited to a distance 5–10 Å between two components,

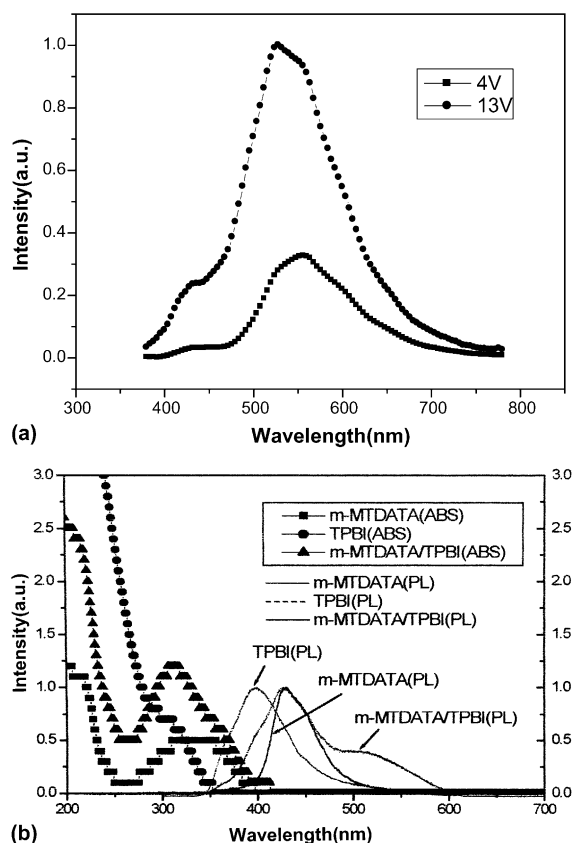


Fig. 2. EL spectra of device (a) at 4 V and 13 V. As voltage increased, emission peak from exciplex (556 nm-main peak and 592 nm-minor peak) decreased comparing to emission of m-MTDATA and Alq₃. (b) ABS and PL spectra of m-MTDATA, TPBI and m-MTDATA/TPBI.

the charge trapping is insufficient and a minor shoulder of 436 nm from m-MTDATA is acquired in EL spectra of device (a). The emissive peaks of 556 nm with a 592 nm-shoulder come from none of singlet materials we have used, as can be seen from PL spectra in Fig. 2(b). From ABS spectra and PL spectra of m-MTDATA/TPBI, we find out no new ABS peak is formed comparing to the individual ABS spectra of m-MTDATA and TPBI. However, from PL spectra of m-MTDATA/TPBI, a new emission peak with a broad bathochromic band occurs according to each PL peak of m-MTDATA and TPBI. We deduce the new PL peak from exciplex emission generated at the interface of m-MTDATA/TPBI.

With increasing of voltage, the emission from exciplex decreases comparing to that from m-MTDATA and Alq₃ (see Fig. 2(a) at 13 V). And this change is consistent with previous report about exciplex [10,11]. There is a long wavelength emission (out to 750 nm) which extends well beyond the emission seen in PL spectra (Fig. 2(b)) for m-MTDATA/TPBI (PL spectra finishes at ≈600 nm). The origin of the weak long wavelength is considered as recombination and emission from trapping of h–e heteropairs at the interface m-MTDATA/TPBI. Disordered interface formed during deposition should devote to generation of these trappings.

The exciplex emission can be explained from energy band theory, too. LUMO and HOMO levels of the organic materials for device (a) are demonstrated in Fig. 3. Since there is a large gap of 1.1 eV between HOMO levels of m-MTDATA and TPBI and 0.8 eV between LUMO levels, most of holes from anode and electrons from cathode are blocked in bulk of m-MTDATA and TPBI near the interface, respectively, and then recombine and emit as exciplex at the interface m-MTDATA/TPBI. As forward bias voltage increases, more electrons and holes overcome barrier (especially in devices (b,c,d), doping processes make charge trapping sufficient) and lead to a stronger emission of m-MTDATA and Alq₃.

In device (a) the exciplex could be formed only at the interface of m-MTDATA and TPBI and recombination for e–h heteropairs was insufficient. The maximum power efficiency of 1.8 lm/W was gotten at 4 V with a luminance 49.6 cd/m².

As Hong Cao's report [9], an exciplex emission can be observed both in a mixture and at the interface of the bilayer film. We doped

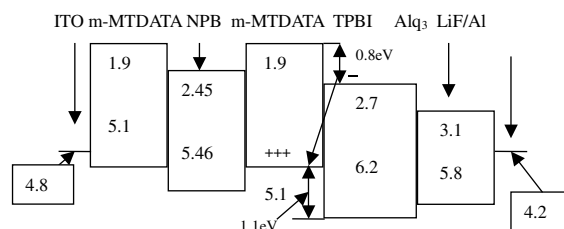


Fig. 3. Energy band characteristics for device (a).

Table 1

Performances of devices (a,b,c,d,e) about maximum luminance (L_{\max}) and maximum power efficiency (MPE) and other performances such as voltage and current density corresponding to L_{\max} and MPE et al.

Device	MWR of m-MTDATA:TPBI for b,c,d and m-MTDATA:Alq ₃ for e	L_{\max} (cd/m ²) and voltage (V) correspondingly	Current density (mA/mm ²)@ L_{\max}	MPE (lm/W) and voltage (V) correspondingly	Luminance and current density (mA/mm ²)@MPE
a		2555@12 V	4.224	1.8@4 V	49.6/0.021
b	3:1	3810@14 V	5.202	3.8@4 V	145.7/0.030
c	1:1	4210@12 V	6.024	3.2@4 V	132/0.033
d	1:3	4583@12 V	4.716	4.6@4 V	170.5/0.029
e	3:1	4027@13 V	14.316	0.18@5 V	77.4/0.265

m-MTDATA into TPBI and observed the appearance of exciplex emission with improved efficiency.

Table 1 shows the maximum power efficiencies reached 3.8 lm/W (at 4 V with a luminance of 145.7 cd/m²), 3.2 lm/W (at 4 V with a luminance of 132 cd/m²) and 4.6 lm/W (at 4 V with a luminance of 170.5 cd/m²) for doped devices (b,c,d) comparing to 1.8 lm/W (at 4 V with a luminance of 49.6 cd/m²) for device (a) when exciplex emission was major for all devices. The maximum luminance was enhanced from 2555 cd/m² (at 12 V with an efficiency 0.158 lm/W) of device (a) to 3810 cd/m² (at 14 V with an efficiency 0.164 lm/W), 4210 cd/m² (at 12 V with an efficiency 0.183 lm/W) and 4583 cd/m² (at 12 V with an efficiency 0.254 lm/W) in devices (b,c,d), respectively. And Figs. 4–6 show current density–voltage, luminance–voltage and power efficiency–luminance characteristics for devices (a,b,c,d), respectively. Table 2 shows CIE coordinates at different voltages in

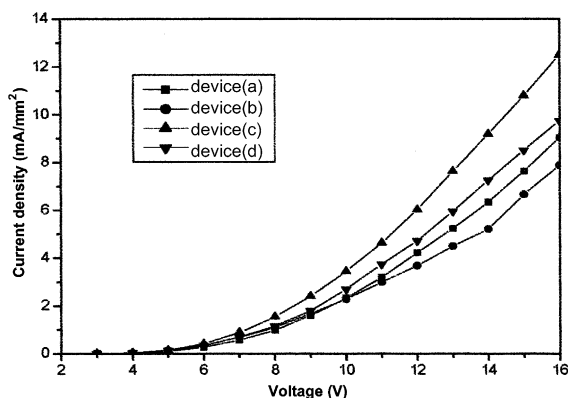


Fig. 4. Current density–voltage curves for devices (a,b,c,d).

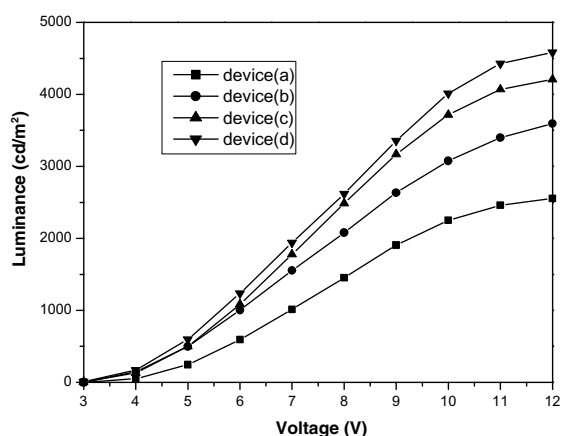


Fig. 5. Luminance–voltage characteristics of devices (a,b,c,d).

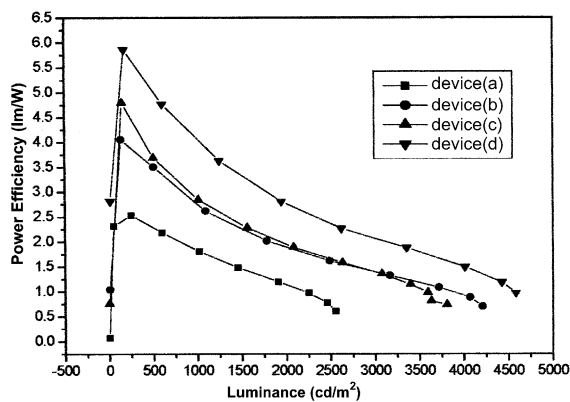


Fig. 6. Power efficiency–luminance characteristics of devices (a,b,c,d).

devices (a,b,c,d). In device (a), only a yellow emission was obtained with CIE coordinate changing

Table 2

CIE coordinates changed with improvement of forward bias voltage in different devices

	4 V	6 V	8 V	12 V	16 V
Device (a)	(0.397, 0.532)	(0.375, 0.517)	(0.351, 0.494)	(0.317, 0.445)	(0.311, 0.413)
Device (b)	(0.406, 0.533)	(0.355, 0.458)	(0.320, 0.400)	(0.286, 0.346)	(0.264, 0.303)
Device (c)	(0.409, 0.533)	(0.352, 0.450)	(0.311, 0.384)	(0.272, 0.317)	(0.246, 0.275)
Device (d)	(0.427, 0.536)	(0.396, 0.510)	(0.361, 0.466)	(0.319, 0.401)	(0.302, 0.363)

from (0.397, 0.532) to (0.311, 0.413) with voltage from 4 to 16 V. While in devices (b,c,d), yellow emission turned into white emission with increase of voltage. The CIE coordinates were (0.406, 0.533), (0.409, 0.533) and (0.427, 0.536) at 4 V for device (b), device (c), device (d), respectively. At 8, 8, 12 V, white emission were obtained with CIE coordinates (0.320, 0.400), (0.311, 0.384), (0.319, 0.401) for device (b), device (c), device (d) and turned into (0.264, 0.303), (0.246, 0.275), (0.302, 0.363) when voltage increased to 16 V. The normalized EL spectra for devices (a,b,c,d) at 13 V are shown in Fig. 7. Analyzing the data above, we get the results as following:

- (1) A white emission was acquired in devices (b,c,d) with increase of voltage while only a yellow emission was gotten in device (a) because doped structures (b,c,d) made charge trapping (typically limited to a dis-

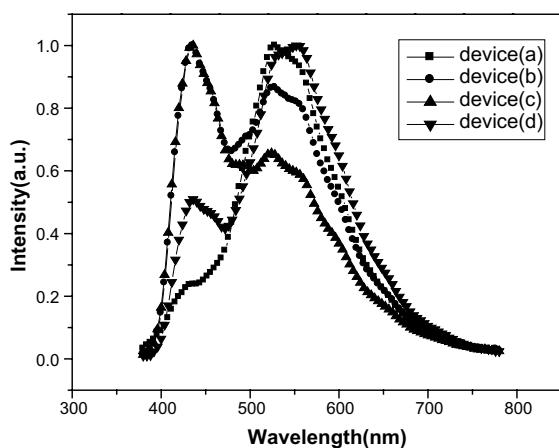


Fig. 7. EL spectra of devices (a,b,c,d) at 13 V. Device (d) showed more remarkable exciplex emission than that of (a,b,c). As voltage increased, exciplex emission in device (d) was major continuously while that of (a,b,c) decreased.

tance 5–10 Å between two components) from TPBI to m-MTDATA sufficient which lead to a stronger emission from m-MTDATA, as is shown in Fig. 7. As a result, white emission was obtained by combination of blue emission from m-MTDATA and green-yellow emission both from Alq₃ and exciplex.

- (2) Table 2 shows a bluish-white emission occurred in device (c) at a high voltage while white emission from device (b) and (d) had a small blue shift. From Fig. 7, we observed the 436 nm-peak from m-MTDATA of device (c) increased differently from that of device (b) and device (d). In device (c), a stronger blue peak occurred comparing to that in devices (b,d). It is because of the more sufficient charge trapping in device (c) with the MWR of 1:1 than that in device (b) and device (d) with the MWR of 1:3 and 3:1, respectively, which might be decided partly by the position and orientation between m-MTDATA and TPBI [11].
- (3) At a high voltage, exciplex emission (556 nm) in device (a,b,c) decreased remarkably comparing with the other emissive components (blue emissive peak from m-MTDATA and green emissive peak from Alq₃) while exciplex emission in device (d) was still major (shown in Fig. 7). And explanation of the phenomenon is not clear yet.
- (4) We selected device (e) as a controlled device. As Koji Itano's report [11], exciplex forms in the mixture between m-MTDATA and Alq₃. From Table 1, we found a low power efficiency of 0.18 lm/W was obtained at 5 V when m-MTDATA:Alq₃ was 3:1 (since at a low forward bias voltage, exciplex emission was major for all devices). Generally speaking, the formation of an exciplex requires a favorable position and orientation of compo-

ment molecules: the molecular planes of donor and acceptor being parallel or nearly parallel to each other and with a small interplanar separation of 3–4 Å [8]. Since the size of TPBI is larger than that of Alq₃, the overlap between TPBI and m-MTDATA is more than that between Alq₃ and m-MTDATA, which results in an increase in the stabilization energy of the complex system and a decrease in the exciplex energy. So exciplex emission efficiency increases which leads to a further enhancement of power efficiency.

4. Conclusion

We fabricated an efficient OLED based on exciplex emission by doping hole-transporting material (m-MTDATA) into electron-transporting material (TPBI). The maximum efficiencies of the devices with different molecular weight ratio (MWR) of 3:1, 1:1 and 1:3 reached 3.8 lm/W (at 4 V), 3.2 lm/W (at 4 V) and 4.6 lm/W (at 4 V) comparing to that of the none-doped device 1.8 lm/W (at 4 V). At such a low voltage, exciplex emission was major for all devices. A yellow emission turned into white emission with voltage increasing in the doped devices while only yellow light was obtained in the none-doped device. The reason was that doping made charge trapping from TPBI to m-MTDATA sufficient which lead to a stronger emission from m-MTDATA and then a white light was obtained by combination of blue emission from m-MTDATA and green-yellow emission from Alq₃ and exciplex. Compared to the device (c) with MWR of 1:1 for m-MTDATA:TPBI, white emission from device (b) and device (d) with MWR of 3:1 and 1:3, respectively, had a less blue shift, as might owing to the more sufficient charge

trapping in device (c) with the MWR of 1:1 than that in device (b) and device (d) with the MWR of 1:3 and 3:1, respectively, which might be decided partly by the position and orientation between m-MTDATA and TPBI. The power efficiencies of both doped devices and none-doped device are higher than that of the controlled device for favorable position and orientation.

Acknowledgements

This work is supported by National Natural Science Foundation of China under Grant No. 60376028 and 20020518, 2003CB314703, 60207003. The author wishes to acknowledge Prof. Chin-Ti Chen (Institute of Chemistry, Academia Sinica) for TPBI provision.

References

- [1] M. Cocchi, D. Virgili, G. Giro, V. Fattori, P. DiMarco, *Appl. Phys. Lett.* 80 (2002) 2401.
- [2] Xuezhong Jiang, Michelle S. Liu, Alex K.-Y. Jen, *J. Appl. Phys.* 91 (2002) 10147.
- [3] Y. Kawabe, J. Abe, *Appl. Phys. Lett.* 81 (2002) 493.
- [4] Fushan Li, Zhijian Chen, WeiWei, Huayu Cao, et al., *J. Phys. D* 37 (2004) 1613.
- [5] Thomas Granlund, Leif A.A. Pettersson, *J. Appl. Phys.* 81 (1997) 8097.
- [6] D.D. Gebler, Y.Z. Wang, J.W. Blatchford, S.W. Jessen, *Appl. Phys. Lett.* 70 (1997) 1644.
- [7] M. Mazzeo, D. Pisignano, F. Della Sala, J. Thompson, et al., *Appl. Phys. Lett.* 82 (2003) 334.
- [8] Jing Feng, Feng Li, Wenbao Gao, Shiyong Liu, et al., *Appl. Phys. Lett.* 78 (2001) 3947.
- [9] Hong Cao, Xicun Gao, Chun-Hui Huang, *Appl. Surf. Sci.* 161 (2000) 443.
- [10] Ching-lan Chao, Show-An Chen, *Appl. Phys. Lett.* 73 (1998) 426.
- [11] Koji itanno, Hiromitsu Ogawa, Yasuhiko Shirota, *Appl. Phys. Lett.* 72 (1998) 636.



High-efficiency electron injection cathode of Au for polymer light-emitting devices

Hongbin Wu, Fei Huang, Junbiao Peng, Yong Cao *

Institute of Polymer Optoelectronic Materials and Devices, Key Laboratory of Specially Functional Materials and Advanced Manufacturing Technology, South China University of Technology, Guangzhou 510640, China

Received 11 February 2005; accepted 14 March 2005

Available online 20 April 2005

Abstract

Polymer light-emitting diodes (PLEDs) have attracted great interests recent years due to their potential application in next generation large-area flat-panel displays. For these devices, however, achieving efficient electron injection from air- and chemicals-stable cathode remains a great challenge. Here we demonstrate for first time that by incorporation of a thin layer of amino-alkyl-substituted polyfluorene copolymer spin-coated from alcohol or water solution, Au, a most noble metal with high work-function, can be a good electron injection cathode. This new type of bilayer cathode can significantly enhance electron injection to red, green and blue electroluminescent (EL) polymers, thereby resulting in high efficiency polymer LEDs, which are comparable to that of using low work-function metals, such as Ca and Ba as cathode. The use of most stable metals such as Au as cathode will open a door for fabrication and patterning of air-stable flat panel displays.

© 2005 Elsevier B.V. All rights reserved.

Keywords: Electron-injection; Electroluminescent; Organic/polymer light-emitting diodes; Polymer–metal interface; Amino-alkyl-substituted polyfluorene copolymer

1. Introduction

Polymer light-emitting diodes (PLEDs) have attracted broad interests due to their potential application in large-area displays since the first prototype demonstrated in 1990 [1]. Charge carri-

ers injection from electrodes into the electroluminescent (EL) polymer layer is a key factor in the determination of device efficiency [2,3] and operating life time [4]. In PLEDs, metal electrodes are utilized to inject carriers (electrons and holes) into polymer and organic layer. Therefore, metal–polymer (MP) and metal–organic (MO) interfaces are crucial for carrier injection. In the first approximation, Schottky–Mott rule of vacuum level

* Corresponding author. Fax: +86 20 87110606.

E-mail address: poycao@scut.edu.cn (Y. Cao).

alignment can be applied to describe MP or MO interface [5,6] although the deviation of it has been frequently found due to the complex nature of MP interface. According to Schottky–Mott rule, the injection efficiency of the diodes is determined by the potential barrier height (difference between the Fermi level of the injection electrodes and the lowest unoccupied molecular orbital (LUMO) (for electron injection) or the highest occupied molecular orbital (HOMO) of the semiconductor (for hole injection). Owing to low electron affinity and low drifting mobility of electrons in common conjugated EL polymers, enhanced electron injection is desired. As a result, low work-function metals, such as Ca (work-function $\phi = 2.9$ eV) and Ba ($\phi = 2.8$ eV), are typically used as a cathode to facilitate electron injection [7]. Since the low work-function metals are susceptible to degradation upon water vapor or oxygen, high work-function metals, therefore more stable electron injection cathodes are desirable, if they are expected to give comparable device efficiency. Previous works have indicated that the simple vacuum alignment rule can be overruled by many ways, such as the formation of interfacial dipole, chemical doping or reactions and presence of interfacial states [5,8–10]. Over the past few years, significant efforts have been made to develop a new electron-injection cathode from high work-function metals in order to reach a high environmental stability, and ease of fabrication, in combination with high device efficiency and a low operating voltage. Great success has been achieved in modification of organic (or polymer)/Al interface by inserting ultrathin alkaline fluoride (LiF, CsF) films, which results in high-efficiency Al injection bilayer cathodes [11]. Although the mechanism of shifting vacuum level is still in debate [12–14], recently, many experimental results are pointing at doping mechanism caused by lithium (or cesium and etc.) from dissociation of alkaline fluorides in the presence of top Al layer [15,16]. This mechanism is consistent with the fact that a high work-function metal such as LiF/Au does not show similar enhancement in electron injection as LiF/Al [17]. Similar cathode metal dependence has been reported for PLEDs with surfactant/metal bilayer cathode which shows high-efficiency (as high as alkaline metals like Ca

and Ba) for the metal Al, while three orders of magnitudes lower in external efficiency was reported for surfactant/Au cathode [18]. On the other hand, Au is a most noble metal with a high work-function ($\phi = 5.2$ eV) and has been previously accepted as a good hole injection electrode [19,20]. In replace of ITO by Au, the device efficiencies of Au/MEH-PPV/Ca or Al or Au were, respectively, 2% for Ca and $1 \times 10^{-2}\%$ for Al, while for Au cathode, there is no light observed due to extremely low efficiency. However, in many applications, a most noble metal like Au is desirable due to its excellent chemical, environmental stability and thermal conductivity (i.e., in VLSI ICs). For example, Lee et al. [21] recently reported the fabrication of OLEDs by soft contact lamination and a significant enhancement in device efficiency (up to $1.5 \times 10^{-3}\%$) with laminated Au cathode, compared to $QE = 5.9 \times 10^{-5}\%$ for thermally evaporated Au cathode, even though, the devices performance was far away from that for practical application.

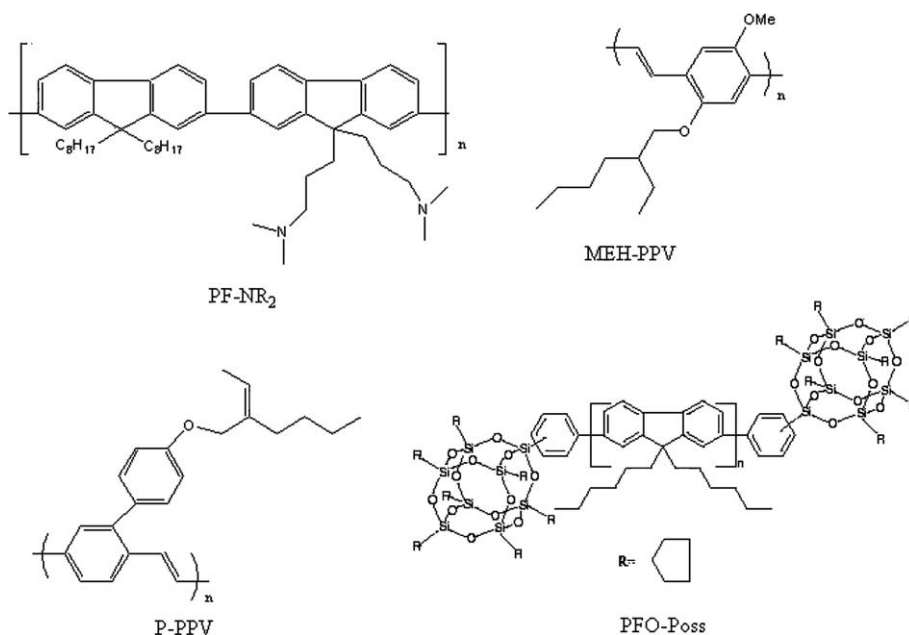
In this paper, we report for first time high-efficiency polymer OLEDs with Au as the cathode with insertion of a thin layer of conjugated aminoalkyl substituted polyfluorene [22] (PF-NR₂) between Au and emitting layer. We have shown previously that the insertion of PF-NR₂ between Al and emitting layer lead to high-efficiency PLEDs comparable with devices from Ca and Ba cathodes [23] and light-emitting devices fabricated from aminoalkyl-substituted polyfluorene copolymers with different contents of narrow band gap comonomer 2,1,3-benzothiadiazole (BTDZ) show high external quantum efficiencies both for the neutral precursor and the quaternized copolymers, with high work-function metals such as Al as a cathode [24]. Here we demonstrate that unlike other bilayer cathode with high work-function metal, such as LiF/Al [11] and surfactant/Al [18], the insertion of PF-NR₂ between varieties of RGB emitting polymers and Au also significantly enhances electron injection to the level as for low work-function metals, such as Ba and Ca as well as for PF-NR₂/Al cathode. We also found that the significant improvement of an electron injection originated from the modification of MP interface by self-assembly of PF-NR₂ interlayer attached to Au

surface via amino or ammonium–Au interaction. Furthermore, we investigated bilayer cathode of PF-NR₂ with varieties of other high work-function metal ($\phi > 4.1$ eV) such as In, Ag, Sn and Cu. We have shown that unlike LiF/Al bilayer cathode which is specific only for Al metal, aminoalkyl-substituted polyfluorenes and their polyelectrolyte can be used in combination with many other higher work-function metals in addition to Al to give comparable device performance as low work-function metal. This fact implies that PF-NR₂/metal bilayer cathode has different mechanism other than LiF/Al bilayer cathode. Electroluminescent properties and mechanism of PF-NR₂/Au cathode are investigated and discussed based on measurement of built-in potential in parallel by photovoltaic (PV) measurement and electroabsorption (EA) measurement and X-ray diffraction pattern. PV and EA confirm that upon incorporation of PF-NR₂ layer, electron injection barrier height for electron injection from high work-function cathode was significantly decreased as a result of an interface dipole formed due to strong interaction and alignment of amino group on metal surface. The particular advantage derived from the use copolymers presented in this study is that the electron injection layer from aminoalkyl-substituted polyfluorene copolymer can be solution processed from solvents, such as methanol and water, in which most of conjugated polymers are insoluble. This feature is expected to be particularly useful for the fabrication of multi-layer PLEDs by solution processing, in which mixing EL layer with adjacent electron injection layer can be avoided.

2. Experimentals

The fabrication of PLEDs with MEH-PPV, P-PPV and PFO, as an electroluminescent layer follows well-established process [23]. Patterned indium tin oxide (ITO) coated glass substrates with a sheet resistance of 15–20 Ω /square undergoes a wet-cleaning process in an ultrasonic bath, beginning with acetone, followed by detergent, deionized water, and isopropanol. After oxygen-plasma treating, a 100 nm-thick anode buffer layer of poly(ethylenedioxythiophene): poly(styrene sulfonic

acid) (PEDOT: PSS, Baytron P 4083, Bayer AG) film was spin-cast on the ITO substrate and dried by baking in a vacuum oven at 80 °C overnight. For blue light-emitting PFO, a 40 nm-thick poly(*N*-vinylcarbazole) (PVK, from Aldrich Co.) was spin-coated at the top of the PEDOT layer from 10 mg/mL 1,1,2,2-tetrachloroethane solution with subsequent drying in vacuum at room temperature. The RGB EL polymers used in this study are poly[2-methoxy,5-(2'-ethyl-hexyloxy)-1,4-phenylene vinylene] (MEM-PPV) [25], poly[2-(4-(3',7'-dimethyloctyloxy)-phenyl)-*p*-phenylenevinylene] (P-PPV) [26] and polyfluorene (PFO-POSS) [27] (see Scheme 1). Of which, MEM-PPV and P-PPV were synthesized according to published procedure, and PFO was kindly provided by Dr. S. Xiao of Organic Vision Inc. RGB active polymer films were casted from 5 mg/mL toluene solution (for P-PPV), 4 mg/mL toluene: xylene (50:50) solution (for MEH-PPV), and 15 mg/mL chloroform solution (for PFO-POSS) to form a uniform 80 nm-thick film at a speed around 2000 rpm. An Alfa-step 500 surface profiler (Tensor) was used to determine the spin-cast film thickness. The aminoalkyl substituted polyfluorene (PF-NR₂) was synthesized according to procedure published elsewhere [22]. A thin PF-NR₂ interlayer (10–300 Å) was spin-coated from 0.4 mg/mL or 2 mg/mL methanol solution with a few drops of acetic acid at a speed of 600–3000 rpm on the top of the emitting layer. Finally, 100 nm-thick gold is evaporated with shadow mask to form the top electrode at a base pressure of 1×10^{-4} Pa. The thickness of the evaporated cathodes was monitored by a calibrated crystal thickness/ratio monitor (Model: STM-100/MF, Sycon). The cross-area between the cathode and anode defined the pixel size of 15 mm². Except the spin coating of PEDOT layer, all the processes were carried out in a controlled atmosphere of nitrogen dry-box (Vacuum Atmosphere Co.) containing less than 10 ppm oxygen and moisture. In order to avoid a contamination of volatile low work-function metal during Au cathode deposition on top of PF-NR₂ layer, an evaporation chamber was thoroughly cleaned by prolonged baking at 120–130 °C under high vacuum ($<1 \times 10^{-4}$ Pa) before Au deposition. The control device with device configuration: ITO/



Scheme 1. Molecular structure of RGB electroluminescent polymers used. Of which, MEM-PPV and P-PPV were synthesized according to published procedure [24,25], and PFO-Poss was kindly provided by Dr. S. Xiao26 of Organic Vision Inc. Synthesis of poly[(9,9-bis(3'-(*N,N*-dimethylamino)propyl)-2,7-fluorene)-alt-2,7-(9,9-dioctylfluorene)] (PF-NR₂) and their quaternized salt (PF-NR₃+X⁻, where X⁻ is I⁻ or Br⁻) was described previously [22].

PEDOT (PVK)/EL polymer/Au is always fabricated as a control along with PF-NR₂/Au devices to make sure that no low work-function metal residue left in the evaporation chamber from previous deposition.

The current density–voltage–luminance (*J–L–V*) characteristic was measured by a Keithley 236 source-measurement unit and a calibrated silicon photodiode which was calibrated for luminance by a PR-705 SpectraScan Spectrophotometer (Photo Research). The external EL quantum efficiency (QE) was collected by measuring the total light output in all directions in an integrating sphere (IS-080, Labsphere). The photovoltaic measurement was carried out under white-light illumination using a xenon lamp (150 W, Oriel) as a light source. Our electroabsorption spectrograph consists of a 250 W halogen tungsten lamp, a monochromator (Zolix BP500) equipped with a 1200 lines/mm grating, an amplifier silicon photodiode and a SRS (Model: SR830) lock-in amplifier. The EL spectra were captured by Instaspec IV CCD spectrometer (Oriel).

For small angle X-ray diffraction (XRD) samples, silicon wafers with polished crystal surface (111) were used as substrate. After undergoing the wet cleaning process in an ultrasonic bath as mentioned above, the wafers were dried by baking in a vacuum chamber. Simulating the PLEDs structure in XRD study, samples in configuration like Si (111)/MEH-PPV (1000 Å)/PF-NR₂ (200 Å)/Au (90 Å) and Si (111)/MEH-PPV (1000 Å)/PF-NR₂ (200 Å) was fabricated in a controlled atmosphere of nitrogen dry-box following a similar process with that of PLEDs fabrication. XRD was taken by an automatic X-ray diffractometer (D/Max-III A, Rigaku) with Cu K α filtered by Sm filter.

3. Results and discussion

Since MEH-PPV, P-PPV and PFO have the lowest unoccupied molecular orbital level (LUMO) of 2.80 eV, 2.34 eV and 2.60 eV [26,27] respectively, a substantial barrier height is expected for electron injection with respect to the plain Au cathode

($\phi = 5.2$ eV) in ITO/PEDOT/polymer/Au devices. As a result, the device efficiency for three polymers from plain Au cathode was very low (Figs. 1, 2 and Table 1), similar as reported by the other groups [18–21]. Fig. 1 compares characteristic of the current density J and luminous efficiency (LE) vs. bias for MEH-PPV device by using Au cathode with or without PF-NR₂ interlayer (ITO/PEDOT/MEH-PPV/PF-NR₂ (0, 20 nm)/Au). As expected, plain Au device shows flat exponential increase in J - V characteristics after turn-on and a low LE in the order of 10^{-3} cd/A, indicating poor-behaved electron injection. In contrast, with a thin PF-NR₂ film (20 nm) incorporated between Au and MEH-PPV, the J - V and LE- V (Fig. 1) characteristics change dramatically, followed by a sharp exponential increase in current flow (Fig. 1) and a three-order of magnitudes increase in the LE approaching 1 cd/A, in the results of the enhanced electron injection. The maximum EL quantum efficiency (QE) measured in an integrating sphere (IS-080, Lab-sphere) for the device with a 30 nm PF-NR₂ layer yields a thousandfold increase to 1.2% (photon/electron) (Table 1). The further evidence for the improved electron injection from PF-NR₂/Au

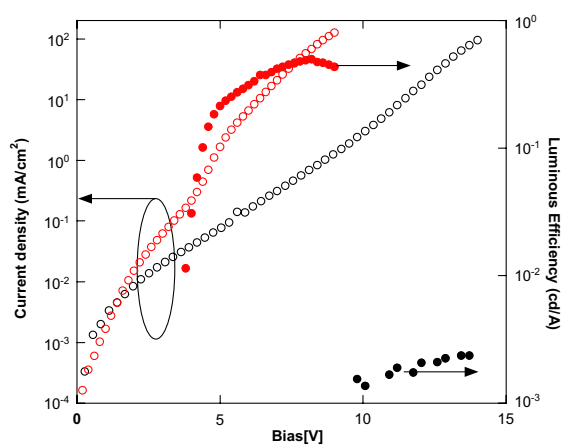


Fig. 1. Performance of PLEDs with an 800 Å MEH-PPV film with Au and PF-NR₂ (20 nm)/Au as cathode, respectively: (a) J - V characteristic: Au cathode (black open circles), PF-NR₂ (20 nm)/Au bilayer cathode (red open circles) and (b) LE- V characteristic: Au cathode (black solid circles), PF-NR₂ (20 nm)/Au cathode (red solid circles). (For interpretation of colours the reader is referred to the web version of this article.)

cathode can be obtained by fact that for the I - V curves from devices with ITO replaced by Au as an anode in structure: Au/MEH-PPV/PF-NR₂/Au (Fig. 3). Diode type I - V (and also the enhanced device efficiency) can be observed only when PF-NR₂/Au is wired negatively.

PLEDs with green emitting P-PPV as EL polymer and PF-NR₂/Au as cathode are shown in Fig. 2. Fig. 2 shows that the enhanced efficiency is also associated with enhanced electron injection and more balanced electrons and holes current in P-PPV devices. As shown in Fig. 2 and Table 1, for P-PPV bilayer (PF-NR₂/Au) device, an external quantum efficiency of 3.83% and a luminous efficiency of 11.7 cd/A with a luminance of 4605 cd/m² have been reached at a current density of 39.3 mA/cm² at 9.6 V, compared with 0.002% for plain Au device. Similarly, with a bilayer cathode, the device from blue-emitting PFO polymer shows an external quantum efficiency of 1.78% at a current density of 35.3 mA/cm². The maximal external quantum efficiency reached 3.12% at 6.7 mA/cm², compared to 0.002% at similar current density for a plain Au device (Table 1).

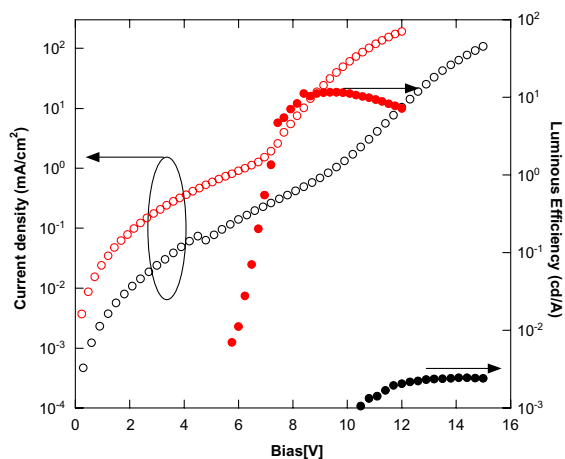


Fig. 2. Performance of PLEDs with an 800 Å P-PPV polymer film with Au and PF-NR₂ (20 nm)/Au as cathode, respectively: (a) J - V characteristic: Au cathode (black open circles), PF-NR₂ (20 nm)/Au bilayer cathode (red open circles). (b) LE- V characteristic: Au cathode (black solid circles), PF-NR₂ (20 nm)/Au bilayer cathode (red solid circles). (For interpretation of colours the reader is referred to the web version of this article.)

Table 1

Device performance of RGB PLEDs using PF-NR₂/Au as a cathode in device configuration ITO/PEDOT (PVK)/EL polymer/PF-NR₂/Au

EL polymers	PF-NR ₂ thickness (nm)	Bias (V)	Current density (mA/cm ²)	Luminance (cd/m ²)	QE (%)	LE (cd/A)
MEH-PPV	3	3.2	35.8	3.7	0.009	0.010
MEH-PPV	20	6.0	34.7	162.5	0.411	0.469
MEH-PPV	30	11.8	39.9	377.5	1.240	0.945
MEH-PPV	–	6.6	166.7	0.8	0.0004	0.0005
P-PPV	3	8.6	34.7	17.7	0.017	0.051
P-PPV	20	9.4	31.3	3648.0	3.843	11.642
P-PPV	30	11.0	34.7	3816.1	3.639	11.008
P-PPV	–	13.2	35.9	0.78	0.002	0.006
PFO	3	11.7	33.3	8.6	0.036	0.026
PFO	20	11.8	35.3	495.7	1.778	1.403
PFO	30	13.4	39.3	271.8	0.876	0.691
PFO	–	24.4	32.0	0.6	0.002	0.002

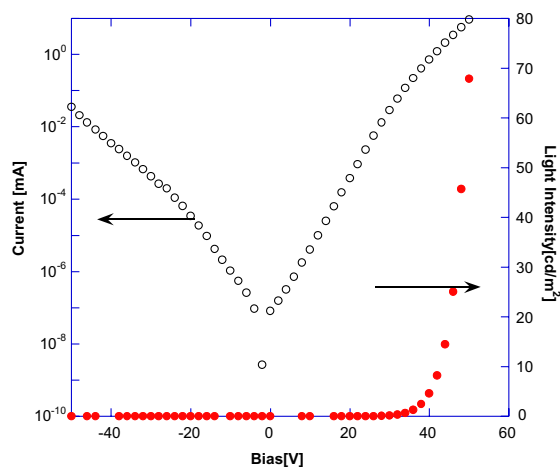


Fig. 3. I – L – V characteristic of PLEDs in configuration like ITO/Au (500 Å)/MEH-PPV/PF-NR₂ (300 Å)/Au.

The device performance based on the RGB EL polymers is summarized in Table 1 for comparison. EL spectra (Fig. 4) show that there is no significant difference between the EL emission profile for MEM-PPV, P-PPV and PFO devices with a PF-NR₂/Au bilayer cathode and with a Ba/Al cathode, which implies that the recombination zone for these devices is located in the bulk of EL polymers, and that the PF-NR₂ plays a role of electron injection layer.

In order to understand the mechanism of this amazing and unexpected enhancement of electron injection from Au, we measure photovoltaic char-

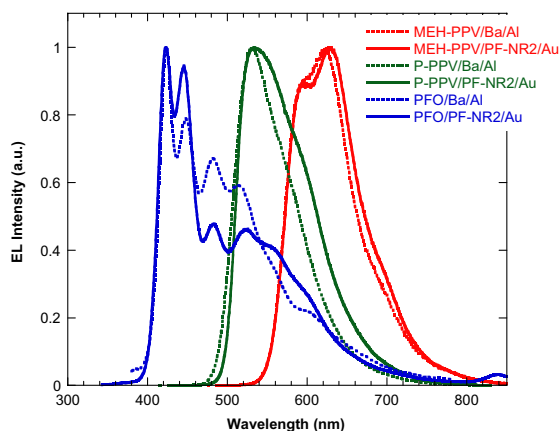


Fig. 4. EL spectra for the RGB devices. Of which, MEH-PPV devices, with PF-NR₂/Au bilayer cathode (red solid line) and Ba/Al cathode (red broken line), P-PPV devices, with PF-NR₂/Au bilayer cathode (green solid line) and Ba/Al cathode (green broken line), and PFO devices, with PF-NR₂/Au bilayer cathode (blue solid line) and Ba/Al cathode (blue broken line). (For interpretation of colours the reader is referred to the web version of this article.)

acteristics for a series of PLEDs in configuration: ITO/PEDOT (or PVK)/MEH-PPV (PFO)/PF-NR₂/Au, which only differ in PF-NR₂ layer thickness range from 0 to 30 nm, to estimate the built-in potential across the devices [28]. As the anode and the EL polymer layer are identical in all devices, the built-in potential (V_{bi}) of the devices should scale with the change of barrier height in the cathode side. We notice that, for MEH-PPV

devices, with an increase in the thickness of the PF-NR₂ layer employed from 0, 1 nm, 2 nm, 3 nm, 10 nm, 20 nm, 25 nm and 30 nm, the built-in potential shifts from 0.15 V, which roughly corresponds to the difference between the work-function of PEDOT (5.0 eV) [29] and Au (5.2 V) [30] to 0.90 V (Fig. 5a). When PEDOT/MEH-PPV is replaced by PVK/PFO, similar V_{bi} increases from 0.45 V, which is in agreement with the work-function difference between PVK (5.6 eV) and Au (5.2 eV) for device with neat Au cathode (without PF-NR₂) to 1.45 V for device with a 30 nm PF-NR₂/Au cathode (Fig. 5(b)). We note that the built-in potential and the electron injection barrier height can be tuned in a wide range of around 0.75 V and 1.0 eV for MEHPPV and PFO devices, respectively, just by insertion of the PF-NR₂ layer with different thickness. It is important to note that the device efficiency increases with increasing the built-in potential (Table 1). Similar correlation between the built-in potential and the device efficiency: the higher V_{bi} corresponds the higher efficiency, was reported recently by Brown et al. [31]. In combination with the J - L - V characteristics of the PLEDs, photovoltaic results indicate that the increase in an electron injection and the device efficiency is due to the reduction of barrier height in the cathode interface. As pointed by many authors, Schottky rule of vacuum level alignment can be broken by strong metal/polymer (organic) interaction (MP and MO), such as the adsorption of molecules on metal surfaces, dipole formation, charge transfer and interface state [10,32–34]. We propose that dipole formation is most likely the origin of the reduction of barrier height between Au and EL polymers due to the presence of PF-NR₂ layer. As a result, an abrupt shift of vacuum level at the interface was observed and the work-function or surface potential of the metal is altered.

In order to gain insight into the electron injection enhancement of the bilayer cathode devices, in parallel with PV measurement, we use electroabsorption spectroscopy to measure the built-in potential of devices in configuration EL polymer/metal and EL polymer/PF-NR₂/metal for comparison. EA measurement takes great advantage over other indirect approaches in quantifying the built-

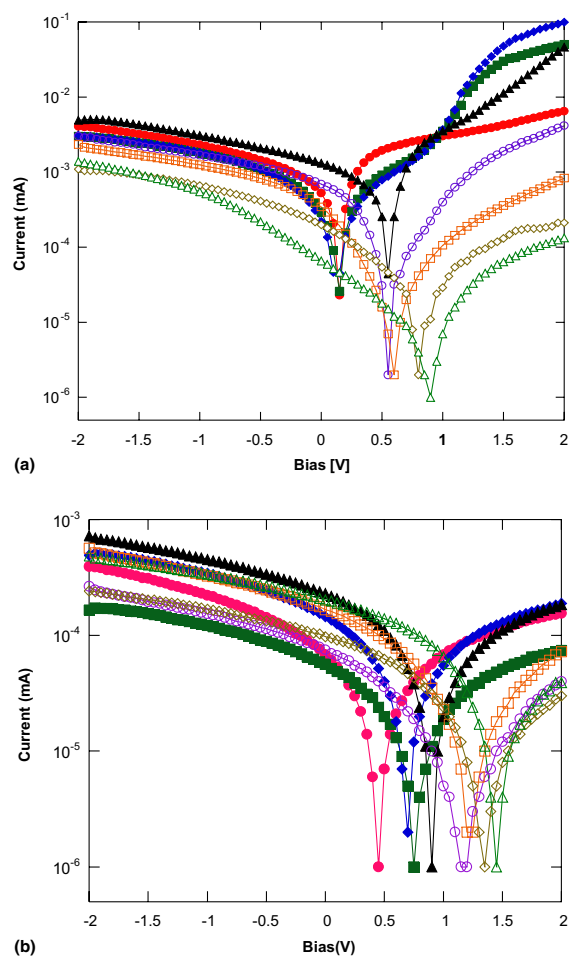


Fig. 5. Photovoltaic characteristics of devices with varied PF-NR₂ layer thickness: (a) in configuration ITO/PEDOT/MEH-PPV/PF-NR₂/Au and (b) in configuration ITO/PEDOT/PVK/PFO/PF-NR₂/Au. Filled circles are for devices without PF-NR₂ layer, filled squares for devices with 1 nm PF-NR₂ layer, filled diamonds for 2 nm, filled triangles for 3 nm, open circles for 10 nm, open squares for 20 nm, open diamonds for 25 nm, and open triangles for 30 nm.

in potential of a device structure; its high reliability lies in direct measurement and noninvasion to the device and had been demonstrated be valid for probe the built-in field in polymer/metal structure [35–38]. Details of electroabsorption technique and apparatus have been described by Campbell et al. [35]. EA signal of a sample, representing the relative change of the optical transmission under the application of electric field, is propor-

tional to the imaginary part of the optical third-order susceptibility $\text{Im}\chi^{(3)}(\hbar\omega)$ and the square of the electric field, then the EA response due to an applied ac bias, $E = E_{\text{DC}} + E_{\text{AC}}\cos\omega t$, follows:

$$-\frac{\Delta T}{T}(\hbar\omega) \propto \text{Im}\chi^{(3)}(\hbar\omega)\{E_{\text{AC}}^2[1 + \cos(2\omega t)]/2 + 2E_{\text{AC}}E_{\text{DC}}\cos(\omega t) + E_{\text{DC}}^2\} \quad (1)$$

Thus, in presence of built-in field, the EA response at the fundamental harmonic frequency is both modulated by V_{AC} and the actual DC component ($V_{\text{DC}} - V_{\text{bi}}$) across the device. So changing the DC component and finding the voltage at which the EA response at fundamental frequency vanishes can determine the built-in field. It is important to note, the equation is based on a uniform distribution of the electric field across the bulk of the EL polymer layer. We have confirmed the existence of a uniform distribution of the electric field in our devices by running capacitance–voltage measurements. In reverse to weak forward bias regime (not shown here), for a typical MEH-PPV/PF-NR₂ (20 nm)/Au device, the capacitance is essentially constant, independent on bias, indicating space charge is negligible [39]. Prior to EA measurement, electroabsorption response for single layer PF-NR₂ was carried out, in that the spectral position of the EA features of the PF-NR₂ layer are quite separated from that of the EL polymer (not shown). The magnitude of the EA response as a function of DC bias for a MEH-PPV/Au PLEDs and a MEH-PPV/PF-NR₂/Au PLEDs, with 2.15 eV photon as probe monochromatic beam under 2 V AC applied bias, was shown in Fig. 6, and the built-in potential of each finished device can straightforwardly be deduced. For a MEH-PPV/PF-NR₂/Au device, a built-in potential about 1800 mV corresponds to a considerable increase over that of the gold-only cathode with a V_{bi} of 400 mV for plain Au device. This result is fully consistent with that of our photovoltaic measurement (Fig. 5). Significant enhancement of the built-in potential indicates that the effective barrier height for the electron injection is substantially lowered by the insertion of a PF-NR₂ layer between Au and the emitting layer, thereby leading to a more balanced injection of electrons and

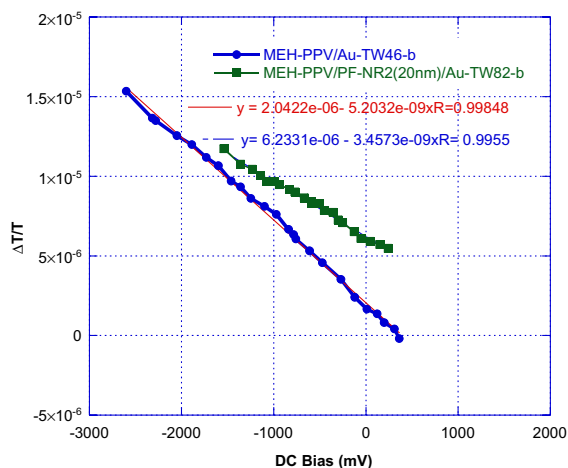


Fig. 6. The magnitude of the EA response as a function of DC bias for a MEH-PPV/Au PLEDs and an MEH-PPV/PF-NR₂ (20 nm)/Au with 2.15 eV photon as probe monochromatic beam under 2 V AC applied bias.

holes. As a result, the quantum efficiency increases, and the turn-on and the operating voltage decreases. Similar trend can be found in other test system investigated by EA measurement. For example, for In based MEH-PPV devices, the built-in potential of a typical MEH-PPV/In device moves from 930 mV (which is approximately equal to the difference between the work-functions of ITO/PEDOT and In in a flat-band configuration) to about 2400 mV for device with a PF-NR₂/In bilayer cathode.

In order to form strong dipole which can shift barrier height up to 1 eV, the PF-NR₂ layer must be self-assembled in each layer to form a positive interface dipole (taking dipole directing outward to be positive). It is well known that amino and ammonium group can form strong interaction with Au metal surface, and it was widely used for self-assembly of organic compounds on Au surface [40–42]. Small-angle X-ray diffraction pattern of PF-NR₂ layer with Au deposited on the top of it (Fig. 7) indicates the existence of an ordered structure around $2\theta = 2.018^\circ$ (corresponding to a spacing of 43.7 Å) after Au deposition on the PF-NR₂ layer in configuration of Si(111)/MEH-PPV-(1000 Å)/PF-NR₂(200 Å)/Au (90 Å), simulating the PLEDs device configuration in this study. The

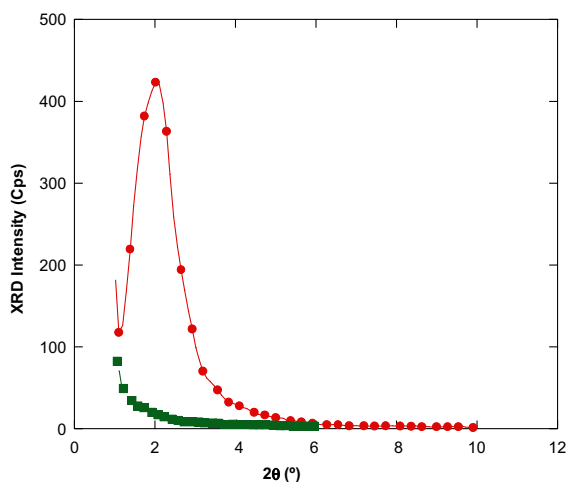


Fig. 7. X-ray diffraction pattern of PF-NR₂ layer with Au deposited on the top of it compared with that without Au deposition. Circles are for Si (111)/MEH-PPV (1000 Å)/PF-NR₂ (200 Å)/Au (90 Å) and squares are for Si (111)/MEH-PPV (1000 Å)/PF-NR₂ (200 Å).

coherent length of $\xi = 70$ nm estimated from the Debye–Scherrer formula [43]: $\xi = 2\pi\lambda/\delta(2\theta)$, where λ is Cu K $_{\alpha}$ wavelength and $\delta(2\theta)$ is the full width at half-maximum of the XRD, indicates a considerably ordered domain size for PF-NR₂ layer. In contrast, for Si(111)/MEH-PPV (1000 Å)/PF-NR₂ (200 Å) structure without Au deposition, no long range ordering structure was recorded (Fig. 7). This implies that Au deposition stimulates a self-assembling of PF-NR₂ layer on the Au surface due to strong interaction between Au and the NR₂ groups. The aligned PF-NR₂ layer provides a large positive interface dipole moment. As a result, significant vacuum level shift to lower energy occurs at the interfaces. We also note that similar diffraction pattern can be observed in reversed structure upon spin of PF-NR₂ on the top of Au layer (Fig. 8). Diffraction pattern show a sharp structure around $2\theta = 1.450^\circ$ corresponding to a spacing of 60.92 Å, which is slightly larger than spacing for PF-NR₂/Au by thermally deposition. This fact indicates that self-assembling of PF-NR₂ layer takes place either by spin-coating of PF-NR₂ solution on Au surface or by thermal deposition of Au on the top of PF-NR₂ surface. Detailed analysis of PF-NR₂/Au interlayer structure is now in progress and will be reported else-

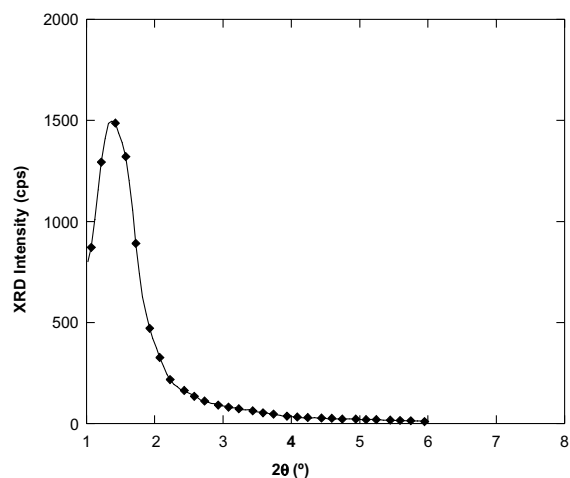


Fig. 8. X-ray diffraction pattern in configuration like Si (111)/Au (90 Å)/PF-NR₂ (200 Å)/MEH-PPV (200 Å).

where. Controllable carrier injection barrier height between the interface of Ag and organic self-assembled monolayer (SAM) with different dipole moment and direction has been reported by Campbell et al. [44]. However, no device data were reported with such modified metal interface by Campbell group. Here we are able to demonstrate for the first time that such a self-assembled structure can lead really to high-efficiency PLEDs.

Our approach is not limited in specific metals such as Au demonstrated here or Al [23], other high work-function metals such as In ($\phi = 4.12$ eV), Ag ($\phi = 4.26$ eV), Sn ($\phi = 4.42$ eV), and Cu ($\phi = 4.65$ eV) are also tested, as summarized in Table 2. Al devices performance is also listed in Table 2 for comparison. At the same time, photovoltaic measurement for all of these devices also confirmed a reduction of barrier height in the cathode interface as inserted with an ultrathin PF-NR₂ layer. Results in Table 2 indicate that device performance with such bilayer cathode exhibit significant metal dependence. Preliminary analysis of all existed data indicates that the variation of device performance with the nature of metals is probably related with interaction of aminoalkyl-substituted polyfluorene with metal surface, rather than work-function of metals. More detailed studies are in progress and the results will be reported in forthcoming report.

Table 2

Device performances of RGB PLEDs using PF-NR₂/metals as a cathode in device configuration ITO/PEDOT/EL polymer/PF-NR₂/metals (for devices from PFO polymer device the configuration is ITO/PEDOT/PVK/PFO/PF-NR₂/metals)

EL polymers	Cathode	Bias (V)	Current density (mA/cm ²)	Luminance (cd/m ²)	QE (%)	LE (cd/A)
MEH-PPV ²³	Al ($\phi = 4.30$ eV)	4.6	34.7	6	0.02	0.02
MEH-PPV ²³	PF-NR ₂ (3 nm)/Al	5.2	36.7	454	1.54	1.2
P-PPV ²³	Al ($\phi = 4.30$ eV)	7.7	34.7	115	0.11	0.3
P-PPV ²³	PF-NR ₂ (20 nm)/Al	8.8	33.3	7923	7.85	23.8
PFO ²³	Al ($\phi = 4.30$ eV)	14.4	34.7	2	0.02	0.01
PFO ²³	PF-NR ₂ (20 nm)/Al	9.7	30	380	1.62	1.3
MEH-PPV	In ($\phi = 4.12$ eV)	4.8	33	1.1	0.003	0.003
MEH-PPV	PF-NR ₂ (20 nm)/In	5.9	37.5	98	0.305	0.261
P-PPV	In ($\phi = 4.12$ eV)	4	31	22.4	0.024	0.072
P-PPV	PF-NR ₂ (25 nm)/In	7.4	29.7	3945.5	4.369	13.299
PFO	In ($\phi = 4.12$ eV)	9	31.2	46.1	0.106	0.148
PFO	PF-NR ₂ (25 nm)/In	9	29.8	326.2	1.391	1.095
MEH-PPV	Ag ($\phi = 4.26$ eV)	5.1	32.9	0.8	0.003	0.002
MEH-PPV	PF-NR ₂ (20 nm)/Ag	6.4	35.7	61	0.199	0.171
P-PPV	Ag ($\phi = 4.26$ eV)	4.3	28.7	5.8	0.007	0.02
P-PPV	PF-NR ₂ (20 nm)/Ag	5.6	29.1	908.5	1.025	3.125
PFO	Ag ($\phi = 4.26$ eV)	20.2	30.3	11.4	0.048	0.038
PFO	PF-NR ₂ (20 nm)/Ag	15	39.1	122.4	0.398	0.313
MEH-PPV	Sn ($\phi = 4.42$ eV)	6.7	35.7	2.4	0.008	0.007
MEH-PPV	PF-NR ₂ (20 nm)/Sn	7.6	31.4	66.4	0.246	0.211
P-PPV	Sn ($\phi = 4.42$ eV)	3.9	31	5.8	0.006	0.019
P-PPV	PF-NR ₂ (20 nm)/Sn	5.8	40.3	1192.8	0.974	2.962
PFO	Sn ($\phi = 4.42$ eV)	20.7	30.1	9.3	0.039	0.031
PFO	PF-NR ₂ (20 nm)/Sn	16.2	34.1	147.1	0.548	0.432
MEH-PPV	Cu ($\phi = 4.65$ eV)	5.6	33.2	2.5	0.009	0.007
MEH-PPV	PF-NR ₂ (25 nm)/Cu	8.9	36.4	334.4	1.071	0.918
P-PPV	Cu ($\phi = 4.65$ eV)	3.2	37.1	4.9	0.004	0.013
P-PPV	PF-NR ₂ (3 nm)/Cu	3.6	35.9	160.4	0.147	0.447
PFO	Cu ($\phi = 4.65$ eV)	16	32.7	14.1	0.089	0.043
PFO	PF-NR ₂ (25 nm)/Cu	13.5	35.1	416.6	1.509	1.188

4. Conclusions

In summary, we successfully demonstrated for the first time that barrier height between a most noble and high work-function metal Au (or other high work-function metal with work-function $\phi > 4.1$ eV, such as In, Ag, Sn and Cu) and organic EL polymer can be turned down to allow highly efficient electron injection into conjugated polymers by the insertion of self-assembled aminoalkyl-substituted polyfluorene and fabrication of high-efficiency PLEDs with a variety of RGB EL polymers of different band-gaps. PV and EA measurement confirm that built-in potential across the device was significantly raised due to

decreasing barrier height. Vacuum level alignment of EL polymer/Au interface was modified by dipole moment caused by self-assembly and alignment of the inserted PF-NR₂ layer on the Au surface. A small-angle X-ray diffraction pattern indicates that such self-assembling in the MP interface takes place. This first example of high-efficiency PLEDs with Au cathode distinctly demonstrates that EL polymer/metal interface, together with the PLEDs architecture, can be engineered by using novel solution-processable materials, which allow using most noble and high work-function metal Au as an efficient electron injection cathode. The results show that interface engineering in polymer and organic LEDs will

lead to essentially new device architecture in the future.

Acknowledgement

The work was financially supported by the Ministry of Science and Technology (Project No. 2002CB613402) and the Natural Science Foundation of China (Project No. 90101019, 50433030). The authors are grateful to Mo, Y.Q. for supplying MEH-PPV, P-PPV and Dr. S. Xiao, for supplying PFO polymer.

References

- [1] J.H. Burroughes, D.D.C. Bradley, A.R. Brown, R.N. Marks, K. MacKay, R.H. Friend, P.L. Burn, A.B. Holmes, *Nature* 347 (1990) 539.
- [2] I.D. Parker, *J. Appl. Phys.* 75 (1994) 1656.
- [3] Y. Cao, G. Yu, I.D. Parker, A.J. Heeger, *J. Appl. Phys.* 88 (2000) 3618.
- [4] I.D. Parker, Y. Cao, C.Y. Yang, *J. Appl. Phys.* 85 (1999) 2441.
- [5] A. Kahn, N. Koch, W.Y. Gao, *J. Polym. Sci. B* 41 (2003) 2529.
- [6] Y.L. Shen, A.R. Hosseini, M.H. Wong, G.G. Malliaras, *Chem. Phys. Chem.* 5 (2004) 16.
- [7] D. Braun, A.J. Heeger, *Appl. Phys. Lett.* 58 (1991) 1982.
- [8] S.C. Veenstra, H.T. Jonkman, *J. Polym. Sci. B* 41 (2003) 2549.
- [9] H. Ishii, K. Seki, in: W.R. Salaneck, K. Seki, A. Kahn, J.J. Pireaux (Eds.), *Conjugated Polymer and Molecular Interfaces: Science and Technology for Photonic and Optoelectronic Applications*, Marcel Dekker, New York, 2002.
- [10] H. Ishii, K. Sugiyama, E. Ito, K. Seki, *Adv. Mater.* 11 (1999) 605.
- [11] L.S. Hung, C.W. Tang, M.G. Mason, *Appl. Phys. Lett.* 70 (1997) 152.
- [12] L.S. Hung, C.H. Chen, *Mater. Sci. Eng. R* 39 (2002) 143.
- [13] S.E. Shaheen, G.E. Jabbour, M.M. Morrell, Y. Kawabe, B. Kippelen, N. Peyghambarian, M.F. Nabor, R. Schlaf, E.A. Mash, N.R. Armstrong, *J. Appl. Phys.* 84 (1998) 2324.
- [14] M.G. Mason, C.W. Tang, L.S. Hung, P. Raychaudhuri, D.J. Giesen, L. Yan, Q.T. Le, Y. Gao, S.T. Lee, L.S. Liao, L.F. Cheng, W.R. Salaneck, D.A. dos Santos, *J. Appl. Phys.* 89 (2001) 2756.
- [15] M.Y. Chan, S.L. Lai, M.K. Fung, S.W. Tong, C.S. Lee, S.T. Lee, *Appl. Phys. Lett.* 82 (2003) 1784.
- [16] Q.T. Le, L. Yan, Y. Gao, M.G. Mason, D.J. Giesen, C.W. Tang, *J. Appl. Phys.* 87 (2000) 375.
- [17] I.G. Hill, A.J. Mäkinen, Z.H. Kafafi, *Appl. Phys. Lett.* 77 (2000) 2003.
- [18] Y. Cao, G. Yu, A.J. Heeger, *Adv. Mater.* 10 (1998) 917.
- [19] R.A. Hatton, M.R. Willis, M.A. Chesters, F.J.M. Rutten, D. Briggs, *J. Mater. Chem.* 13 (2003) 38.
- [20] G.G. Malliaras, J.R. Salem, P.J. Brock, C. Scott, *Phys. Rev. B* 58 (1998) R13411.
- [21] T.W. Lee, J. Zaumseil, Z. Bao, J.W.P. Hsu, J.A. Rogers, *PNAS* 101 (2004) 429.
- [22] F. Huang, H.B. Wu, D.L. Wang, W. Yang, Y. Cao, *Chem. Mater.* 16 (2004) 708.
- [23] H.B. Wu, F. Huang, Y.Q. Mo, W. Yang, D.L. Wang, J.B. Peng, Y. Cao, *Adv. Mater.* 16 (2004) 1826.
- [24] F. Huang, L.T. Hou, H.B. Wu, X.H. Wang, H.L. Shen, W. Cao, W. Yang, Y. Cao, *J. Am. Chem. Soc.* 126 (2004) 9845.
- [25] Y.Q. Mo, J. Huang, J.X. Jiang, X.Y. Deng, Y.H. Niu, Y. Cao, *Chinese J. Polym. Sci.* 20 (2002) 461.
- [26] H. Becker, H. Spreitzer, W. Kreuder, E. Kluge, H. Schenk, I.D. Parker, Y. Cao, *Adv. Mater.* 12 (2000) 42.
- [27] S. Xiao, M. Nguyen, X. Gong, Y. Cao, H.B. Wu, D. Moses, A.J. Heeger, *Adv. Funct. Mater.* 13 (2003) 25.
- [28] C.J. Brabec, A. Cravino, D. Meissner, N.S. Sariciftci, F. Fromherz, M.T. Rispens, L. Sanchez, J.C. Hummelen, *Adv. Funct. Mater.* 11 (2001) 374.
- [29] T.M. Brown, T.J. Cacialli, *Polym. Sci. B* 41 (2003) 2649.
- [30] W.N. Hansen, K.B. Johnson, *Surf. Sci.* 316 (1994) 373.
- [31] T.M. Brown, R.H. Friend, I.S. Millard, D.J. Lacey, T. Butler, J.H. Burroughes, F. Cacialli, *J. Appl. Phys.* 93 (2003) 6159.
- [32] C.J. Christoph, S.E. Shaheen, C. Winder, N.S. Sariciftci, P. Denk, *Appl. Phys. Lett.* 80 (2003) 1288.
- [33] D.P. Woodruff, T.A. Delchar, *Modern Techniques of Surface Science*, Cambridge University Press, Cambridge, 1986.
- [34] J.H. Lzél, F.K. Schulte, H. Wagner, *Solid State Surface Physics*, Springer, Berlin, 1979.
- [35] I.H. Campbell, T.W. Hagler, D.L. Smith, J.P. Ferraris, *Phys. Rev. Lett.* 76 (1996) 1900.
- [36] I.H. Campbell, M.D. Joswick, I.D. Parker, *Appl. Phys. Lett.* 67 (1995) 3171.
- [37] T.M. Brown, F. Cacialli, *IEE Proc. Optoelectron.* 74 (2001) 148.
- [38] T.M. Brown, R.H. Friend, S. Millard, D.J. Lacey, T. Butler, J.H. Burroughes, F. Cacialli, *J. Appl. Phys.* 93 (2003) 6159.
- [39] I.H. Campbell, D.L. Smith, J.P. Ferraris, *Appl. Phys. Lett.* 66 (1995) 3030.
- [40] L. Xu, Y. Guo, R. Xie, J. Zhuang, W. Yang, T. Li, *Nanotechnology* 13 (2002) 725.
- [41] A. Michota, A. Kudelski, J. Bukowska, *Surf. Sci.* 502–503 (2002) 214.
- [42] J.F. Liu, L. Zhang, N. Gu, Q. Hong, J. Ren, Y. Wu, P. Mao, P.D. Chen, *Supramolec. Sci.* 5 (1998) 705.
- [43] C.Y. Yang, P. Smith, A.J. Heeger, Y. Cao, J.E. Osterholm, *Polymer* 35 (1994) 1142.
- [44] I.H. Campbell, S. Rubin, T.A. Zawodzinski, J.D. Kress, R.L. Martin, *Phys. Rev. B* 54 (1996) R14321.



Photovoltaic properties of NiPc/p-Si (organic/inorganic) heterojunctions

M.M. El-Nahass, K.F. Abd-El-Rahman^{*}, A.A.M. Farag, A.A.A. Darwish

Department of Physics, Faculty of Education, Ain Shams University, Heliopolis, Cairo 11757, Egypt

Received 15 April 2003; received in revised form 3 April 2004; accepted 10 March 2005
Available online 19 April 2005

Abstract

Current–voltage (I – V) and capacitance–voltage (C – V) characteristics of NiPc thin films deposited on p-Si as heterojunction have been investigated. For I – V measurements, the conventional rectifying properties were shown with rectification ratio of 1750. At low voltages, current in the forward direction was found to obey the diode equation and the conduction was controlled by thermionic emission mechanism. For relatively higher voltages, conduction was dominated by a space-charge-limited conduction mechanism with single trap level of 0.36 eV. On the other hand, the carrier generation-recombination process limits the reverse current. Also, various electrical parameters were determined from the I – V and C – V analysis. The junction exhibits photovoltaic characteristics with open-circuit voltage (V_{oc}) of 0.32 V, a short-circuit current (I_{sc}) of 186 μ A and a power conversion efficiency (η) of 1.11%. These parameters have been estimated at room temperature and under illumination of 6 mWcm^{-2} white light.

© 2005 Elsevier B.V. All rights reserved.

PACS: 73.61.Ph; 84.37.+q; 73.40.Lg

Keywords: Phthalocyanines; Thin films; Photovoltaic; Organic/inorganic heterojunctions

1. Introduction

Organic semiconductors are promising candidates for future technological devices due to their function and variety. Phthalocyanines are proto-

type organic semiconductors and are characterised by high thermal and chemical stability. They form a large group of organic compounds, which have been the main basis for the search of molecular semiconductors for more than 40 years. Therefore, numerous searches have been done for phthalocyanines mainly in thin films form. Despite that they have been studied since 1930 [1], the interest in their properties is still attractive because of their

^{*} Corresponding author.

E-mail address: elrahman99@hotmail.com (K.F. Abd-El-Rahman).

potential applications as semiconducting devices such as: photovoltaic cells [2], laser printers [3], dyes, pigments, photocopying agents [4], gas sensors [5,6], optical data storage systems [7], solar cells [8], light emitting diodes [9] and also in nuclear reactor systems [10].

Despite that most of the organic photovoltaic cells have been fabricated with low efficiencies ($\sim 1\%$) [11–14], a significant jump in the conversion yield of organic photovoltaic (PV) solar cells, passing from 1% [15] yield to about 5% [16].

Nickel phthalocyanine (NiPc) is a p-type material [17]. Therefore, previous work on NiPc thin films has reported a relatively high mobility value ($\sim 10^{-5} \text{ m}^2 \text{ V}^{-1} \text{ s}^{-1}$) [18], when compared with mobility values reported for several other phthalocyanine compounds ($7.6 \times 10^{-9} \text{ m}^2 \text{ V}^{-1} \text{ s}^{-1}$ for ZnPc [19], $3 \times 10^{-7} \text{ m}^2 \text{ V}^{-1} \text{ s}^{-1}$ for CoPc [20] and $10^{-8} \text{ m}^2 \text{ V}^{-1} \text{ s}^{-1}$ for CuPc [21]). This particular feature makes NiPc a potential candidate for the development of future electronic devices.

In the present work, Au/NiPc/Si/Al as p–p⁺ heterojunctions were fabricated by deposition of NiPc thin films using the thermal evaporation technique onto p-Si single crystals. The temperature dependence of the current–voltage (I – V) characteristics in both forward and reverse bias was studied in an attempt to obtain information about the transport mechanisms of the device. In addition, capacitance–voltage (C – V) measurements were applied for the characterisation of these heterojunction solar cells. Also photovoltaic properties have been investigated by illuminated I – V characteristics.

2. Experimental details

The NiPc powder used in this study is obtained from Kodak, UK. The p-type Si (100) single crystal wafers with carrier concentration of 10^{22} m^{-3} is obtained from Nippon Mining Co. Pieces of 1 cm^2 each and $450 \mu\text{m}$ thick were cleaned and etched by using the CP4 solution ($\text{HF}:\text{HNO}_3:\text{CH}_3\text{COOH}$ in ratio 1:6:1). After etching, the Si wafers were washed with distilled water and then with ethyl alcohol. The Si wafers after being etched and cleaned were coated from the front side by NiPc thin films with different thicknesses using the con-

ventional thermal evaporation technique, and then the NiPc layer was overcoated by an Au mesh to be used as ohmic electrode. The back side of Si was coated by a thick layer of aluminium electrode. It was found that the annealing of the fabricated junction at 373 K for 2 h is needed to enhance the performance of the junction. This annealing might remove any channels, which could be raised during the fabrication. It was found also that the thinner layer of NiPc is most efficient one. Therefore it is used for the data displaying.

Measurements of dark current–voltage characteristics within the temperature range 298–373 K were made in air. The current flowing through the cell was determined using a stabilized power supply and a Keithley 617 electrometer. The temperature was measured directly by mean of Pt–PtRh thermocouple with monitor (Philips thermostat PT 2282 A). A proportional temperature controller (Eurotherm model no. 390-200) was used to avoid the sudden drop in the heater temperature. The cells were exposed to light coming from a light source (white light) to get an intensity of incident power of about 6 mW/cm^2 . The dark C – V characteristics were measured at 1 MHz using Model 410 CV Meter.

3. Results and discussion

3.1. Dark current–voltage characteristics

To study the junction properties, current–voltage characteristics (I – V) have been made. These measurements, usually, provide a valuable source of information about the junction properties such as the rectification ratio (RR), the diode quality factor (n), the reverse saturation current (I_0), the series (R_s) and the shunt (R_{sh}) resistances. Analysis of the I – V characteristics is also extremely useful to identify the transport mechanisms controlling the conduction.

The current–voltage characteristics of NiPc films with thickness 55 nm deposited onto p-Si at different temperatures ranging from 298 to 373 K are illustrated in Fig. 1. The curves exhibited a diode-like behaviour, with the forward direction to the positive potential on Si. This behaviour

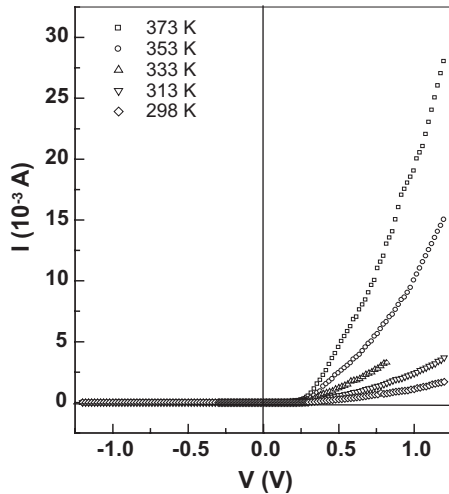


Fig. 1. Current–voltage characteristics of NiPc/p-Si heterojunction at different temperatures in both forward and reverse bias.

can be understood by the formation of p–p⁺ heterojunction, in which the barrier at the interface limits the forward and reverse carrier's flow across the junction, where the built-in potential could be developed.

Fig. 2 shows a semilogarithmic plot of the forward and reverse currents versus the applied voltage. It shows an exponential increase in the

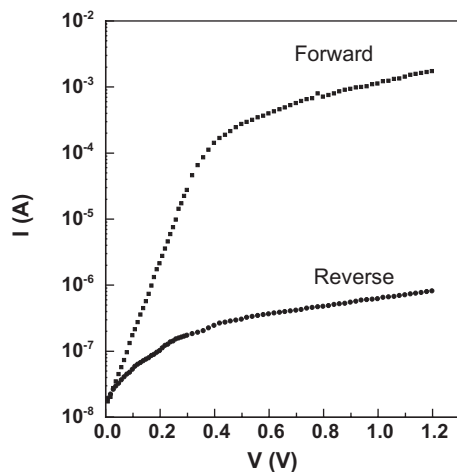


Fig. 2. Semilogarithmic plots of the forward and reverse bias at room temperature.

forward current with applied voltage for the junction at low voltage range. This exponential dependence at lower voltage range can be attributed to the formation of depletion region between Si and NiPc thin film. From Fig. 2, the junction parameters can be easily determined. The rectification ratio, RR, is calculated as the ratio of the forward current to the reverse current at a certain applied voltage, i.e. $RR = (I_F/I_R)_{V=\text{const}}$.

For nonideal diode, the experimentally measured characteristics often present a more complex behaviour than the ideal diode due to the presence of various conduction mechanisms. A summation of two (or sometimes more) exponential expressions is frequently used to model the various conduction mechanisms [22]:

$$I = I_{01} \left[\exp \frac{q(V - IR_s)}{n_1 k_B T} - 1 \right] + I_{02} \left[\exp \frac{q(V - IR_s)}{n_2 k_B T} - 1 \right] + \frac{V - IR_s}{R_{sh}} \quad (1)$$

where I_0 is the reverse saturation current, n is the diode quality factor, R_s is the series resistance and R_{sh} is the shunt resistance. The equation also includes the effects of parasitic series and parallel resistance, which can obscure the intrinsic parameters of the device. The series resistance, R_s , and the shunt resistance, R_{sh} , are determined from the plot of the diode junction resistance, R_J , against voltage [23], where $R_J = \partial V / \partial I$, which can be determined from the current–voltage curves. A plot of R_J against V is shown in Fig. 3 for NiPc/p-Si heterojunction. As observed at sufficiently high forward bias the junction resistance approaches a constant value, this value is the series resistance, R_s . On the other hand, the junction resistance is also constant at sufficiently high reverse bias, which is equal to the diode shunt resistance, R_{sh} . However, junction series and shunt resistances are important factors in improving cell performance and design. The obtained values of the rectification ratio (RR), the series resistance (R_s) and the shunt resistance (R_{sh}) are determined as 1750, 750 Ω and 1.7 M Ω , respectively.

The information about the conduction mechanism can be obtained from current–voltage characteristics at different temperatures. The

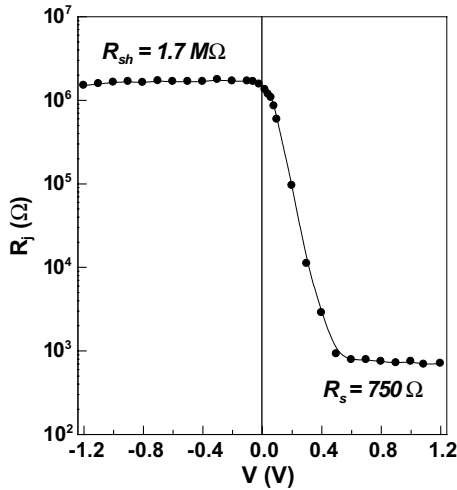


Fig. 3. Junction resistance, R_J , versus V for NiPc/p-Si heterojunction.

semilogarithmic plots of the forward current–voltage characteristics of NiPc/p-Si heterojunction at different temperatures ranging from 298 to 373 K are shown in Fig. 4. Two distinct regions characterise these curves indicating different conduction mechanisms. As it is observed in Fig. 4, within the narrow low forward voltage ($V \leq 0.30$ V), the current increases exponentially. Thus, the voltage

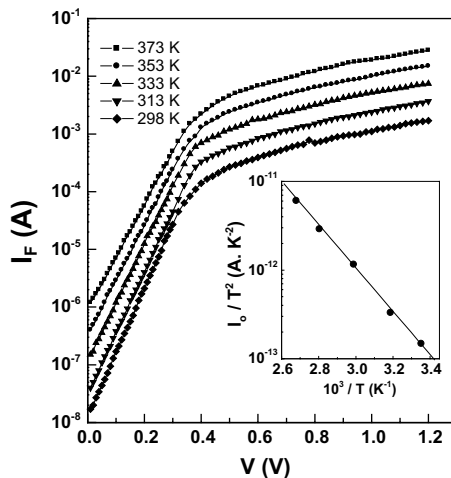


Fig. 4. Semilogarithmic plots of the forward bias of I – V characteristics at different temperature and semilogarithmic plot of $\ln(I_0/T^2)$ versus $10^3/T$ for NiPc/p-Si heterojunction.

dependence of the junction current can be expressed in the simplified form as

$$I = I_0 \exp\left(\frac{eV}{nk_B T}\right) \quad (2)$$

where I_0 is the saturation current which can be obtained by extrapolation of the linear $\ln(I)$ – V portion to the $\ln(I)$ axis at zero voltage and n is the diode quality factor. The parameters I_0 and n can be readily determined from the curve (room temperature measurement) shown in Fig. 4 together with Eq. (2). The values of I_0 and n are calculated as 1.2×10^{-8} A and 1.51 ± 0.05 , respectively. Deviation of n from unity may be attributed to either recombination of electrons and holes in the depletion region, and/or the increase of the diffusion current due to increasing the applied voltage [24]. The diode quality factor is almost found to be constant at different temperatures. This behaviour is in accordance with the thermionic emission mechanism.

To confirm that the thermionic emission is the operating conduction mechanism, more analysis was carried out. According to the thermionic conduction, the saturation current is given by [25]

$$I_{01} \propto T^2 \exp\left(-\frac{e\phi_b}{k_B T}\right) \quad (3)$$

where ϕ_b is the barrier height. Obtaining a straight line from the plot of the logarithm of I_0/T^2 against $1/T$ supports the thermionic mechanism. The inset of Fig. 4 represents this plot, which clearly shows a linear behaviour. From the slope of this straight line the potential barrier height, ϕ_b , is determined as 0.48 eV.

At relatively high forward voltages ($0.5 \leq V \leq 1.2$ V), a different mechanism is operating. As observed in Fig. 5, the current shows a power-law exponent of the form $I \sim V^m$. The slope of the $\log(I)$ – $\log(V)$ characteristics, is about 2, clarifying that the forward biased current is space-charge-limited current (SCLC) controlled by a single dominating trap level. Separate SCLC measurements, supporting this result, were also done for the samples in form of Au/NiPc/Au and it is under processing with other transport measurements. The current in this case is expressed as [26]

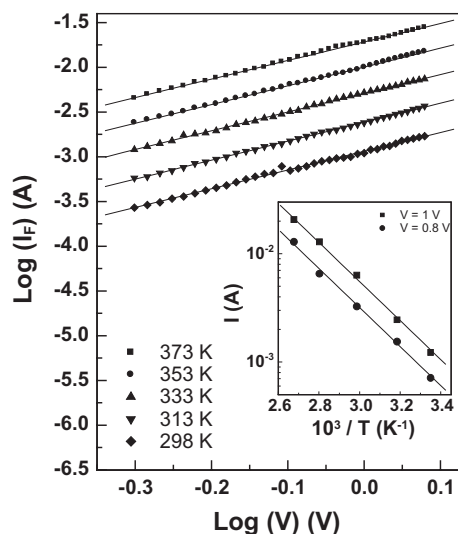


Fig. 5. Variation of $\log I$ with $\log V$ at higher forward voltage bias for NiPc/p-Si heterojunction and variation of $\log I$ with $1000/T$ in SCLC for NiPc/p-Si heterojunction.

$$I = (9/8)\epsilon\mu A \frac{V^2}{d^3} (N_v/N_t) \exp\left(\frac{-E_t}{k_B T}\right) \quad (4)$$

where ϵ is the permittivity of NiPc film taken as $2.425 \times 10^{-11} \text{ Fm}^{-1}$ [27,28], μ is the holes mobility ($10^{-5} \text{ m}^2 \text{ V}^{-1} \text{ s}^{-1}$) [18], N_v is the effective density of states which equals to 10^{27} m^{-3} [29] and N_t is the concentration of traps at energy level E_t , above the valence band edge calculated as $1.15 \times 10^{11} \text{ m}^{-3}$ and 0.36 eV, respectively, by plotting I against $1/T$ as shown in the inset of Fig. 5.

On the other hand, the reverse current–voltage characteristics of NiPc/p-Si heterojunction at different temperatures ranging from 298 to 373 K are shown in Fig. 6. As usual for reverse direction of a rectifier, the current does not nearly depend on voltage. At relatively high voltage, the dependence of the current on voltage is stronger than predicted by pure thermionic emission or Schottky effect, that leads to the assumption that nearly flat reverse I – V characteristics could be fit over a wide range of voltages assuming that generation and recombination of carriers in the Si substrate is the dominant source of the reverse current [4]. The reverse current due to carrier recombination is thermally activated according to the form [7]

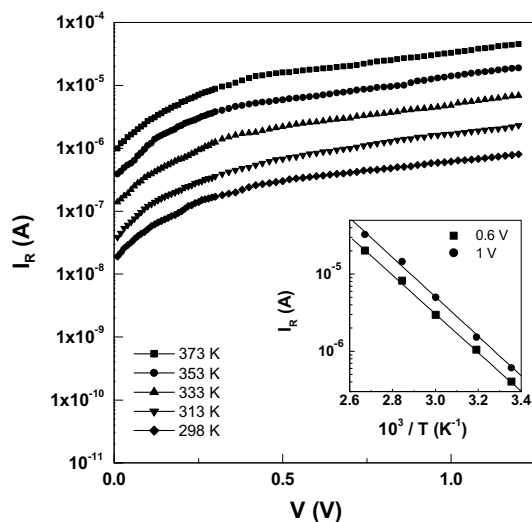


Fig. 6. A Semilogarithmic plots of the reverse bias of I – V characteristics at different temperature and semilogarithmic plots of I_R versus $1000/T$ for NiPc/p-Si heterojunction at different voltage.

$$I_R \propto \exp(-\Delta E/k_B T) \quad (5)$$

where ΔE is the minority carrier activation energy. The semilogarithmic plot of the reverse current versus $1/T$ is shown in the inset of Fig. 6. The activation energy was determined from the slope of the straight line to have a value of 0.51 eV. The obtained activation energy is approximately equal to half the band gap of Si. This suggests that the main source of the reverse current is the Si substrate and indicates that the reverse current should be limited by the carrier generation-recombination process.

3.2. Dark capacitance–voltage characteristics

Fig. 7(a) shows the C^{-2} – V characteristic of NiPc/p-Si heterojunction at room temperature, which is reasonably interpreted by assuming an abrupt heterojunction. This characteristic can be discussed in terms of the junction type analysis [30] in which the quasi-Fermi level for electrons is separated from that for holes in the depletion region when a voltage is applied across the junction, i.e. a net current flows across the NiPc/p-Si heterojunction.

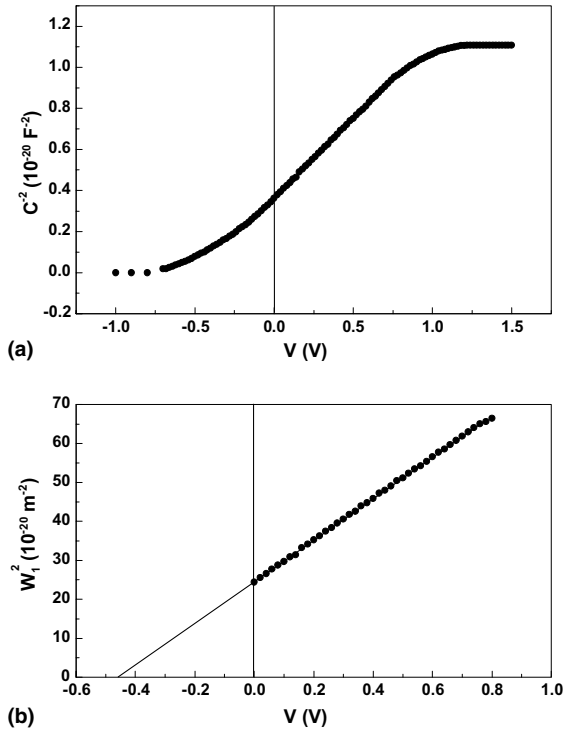


Fig. 7. (a) C^{-2} - V characteristics for NiPc/p-Si heterojunction. (b) Width of the depletion region in p-Si as a function of voltage.

The capacitance was measured using a small a.c. voltage of 1 MHz. The resistivity, ρ_1 , of p-Si used in this study was found to be lower than $0.1 \Omega\text{m}$, so that the dielectric relaxation time ($\rho_1\epsilon_1$, where ϵ_1 is the permittivity of Si) became 10^{-12}s , which indicated that the redistribution of holes (majority carriers of p-Si) can respond to the 1 MHz a.c. voltage. On the other hand, the minimum value of resistivity, ρ_2 , for the p-NiPc films was $10^{10} \Omega\text{m}$. Therefore, the dielectric relaxation time became 10^{-2}s , which suggested that the redistribution of holes (majority carriers of NiPc) can not respond to an a.c. voltage higher than 100 Hz. Thus, the films may be considered as a dielectric material in its behaviour in the case of the 1 MHz a.c. voltage. This indicated that the capacitance of NiPc film equals to its geometric capacitance due to its longer dielectric relaxation time. Since the capacitance of NiPc films measured at 1 MHz showed a constant value of 129.1 pF,

independent of the applied voltage as shown in Fig. 7(a), one can obtain information on the depletion layer extending in the p-Si side regardless that of NiPc side. Therefore, the total capacitance, C , of the junction can be expressed by the relation [31,32]:

$$\frac{1}{C} = \frac{1}{C_1} + \frac{1}{C_2} = \frac{1}{\epsilon_0 A} \left(\frac{W_1}{\epsilon_1} + \frac{d}{\epsilon_2} \right) \quad (6)$$

where C_1 , W_1 and ϵ_1 are, respectively, the capacitance, the width of the depletion region in the p-Si side and the dielectric constant of p-Si, which has a value of 11.9. A is the effective area of the junction, and d , ϵ_2 , and C_2 are, respectively, the thickness, the dielectric constant, 3.35 [28], and the capacitance of the NiPc films which is given by:

$$C_2 = \epsilon_0 \epsilon_2 \frac{A}{d} \quad (7)$$

According to the abrupt heterojunction model [30], the following two relations are easily derived:

$$\frac{V_{D1} - V_1}{V_{D2} - V_2} = \frac{N_2 \epsilon_2}{N_1 \epsilon_1} \quad (8)$$

and

$$W_1^2 = \frac{2\epsilon_0 \epsilon_1}{eN_1} (V_{D1} - V_1) \quad (9)$$

where V_1 and V_2 are the d.c. bias voltages being supported in the depletion region in p-Si and NiPc, respectively, N_2 is the effective density of localized gap states in NiPc, N_1 is the donor concentration in the p-Si, $\sim 10^{22} \text{m}^{-3}$. Eq. (8) can be rewritten in the following form:

$$\frac{V_{D1} - V_1}{V_D - V} = \frac{N_2 \epsilon_2}{N_1 \epsilon_1 + N_2 \epsilon_2} \quad (10)$$

where $V = V_1 + V_2$ is the total applied voltage through the heterojunction and $V_D = V_{D1} + V_{D2}$ is the total built-in voltage.

From Eqs. (6), (7) and (10), the following relations can be easily derived as:

$$W_1^2 = \left[\epsilon_0 \epsilon_1 A \left(\frac{1}{C} - \frac{1}{C_2} \right) \right]^2 \quad (11)$$

$$W_1^2 = \frac{2\epsilon_0 \epsilon_1 \epsilon_2 N_2}{eN_1 (N_1 \epsilon_1 + N_2 \epsilon_2)} (V_D - V) \quad (12)$$

The saturated capacitance value, C_2 , of 129.1 pF with the forward bias has been used to calculate W_1 in Eq. (11). The calculated values of W_1^2 are plotted versus V as shown in Fig. 7(b). This plot reveals a good linear relationship indicating that the abrupt heterojunction model is applicable to the NiPc/p-Si structure.

It is clear from Eq. (12) that both N_2 and V_D can be determined graphically from the slope of the curve shown in Fig. 7(b) and the intercept on the horizontal axis respectively; their values were found to be $1.03 \times 10^{16} \text{ m}^{-3}$ and 0.46 eV, respectively.

3.3. Photovoltaic properties

The current–voltage characteristics of a NiPc/p-Si heterojunction solar cell in the dark and under white light illumination of 6 mWcm^{-2} and active area of 0.25 cm^2 are shown in Fig. 8. It can be seen from this figure that the current value at a given voltage for NiPc/p-Si cell under illumination is higher than that in the dark. This indicates that the light generates carrier-contributing photocurrent due to the production of electron–hole pairs as a result of the light absorption. It is well known that the absorption region of all phthalocyanines

corresponds to the UV–VIS region [32]. Solar cells based on monocrystalline silicon convert up to 24% of solar energy to electrical energy [33]. So, it has been suggested that the light is absorbed at both NiPc and Si. The generation of photoelectrons, via both NiPc and Si exciton intermediate, followed by electron transfer from p-Si into NiPc through the potential barrier at the interface. This is a result of a difference in electron affinities between the two semiconductors. It is note worthy that the photocurrent in the reverse direction is strongly enhanced by photo-illumination. This behaviour yields useful information on the electron–hole pairs, which were effectively generated in the junction by incident photons. Under the influence of the electric field at the junction, electrons were accelerated towards the NiPc, while the generated holes were swept towards the Si along the potential barrier at the interface.

Different junctions were fabricated with different thicknesses of NiPc layers. In agreement with a previous work [34], the most effective junction was with the thinner layer. This can be explained as the increasing of the thickness, increases the series resistance of the junction. It can be also explained by considering that the thinner layer allows higher intensity of light to reach the Si substrate.

It can be seen from Fig. 8 that the NiPc/Si junction shows a photovoltaic characteristic with short circuit current (I_{sc}) of $186 \mu\text{A}$, open circuit voltage (V_{oc}) of 0.32 V, fill factor (FF) of 0.28 and power conversion efficiency (η) of 1.11%. The value of the fill factor is lower in comparison to those of solar cells based on inorganic materials. The main cause of this effect is generally found to be the field dependent nature of the charge photogeneration process or high series resistance of the organic layer. However, the obtained value of η is in the order of the values, previously, reported for phthalocyanines heterojunction cells having Si as substrates [34].

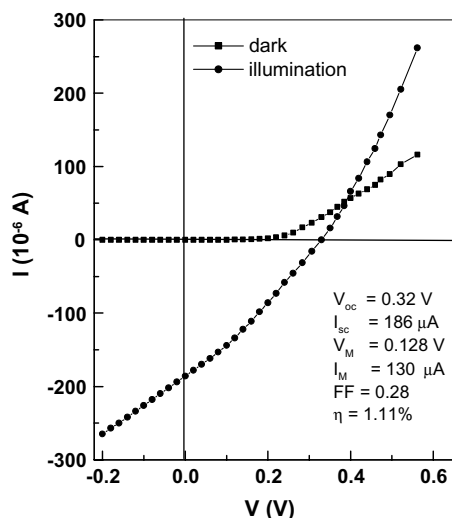


Fig. 8. Current–voltage characteristics under illumination for NiPc/p-Si heterojunction.

4. Conclusions

The organic/inorganic heterojunctions were studied. The NiPc films were deposited onto p-Si

$\langle 100 \rangle$ substrates by evaporation technique. The current–voltage (I – V) and capacitance–voltage (C – V) measurements have been performed to determine the electrical properties of the junctions. The junctions exhibit rectifying characteristics showing p–p⁺ diode-like behaviour. Measurements of the forward current versus voltage, and the saturation current versus inverse temperature suggest the existence of a potential barrier ϕ_b at NiPc/Si interface, which has a value of 0.48 eV. The rectification ratio of the junction was also calculated at ± 1 V, yielding a value of 1750. The dark current–voltage measurements suggest that the forward current in these junctions involves thermionic emission mechanism, while at high-applied voltage a space-charge-limited current mechanism was operated with single trap, which has a value of 0.35 eV. On the other hand, the reverse current may be reasonably ascribed to a generated-recombination current. From the capacitance–voltage measurements at high frequency of 1 MHz, one can obtain information on the depletion layer extending in the Si side regardless of that in the NiPc side. To study the photovoltaic conversion properties at interface, current–voltage characteristics in the transverse direction have been measured under illumination of 6 mWcm^{-2} . These measurements revealed the occurrence of electron transfer at the interface supporting a spatial separation of the electrons and holes in this optoelectronic system.

References

- [1] R.P. Listead, J. Chem. Soc. part I (1934) 1016.
- [2] D. Wohrle, D. Meissner, Adv. Mater. 3 (1991) 129.
- [3] P. Gregory, High-technology Applications of Organic Colorants, Plenum Press, New York, 1991, 759.
- [4] P. Haisch, G. Winter, M. Hanack, L. Lürer, H.J. Egelhaaf, D. Oelkrug, Adv. Mater. 9 (1997) 316.
- [5] J.W. Gardner, M.Z. Iskandari, B. Bott, Sensors Actuators B9 (1992) 133.
- [6] A. Mrwa, M. Friedrich, A. Hofman, Sensors Actuators B24–25 (1995) 596.
- [7] R. Ao, L. Kilmert, D. Haarer, Adv. Mater. 7 (1995) 495.
- [8] H.R. Kerp, E.E. van Faassen, Chem. Phys. Lett. 5 (2000) 332.
- [9] S.T. Lee, Y.M. Wang, X.Y. Hou, C.W. Tang, Appl. Phys. Lett. 74 (1999) 670.
- [10] P. Cerny, Chem. Zvesti 9 (1955) 94.
- [11] P.J. Reucroft, H. Ullai, Solar Energy Mater. 2 (1980) 217.
- [12] A.K. Ghosh, D.L. Morel, T. Feug, R.F. Shaw, C.A. Rowe, J. Appl. Phys. 45 (1974) 230.
- [13] M. Khelifi, M. Mejatty, J. Berrehar, H. Bouchrriha, Rev. Phys. Appl. 20 (1985) 511.
- [14] A.K. Mahapatro, S. Ghosh, IEEE Trans. Electron Dev. 48 (9) (2001) 1911.
- [15] C.W. Tang, Appl. Phys. Lett. 48 (1986) 183.
- [16] J.H. Schön, Ch. Kloc, B. Batlogg, Appl. Phys. Lett. 77 (2000) 2473.
- [17] T.G. Abdel-Malik, A.A. Aly, A.M. Abdeen, H.M. El-Labany, Phys. Status Solidi (a) 76 (1983) 651.
- [18] T.G. Abdel-Malik, R.M. Abdel-Latif, A.E. El-Samahy, S.M. Khalil, Thin Solid Films 256 (1995) 139.
- [19] G.D. Sharma, S.G. Sangodkar, M.S. Roy, Mater. Sci. Eng. B41 (1996) 222.
- [20] S. Gravano, A.K. Hassan, R.D. Gould, Int. J. Electron. 70 (1991) 477.
- [21] R.D. Gould, J. Phys. D: Appl. Phys. 9 (1986) 1785.
- [22] J.C. Ranuárez, F.J. Garcia Sánchez, A. Ortiz-conde, Solid-State Electron. 43 (1999) 2129.
- [23] A.S. Darwish, A.S. Riad, H.S. Soliman, Semicond. Sci. Technol. 10 (1995) 1.
- [24] E.H. Rhoderick, Metal Semiconductor Contacts, Oxford University Press, Oxford, 1978.
- [25] M.S. Sze, Physics of Semiconductor Devices, second ed., Wiley, New York, 1981.
- [26] M.A. Lampert, Rep. Prog. Phys. 27 (1964) 329.
- [27] T.D. Anthopoulos, T.S. Shafai, Phys. Status Solidi (a) 569 (2000) 181.
- [28] M.M. El-Nahass, K.F. Abd-El-Rahman, A.A.M. Farag, A.A.A. Darwish, Int. J. Modern Phys. B 18/3 (2004) 421.
- [29] A. Sussuman, J. Appl. Phys. 2738 (1967) 38.
- [30] H. Matsuura, J. Appl. Phys. 64 (1988) 1964.
- [31] K. Aguir, A. Fennouh, H. Carchano, J. Lseguin, B. Elhadadi, F. Lalonde, Thin Solid Films 257 (1995) 98.
- [32] A.T. Davidson, J. Chem. Phys. 77 (1982) 168.
- [33] M. Green, K. Emery, K. Bueher, D.I. King, S. Igari, Prog. Photovoltaic: Res. Appl. 5 (1997) 51.
- [34] A.S. Riad, Thin Solid Films 370 (2000) 253.



Trap states as an explanation for the Meyer–Neldel rule in semiconductors

P. Stallinga^{*}, H.L. Gomes

Universidade do Algarve, Optoelectronics, UCEH, FCT, Campus de Gambelas, Faro 8000, Portugal

Received 19 October 2004; accepted 14 March 2005
Available online 19 April 2005

Abstract

It is shown that whenever traps, distributed exponentially in energy, are governing the conduction in electrical materials, a Meyer–Neldel observation is expected. This is a direct result of the model incorporating a high density of traps by Shur and Hack. Since this type of conduction is common for low mobility materials, such as organic semiconductors or amorphous silicon, they are therefore likely to obey the Meyer–Neldel rule.

© 2005 Elsevier B.V. All rights reserved.

PACS: 72.80.Le; 73.50.–h; 72.20.Jv

Keywords: Meyer–Neldel rule; Electronic transport; Traps; Semiconductors

The Meyer–Neldel rule (MNR) [1] is observed in many processes in nature. Applied to semiconductor materials, the Meyer Neldel rule states that the prefactor of the thermally activated mobility increases exponentially with the activation energy. What this means is that (1) the activation energy of current or carrier mobility depends on the bias conditions, (2) there exists a temperature, known as the isokinetic temperature T_{MN} , where the dependence on bias disappears. In other words,

when presented in an Arrhenius plot (logarithm of the measured quantity vs. reciprocal temperature), the curves of current or mobility are straight lines that pass through or converge to a common point not coinciding with infinite temperature. The MNR is frequently observed in low-conductivity disordered materials. As examples: porous and amorphous silicon [2,3], microcrystalline silicon films [4], ionic conductivity [5], glassy materials [6] and organic materials [7]. The common factor to all these materials is the existence of a large density of localized states with high activation energy (traps). In this article we discuss the link between trap states and the Meyer–Neldel rule

^{*} Corresponding author. Tel.: +351 969541198; fax: +351 289800030.

E-mail address: pjotr@ualg.pt (P. Stallinga).

using a model of Shur and Hack [8]. As an example we show results of thin-film field-effect-transistors of α -sexithiophene (α -T6), although the idea is equally well applicable to other low mobility materials.

In the standard model for field effect transistors, the current in the linear region ($V_{ds} \ll V_g - V_t$) is of the form

$$I_{ds} = \frac{W}{L} \mu C_{ox} V_{ds} (V_g - V_t). \quad (1)$$

Here W and L are the source and drain electrode length and distance respectively, μ is the carrier mobility, C_{ox} is the insulator capacitance density and V_{ds} and V_g the drain–source voltage and gate–source voltage respectively. V_t is the voltage needed at the gate to open the channel. The above equation allows for a definition of the as-measured mobility via the derivative of a transfer curve (I_{ds} vs. V_g):

$$\mu = \frac{L}{WC_{ox}V_{ds}} \frac{\partial I_{ds}}{\partial V_g}. \quad (2)$$

Actually, this is the de facto standard used for determining the carrier mobility in field effect transistors and is also sometimes called the field effect mobility, μ_{FET} , to distinguish it from mobilities measured by other techniques such as time-of-flight or Hall effect. For various reasons, this mobility can still depend on the bias conditions and the temperature.

In the multi-trap-and-release model, the charges spend most of their time on localized trap states, where the mobility is zero. To contribute to conduction, a charge first has to be (thermally) excited to a delocalized band where the mobility is high. The field-effect mobility now, by the way it is measured, is a weighed average of the trap states and the conduction bands and is not the intrinsic mobility of free carriers. Since the thermal equilibrium of the distribution over the levels depends on the temperature, the as-measured mobility depends on the temperature. Parameters in this are the band state density and the trap state density and depth. Poole and Frenkel [9] have shown that the effective trap depth can be lowered by the application of an in-plane field. This makes the as-measured mobility also field (drain–source

voltage) dependent. Many authors have shown that non-crystalline low-conductivity materials such as most organic materials or amorphous silicon are well described by this Poole–Frenkel conduction model [10], thereby showing that traps is the limiting factor in the conductivity. In a recent publication we have shown this to be true for α -sexithiophene [11].

As shown by Shur and Hack, a high density of trap states also causes the mobility to depend on the gate voltage [8,12]. Because the ratio of free-to-trapped charges increases with the gate voltage, the transfer curves are supra-linear [8,11]. They present a model with a density of traps that is exponentially decreasing with depth. Their model dictates that the drain–source current is of the form [8, Eq. 53]

$$I_{ds} = \frac{q\mu_0 W}{L} f(T, T_2) [C_{ox}(|V_g - V_t|)]^{(2T_2/T-1)} V_{ds} \quad (3)$$

with

$$f(T, T_2) = N_V \exp\left(\frac{-E_{F0}}{kT}\right) \frac{kT\epsilon}{q} \left(\frac{\sin(\pi T/T_2)}{2\pi\epsilon T_2 k T g_{F0}}\right)^{T_2/T}. \quad (4)$$

Here T_2 is a parameter describing the slope of the distribution of deep trap states in a logarithmic energy diagram: $d \ln(N_T)/dE = 1/kT_2$. N_V is the effective density of band states which is considered independent of temperature (assuming a more accurate slowly-varying function, such as $N_V \propto T^{3/2}$ [9], does not change the analysis). g_{F0} is the density of deep localized states at the Fermi level E_{F0} , which can be as large as N_V . μ_0 is the band mobility, ϵ the semiconductor permittivity, q the elementary charge and k the Boltzmann constant. Note that a factor q has been removed from the last term of the original form of Eq. (4) in order to make the units correct.

Eq. (3) directly predicts the second part of the Meyer–Neldel observation, namely a temperature where the current does not depend on the gate voltage:

$$T_{MN} = 2T_2. \quad (5)$$

In other words, the Meyer–Neldel temperature is a direct measure of the distribution of deep

trap states and this temperature can rapidly be determined by taking temperature-scanned-current curves at different biases.

For temperatures well below T_2 , the approximation $\sin(\pi T/T_2) \approx \pi T/T_2$ can be made and, together with the relation $a^x = \exp(x \ln(a))$ it is easily shown that the Arrhenius plots of current are linear and the effective activation energy depends on the gate bias (demonstrating the first part of the Meyer–Neldel rule):

$$E_A = E_{F0}$$

$$-kT_2 \left[\ln \left(\frac{1}{2\epsilon(kT_2)^2 g_{F0}} \right) - 2 \ln(C_{\text{ox}}(|V_g - V_t|)) \right]. \quad (6)$$

This activation energy can thus substantially deviate from the depth of the traps at the Fermi level, E_{F0} . Moreover, because of the linearity of the Arrhenius plots, one can easily make the mistake of assuming a single discrete trap level to be responsible for the activation of the current.

Eq. (6) also shows that the activation energy depends on the bias condition V_g . Fig. 1 shows a simulation of a temperature-dependent-current (I – T) experiment of a system with deep traps with the parameters as of Table 1. In the inset, the as-measured

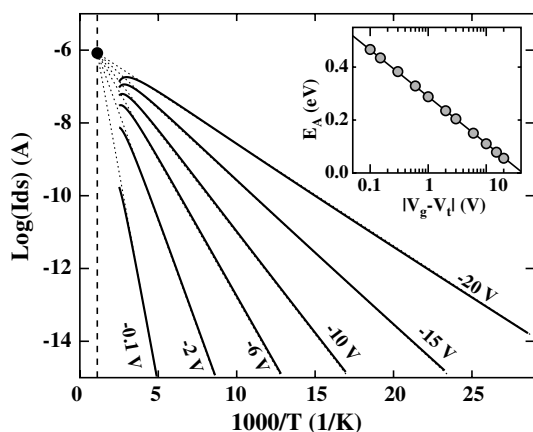


Fig. 1. Simulation of temperature-dependent currents (IT) based on parameters of Table 1, with gate biases from 0.1 V to 20 V as indicated. The solid dot (●) represents the Meyer–Neldel point (T_{MN}, I_{MN}). The inset shows the effective activation energy as a function of bias.

Table 1
Simulation parameters used to generate Fig. 1

Parameters	Value	Unit
N_V	10^{19}	cm^{-3}
C_{ox}	1.92×10^{-4}	F/m^2
E_{F0}	484	meV
V_{ds}	−0.1	V
g_{F0}	10^{16}	$\text{cm}^{-3} \text{eV}^{-1}$
T_2	450	K
W	1	cm
L	30	μm
μ_0	3	$\text{cm}^2 \text{V}^{-1} \text{s}^{-1}$
ϵ	$5\epsilon_0$	

sured activation energy is shown as a function of bias, $|V_g - V_t|$. This is indeed very similar to the Meyer–Neldel observation seen in a wide variety of materials. (Note: Since the parameters are interdependent, the same results can be obtained for other combinations of E_{F0} and g_{F0} .)

Applying Eq. (2) for the as-measured mobility to Eqs. (3) and (4) we find that the observed mobility has a similar behavior but becomes gate-voltage independent at a Meyer–Neldel temperature of $T_{MN} = T_2$. Moreover, the as-measured mobility is much smaller than the band conduction mobility μ_0 . As an example, for the parameters of Table 1 and $|V_g - V_t| = 6$ V and $T = 300$ K, the measured mobility is $8.0 \times 10^{-3} \text{ cm}^2/\text{Vs}$ —three orders of magnitude below the band mobility μ_0 .

For a specific α -sexithiophene p-channel FET, with geometric parameters W , L and C_{ox} as given in Table 1, I – T scans were made for various bias conditions [11]. An example of an I – T curve for $V_g = -10.5$ V and $V_{\text{ds}} = -0.5$ V, together with a simulation on basis of Eq. (3) is shown in Fig. 2. A summary of the measured activation energies of current as a function of gate bias is given in Fig. 3. Unfortunately, in these experiments, the scanning had to be limited to below 210 K to avoid the phenomenon known as stress [14], substantial shifts of the threshold voltage V_t with time and upon changes of bias. This is especially pertinent because the effect of bias on the measured activation energy is expected to be largest for V_g close to V_t , as predicted by Eq. (6). Thus, small changes of V_t influence the results dramatically. Recently, Gomes et al. [13] have shown that α -sexithiophene also suffers from this phenomenon for higher

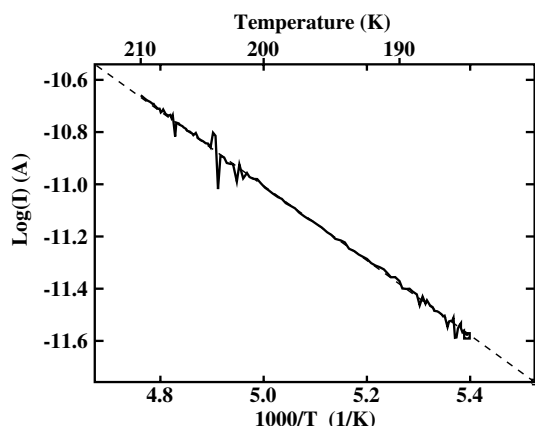


Fig. 2. Arrhenius plot of the current of an FET based on sexithiophene with bias $V_{ds} = -0.5$ V and $V_g = -10.5$ V. The dashed line shows a simulation with $E_{F0} = 535$ meV, $N_V = 1.7 \times 10^{19}/\text{cm}^3$, $V_g - V_t = -2$ V and other parameters as of Table 1. The slope of the curve yields an effective activation energy of 296 meV.

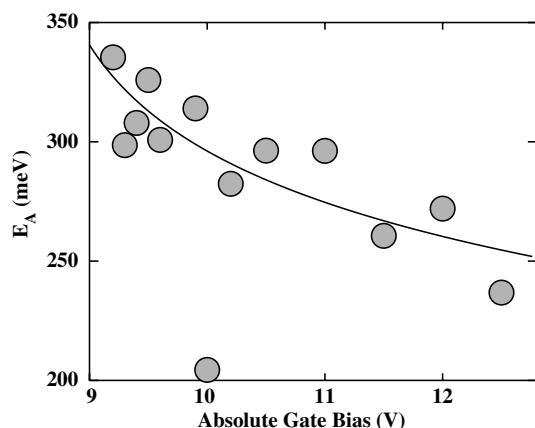


Fig. 3. Measured activation energy as a function of bias of an FET based on sexithiophene. The solid line is a fit to the data yielding $T_2 = 250 \pm 200$ K and $V_t = -8.5 \pm 1.4$ V. To avoid systematic error, the measurements were carried out in random order. Each point represents a curve such as shown in Fig. 2.

temperatures and we expected to obtain distorted results when stressing becomes important above 210 K. Even in the low temperature range chosen for the experiment, we cannot exclude small changes of V_t . However, it is clear from Fig. 3 that the activation decreases with V_g as predicted by the above theory. Moreover, to avoid systematic

errors in the measurement caused by stress, the experiments were carried out in random order.

In another experiment [11], measuring the mobility of the carriers as a function of temperature, Meyer–Neldel temperatures ($T_{MN} = T_2$) were found to vary from sample to sample and different T_2 's were sometimes found in the high and low temperature range, sometimes with an abrupt change at around 200 K [11]. Using the above theory this implies a change in the energetic distribution of deep trap states.

One final thing to note is that Eqs. (3) and (4) also predict a current that is dropping for temperatures approaching T_2 (see Fig. 1). For temperatures beyond T_2 (up to $2T_2$), the equations do not yield a real value for the current. Interesting in this respect is the lack of presented results in literature for measurements at the isokinetic temperature. In all cases the Meyer–Neldel point is found by extrapolation of the curves.

In a conclusion, we showed that the observation of the MNR is a direct result of traps. Therefore, the MNR is a sign of conduction governed by trap states and the isokinetic temperature T_{MN} , the temperature where the current or the mobility is independent of bias, is a parameter describing the distribution of these trap states. As such, the Meyer–Neldel temperature is a reliable and easily measured parameter to determine trap states. T_{MN} can be called a figure-of-merit as suggested by Pichon et al. [15]. The theory was applied to an FET of sexithiophene which shows to conform to this model, although, due to stressing, the parameters were difficult to extract.

As a final remark, we do not exclude the possibility that other systems or factors will result in the observation of the MNR. Moreover, even for trap-rich systems there might be various explanations for the MNR observation. Shur and Hack [8], Crandall [16] and Vissenberg and Matters [17] all use models of trap-rich systems resulting in similar temperature and gate-bias dependence. We can apply the same analysis to show that these models will thus predict the MNR observation. Vissenberg et al. do not include the band states and the conduction is solely through hopping from trap state to trap state. In a recent work we have shown the model of Shur and Hack to be most adequate

for describing the α -T6 FETs [11]. In the current work we have shown how this then predicts a Meyer–Neldel rule.

We would like to acknowledge D.M. De Leeuw for valuable discussion. This work has been financed by Portuguese grant POCTI/FAT/47956/2002.

References

- [1] W. Meyer, H. Neldel, *Z. Tech.* 18 (1937) 588.
- [2] Y. Lubianiker, I. Balberg, *J. Non-Cryst. Solids* 227–230 (1998) 180.
- [3] M. Kondo, Y. Chida, A. Matsuda, *J. Non-Cryst. Solids* 198–200 (1996) 178.
- [4] S.K. Ram, S. Kumar, R. Vanderhaghen, P. Roca i Cabarrocas, *J. Non-Cryst. Solids* 299–302 (2002) 411.
- [5] K.L. Ngai, *Sol. Stat. Ionics* 105 (1998) 231.
- [6] K. Shimakawa, F. Abdel-Wahab, *Appl. Phys. Lett.* 70 (1997) 652.
- [7] E.J. Meijer, M. Matters, P.T. Herwig, D.M. de Leeuw, T.M. Klapwijk, *Appl. Phys. Lett.* 76 (2000) 3433.
- [8] M. Shur, M. Hack, *J. Appl. Phys.* 55 (1984) 3831.
- [9] S.M. Sze, *Physics of Semiconductor Devices*, second ed., Wiley Interscience, 1981.
- [10] See for example S.V. Rakhmanova, E.M. Conwell, *Appl. Phys. Lett.* 76 (2000) 3822, and other papers by the Conwell group.
- [11] P. Stallinga, H.L. Gomes, F. Biscarini, M. Murgia, D.M. De Leeuw, *J. Appl. Phys.* 96 (2004) 5277.
- [12] M. Shur, *Physics of Semiconductor Devices*, Prentice Hall, New Jersey, 1990.
- [13] H.L. Gomes, P. Stallinga, F. Dinelli, M. Murgia, F. Biscarini, D.M. De Leeuw, T. Muck, J. Geurts, L.W. Molenkamp, V. Wagner, *Appl. Phys. Lett.* 84 (2004) 3184.
- [14] M.J. Powell, *IEEE Trans. Electr. Dev.* 36 (1989) 2753.
- [15] L. Pichon, A. Mercha, J.M. Routoure, R. Carin, O. Bonnaud, T. Mohammed-Brahim, *Thin Solid Films* 427 (2003) 350.
- [16] R.S. Crandall, *Phys. Rev. B* 43 (1991) 4057.
- [17] M.C.J.M. Vissenberg, M. Matters, *Phys. Rev. B* 57 (1998) 12964.



Insulators and device geometry in polymer field effect transistors

Henrik G.O. Sandberg^{a,b,*}, Tomas G. Bäcklund^b, Ronald Österbacka^b, Maxim Shkunov^c, David Sparrowe^c, Iain McCulloch^c, Henrik Stubb^b

^a VTT Information Technology, Microelectronics, Polymer Electronics, P.O. Box 1208, FI-02044 VTT, Espoo, Finland

^b Department of Physics, Åbo Akademi University, FI-20500 Turku, Finland

^c Merck Chemicals, Chilworth Science Park, Southampton SO16 7QD, United Kingdom

Received 12 March 2004; received in revised form 1 April 2005; accepted 1 April 2005

Available online 2 May 2005

Abstract

In order to increase the stability and practicality of polymer field effect transistor (FET) devices, different manufacturing parameters are investigated, including choice of material, processing solvent, and device geometry. It is found that the performance of the devices is closely related to the choice of gate insulator material, the applied sample configuration and the order of layer deposition. Thermally cross-linked polymers are investigated as insulator materials. For a top gate configuration the key parameter is the choice of insulator material (and solvent) while for the bottom gate configuration, device performance is largely dependent on interfacial properties, which may be controlled for example by surface treatment. This study shows that care must be taken in designing and applying the gate insulator layer of a FET.

© 2005 Elsevier B.V. All rights reserved.

PACS: 73.40.Qv; 85.65.+h; 73.61.Ng; 73.61.Ph

Keywords: Organic; Field effect transistor; Insulator; Polyvinylphenol; Polyhydroxystyrene; Polyalkylthiophene

Electronic products based on polymers and other organic materials have emerged recently,

such as transistors, sensors, displays, and photovoltaic devices [1–3]. The transistor is a basic component in modern electronics and high performing organic transistors are thus the key to all-polymer electronics.

Organic transistors, however, still lag behind inorganic competitors in both peak performance and stability. Still, there is great potential for

* Corresponding author. Address: VTT Information Technology, Microelectronics, Polymer Electronics, P.O. Box 1208, FI-02044 VTT, Espoo, Finland. Tel.: +358 20 722111; fax: +358 20 7227012.

E-mail address: henrik.sandberg@vtt.fi (H.G.O. Sandberg).

organic electronics to replace current alternatives in some areas due to its low cost and simple processing capabilities, such as a continuous additive printing type manufacturing process.

This paper addresses the influence of device geometry and particularly the gate configuration, and the choice of gate insulator material. The organic transistor is a thin film transistor (TFT) device and it is well known that the field effect is determined largely by the insulator layer that forms the metal–insulator–semiconductor (MIS) capacitor [4]. For comparison all process parameters, such as electrode material, drying times and temperatures, annealing temperatures etc. are the same in all devices. The field effect transistor (FET) channel width and length are 1500 and 100 or 35 μm , respectively. Regioregular poly(3-hexylthiophene) (RR-P3HT) from Merck Chemicals dissolved in *p*-xylene (anhydrous, from Aldrich) is used as an organic semiconductor, spun at room temperature from a filtered 2 mg/ml solution giving a film thickness of 20–30 nm on glass.

The two types of samples are of bottom gate (BG) or top gate (TG) configuration, as shown in Fig. 1. The insulators are deposited by spin casting and the gold electrodes by shadow mask vacuum evaporation.

Four different insulating materials are compared; poly(hydroxy styrene) (PHS) from Electronic Polymers (DuPont); PHS and the cross-linking agent poly(melamine-*co*-formaldehyde) (PMF) in a mixture (PHS:PMF) with 15 wt% PMF; a precursor polyimide (pPI) (PI2610 DuPont, purchased from Aldrich) in solution; and a butanol based insulator formulation from Merck Chemicals (TCI01), which is an aromatic oligomeric resin. PHS and PHS:PMF are dissolved in anhydrous ethyl acetate (from Aldrich). Typi-

cally TCI01 was spun at 2000 rpm, PHS (150 mg/ml) at 1000 rpm and PHS:PMF (100 mg/ml) at 600 rpm. The pPI solution was diluted to 7 wt% with *N*-methyl-2-pyrrolidone (NMP) to yield a film thickness of $\sim 1 \mu\text{m}$ when spun at 2000 rpm. The addition of PMF changes the wetting properties significantly for the PHS material mixture. An insulator thickness of around 1 μm was chosen to minimize the risk of pinholes and current leakage to the gate electrode.

Transistor devices are characterized using an Agilent HP4142B semiconductor analyzer. Insulator capacitance is estimated by applying a linearly increasing voltage with a voltage rise speed, $A = 100 \text{ V/s}$, over a plate capacitor device using gold electrodes with an overlap of 1 mm^2 , and measuring the charging current. This technique [5] allows for accurate direct measurements of the capacitance using simple laboratory equipment and gives estimates for the capacitance even for samples with a high conductivity. Mean values for capacitance per unit area, C_i , for the different insulator layers are for PHS 1.8 nF/cm^2 , for pPI 4.9 nF/cm^2 , for PHS:PMF 2.1 nF/cm^2 , and for TCI01 2.5 nF/cm^2 . Mobility, μ , is mainly estimated from the modulation of the drain current in the saturated region, see e.g. [6] for details. The conductivity, σ , of the RR-P3HT film is estimated from the source current at a low drain voltage when the gate voltage is 0 V. Contact resistance was assumed to be negligible as gold electrodes are known to form good contacts to RR-P3HT [7]. The leakage currents were reduced by carefully wiping off the RR-P3HT around the edges of the sample.

Using silicon substrates as a working gate electrode inevitably results in a BG device configuration. Polymer based devices are normally of a TG configuration due to solvent compatibility reasons between layers. One of the main topics of this work is to investigate the influence of using different insulator materials that can be thermally cross-linked to form insoluble thin films thus providing more freedom in device configuration. The chemical process involved in the cross-linking is not investigated, the materials are used as received and all films are cured/baked at 100 $^\circ\text{C}$ for 1 h. The three cross-linkable materials are designed to

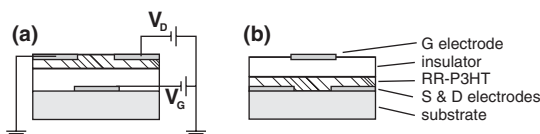


Fig. 1. Sample configurations used in this study; (a) bottom gate, BG, with the measurement setup schematically shown, and (b) top gate, TG, indicating the different layers and materials of the device. The hatched area is the RR-P3HT semiconductor layer. Layer thicknesses are not to scale.

be curable at low temperature and have been tested for compatibility with xylene, the solvent used for RR-P3HT deposition. Pure PHS can be used for working devices when RR-P3HT is quickly spun, despite the fact that the material is not cross-linked. Sample preparation and measurements are performed under controlled atmosphere.

Fig. 2 shows the influence of gate configuration on I - V characteristics for PHS samples. In general, the I - V characteristics are more typical of transistor behaviour in the BG configuration. A high conductivity in the TG configuration is assigned to increased doping of the semiconductor by the addition of the insulator layer solution or the introduction of impurities in the interface during sample preparation. The latter may be due to the fact that in this configuration the exposed top surface of the semiconductor is where the FET channel is formed [8]. For samples using TCI01 as an insulator, however, the difference between TG and BG configuration is fairly small. An output curve for a TG TCI01 transistor is shown in Fig. 3. This sample features a low conductivity

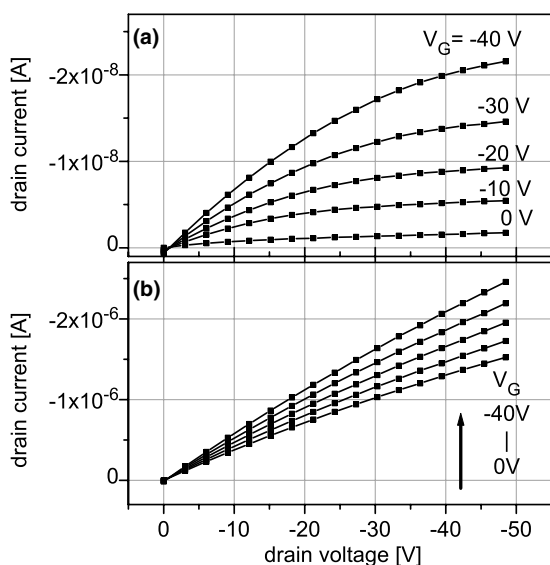


Fig. 2. Output curves for (a) BG and (b) TG configurations using PHS as gate insulator material. There is a typical difference in current (and conductivity) of 100 between the two geometries.

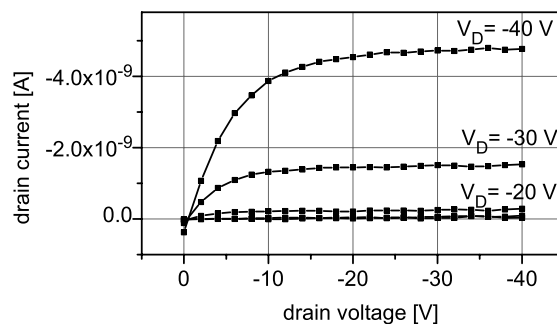


Fig. 3. Output curves for a TG device with low conductivity using TCI01 as the gate insulator. Field effect modulation is pronounced, with a clear saturated region typical of FETs. The small offset between curves at low drain fields indicates a leakage current on the gate electrode, occasionally a severe problem especially on unpatterned low conductivity samples.

RR-P3HT film and shows typical transistor behaviour. The quality of a FET can be estimated by comparing the mobility values extracted from the linear and saturated regions, which in this sample are $3.7 \times 10^{-4} \text{ cm}^2/\text{Vs}$ and $2.2 \times 10^{-4} \text{ cm}^2/\text{Vs}$, respectively.

A low conductivity in both configurations for the TCI01, provides indication that the RR-P3HT layer is not affected by the curing of the TCI01 film or by the solvent used for the insulator solution. As will be discussed further in the context of Fig. 4, the TG results may even suggest that this configuration provides enhanced charge carrier transport when using TCI01. This could be due to a higher mobility or a change of density of states as a result of improved film morphology or local polarisation effects [9]. Apart from the insulator material, the device properties are influenced by other processing parameters relating to the changed device configuration, such as the insulator solvents, the cross-linking procedure and the different semiconductor-insulator interface.

The PHS insulator works well in transistor devices and is widely used for organic electronics [10]. The material has good dielectric properties but has been shown to be hygroscopic and therefore absorb humidity in ambient atmosphere affecting the I - V characteristics of the unshielded device [11]. PHS is soluble in many common solvents, normally restricting applicability to TG devices. PI, on

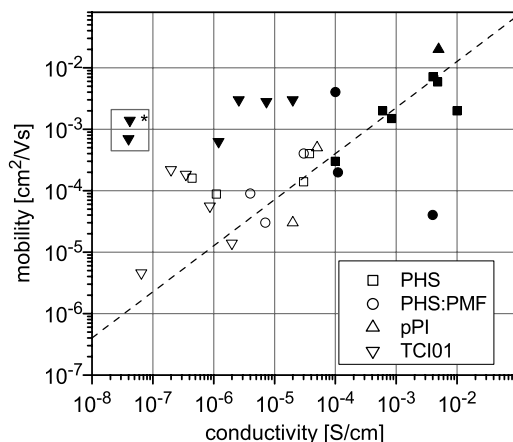


Fig. 4. Mobility vs. conductivity for the different device configurations using the four different insulator materials. Open and solid symbols correspond to BG and TG device configurations, respectively. The dashed line represents the universal rule [14] between the conductivity and mobility for disordered conjugated material. The samples marked with an * exhibit threshold voltage ≤ 0 V resulting in unreliable conductivity measurement using the chosen technique.

the other hand, is a well-known insulator with excellent electrical and mechanical properties. Low-temperature precursors, however, are few. To avoid degrading the RR-P3HT film, samples must not be heated above ~ 150 °C [12, p. 480].

Fig. 4 shows the collected results for the four different materials and both device configurations. Additionally, the graph displays the general rule, $\mu \sim \sigma^\delta$ with $\delta = 0.76$, relating the mobility value and the conductivity of the semiconductor for RR-P3HT [13,14]. This “universal rule” is valid for amorphous (disordered) material. However, the rule serves as a measure to indicate the difference between increased mobility due to e.g. structural or interface changes and mobility due to unintentional doping (high conductivity). In general, samples with better performance are found in the upper left corner of Fig. 4. At low conductivity values, a small gate leakage current affects the measurement and the estimation of the conductivity is more complicated. This gives a larger spread in the data at low conductivities, as seen in Fig. 4.

All samples follow the general rule marked with the dashed line within a factor of 10–100, except the TG TCI01 samples (marked by \blacktriangledown), which ap-

proach the upper left corner in Fig. 4. Recorded values are consistent with results reported in the literature. Furthermore, BG configuration generally result in a lower conductivity than TG configuration. A proposed explanation is that for BG the insulator is converted before the semiconductor is applied. Using the TG configuration any conversion products and solvents can interact with the semiconductor during the cross-linking procedure. The TCI01 in a TG configuration is the exception since both a high mobility and a low conductivity is obtained. BG gives very low conductivity values, but mobility is correspondingly lower, following the universal rule.

Film quality may have been an issue in the PHS:PMF samples since this material combination had a large failure rate among the measured samples. During the cross-linking step of TG PHS:PMF (marked by \bullet) it is speculated that there could be structural changes in the film that translate to the underlying RR-P3HT film causing changes in film morphology and thus charge carrier mobility.

There was a very high failure rate for TG pPI (marked by \blacktriangle) which is assigned to unidentified harmful reactions taking place during the conversion of the polyamic acid precursor polymer. Even the presently used low curing temperature precursor is more efficient, and would produce polyimide of a higher quality with better insulator properties, if cured at higher temperatures. BG structures can be cured at higher temperatures if metal gate electrodes are used, but for TG structures pPI is not well suited.

The conversion of TCI01 does not seem to affect RR-P3HT as much. The spread of values for TCI01 (marked by ∇) is partly due to uncertainty in the low currents. These samples show the best transistor characteristics and exhibit turn on voltages close to 0 V (in some cases even negative) but accurate conductivity determination for such samples is not straightforward. The TCI01 insulator provides the best performance in this study and a TG device structure could even be beneficial for practical TFTs, additionally providing a natural encapsulation of the sensitive FET channel region. It is speculated that the thermal cross-linking procedure for TG TCI01 samples (marked by \blacktriangledown)

result in structural changes in RR-P3HT, which maintains the high mobility even at low conductivity values. If the semiconductor is unchanged a decreased conductivity would result in lowering the mobility following the general rule.

This study implies that the device structure and the curing process must be controlled with great care. A generally higher conductivity and a slightly better reproducibility is obtained using the TG structure. A generally poor ON–OFF ratio of the FETs in this study (about 10^2 – 10^3 for the sample in Fig. 3 at -40 V) could be improved by optimizing FET geometry thus minimizing the interference of the gate leak currents present on the transfer characteristics. In this work FET structures were used with a non-optimized channel size and the semiconductor was not patterned, resulting in significant parasitic gate leakage, the impact of which would be much less if a shorter channel, and minimized gate electrode overlap, was used. However, the experiment was designed to reveal the differences between samples using different gate configuration and insulator material, and the device structure was thus kept the same in all measurements.

As a conclusion, it is seen that the TG geometry, often the device configuration of choice for organic FETs, generally gives higher mobility values. We note, however, that mobility and conductivity are related properties. The variations in conductivity is large and the device properties depend highly on the choice of insulator material. The spread in recorded parameters is smaller using the BG configuration and conductivity is also generally lower, which gives better current modulation at low voltages. Surface treatment procedures may provide means for improving the interface to the semiconductor and thus increase the mobility. The insulator TCI01 from Merck is in this work the material of choice and would be used in the TG configuration due to the excellent μ – σ characteristics of these devices.

Acknowledgements

Niklas Björklund is acknowledged for his work on the PHS:PMF cross-linking procedure. This work has been done partly within the framework of the MUOELE project of the Finnish Develop-

ment Fund (TEKES) and Academy of Finland project 50575.

References

- [1] J.A. Rogers, Z. Bao, Printed plastic electronics and paper-like displays, *J. Polym. Sci. Pol. Chem.* 40 (2002) 3327–3334.
- [2] H. Sirringhaus, N. Tessler, R.H. Friend, Integrated optoelectronic devices based on conjugated polymers, *Science* 280 (1998) 1741.
- [3] G. Gelinck, H. Huitema, E.V. Veenendaal, E. Cantatore, L. Schrijnemakers, J.V. der Putten, T. Geuns, M. Beehakkers, J. Giesbers, B. Huisman, E. Meijer, E. Benito, F. Touwslager, A. Marsman, B.V. Rens, D.D. Leeuw, Flexible active-matrix displays and shift registers based on solution-processed organic transistors, *Nature Mater.* 3 (2) (2004) 106–110.
- [4] R.F. Pierret, *Field Effect Devices*, second ed. Modular series on solid state devices, vol. IV, Addison-Wesley Publishing Company, Reading, MA, 1990.
- [5] G. Juška, K. Arlauskas, M. Viliunas, J. Kočka, Extraction current transients: New method of study of charge transport in microcrystalline silicon, *Phys. Rev. Lett.* 84 (21) (2000) 4946–4949.
- [6] S.M. Sze, *Physics of Semiconductor Devices*, second ed., John Wiley & Son, New York, 1981.
- [7] L. Bürgi, T.J. Richards, R.H. Friend, H. Sirringhaus, Close look at charge carrier injection in polymer field-effect transistors, *J. Appl. Phys.* 94 (9) (2003) 6129–6137.
- [8] S. Hoshino, M. Yoshida, S. Uemura, T. Kodzasa, N. Takada, T. Kamata, K. Yase, Influence of moisture on device characteristics of polythiophene-based field-effect transistors, *J. Appl. Phys.* 95 (9) (2004) 5088–5093.
- [9] J. Veres, S.D. Ogier, S.W. Leeming, D.C. Cupertino, S.M. Khaffaf, Low- k insulators as the choice of dielectrics in organic field effect transistors, *Adv. Funct. Mater.* 13 (2003) 199–204.
- [10] M. Halik, K. Hagen, U. Zschieschang, G. Schmidt, W. Radlik, W. Weber, Polymer gate dielectrics and conducting polymer contacts for high-performance organic thin-film transistors, *Adv. Mater.* 14 (23) (2002) 1717.
- [11] H.G.O. Sandberg, T.G. Bäcklund, R. Österbacka, H. Stubb, High-performance all-polymer transistor utilizing a hygroscopic insulator, *Adv. Mater.* 16 (13) (2004) 1112.
- [12] D. Fichou, *Handbook of Oligo- and Polythiophenes*, Wiley-VCH, Weinheim, 1999.
- [13] M. Raja, G. Lloyd, N. Sedghi, W. Eccleston, R.D. Lucrezia, S. Higgins, Conduction processes in conjugated, highly regio-regular, high molecular mass, poly(3-hexylthiophene) thin-film transistors, *J. Appl. Phys.* 92 (3) (2002) 1441–1445.
- [14] A. Brown, C. Jarrett, D. de Leeuw, M. Matters, Field-effect transistors made from solution-processed organic semiconductors, *Synth. Met.* 88 (1997) 37–55.



Call for papers

Special Issue on Coupled States of Excitons, Photons, and Plasmons in Organic Structures

Special Issue Editors: Vladimir Bulović and Chihaya Adachi

Manuscripts due by: 1 February 2006

Organic Electronics announces its first special issue on the subject of Coupled States of Excitons, Photons, and Plasmons in Organic Structures.

Coupling of the excited states of organic films with modes of optical cavities can lead to lasing action in the weak coupling limit or exciton–polariton phenomena in strongly coupled systems. Lasing action in organic semiconducting thin films has been actively pursued over the last decade with goals of demonstrating tunable light sources for applications such as high sensitivity chemical probes and organic photonic integrated circuits, and with emphasis on design of electrically pumped organic lasing structures. In the field of strongly coupled organic-optical cavity systems, researchers are in pursuit of thresholdless lasing, quantum computing, electromagnetically induced transparency, and related manifestations of room temperature cavity quantum electrodynamics. Related work on coupling of organic excited states to the plasmon modes of metals, metal nanocrystals, and inorganic semiconductor nanocrystals (quantum dots), complements the above studies by investigating near-field phenomena. Today's experimental demonstrations suggest tomorrow's practical optoelectronic devices that reconcile the demands and balance the opportunity of coupled optical and electronic phenomena in room temperature organic structures.

In response to the recent advances and projected opportunity of this emerging field, Organic Electronics is launching a special issue in this topical area. We therefore welcome submissions in all areas of Coupled States of Excitons, Photons, and Plasmons in Organic Structures including:

- organic lasers and optical amplifiers (containing polymers, small molecules, dendrimers, etc.);
- hybrid organic/inorganic nanostructured materials for lasers and optical amplifiers;
- applications of lasing action in organic and hybrid structures;
- Photonic Integrated Circuits;
- organic and hybrid materials in photonic band gap structures;
- observation of exciton–polaritons in organic and hybrid thin films and crystals;
- organic and hybrid devices that exhibit strong coupling limit of quantum electrodynamics;
- observation of exciton coupling to fields of metal plasmons;
- device structures utilizing exciton–plasmon coupling;
- interaction of free/trapped charges with exciton–photon–plasmon coupled states;
- influence of free/trapped charge on the operation of above devices.

All manuscripts should be sent to:

Vladimir Bulović

Department of Electrical Engineering and Computer Science

Room 13-3138, Massachusetts Institute of Technology, Cambridge, MA 02139, USA

For instructions on how to prepare the manuscript or how to submit online, please consult the Author Gateway at <http://authors.elsevier.com/journal/orgel>. Note that authors should indicate in the cover letter to the Editor that the manuscript is submitted for this Special Issue.

Properties of organic light-emitting diodes by aluminum cathodes modification using Ar⁺ ion beam

Soon Moon Jeong, Won Hoe Koo, Sang Hun Choi, Hong Koo Baik *

*Department of Metallurgical Engineering, School of Materials Science and Engineering, Yonsei University,
134 Shinchon-dong, Seodaemun-ku, Seoul 120-749, Republic of Korea*

Received 20 September 2004; received in revised form 14 March 2005; accepted 30 March 2005

Available online 12 May 2005

Abstract

Organic light-emitting diodes (OLEDs) with aluminum cathodes prepared by the ion beam-assisted deposition (IBAD) have a longer lifetime than thermally evaporated ones. The electroluminescent features were examined to compare the rate of degradation in the devices with thermal evaporated Al cathodes and ion beam-assisted Al cathodes. The dense and highly packed Al cathode effectively prevents the permeation of H₂O and O₂ through pinhole defects, which results in retarding dark spot growth. Employing thin Al buffer layer diminished Ar⁺ ion-induced damages in phenyl-substituted poly-*p*-phenylene-vinylene (Ph-PPVs) and limited permeation against H₂O and O₂. The interface between Al and Ph-PPV may be modified in IBAD case, even though buffered Al layer was deposited to 30 nm by thermal evaporation prior to Ar⁺ ion beam irradiation. It is believed that the buffered Al film cannot screen the Ar⁺ ions or Al atoms wholly due to the existence of pinholes or non-deposited regions among the columnar structures.
© 2005 Elsevier B.V. All rights reserved.

Keywords: OLED; Ion beam-assisted deposition; Passivation; Lifetime

1. Introduction

Since efficient electroluminescence (EL) from an organic light emitting device (OLED) was first reported, there has been considerable interest in utilizing OLEDs for full color flat panel display

applications [1]. However, the OLED devices still suffered from limitation of short lifetime due to degradation such as crystallization of organic materials [2,3], chemical reactions including oxidation [4] and gas evolution [5,6], there has been little mention of passivation layer that protect OLED devices from water and oxygen in a room ambient. As a result, conventional OLEDs exhibit a short lifetime (generally defined as the time necessary to reduce luminance to 50% of initial luminance

* Corresponding author. Tel.: +82 2 2123 2838; fax: +82 2 312 5375.

E-mail address: thinfilm@yonsei.ac.kr (H.K. Baik).

value at constant current) as a usable device in atmospheric conditions.

To increase the lifetime of OLEDs, various methods and techniques have been devised for encapsulating OLEDs with protective layers of varying compositions. At present, a hermetic encapsulation technique using a glass or metal lid attached by a bead of UV cured epoxy resin has been extensively performed to protect OLEDs from oxygen and water vapors [4]. However, these types of seals are very expensive to fabricate and require extensive labor to assemble. In addition, these seals are large and heavy so that they severely limit the applications of OLEDs.

Polymer materials formed by using dry or wet process have a relatively high H₂O permeation rate of 10⁰–10² g/m² [day] and are therefore inadequate for encapsulating OLEDs. In addition, the moisture barrier property below 5 × 10⁻³ g/m² [day] is difficult to achieve using inorganic materials deposited at or near room temperature.

In the food packaging or medical device industries it is desirable to manufacture thin, flexible and transparent films that act as a protection against oxygen and moisture. Some researchers proposed a quantitative model for inorganic/polymer films which estimate the degree of oxygen permeation through the lattice (pore size < 0.3 nm), nano-defects (0.3–1.0 nm) and micro-defects (>1 nm) at a given oxidant layer. The existence of nano-defects in silica glasses has been previously found based on observed decrease in the activation energy of permeation at low temperatures [7]. The role of nano-defects was reported to be effective for relatively large molecules (e.g., O₂ and H₂O) since their lattice permeabilities at room temperature are virtually negligible. So note that the passivation layer should not contain nano-defects to protect the OLED device from O₂ and H₂O.

However, there have been few reports about enhancing passivation property through cathode modification. To minimize damage in organic materials, the cathode has been deposited by the thermal evaporation process with low adatom mobility. This process allows the porous thin film cathode having many pinholes, even though damage is not produced.

In this paper, we develop the highly packed aluminum cathode using the IBAD technique, leading to an increase lifetime of the OLED device through the improvement of protection ability against O₂ and H₂O.

2. Experiment

Indium tin oxide (ITO) coated glass was used as the substrate for OLEDs which was about 200 nm thick with a sheet resistance of approximately 15 Ω/square. ITO was patterned using a gas mixture of hydrochloric acid (HCl) and nitric acid (HNO₃) with same volume quantity and then 3 mm-sized ITO stripes were obtained. After ITO patterning, the standard cleaning procedure including the sonication in a detergent, acetone, and isopropyl alcohol successively, and then rinsing in deionized water. A layer which has been used as a dispersion of poly(3,4-ethylenedioxythiophene) (PEDOT) and poly(styrenesulfonic acid)

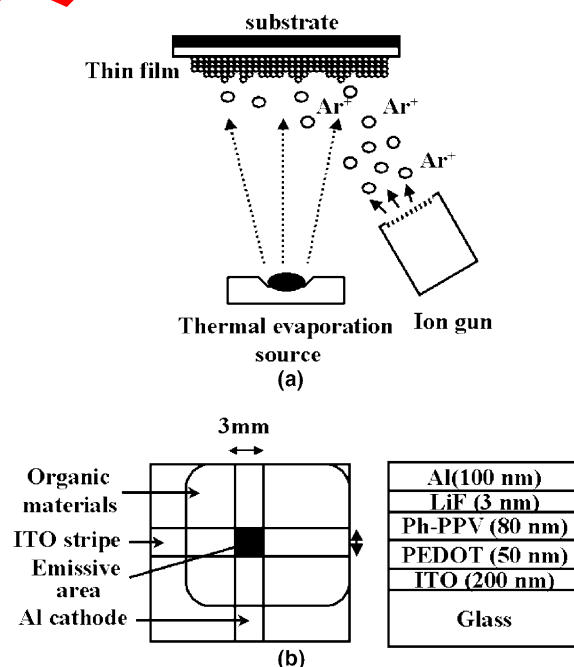


Fig. 1. Schematic diagram of (a) ion beam-assisted deposition (IBAD) system and (b) device structure (ITO/PEDOT/Ph-PPV/LiF/Al).

(PSS), commercialized by Starck (AI 4083), was spin-coated up with 4000 rpm to a thickness of 50 nm as a hole transport layer (HTL). The residual water was removed at 200 °C for 5 min in air condition. After heat treatment, yellow light emitting polymer, phenyl-substituted poly-*p*-phenylene-vinylene (Ph-PPVs) provided by Covion, was spin-coated with 4000 rpm to have a thickness of 80 nm as an emissive layer on the HTL layer in air condition successively, and they were transferred in air to the evaporation chamber. Then, Al cathodes were deposited up to about 100 nm in thickness by the conventional thermal evaporation method and IBAD process, respectively. The schematic diagram of an IBAD system and the device are shown in Fig. 1. The Kaufman ion gun was used to increase aluminum ad-atom mobility. Ar⁺ ion energy and current density were 150 eV and 70 μA/cm², and Al deposition rate was 1–2 Å/s. In all cases of ion beam irradiation conditions, the incident angle of the ion beam was 45°. To avoid Ph-PPV damages by Ar⁺ ion bombardment,

thermally evaporated Al is deposited up to 30 nm in thickness prior to ion beam-assisted deposition.

3. Results and discussion

It was reported that smooth barrier coatings have low values of diffusivity [whereas for rougher coatings the diffusivity is much worse [5]]. To achieve highly flat aluminum thin films, the surface morphology of Ph-PPV used as a substrate should be flat because depositing film was influenced largely by substrate surface conditions. The surface roughness and thickness of spin coated organic materials is determined by two factors, one is a spin speed and the other is a solution viscosity. The viscosity that can be varied by volume ratio between polymer and solvent is fixed, so the roughness and thickness of Ph-PPV is decreased with increasing spin speed. Fig. 2 shows the surface morphology of spin coated Ph-PPV with

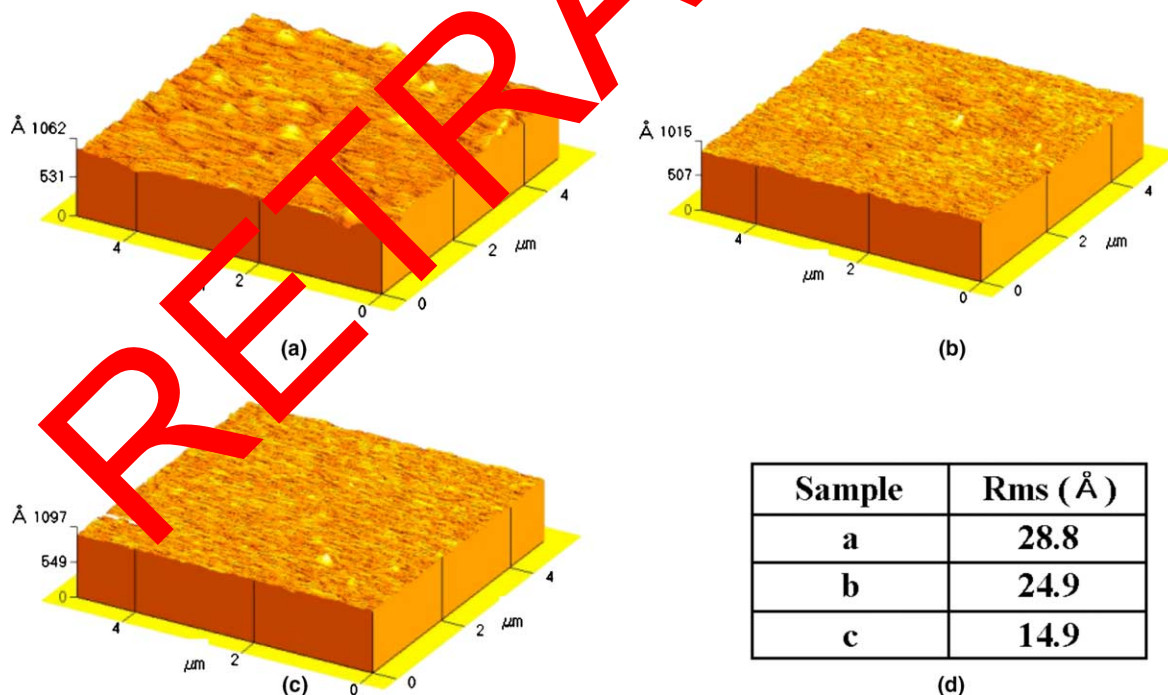


Fig. 2. Atomic force microscopy (AFM) images of various spin coated phenyl substituted poly-*p*-phenylene-vinylene (Ph-PPV) (a) 1000 rpm (b) 3000 rpm (c) 4000 rpm and (d) root mean square (rms) values.

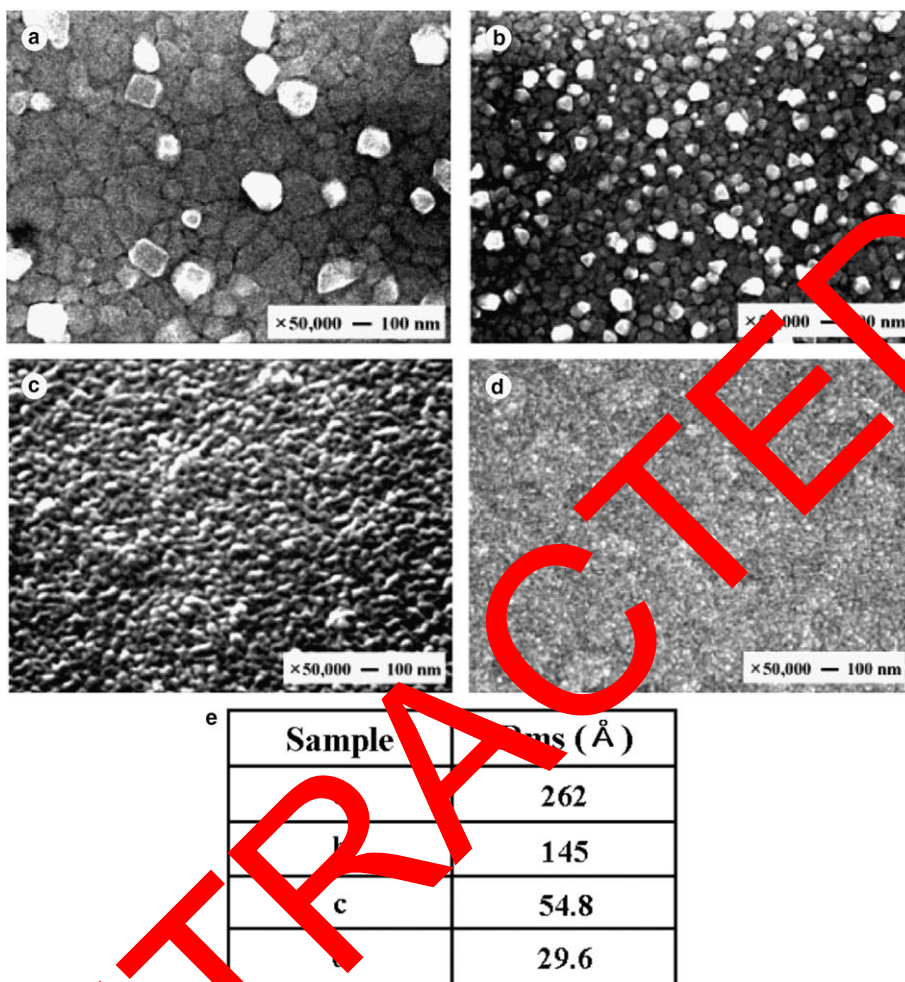


Fig. 3. The scanning electron microscopy (SEM) images of (a)–(c) thermally evaporated Al on LiF/Ph-PPV/PEDOT/ITO structure with deposition rates of 50, 10, 1 Å/s respectively (d) ion beam-assisted Al with deposition rate of 1 Å/s and (e) root mean square (rms) values obtained from atomic force microscopy (AFM).

various spin speed using AFM. The larger spin speed, the smoother the surface roughness of Ph-PPV. We determined the optimized spin speed to 4000 rpm because the thickness of Ph-PPV at that spin speed is 80 nm that was usually used in other reports.

In order to investigate the effects of deposition rate on the roughness, we manipulated aluminum deposition rate from 1 Å/s to 50 Å/s. It has been generally accepted that the surface morphology is flat at slow deposition rate because adatom moving time is longer than that of higher deposition speed.

Fig. 3 shows the SEM images and root mean square (rms) value of aluminum thin films on LiF/Ph-PPV/PEDOT/ITO substrate having different deposition rates. The aluminum deposition rate varies from 1 Å/s to 50 Å/s and the spin coating speed of Ph-PPV and PEDOT layer is fixed at 4000 rpm spin. In Fig. 3(a)–(c), the surface of aluminum thin films obtained at low deposition speed is smoother than that at high deposition speed.

We must now relate the surface diffusion which an adsorbate molecule travels during film deposition. This is an adaptation of the classic random-

walk problem. Since each hop is equally likely to be forward or backward in any given direction on the surface, there is no net motion in any one direction. However, as time ($=t$) passes, the molecule is more likely to be found further from its starting point. This is equivalent to saying that if one carries out a large number of trials of starting a molecule diffusing from a single point at $t = 0$, then with increasing t the final locations of these molecules become more widely dispersed from the starting point [9]. As a result, the roughness decrease in slowly deposited Al film because adatom can diffuse further distance if the deposition rate is lower.

Fig. 3(e) indicates the root mean square (rms) value obtained from Atomic Force Microscopy (AFM) measurement. This is might be due to prolonged adatom moving time.

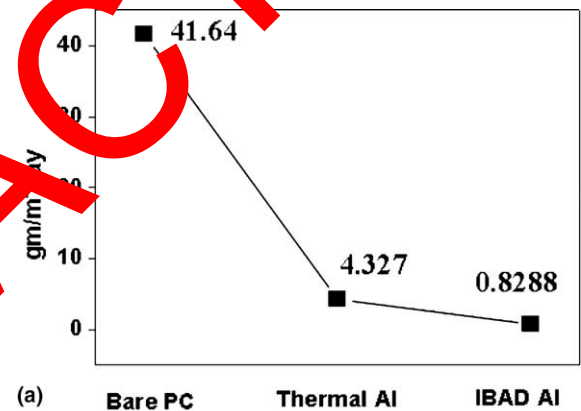
The impingement of energetic ions or atoms upon a solid surface produces a wide variety of effects, and there has been a vast amount of experimental and theoretical work on the subject. Many of these effects are beneficial to thin film deposition, thus ion bombardment is one of the most important thin film process parameters. Careful studies of atomic trajectories during ion impact onto a porous microcolumnar surface structure clarified the essential mechanisms which contribute to an improvement in layer growth: (i) ion bombardment during growth removes overhanging atoms and causes void regions to remain open until filled by new depositing atoms, (ii) sputtered atoms are redeposited mainly in voids, (iii) ions induce surface diffusion (diffusion distance is a few interatomic spacings), local heating, collapse of voids and recrystallization [10].

The ion beam-assisted deposition process was adopted to obtain highly flat and packed aluminum structure. Fig. 3(d) shows the SEM data of the Al cathodes deposited by thermal evaporation and IBAD process. In the thermally evaporated Al cathode, islands and voids are very large. On the other hand, the Al cathode deposited by IBAD contains the fine islands and voids that may restrict the permeation of H_2O and O_2 . The Al atoms bombarded by energetic Ar^+ ion produce the cathode having the highly packed structure due to their high surface adatom mobility. The

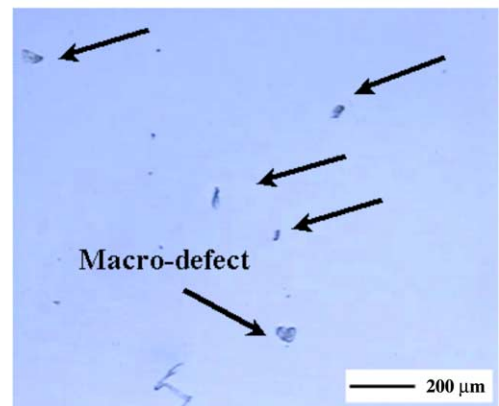
degree of surface roughness of the Al films deposited by IBAD is lowered remarkably for Ar^+ ion energy of 150 eV.

To study the effect of ion beam-assisted Al on the protection against H_2O , the water vapor transmission rate (WVTR) of bare PC (polycarbonate) and cathodes obtained from different deposition processes, thermal evaporation and IBAD with 1 Å/s, on PC substrate was measured using a MOCON instrument at 37.8 °C. All WVTR values are reported in units of g/m^2 per day.

In Fig. 4(a), it can be seen that the Al layers from thermal evaporation and IBAD have much lower WVTR value than the bare PC substrate does. Further, the WVTR value of the Al layer



(a) Bare PC Thermal Al IBAD Al



(b) Macro-defect
200 μm

Fig. 4. (a) Water vapor transmission rate (WVTR) of Al layer prepared by thermal evaporation and ion beam-assisted deposition on polycarbonate (PC) substrate (b) Optical image of bare polycarbonate (PC) substrate.

from IBAD is even lower than that from thermal evaporation. But these values are somewhat higher than those reported for the most commonly used coatings on PET (poly ethylene terephthalate): Al [11,12]; SiO [13–15]; and AlO_x [16]. This might be due to the macro-defects existed in the bare PC substrate as shown in Fig. 4(b). These macro-defects induce the pinholes in Al films that act as a pathway of H₂O due to the shadowing effect. However, the shadowing effect can be minimized in the ion beam-assisted Al layer because of its relative high adatom mobility, resulting in a decrease in the value.

The lowest value of WVTR may be caused by not only macro-defects existed in bare PC substrate but also nano-defects or lattice interstices. Roberts et al. reported that macro-defects (>1 nm), nano-defects (0.3–0.4 nm) and the lattice interstices (<0.3 nm) all contribute to total permeation [7]. The relative contribution of each component depends on the size of the permeant molecule (or atom), and the number and size of each class of defect. Although the relative contribution of each factor were not clearly examined in this experiment, it is obvious that films prepared with ion bombardment have packed grain structure and flat grain morphology resulting in smaller size of nano-defects or lattice interstices [17]. They may induce the lower WVTR value in ion beam-assisted Al sample.

In order to compare the passivation properties of the thermally evaporated Al and ion beam-assisted Al cathode, the storage lifetime test was performed. The samples used for storage lifetime test are thermally evaporated Al device and ion beam-assisted Al device with 1 Å/s and substrates were fabricated identically for the comparison of two different methods. The resulting specimens were stored in air condition and electroluminescent features were captured using optical microscopy to investigate the growth of dark spots. The corresponding devices consisted of multi-layers, ITO/PEDOT/Ph-PPV/LiF/Al, without any encapsulation or passivation layer.

Fig. 5 shows the optical images of both Al cathodes. Driving conditions of the thermal evaporated Al device and ion beam-assisted Al device were 10 V, 2 mA, 2500 cd/m² and 10 V, 3 mA,

3500 cd/m², respectively. Dark spots induced by dust particles were formed inevitably since the devices were fabricated at an ordinary laboratory without filtering process from the air. In the thermally evaporated Al device, the dark spots were growing gradually with time whereas in the ion beam-assisted Al device remained almost steady. It was believed that the formation of pinholes resulting from dust particles was minimized due to high surface adatom mobility for the IBAD-related device. However, some of the dark spots in the thermally evaporated Al device may be almost steady with time. Wang and coworkers [18] reported that the growth rate of dark spot is correlate with the pinhole size and diffusion controlled process. Although the Al has a porous structure in thermal device, dark spot growth can be slow if the pinhole size is very small. However, it is certain that the growth rate of all dark spot in thermal device is faster than the IBAD one.

Moreover, this enhanced passivation property can be examined by dense Al structure using Ar⁺ ion irradiation resulting in reduced pinholes.

Atomic force microscopy has been employed to identify differences arising in surface morphology and roughness of samples prepared by thermal evaporation and IBAD exhibiting barrier efficiencies.

To ascertain if morphological features are at least partly responsible for the differences in H₂O, higher resolution 2 μm—2 μm phase and oblique (3D) images are presented in Fig. 6. These images reveal that the surface of Al films can be described as columnar or granular structure. The phase images displayed in Fig. 6(a) show that the Al film surface prepared by IBAD consists of densely packed small spherical clusters (grains) with well-defined boundaries.

Such fine uniform features are responsible for the lower WVTR value because the penetrant molecules locate and diffuse through the relatively few and small defect sites (due to the dense packing of particles) within the Al film. In case of Al film prepared by thermal evaporation, a poorer barrier coating is produced. An increase in particle size is accompanied by an increase in grain boundary area. When this effect is combined with the irregular grain texture, it is anticipated that a greater

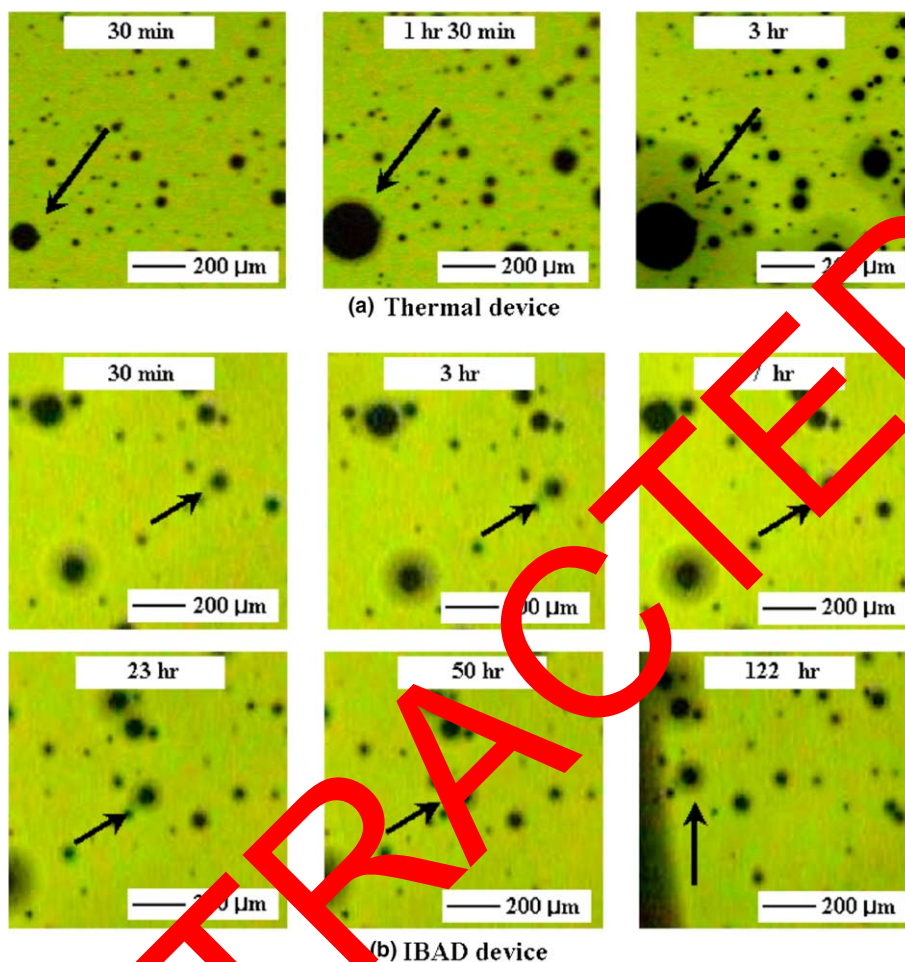


Fig. 5. Optical images of the electroluminescent features with time in Al cathodes with 1 \AA/s prepared by thermal evaporation (a) and ion beam-assisted deposition (b).

number of penetrant molecules will diffuse through intergranular pores. When compared on a fixed vertical scale (a range of 50 nm), the topography of the IBAD sample (Fig. 6(b)) appears to be composed of uniformly distributed, small columnar features, whereas large domes create valleys that may not be completely covered with Al, thereby forming diffusive pathways in coatings that exhibit poor barrier quality in thermal sample. Such megalithic structures increase the rms surface roughness, which is shown in Fig. 6(b).

In addition, the cell even degraded due to the permeation of H_2O and O_2 at its edge. This is because the present device was a passive matrix hav-

ing the structure exposed to air at the interface between Al and Ph-PPV, and so we failed to show the optical image of electroluminescence only after 3 hours for the thermal evaporated Al device. However, edge permeation in the IBAD device is much smaller than the thermal device due to its high packed Al structure.

Fig. 7(a) shows H_2O or O_2 permeation progress in thermal evaporated Al device through the edge structure with increasing time. When the device was stored in air condition, dark spots were growing with increasing time. However, the degradation of edge was too fast to observe growth of dark spots.

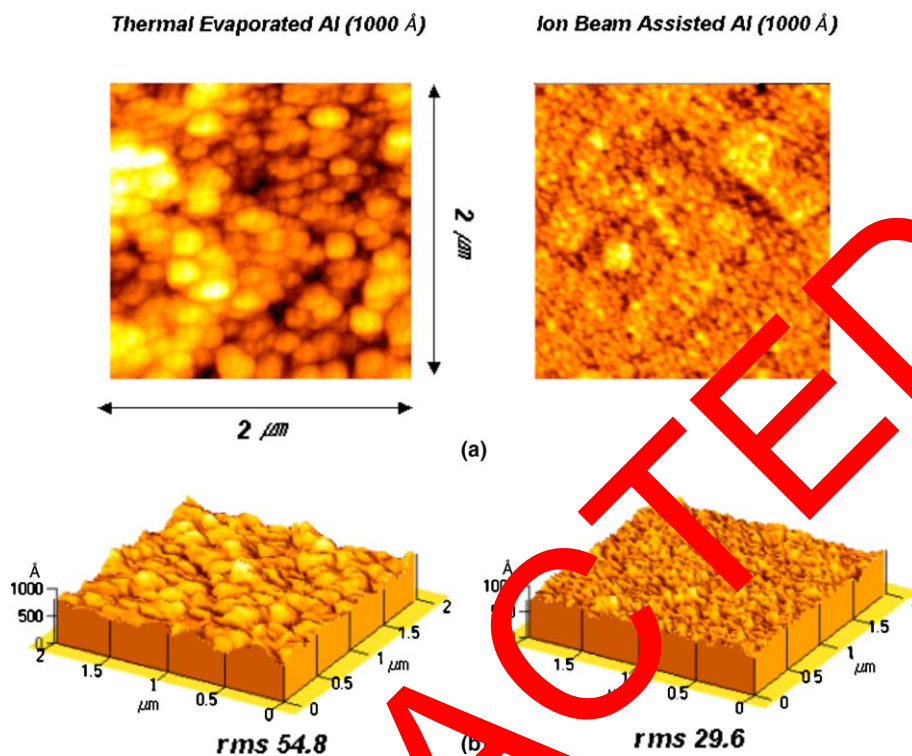


Fig. 6. Atomic force microscopy (AFM) images of Al films prepared by thermal evaporation and ion beam-assisted deposition on LiF/Ph-PPV/PEDOT/ITO structure with same deposition rate of 1 Å/s (a) phase (2D) images (b) oblique (3D) images.

After storing the device in air condition for 3 hours, electroluminescence region was shrunk by edge permeation as shown in Fig. 7(a). This Al cathode oxidation by edge permeation of H_2O and O_2 can be observed even when bias is not applied to the device. The dashed vertical line is an indication to the area of oxidation region with time by edge permeation. It shows that the bright region was shrunk to the center of active area with time due to the edge permeation. In Fig. 7(b), gas bubbles can be seen in the oxidation region when the EL is switched off and these bubbles have donut-like structure filled with gases (mostly oxygen) presumably evolved during electrochemical and photoelectrochemical processes in the presence of water [19]. Gases stimulated by significant heating during the device operation form these bubbles, and then cause cathode delamination at metal/organic material interface [20].

On the other hand, in case of IBAD sample, edge permeation is reduced compared than thermal case even though an Al buffer layer is deposited to 30 nm in thickness by thermal evaporation prior to ion beam-assisted deposition to avoid ion bombardment induced damages in Ph-PPV. This indicates that IBAD process may influence the interfacial state because edge permeation is slower than thermal case.

Although an Al buffer layer is deposited to 30 nm in thickness by thermal evaporation prior to ion beam-assisted deposition to avoid ion bombardment induced damages in Ph-PPV, IBAD process may influence the interfacial state because edge permeation is slower than thermal case. Hung and Madathil [21] reported that catastrophic failure still occurs even though 10 nm of MgAg is sufficient thick to protect the organic layer stack, when organic films are subjected to irradiation through pinholes. The formation of pinholes is

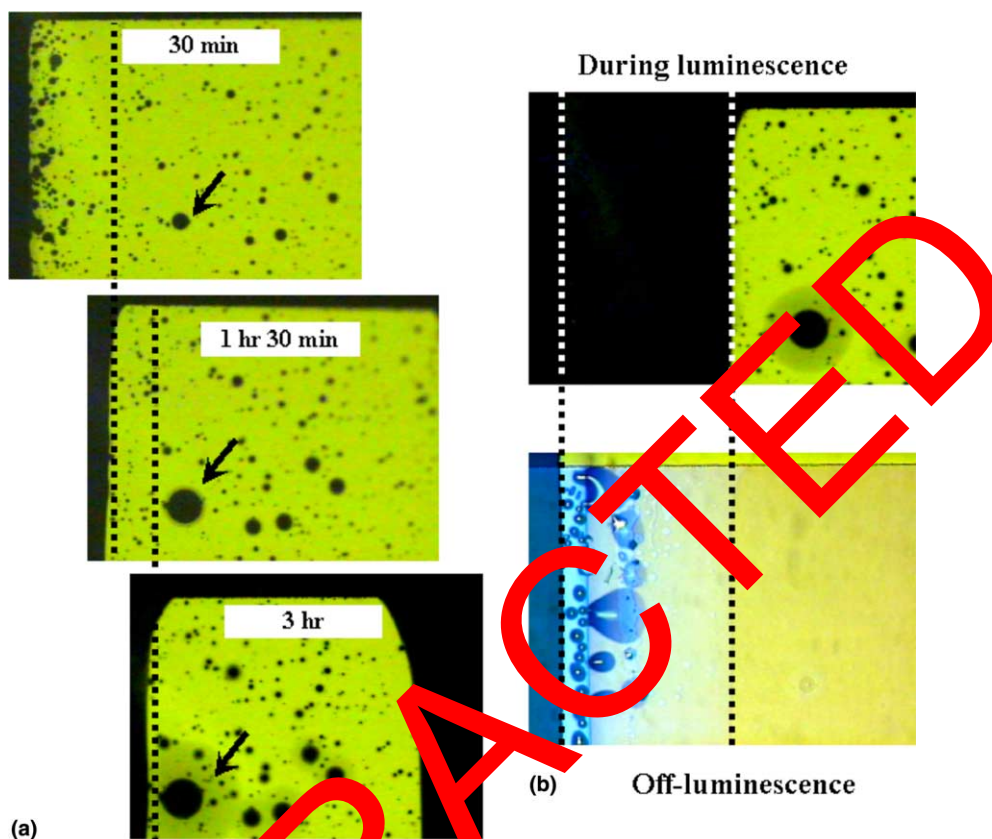


Fig. 7. Optical images of edge permeation in electroluminescent devices of thermal evaporated Al (a) during luminescence (b) comparison with off-luminescence. The dashed vertical line is an indication to the degree of oxidation region with time by edge permeation.

possibly related to the island-like growth of thin films of MgAg or Alq [22].

Fig. 8 illustrates the deposition process of Al to make the buffered SAD device. As thermally evaporated Al is deposited to 30 nm in thickness prior to Ar^+ ion irradiation, the buffered Al film may have many pinholes and porous structure due to its low surface adatom mobility. When the Ar^+ ions or their activated Al atoms are irradiated to the buffered Al film surface, they cannot be screened by the buffered Al film wholly because they can transmit to Ph-PPV through the pinholes or non-deposited regions among the columnar structures. This idea can be supported by TEM data indirectly.

Fig. 9 is TEM images showing the plane views of Al specimens prepared by three different pro-

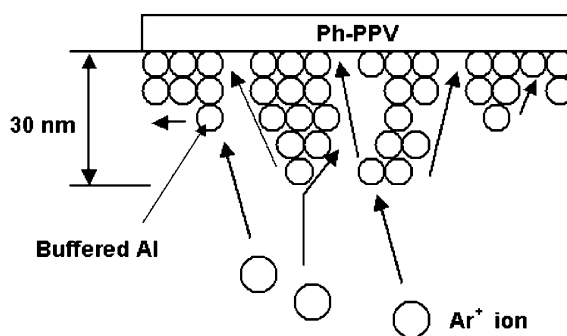


Fig. 8. Schematic diagram of ion beam-assisted deposition process in buffered Al layer.

cesses. In this experiment, the thickness of the Al film is fixed at 30 nm for transmitting the electron beam through it in a given transmission electron

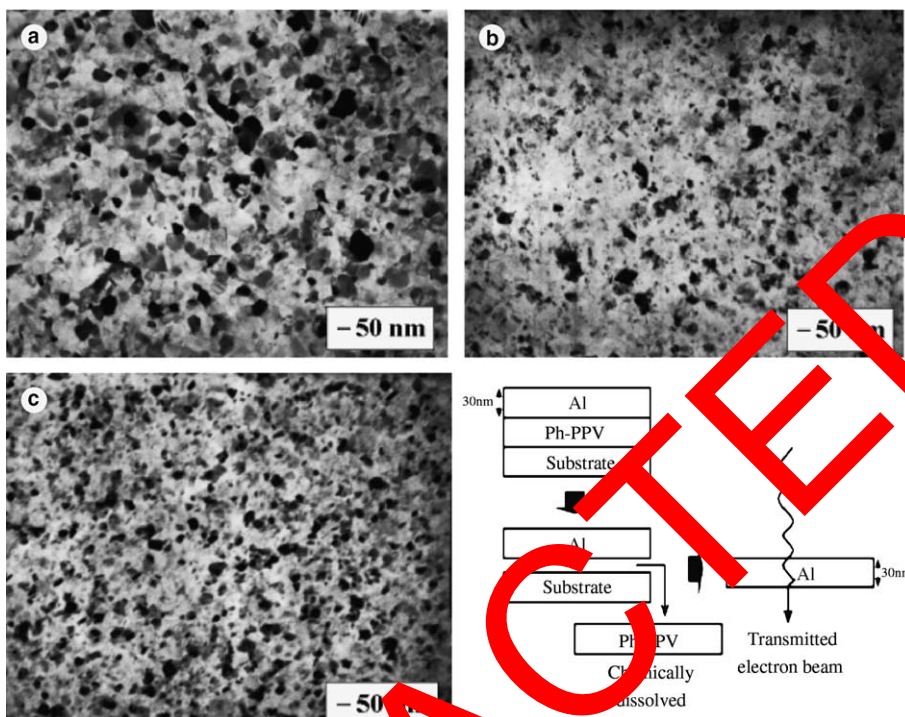


Fig. 9. TEM images ($\times 100,000$) of Al prepared by (a) thermal evaporation (30 nm) (b) thermal (20 nm) + IBAD (10 nm) (c) IBAD Al (30 nm) on Ph-PPV/ITO structure.

microscopy. Here, the conventional TEM sample preparation method cannot be used for the present organic samples. Fig. 9(a) is a TEM image of the Al film (30 nm) deposited by thermal evaporation. The resulting buffered Al film consists of thermally evaporated Al (20 nm) prior to the Al film (10 nm), which is obtained by only Ar^+ ion beam-assisted deposition, as shown in Fig. 9(b) and (c).

Although they differ from the previous buffered Al film which is deposited up to 30 nm just by thermal evaporation, TEM data show the decreased average grain size in buffered Al film (Fig. 9) compared with thermally evaporated Al (Fig. 9(a)). That might be caused by transmitting Ar^+ ion or activated Al atoms through the pinholes resulting in breakup of 3D structure (Fig. 8). So the significant enhancement in the passivation properties of the OLEDs prepared with ion bombardment result from not only densification of the Al structure but also interface modification between Al and Ph-PPV retarding H_2O and O_2 permeation at edge structure.

In order to observe whether Ar^+ ions or activated Al atoms transmit through the pinholes or non-deposited regions, we investigated the electrical characteristics of OLED device to measure damages in buffered IBAD device. Fig. 10 shows the current–voltage (I – V) characteristics of the OLEDs with ion beam-assisted Al cathodes were measured and compared with that of a conventional Ph-PPV based device. The Al cathode depositions by IBAD were made with the thermally evaporated Al buffer layer about 300 Å before using IBAD process to avoid Ph-PPV damages by Ar^+ ion bombardment. The measurements have been carried out in a glove box filled with argon gas of 99.9999% purity to exclude the permeation effect of H_2O and O_2 because dark spots formed by the cathode oxidation restrain the current injection.

There is some leakage current even in buffered IBAD device as shown in Fig. 10. Although above I – V data cannot be related directly with the generation of damages through pinholes in buffered Al

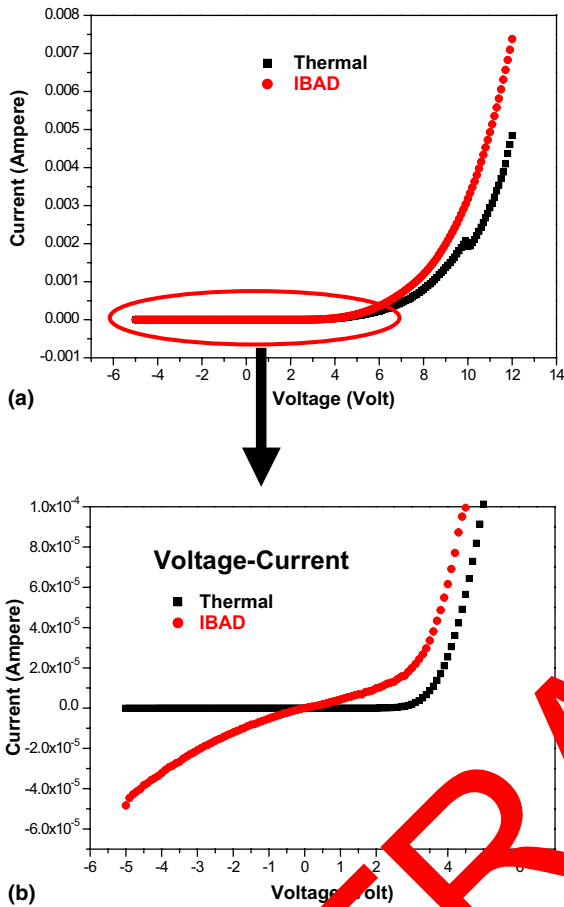


Fig. 10. I - V plot of OLED device with Al cathode deposited by thermal evaporation and ion beam-assisted deposition. (a) voltage-current (b) magnified voltage-current

film, it is certain that the leakage current is induced by Ar^+ ion induced damage because the leakage current must not be generated at reverse bias regime due to the potential barrier for electrons and holes injection.

More physical information about the device characteristics can be extracted from a logarithmic representation. In $\log I$ - $\log V$ plots, we can reveal the complex nature of device performance, and demonstrate the physics of the injection, transport, and recombination processes (Fig. 11).

From the $\log I$ - $\log V$ plot, charge-carrier injection and transport processes of conventional thermal evaporated Al device can be explained by

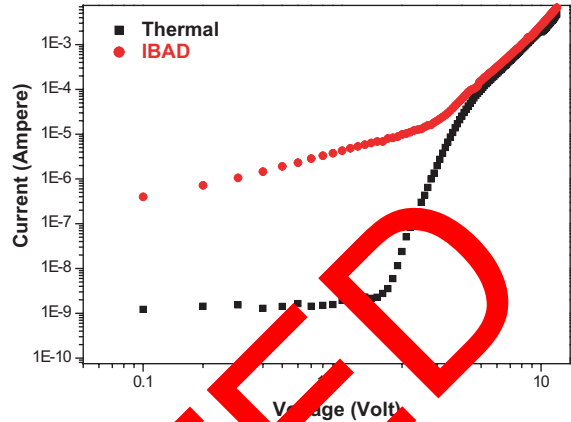


Fig. 11. $\log I$ - $\log V$ plot of OLED device with Al cathode deposited by thermal evaporation and ion beam-assisted deposition.

Schottky barrier model, where the current is predominantly carried by holes and is limited by the Schottky contact at the PPV/metal interface and the series resistance. The contact of PPV with the high work function metal ITO is regarded as ohmic which, in the ideal case, has negligible resistance [23].

In forward bias ($V > 0$), the I - V curve of thermally evaporated Al device shows an exponential current rise with increasing voltage between 2 V and 4 V. This is because holes surmount the built in potential barrier formed at Al/PPV interface with increasing voltage. Schottky barrier model can be applied well in thermally evaporated Al device. With increasing voltage, the slope of the $\log V$ - $\log I$ plot is decreased. The power-law dependence of the I - V was observed consistent with the previous work, where it was suggested that current in OLED was limited basically by traps and space charge effects [24–27]. Most researchers demonstrated that the current I depends quadratically on the voltage V at higher bias regime which current transport is limited by bulk PPV resistance because injected charge is very large [25]. This behavior is characteristic for trap free space charge limited current (SCLC), but SCLC behavior was not observed in our data because of the large trap concentration and low mobility in organic semiconductors. It has been

proposed that the carrier transport in OLEDs is trap charge limited (TCL) [26,27].

The I - V curves of ion beam-assisted Al devices were different from thermally evaporated Al device. The increase of leakage current is induced by Ar^+ ion irradiation during Al electrode deposition. In case of the IBAD device, although thermally evaporated Al film is deposited to 30 nm prior to Ar^+ ion irradiation, the buffered Al film cannot screen the Ar^+ ions wholly because that may have many pinholes and porous structure due to the low surface adatom mobility. So Ar^+ ions or Al atoms can transmit to PPV through the pinholes or non-deposited regions among the columnar structures resulting in increase of leakage current.

4. Conclusion

It was investigated in the present work that the Al cathode generated by IBAD has the more improved passivation properties than that by thermal evaporation by allowing the more dense structure that restricts the permeation of H_2O and O_2 . Employing thin Al buffer layer diminishes Ar^+ ion-induced damages in Ph-PPV and limited permeation against H_2O and O_2 to the device structure exposed to air. It might result from transmitting Ar^+ ions through porous buffered Al film leading to prolonged lifetime.

References

- [1] C.W. Tang, S.A. Van Slyke, Appl. Phys. Lett. 51 (1987) 913.
- [2] T. Sato, H. Yanai, Mol. Cryst. Liq. Cryst. 253 (1994) 143.
- [3] H. Aziz, S. Popovic, J. Xie, A. Hor, N. Hu, C. Tripp, G. Xu, Appl. Phys. Lett. 72 (1998) 756.
- [4] P.E. Burrows, V. Bulovic, S.R. Forrest, L.S. Sapochak, D.M. McCarty, M.E. Thompson, Appl. Phys. Lett. 65 (1994) 2922.
- [5] L.M. Do, E.M. Han, Y. Niidome, M. Fujihira, T. Kanno, S. Yoshida, A. Maeda, A.J. Ikushidma, J. Appl. Phys. 76 (1994) 5118.
- [6] H. Aziz, G. Xu, Synth. Met. 80 (1996) 7.
- [7] A.P. Roberts, B.M. Henry, A.P. Sutton, C.R.M. Grovenor, G.A.D. Briggs, T. Miyamoto, M. Kano, Y. Tsukahara, M. Yanaka, J. Membrane Sci. 208 (2002) 75.
- [8] G. Garcia-Ayuso, L. Vazquez, J.M. Martinez-Duart, Surf. Coat. Tech. 80 (1996) 203.
- [9] D.L. Smith, Thin-film Deposition (Principles and Practice), McGraw-Hill, Inc., NY, 1997.
- [10] J.J. Cuomo, S.M. Rossnagel, R. Kaufman, Handbook of Ion Beam Processing Technology, Noyes Publications, NJ, 1989.
- [11] B.M. Henry, F. Dinelli, K.-Y. Zhao, C.R.M. Grovenor, O.V. Kolosov, G.A.D. Briggs, A.P. Roberts, R.S. Kumar, R.P. Howson, Thin Solid Films 357 (1999) 500.
- [12] E.H.H. Johnson, A.H. Venable, Mater. Sci. 18 (1983) 64.
- [13] Y.G. Topsoe, N.G. Harvey, Phys. Chem. B 101 (1997) 2259.
- [14] A.G. Erlat, R.J. Montak, R.P. Clarke, T.C. Robinson, P.D. Haaland, Y. Topsoe, N.G. Harvey, E.A. Vogler, J. Phys. Chem. B 103 (1999) 6047.
- [15] A.S. da Silva Sobrinho, G. Czeremuszkin, M. Latreche, M.R. Wertheimer, J. Vac. Sci. Tech. A 18 (2000) 149.
- [16] B.M. Henry, F. Dinelli, K.-Y. Zhao, A.G. Erlat, C.R.M. Grovenor, G.A.D. Briggs, in: Proceedings of the Society of Vacuum Coaters Soc. 42nd Annual Tech. Conf. Proc., Chicago, USA, April 17–22, 1999, p. 403.
- [17] J.S. Kwak, H.K. Baik, J.H. Kim, S.M. Lee, Appl. Phys. Lett. 71 (1997) 2451.
- [18] S.F. Lim, L. Ke, W. Wang, S.J. Chua, Appl. Phys. Lett. 78 (2001) 2116.
- [19] L.M. Do, M. Oyamada, A. Koike, E.M. Han, N. Yamamoto, M. Fujira, Thin Solid Films 273 (1996) 209.
- [20] V.N. Savvateev, A.V. Yakimov, D. Davidov, R.M. Pogreb, R. Neumann, Y. Avny, Appl. Phys. Lett. 71 (1997) 3344.
- [21] L.S. Hung, J. Madathil, Thin Solid Films 410 (2002) 101.
- [22] P.E. Burrows, G. Gu, S.R. Forrest, E.P. Vicenzi, T.X. Zhou, J. Appl. Phys. 87 (2000) 3080.
- [23] M. Meier, S. Karg, W. Riess, J. Appl. Phys 82 (1997) 1961.
- [24] P.W.M. Blom, M.J.M. de Jong, J.J.M. Vlegaar, Appl. Phys. Lett. 68 (1996) 3308.
- [25] H. Antoniadis, M.A. Abkowitz, B.R. Hsieh, Appl. Phys. Lett. 65 (1994) 2030.
- [26] P.E. Burrows, S.R. Forrest, Appl. Phys. Lett. 64 (1994) 2285.
- [27] P.E. Burrows, Z. Shen, V. Bulovic, D.M. McCarty, S.R. Forrest, J. Appl. Phys. 79 (1996) 7991.



Polymer field effect transistors made by laser patterning

M. Schrödner *, R.-I. Stohn, K. Schultheis, S. Sensfuss, H.-K. Roth

TITK Institute, Breitscheidstrasse 97, 07407 Rudolstadt, Germany

Received 6 January 2005; received in revised form 18 March 2005; accepted 29 April 2005

Available online 31 May 2005

Abstract

Polymer field effect transistors (PFETs) were made from polymeric semiconductors and insulators on flexible polymeric substrates. The electrodes were patterned from thin films of conducting polymers or metals using an excimer laser. This technique yields highly resolved source and drain electrode patterns with channel lengths below 10 μm which is a preposition for fast transistors and electronic circuits. Together with the available processing rates this technique makes a well-balanced compromise between pattern resolution and processing demands. Moreover, these PFETs show a long-term stability of more than two years without any special protection.

© 2005 Elsevier B.V. All rights reserved.

PACS: 85.30.Tv; 79.20.Ds; 73.61.Ph

Keywords: Organic field effect transistor; Laser patterning; Conjugated polymers; Poly(3-alkylthiophene)

1. Introduction

Plastic electronics based on organic semiconductors is a very promising technology to enter the low cost low performance segment of the electronic market. Radio frequency identification systems like ident tags, electronic watermarks, smart cards, electronic labels can be produced in a large

scale. Thin film transistors for active matrix displays seem to be possible as well.

Organic field effect transistors (OFETs) with the conjugated polymer polythiophene as semiconductor were first reported by Kozuka and co-workers [1,2] in 1987. Since this time, many progress concerning device parameters as well as fabrication technologies could be achieved. The polythiophene as semiconductor was followed by soluble poly(3-alkylthiophenes), polyfluorenes, poly(thienylene-vinylene) [3–9] and low molecular compounds like oligothiophenes [10–12] or pentacene [12,13]. The polymers have the advantage of easy processability

* Corresponding author. Tel.: +49 3672 379553; fax: +49 3672 379379.

E-mail address: schroedner@titk.de (M. Schrödner).

from solution whereas the low molecular compounds possess a high carrier mobility exceeding $0.1 \text{ cm}^2/\text{V s}$ for polycrystalline materials and more than $1 \text{ cm}^2/\text{V s}$ for single crystallites [11,14].

The prerequisite for a successful application of OFETs is the realisation of sufficiently good device parameters using extreme low-cost technologies in high throughput processes. The selection of suitable technologies depends among others on the materials used. The use of soluble polymers which can be easily processed from solutions or pastes should be favoured. This holds for all functional layers (electrodes, semiconductor, insulator) and processing steps necessary, i.e., the resulting device is an all-polymer field effect transistor (PFET).

At the sight of these demands, several technological approaches have been proposed and tested. For patterning of source–drain electrodes, which is one of the most important steps, printing techniques like ink-jet printing [9], microcontact printing (μCP) [15–17], offset printing [18] and pad printing [19] are under investigation.

To achieve good dynamic parameters, i.e., a high cut-off frequency, the channel length L should be as low as possible, possibly smaller than $15 \mu\text{m}$. Lithographic processes can yield such fine patterns, but they do not fit well to high throughput processes. Laser assisted techniques can partially close this gap. In [20] a laser generated thermo-transfer process is described, which allows the generation of conducting tracks by a selective transfer of $5 \mu\text{m} \times 2.7 \mu\text{m}$ pixels of a conducting polymer. The throughput is $0.1 \text{ m}^2/\text{min}$.

In this paper, we present results on PFETs using electrodes patterned by UV-laser ablation. This method can be applied to several conductors like polymers, metals or oxides. It has the potential to combine a high pattern resolution with a moderate throughput. In a previous paper, we already demonstrated patterns down to $1 \mu\text{m}$ spacing made by UV-laser ablation of the conducting polymer poly-3,4-ethylenedioxythiophene (PEDOT) [7].

The combination of PFETs to integrated circuits (IC) like inverters and ring oscillators was also successfully demonstrated by several groups [3,4,6,9,13,17,21,22]. Ring oscillators made from semiconducting polymers could be operated at

106 kHz using channel lengths of 2 and $5 \mu\text{m}$ [21]. De Leeuw and co-workers realised a fully functional 64-bit-code generator which consists of about 700 OFETs [22].

Despite the progress made, much further research is still necessary to develop organic based electronics inclusive appropriate techniques for commercial production. Besides, a further improvement of transistor and IC parameters many groups in the world work on the development of a suitable technology for a mass production of low-cost polymer ICs.

2. Experimental

PFETs were prepared in top-gate architecture (Fig. 1) by spin coating of regioregular poly(3-alkylthiophene) solutions (Aldrich) on polyethylene terephthalate (PET) or polyimide films. The plastic films contain the source and drain electrodes which were patterned by laser ablation from thin layers of conducting films. We used an excimer laser Compex 205 (Lambda Physik) operating at 248 nm wavelength and about 20 ns pulse length. The maximum repetition rate is 50 s^{-1} . The source–drain geometry is comb-like structured with geometry factors W/L ranging from 200 to 6000. The insulator was spin coated from a solution of poly(4-vinylphenol) (P4VP). The gates were made from gold, a graphite dispersion or a polyaniline (PANI)/polyamide (PA) composite (Ormecon L5000).

The electrical characterisation was done at ambient conditions with the help of source monitor units (SMUs) HP 4142 (Agilent) controlled

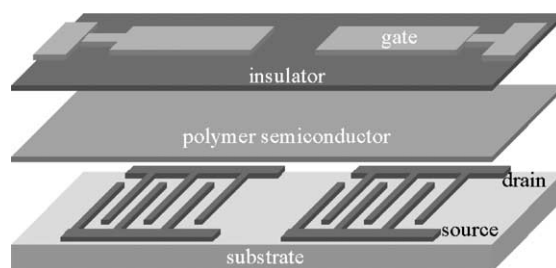


Fig. 1. Exploded view of two top-gate polymer FETs.

by the ICS software of Metrics Technol. Inc. The electrodes were contacted by use of a Suss wafer prober PM 5. The layer thickness was determined ellipsometrically using a Wollam spectral ellipsometer. Pattern quality was tested using the μ -surf confocal microscope (Nanofocus).

3. Results and discussion

3.1. Laser patterning of SID electrodes

The patterning of fine electrodes by laser ablation of thin films can be applied to many conducting materials like metals and conducting polymers. This is an one-step process without any subsequent treatment like developing, etching, stripping and so on. The material can be locally removed by an intense laser pulse of a fluence of 200–1000 mJ/cm². The photon energy, which in our case is 5 eV, is high enough to break chemical bonds of the illuminated material resulting in low molecular mass fragments moving away from the surface as an explosively expanding plasma cloud (plume).

The electrode pattern in the substrate plane is obtained by a 1:5 image projection of a positive

mask (chromium on quartz) using a special UV-objective. The illuminated area is 5 mm \times 5 mm for the optical setup used. Before passing the mask, the laser beam has been expanded and homogenized by an fly's-eye homogenizer which consists of an array of 7 \times 7 lenses at each side. For more details see [23].

We used this technique to generate source and drain electrodes from gold, copper, carbon black composites, PEDOT and polyaniline [24]. It is possible to remove the layers by only one or two laser pulses depending on the optical properties of the coating and base materials, the chemical structure, the layer thickness and the incident light energy. Pattern resolutions down to 1 μ m could already be demonstrated [7]. The quality of the electrode patterns can be examined by e.g., confocal microscopy (Fig. 2). The figure shows a well-defined PEDOT pattern of about 8 μ m channel length with sharp edges and low roughness.

3.2. Organic–inorganic hybrid FETs

PFETs with poly(3-hexylthiophene) (P3HT) and poly(3-dodecylthiophene) (P3DDT) as semiconductor were processed as described above.

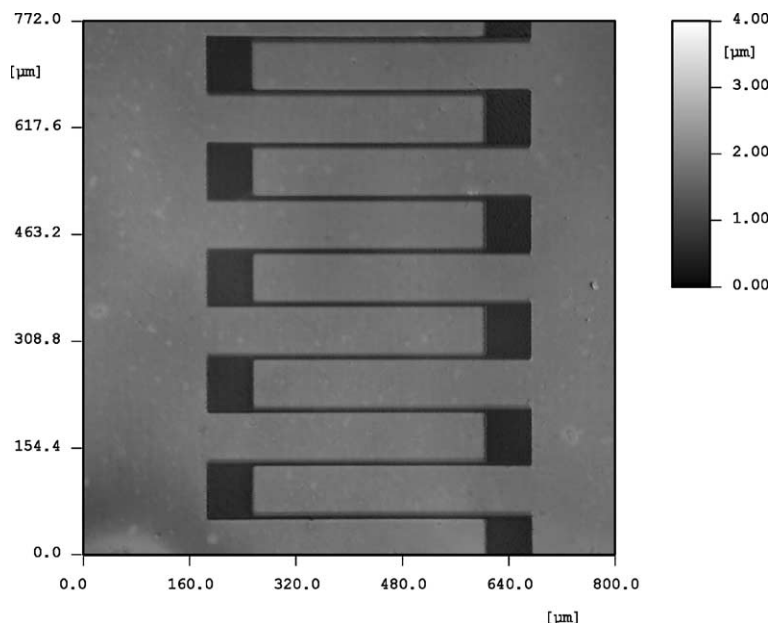


Fig. 2. Confocal micrograph of laser patterned PEDOT electrodes; the z -dimension is given as a gray scale; channel length $L = 8 \mu\text{m}$.

The FET structure is schematically drawn in Fig. 1. The thickness of the semiconductor and the insulator were typically about 20 nm and 400 to 1000 nm, respectively. Source, drain and gate electrodes were made by laser patterning of gold. Typical output and transfer characteristics are shown in Fig. 3. The transistors have low threshold voltages in a range of slightly negative values up to 0 V and an on/off ratio of about 10^3 (determined at $\Delta V_G = 25$ V). The inverse subthreshold slope of our devices normally exceeds 1 V/dec which is often found for organic FETs. Such high values can be ascribed to traps, originating from unintentional doping at the semiconductor–insulator interface or in the semiconductor bulk [25]. The charge carrier mobility, which has been derived from the slope of the transfer characteristics, is in the order of 10^{-2} cm²/V s which is a rather

high value for polymer semiconductors. One possible explanation can be again unintentional doping in the channel.

An important characteristic for applications is the long-term stability of the polymer or organic transistors. To get a first clue we have repeatedly measured some FETs from time to time. (These transistors were still patterned by conventional lithography, but in principle have the same layer setup as described above.) Surprisingly, we found that the transistors work over a long period of time with only small changes in their characteristics. Fig. 4 shows the output characteristics of one and the same transistor shortly after preparing and more than two years later (825 days). In the time between the transistor has been stored in the laboratory under ambient conditions without any special protection. This effect possibly can

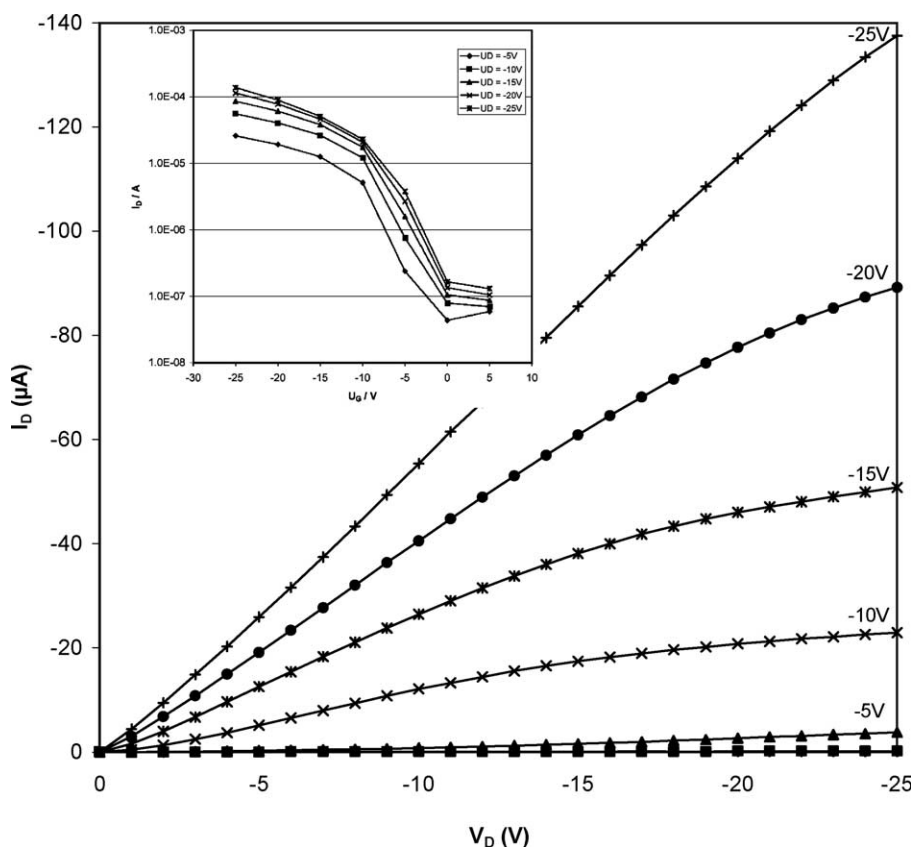


Fig. 3. Output characteristics of a PFET with gold as source–drain electrodes, P3HT as semiconductor, P4VP as insulator and gold as gate electrode ($W = 60$ nm; $L = 10$ μm); transfer characteristics is given as an insert.

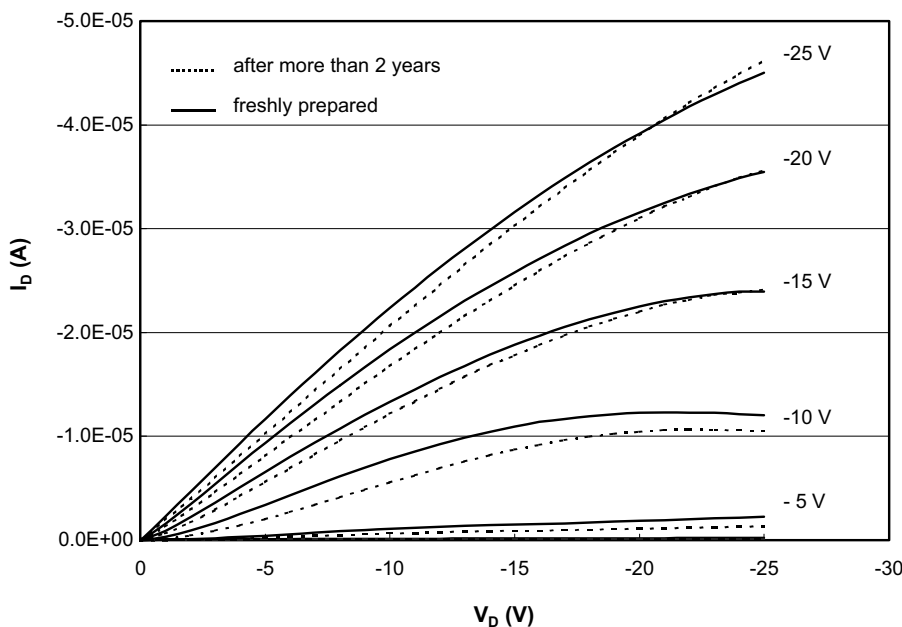


Fig. 4. Characteristics of one and the same transistor: freshly prepared (solid line) and after more than two years (825 days) storage in air (dashed line); electrodes: gold; semiconductor: P3DDT; insulator: P4VP.

result from the top-gate architecture used in our experiments. It provides a more or less effective encapsulation of the polymer semiconductor by the substrate from the bottom side and by the insulator and gate from the top side. The results are in accordance to [6], who used also a top-gate setup with similar materials.

3.3. All-polymer FETs

For the preparation of all-polymer FETs the metallic source and drain electrodes were replaced by the conducting polymer PEDOT which was patterned as described in Section 3.1. The semiconductor (P3DDT) and the insulator were coated as described above with the same thickness of the layers. The gate electrode was made from a graphite composite. The output and transfer characteristics of such an all-polymer FET is shown in Fig. 5. From the transfer characteristics a charge carrier mobility of $1.5 \times 10^{-3} \text{ cm}^2/\text{V s}$ and an on/off ratio of about 10^2 have been calculated. The transistors again have a slightly negative threshold voltage of about -5 V .

In another version, we used a polyaniline/polyamide composite as gate electrode material. The so obtained FETs had high drain currents of more than $100 \mu\text{A}$ and on/off ratios up to about 4.7×10^3 [26], but the lifetime was only a few days. These high currents, which significantly differ from those shown in Fig. 5, can be due to different solvent constituents of the gate polymer suspension which can cause partially swelling of the insulator and a subsequent penetration by polyaniline resulting in a reduction of the effective thickness of the insulator. This, together with the migration of counter ions may also cause the relatively low shelf life of this type of PFET.

4. Summary and conclusions

Our results demonstrate the feasibility of polymer FETs, inclusive all-polymer FETs, using UV-pulse lasers for electrode patterning. The high resolution capability of this technique allows the production of FETs with small channel lengths L in the lower micron range. Using state of the art

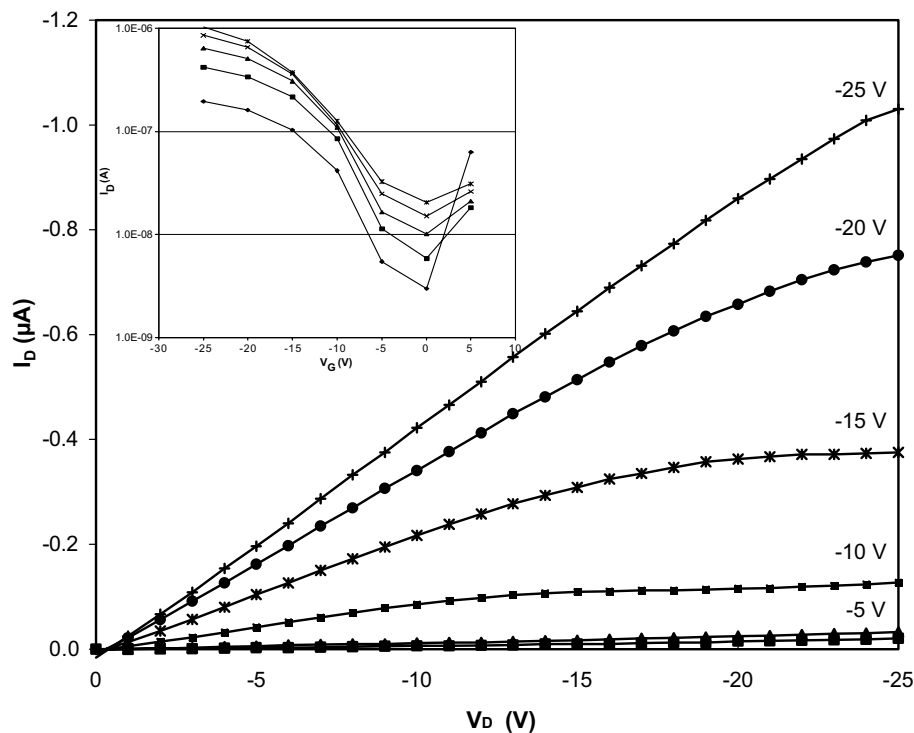


Fig. 5. Output characteristics of an all-polymer FET with PEDOT as source–drain electrodes, P3DDT as semiconductor, P4VP as insulator and graphite as gate electrode ($W/L \approx 320$); transfer characteristics is given as an insert.

excimer lasers it is possible to emit up to 300 light pulses per second. Assuming an illuminated area of about $0.5\text{--}2\text{ cm}^2$ per pulse, one can process an area of between 0.9 m^2 and 3.6 m^2 per minute. This is much higher compared to e.g., ink-jet printing, microcontact printing or the thermo-transfer laser process of [20]. On the other hand, it is much lower compared to high-volume offset or gravure printing which can process an area of more than $1000\text{ m}^2/\text{min}$ [18]. But taking into account the higher resolution of our laser technique it is possible to produce more transistors or electronic circuits per unit area. Furthermore, the dynamic performance of PFETs of smaller channel length should be much better due to the L^{-2} dependence of the cut-off frequency.

Taking into consideration all aspects, we believe that excimer laser patterning represents a good compromise between pattern resolution, which determines the device performance and processing speed. Moreover, this technique can be applied to

a lot of materials. The method enables cost-effective sheet as well as reel to reel patterning processes.

Long-term investigations demonstrated a rather high shelf life of more than two years without any additional protection for the FET build-up used.

Acknowledgement

Financial support from the German Bundesministerium fuer Wirtschaft und Technologie (project No. 1014/99 and 277/02) is gratefully acknowledged.

References

- [1] H. Koezuka, A. Tsumura, T. Ando, *Synth. Met.* 18 (1987) 699.
- [2] A. Tsumura, H. Koezuka, T. Ando, *Synth. Met.* 25 (1988) 11.

- [3] C.J. Drury, C.M.J. Mutsaers, C.M. Hart, M. Matters, D.M. de Leeuw, *Appl. Phys. Lett.* 73 (1998) 108.
- [4] G.H. Gelinck, T.C.T. Geuns, D.M. de Leeuw, *Appl. Phys. Lett.* 77 (2000) 1487.
- [5] A. Ullmann, J. Ficker, W. Fix, H. Rost, W. Clemens, I. McCulloch, M. Giles, *Mat. Res. Soc. Symp. Proc.* 665 (2001) C7.5.1.
- [6] J. Ficker, A. Ullmann, W. Fix, H. Rost, W. Clemens, *SPIE Int. Soc. Opt. Eng.* (2001) 4466.
- [7] H.-K. Roth, S. Sensfuss, M. Schrödner, R.-I. Stohn, A. Bernds, W. Clemens, *Materialwiss. u. Werkstofftechnik.* 32 (2001) 789.
- [8] Sirringhaus, N. Tessler, R.H. Friend, *Synth. Met.* 102 (1999) 857.
- [9] H. Sirringhaus, T. Kawase, R.H. Friend, T. Shimoda, M. Inbasekaran, W. Wu, E.P. Woo, *Science* 290 (2000) 2123.
- [10] G. Horowitz, D. Fichou, X. Peng, Z. Xu, F. Garnier, *Solid State Comm.* 72 (1989) 381.
- [11] G. Horowitz, R. Hajlaoui, F. Kouki, *Eur. Phys. J. Appl. Phys.* 1 (1998) 361.
- [12] G. Horowitz, D. Fichou, X. Peng, F. Garnier, *Synth. Met.* 41–43 (1991) 1127.
- [13] A.R. Brown, A. Pomp, C.M. Hart, D.M. de Leeuw, *Science* 270 (1995) 972.
- [14] T.W. Kelley et al., *Mater. Res. Soc. Symp. Proc.* 771 (2003) L6.5.1.
- [15] Y. Xia, D. Qin, G.M. Whiteside, *Adv. Mater.* 8 (1996) 1015.
- [16] T. Granlund, T. Nyberg, L. Stolz Roman, M. Svensson, O. Inganäs, *Adv. Mater.* 12 (2000) 269.
- [17] U. Zschieschang, H. Klauk, M. Halik, G. Schmid, C. Dehm, *Adv. Mater.* 15 (2003) 1147.
- [18] A. Huebler, U. Hahn, W. Beier, N. Lasch, T. Fischer, in: *Proc. 2 Int. IEEE Conf. Polym. Adhesives Microelectron. Photon.*, 2002, p. 172.
- [19] A. Knobloch, A. Bernds, W. Clemens, in: *Proc. 1 Int. IEEE Conf. Polym. Adhesives Microelectron. Photon.*, 2001, pp. 84–90.
- [20] G.B. Blanchet, Y.-L. Loo, J.A. Rogers, F. Gao, C.R. Fincher, *Appl. Phys. Lett.* 82 (2002) 463.
- [21] W. Fix, A. Ullmann, J. Ficker, W. Clemens, *Appl. Phys. Lett.* 81 (2002) 1735.
- [22] D.M. de Leeuw, G.H. Gelinck, T.C.T. Geuns, E. van Veenendaal, E. Cantatore, B.H. Huisman, *IEDM 2002 Tech Digest* 293 (2002).
- [23] H.-K. Roth, R.-I. Stohn, M. Schrödner, K. Schultheis, in: *Proc. 1 Int. Conf. Technol. Polym. Electron. (TPE04)*, 2004, pp. 65–70.
- [24] M. Schrödner, H.-K. Roth, S. Sensfuss, K. Schultheis, *e & i* (6) (2003) 2056.
- [25] S. Scheinert, G. Paasch, M. Schrödner, H.-K. Roth, S. Sensfuss, T. Doll, *J. Appl. Phys.* 92 (2002) 330.
- [26] M. Schrödner, S. Sensfuss, H.-K. Roth, R.-I. Stohn, W. Clemens, A. Bernds, *Proc. 2. Internat. IEEE Conf. on Polymers and Adhesives in Microelectron. and Photonics*, 2002, p. 188.



“Band bending” in copper phthalocyanine on hydrogen-passivated Si(1 1 1)

M. Gorgoi *, D.R.T. Zahn

Institut für Physik, Technische Universität Chemnitz, D-09107 Chemnitz, Germany

Received 18 March 2005; accepted 25 May 2005

Available online 17 June 2005

Abstract

Ultraviolet photoemission spectroscopy (UPS) and inverse photoemission spectroscopy (IPES) were employed to study the electronic density of states of copper phthalocyanine (CuPc) layers deposited onto hydrogen passivated Si(1 1 1) substrates. The highest occupied and lowest unoccupied molecular orbital (HOMO respectively LUMO) features are found to shift gradually in the same direction with increasing film thickness. At approximately 15 nm, the shifts saturate with a total amount of about 0.4 eV.

© 2005 Elsevier B.V. All rights reserved.

PACS: 79.60.-i; 79.20.Kz; 71.20.Rv

Keywords: Copper phthalocyanine; Ultraviolet photoemission; Inverse photoemission; LUMO; HOMO

1. Introduction

Considerable attention has been given to phthalocyanine materials in the last years because of their increasing importance in organic-based devices. Their attributes such as chemical and thermal stability and the tendency to form highly ordered layers result in an increase of device effi-

ciency [1]. Therefore, metal phthalocyanines are promising candidates for applications, e.g. in organic light emitting diodes, organic field effect transistors, photovoltaic solar cells and gas sensors. While a large number of articles were published regarding the characterization of bulk CuPc, only very few studies describe the interface formation between CuPc and different types of substrates, e.g. metals or semiconductors. Metal–organic interfaces have received considerable attention due to their important role in the injection of carriers into the organic layer [2–5]. Organic–organic heterojunctions were investigated

* Corresponding author. Tel.: +49 03715313009; fax: +49 03715313060.

E-mail address: mihaela.gorgoi@physik.tu-chemnitz.de (M. Gorgoi).

regarding carrier transport in multilayer light emitting structures [6]. Organic–inorganic semiconductor heterojunctions did not receive the same attention. They could, however, become relevant for future devices, in particular hybrid solar cells.

With respect to energy level alignment, it was shown for metal–organic interfaces that the vacuum levels in general do not align [4,7,8]. This assertion is also accepted for organic–inorganic semiconductor interfaces [3]. The difference in vacuum levels is attributed to interface dipoles, for which values between 0.2–1 eV were found for several metal–organic interfaces using photoemission spectroscopy. Another important issue is the occurrence of a “band bending”-like electrostatic energy shift for organic layers which was observed in many metal–organic systems [9]. In most cases, this shift is confined to a regime of only a few nanometres, which cannot be accounted for using the conventional band bending theory of inorganic semiconductors. Considering the Schottky model [10], at the CuPc/Au interface which has a built-in potential of 1.2 eV (interface dipole), for a depletion width of 10 nm the calculated density of carriers has a value of $1.2 \times 10^{17} \text{ cm}^{-3}$. This value is 10 orders of magnitude higher than the carrier concentration estimated from electrical measurements for undoped organic semiconductors such as metal phthalocyanines [11].

Energy shifts occurring in small thickness ranges i.e. 15 nm can be due to a change in the intermolecular interaction, for instance, due to a change in the molecular orientation as a function of the film thickness. This observation has been made for CuPc films grown on MoS₂ substrates [12]. Angular resolved ultraviolet photoemission spectroscopy using synchrotron radiation was used to determine the energy position of the HOMO and the orientation of the molecules as a function of the film thickness. For a layer thickness of 0.3 nm, the HOMO is found ≈ 1.05 eV below the Fermi level, while for films of 5 nm thickness, the HOMO shifts by about 0.3 eV to higher binding energies. Following the intensity of the HOMO as a function of emission angle and sample azimuth, the tilt angle of the CuPc molecular plane with respect to the substrate sur-

face is determined to be 0° and 10° for the 0.3 and 5 nm thick films, respectively.

Shimada et al. [13] studied the behaviour of CuPc on three types of layered substrates (no dangling bonds): semiconducting MoTe₂, semi-metallic highly oriented pyrolytic graphite (HOPG) and metallic TaSe₂. The substrates were chosen due to their different work function. Flat band condition—absence of both energy shifts and interface dipoles—was observed on HOPG and MoTe₂. In the case of CuPc on TaSe₂, two mechanisms were proposed: an interface dipole and “band bending” by n-type carriers with an overall value of 0.5 eV. Moreover Peisert et al. [14] demonstrated the presence of both mechanisms: interface dipole and “band bending” at the CuPc/Au interface. The value for the interface dipole was estimated to be 1.2 eV. On the other hand, for the CuPc/GeS(110) interface no “band bending” is present and the determined interface dipole has a value of 0.5 eV. All these studies employ a combination of ultraviolet photoemission spectroscopy and X-ray photoemission spectroscopy, which allows the determination of HOMO position of the organic material and the interface chemistry, but not the LUMO position. The LUMO can be determined by employing inverse photoemission (IPES) experiments. Having the energy position for both HOMO and LUMO, the transport gap E_t can be determined.

It is known that wet chemical etching of silicon produces ideally H-terminated Si(111) surfaces [15]. This type of non-reactive surface is preferred for organic molecular beam deposition (OMBD) since it favours ordered arrangement of the organic molecules. The present paper focuses on characterizing the interface formation between CuPc and H-Si(111) using UPS and IPES measurements as a function of film thickness. The results of this work complement the picture of thickness dependent energy level shifts in organic materials, particularly in the class of phthalocyanine materials.

2. Experimental

Hydrogen-passivated p-type, (111) oriented silicon with a doping concentration of approximately

$1.5 \times 10^{15} \text{ cm}^{-3}$ was used as the substrate. The passivation process consists of a wet chemical etching in a solution containing HF 40%. After the passivation process, the samples were transferred into UHV. All measurements were performed on freshly evaporated organic layers. Sublimed CuPc provided by Sensient Imaging Technologies GmbH (former SynTec) was employed with no further purification. The organic material was evaporated from Knudsen cells kept in a temperature range of 340–370 °C. During OMBD, the pressure was better than 2×10^{-8} mbar. The evaporation rates were in the range of 0.1–2 nm/min and the substrate was kept at room temperature. The film thickness and the evaporation rate were determined by means of a quartz crystal microbalance and confirmed by post-growth ellipsometry measurements. The UPS and IPES measurements were performed on two UHV systems (base pressures 3×10^{-10} and 8.5×10^{-10} mbar, respectively), each comprising an analysis and a preparation chamber. UPS spectra were recorded in normal emission with a hemispherical analyser and using He I radiation (21.22 eV), providing an overall resolution of 0.1 eV. The IPES experimental set-up working in the isochromat mode is a “home” built system. The fixed-energy photon detector [16] consists of a Geiger–Müller tube with a magnesium fluoride (MgF_2) window filled with a gas mixture containing ethanol and argon. The ionisation energy of ethanol and the transmission function of the MgF_2 provide a value of 10.9 eV as the nominal detection energy of the detector. A low energy electron gun [17] was used to produce a monoenergetic electron beam. The overall IPES instrumental resolution, estimated from the width of the Fermi edge measured on an Ar sputtered nickel sample, is 0.4 eV. Spectra were recorded at normal incidence with a current density in the range of 10^{-6} A/cm^2 . This value is low enough in order not to damage the organic film [3].

3. Results and discussion

Fig. 1 depicts the thickness-dependent ultraviolet photoemission and inverse photoemission spectra of CuPc deposited on H–Si(111). The spectra

were normalized with respect to the highest peak and shifted vertically for clarity. The HOMO and LUMO peak and onset positions are marked by vertical bars. The three UPS characteristic peaks for CuPc³ already appear at very low coverage (0.5 nm). Zooming into the HOMO region as shown on the right hand side of Fig. 1(a), a strong shift of the HOMO peak and onset positions towards higher binding energies is observed with increasing thickness. The shift shows a saturation tendency above 10 nm. The overall value of the shift is approximately 0.4 ± 0.07 eV. The same amount of shift is found in the LUMO position as a function of thickness as shown in Fig. 1(b). Similar to the UPS case, the CuPc features appear for 0.5 nm and become better resolved for higher thicknesses. The LUMO shifts towards the Fermi level with increasing film coverage. To determine the LUMO peak positions, a polynomial background was subtracted and the remaining peaks were fitted with Gaussian functions. In addition, the LUMO onsets were determined with respect to the Fermi level by a linear extrapolation of the low energy edge of the LUMO feature after background removal. The determination of the LUMO onsets in IPES presents an experimental difficulty due to the broadening effects as a consequence of the resolution (0.4 eV) which leads to a smearing out of the features. However, the onset positions are determined after deconvoluting the spectra with a Gaussian function that has a FWHM of 0.4 eV. In this manner, the effect of the IPES resolution is more or less eliminated.

Fig. 2 summarizes the resulting HOMO–LUMO peak and onset positions as a function of film thickness and with respect to the Fermi level. The HOMO–LUMO peak-to-peak difference calculated for all coverages is approximately 2.9 ± 0.2 eV. The transport gap determined as the difference between the onset positions of LUMO and HOMO is found to be 2.2 ± 0.2 eV. This value is in rather good agreement with the one determined by Hill et al. using UPS–IPES [3] (2.3 ± 0.4 eV), but somewhat larger than the one determined by cyclic voltammetry [18] (1.71–1.84 eV).

The evolution of the electron affinity (EA) determined using the LUMO onset energy

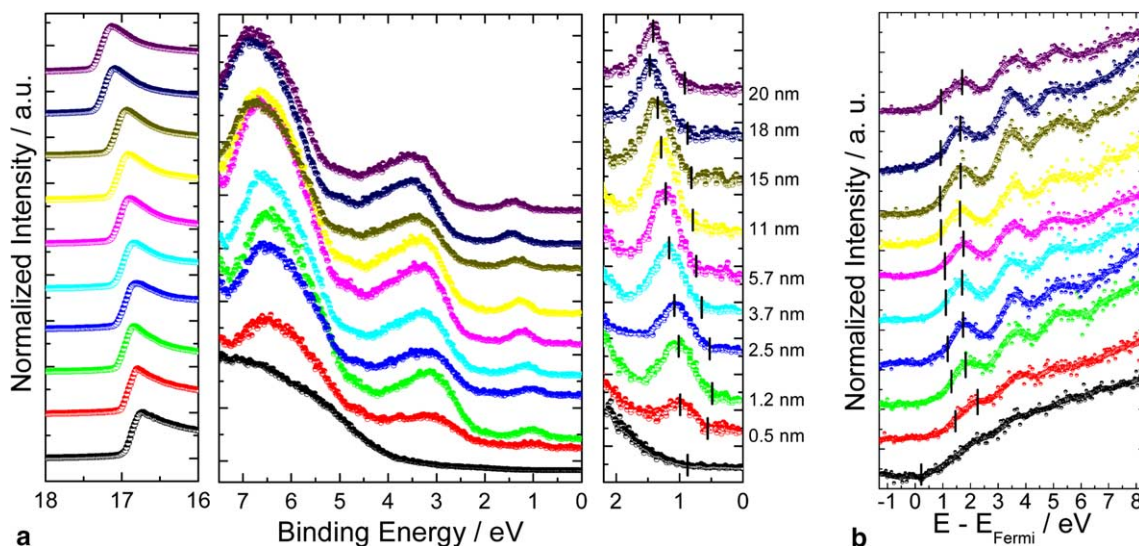


Fig. 1. (a) UPS thickness dependent measurements on CuPc/H-Si(111); (b) IPES thickness dependent measurements on CuPc/H-Si(111).

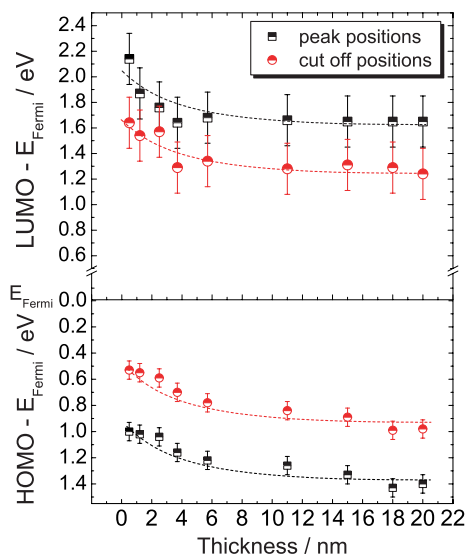


Fig. 2. The HOMO–LUMO peak and onset positions. The dotted curves are plotted as a guide for the eye.

position, work function (ϕ) and ionisation energy (IE) as a function of the CuPc thickness is presented in Fig. 3. For simplicity, the band bending of the substrate is omitted so that the energy levels corresponding to the substrate represent those of

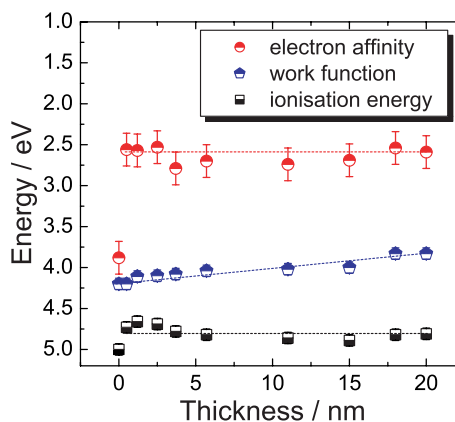


Fig. 3. EA, ϕ and IE of the CuPc film as a function of its thickness. The 0 point thickness represents the values for the H-Si surface.

the substrate surface. At zero coverage, the values of EA, ϕ and IE of the hydrogen-passivated silicon were included. The EA of H-Si was estimated using the known transport gap of silicon 1.12 eV and the onset position of the valence band maximum (VBM) from the UPS measurement. The dashed lines are plotted as a guide to the eye. When 0.5 nm of CuPc is deposited, a sudden

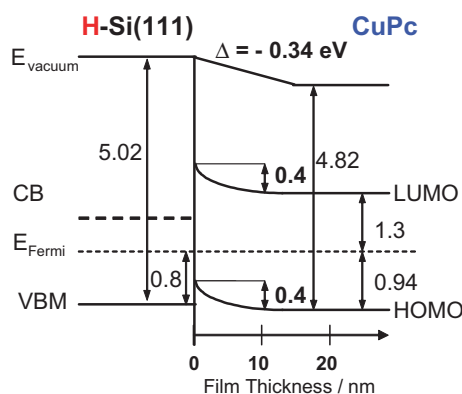


Fig. 4. Schematic energy level diagram of the CuPc/H-Si(111) interface.

change of EA and IE occurs. Proceeding to larger CuPc thicknesses, EA and the IE remain constant. On the other hand, the work function linearly increases as a function of thickness.

Fig. 4 summarizes the measurements by showing the energy band diagram of CuPc/H-Si(111) interface. The determined values for thick CuPc layer (20 nm) are $IE = 4.82 \pm 0.07$ eV, $\phi = 3.88 \pm 0.07$ eV and $EA = 2.5 \pm 0.2$ eV. An interface dipole of 0.34 ± 0.07 eV is measured as well. The onset positions of the HOMO and LUMO were employed in order to sketch the energy band diagram and to calculate these values. In the case of H-Si(111), the onset position of the VBM was taken into consideration for determining the $IE = 5.02 \pm 0.07$ eV and $\phi = 4.22 \pm 0.07$ of the surface. The VBM is obtained in the direction perpendicular to the (111) plane of silicon. However, the conduction band minimum is not situated in the same direction [10]. The conduction band (CB) position of H-Si(111) was determined by IPES and it represents a local minima in the energy scale of the unoccupied states of the hydrogen-passivated silicon surface.

Considering again the spectra in Fig. 1(a) and (b), it should be noted that all the peaks shown are gradually shifting with increasing CuPc thickness while the relative distance between the peaks remains unchanged. This indicates that no chemical interaction occurs during the interface formation process. Furthermore, no marked changes in

the peak shape of the HOMO as well as LUMO features are observed. The values of the full width half maximum (FWHM) for the HOMO and the LUMO are almost constant as a function of film thickness and have values of 0.50 and 1.1 eV without deconvoluting with the instrumental resolution, respectively. Calculations of the band structure for the β -metal free phthalocyanine suggest that the FWHM of the HOMO and LUMO are in the range of 0.1–0.4 eV along the molecular stacks where the molecules have the greatest π – π overlap [19]. The FWHM of the HOMO observed for individual phthalocyanine molecules in the gas phase has a value of 200 meV [20]. In the gas phase, molecule–molecule interaction is negligible and as a consequence, the observed HOMO does not have a contribution from the vibrational coupling of adjacent molecules. Consequently, the broadening of the HOMO even at a low CuPc coverage suggests the development of a band structure, i.e. molecule–molecule interaction.

Above 15 nm CuPc coverage, the energy shift saturates. At this point, the CuPc layer has reached the characteristics of the bulk-like organic material. The CuPc molecular bulk configuration presents the HOMO state at ~ 1.6 eV binding energy (BE) and two other molecular levels at higher BE [3,21] with respect to the Fermi level.

The energy shift that appears at the H-Si(111)/CuPc interface might have several explanations. As already discussed for metal–organic interfaces [3,14], the formalism of electrostatic band bending model can hardly explain the formation of these interfaces. Applying Poisson's equation as for inorganic semiconductors, using a depletion width of 15 nm, the built-in potential calculated from the difference of ϕ of H-Si and CuPc, and the reported relative dielectric constant of CuPc (about 5) [22], the charge carrier density is found to be very high, i.e. 2.3×10^{16} cm^{-3} . Consequently, the results of such an interpretation would be unreasonable since the intrinsic carrier concentration of CuPc¹¹ was previously estimated to be $\sim 10^7$ cm^{-3} .

Even though the conventional band bending model is quite unlikely to explain the energy shifts at the CuPc/H-Si interface, this model was not completely ruled out in previous publications

[13,23]. The formation of inorganic–organic semiconductor interfaces is still under discussion. Possible factors which can affect the interfacial layer are chemical interaction, polarization in the molecular layer and a surface rearrangement. The appearance of the energy shift due to charge transfer occurring as a result of chemical interaction may be excluded since the distance between the gradually shifting peaks as well as their line shape remains unchanged. In the case of chemical interaction, the appearance or disappearance or at least changes in the line shape of features in the valence band is expected. Polarization in the molecular layer is consistent with such energy shifts in the HOMO position as found by Peisert et al. [14] and initially considered for other organic molecules as well, i.e. perylene derivatives [3]. The distribution of charge on the molecules changes with the changing of environment from the hydrogen-passivated silicon substrate to the thick CuPc film. Moreover, this is also influenced by the slightly different arrangement of the molecules in the vicinity of the substrate compared with the ones in the thick film. Furthermore, the surface roughness of the substrate may also play a role in the overall molecular arrangement. Nakamura et al. [24] determined the growth mode of CuPc on a NH_4F passivated Si(111) substrate. The molecular column of CuPc was found to be parallel to the surface on a relatively rough substrate, while the column was found perpendicular to the Si(111) plane on an atomically flat substrate. The hydrogen passivation involving HF immersion was already proven to produce a relatively rough substrate surface [25,26]. Considering that the FWHM values of the HOMOs are not changing, the adsorption geometry of CuPc molecules may be estimated. The molecules seem to form clusters even at a monolayer coverage, which would grant them already bulk like properties and result in band formation. Peisert et al. [14] determined that CuPc on polycrystalline gold behaves in a similar way. Comparing the polycrystalline gold surface and the H–Si(111) surface, a common characteristic is found: namely the relative large roughness of both substrates. Although the wet chemical treatment based on HF dip gives

an ideally hydrogen terminated surface, this surface is non-uniform [27]. By means of STM, the estimated value of the roughness is about 3–4 Å. This may favour the clustering of the molecules in the first monolayers. Furthermore, in order to determine the influence of the surface roughness on the energy shifts, we performed another set of UPS-IPES experiments on CuPc/H–Si(111) systems with a slightly different hydrogen-passivation treatment (spectra are not shown here). The details of the passivation procedure are given elsewhere [28]. The roughness of H–Si(111) is then in the range of 2–3 Å as judged from STM images. The ionisation energy and the work function of the H–Si(111) are in excellent agreement with the ones determined above. The values are 4.94 ± 0.07 and 4.24 ± 0.07 eV, respectively. Moreover, the same value of 0.4 ± 0.07 eV is found to represent the energy shift of HOMO and LUMO as a function of CuPc film thickness. The shift saturates in the same manner above 15 nm. These results indicate that the surface roughness of the substrate does not play a major role for the energy shifts at the interface.

Several other studies have shown that the molecules change their orientation as a function of layer thickness [29–31]. An incomplete overlapping of the CuPc molecules results in a partial superposition of the π -orbitals. As a consequence, when a change in molecular orientation occurs, it will result in a change of the intermolecular interaction and will affect of the π -electron system. The HOMO and LUMO features correspond to π -character molecular orbitals [21,32]. Consequently, any change of molecular orientation will influence the recorded UPS and IPES spectra and the HOMO and LUMO features, respectively. Following this hypothesis, angular dependent NEXAFS was performed on the CuPc/H–Si(111) system. These NEXAFS spectra reveal a change in the molecular orientation of CuPc from monolayer range to thick films. At 0.5 nm CuPc, the orientation of molecular plane with respect to the substrate was found to be $70^\circ \pm 2^\circ$ while for 20 nm the angle is $90^\circ \pm 1^\circ$ [33]. Thus, the rearrangement of the CuPc molecules is most likely the reason for the observed energy shifts at the

CuPc/H–Si(111) interface, since the energy shifts are independent of surface treatment and surface roughness.

4. Summary

The interface between CuPc and hydrogen-passivated silicon was investigated using UPS and IPES and their electronic properties were determined. The measurements as a function of film thickness show a energy shift of 0.4 eV of the HOMO and LUMO bands at the CuPc/H–Si(111) interface. The transport band gap, however, remains constant at 2.2 ± 0.25 eV. The rearrangement of the CuPc molecules is attributed as being the cause of such type of energy shifts. The energy level alignment was determined for the CuPc/H–Si(111) system.

Acknowledgement

The authors acknowledge the EU funded Human Potential Research Training Network DIODE (Contract No.: HPRN-CT-1999-00164) for the financial support.

References

- [1] S. Forrest, *Chem. Rev.* 97 (1996) 1793.
- [2] H. Peisert, M. Knupfer, J. Fink, *Appl. Phys. Lett.* 81 (13) (2002) 2400–2402.
- [3] I.G. Hill, A. Kahn, Z.G. Soos, R.A. Pascal Jr., *Chem. Phys. Lett.* 327 (2000) 181.
- [4] I.G. Hill, A. Rajagopal, A. Kahn, Y. Hu, *Appl. Phys. Lett.* 73 (1998) 662.
- [5] I.G. Hill, A. Kahn, *J. Appl. Phys.* 86 (1999) 42116.
- [6] Y. Hirose, W. Chen, E.I. Haskal, S.R. Forest, A. Kahn, *Appl. Phys. Lett.* 64 (1994) 3482.
- [7] H. Ishii, K. Sugiyama, E. Ito, K. Seki, *Adv. Mater.* 11 (1999) 605.
- [8] Narioka.H. Ishii, D. Yoshimura, M. Sei, Y. Ouchi, K. Seki, S. Hasegawa, T. Miyazaki, Y. Harima, K. Yamashita, *Appl. Phys. Lett.* 67 (1995) 1899.
- [9] I.G. Hill, A.J. Makinen, Z.H. Kafa, *Appl. Phys. Lett.* 77 (2000) 1825.
- [10] W. Mönch, *Semiconductor Surfaces and Interfaces*, Springer-Verlag, Berlin, Heidelberg, 1995.
- [11] N.B. McKeown, *Pthalocyanine Materials: Synthesis, Structure and Function*, Cambridge University Press, Cambridge, MA, 1998.
- [12] K.K. Okudaira, S. Hasegawa, H. Ishii, K. Seki, Y. Harada, N. Ueno, *J. Appl. Phys.* 85 (1999) 6453.
- [13] T. Shimada, K. Hamaguchi, A. Koma, F.S. Ohuchi, *Appl. Phys. Lett.* 72 (1998) 15, 1869.
- [14] H. Peisert, M. Knupfer, T. Schwieger, J.M. Auerhammer, M.S. Golden, J. Fink, *J. Appl. Phys.* 91 (2002) 4872–4878.
- [15] S. Bouzidi, F. Coletti, J.M. Debever, P.A. Thiry, P. Dumas, Y.J. Chabal, *Phys. Rev. B* 45 (1992) 1187.
- [16] K.C. Prince, *Rev. Sci. Instrum.* 59 (1988) 741.
- [17] P.W. Erdman, E.C. Zipf, *Rev. Sci. Instrum.* 53 (1982) 225.
- [18] J. Simon, J.-J. Andre, *Molecular Semiconductors*, Springer-Verlag, Berlin, Heidelberg, 1985.
- [19] E. Orti, J.L. Bredas, *Synth. Met.* 29 (1989) 115.
- [20] D. Schlettwein, K. Hesse, N.E. Gruhn, P.A. Lee, K.W. Nebesny, N.R. Armstrong, *J. Phys. Chem. B* 105 (2001) 4791.
- [21] D. Schlettwein, N.R. Armstrong, *J. Phys. Chem.* 98 (1994) 11771.
- [22] M.K. Debe, *J. Vac. Sci. Technol. A* 10 (1992) 2816.
- [23] G. Paasch, H. Peisert, M. Knupfer, J. Fink, S. Scheinert, *J. Appl. Phys.* 93 (2003).
- [24] M. Nakamura, Y. Morita, Y. Mori, A. Ishitani, H. Tokumoto, *J. Vac. Sci. Technol. B* 14 (1996) 1109.
- [25] V.A. Burrows, Y.J. Chabal, G.S. Higashi, K. Raghavachari, S.B. Christman, *Appl. Phys. Lett.* 53 (1988) 998.
- [26] G.S. Higashi, Y.J. Chabal, G.W. Trucks, K. Raghavachari, *Appl. Phys. Lett.* 56 (1990) 656.
- [27] G.S. Higashi, R.S. Becker, Y.J. Chabal, A.J. Becker, *Appl. Phys. Lett.* 58 (1991) 1656.
- [28] T. Yasuda, D.E. Aspnes, D.R. Lee, C.H. Bjorkman, G. Lucovsky, *J. Vac. Sci. Technol. A* 12 (1994) 1152.
- [29] H. Ishii, K. Sugiyama, D. Yoshimura, E. Ito, Y. Ouchi, K. Seki, *IEEE J-STQE* 4 (1998) 24.
- [30] H. Peisert, T. Schwieger, J.M. Auerhammer, M. Knupfer, M.S. Golden, J. Fink, P.R. Bressler, M. Mast, *J. Appl. Phys.* 90 (2001) 466.
- [31] H. Yamane, S. Kera, S. Tanaka, H. Honda, T. Nakamura, H. Setoyama, K.K. Okudaira, N. Ueno, *PC74 ERPOS*, Prague, 2002.
- [32] H. Yoshida, K. Tsutsumi, N. Sato, *J. El. Spectrosc. Relat. Phenom.* 121 (2001) 83.
- [33] M. Gorgoi, G.N. Gavrila, W. Braun, D.R.T. Zahn, *BESSY Jahresbericht* 2004, p. 165.



Importance of ITO surface conditions for the interaction with thin CuPc layers

M. Andreasson^{a,*}, M. Tengelin-Nilsson^b, T.G. Andersson^a,
L. Ilver^b, J. Kanski^b

^a *Applied Semiconductor Physics, Microtechnology and Nanoscience, Chalmers University of Technology, S41296 Göteborg, Sweden*

^b *Department of Experimental Physics, Chalmers University of Technology and Göteborg University, Göteborg, Sweden*

Received 21 December 2004; received in revised form 17 June 2005; accepted 22 June 2005

Available online 21 July 2005

Abstract

The electronic interaction between the transparent anode material indium tin oxide (ITO) and the common organic hole injection material copper phthalocyanine has been investigated by means of angle-resolved UV photoemission. The study was made on two differently treated ITO substrates, both cleaned in common organic solvents and one of them heated in air after the cleaning. The heat treatment efficiently removes surface carbon-containing contamination, and has also an oxidizing effect. As a result, the ITO work function is increased by 0.4–0.6 eV. This surface preparation has significant impact on the electronic properties of adsorbed CuPc. We find that the Pc HOMO level, important for transport properties, is shifting by 0.5 eV depending on surface conditions. This is interpreted as an effect of Fermi level pinning within the gap of the spin-split Cu derived b_{1g} molecular orbitals.

© 2005 Elsevier B.V. All rights reserved.

PACS: 73.61.Ph; 79.60.Fr

Keywords: CuPc; ITO; UPS

1. Introduction

There is currently a growing interest in evaporated organic molecular layers due to the versatility of the molecular materials. Multilayer structures are implemented in devices like transistors, solar cells, and light emitters (OLEDs) [1–3]. OLEDs consist typically of an anode for hole injection, a

* Corresponding author. Tel.: +46 31 772 3327; fax: +46 31 772 3385.

E-mail address: mans.andreasson@mc2.chalmers.se (M. Andreasson).

hole transport layer (HTL), a recombination layer, an electron transport layer (ETL), and a cathode. Carriers are injected into the device by an applied electric field and are transported to the emissive region. The charge injection and transport properties are to a large extent controlled by the interfaces at the electrodes and between the active layers. The most common anode material is indium tin oxide (ITO), which has a relatively high work function, good transport properties, and high optical transparency in the visible range. The ITO work function is very sensitive to different surface treatments, such as chemical etching, oxygen or argon plasma treatment, as well as irradiation with UV light. After such treatments the work function can take values ranging from below 4 to above 5 eV [4,5]. The HTL layer is usually added to reduce the voltage needed to inject holes from the ITO into the optically active region. The HTL material is chosen such that its highest occupied molecular orbital (HOMO) is positioned between the Fermi level and the HOMO of the active layer. In addition to the HTL a thin buffer layer is sometimes grown in-between the ITO and the HTL, which further improves the OLED functionality. The predominantly used material for this purpose is copper phthalocyanine (CuPc) [6–9]. It has been suggested that the CuPc layer improves the mechanical properties of the devices, and experiments show that a thin film of CuPc makes it possible to obtain a continuous HTL layer of NPB on ITO [10]. Without this layer the NPB form islands.

The CuPc/ITO interface is of great interest, and particularly so the structural and electronic properties of the first few molecular layers. In this study we have used angle-resolved ultraviolet photoelectron spectroscopy (ARUPS) to examine this system on two differently treated ITO substrates. ARUPS is a highly surface sensitive probe and provides information about the electrostatic situation in the interface region, such as interface dipoles and the band offset situation.

2. Experimental

ITO films on glass substrates with a surface resistivity of $15 \Omega/\square$ and a thickness of 100 nm

were ultrasonically cleaned with acetone and methanol (15 min in each), and rinsed with deionised water. After this chemical cleaning one of the sheets was additionally heated in air at 400 °C for 20 min. The two samples were characterized with Auger electron spectroscopy (AES) for surface composition, and atomic force (AFM) and scanning tunnelling microscopy (STM) for surface morphology. The samples were then mounted on the same substrate holder and introduced into a combined ultra high vacuum (UHV) photoemission and deposition system. Commercially available CuPc (Sigma–Aldrich, purity >99% sublimation grade) was out gassed for ~5 h before evaporation onto the ITO substrates from a quartz crucible, mounted at a distance of approximately 15 cm from the substrate. The growth was monitored with a quartz crystal microbalance. The CuPc was deposited incrementally, to the total amount shown in Table 1. Assuming formation of the CuPc α -polymorph with the crystallographic *b*-axis oriented perpendicular to the surface (i.e., the molecules lying flat on the surface) and a density of 1.64 g/cm³ [11,12], the depositions would correspond to 1, 2, 4, 8, 16, 40 nominal monolayers on the heated surface, and 0.5, 1, 2, 4, 8 and 20 nominal monolayers on the wet-cleaned substrates. However, one should note that in an earlier study (of which we were unaware at the time of the present experiments) CuPc was found to grow in a standing orientation [13]. The UPS measurements were performed in a VG ADES 400 system connected to the evaporation chamber. The photoelectron spectra were excited with HeI light (21.2 eV) incident at 45° relative to the surface normal, and all spectra discussed in this paper were recorded in normal emission. The angular resolution was around 3°, and the energy resolution was set to 0.1 eV.

Table 1
The amount of CuPc deposited on the two substrates in nm

Substrate	Thickness (nm)					
Heated ITO	0.4	0.7	1.3	2.6	5.2	10.4
Wet cleaned	0.2	0.4	0.7	1.3	2.6	5.2

Using a density of 1.64 g/cm³ [12] and assuming unit sticking coefficients on the quartz crystal and the ITO substrate.

3. Results and discussion

Auger electron spectroscopy (AES) of the ITO substrates showed that the surface carbon, was significantly reduced after heating in air (see Fig. 1). Judging from the attenuation of the In and Sn signals, the initial thickness of the contamination layer was about 0.5 nm. The metal/oxygen ratio was estimated from Auger amplitudes, corrected for element sensitivities, but not for matrix effects. The observed metal/oxygen ratio was reduced from 1.4 to 1.2 in the heating process. Any oxygen content in the initial contamination layer, as adsorbed CO, would have changed the ratio in the opposite direction. We conclude that the ITO surface must have been oxidized by the heat treatment. The surface RMS roughness of the two samples was basically the same, about 1.4 nm as determined by atomic force microscopy (AFM) and scanning tunnelling electron microscopy (STM) measurements. Also the structures of the surfaces were similar, consisting of grains 20–50 nm in size. However, the image of the wet-cleaned surface reveals a smooth over-layer covering the ITO grains (see Fig. 2). Local spots with reduced conductivity on the heat-treated surface were also observed in the STM scans, mainly at the highest region of the grains.

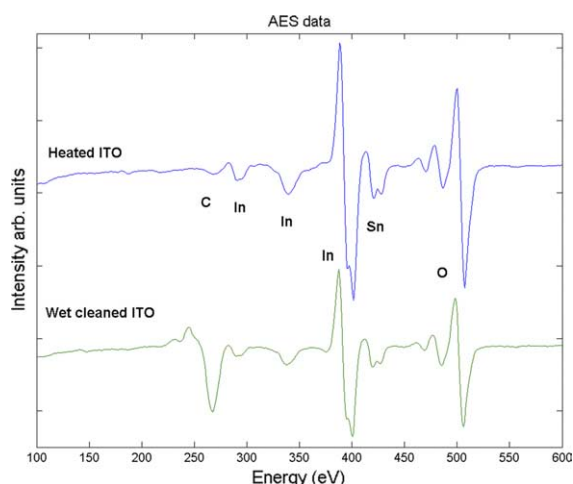


Fig. 1. Auger electron spectra of the two ITO substrates with the spectra on top from the heated substrate.

In the initial stages of deposition, the quantity of the deposited material is reflected by the spectral intensity of the species characteristic features. For non-clustered growth one expects the peak area (intensity) to increase linearly as a function of the amount of deposited material up to full monolayer coverage. A linear dependence can indeed be seen in the photoemission data, but the linearity is broken at a nominal coverage of about 2 ML (0.7 nm). From this we conclude that the growth geometry is not that assumed at the outset, i.e., a flat lying molecular structure, but closer to the standing orientation assessed in a previous study [13]. With such an arrangement the full densely packed monolayer would correspond to roughly 3 monolayers of flat lying molecules. The break observed at 2 ML of nominal thickness (0.7 nm) can be taken as an indication that the molecular orientation is slightly tilted, i.e., neither oriented perpendicular nor flat. We also note that the HOMO intensity develops differently for the two films, which indicates different structural properties.

In photoemission, the first important result is the observation of a modified ITO work function by the heat treatment. The spectral cut-off is shifted by about 0.5 eV to higher kinetic energy (reflecting the work function increase) and becomes significantly broadened (from ~50 meV to ~250 meV). The broadening of the cut-off on the heated surface shows that it is electronically more inhomogeneous, which may be connected with the local reduction in conductivity observed in the STM scans and/or different surface morphologies. The different electronic characteristics of the two surfaces are also reflected in the detailed electronic properties of the subsequently deposited CuPc, as will be shown in the following.

The photoemission spectra from the CuPc layers deposited on the two surfaces are on the whole very similar, except for a slight overall shift in energy. More detailed examinations reveal, however, some significant differences. In the remaining part of the paper we focus on the properties of the HOMO emission, since this structure is separated from other features, and hence easiest to analyze. The peak positions and widths were determined using a numeric peak fitting routine. Fig. 3 shows

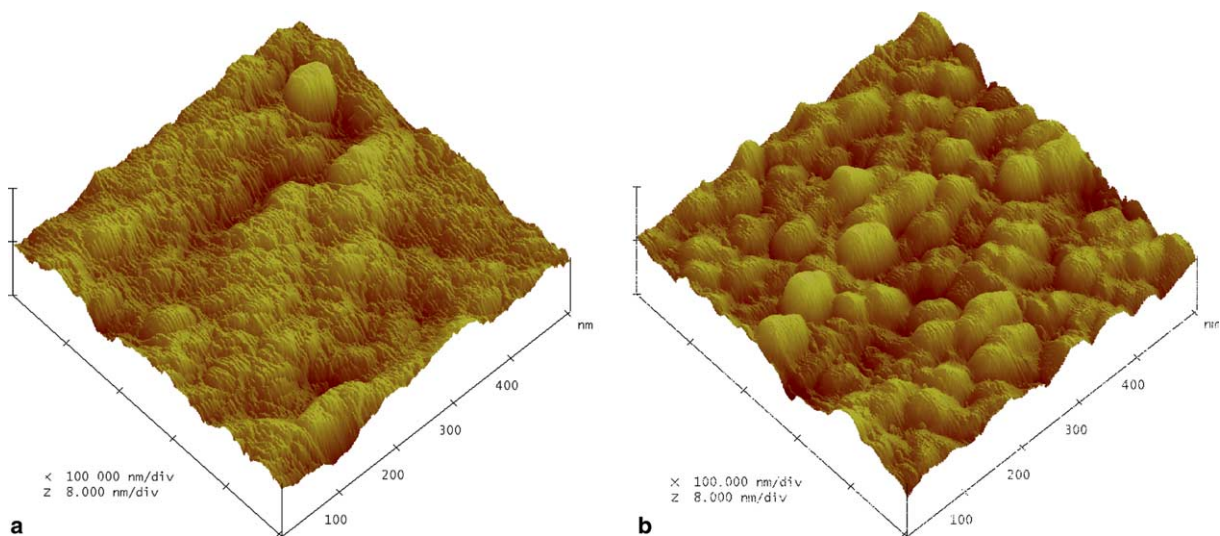


Fig. 2. AFM scans of the two ITO surfaces. (a) Shows the wet treated substrate and (b) the heat-treated substrate. The AFM measurements were performed in tapping mode.

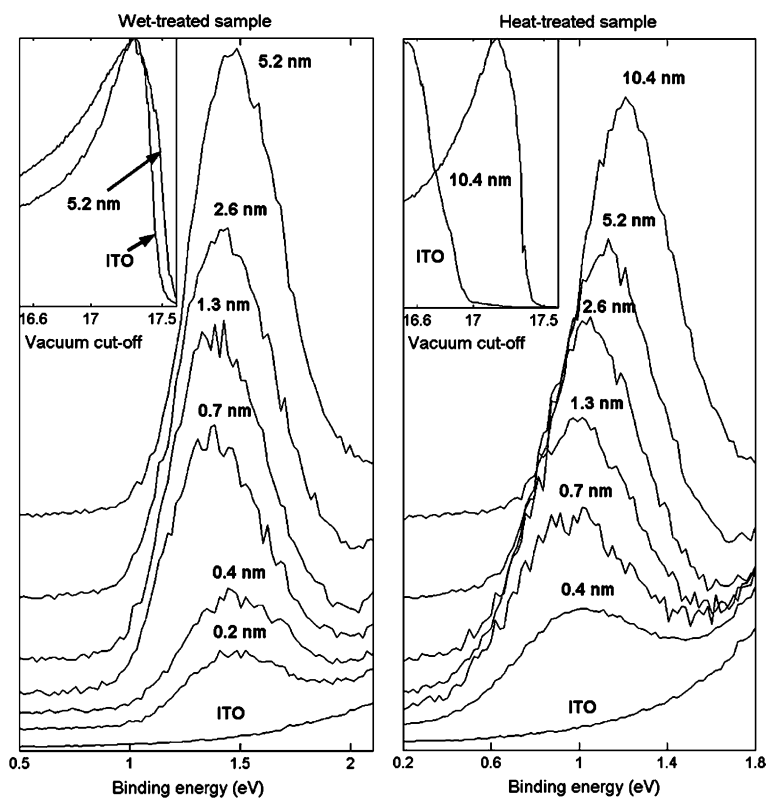


Fig. 3. HOMO evolution on the two substrates as a function of deposited film thickness. The wet-cleaned substrate is shown in the left spectra and the heated substrate in the right one.

spectra of the HOMO peak for the two samples and progressing film thickness. For the first layer, the HOMO on the wet-cleaned sample is located at about 0.5 eV higher binding energy compared to the heat-treated sample. For thicker films the difference is gradually reduced (see below). In agreement with previous studies we thus find that the energy difference between the ITO Fermi level and the HOMO of the CuPc varies with different ITO work functions [14–16]. This is in contrast to the results in [6] where the difference was found to be independent of the ITO work function. It should however be mentioned that the work function for all data in that study is very high ~ 5.1 – 5.35 eV [6]. The peak positions as well as their development as a function of thickness are clearly different on the two substrates. The variation in peak energy (shown in Fig. 4a) is larger for the heat-treated substrate, where for the first monolayer the HOMO peak appears around 1.0 eV below the Fermi level, and shifts to about 1.3 eV for the thickest layer. On the wet-cleaned substrate the HOMO peak behaves differently. At low coverage the energy changes rapidly, but becomes quite constant (around 1.5 eV) above 4 ML (1.3 nm) nominal coverage.

The differences in HOMO energies can be understood in terms of the detailed electronic structure of CuPc. According to spin-unrestricted calculations [17], two Cu 3d derived states (~ 0.5 eV separation) are located in the HOMO-LUMO gap of the Pc, one of them is filled, the other empty. The density of states (DOS) between these two is very low in the molecular film, and by virtue of their relatively high DOS they define two intrinsic pinning levels.

The formation of molecular solid interfaces is usually described within the Shottky model, i.e., emphasising the role of the work functions and affinities of the free surfaces. Deviations from the “intrinsic” alignment are then accumulated in interface dipoles. Adsorption on a low work function surface will thus result in pinning at the upper of the two states, and for a high work function surface the pinning will be shifted to the lower state. For moderate differences in electronegativities the charge transfer is small, and the pinning should occur at the high (low) energy side of the lower

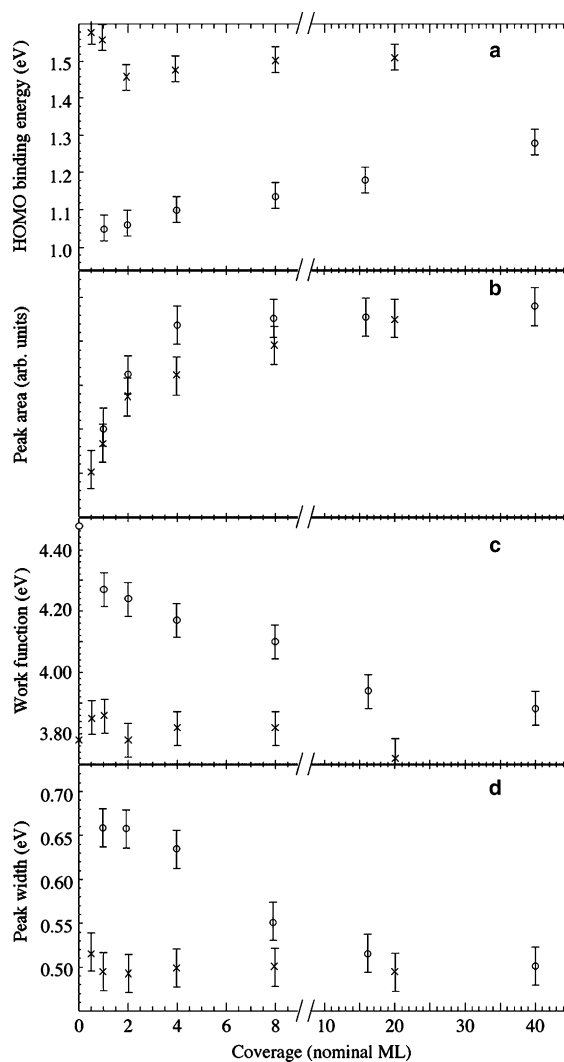


Fig. 4. The four figures show the energy position, HOMO peak area, work function, and peak width for the CuPc thin films on the two substrates, as a function of deposited thickness in no. of nominal ML. The symbol (x) means the wet cleaned and (o) the heat-treated substrate.

(higher) lying d-state. This account for the occurrence of two distinctly different initial pinning situations found in our data, and explains also similar observations in a recent spatially resolved photoemission study of CuPc [18]. With this reasoning we can also understand the changes of the HOMO energy with increasing CuPc coverage. On the heated substrate we have electron transfer

from CuPc to ITO forming a small interface dipole. Each additional CuPc layer will contribute filled Cu-derived band-gap states, which will be shared with the previously deposited layers. In this way the CuPc charging will be “diluted” and the HOMO should shift gradually towards the position of the neutral molecule. For each given thickness the electrostatic situation in the CuPc layer can of course be described in terms of band bending, and the discussion above describes the gradual development of a band bending situation. The difference from a “conventional” band bending is that the charge depletion does not involve defect states (impurities), but intrinsic Cu-derived states. Another distinction from band bending at inorganic semiconductor surfaces is that the present effects are not induced by surface defects. Band bending has earlier been reported for CuPc films on ITO treated with UV-ozone [6], and argon/oxygen ion sputtering [16]. This indicates that more aggressive cleaning methods produce a more reactive surface.

The carbon-contaminated surface shows a much smaller thickness dependent shift. In this case the alignment occurs close to the charge neutrality level of the molecule, i.e., between the Cu-derived gap states and the situation resembles a “flat band” system. In this respect the data are similar to those reported by Hill and Khan [15], who studied deposition on ITO prepared in a similar way as our wet treatment.

Out-diffusion of oxygen from the ITO substrate could also modify the electrostatic situation within the CuPc layer [19]. We do not believe that this occurs in the present case, because similar thickness dependence is observed for CuPc layers on clean Cu surfaces [16]. Spectral shifts in photoemission can also be due to final state effects. However, the dielectric properties of CuPc and ITO are comparable (with dielectric constants between 3 and 4) [20,21], which means that screening effects should not give any significant energy shifts as function of film thickness. Therefore, we ascribe the major part of the thickness dependence of the HOMO to the mechanism described above. The changes at low coverage up to 1 ML (0.4 nm) can be explained by increasing efficiency of intra-layer screening, going from individually adsorbed molecules to a complete layer. The increased CuPc

adlayer–substrate distance on the wet-cleaned surface, as a consequence of the contamination layer, implies a reduced substrate related screening of the ionized final state. For the heated surface, the CuPc molecules interact directly with the ITO surface, and the substrate related screening is initially more efficient.

The ionization potentials (IP) of the two samples (determined from the relation $IP = h\nu - (E_{\text{HOMO}} - E_{\text{cut}})$) are also different. Even after deposition of relatively thick layers the IP of CuPc on the heated ITO is about 70 meV smaller than for CuPc on the wet-cleaned substrate. This difference is small but nevertheless significant, as the spectra were recorded under identical experimental conditions (the two samples were studied in parallel, just by shifting the sample holder vertically in front of the electron energy analyzer). We can thus conclude that the two layers have different electronic properties.

We note that the shift in the HOMO energy level does not match the shift in vacuum cut-off energies which results in a thickness dependence of the ionization potential, see Fig. 4a and c, for both surfaces. We can thus conclude that the spectral energy shifts are *not purely* a result of different interfacial dipoles. The different ionization potentials of the two samples indicate that the CuPc layers are structurally dissimilar, confirming the conclusion drawn from the development of the HOMO intensity. The large difference in peak widths shown in Fig. 4d, where the peaks are wider for the heated substrate, can be explained by the fact that the heated surface is more inhomogeneous. This has already been commented in connection with the broadening of the low energy spectral cut-off. Such inhomogeneity may be very important for the electronic performance and stability of devices based on such structures.

4. Conclusions

From the combined spectroscopic data we conclude that in-air heat treatment of ITO is very effective in removing adsorbed carbon-containing species as well as changing the surface oxide composition. The electronic properties differ between

the two substrates, with a significantly higher work function for the heated one. The heated surface is also electronically more inhomogeneous. The binding energy of the CuPc HOMO is found to be lower on the heated substrate, which is interpreted as an effect of different pinning situations on the two surfaces. This indicates that the heat-treated substrate would be preferable for OLED fabrication over the wet-cleaned one because of the lower injection barrier due to a closer alignment of the ITO work function and CuPc HOMO level. However, the surface inhomogeneity may be disadvantageous for the stability of such devices.

References

- [1] C. Reese, M. Roberts, M. Ling, Z. Bao, *Mater. Today* 7 (8) (2004) 20–27.
- [2] J. Drechsel, B. Männig, D. Gebeyehu, M. Pfeiffer, K. Leo, H. Hoppe, *Org. Electron.* 5 (4) (2004) 175–186.
- [3] Z. Shen, P.E. Burrows, V. Bulovic, S.R. Forrest, M.E. Thompson, *Science* 276 (1997) 2009–2011.
- [4] L. Chkoda, C. Heske, M. Sokolowska, E. Umbach, F. Steuber, J. Staudigel, M. Stoßel, J. Simmerer, *Synth. Met.* 111–112 (2000) 315–319.
- [5] F. Nüesch, L.J. Rothberg, E.W. Forsythe, Q.T. Le, Y. Gao, *Appl. Phys. Lett.* 74 (6) (1999) 880–882.
- [6] S.M. Tadayyon, H.M. Grandin, K. Griffiths, P.R. Norton, H. Aziz, Z.D. Popovic, *Org. Electron.* 5 (2004) 157–166.
- [7] J. Kido, Y. Izumi, *Appl. Phys. Lett.* 73 (1998) 2721–2723.
- [8] H. Aziz, Z.D. Popovic, N.X. Hu, A.M. Hor, G. Xu, *Science* 283 (1999) 1900–1902.
- [9] S.A. Van Slyke, C.H. Chen, C.W. Tang, *Appl. Phys. Lett.* 69 (1996) 2160–2162.
- [10] E.W. Forsythe, M.A. Abkowitz, Y. Gao, C.W. Tang, *J. Vac. Sci. Technol. A* 18 (4) (2000) 1869–1874.
- [11] R. Hiesgen, M. Rübisch, H. Böttcher, D. Meissner, *Solar Energy Mater. Solar Cells* 61 (2000) 73–85.
- [12] A. Hoshino, Y. Takenaka, H. Miyaji, *Acta Cryst. B* 59 (2003) 393–403.
- [13] H. Peisert, T. Schwieger, J.M. Aurehammer, M. Knupfer, M.S. Golden, J. Fink, P.R. Bressler, M. Mast, *J. Appl. Phys.* 90 (1) (2001) 466–469.
- [14] S.T. Lee, Y.M. Wang, X.Y. Hou, C.W. Tang, *Appl. Phys. Lett.* 74 (5) (1999) 670–672.
- [15] I.G. Hill, A. Khan, *J. Appl. Phys.* 86 (4) (1999) 2116–2122.
- [16] H. Peisert, M. Knupfer, T. Schwieger, J. Fink, *Appl. Phys. Lett.* 80 (16) (2002) 2916–2918.
- [17] L. Guo, E. Ellis, K.C. Mundim, B.M. Hoffman, J. Porphyrins Phtalocyanines 3 (1999) 196–209.
- [18] T. Munakata, T. Sugiyama, T. Matsuda, M. Aida, N. Ueno, *Appl. Phys. Lett.* 85 (16) (2004) 3584–3586.
- [19] D. Zheng, Z. Gao, X. He, F. Zhang, L. Liu, *Appl. Surf. Sci.* 211 (2003) 24–30.
- [20] J. Zhang, J. Wang, H. Wang, D. Yan, *Appl. Phys. Lett.* 84 (1) (2004) 142–144.
- [21] S.H. Brewer, S. Franzen, *J. Phys. Chem. B* 106 (50) (2002) 12986–12992.



Fullerene based n-type organic thin-film transistors

Joshua N. Haddock, Xiaohong Zhang, Benoit Domercq, Bernard Kippelen *

*Center for Organic Photonics and Electronics, School of Electrical and Computer Engineering,
Georgia Institute of Technology, 777 Atlantic Dr NW, Atlanta, GA 30332, USA*

Received 27 April 2005; accepted 24 June 2005

Available online 19 July 2005

Abstract

Significant progress has been made in the area of p-type organic field effect transistors while progress in developing n-type materials and devices has been comparatively lacking, a limiting factor in the pursuit to develop complementary organic electronic circuits. Given the need for n-type organic semiconductors we have carried out studies using two different fullerene molecules, C₆₀ and C₇₀. Here, we report mobilities for C₆₀ ranging from 0.02 cm²/V s up to 0.65 cm²/V s (depending on channel length), and mobilities from 0.003 cm²/V s up to 0.066 cm²/V s for C₇₀. All devices were fabricated with organic films deposited under high vacuum but tested at ambient pressures under nitrogen.

© 2005 Elsevier B.V. All rights reserved.

PACS: 85.30.Tv; 85.65.+h; 73.61.Wp

Keywords: Organic electronics; Complementary logic; Thin-film transistors; Fullerenes

1. Introduction

Organic field-effect transistors (OFETs) hold promise for electronic applications where low cost, large area, simplified processing and mechanical flexibility are of interest. Individual transistors with field-effect mobilities greater than 1 cm²/V s, threshold voltages near 0 V, and on/off current ratios greater than 10⁶ are routinely achieved in thin films

of the p-type (hole transport) organic semiconductor pentacene [1]. This level of performance is comparable to that of amorphous silicon thin-film transistors used to drive some liquid-crystal displays. However, in order to realize applications such as organic complementary logic circuits [2], both p-type and n-type organic semiconductors are needed and should exhibit comparable electrical performance. In contrast, electron field-effect mobilities have only recently exceeded 1 cm²/V s; where the highest value reported in a thin-film device was 1.7 cm²/V s using the perylene-based compound PTCDI-C₈ [3]. The fullerenes are

* Corresponding author. Tel.: +1 404 385 5163; fax: +1 404 385 5162.

E-mail address: kippelen@ece.gatech.edu (B. Kippelen).

another well known class of n-type organic semiconductor that have previously been used for OFETs. In thin films of the fullerene C_{60} , reported field-effect mobility values have increased over time from $0.08 \text{ cm}^2/\text{V s}$, reported by Haddon et al. [4] to $0.56 \text{ cm}^2/\text{V s}$, reported by Kobayashi et al. [5,6]. In both cases threshold voltages were approximately 15–20 V, and on/off current ratios increased from $>10^6$ for Haddon to $>10^8$ for Kobayashi. Thin films of the fullerene C_{70} have also been studied in OFET devices by Haddon [7] and the field effect mobility was two orders of magnitude lower than C_{60} , $0.002 \text{ cm}^2/\text{V s}$. Compared to Haddon's C_{60} OFETs, these devices also exhibited higher threshold voltages (27 V compared to 15 V) and on–off current ratios that were one order of magnitude lower (10^5 compared to 10^6).

Because n-type organic semiconductors are susceptible to the effects of oxygen [8], fullerene devices exhibiting the highest mobility values [4–7] have been both fabricated and tested under ultra-high vacuum (UHV) conditions. One report of stable operation of C_{60} OFETs in air used an Ar sputtered, low oxygen content alumina (Al_2O_3) passivation layer that resulted in no degradation in transistor performance for more than one month but the mobility was only $0.1 \text{ cm}^2/\text{V s}$ [9].

Here, we present results on thin-film C_{60} and C_{70} OFETs fabricated under high vacuum and tested in nitrogen at ambient pressure. These devices exhibit electron field-effect mobilities as high as $0.65 \text{ cm}^2/\text{V s}$ in C_{60} and $0.066 \text{ cm}^2/\text{V s}$ in C_{70} .

2. Experiment

Transistors were fabricated on heavily n-doped silicon substrates (as the gate electrode) with 200 nm of thermally grown silicon dioxide as the gate dielectric ($\epsilon_r = 3.9$) and Ti/Au (10 nm/100 nm) backside metalization as the external gate contact. Bottom contact geometry Ti/Au (10 nm/100 nm) source and drain electrodes defining channels with $500 \mu\text{m}$ and $1000 \mu\text{m}$ widths and lengths ranging from $1 \mu\text{m}$ to $50 \mu\text{m}$ were patterned on the SiO_2 layer using lift-off photolithography (Fig. 1).

Commercially obtained (Alfa Aesar) C_{60} and C_{70} were first purified using gradient zone sublima-

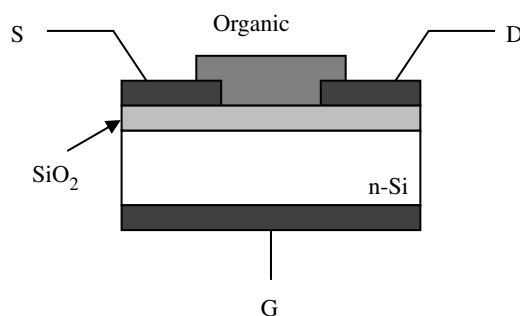


Fig. 1. Diagram of the OFET device geometry where the source (S), drain (D), and gate (G) electrodes are electron-beam evaporated Ti/Au (10 nm/100 nm).

tion and then deposited at 0.6 \AA/s onto the source and drain electrodes to a thickness of 50 nm. Depositions were performed at room temperature using physical vapor deposition at a pressure of 5×10^{-8} Torr. Subsequent to organic layer deposition the devices were transferred into a nitrogen glove box (O_2 , $\text{H}_2\text{O} < 1 \text{ ppm}$) connected to the vacuum deposition system and then transferred in an air-tight vessel to a second glove box filled with nitrogen (O_2 , $\text{H}_2\text{O} < 0.1 \text{ ppm}$) for electrical characterization. During testing electrical connections were made with a micro-probe station contained within the second glove box and an Agilent E5272A medium power source/monitor unit, connected to the probe station, was used to perform the electrical measurements. At no point after deposition of the organic layer were the devices exposed to air. For each individual device output characteristics (I_{DS} vs. V_{DS} at multiple, discrete V_{GS} values) and transfer characteristics (I_{DS} vs. V_{GS} at fixed V_{DS}) were measured. Field-effect mobilities and threshold voltages were calculated in the saturation regime by fitting the $\sqrt{I_{\text{DS}}}$ vs. V_{GS} data to the square law:

$$I_{\text{DS}} = \mu C_{\text{OX}} \frac{W}{2L} (V_{\text{GS}} - V_{\text{T}})^2 \quad (1)$$

where μ is the field-effect mobility, C_{OX} is the capacitance density of the gate dielectric [F/cm^2], V_{T} is the threshold voltage, and W (width) and L (length) are the dimensions of the semiconductor channel defined by the source and drain electrodes.

3. Results

For the C_{60} OFETs mobility values generally increased with channel length and ranged from a minimum of $0.02 \text{ cm}^2/\text{V s}$ for the width $1000 \mu\text{m}$, length $1 \mu\text{m}$ device to the maximum value of $0.65 \text{ cm}^2/\text{V s}$ for the width $500 \mu\text{m}$, length $50 \mu\text{m}$ device (Fig. 2). This field effect mobility value is greater than the $0.56 \text{ cm}^2/\text{V s}$ value reported by Kobayashi et al. [5,6] and, more recently, the $0.5 \text{ cm}^2/\text{V s}$ value reported by Tapponnier et al. [10], for devices fabricated and tested under UHV. Transfer characteristics for this device are shown in Fig. 3b. In addition to the mobility value, the linear fit to the $\sqrt{I_{DS}}$ vs. V_{GS} data yielded a threshold voltage of approximately 32 V. Semilogarithmic plots of I_{DS} vs. V_{GS} yielded an on/off current ratio $>10^6$ and a sub-threshold slope of 3.2 V/decade. Output characteristics for the width $500 \mu\text{m}$, length $50 \mu\text{m}$ device are shown in Fig. 3a for V_{DS} between 0 V and 60 V and V_{GS} between 0 V and 60 V. Results for the C_{70} OFETs behaved similarly to those of C_{60} where mobility values increased with channel length and ranged from a minimum of $0.003 \text{ cm}^2/\text{V s}$ for the width $500 \mu\text{m}$, length $1 \mu\text{m}$ device to the maximum value of $0.066 \text{ cm}^2/\text{V s}$ for the width $500 \mu\text{m}$, length $50 \mu\text{m}$ device (Fig. 2). This field-effect mobility value is

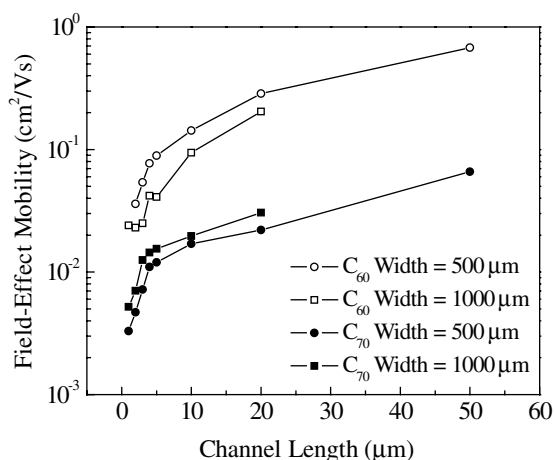


Fig. 2. C_{60} and C_{70} field-effect mobility values as a function of channel length for devices with $500 \mu\text{m}$ and $1000 \mu\text{m}$ wide channels.

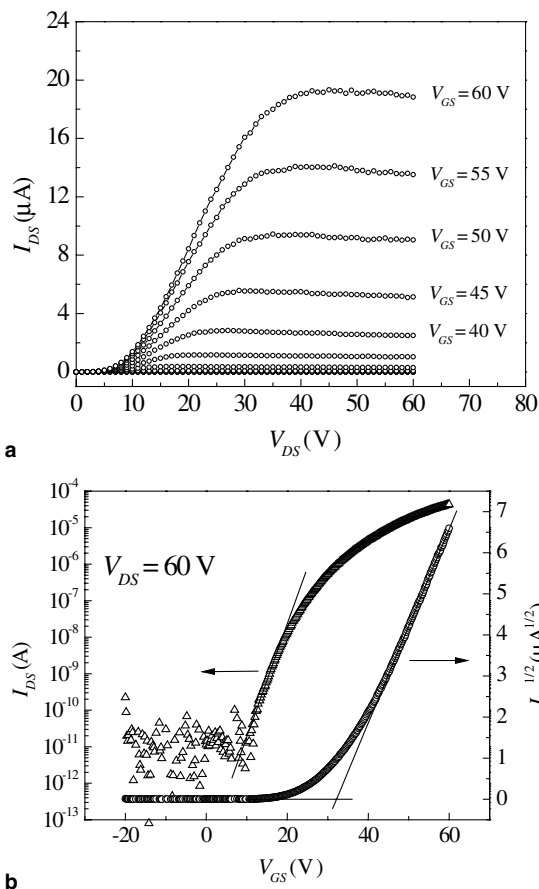


Fig. 3. Output characteristics (a) and transfer characteristics (b) of a C_{60} OFET with a $500 \mu\text{m}$ wide and $50 \mu\text{m}$ long channel.

more than 30 times the $0.002 \text{ cm}^2/\text{V s}$ value reported by Haddon et al. for devices fabricated and tested under UHV [7]. Transfer characteristics for this device are shown in Fig. 4b. The linear fit to the $\sqrt{I_{DS}}$ vs. V_{GS} data yielded a higher threshold voltage of approximately 40 V and semilogarithmic plots of I_{DS} vs. V_{GS} yielded an on/off current ratio $>10^5$. The lower mobility and higher threshold voltage in C_{70} reflect the same trend observed by Haddon. C_{70} however, did exhibit a lower sub-threshold slope of 2.2 V/decade. Output characteristics for the width $500 \mu\text{m}$, length $50 \mu\text{m}$ C_{70} OFET are shown in Fig. 4a for V_{DS} between 0 V and 60 V and V_{GS} between 0 V and 60 V.

One significant difference in the performance of the two materials is the non-ohmic behavior in the

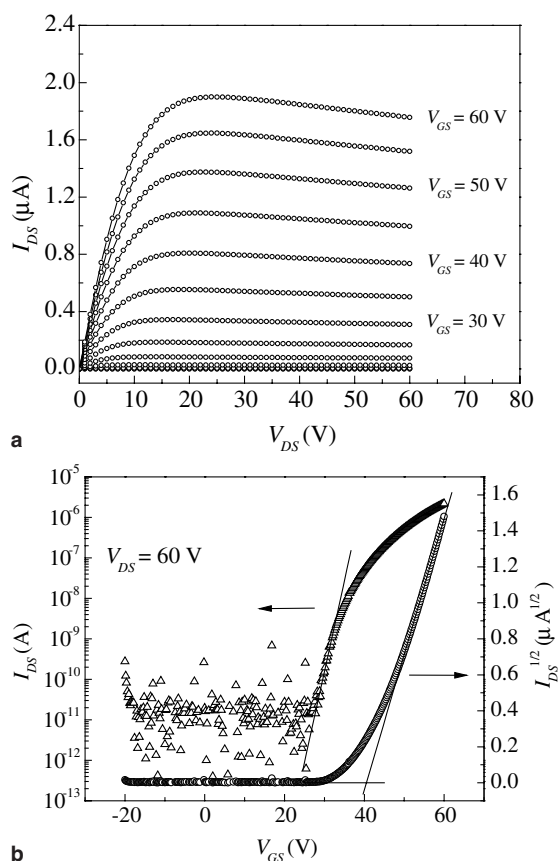


Fig. 4. Output characteristics (a) and transfer characteristics (b) of a C_{70} OFET with a $500\ \mu\text{m}$ wide and $50\ \mu\text{m}$ long channel.

output characteristics at low V_{DS} in the C_{60} device compared to the C_{70} device. Such behavior suggests the presence of contact resistance between the organic semiconductor and the source and drain electrodes. While contact resistance can be attributed to many factors including film morphology at the electrode/organic interface [11] and interactions between the electrode and organic semiconductor [12] it is difficult to determine an absolute cause for the non-ohmic behavior in our devices. However, bottom contact Ti/Au electrodes have shown in the literature to produce more ohmic output characteristics than what we have presented here [6]. Common to both materials is a decrease in the drain current in the usual saturation regime above pinch-off. This phenomenon is as of yet unexplained but it has been

observed in other n-type organic field-effect transistors [13].

Our devices were also sensitive to ambient atmosphere exposure. When C_{60} devices similar to those discussed previously were exposed to ambient atmosphere for 1 h and then returned to the glove box for testing, drain currents were found to drop by half (Fig. 5b) relative to those measured in the pristine state (Fig. 5a). This was accompanied by a drop in mobility and on/off current ratio as well as an increase in threshold voltage (Table 1). Similar to other reports in the literature [8,10], post-exposure device performance (drain current, mobility, threshold voltage, on/off current ratio) could be improved by storing the devices in the inert atmosphere for 24 h prior to retesting (Fig. 5c, Table 1). Compared to pristine devices (Fig. 6a), C_{70} OFETs showed a factor of

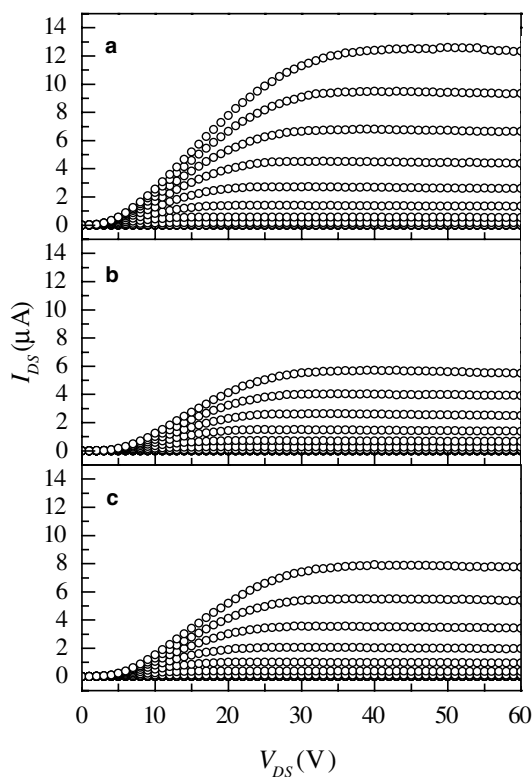


Fig. 5. Output characteristics for a C_{60} OFET as a function of exposure to ambient and nitrogen atmospheres. Data shown is for $0\ \text{V} \leq V_{GS} \leq 60\ \text{V}$ in $5\ \text{V}$ steps for a device with a channel width of $500\ \mu\text{m}$ and a channel length of $50\ \mu\text{m}$.

Table 1

Values of the field-effect mobility, threshold voltage and on/off current ratio for the C₆₀ and C₇₀ devices shown in Figs. 5 and 6 (respectively) as a function of exposure to ambient and nitrogen atmospheres

	C ₆₀ /C ₇₀	C ₆₀ /C ₇₀	C ₆₀ /C ₇₀
Pristine device	$\mu = 0.192/0.060 \text{ cm}^2/\text{V s}$	$V_T = 29.7/34.7 \text{ V}$	$I_{\text{on}}/I_{\text{off}} = 1.5 \times 10^6/3.9 \times 10^5$
Post 1 h ambient exposure	$\mu = 0.159/0.042 \text{ cm}^2/\text{V s}$	$V_T = 35.6/40.1 \text{ V}$	$I_{\text{on}}/I_{\text{off}} = 8.3 \times 10^5/1.5 \times 10^5$
Post 24 h nitrogen exposure	$\mu = 0.170/0.041 \text{ cm}^2/\text{V s}$	$V_T = 33.5/42.2 \text{ V}$	$I_{\text{on}}/I_{\text{off}} = 1.0 \times 10^6/1.2 \times 10^5$

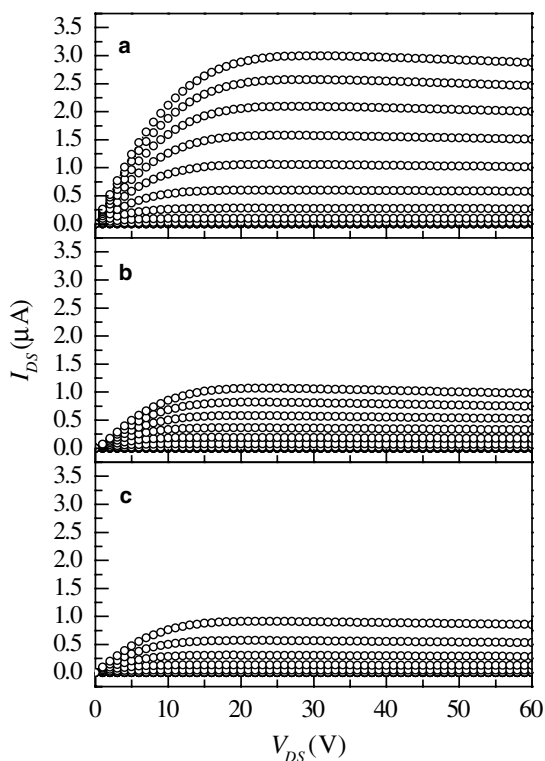


Fig. 6. Output characteristics for a C₇₀ OFET as a function of exposure to ambient and nitrogen atmospheres. Data shown is for $0 \text{ V} \leq V_{\text{GS}} \leq 60 \text{ V}$ in 5 V steps for a device with a channel width of 500 μm and a channel length of 50 μm .

three reduction in drain currents after a 1 h exposure to ambient atmosphere (Fig. 6b) along with a decrease in mobility and on/off current ratio and an increase in threshold voltage (Table 1). Unlike the C₆₀ device however, performance continued to degrade after storage under inert atmosphere for 24 h (Fig. 6c, Table 1).

Another point of interest regarding our results on C₆₀ is that the mobility value of $0.65 \text{ cm}^2/\text{V s}$ is slightly higher than the highest mobility mea-

sured in single crystals of C₆₀ ($0.5 \text{ cm}^2/\text{V s}$) by the time-of-flight technique [14]. Material morphology plays a significant role in charge transport and mobility measurements in organic single crystals are usually considered upper values. For instance, recent work has shown that hole mobilities as large as $35 \text{ cm}^2/\text{V s}$ could be measured in single crystals of pentacene as measured by space-charge limited current methods [15]. These values should be compared with hole mobilities of $5 \text{ cm}^2/\text{V s}$ measured in thin films of pentacene in a field-effect transistor geometry [16]. Our results would then suggest that the mobility of $0.5 \text{ cm}^2/\text{V s}$ measured in single crystals of C₆₀ was limited by extrinsic effects such as impurities and structural defects and that the intrinsic electron mobility of C₆₀ can possibly be significantly higher than $1 \text{ cm}^2/\text{V s}$.

4. Conclusions

Organic field-effect transistors have been fabricated from thin films of C₆₀ and C₇₀ purified by zone sublimation and deposited into thin films under high vacuum. These devices have been tested in an inert nitrogen atmosphere at ambient pressure and have exhibited saturation regime electron field-effect mobilities as large as $0.65 \text{ cm}^2/\text{V s}$ for C₆₀ and $0.066 \text{ cm}^2/\text{V s}$ for C₇₀. The mobility value for C₆₀ is slightly higher than the state of the art value obtained from devices tested under ultra-high vacuum and the mobility value for C₇₀ is more than an order of magnitude improvement over the state of the art value in that material (also obtained from devices tested under ultra-high vacuum). Our results indicate that carefully passivated devices fabricated from a highly purified fullerene and pentacene could be good candidates for complementary organic semiconductor circuits.

Acknowledgement

This material is based upon work supported in part by the STC program of the National Science Foundation under Agreement Number DMR-0120967, by the Office of Naval Research, by an NSF CAREER program (B.K.), and by the Defense Advanced Research Projects Agency.

References

- [1] C.D. Dimitrakopoulos, P.R.L. Malenfant, *Adv. Mater.* 14 (2002) 99.
- [2] T. Kanbara, K. Shibata, S. Fujiki, Y. Kubozono, S. Kashino, T. Urisu, M. Sakai, A. Fujiwara, R. Kumashiro, K. Tanigaki, *Chem. Phys. Lett.* 379 (2003) 223.
- [3] R.J. Chesterfield, J.C. McKeen, C.R. Newman, P.C. Ewbank, D.A. da Silva Filho, J.L. Brédas, L.L. Miller, K.R. Mann, C.D. Frisbie, *J. Phys. Phys. Chem. B.* 108 (2004) 19281.
- [4] R.C. Haddon, A.S. Perel, R.C. Morris, T.T.M. Palstra, A.F. Hebard, R.M. Fleming, *Appl. Phys. Lett.* 67 (1995) 121.
- [5] S. Kobayashi, T. Takenabu, S. Mori, A. Fujiwara, Y. Iwasa, *Appl. Phys. Lett.* 82 (2003) 4581.
- [6] S. Kobayashi, T. Takenabu, S. Mori, A. Fujiwara, Y. Iwasa, *Sci. Technol. Adv. Mater.* 4 (2003) 371.
- [7] R.C. Haddon, *J. Am. Chem. Soc.* 118 (1996) 3041.
- [8] C.P. Jarret, K. Pichler, R. Newbould, R.H. Friend, *Synth. Met.* 77 (1996) 35.
- [9] K. Horiuchi, K. Nakada, S. Uchino, S. Hashii, A. Hashimoto, N. Aoki, Y. Ochiai, M. Shimizu, *Appl. Phys. Lett.* 81 (2002) 1911.
- [10] A. Tapponnier, I. Biaggio, P. Günter, *Appl. Phys. Lett.* 86 (2005) 112114.
- [11] K.P. Puntambekar, P.V. Pesavento, C.D. Frisbie, *Appl. Phys. Lett.* 83 (2003) 5539.
- [12] P.V. Pesavento, R.J. Chesterfield, C.R. Newman, C.D. Frisbie, *J. Appl. Phys.* 96 (2004) 7312.
- [13] P.R.L. Malenfant, C.D. Dimitrakopoulos, J.D. Gelorme, L.L. Kosbar, T.O. Graham, *Appl. Phys. Lett.* 80 (2002) 2517.
- [14] E. Frankevich, Y. Maruyama, H. Ogata, *Chem. Phys. Lett.* 214 (1993) 39.
- [15] O.D. Jurchescu, J. Baas, T.M. Palstra, *Appl. Phys. Lett.* 84 (2004) 3061.
- [16] T.W. Kelley, P.F. Baude, C. Gerlach, D.E. Ender, D. Muyres, M.A. Haase, D.E. Vogel, S.D. Theiss, *Chem. Mater.* 16 (2004) 4413.



Letter

Fullerene-based bistable devices and associated negative differential resistance effect

Himadri S. Majumdar ^{a,*}, Jayanta K. Baral ^a, Ronald Österbacka ^a,
Olli Ikkala ^b, Henrik Stubb ^a

^a Department of Physics, Åbo Akademi University, Porthansgatan 3, Turku 20500, Finland

^b Optics and Molecular Materials, Helsinki University of Technology, Finland

Received 4 May 2005; received in revised form 25 June 2005; accepted 27 June 2005

Abstract

We have observed bistability in single layer devices made from fullerenes (C₆₀) mixed with polystyrene (PS) and sandwiched between two Al electrodes. By merely changing the concentration of C₆₀ in PS we found three distinctly different device properties, namely a true insulator, a bistable device switching between an OFF and an ON state having ON–OFF current ratios larger than 10⁴ and a write-once, read-many times (WORM) device. An additional negative differential resistance (NDR) was observed in the ON state of both the bistable and WORM devices leading to multi-level switching capability of the devices. This opens up a wide range of application possibilities of such devices in disposable printable electronics.

© 2005 Elsevier B.V. All rights reserved.

PACS: 73.61.Wp; 85.65.+h; 73.40.Sx; 84.37.+q

Keywords: Fullerene; Conductance switching; Memory applications; Negative differential resistance; Tunneling

1. Introduction

The past few years have seen an upsurge in fabrication and characterization of two-terminal

nonvolatile memory devices using organic semiconductors and polymers [1–7]. These devices can switch between a high- and a low-impedance state upon application of an electric field. Different active materials and device architectures have been suggested for this purpose. Small molecules and conjugated polymers used as semiconductors in a metal/semiconductor/intermediate metal/semiconductor/metal (MSIMSM) structure reported

* Corresponding author. Tel.: +358 2 2154606; fax: +358 2 2154776.

E-mail address: himadri.majumdar@abo.fi (H.S. Majumdar).

switching of $\sim 10^6$ times [1–3]. The MSIMSM devices switch to an ON state under a certain bias and retained the state even after the bias was switched off. There is, however, a difference in the nonvolatile nature of the memory as the devices can get back to its OFF state upon application of bias of same magnitude but with reverse polarity [1], shortening (i.e., application of 0 V) [2], or application of higher magnitude of bias with same polarity [3]. The switching mechanism suggested in all the cases is different as well. For devices where the ON state is erased by application of a bias of opposite polarity, the explanation was based on a model proposed by Sheng et al. [8]. The electrons tunnel through the insulating barriers between the metallic grains (grain size 5–10 nm) dispersed in the insulator matrix. This causes the charging of the granular intermediate metal layer in the MSIMSM devices.

Simmons and Verderber [9] observed multistability in SiO films with electroforming due to diffusion of Au particles upon evaporation forming an impurity band of charge transport levels as well as deeper charge-trapping levels. Charging of these levels under bias leads to a N-shaped current curve and is seen as negative differential resistance (NDR). A similar NDR effect was also observed upon deliberate introduction of metal particles within a semiconductor layer in a MSIMSM architecture [3]. In this letter, we will show that memory switching can be achieved using single layer devices with a dispersed solution of Buckminsterfullerenes (C60) in a polystyrene insulating matrix (PS:C60) as the active layer suitable for printed electronics. The solution processibility of the device and its easy and inexpensive fabrication makes it a good candidate for roll-to-roll printing and manufacturing of cheap throw-away electronics.

2. Experiments

The Al/PS:C60/Al thin films were fabricated on a glass substrate in a nitrogen atmosphere inside a glove-box. The PS:C60 solution was mixed from 150 mg/ml and 1 mg/ml solutions of PS and C60 in *p*-xylene, respectively. Both PS and C60 were

bought from Aldrich Chemical co. and were used as such. 5% concentration of PS:C60 solution is defined as PS and C60 weight ratio of 20:1 in the mixed solution. To fabricate the device the PS:C60 solution was spin coated on a ~ 50 nm Al-coated glass substrate at a speed of 1000 rpm. The top Al electrode layer was vacuum-evaporated on the film. Both the top and bottom Al were evaporated at a pressure of $\sim 1 \times 10^{-5}$ mbar with a uniform rate of 0.7–1.0 nm/s to avoid penetration into the active layer. The device thickness was in the range of 50–60 nm and the active area of the devices was 6 mm^2 . We divide the devices in three categories depending on their different electrical characteristics observed. Device I denotes devices from 1% concentration, device II from 5% and device III from concentrations between 7.5% and 20%.

The devices were characterized using both constant wave (cw) and transient measurements. A Keithley 2400 programmable source meter was used for the cw measurements and the transient measurements were carried out using a Stanford Research Systems DS345 function generator and Tektronix TDS 680B oscilloscope. The details for the transient measurements are provided elsewhere [11]. All cw measurements were carried out in voltage steps of 0.4 V and a delay of 2 s between successive steps, if not mentioned otherwise. The bottom Al electrode was used for positive bias for all the measurements reported here, but all the devices (I–III) work identically even when the top Al electrode is used to apply the positive bias. Electrical characterization was done on the devices after they were kept in the measurement chamber under dynamic vacuum of $\sim 10^{-5}$ bar overnight.

3. Results and discussions

The cw current–voltage (J – V) characteristics shown in Fig. 1 provide the first idea of the Al/PS:C60/Al device working as a memory device. The figure shows currents for typical devices I–III. The voltage across the devices was varied in the cycle 0 V to 7.5 V to -7.5 V to $+7.5$ V to 0 V in all the cases shown in figure. We find that the current values for device I are orders of magnitude smaller

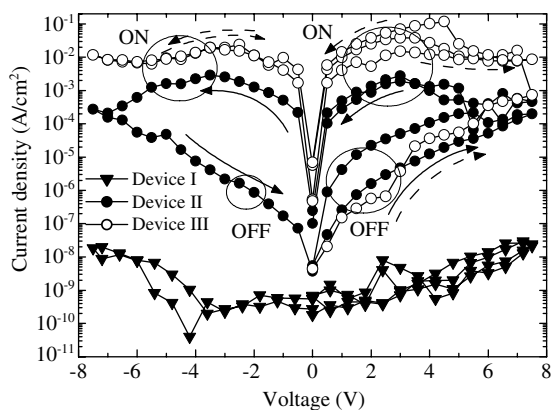


Fig. 1. Current density vs. voltage plots for devices I (\blacktriangledown), II (\bullet) and III (\circ). The voltage was varied between ± 7.5 V and the scan rate was 200 mV/s. Current under applied bias directions for device II (\rightarrow) and device III (\dashrightarrow) are indicated. The ON and the OFF state current ranges are indicated by the circles. Absolute values of current under reverse bias were taken to obtain a semi-logarithmic plot.

than for the devices II and III, suggesting that the device works like an insulator for such a low concentration of C60. Device II started from a high-impedance OFF state and went to a low-impedance, high-current-conducting ON state when voltage was increased to $+7.5$ V. The ON state is retained during the voltage scan back from $+7.5$ V to -7.5 V. The device II current once again decreased by 3 orders of magnitude and came back to its original high-impedance OFF state during the -7.5 V to 0 V scan. This voltage cycle was repeated over again showing current level tracing the same path always. There is, however, a threshold voltage below which the device did not switch ON when the voltage cycle was done. The threshold voltage varies between 4.5 V and 5.5 V. Hence we have obtained a bistable device that switches between two different impedance states similar to the observations in the MSIMSM devices by Ma et al. [1].

Device III also started from a high-impedance OFF state and went to a low-impedance ON state with increasing voltage to $+7.5$ V in the first scan. It then retained the ON state even for a scan to bias of opposite polarity and back, unlike device II. Hence the possibility of obtaining a write-once, read-many (WORM) device is realized. Such

WORM application has previously been reported in polymeric devices working as fuses [13] and silica-based devices working as anti-fuses [14 and references therein]. The threshold voltage for device III is similar to device II (between 4.5 V and 5.5 V) meaning that the WORM memory requires a probe voltage higher than the threshold voltage in order to disturb the OFF state. When device III was brought in contact with air by breaking the vacuum, the current level immediately came down to one similar to the pristine device. The device behaved identically as before when we got it back into vacuum once again, suggesting that the sudden rise of conductivity is not due to degradation of the device. The decrease of conductivity of the C60-based devices in air is a known phenomenon [15,16]. C60 molecules adsorb oxygen from atmosphere even at room temperature which creates new defect and impurity states acting as efficient traps for electrons in the conduction band of C60. This decreases the carrier lifetime and, in turn, brings down the conductivity of the device [16].

Thus, we have obtained two different memory devices—multiple read–write devices, commonly called bistable devices, (device II) and WORM devices (device III) from an all-organic single layer device merely by changing the concentration of C60 in PS. We found that the ON state decreased less than 5% in devices II and III even after 30 days, suggesting a very high retention time with applications in disposable printed electronics in mind.

The observations in all three devices above are in accordance with prior experimental observations [1–3] and a recent proposal [10] where tunneling is identified as the basic device mechanism. In device I there is no tunneling between the C60 particles as the C60 particles are far apart. So, we never get a change in conductivity upon application of bias—making it a mere insulator. For device II tunneling occurs since the C60 molecules are separated by a proper distance for the electrons to tunnel from one C60 to the other without forming a continuous network. We estimated the average distance between the C60 molecules in device II to be ~ 3 nm from concentration and structural parameters. The charged C60 molecules increase

the conductivity of the device. The C60 molecules loose the charged state upon injection and/or extraction from/to the other electrode under bias of opposite polarity and the device falls back to its initial low-conducting state. For device III, the C60 molecules are more closely packed and form increasingly large conducting networks within the bulk of the device, allowing the C60 network to be charged by tunneling. It has been previously seen that charge can delocalize in systems of C60 if the intermolecular coupling is large enough [12]. We suggest that the charge delocalization in the (unconnected) networks create an environment where some charges will always be stored in the device even after application of bias of reverse polarity. We note that for devices with C60 well above the percolation threshold i.e., higher concentration of C60 in solutions, no switching was observed.

We now turn our attention to the NDR observed in the ON state of both devices II and III. In Fig. 1 NDR occurred for both polarities of bias and for all scan directions only when the device is in the ON state. This phenomenon has previously been observed both in devices with intermediate metal layers [3] and with electroformed metal in SiO [9]. In Fig. 2 we apply a linearly increasing voltage of different amplitudes but with the same

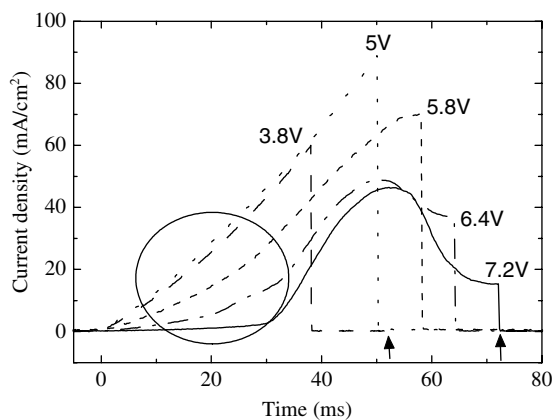


Fig. 2. Current density (J) characteristics of device III for different linearly increasing voltages at a scan speed of 100 V/s. The current for successive voltage scans are indicated in the figure. The circled area indicates the variation of current in the low-voltage regime. The arrows indicate the V_{\max} (~ 5.2 V) and V_{\min} (7.2 V).

scan speed of 100 V/s over device III, which is already in the ON state, and measure the current [11]. For voltage ramps with amplitudes up to $V_{\max} \approx 5.2$ V we observe the same high-current density through the device. By further increasing the voltage amplitude above 5.4 V the current starts to decrease till it reaches a minimum at $V_{\min} \approx 7.2$ V making it an N-shaped current curve [3,9]. This allows for an additional memory effect in the ON state of the already observed bistable and WORM devices. We note, however, that the OFF state current in device II and III are still orders of magnitude lower than the current at V_{\min} (see Fig. 1).

The current difference in the low-voltage regime (circled) in Fig. 2 is especially of interest. It shows that if we apply a certain bias within the NDR regime (5–7.2 V), the consequent low-voltage probes will show a device history, i.e., memory. This leads to multistability response of the device as seen in Ref. [9]. We applied a ramp “pump” write voltage varying between 2.5 V and 7.2 V and probed the device current using a smaller read voltage (1 V) as shown in the inset of Fig. 3. We find distinct read current values for all write voltages. Thus, we can create different “states” of the device that respond differently to the same probe voltage, leading to multistability.

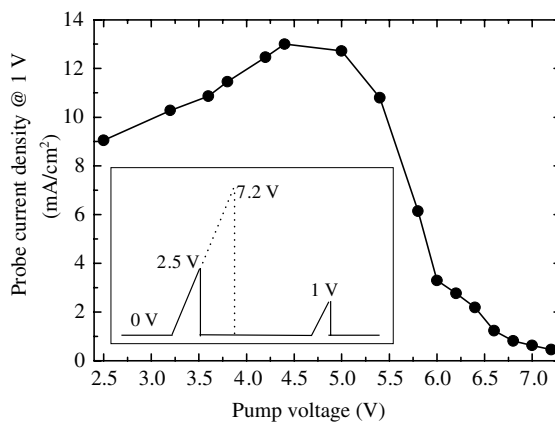


Fig. 3. Current density of the probe pulse in device III. The device current was “read” with a 1 V ramp after a state is “written” by applying linearly increasing pump voltages in the 2.5–7.2 V range. Inset shows the scheme of the experiment.

Measurements on devices with various thicknesses reveal that both the bistability and NDR in devices II and III are voltage driven phenomenon. We have also observed that the NDR is independent of temperature down to 240 K.

4. Conclusions

In conclusion, we have fabricated a simple memory switching device. The device was fabricated by using C60 mixed into a common organic insulator—polystyrene. By merely changing the concentration of the C60 in PS we found three distinctly different device mechanisms, namely a true insulator, a bistable device switching between an OFF and ON state (device II) and a write-once, read-many switch (device III). Furthermore, both devices II and III show NDR in their ON states allowing for fabrication of multistable devices. The device physics can be quantitatively understood based on a mechanism similar to tunneling and impurity band conduction.

Acknowledgements

Financial support from the Academy of Finland Project Nos. 50575 and 204844 is acknowledged.

References

- [1] L. Ma, J. Liu, S. Pyo, Y. Yang, *Appl. Phys. Lett.* 82 (2003) 1419.
- [2] T. Ouisse, O. Stéphan, *Org. Electron.* 5 (2004) 251.
- [3] L.D. Bozano, B.W. Kean, V.R. Deline, J.R. Salem, J.C. Scott, *Appl. Phys. Lett.* 84 (2004) 607.
- [4] T. Oyamada, H. Tanaka, K. Matsushige, H. Sasabe, C. Adachi, *Appl. Phys. Lett.* 83 (2003) 1252.
- [5] J.B. Cui, R. Sordan, M. Burghard, K. Kern, *Appl. Phys. Lett.* 81 (2001) 3260.
- [6] H.S. Majumdar, A. Bolognesi, A.J. Pal, *Synth. Met.* 140 (2004) 203.
- [7] D. Tondelier, K. Lmimouni, D. Vuillaume, C. Fery, G. Haas, *Appl. Phys. Lett.* 85 (2004) 5763.
- [8] P. Sheng, B. Abeles, Y. Arie, *Phys. Rev. Lett.* 31 (1973) 44, and Ref. [7] therein.
- [9] J.G. Simmons, R.R. Verderber, *Proc. R Soc. Lond. Ser. A* 301 (1967) 77.
- [10] M.J. Rozenberg, I.H. Inoue, M.J. Sánchez, *Phys. Rev. Lett.* 92 (2004) 178302.
- [11] G. Juška, K. Arlauskas, M. Viličnas, J. Kočka, *Phys. Rev. Lett.* 84 (2000) 4946.
- [12] Å. Johansson, S. Stafström, *Phys. Rev. B* 68 (2003) 035206.
- [13] S. Möller, C. Perlov, W. Jackson, C. Taussig, S.R. Forrest, *Nature* 426 (2003) 166.
- [14] J. Hu, H.M. Branz, P. Stradins, S. Ward, A. Duda, Q. Wang, C. Perlov, W.B. Jackson, C. Taussig, *IEEE Electron Device Lett.* 26 (2005) 17.
- [15] A. Hamed, Y.Y. Sun, Y.K. Tao, R.L. Meng, P.H. Hor, *Phys. Rev. B* 47 (1993) 10873.
- [16] G. Shervoglieri, G. Faglia, C. Perego, P. Nelli, R.N. Marks, T. Virgili, C. Taliani, R. Zamboni, *Synth. Met.* 77 (1996) 273.



Surface photocurrents in tetracene layers

D. Kotowski*, B. Kutrzeba-Kotowska, M. Obarowska,
R. Signerski, J. Godlewski

Department of Physics of Electronic Phenomena, Gdańsk University of Technology, Narutowicza 11/12, 80-952 Gdańsk, Poland

Received 29 December 2004; received in revised form 30 May 2005; accepted 7 September 2005

Available online 14 July 2005

Abstract

The surface current stimulated by light in tetracene layers was investigated. The tetracene sample was prepared by evaporation in vacuum on the glass substrate. The sample was equipped with the gold electrodes deposited on the glass or on the top of the tetracene layer. Illumination of the tetracene layers was perpendicular to the flat area. Two methods of illumination were applied—from glass substrate side (S) or from non-substrate side (NS).

Photocurrent characteristics as a function of wavelength (λ), light intensity (I_0) and voltage (U) were measured.

We concluded that mechanism of the photocurrent stimulation results from triplet exciton-trapped charge carrier interaction, which leads to detrapping of charge carriers and enhancement of the current.

It was shown that current–wavelength characteristics have antibatic behaviour (reverse proportionally to the absorption coefficient) under illumination of non-substrate side, and symbatic (proportionally to the absorption coefficient) under illumination of substrate side of the sample.

Based on the experimental results, it is thought that the phenomenon results from non-uniform distribution of the trapping charge carriers in the tetracene layers in perpendicular direction, which leads to non-uniform detrapping of charge carriers by excitons.

© 2005 Elsevier B.V. All rights reserved.

PACS: 73.25.+i; 72.80.Le; 85.60.–q; 73.50.Pz

Keywords: Excitons; Injection; Photoenhanced current; Tetracene

1. Introduction

The increase of current, resulting from illumination of the sample, is usually induced by exciton detrapping of trapped carriers [1–4]. The phenomenon is known as a photoenhancement of current

* Corresponding author. Tel.: +48 58 347 20 12; fax: +48 58 347 28 21.

E-mail address: dako@mifgate.pg.gda.pl (D. Kotowski).

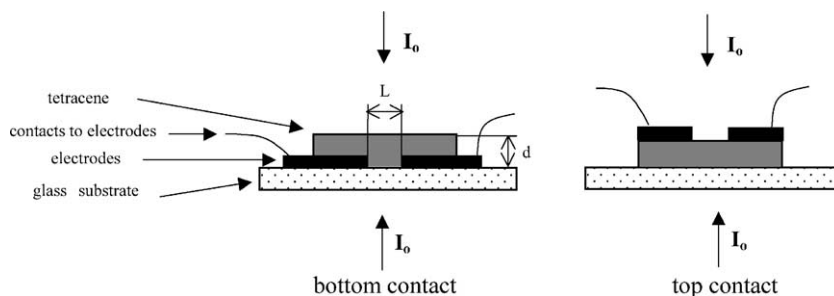


Fig. 1. Scheme of experimental arrangement of the vacuum deposited tetracene layers with bottom and top contacts. Direction of possible illumination by flux of light (I_0) is shown.

(PEC). Optical processes are based on the assumption that charge carriers are detrapped out from the traps by excitons created by the exciting light in the organic material. In the tetracene, the first singlet exciton energy is $E_S = 2.2$ eV and the lowest triplet exciton energy is $E_T = 1.2$ eV [2], so the difference energy $2E_T - E_S$ is equal 0.2 eV [5,6]. As a consequence the probability of intersystem crossing is very low in tetracene crystals. As a result of very effective singlet fission process, the triplet excitons play an important role in charge carrier detrapping processes. From these reasons PEC reaches extremely high values in organic molecular materials when the examined samples are illuminated by light from the region of singlet exciton absorption. Under such conditions, the charge carriers detrapping by exciton significantly dominates over the photon detrapping. The behaviour results from much smaller value of the cross-section for photon absorption by trapped charge carrier than for the exciton-trapped charge carrier interaction [1,2].

PEC in organic materials was the subject of many experimental and/or theoretical investigations. However, all of these works were carried out on samples with electrodes in sandwich arrangement, on both monocrystals and vacuum-evaporated layers [3,7–12].

Our analysis of PECs concerns the conductivity of vacuum-evaporated tetracene samples in surface arrangement (see Fig. 1). The investigations of these type of samples, illuminated perpendicular to the flat part of the layer, give us information about some properties of the surface region of the layers from the substrate (S) and non-substrate (NS) side (where S is the side contiguous to the

substrate glass and NS is the opposite side of the layer, see Fig. 5).

In this paper we present the experimental results concerning the photoenhanced current obtained for samples in surface arrangement with electrodes deposited on substrate (bottom contacts—BC) or on non-substrate (top contacts—TC) side of the organic layers (see Fig. 1). In both cases the layers were illuminated from S and NS side. The conclusions resulting from experimental measurements are completed by a theoretical model which particularly explains the photocurrent dependence on wavelength under the illumination from S and NS side.

2. Experimental details

Tetracene (Aldrich, 98% pure), purified by repeated vacuum sublimation has been used for deposition. The thin films samples were obtained by evaporation in vacuum of gold electrodes (thickness about 20 nm) directly onto a microscope slide 150 μm thick at a pressure of 10^{-3} Pa at room temperature for bottom contacts or on the tetracene layer for top contacts, with tetracene deposition rate of about 2 $\text{\AA}/\text{s}$. The evaporation parameters were controlled by EDWARDS Auto 306 turbo, turbomolecular vacuum evaporation system.

The electrical contact of samples with terminals was achieved by means of silver paste. The samples were placed in the measurement chamber and resulting currents were measured by Keithley 487 electrometer. The thin layer samples were

illuminated with a KB 5703 Xenon lamp through a monochromator SPM-2. All measurements have been done in air, at room temperature. The entrance slit of the monochromator was adjusted to give the same quantum light intensity at different wavelengths.

For investigations the samples with different thickness of the tetracene layers from $d = 0.75\mu\text{m}$ to $d = 1.5\mu\text{m}$ and with different distances between electrodes “ L ” (Fig. 1) have been used. Layers were illuminated from both substrate and non-substrate side. The samples had ohmic electrodes, formed from gold contacts. In the paper the results are presented on the layer of $0.75\mu\text{m}$ thickness.

2.1. Experimental results and their analysis

The experimental analysis were based on the measurements of photoenhanced current as a function of the wavelength, light intensity and applied voltage. The current–wavelength characteristics obtained for the tetracene layer at two directions of illumination is shown in Fig. 2. It can be noticed that under the illumination of the layer from S side, the PEC characteristic shows symbatic dependence (proportional to the absorption coefficient) which is independent from position of electrodes, TC or BC. When the NS side

of the layer is illuminated, spectral characteristics transform into an antibatic relation (inversely proportional to the absorption coefficient). It is noteworthy that the values of photoenhanced currents are generally higher when the S side is illuminated.

Next, we present the experimental data of the photocurrent vs. intensity of incident light (Fig. 3) for BC only. The samples were illuminated by the monochromatic lights of $\lambda = 505\text{ nm}$ and $\lambda = 530\text{ nm}$ wavelengths, which correspond to the strong and weak region of light absorption of the tetracene layer, respectively. Analysing these plots difference between the value of the currents slope obtained for the illumination from S and/or NS side of the investigated layer can be observed. In every case the curves start from horizontal position, which corresponds to the dark currents. It can be noticed, that for weak light absorption (Fig. 3b, $\lambda = 530\text{ nm}$) differences between values of the photoenhanced current for illumination from S and NS side of the layer are much smaller than for strong light absorption region (Fig. 3a, $\lambda = 505\text{ nm}$). Moreover, it can be seen, that the increase of photocurrent under the illumination from S side starts later, that for illumination from NS side of the layer.

In Fig. 4. the photocurrent as a function of the applied voltage obtained for the samples with BC arrangement under the light illumination from

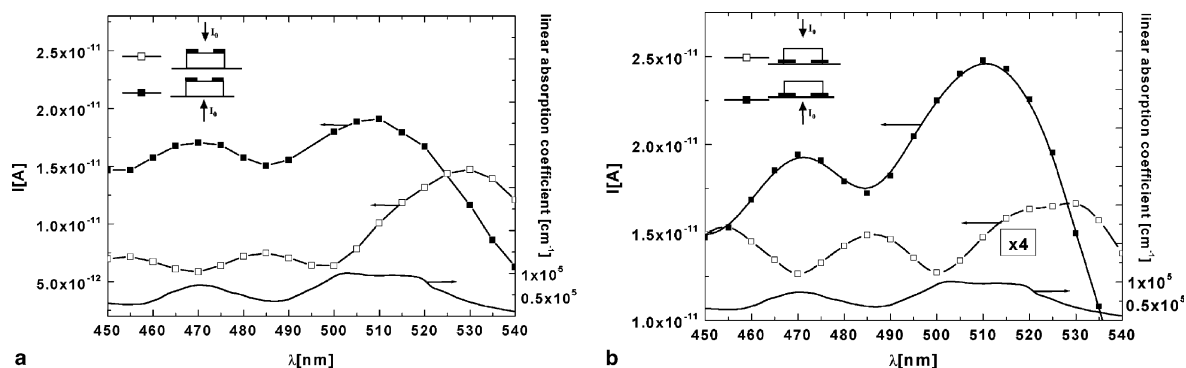


Fig. 2. Spectral characteristics of the surface photocurrent in tetracene layers for distance between electrodes $L = 0.2\text{ mm}$, in the case of top contact (a) and bottom contact (b). The illumination of the layers was through S or NS side of the layer (see schematic drawing in the top left corner). Results were obtained at $U = 20\text{ V}$, $I_0 = 10^{15}\text{ photons/cm}^2\text{ s}$ and for the thickness of the sample $d = 0.75\mu\text{m}$. Values of photocurrent for the sample with bottom contact under illumination from NS side were multiplied by the factor of 4. For comparison with photocurrent spectrum the absorption spectrum of the tetracene layer is presented on the basis on the literature data [14].

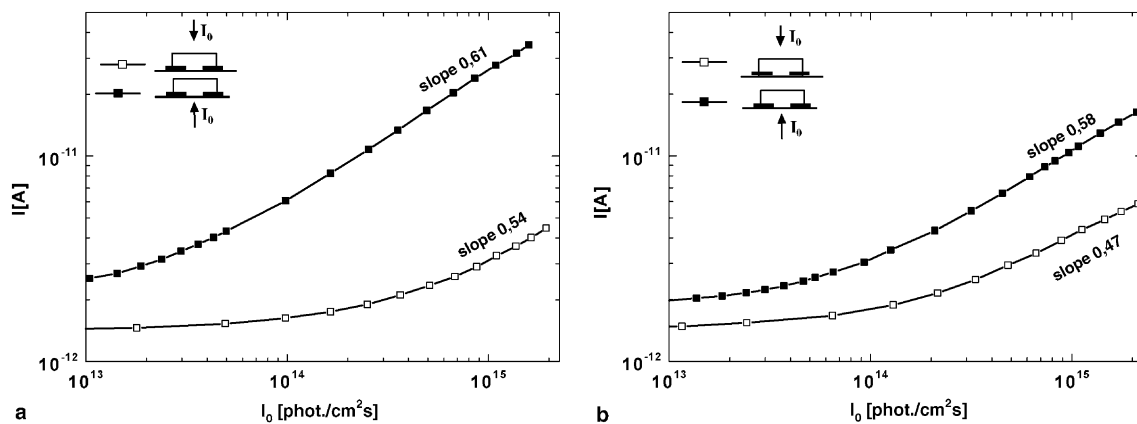


Fig. 3. Characteristics of photocurrent vs. intensity of incident light for layers with bottom contact (see schematic drawing in the top left corner). Results were obtained for wavelengths $\lambda = 505$ nm (plot (a)) and $\lambda = 530$ nm (plots (b)) at $U = 20$ V, $L = 0.2$ mm and for the thickness of the sample $d = 0.75$ μm .

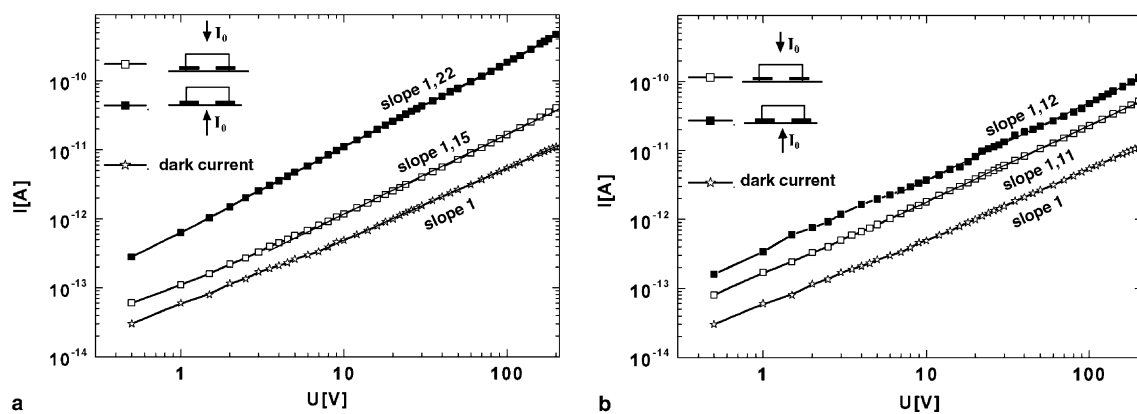


Fig. 4. The photocurrent–voltage curves for layers with bottom contacts (see schematic drawing in the top left corner). Results were obtained for wavelengths $\lambda = 505$ nm (plots (a)) and $\lambda = 530$ nm (plots (b)) at intensity of incident light $I_0 = 10^{15}$ photons/cm² s, $L = 0.2$ mm, $d = 0.75$ μm .

strong and weak absorption region of tetracene crystal is shown. According to the experimental results presented in Fig. 4, it can be seen that the dark current dependence on applied voltage is linear with slope close to 1, and the relationship between photocurrent and applied voltage is derived for the light illumination from weak and strong absorption region of tetracene crystal is superlinear with slope > 1 .

It is worth to point out that the difference between the values of photocurrent obtained under the illumination of the sample from S and NS side

is bigger for $\lambda = 505$ nm (left plot) than for $\lambda = 530$ nm (right plot).

3. Simple model describing surface photoenhanced current in the layer

Charge carrier detrapping process in molecular layer, due to its illumination, depends on trapped charge carrier and excitons [1–10].

The charge carrier distribution in the thin insulator layers, in the direction perpendicular to the

layer, was analysed in [13]. According to that approach it can be assumed that the charge carriers in the layer are mostly situated near the surfaces of the layer due to coulombic repulsion. In order to explain experimental results, the simple model of the processes has been used. For the sake of the present discussion, it suffices to recall the most important assumptions:

- (i) the trapped charge carriers are localised only in the short distance equals $a/2$ from each surface of the layer,
- (ii) the thickness of the layer where the trapped charge carriers are situated (a) is small in comparison to the layer thickness,
- (iii) there is no current flow in the direction perpendicular to the layer because there is no permanent source of charge carrier.

From the last assumption it follows that electric field intensity is close to zero in the direction perpendicular to the layer and the trapped charge carrier concentration (n_{t0}) is the same for S and NS side of the sample. The schematic representation of the sample is presented in Fig. 5.

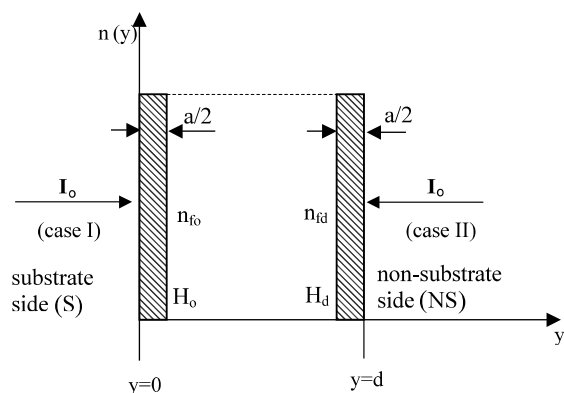


Fig. 5. Scheme of assumed trapped charge carrier distribution in direction perpendicular to the layer (a), where: n_{f0} and n_{fd} are concentrations of free charge carrier near position $y = 0$ (S side) and $y = d$ (NS side), $a/2$ is thickness of the layer which contain the trapped charge carrier near the surface H_0 and H_d is concentration of the traps correlated with position $y = 0$ and $y = d$, respectively. I_0 is intensity of the light flux, n_{t0} is concentration of trapped charge carriers.

According to the above, the current flow in the direction parallel to the layer is realised in narrow part of the sample equals a . As a result the value of measured current can be described as

$$I = (n_{f0} + n_{fd})\mu e E_0 a b, \quad (1)$$

where n_{f0} and n_{fd} are concentrations of free charge carrier near substrate side and non-substrate side, respectively, e is elementary charge carrier, μ is mobility of a charge carrier, E_0 is an average value of the electric field in the direction parallel to the layer, a is total thickness of the layer which contains the trapped charge carrier and b is width of the layer in the active region for the charge carrier transport.

After illumination of the layer, via singlet excitons fission process triplet excitons are generated. The triplet excitons can interact with the trapped charge carriers. As a consequence we expect an efficient free charge carriers production.

Taking into account the exponential distribution of traps according to the energy,

$$h(E) = \frac{H}{\ell kT} \exp\left(-\frac{E}{\ell kT}\right) \quad (2)$$

and for efficient charge carriers detrapping process the relation between free and trapped charge carrier, can be described as follows [3]:

$$n_f(y) = \frac{N_{\text{eff}}}{H} \left(\frac{\eta \tau_0 \kappa I_0 e^{-ky}}{v} \right)^{1-1/\ell} n_t(y), \quad (3)$$

where H is the concentration of the traps, ℓ is the parameter describing energetically distribution of the traps, N_{eff} is effective density of the states, η is efficiency of charge carrier detrapping by excitons, τ_0 is the life time of excitons, κ is linear absorption coefficient, I_0 is intensity of the incident light flux and y is the direction perpendicular to plane of the layer.

Due to the beam of light can be applied from substrate side and from non-substrate side of the sample, two different cases have been taken into consideration.

For case $I(y \rightarrow 0)$ (see Fig. 5), using Eqs. (1) and (3) and the assumption that $E_0 \approx U/L$, where U is voltage applied to the sample and L is the distance between electrodes, the current may be expressed as

$$I_I = \underbrace{\frac{N_{\text{eff}}n_{t0}e\mu Uab}{L} [\eta\tau_0\kappa I_0]^{1-1/\ell}}_A \underbrace{\left[\frac{1}{H_0} + \frac{e^{-\kappa d(1-1/\ell)}}{H_d} \right]}_B. \quad (4)$$

An analogous relationship for the case II ($y \rightarrow d$), may be obtained:

$$I_{II} = \underbrace{\frac{N_{\text{eff}}n_{t0}e\mu Uab}{L} [\eta\tau_0\kappa I_0]^{1-1/\ell}}_A \underbrace{\left[\frac{e^{-\kappa d(1-1/\ell)}}{H_0} + \frac{1}{H_d} \right]}_B. \quad (5)$$

Eq. (4) (for the case I) and (5) (for the case II) represent the photocurrent flowing through the sample in direction parallel to the layer, under the light illumination perpendicular to the layer in presence of trapped charge carriers near the surface with different concentration of traps at the substrate (H_0) and non-substrate side (H_d) and with exponential distribution of the traps according to the energy.

4. Results and discussion

According to Eqs. (4) and (5), the term A describes photocurrent as a function of light intensity (I_0) and the term B describes the photocurrent dependence on the absorption coefficient (κ). Taking into account traps concentration and analysing Eq. (4) for the case I we can finally show, that

$$\frac{1}{H_0} \gg \frac{e^{-\kappa d(1-1/\ell)}}{H_d}, \quad (6)$$

the surface photoenhanced current is directly proportional to the light intensity and absorption coefficient ($j \sim (I_0\kappa)^{1-1/\ell}$). This type of relationship is usually called as symbatic and it has been observed under the sample illumination in the case I (Fig. 2a and b). The symbatic behaviour of the photocurrent is possible when $H_0 \ll H_d$. When $H_0 \gg H_d$, based on Eq. (4) the antibatic relationship for the measured photocurrent can be obtained. Antibatic relation was not obtained experimentally under the illumination in the case II.

Analysing the relationship (5), under the case II, we can conclude that

$$\frac{1}{H_d} \ll \frac{e^{-\kappa d(1-1/\ell)}}{H_0}. \quad (7)$$

From the above we obtained antibatic relation describing the surface photoenhanced current.

Conclusion presented above, from Eqs. (6) and (7), stay in a good agreement with experimental results presented in Fig. 2. Eqs. (4) and (5) follow underlinear photocurrent–light intensity characteristics. Slope of photocurrent–light intensity characteristics is equal $n = 1 - 1/\ell$. Based on experimental data presented in Fig. 3, we can find $\ell_I \cong 2.5$ for substrate side and $\ell_{II} \cong 2$ for non-substrate side of the layer. It seems that energetical distribution of traps is not so different, at different value of concentration of the traps. The photocurrent dependence on applied voltage is presented in Fig. 4. Based on experimental data and results of theoretical analysis we can conclude, that in tetra-cene layers concentration of traps is much smaller at the substrate side (H_0) than at non-substrate side (H_d) of the sample.

The last statement leads to conclusion, that greater value of the enhanced photocurrent can be obtained under low concentration of traps and with the value of traps distribution parameter from the range ($\ell \cong 2$ to 2.5) from both sides.

These results can be understood that after detrapping of charge carrier, electrical currents are function of Schubweg distance (S).

The distance of Schubweg can be estimated as follows:

$$S = \mu E_0 \tau, \quad (8)$$

where μ is charge carriers mobility and τ is charge carriers lifetime in the band.

The charge carrier lifetime can be described as follows:

$$\tau = (Hv\sigma)^{-1}, \quad (9)$$

where σ is the cross-section for charge carrier trapping, v is the charge carrier thermal velocity.

When charge carrier traps concentration at substrate side (H_0) is smaller than at non-substrate side (H_d) the charge carrier lifetime at the substrate side can be represented as follows:

$$\tau_0 = (H_0 v \sigma)^{-1} \quad (10)$$

and its value is greater than the lifetime at non-substrate side which is given by

$$\tau_d = (H_d v \sigma)^{-1}. \quad (11)$$

The results following from the above relationships can be closed by the statement that the distance of Schubweg at the substrate side S_0 is greater than at non-substrate side S_d . Longer distance of Schubweg leads to higher enhancement of the photocurrent.

5. Final conclusion

The surface photoenhanced current transport investigation in the direction parallel to the layers show that charge carrier transport is realised near

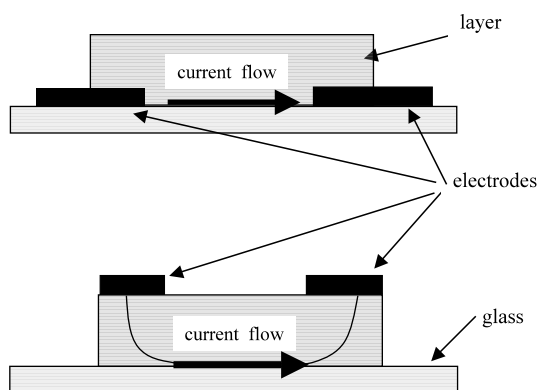


Fig. 6. Possible direction of current flow in layer for a different configuration of the experimental system for the sample.

the substrate surface (Fig. 6). This effect results from non-uniform distribution of the charge carriers traps in the tetracene layers in direction perpendicular to the layer, which causes non-uniform detrapping of charge carriers by excitons. This conclusion is very important for the construction of field effect transistors and phototransistors for molecular physics.

References

- [1] K.C. Kao, W. Hwang, *Electrical Transport in Solids*, Pergamon Press, Oxford/New York, 1981.
- [2] M. Pope, C.E. Swenberg, *Electronic Processes in Organic Crystals*, Clarendon Press, New York, 1982.
- [3] J. Godlewski, J. Kalinowski, *Phys. Status Solidi (a)* 53 (1979) 161.
- [4] D. Kotowski, J. Godlewski, *Mol. Phys. Rep.* 36 (2002) 174.
- [5] M. Pope, N.E. Geactinow, F. Vogel, *Mol. Cryst. Liq. Cryst.* 6 (1969) 83.
- [6] R.P. Groff, P. Avakian, R.E. Merrifield, *Phys. Rev. B* 1 (1970) 815.
- [7] W. Helfrich, *Physics and Chemistry of the Organic Solid States*, Wiley Interscience, New York, 1967.
- [8] H. Bauser, H.H. Ruf, *Phys. Status Solidi* 32 (1969) 135.
- [9] J. Godlewski, J. Kalinowski, *Solid State Commun.* 25 (1978) 473.
- [10] G. Jarosz, R. Signerski, J. Godlewski, *Acta Phys. Pol. A* 87 (1995) 855.
- [11] J. Godlewski, G. Jarosz, R. Signerski, *Phys. Status Solidi (b)* 226 (2001) 185.
- [12] J. Godlewski, G. Jarosz, R. Signerski, *Appl. Surf. Sci.* 175 (2001) 344.
- [13] A.G. Tangena, J. Middehoek, N.F. de Rooij, *J. Appl. Phys.* 49 (5) (1978) 2876.
- [14] N.E. Geactinow, M. Pope, H. Kallman, *J. Chem. Phys.* 45 (1966) 2639.



Amorphous organic molecule/polymer diodes and transistors—Comparison between predictions based on Gaussian or exponential density of states

Nir Tessler*, Yohai Roichman

Electrical Engineering Department, Technion Israel Institute of Technology, Haifa 32000, Israel

Received 5 May 2005; received in revised form 13 June 2005; accepted 30 June 2005

Available online 25 July 2005

Abstract

We examine the role of the density of states in determining the performance of amorphous organic devices. Specifically we compare the exponential density of states and the Gaussian density of states. We find that the shape of the density of states affects dramatically the ideality factor of P–N diodes and the gate voltage dependence of the mobility in field effect transistors. By comparing to experimental results we conclude that a real DOS should have the attributes found in Gaussian density of states. Also, since the Gaussian density of states do not easily allow to produce simple analytical expressions, methods that are developed for Gaussian density of states can more easily be adapted to real shapes of density of states which are not necessarily described by a single Gaussian.

© 2005 Elsevier B.V. All rights reserved.

PACS: 72.20.Ee; 72.80.Le; 72.80.Ng; 73.61.Ph

Keywords: Transport; Diode; FET; Organic; Polymer; Molecule

1. Introduction

In organic polymers or small molecule devices one often finds that the classical models found in inorganic device textbooks [1] and the I – V characteristics that they predict do not fit experimental data. In the literature there exist models that focus

on the charge transport phenomena or charge injection. In the charge transport context one can find models based on charge density effects only, as in trap-filling [2–5], models based only on field induced lowering of transport barriers [6–10], or even non-equilibrium models [11–14], where the concept of mobility is a bit vague. Similarly, one can find models for contact injection which are based on the assumption of equilibrium at the contact interface [15–18] or non-equilibrium [19–22].

* Corresponding author. Tel./fax: +97 248294719.
E-mail address: nir@ee.technion.ac.il (N. Tessler).

(We restrict the discussion here to amorphous films and we only mention that the balance of processes is different in high purity organic crystalline materials [23,24].) An outsider to this field may be tempted to conclude that these materials are so ill-defined that each group is actually studying a different material and hence must resort to a different physical picture in order to achieve a perfect overlap between theory and experiment. However, if one looks carefully, it is apparent that sometimes even a single group studying the same material is using a different physical model each time. This indicates that the materials are not at fault and that better self-consistency is required.

In the past 5 years there have been extensive efforts to extend the physical picture developed, at the early stages of the field, originally for low charge density experiments [6,7,11,12,22], as the time of flight, to the LED, FET and solar cell operating conditions [14,25–27]. In our study we have been insisting on using a single physical picture for all device architectures and operating conditions [18,26–28] and we chose the most popular physical picture that was put forward by Bassler and coworker, i.e. hopping in a Gaussian density of states. While the immediate result was that many experimental curves could not be perfectly fitted any more it had positive effects on our theoretical and experimental work. In the theoretical part it forced us into expanding the Bassler model to account for both charge-density and electric-field effects [26,27,29,30] and find methods where it can be directly integrated into device models [18] and thus describe also the contact phenomena. The contribution of Arkhipov et al. in expanding [20,25,31,32] the Gaussian DOS model is of great importance in the current context. In the experimental part it made us realize that many “standard” methods to extract parameters, such as mobility or contact barrier height, are not suitable for disordered organic materials [30,33,34]. Such single-model attitude has led us to the conclusion that the most important and missing parameter is the actual density of states of a pristine material that is embedded in a realistic device configuration. This implies that any formalism that is to be developed must be simple and flexible enough to allow for any DOS shape that would eventually

be measured. We do not believe we have found the bench-mark model that would solve all problems or unify all physical scenarios but we believe that the approach that led us to this model would yield the most useful device-related models. Our goal here is to demonstrate the importance of the density of state shape for device applications and of self-consistency or single physical picture approach.

We limit ourselves here to the regime where the device is close to the steady state and hence (in most cases) one can apply standard device model approach that relies on the existence of equilibrium (or quasi-equilibrium) in the sample. In other words, from the device point of view, it is important to be able to define the shape of the charge density of states (DOS) and the value of the quasi-Fermi-level. Since all expressions for the I - V characteristics of devices start with the current equation

$$J_h = q\mu_h n_h E - qD_h \frac{d}{dx} n_h$$

it is important to examine the mobility (μ) and the diffusion coefficient (D) and again, in the context of devices, the ratio between the two (generalized Einstein relation [26,35,36]) is the most important factor.

2. The diffusion coefficient

The generalized Einstein relation is derived from the current equation under the assumption that the net current that flows is much smaller than the drift or diffusion currents and it can be regarded as a very small perturbation ($q\mu_h n_h E \approx qD_h \frac{d}{dx} n_h \gg J_h$). This is then expressed as $\mu_h = D_h \frac{1}{n_h} \frac{dn_h}{E dx} = -D_h \frac{1}{n_h} \frac{dn_h}{dV}$ where in order to intuitively understand its meaning we need to remember that the role of diffusion is in smoothing and averaging out charge density differences. Having that in mind, the last expression actually implies that if the system (DOS) is such that a change in potential (Fermi-level) should result in a very small increase of the charge density ($\frac{dn_h}{dV} \ll 1$) then, for the current equation to still hold, the diffusion coefficient must become large so as not to allow

a voltage drop to create large density differences. To make the derivation more formal we use the fact that a difference in potential between two points is defined as the difference between the quasi-Fermi-levels [26,35]:

$$\frac{D}{\mu} = -n \left(\frac{dn}{dE_f} \right)^{-1} \quad (1)$$

For a Gaussian DOS, $\text{DOS}_{\text{gauss}} = \frac{N_V}{\sqrt{2\pi}\sigma} \exp \left[-\left(\frac{\varepsilon - \varepsilon_0}{\sqrt{2}\sigma} \right)^2 \right]$ we find:

$$\begin{aligned} \frac{D}{\mu} &= \frac{kT}{q} \frac{\int_{-\infty}^{\infty} \exp \left[-\left(\frac{\varepsilon - \varepsilon_0}{\sqrt{2}\sigma} \right)^2 \right] \cdot \frac{1}{1 + \exp \left(\frac{\varepsilon - \varepsilon_F}{kT} \right)} d\varepsilon}{\int_{-\infty}^{\infty} \exp \left[-\left(\frac{\varepsilon - \varepsilon_0}{\sqrt{2}\sigma} \right)^2 \right] \cdot \frac{\exp \left(\frac{\varepsilon - \varepsilon_F}{kT} \right)}{[1 + \exp \left(\frac{\varepsilon - \varepsilon_F}{kT} \right)]^2} d\varepsilon} \\ &= \frac{kT}{q} \eta_G \end{aligned} \quad (2)$$

And for an exponential DOS, $\text{DOS}_{\text{exp}} = \frac{N_V}{kT_0} \exp \left(\frac{\varepsilon}{kT_0} \right)$, we find:

$$\begin{aligned} \frac{D}{\mu} &= \frac{kT}{q} \frac{\int_{-\infty}^{\infty} \exp \left(\frac{\varepsilon}{kT_0} \right) \cdot \frac{1}{1 + \exp \left(\frac{\varepsilon - \varepsilon_F}{kT} \right)} d\varepsilon}{\int_{-\infty}^{\infty} \exp \left(\frac{\varepsilon}{kT_0} \right) \cdot \frac{\exp \left(\frac{\varepsilon - \varepsilon_F}{kT} \right)}{[1 + \exp \left(\frac{\varepsilon - \varepsilon_F}{kT} \right)]^2} d\varepsilon} \\ &= \frac{kT}{q} \eta_{\text{exp}} \approx \frac{kT_0}{q} \end{aligned} \quad (3)$$

Fig. 1A shows the calculation of the enhancement of the Einstein relation $\left(\frac{D}{\mu} \frac{q}{kT} \right)$ assuming a Gaussian DOS, for several DOS widths (σ). We note that at very low charge density the Einstein relation enhancement tends towards 1 $\left(\frac{D}{\mu} = \frac{kT}{q} \right)$ indicating that the material is non-degenerate at low charge densities and becomes degenerate at device related densities. Fig. 1B shows the calculation of the enhancement of the Einstein relation $\left(\frac{D}{\mu} \frac{q}{kT} \right)$

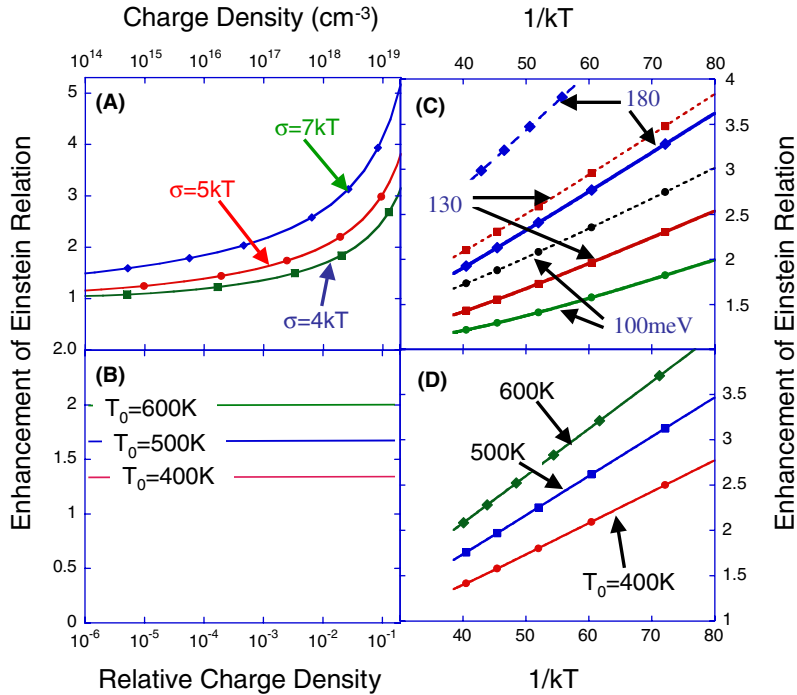


Fig. 1. Enhancement of the Einstein relation as a function of charge density (A and B) and of temperature (C and D). (A) Assuming the DOS is Gaussian and for widths of 100 meV, 130 meV, 180 meV. (B) Assuming the DOS is exponential and for characteristic temperatures of 400 K, 500 K, and 600 K. (C) Assuming Gaussian DOS of 100 meV (circles), 130 meV (squares), 180 meV (diamonds). The solid line was calculated for relative charge density of 10^{-4} (10^{16} cm $^{-3}$) and the dashed lines for relative charge density of 10^{-2} (10^{18} cm $^{-3}$). (D) Assuming the DOS is exponential and for characteristic temperatures of 400 K, 500 K, and 600 K.

assuming an exponential DOS, for several characteristic temperatures (T_0). We note that unlike the Gaussian DOS the generalized Einstein relation for exponential DOS is independent of the charge density and is always higher than kT/q .

In order to gain some insight as to the origin of the above differences we plot in Fig. 2 the average energy of the charge population as a function of the quasi-Fermi-level (charge density).

The line with rectangle markers was calculated for exponential DOS with $T_0 = 450$ K and the line with circular markers was calculated for a Gaussian density of states with $\sigma = 100$ meV. We note that for the exponential DOS the average energy tracks the value of the quasi-Fermi-level for any value. The position of the charge population close to the Fermi-level is an indication that the material would be degenerate at any charge density and indeed the generalized Einstein relation shown in Fig. 1B is larger than one. The straight line dependence indicates that the exponential DOS is never empty nor full. This difference between the two distributions have been noted in different ways in the past and was also used to explain why an exponential DOS will more easily tend towards non-equilibrium transport and hence transport in such system will be highly dispersive [37–39]. This no-bottom effect have been linked to the basic description of dispersive transport [11,12] measurements that seem to exhibit any time scale and specifically as long as one would be able to measure. Very few

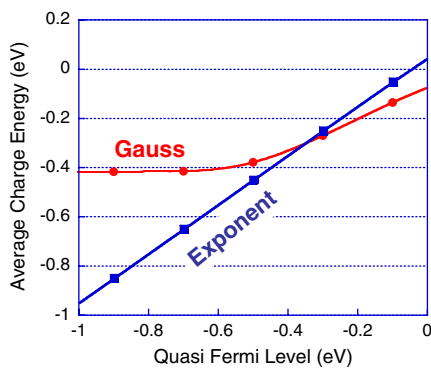


Fig. 2. Average energy of the carrier population as a function of the position of the quasi-Fermi-level for an exponential DOS characterized by $T_0 = 450$ K (squares) and for a Gaussian DOS characterized by $\sigma = 100$ meV (circles).

experiments did attempt to test the hypothesis of “as long as one would be able to measure” but for example in [40] it is shown that there is a cut-off at long time scales or slow rates and in [41] a detailed discussion of dispersive to non-dispersive transition may also be found. Such a cut off indicates that while in some cases one can ignore the existence of a bottom to the DOS it is still there. In fact one can realize that a physical DOS must have a bottom simply by realizing that it is not possible to have the electron population belonging to the LUMO level residing below the HOMO level.

The Gaussian DOS however, exhibits a bottom like effect where the average carrier energy cannot go below a certain value ($-\sigma^2/kT$). Since the energy distribution of the charge carrier is dictated by the DOS multiplied by the Fermi–Dirac distribution a bottom like effect will occur where the DOS decays much faster than the Fermi–Dirac function, that asymptotically behave like $\exp(\frac{E-E_F}{kT})$. Such faster decay cannot be found in an exponential distribution and for a Gaussian DOS it occurs at $\sim\sigma^2/kT$ below the center of the Gaussian.

Having said the above one should still remember that models based on exponential DOS have been very successful over the years and specifically are reported to be good enough to describe certain aspects of organic FETs [5,42].

3. Low field mobility

Using the mean medium approximation [30] it becomes possible to calculate the effect of both the charge density and electric field on the mobility value. As other models typically address only one or the other we start with examining the charge density dependence at the low field limit (see Fig. 3). It turns out that the results from the full calculation can be approximated using the following expression:

$$\mu = \mu_{\max} \cdot \psi \cdot (1 + (\tanh((\bar{p}/0.05)^\lambda))/\psi) \quad (4)$$

where $\bar{p} = \frac{P_{3D}}{P_{DOS}}$ is the 3D charge density normalized to the total DOS, μ_{\max} is the maximum mobility, and $\psi = \mu_{\min}/\mu_{\max}$. For $\bar{\sigma} = \frac{\sigma}{kT}$ between 4 and 8 $\psi \simeq 10^{-(\bar{\sigma}-3)}$ and in this range the parameter λ is expressed as:

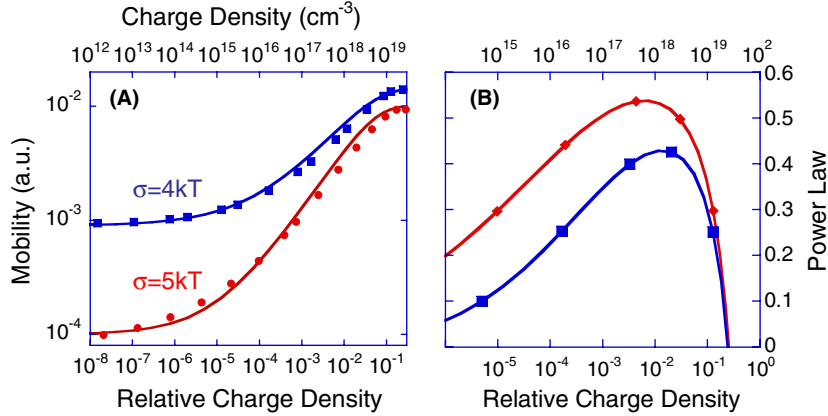


Fig. 3. The calculated charge density dependent mobility assuming negligibly small electric field. The symbols were obtained using the full MMA calculation [30] and the full lines were computed using Eq. (4) in the text.

$$\lambda = 0.73 - 1.17 \cdot (\bar{\sigma} + 1) \cdot \exp\left(-\frac{\bar{\sigma} + 1}{1.65}\right) \quad (5)$$

The good agreement between the expression shown in Eq. (4) and the full calculation is shown in Fig. 3A. Fig. 3B shows the slope of the log–log plot (power law) as a function of charge density. This figure demonstrates two issues: (a) The parameter λ in Eq. (5) is the maximum slope which is positioned at the high density regime. (b) At lower densities (found in LED/diodes) the density dependence of the mobility is much weaker and in certain circumstances can be neglected.

If one examines Fig. 3A in the experimentalist eyes and try to make the best linear fit across as wide as possible range then such an averaging will approximate the mobility as $\mu \propto P^\kappa$ [30] where

$$\kappa = 0.73 - 1.17 \cdot \bar{\sigma} \cdot \exp\left(-\frac{\bar{\sigma}}{1.65}\right) \quad (6)$$

Next, we compare the results with those obtained using exponential DOS where it has been shown [5,43] that the mobility can be described as a power law of the form:

$$\mu \propto P^{\left(\frac{T_0}{T} - 1\right)} \quad (7)$$

This expression is supposed to be valid for all charge densities and hence cannot be compared with the Gaussian model predictions. However, if we limit ourselves to a narrow range (of normalized charge concentration near 10⁻³ or 10⁻²), as

may be found in a single experiment, we can compare Eqs. (6) and (7). Doing so we find that $\bar{\sigma} = 5 \rightarrow T_0 = 435$ and $\bar{\sigma} = 7 \rightarrow T_0 = 485$.

4. Field and density dependent mobility

In Ref. [30] we reported that the electric field dependence of the mobility predicted by the MMA model for the low charge density regime (μ_{\min} in Eq. (4)) is identical to the predictions previously made by Bassler et al. for the Gaussian model using Monte Carlo simulations at the low density limit [6]:

$$\mu = \mu_{E=0} \exp\{c[\bar{\sigma}^2 - 2.25]\sqrt{E}\} \quad (8)$$

where $c \approx 2 \times 10^{-4} \text{ (cm/V)}^{0.5}$. Using this we can extend expression (4) to account for it simply by redefining ψ as:

$$\psi = \mu_{\min} \cdot \exp\{c[\bar{\sigma}^2 - 2.25]\sqrt{E}\} / \mu_{\max} \quad (9)$$

Namely, Eqs. (4), (5) and (9) reproduce empirically the results of the field and density dependent mobility obtained by the MMA method [30].

5. Temperature dependence

The MMA model as developed in [30,44] (using the Miller Abraham rate) is not expected to fully reproduce temperature dependence of the

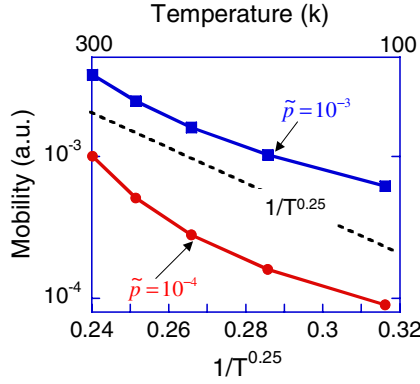


Fig. 4. Calculated mobility as a function of inverse temperature for two relative charge densities of 10^{-3} ($\sim 10^{17} \text{ cm}^{-3}$) and 10^{-4} ($\sim 10^{16} \text{ cm}^{-3}$).

mobility. The applicability of the MMA model, as developed in [30,44], to any DOS, to any charge density, and to a wide range of electric fields comes with a penalty that it is not valid at very low temperatures. This is due to the fact that the polaronic effects such as polaron binding energy (0.2–0.4 eV) and phonon temperature (350–500 K) [45,46] are not included. Also, the notion of the conductivity being determined by percolation paths [47,48], that is important primarily at low temperatures, is not included. Nevertheless, for the sake of completeness we show the prediction of this model for the temperature dependence of the mobility. Fig. 4 shows the mobility calculated using the MMA model versus $1/T^{0.25}$, following Mott's notion of variable range hopping [47]. The upper curve was calculated for a filling factor (relative to the total DOS) of 10^{-3} and the lower for 10^{-4} . The dashed line shows the slope of $\exp(1/T^{0.25})$ dependence.

6. Device performance and analysis

6.1. Diode or P–N junction

Our aim here is to examine how the I – V characteristics of a classic diode structure are altered due to charge density dependence of the mobility and of the Einstein relation. More specifically we will derive an expression for the effective ideality factor. The motivation for this analysis is the appear-

ance of high quality organic-diodes based on N and P doping [36]. For simplicity of the calculations we assume a N^+P where the current across the junction is carried mainly by electrons and the P side is long (wide diode). We start with the equation relating the built in electric field (E) to the charge distribution across the junction:

$$E = -\frac{D}{\mu} \frac{1}{\bar{n}} \frac{d\bar{n}}{dx} \quad (10)$$

The built in voltage (V_B) is then:

$$V_B = -\int_{-\infty}^{\infty} E(x) dx = \int_{x_1}^{x_2} \frac{D}{\mu} \frac{1}{\bar{n}} \frac{d\bar{n}}{dx} dx \quad (11)$$

where x_1 and x_2 are well outside the junctions. If D/μ is varying slowly, compared to the charge density, across the junction one can relate the built in potential (V_B) to the equilibrium electron density on the N (\bar{n}_N) and P (\bar{n}_P) sides of the junction in the form:

$$V_B = -\int_N^P \frac{D_c}{\mu_c} \frac{1}{n} dn = -\frac{D_c}{\mu_c} \cdot \ln(n)|_N^P \quad (12)$$

which yields:

$$V_B = \frac{D_c}{\mu_c} \Big|_N \cdot \ln(\bar{n}_N) - \frac{D_c}{\mu_c} \Big|_P \cdot \ln(\bar{n}_P) \quad (13)$$

Once an external voltage is applied (V_A) the actual voltage drop across the junction (V_i) is related to the charge density under current/voltage excitation (n_N and n_P):

$$\begin{aligned} V_i &= V_B - V_A \\ &= \frac{D_c}{\mu_c} \Big|_N \cdot \ln(\bar{n}_N) - \frac{D_c}{\mu_c} \Big|_P \cdot \ln(n_P) \end{aligned} \quad (14)$$

where we have used $n_N \cong \bar{n}_N$ due to electrons being the majority carrier on the N side. After rearranging the terms:

$$\begin{aligned} n_P &= \exp \left\{ \frac{\mu_c}{D_c} \Big|_P \left[\frac{D_c}{\mu_c} \Big|_N \cdot \ln(\bar{n}_N) - V_B + V_A \right] \right\} \\ &= n_0 \exp \left\{ \frac{\mu_c}{D_c} \Big|_P V_A \right\} \end{aligned} \quad (15)$$

where n_0 is a constant defined by Eq. (15) and its value is dictated by the junction profile. The excess minority charge profile on the P side takes then its usual form:

$$\hat{n}_p(x)|_{x>0^+} = n_0 \left(e^{\frac{\mu V_A}{D}} - 1 \right) e^{-\frac{x}{\sqrt{D\tau}}} \quad (16)$$

where τ is the minority (electron) recombination rate in side P.

The electron current can thus be deduced as:

$$\begin{aligned} I_e|_{0^+} &= qAD_e \frac{d}{dx} (\hat{n}_p) \Big|_{x>0^+} \\ &= -\frac{qAn_0}{\sqrt{\tau_e}} \sqrt{\mu_e} \sqrt{\frac{D_e}{\mu_e}} \left(e^{\frac{\mu_e V_A}{D_e}} - 1 \right) \end{aligned} \quad (17)$$

Using the general Einstein relation (see Eq. (2) or (3)) of $\frac{D}{\mu} = \eta \frac{kT}{q}$:

$$I_e|_{0^+} = -\frac{qAn_0}{\sqrt{\tau_e}} \sqrt{\frac{\eta_e kT}{q}} \mu_e \left(e^{\frac{qV_A}{\eta_e kT}} - 1 \right)$$

If we recall that the mobility is density dependent:

$$\mu_e \propto n_p^\kappa \propto e^{\frac{\kappa \mu_e V_A}{D_e}}$$

Eq. (17) then takes the form:

$$\begin{aligned} I_e|_{0^+} &\equiv -R_0 \sqrt{\frac{D}{\mu}} e^{\frac{\kappa \mu V_A}{2D}} \left(e^{\frac{\mu V_A}{D}} - 1 \right) \\ &\cong -R_0 \sqrt{\frac{D}{\mu}} \left(e^{V_A \frac{\kappa}{2} \left(1 + \frac{\kappa}{2} \right)} \right) \end{aligned} \quad (18)$$

which accounting for the general Einstein relation results in:

$$I_e|_{0^+} \approx -R_0 \sqrt{\frac{D}{\mu}} \exp \left(\frac{V_A q}{1 + \kappa/2} \right) \quad (19)$$

And the ideality factor n_f is:

$$n_f = \frac{\eta}{1 + \kappa/2} \quad (20)$$

Using Eqs. (2), (3), (6) and (7) in (20) we can calculate the ideality factor predicted by a Gaussian DOS or exponential DOS models.

Fig. 5 describes the ideality factor as a function of inverse temperature for a device made with a semiconductor comprising of a Gaussian DOS (Fig. 5A) or exponential DOS (Fig. 5B). In the exponential DOS case the interplay between the enhancement of the Einstein relation and of the mobility nearly cancel out the dependence on T_0 and makes the ideality factor almost constant

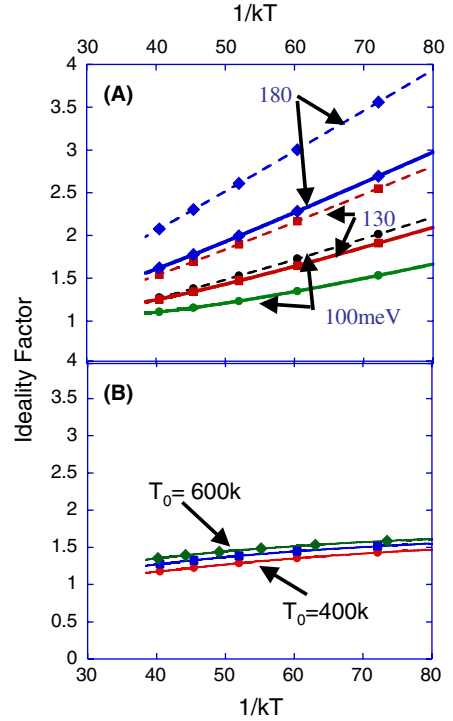


Fig. 5. Calculated ideality factor for P–N junction type device. (A) Assuming Gaussian DOS width (σ) of 100 meV (circles), 130 meV (squares), 180 meV (diamonds). The solid lines were calculated for relative charge density of 10^{-4} (10^{16} cm $^{-3}$) and the dashed lines for relative charge density of (\Rightarrow) 10^{-2} (10^{18} cm $^{-3}$). (B) Assuming exponential DOS (the result is almost independent of the T_0 parameter).

and smaller than 2. In the Gaussian DOS case (Fig. 5A) we note a relatively strong temperature dependence which varies with the amount of disorder found in the sample (σ). The solid lines in Fig. 5A were calculated for relative charge density of 10^{-4} (10^{16} cm $^{-3}$) and the dashed lines for relative charge density of 10^{-2} (10^{18} cm $^{-3}$). This shows that for a Gaussian DOS the ideality factor would also be density dependent (or bias dependent). We now refer the reader to the experimental data obtained by Harada et al. [36] who studied high quality organic diodes. Especially we refer to Fig. 3A of that paper which shows the experimentally determined ideality factor as a function of the inverse temperature. The data presented in this paper looks very similar to the predictions made by the Gaussian model (Fig. 5A). Namely, the DOS in

the real device is very likely to have the attributes of a Gaussian DOS [49] and is by no means exponential.

7. Field effect transistor

The field effect transistor is a well studied device structure where the common equations used to describe it are:

$$I_{DS_Lin} = \frac{W}{L} \mu C_{ins} \left[(V_{GS} - V_T) V_{DS} - \frac{V_{DS}^2}{2} \right]$$

for V_{GS} in accumulation regime and
 $|V_{DS}| \leq |V_{GS}|$ (21)

$$I_{DS_Sat} = \frac{W}{L_{EFF}} \mu C_{ins} [V_G - V_T]^2$$

for V_{GS} in accumulation regime and
 $|V_{DS}| \geq |V_{GS}|$ (22)

The derivation of the above equations for the linear (21) and saturation (22) regime assumes a constant mobility. However, for an FET based on the conductor–insulator, π -conjugated technology (CI π -FET) one has to account for charge density and possibly also electric field dependence [33,42,43] and hence, one has to recalculate the current equations. The charge 2D-density at the channel can be written as:

$$n_s(x) = (C_g/q)[V_{GS} - V_T - v(x)] \quad (23)$$

Where $v(x)$ is the potential in the channel at point x . The current at each point can be written then as:

$$I_{DS} = W q n_s(x) \mu(x) \frac{-dv(x)}{dx} \quad (24)$$

Integrating Eq. (24) from 0 to L :

$$\int_0^L I_{DS} dx = \int_0^L W q n_s(x) \mu(x) \frac{-dv(x)}{dx} dx$$

$$I_{DS} = \frac{W}{L} \int_0^L C_g [V_{GS} - V_T - v(x)] \mu(x) \frac{dv(x)}{dx} dx \quad (25)$$

And finally replacing the integration over x with that of the channel potential:

$$\begin{cases} |I_{DS_Lin}| = \frac{W}{L} \int_0^{V_{DS}} C_g [V_{GS} - V_T - v] \\ \quad \times \mu(V_{GS} - V_T - v) dv \\ |I_{DS_Sat}| = \frac{W}{L} \int_0^{V_{GS} - V_T} C_g [V_{GS} - V_T - v] \\ \quad \times \mu(V_{GS} - V_T - v) dv \end{cases} \quad (26)$$

For example, the simplest way of fitting the mobility is through a simple polynomial [33] function:

$$\mu(V_{GS} - V_T - v) = \sum_{n=0}^N \mu_n [V_{GS} - V_T - v]^n \quad (27)$$

where μ_n are coefficients to be fitted. The equations describing the current take the form (assuming $V_{GS} - V_T > 0$):

$$I_{DS_Lin} = C_g \frac{W}{L} \sum_{n=0}^N \frac{\mu_n}{n+2} [(V_{GS} - V_T)^{n+2} - (V_{GD} - V_T)^{n+2}] \quad (28)$$

for V_{GS} in accumulation regime and $V_{DS} \leq V_{GS}$ and

$$I_{DS_Sat} = C_g \frac{W}{L} \sum_{n=0}^N \frac{\mu_n}{n+2} (V_{GS} - V_T)^{n+2} \quad (29)$$

for V_{GS} in accumulation regime and $V_{DS} \geq V_{GS}$. Using this formalism it is possible to fit the current and find the coefficients ($\mu_0 \dots \mu_N$) and thus derive the mobility even for the low density regime which is inevitably associated with non-uniform charge distribution across the channel.

Eqs. (28) and (29) look very similar to equations derived under the assumption that the mobility can be described using a single power law [4,5,42,50,51] which have their physical origin in the exponential distribution of trapping states. The advantage of Eqs. (28) and (29) is that one does not force a specific DOS and it allows for both exponential DOS as well as DOS that results in an onset and a saturation of the density dependence (see for example Fig. 3A). Moreover, as we will show below, it also shows where electric field dependence has to be taken into account too. There is no doubt that a single power law can give an excellent fit over an order of magnitude however, some details of the physical picture are lost in the process.

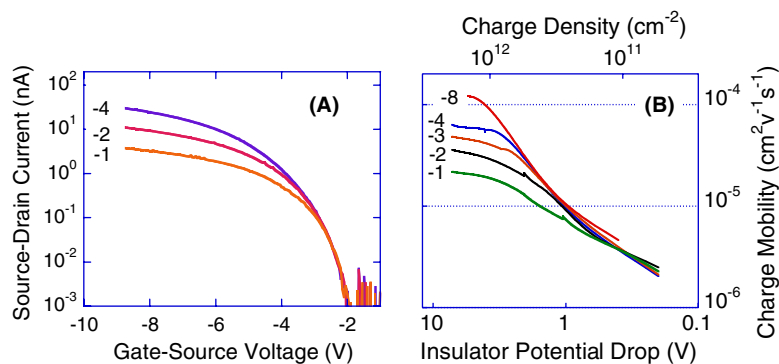


Fig. 6. (A) Source–drain current as a function of gate bias for several drain source voltages. (B) The hole mobility dependence on the 2D charge density (divided by $C_{\text{ins}} = 43 \text{ nF cm}^{-2}$) derived based on Eqs. (28) and (29) using $V_T = -1.8 \text{ V}$, $W = 0.6 \text{ cm}$, $L = 9.5 \text{ }\mu\text{m}$.

Fig. 6A shows the transfer characteristics of Cl π -FET made using Si/SiO₂ and MEH-PPV. The current shows an onset at about 2 V gate–source voltage for the range of drain source bias measured (only $V_{DS} = -1, -2, -4$ are shown). These I - V curves were fitted using Eqs. (28) and (29) from the very onset of current (determined by our measurement set-up sensitivity) and up to the high voltage regime. This fit results in a set of coefficients, μ_n , which are used in Eq. (27) to calculate the mobility. The results of such procedure are shown in Fig. 6B. The x-axis corresponds to the voltage that drops across the insulator and the 2D charge density is directly related to it through $n_{2D} = C_{\text{ins}}V_{\text{ins}}/q$ (see top axis). The results show that the lowest bias is not low enough to prove or disprove the existence of an onset of charge density dependence of the mobility. However, if one considers also values extracted from light emitting device configuration such an onset can be found. The high voltage (charge density) range clearly shows the appearance of saturation. This feature can not be explained using exponential DOS and would be missed if the analysis would have been based on such assumption.

Turning our attention to the relative shapes of the curves. As long as V_{GS} is below V_{DS} the transistor is in saturation and the potential across the channel is changing and equal V_{GS} . Once V_{GS} is larger than V_{DS} the potential across the channel is fixed at V_{DS} and the electric field along the channel stops changing. Based on the above we would expect all the mobility curve to be the same for the

low bias range regardless on the value of V_{DS} , which indeed is the case. If the mobility is electric field dependent we would expect the curves to gradually depart from each other as we cross the relevant V_{DS} values. This again is exactly what we see in Fig. 6B. Since the curve for $V_{DS} = -1 \text{ V}$ is almost a perfect straight line up to the saturation point we tend to conclude that up to the corresponding electric field of $\sim 10^3 \text{ V cm}^{-1}$ the mobility is practically field independent. Examining the maximum mobility derived for each V_{DS} value we find that the mobility varies by less than an order of magnitude ($\sim \times 6$) between $\sim 10^3 \text{ V cm}^{-1}$ and $\sim 10^4 \text{ V cm}^{-1}$. Again, we see that a DOS that is close to Gaussian is more appropriate to capture a wide angle of the physical picture. If we insist on fitting the mobility data using a single Gaussian then the best fit would be for $\sigma \approx 130 \text{ meV}$.

8. Conclusions

We have compared the analysis of organic devices assuming an exponential DOS and Gaussian DOS. We found that while the exponential DOS approach can provide excellent fits over a limited physical picture (as found in a single device experiment) it can not capture the full physical picture. It was shown that the approach that relies on a DOS that has the attributes found in a Gaussian (top and bottom) is more readily compatible with real device analysis and can help to bridge across different devices. Specifically we have presented a

calculation of the ideality factor in organic diodes and of the mobility in field effect transistors. We also emphasized that the “true” DOS is not necessarily described by a single Gaussian and hence device analysis must allow for different DOS shapes. In this context we highlighted the use of polynomial expansion of the mobility in FETs and of the general Einstein relation in diodes.

References

- [1] S.M. Sze, *Physics of Semiconductor Devices*, Wiley, New York, 1981.
- [2] P.E. Burrows, Z. Shen, V. Bulovic, D.M. McCarty, S.R. Forrest, J.A. Cronin, M.E. Thompson, Relationship between electroluminescence and current transport in organic heterojunction light-emitting devices, *J. Appl. Phys.* 79 (1996) 7991–8006.
- [3] M.A. Lampert, P. Mark, *Current Injection in Solids*, Academic Press, New York, 1970.
- [4] G. Horowitz, M.E. Hajlaoui, R. Hajlaoui, Temperature and gate voltage dependence of hole mobility in polycrystalline oligothiophene thin film transistors, *J. Appl. Phys.* 87 (2000) 4456–4463.
- [5] M. Vissenberg, M. Matters, Theory of the field-effect mobility in amorphous organic transistors, *Phys. Rev. B* 57 (1998) 12964–12967.
- [6] H. Bassler, Charge transport in disordered organic photoconductors, *Phys. State Sol. (b)* 175 (1993) 15–56.
- [7] H. Bassler, G. Schonherr, M. Abkowitz, D.M. Pai, Hopping transport in prototypical organic glasses, *Phys. Rev. B—Condens. Matter* 26 (1982) 3105–3113.
- [8] M. Van der Auweraer, F.C. Deschryver, P.M. Borsenberger, H. Bassler, Disorder in charge-transport in doped polymers, *Adv. Mater.* 6 (1994) 199–213.
- [9] W.D. Gill, Drift mobilities in amorphous charge-transfer complexes of trinitrofluorenone and poly-*n*-vinylcarbazole, *J. Appl. Phys.* 43 (1972) 5033.
- [10] V. Savvateev, A. Yakimov, D. Davidov, Transient electroluminescence from poly(phenylenevinylene)-based devices, *Adv. Mater.* 11 (1999) 519–532.
- [11] H. Scher, E.M. Montroll, Anomalous transit-time dispersion in amorphous solids, *Phys. Rev. B* 12 (1975) 2455–2477.
- [12] H. Scher, M.F. Shlesinger, J.T. Bendler, Time-scale invariance in transport and relaxation, *Phys. Today* 44 (1991) 26–34.
- [13] P.W.M. Blom, M. Vissenberg, Dispersive hole transport in poly(*p*-phenylene vinylene), *Phys. Rev. Lett.* 80 (1998) 3819–3822.
- [14] J. Nelson, R.E. Chandler, Random walk models of charge transfer and transport in dye sensitized systems, *Coord. Chem. Rev.* 248 (2004) 1181–1194.
- [15] P.S. Davids, S.M. Kogan, I.D. Parker, D.L. Smith, Charge injection in organic light-emitting-diodes—tunneling into low mobility materials, *Appl. Phys. Lett.* 69 (1996) 2270–2272.
- [16] J.C. Scott, G.G. Malliaras, Charge injection and recombination at the metal–organic interface, *Chem. Phys. Lett.* 299 (1999) 115–119.
- [17] M.A. Baldo, S.R. Forrest, Interface-limited injection in amorphous organic semiconductors, *Phys. Rev. B* 64 (2001) 85201.
- [18] Y. Preezant, N. Tessler, Self-consistent analysis of the contact phenomena in low-mobility semiconductors, *J. Appl. Phys.* 93 (2003) 2059–2064.
- [19] A.J. Heeger, I.D. Parker, Y. Yang, Carrier injection into semiconducting polymers—Fowler–Nordheim field-emission tunneling, *Synth. Metals* 67 (1994) 23–29.
- [20] V.I. Arkhipov, U. Wolf, H. Bassler, Current injection from metal to disordered hopping system. II. Comparison between analytic theory and simulation, *Phys. Rev. B* 59 (1999) 7514–7520.
- [21] T. van Woudenberg, P.W.M. Blom, M. Vissenberg, J.N. Huiberts, Temperature dependence of the charge injection in poly-dialkoxy-*p*-phenylene vinylene, *Appl. Phys. Lett.* 79 (2001) 1697–1699.
- [22] R. Metzler, J. Klafter, The random walk’s guide to anomalous diffusion: a fractional dynamics approach, *Phys. Rep.—Rev. Sec. Phys. Lett.* 339 (2000) 1–77.
- [23] N. Karl, Charge carrier transport in organic semiconductors, *Synth. Metals* 133 (2003) 649–657.
- [24] N. Karl, K.H. Kraft, J. Marktanner, M. Munch, F. Schatz, R. Stehle, H.M. Uhde, Fast electronic transport in organic molecular solids?, *J. Vac. Sci. Technol. A* 17 (1999) 2318–2328.
- [25] V.I. Arkhipov, E.V. Emelianova, H. Bassler, Equilibrium carrier mobility in disordered hopping systems, *Philos. Mag. B* 81 (2001) 985–996.
- [26] Y. Roichman, N. Tessler, Generalized Einstein relation for disordered semiconductors—Implications for device performance, *Appl. Phys. Lett.* 80 (2002) 1948–1950.
- [27] S. Shaked, S. Tal, Y. Roichman, A. Razin, S. Xiao, Y. Eichen, N. Tessler, Charge density and film morphology dependence of charge mobility in polymer field-effect transistors, *Adv. Mater.* 15 (2003), pp. 913–+.
- [28] Y. Preezant, Y. Roichman, N. Tessler, Amorphous organic devices—degenerate semiconductors, *J. Phys. Condens. Matter.* 14 (2002) 9913–9924.
- [29] Y. Roichman, N. Tessler, Charge transport in conjugated polymers—the influence of charge concentration, *Synth. Metals* 135–136 (2003) 443–444.
- [30] Y. Roichman, Y. Preezant, N. Tessler, Analysis and modeling of organic devices, *Phys. Status Solidi A* 201 (2004) 1246–1262.
- [31] V.I. Arkhipov, E.V. Emelianova, G.J. Adriaenssens, Effective transport energy versus the energy of most probable jumps in disordered hopping systems, *Phys. Rev. B* 6412 (2001), pp. art. no.-125125.

- [32] V.I. Arkhipov, P. Heremans, E.V. Emelianova, G.J. Adriaenssens, H. Bassler, Equilibrium trap-controlled and hopping transport of polarons in disordered materials, *Chem. Phys.* 288 (2003) 51–55.
- [33] O. Katz, Y. Roichman, G. Bahir, N. Tessler, J. Salzman, Charge carrier mobility in field effect transistors: analysis of capacitance–conductance measurements, *Semicond. Sci. Technol.* 20 (2005) 90–94.
- [34] J.H. Werner, H.H. Guttler, Barrier inhomogeneities at Schottky contacts, *J. Appl. Phys.* 69 (1991) 1522–1533.
- [35] N.W. Ashcroft, N.D. Mermin, *Solid State Phys.*, Holt, Rinehart and Winston, New York, 1988.
- [36] K. Harada, A.G. Werner, M. Pfeiffer, C.J. Bloom, C.M. Elliott, K. Leo, Organic homojunction diodes with a high built-in potential: interpretation of the current-voltage characteristics by a generalized Einstein relation, *Phys. Rev. Lett.* 94 (2005) 36601.
- [37] E.A. Schiff, Trap-controlled dispersive transport and exponential band tails in amorphous-silicon, *Phys. Rev. B* 24 (1981) 6189–6192.
- [38] D. Monroe, Hopping in exponential band tails, *Phys. Rev. Lett.* 54 (1985) 146–149.
- [39] Q. Gu, E.A. Schiff, S. Grebner, F. Wang, R. Schwarz, Non-Gaussian transport measurements and the Einstein relation in amorphous silicon, *Phys. Rev. Lett.* 76 (1996) 3196–3199.
- [40] E.M. Horsche, D. Haarer, H. Scher, Transition from dispersive to nondispersive transport: photoconduction of polyvinylcarbazole, *Phys. Rev. B* 35 (1987) 1273–1280.
- [41] P.M. Borsenberger, L.T. Pautmeier, H. Bassler, Non-dispersive-to-dispersive charge-transport transition in disordered molecular-solids, *Phys. Rev. B* 46 (1992) 12145–12153.
- [42] G. Horowitz, P. Lang, M. Mottaghi, H. Aubin, Extracting parameters from the current–voltage characteristics of field-effect transistors, *Adv. Funct. Mater.* 14 (2004) 1069–1074.
- [43] A. Cerdeira, M. Estrada, B. Iniguez, J. Pallares, L.F. Marsal, Modeling and parameter extraction procedure for nanocrystalline TFTs, *Solid-State Electron.* 48 (2004) 103–109.
- [44] Y. Roichman, Charge transport in conjugated polymers, in: *Electrical Engineering*, Technion, Haifa, 2004.
- [45] D. Emin, Small polarons, *Phys. Today* 35 (1982) 34–40.
- [46] S. Guha, J.D. Rice, Y.T. Yau, C.M. Martin, M. Chandrasekhar, H.R. Chandrasekhar, R. Guentner, P.S. de Freitas, U. Scherf, Temperature-dependent photoluminescence of organic semiconductors with varying backbone conformation, *Phys. Rev. B* 67 (2003).
- [47] N.F. Mott, *Electronic Processes in Non-crystalline Materials*, Clarendon Press, Oxford, 1979.
- [48] Y. Meir, Universal crossover between Efros-Shklovskii and Mott variable-range-hopping regimes, *Phys. Rev. Lett.* 77 (1996) 5265–5267.
- [49] I.N. Hulea, H.B. Brom, A.J. Houtepen, D. Vanmaekelbergh, J.J. Kelly, E.A. Meulenkaamp, Wide energy-windowview on the density of states and hole mobility in poly(*p*-phenylene vinylene), *Phys. Rev. Lett.* 93 (2004) 166601.
- [50] A. Ortiz-Conde, A. Cerdeira, M. Estrada, F.J.G. Sanchez, R. Quintero, A simple procedure to extract the threshold voltage of amorphous thin film MOSFETs in the saturation region, *Solid-State Electron.* 45 (2001) 663–667.
- [51] L. Resendiz, M. Estrada, A. Cerdeira, New procedure for the extraction of a-Si: H TFTs model parameters in the subthreshold region, *Solid-State Electron.* 47 (2003) 1351–1358.



Forming oriented organic crystals from amorphous thin films on patterned substrates via solvent-vapor annealing

Debra J. Mascaro ^{a,1}, Mark E. Thompson ^b,
Henry I. Smith ^c, Vladimir Bulović ^{c,*}

^a Department of Materials Science and Engineering, Massachusetts Institute of Technology, Cambridge, MA 02139, USA

^b Department of Chemistry, University of Southern California, Los Angeles, CA 90089, USA

^c Department of Electrical Engineering and Computer Science, Massachusetts Institute of Technology, Cambridge, MA 02139, USA

Received 21 March 2005; received in revised form 20 July 2005; accepted 25 July 2005

Available online 26 August 2005

Abstract

The challenge of generating crystals of organic materials has been pursued by many research groups who aim to develop materials sets for active electronic and optoelectronic devices, including field-effect transistors [C.D. Dimitrakopoulos, P.R.L. Malenfant, *Adv. Mater.* 14 (2002) 99; H.E. Katz, Z. Bao, *J. Phys. Chem. B* 104 (2000) 671; Y.Y. Lin, D.J. Gundlach, S.F. Nelson, T.N. Jackson, *IEEE Trans. Electron Dev.* 44 (1997) 1325], photodetectors [P. Peumans, V. Bulović, S.R. Forrest, *Appl. Phys. Lett.* 76 (2000) 2650] and optical modulators [S.R. Marder, J.W. Perry, C.P. Yakymyshyn, *Chem. Mater.* 6 (1994) 1137]. Here we describe a method for in-plane growth of millimeter-scale crystalline organic needles from initially amorphous thin films of the molecular organic semiconductor tris(8-hydroxyquinoline)aluminum (Alq₃). The needles form when the vacuum-deposited amorphous films are exposed to chloroform vapor at room temperature and pressure, and can be as large as several microns thick, several microns wide, and one centimeter long (limited in length by the substrate dimensions). As such, the Alq₃ needles are more than 1000 times longer than any previously reported organic crystals formed via a similar solvent-vapor annealing process [F. Iwatsu, T. Kobayashi, N. Uyeda, *J. Phys. Chem.* 84 (1980) 3223; F. Iwatsu, *J. Cryst. Growth* 71 (1985) 629; A.M. Hor, R.O. Loutfy, *Thin Solid Films* 106 (1983) 291; B.A. Gregg, *J. Phys. Chem.* 100 (1996) 852; J.C. Conboy, E.J.C. Olson, D.M. Adams, J. Kerimo, A. Zaban, B.A. Gregg, P.F. Barbara, *J. Phys. Chem. B* 102 (1998) 4516; M. Brinkmann, J.C. Wittmann, C. Chaumont, J.J. Andre, *Thin Solid Films* 292 (1997) 192; F. Toffolo, M. Brinkmann, O. Greco, F. Biscarini, C. Taliani, H.L. Gomes, I. Aiello, M. Ghedini, *Synth. Met.* 101 (1999) 140]. Moreover, the Alq₃ needles are spatially separated from one another and oriented with their long axes parallel to lithographically pre-defined periodic submicron grooves in the substrate surface.

© 2005 Published by Elsevier B.V.

* Corresponding author. Tel.: +1 617 253 7012; fax: +1 617 452 5110.

E-mail address: bulovic@mit.edu (V. Bulović).

¹ Present address: Department of Mechanical Engineering, University of Utah, Salt Lake City, UT 84112, USA.

PACS: 81.10.-h; 78.66.Qn

Keywords: Organic single crystal; Crystal growth; Solvent-vapor annealing; Organic thin film morphology; Tris(8-hydroxyquinoline)aluminum (Alq_3)

1. Introduction

The growth of free-standing organic crystals millimeters in size has been previously demonstrated by resublimation [13–18] and solvent recrystallization [5,13,14], and in a few studies discrete active devices have been fabricated using such crystals [19–22]. However, in order to enable monolithic integration of active organic components [1–5] into all-organic or hybrid integrated systems, it is necessary to form organic crystals in the plane of a large area (cm^2) substrate. The deposition of high purity molecular organic materials onto planar substrates is most often accomplished by vacuum sublimation, but the deposited thin films are typically amorphous or at best polycrystalline with grain sizes on the scale of microns [23–26]. Substrate temperatures are often elevated during deposition in order to improve crystallinity or select a particular crystalline phase [3,11,23–28]. In addition, post-deposition thermal treatment, solvent exposure, and solvent-vapor exposure have been shown to induce grain growth as well as amorphous-to-crystalline or polymorphic transformations in molecular organic thin films [6–12,29,30]. In the case of solvent-vapor annealing, a solvent in which the thin film material has only slight solubility is typically used. The results reported here differ in that Alq_3 is readily soluble in common organic solvents including chloroform.

We demonstrate the crystal formation method using Alq_3 since it is among the most extensively studied molecular organic semiconductors. Vacuum-sublimed thin films of Alq_3 are typically amorphous and have been shown to be morphologically stable under inert atmosphere and room temperature conditions [31]. It has been observed, however, that micron-scale disk-like clusters of crystals form [32] when amorphous thin films of Alq_3 are thermally annealed above the Alq_3 glass transition temperature ($T_g = 175^\circ\text{C}$) [33]. More-

over, vacuum evaporation of Alq_3 onto heated glass substrates pre-rubbed with polytetrafluoroethylene (PTFE) was shown to yield polycrystalline Alq_3 films of planar $\sim 1\text{--}2\ \mu\text{m}$ crystallites [23]. In the PTFE study, the Alq_3 crystallites were also oriented relative to the PTFE sliding direction, with the orientation primarily attributed to the van der Waals interaction of Alq_3 molecules with the aligned PTFE chains. Such ordering is driven by the minimization of interfacial tension between the crystal and the substrate, and has been demonstrated in other studies that used lithographically-defined periodic surface relief to influence the growth and orientation of inorganic crystalline overlayers [34,35], to uniaxially orient liquid crystalline molecules over large areas [36], and to generate long-range order in self-assembling block copolymer thin films [37].

Similar to thermally-assisted Alq_3 crystal formation [23,32], exposure of Alq_3 films to acetone vapor was previously reported to yield micron-scale crystallized regions [12]. In this study we demonstrate that much larger (millimeter-scale) Alq_3 crystalline needles can be formed by solvent-vapor annealing amorphous Alq_3 films on submicron surface-relief gratings.

2. Experimental

Interference lithography was used to fabricate grating lines in Si or SiO_2 with periods ranging from 180 nm to 300 nm and etch depths from 30 nm to 70 nm. The trilayer resist stack consisted of an anti-reflection coating (ARC) layer, an evaporated silica interlayer, and a photoresist layer, with the layers deposited sequentially onto silicon or thermally oxidized silicon wafers. A 325 nm wavelength HeCd laser was used to expose grating lines in the resist. After exposure and development of the resist, the pattern was transferred through

the silica interlayer and ARC layer and into the Si or SiO₂ via reactive ion etching. After removal of the residual resist stack by cleaning in 5:1:1 H₂O:H₂O₂:NH₄OH at 80 °C for ~10 min, a square-wave grating topography remained in the Si or SiO₂.

After the patterned wafers were diced into ~cm² pieces, the substrates were cleaned via the following steps: ultrasonication in dilute detergent, ultrasonication in deionized water, ultrasonication in acetone, immersion in boiling 1,1,1-trichloroethane, ultrasonication in acetone, and immersion in boiling 2-propanol. The substrates were then dried in a stream of nitrogen and further cleaned by UV-ozone treatment for 30 min. The substrates were subsequently treated with octadecyltrichlorosilane (OTS). The vapor phase OTS treatment was accomplished by placing the substrates in a vessel together with a crucible containing ~0.03 ml of OTS. The vessel was evacuated to a pressure of <1 Torr and heated to 120 °C in an oil bath for ~2 h. The OTS-treated substrates were hydrophobic, with contact angles (measured on unpatterned substrates) of ~87°.

Alq₃ films of 10–20 nm thickness were deposited by thermal evaporation in vacuum (<10⁻⁶ Torr) onto room temperature substrates at rates of 0.1–0.3 nm/s as measured by a quartz crystal thickness monitor. Following the evaporation of Alq₃, the substrates were placed in a glass jar together with a beaker of chloroform, and the jar was sealed with a Teflon-lined cap. Exposure times ranged from several hours to two days. The dimensions of the Alq₃ needles formed via chloroform-vapor annealing were characterized by optical microscopy (needle length), and scanning electron microscopy (SEM) and atomic force microscopy (AFM) (needle width, thickness). Optical properties of the needles were investigated via fluorescence microscopy and confocal microscopy (365 nm excitation wavelength).

In order to monitor the growth of Alq₃ crystals during chloroform-vapor exposure, an alternate annealing chamber was constructed from stainless steel and quartz vacuum components. A stereomicroscope was used to view a substrate mounted beneath a quartz view port, and video was captured via an attached CCD camera.

3. Experimental results

Exposure of the Alq₃ thin films to chloroform vapor for times ranging from several hours to two days results in the formation of elongated and oriented Alq₃ needles such as those shown in the optical and SEM micrographs of Fig. 1. The narrowest needles are two to three hundred nanometers wide, spanning a single grating groove (Fig. 3(c)), while the widest are several microns wide and span tens of grooves (Fig. 1(d)). Needle thicknesses range from one hundred nanometers to several microns, exceeding the depth of the grating grooves by as much as a factor of 50, and the thickness of the initial amorphous Alq₃ film by as much as a factor of 200. The needles are often 1000 times longer than they are wide or thick, ranging in length from hundreds of microns to one centimeter (the size of the substrate). In some cases the needles extend several microns beyond the substrate edge, retaining their elongated geometry, consistent with the growth of a crystal (Fig. 1(c)).

The distinct facets (Fig. 1(d)) and diamond-shaped cross sections (Fig. 1(e)) of the Alq₃ needles are also indicative of crystallinity. The optical smoothness of the needle facets is evidenced in fluorescence micrographs that show waveguiding of the Alq₃ fluorescence with outcoupling occurring at the needle edges and defects (Fig. 1(c)). Polarized fluorescence measurements show a change in luminescence intensity with polarization angle, with a maximum at ~15° from the long axis of the needle (Fig. 2(a)). Fluorescence spectra of the crystal needles, obtained via confocal microscopy, peak at $E_{\text{peak}} = 2.36$ eV ($\lambda_{\text{peak}} = 525$ nm) in agreement with the previously reported spectrum of polycrystalline α -Alq₃ (Fig. 2(b)) [38].

Not all of the Alq₃ is incorporated into the needles during the chloroform-vapor exposure. In fact, two regimes of residual Alq₃ are observed alongside the needles (Fig. 3). In the first regime (“Regime I” in Fig. 3), the Alq₃ is in the form of ~100 nm diameter convex globules and microcrystallites that cluster in the grating grooves to form ~1 μ m long features (Fig. 3(d)). The Regime I residual Alq₃ is visible in the optical micrographs as shade/color variations (darker region on the left in Fig. 1(a), green background in Fig. 1(b)).

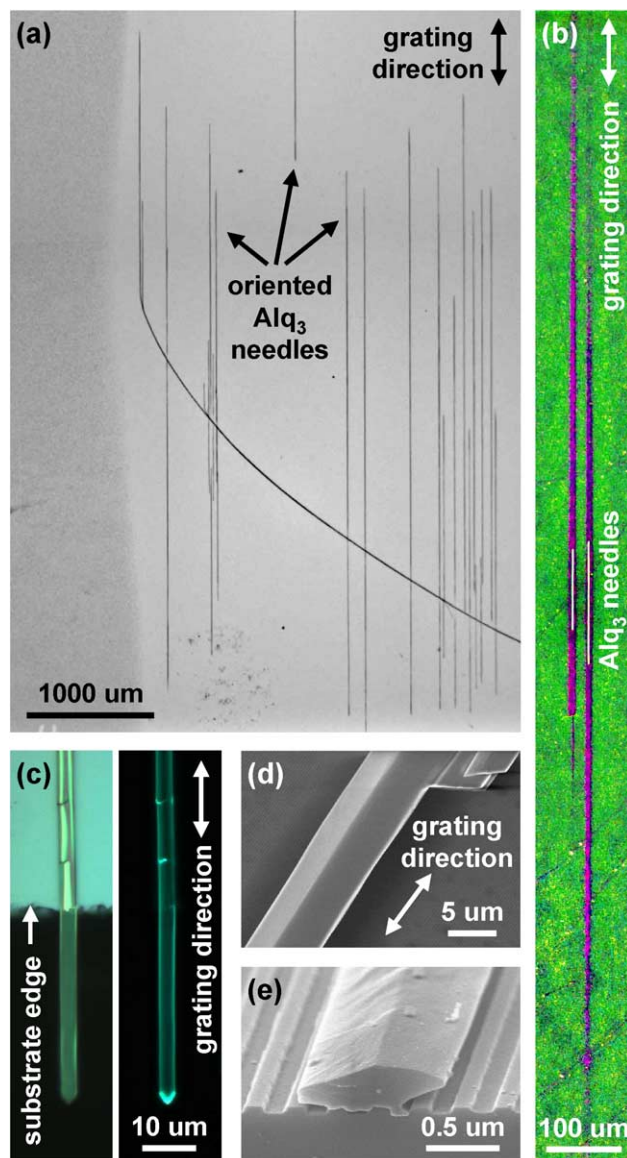


Fig. 1. Alq₃ crystalline needles formed by exposure of amorphous Alq₃ thin films to chloroform vapor at room temperature. (a) Optical micrograph of oriented Alq₃ crystal needles that formed from a 10 nm thick film of amorphous Alq₃. (b) False-color optical micrograph showing Alq₃ needles colored white, regions containing “Regime I” residual Alq₃ colored green, and regions containing “Regime II” residual Alq₃ colored magenta. (c) Optical micrograph (left) and fluorescence micrograph (right, 365 nm excitation wavelength) of an Alq₃ needle that extends ~35 μm beyond the substrate edge. (d) SEM micrograph (top view) showing the distinct facets of an Alq₃ needle. (e) SEM micrograph showing the typical diamond-shaped cross section of an Alq₃ needle.

Although it appears from the optical micrographs that the Alq₃ has been cleared from the substrate in the vicinity of the needles (bulk of the substrate in Fig. 1(a), elongated magenta regions in

Fig. 1(b)), SEM and AFM characterization reveals a second regime of residual Alq₃ (“Regime II” in Fig. 3). In contrast to the non-wetting globules and microcrystallites of Regime I, the residual

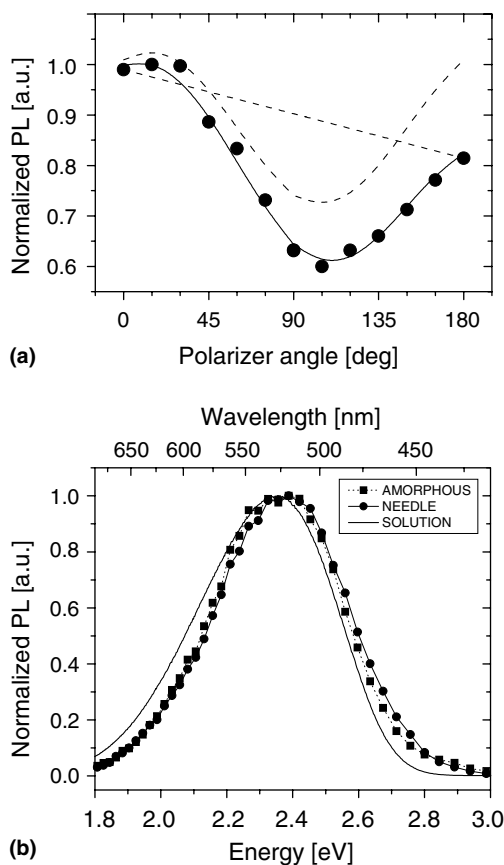


Fig. 2. Fluorescence of Alq₃ needles. (a) Plot of the normalized photoluminescence (PL) intensity (365 nm excitation wavelength) as a function of polarizer angle, where 0° corresponds to the polarizer aligned with the long axis of the needle. The decrease in fluorescence intensity from 0 to 180° is due to gradual photooxidation of the Alq₃ during the measurement as indicated by the straight dashed line. The sinusoidal response of PL with polarizer angle and the composite of the PL response and the gradual oxidation are plotted in dashed and solid lines, respectively. (b) Fluorescence spectra (365 nm excitation wavelength) of an as-deposited Alq₃ thin film and an Alq₃ crystal needle, obtained via confocal microscopy. The solution fluorescence spectrum (408 nm excitation wavelength) of Alq₃ in chloroform is also plotted.

Alq₃ in the grooves adjacent to the needles appears fluid-like and wets the substrate, forming strips that span individual grating grooves, and smaller droplets clinging to the groove sidewalls (Fig. 3(c) and (d)). In general, the area of the Regime II region surrounding a needle increases with increasing needle size (e.g., compare Fig. 1(a) and 1(b)), and

these regions are elongated in the grating direction (Fig. 1(b)).

Time-based experiments provide insight into the relationship between the Regime I and Regime II Alq₃ morphologies. The structural evolution shown in the Fig. 4 AFM images was produced by exposing identical Alq₃ thin film samples to chloroform vapor for different lengths of time. The as-deposited Alq₃ film shown in Fig. 4(a) is continuous, conforming to the underlying grating, but is rough due to the OTS pre-treatment. (Unlike Alq₃ on clean Si or SiO₂, which forms smooth, continuous films even when very thin (~1 nm), Alq₃ on OTS-treated surfaces forms isolated islands during the initial stages of growth due to increased interfacial tension.) Film continuity is lost during the first 5 min of exposure to chloroform vapor (Fig. 4(b)). After exposure for 30 min, the Alq₃ resides primarily in the grating grooves in the form of Regime I globules and microcrystallites (Fig. 4(c)). Increasing the exposure time to 60 min yields aggregation of the globules/microcrystallites to form micron-long clusters (Fig. 4(d), see also Fig. 3(d)). During an additional 30 min of exposure, the aggregated globules/microcrystallites begin to dissolve into Regime II liquescent strips that extend along the grating grooves (Fig. 4(e), see also Fig. 3(d) inset). Chloroform uptake in the Alq₃ film should increase with prolonged vapor exposure, suggesting that the Alq₃ transitions from Regime I to Regime II with increasing chloroform concentration.

Most of our experiments were carried out as described above, with samples characterized after being removed from the annealing chamber. While it is conceivable that the evaporation of chloroform upon removal from the saturated chamber atmosphere may influence or even produce the observed Alq₃ structures, we have disproved the latter by monitoring the growth of Alq₃ needles during chloroform-vapor exposure as described in the Experimental section. The sequence of optical micrographs shown in Fig. 5 corresponds to a 50 nm thick Alq₃ film on a grating pre-treated with phenyltrichlorosilane. In this case, chloroform-vapor exposure produced a tree-like structure of crystalline Alq₃ with branching needles aligned predominantly parallel to the grating direction.

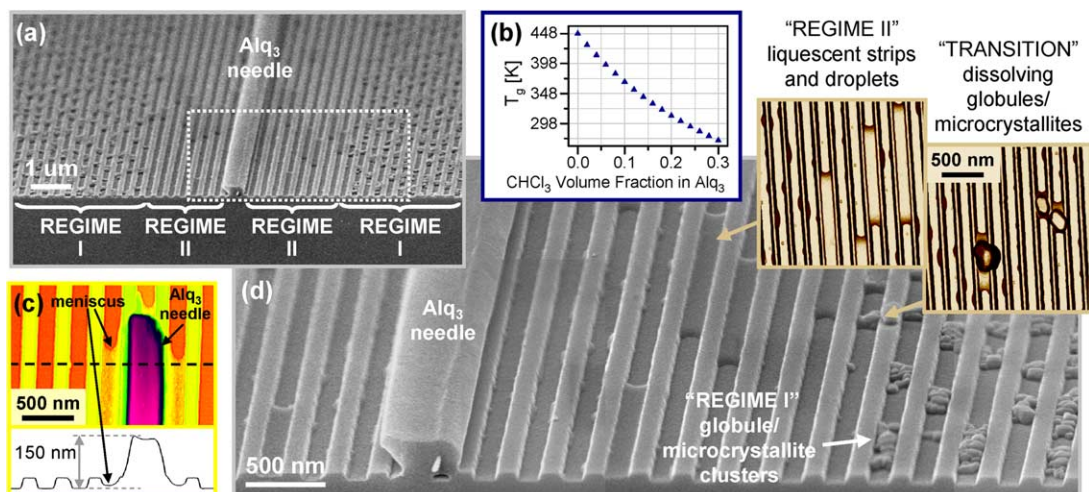


Fig. 3. Residual Alq₃ structural regimes. (a) SEM micrograph of an Alq₃ needle (in cross section) showing the morphological transition of the residual Alq₃ near the needle with Regimes I and II indicated. (b) Plot of the predicted T_g of Alq₃ solvated with chloroform as a function of chloroform volume fraction, calculated from Eq. (1). (c) AFM height image of the tip of an Alq₃ needle showing liquescent Alq₃ in the immediately adjacent grooves. (d) SEM micrograph corresponding to the dashed box in (a), and AFM height image insets (displayed with top illumination to highlight edges and contours).

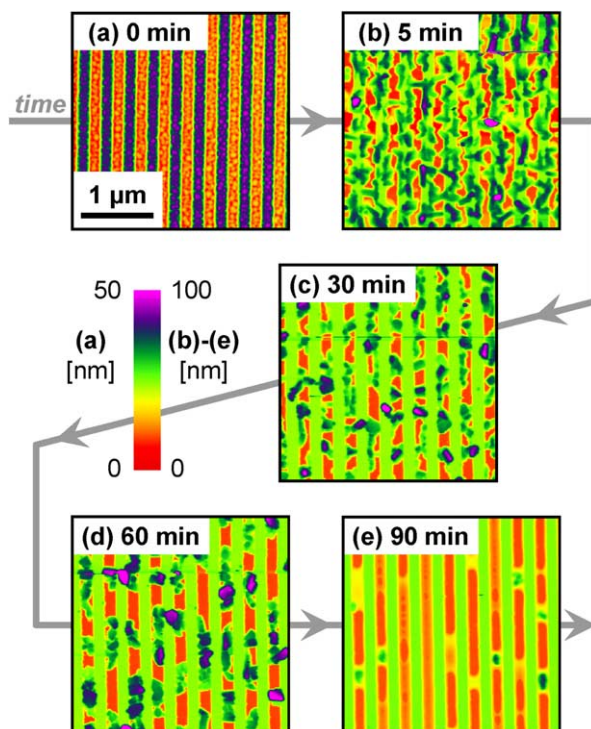


Fig. 4. AFM height images showing the structural evolution of Alq₃ thin films when exposed to chloroform vapor for increasing times. The initial film was 10 nm thick, deposited onto an OTS-treated surface-relief grating.

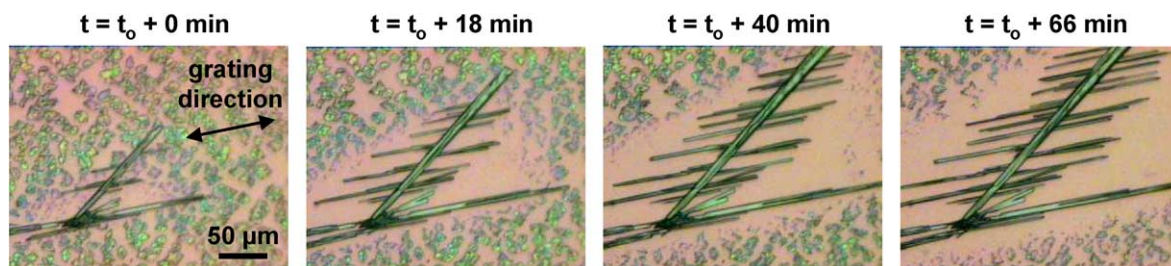


Fig. 5. Time-lapse optical micrographs showing the growth of Alq₃ crystalline needles during chloroform-vapor exposure. The initial film was 50 nm thick, deposited onto a phenyltrichlorosilane-treated surface-relief grating.

During the course of an hour-long exposure to chloroform vapor, new branches formed, the “trunk” and branches grew larger, and the surrounding “cleared” region increased in area.

As evidenced by the Fig. 5 micrographs, the formation of Alq₃ crystals via chloroform-vapor exposure is not limited to OTS-treated substrates. In fact, we have also observed millimeter-scale Alq₃ crystals on untreated Si gratings and on gratings having a thin (<10 nm) coating of copper phthalocyanine (deposited by thermal evaporation immediately prior to deposition of the Alq₃ film), but we have not studied these substrate systems as thoroughly as the OTS-treated system. We have also observed formation of Alq₃ crystalline needles on unpatterned substrates; however, these needles are generally slower to form, fewer in number, shorter, and have random in-plane orientations, highlighting the influence of the grating grooves on both nucleation and mass transport.

The chloroform uptake of Alq₃ thin films was quantified using a quartz crystal thickness monitor. A beaker of chloroform was placed beneath the thickness monitor such that the quartz crystal was ~1 cm above the chloroform level. The beaker and thickness monitor were capped with aluminum foil to simulate the sealed annealing chamber. This experiment was performed first on a blank quartz crystal, and was then repeated for the same crystal after deposition of a 50 nm thick film of Alq₃. The maximum mass increase after exposure to chloroform vapor was 10 times larger for the Alq₃ coated crystal than for the blank quartz crystal, and corresponds to a chloroform mass fraction of 0.21.

4. Discussion

Previous reports of solvent-vapor annealing of amorphous or polycrystalline molecular organic thin films focused on metal phthalocyanines [6–8,11] and perylene derivatives [9,10], where the goal was to improve photoactivity for applications such as xerography or photovoltaic devices. The films tended to have low solubility in the annealing solvents, and adsorption of solvent molecules during solvent-vapor exposure was presumed to result in a saturated solvent solution on the film surface. Two main mechanisms were proposed for the observed crystalline transformations. First, solvent molecules may interact electronically with the thin film molecules to change their π -electron distributions, triggering a change in molecular packing. Alternately, adsorbed solvent molecules may cause a relaxation of a metastable crystal lattice or an increase in molecular motility at the surface of an amorphous thin film, thereby enabling nucleation of a stable crystalline form. The latter mechanism was consistent with observations that (1) transformation rates tend to increase with increasing solubility [6] and (2) similar transformations can be activated via thermal treatment [11]. In cases where an increase in crystal size was observed (rather than a polymorphic transition), the growth was attributed to Ostwald ripening, with the solvent solution serving as a transport medium. The largest reported crystals were a few microns in length.

Although we observe some similarities in the structural changes of vapor-annealed Alq₃ films, the higher solubility of Alq₃ in chloroform

influences the active mechanisms. First, adsorbed chloroform molecules have an increased tendency to diffuse into the amorphous Alq₃ film, enabling “bulk” rather than surface transformations. The imbibed chloroform imparts motility to the Alq₃ molecules via a plasticization effect, whereby the T_g of a glassy material is reduced by the presence of low molecular weight additives (such as solvent molecules). The effect of plasticization on T_g can be estimated from semi-empirical equations based on free-volume considerations [39]:

$$T_g \approx \frac{T_{go}}{1 + \left(\frac{T_{go}}{T_{gs}} - 1\right) \Phi_s} \quad (1)$$

$$T_{gs} \approx \frac{2}{3} T_{ms} \quad (2)$$

where T_{go} and T_{gs} are the glass transition temperatures of the pure glassy material and pure solvent, respectively, and Φ_s is the volume fraction of the solvent. The melting temperature of the solvent T_{ms} is used to estimate T_{gs} using the relationship given in Eq. (2). Using $T_{go} = 448$ K for Alq₃ and $T_{ms} = 210$ K for chloroform, the Alq₃ T_g is calculated to drop below room temperature (298 K) when the film is 23% chloroform by volume (Fig. 3(b)). This value is in good agreement with our quartz crystal measurement of 21% by mass chloroform uptake for a 50 nm thick Alq₃ film. In order to compare mass and volume fractions, we are assuming that the density of the film does not change significantly with chloroform uptake; that is to say, the density of chloroform in Alq₃ is assumed to be closer to the density of neat Alq₃ (1.16 g/cm³ [40]) than to the density of neat chloroform (1.48 g/cm³) due to less dense packing in the solvated structure. The reduction of T_g via chloroform uptake provides the molecular motility necessary for the Alq₃ to minimize interfacial tension by dewetting from the substrate (Fig. 4(b)), and overall free-energy by forming the Regime I globule/microcrystallite clusters (Figs. 3(d), 4(c) and (d)), both at room temperature. Nucleation of the larger crystalline needles also likely results from the reduced Alq₃ T_g , although the seeding process is not yet understood.

Initially the level of chloroform uptake is such that, in effect, chloroform is dissolved in Alq₃

“solvent”. However, due to the solubility of Alq₃ in chloroform, the chloroform concentration is able to increase to the point of dissolving the Alq₃ globules and microcrystallites. Since solubility decreases with increasing size, the larger crystalline needles do not dissolve, but rather grow at the expense of the submicron residual Alq₃ structures (i.e., via Ostwald ripening). When the Regime I residual Alq₃ dissolves, the solvated Alq₃ begins to wet the substrate as evidenced by the shapes of the Regime II strips and droplets (Figs. 3(c), (d) and 4(e)). This wetting behavior is consistent with the observed spreading of a drop of neat chloroform on an OTS-treated substrate.

Although the morphological transition from Regime I globules/microcrystallites to Regime II fluid-like strips/droplets can be effected by increased annealing time, as illustrated in Fig. 4, the coexistence of both regimes on a single substrate (Fig. 3) suggests that other factors influence the local chloroform concentration. For example, the exclusion of chloroform when Alq₃ molecules crystallize at the needle/solution interface would result in an increase in chloroform concentration near the needle. This would explain the observed collocation of Regime II regions containing liquescent Alq₃ (i.e., high chloroform concentration) and the Alq₃ needles. In fact, needle growth not only contributes to but also benefits from the increased local chloroform concentration, since needle growth relies on transport of Alq₃ to the needle/solution interface and in general transport is facilitated by an increase in fluidity. Moreover, the submicron grating grooves provide a means for capillary flow of liquescent Alq₃, greatly enhancing the transport of Alq₃ along the grooves [41]. The resulting anisotropic mass transport is evidenced by elongation of the Regime II “flow regions” in the grating direction (Fig. 1(b)) and is responsible for growth of the needles parallel to the grating direction.

5. Conclusions

In summary, we have formed millimeter-scale crystalline Alq₃ needles via room temperature solvent-vapor exposure of initially amorphous thin

films on patterned substrates. The remarkable size of the needles results from enhanced mass transport due to (1) the solubility of Alq₃ in chloroform and (2) capillary flow along the substrate grooves. The crystallization method has been demonstrated for Alq₃ thin films annealed in chloroform vapor, but is expected to be generally applicable to other material/solvent/substrate systems. An understanding of the crystal seeding process, which would enable placement of the oriented needles at specified locations on a substrate, will be valuable in optimizing the method for potential device fabrication. Organic crystalline needles generated via this technique may have enhanced charge carrier mobilities necessary for organic electronic applications such as low-voltage field-effect transistors and high-efficiency solar cells, or non-linear optical properties required for organic optoelectronic devices such as modulators, optical filters, and polarization rotators.

Acknowledgements

We thank C.A. Breen, J. Chen, S.A. Claussen, I. Kymissis, C.F. Madigan, M.E. Walsh, and J.J. Zartman for technical assistance, and T.M. Swager for technical discussions. We received support for this work from the MARCO Focused Research Center on Materials, Structures, and Devices which is funded at the Massachusetts Institute of Technology, in part by MARCO under contract 2001-MT-887 and DARPA under grant MDA972-01-1-0035. This work made use of the Shared Experimental Facilities supported in part by the MRSEC Program of the National Science Foundation under award number DMR 02-13282.

References

- [1] C.D. Dimitrakopoulos, P.R.L. Malenfant, *Adv. Mater.* 14 (2002) 99.
- [2] H.E. Katz, Z. Bao, *J. Phys. Chem. B* 104 (2000) 671.
- [3] Y.Y. Lin, D.J. Gundlach, S.F. Nelson, T.N. Jackson, *IEEE Trans. Electron Dev.* 44 (1997) 1325.
- [4] P. Peumans, V. Bulović, S.R. Forrest, *Appl. Phys. Lett.* 76 (2000) 2650.
- [5] S.R. Marder, J.W. Perry, C.P. Yakymyshyn, *Chem. Mater.* 6 (1994) 1137.
- [6] F. Iwatsu, T. Kobayashi, N. Uyeda, *J. Phys. Chem.* 84 (1980) 3223.
- [7] F. Iwatsu, *J. Cryst. Growth* 71 (1985) 629.
- [8] A.M. Hor, R.O. Loutfy, *Thin Solid Films* 106 (1983) 291.
- [9] B.A. Gregg, *J. Phys. Chem.* 100 (1996) 852.
- [10] J.C. Conboy, E.J.C. Olson, D.M. Adams, J. Kerimo, A. Zaban, B.A. Gregg, P.F. Barbara, *J. Phys. Chem. B* 102 (1998) 4516.
- [11] M. Brinkmann, J.C. Wittmann, C. Chaumont, J.J. Andre, *Thin Solid Films* 292 (1997) 192.
- [12] F. Toffolo, M. Brinkmann, O. Greco, F. Biscarini, C. Taliani, H.L. Gomes, I. Aiello, M. Ghedini, *Synth. Met.* 101 (1999) 140.
- [13] F.R. Lipsett, *Can. J. Phys.* 35 (1957) 284.
- [14] F. Gutmann, L.E. Lyons, *Organic Semiconductors*, John Wiley & Sons, Inc., New York, 1967.
- [15] D. Fichou, *J. Mater. Chem.* 10 (2000) 571.
- [16] C. Kloc, P.G. Simpkins, T. Siegrist, R.A. Laudise, *J. Cryst. Growth* 182 (1997) 416.
- [17] R.A. Laudise, C. Kloc, P.G. Simpkins, T. Siegrist, *J. Cryst. Growth* 187 (1998) 449.
- [18] G. Horowitz, B. Bachet, A. Yassar, P. Lang, F. Demanze, J.L. Fave, F. Garnier, *Chem. Mater.* 7 (1995) 1337.
- [19] M. Pope, H.P. Kallmann, P. Magnante, *J. Chem. Phys.* 38 (1963) 2042.
- [20] G. Horowitz, F. Garnier, A. Yassar, R. Hajlaoui, F. Kouki, *Adv. Mater.* 8 (1996) 52.
- [21] V. Podzorov, V.M. Pudalov, M.E. Gershenson, *Appl. Phys. Lett.* 82 (2003) 1739.
- [22] F. Pan, K. McCallion, M. Chiappetta, *Appl. Phys. Lett.* 74 (1999) 492.
- [23] J.F. Moulin, M. Brinkmann, A. Thierry, J.C. Wittmann, *Adv. Mater.* 14 (2002) 436.
- [24] E.L. Granstrom, C.D. Frisbie, *J. Phys. Chem. B* 103 (1999) 8842.
- [25] W.A. Schoonveld, J. Vrijmoeth, T.M. Klapwijk, *Appl. Phys. Lett.* 73 (1998) 3884.
- [26] G.Z. Wang, Y. Luo, P.H. Beton, *Appl. Phys. Lett.* 83 (2003) 3108.
- [27] C.D. Dimitrakopoulos, A.R. Brown, A. Pomp, *J. Appl. Phys.* 80 (1996) 2501.
- [28] Z. Bao, A.J. Lovinger, A. Dodabalapur, *Appl. Phys. Lett.* 69 (1996) 3066.
- [29] Y.L. Lee, W.C. Tsai, C.H. Chang, Y.M. Yang, *Appl. Surf. Sci.* 172 (2001) 191.
- [30] D.J. Gundlach, T.N. Jackson, D.G. Schlom, S.F. Nelson, *Appl. Phys. Lett.* 74 (1999) 3302.
- [31] C.W. Tang, S.A. Vanslyke, *Appl. Phys. Lett.* 51 (1987) 913.
- [32] E.M. Han, L.M. Do, N. Yamamoto, M. Fujihira, *Thin Solid Films* 273 (1996) 202.
- [33] K. Naito, A. Miura, *J. Phys. Chem.* 97 (1993) 6240.
- [34] H.I. Smith, M.W. Geis, C.V. Thompson, H.A. Atwater, *J. Cryst. Growth* 63 (1983) 527.
- [35] T. Kobayashi, K. Takagi, *Appl. Phys. Lett.* 45 (1984) 44.

- [36] D.C. Flanders, D.C. Shaver, H.I. Smith, *Appl. Phys. Lett.* 32 (1978) 597.
- [37] J.Y. Cheng, C.A. Ross, E.L. Thomas, H.I. Smith, G.J. Vancso, *Appl. Phys. Lett.* 81 (2002) 3657.
- [38] M. Brinkmann, G. Gadret, M. Muccini, C. Taliani, N. Masciocchi, A. Sironi, *J. Am. Chem. Soc.* 122 (2000) 5147.
- [39] J. Bicerano, *Prediction of Polymer Properties*, Marcel Dekker, Inc., New York, 1996.
- [40] C.F. Madigan, V. Bulović, unpublished work.
- [41] R. Seemann, M. Brinkmann, E.J. Kramer, F.F. Lange, R. Lipowsky, *Proc. Natl. Acad. Sci. USA* 102 (2005) 1848.

Laser-assisted patterning of conjugated polymer light emitting diodes

David G. Lidzey^{a,*}, Monika Voigt^{a,1}, Carsten Giebeler^b, Alastair Buckley^b,
Jeff Wright^b, Karl Böhlen^c, Jim Fieret^c, Ric Allott^c

^a Department of Physics and Astronomy, The University of Sheffield, Hicks Building,
Hounsfield Road, Sheffield S3 7RH, United Kingdom

^b MicroEmissive Displays Ltd., Scottish Microelectronics Centre, The Kings Building, West Mains Road, Edinburgh EH9 3JF,
United Kingdom

^c Exitech Ltd., Oxford Industrial Park, Yarnton, Oxford OX5 1QU, United Kingdom

Received 1 April 2005; received in revised form 3 June 2005; accepted 9 June 2005
Available online 22 September 2005

Abstract

We have developed a patterning procedure based on laser-ablation in combination with the use of water-soluble sacrificial-resists that we use to pixelate different light emitting polymers (LEPs) on a surface, creating a simple array of light emitting diodes (LEDs). We demonstrate that our patterning process is capable of high spatial resolution, with structures having a characteristic length-scale of 10 μm achieved. Importantly, we demonstrate that the patterning process has no detrimental effect on the electronic properties of the LEPs or of the underlying polymeric anode. Our process is compatible with a high-volume manufacturing environment and furthermore it could also be applied to pattern and integrate a wide range of functional polymeric materials for use in other applications.

© 2005 Elsevier B.V. All rights reserved.

PACS: 85.60.Jb; 75.88.Kz; 72.80.Le; 42.62.Cf

Keywords: Conjugated polymer; LEP; LED; Laser-ablation; Patterning; Displays

Patterning semiconducting polymers on a surface is an important enabling technology in the creation of devices such as LED displays and low-cost elec-

tronics [1,2]. The integration of different conjugated polymers into a full colour display necessarily requires the definition of different pixels emitting red, green or blue (RGB) light. The methods that have been previously explored to pattern π -conjugated polymers broadly divide into either reactive or non-reactive processes [1]. Reactive methods usually involve using radiation to locally initiate a chemical reaction in a polymer or precursor-polymer film [3–5], usually creating insoluble

* Corresponding author. Fax: +44 114 272 8079.

E-mail address: d.g.lidzey@sheffield.ac.uk (D.G. Lidzey).

¹ Present address: Blakett Laboratory, Imperial College of Science Technology and Medicine, Prince Consort Road, London SW7 2AZ, United Kingdom.

regions in an otherwise soluble film [6–9]. High-energy electrons can also be used to selectively initiate cross-linking in a conjugated polymer [10], allowing a second polymeric material to be deposited onto the first material without removing the original patterned material. Perhaps the most promising demonstration of reactive-patterning of conjugated polymers has been the direct UV initiated cross-linking of various precursor polymers to form a simple three-colour display [11].

Non-reactive patterning methods involve using lithographic techniques to pattern a polymer in its final form without the requirement of further chemical or thermal treatments. These include screen printing [12,13] and soft-lithography. Soft-lithography involves using an elastomeric stamp that has been ‘inked’ using conjugated polymers. This is then used to print different pixels, often permitting structures having length-scales of several microns to be realized [14]. Alternatively, elastomeric materials can be used as a contact mask, also permitting micron-scale pixels based on thermally-evaporated small-mass dyes to be created [15]. Ink-jet printing has been widely explored to directly pattern both conjugated polymers and conductive films [16–21]. To improve the spatial resolution of the patterns that are printed, surfaces can be pre-patterned using conventional lithographic techniques to define hydrophobic and hydrophilic surface layers. These surface layers direct the deposition of the electronically functional polymer and thus improve the resolution of the technique. This has permitted field effect transistors to be created having gate channel widths as narrow as 500 nm [22].

In this paper, we describe a non-reactive patterning technique that we have developed that is based on laser-ablation combined with the use of sacrificial-resists. Laser processing is already recognized as a highly versatile and accurate manufacturing process [23] that can be used to directly pattern organic thin films for LED applications via ablation [24,25]. The attraction of laser-machining is that the size of the features that can be written is often only limited by optical-diffraction. By using short-wavelength light-sources ($\lambda = 157$ nm) ablation patterns can be written with a resolution as small as 100 nm [26]. Laser-machining can also be used to pattern moving substrates, permitting large-areas to be exposed at speed. One technique that has been recently developed to pattern functional organic materials is that of laser-assisted thermal-imaging [27,28]. Here, the surface of a flexible ‘receiver’ film

is held in direct contact with a ‘donor’ film using a vacuum. The donor film consists of a light-to-heat conversion layer coated with the organic material of interest. When a laser-beam is focused onto the film, the heat generated within the light-to-heat layer creates an expanding bubble of gas that propels the functional organic material onto the receiver substrate. The two films are then separated to leave a patterned structure on the receiver. As we report here, our laser-assisted patterning technique permits all processing to be done on a single substrate, with the functional polymeric films being directly deposited via spin-casting. Importantly the functional organic materials that we deposit are never directly exposed to the laser-radiation that is used to define their location. As we demonstrate below this largely eliminates any possible photo-induced oxidation. The strength of our patterning process is that it is not material specific and we are thus able to pattern state-of-the-art electronic polymers. The resolution that we have demonstrated is as good as (or in some cases better than) other patterning techniques used to pattern conjugated polymers. Our process could also be readily scaled-up into a high-volume manufacturing environment.

The patterning process—shown schematically in Fig. 1—is based on the ablation of polymer films using pulses from a 248 nm excimer laser (pulse duration approximately 25 ns), followed by a lift-off process using a resist that is soluble in a range

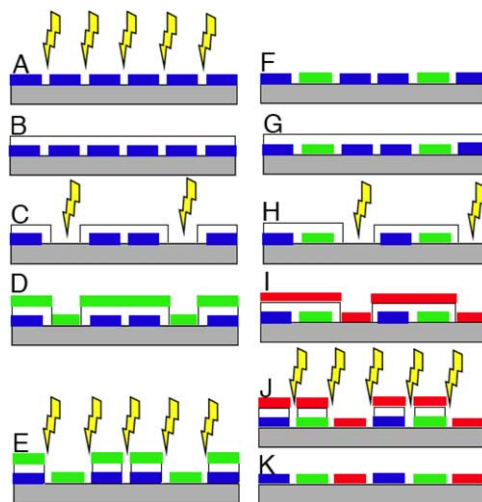


Fig. 1. A schematic of the laser-assisted patterning process described in the text.

of solvents that are orthogonal to those used to process conjugated polymers. The process starts by spin-coating a 100 nm thick film of a light emitting polymer (LEP) film onto a surface from toluene. An excimer laser is then used to ablate selective regions of the polymer (step A). For laser-ablation, the laser light is imaged onto the film surface using a 0.13 numerical aperture lens in the shape of a line whose width can be varied between 10 and 200 μm . All laser patterning was done in air and at room temperature. The regions of the surface that are ablated in this first step are the regions that will eventually separate the different LED pixels in the array. After ablating a series of lines into the film, the substrate is rotated by 90° and the process is repeated to create a grid. The regions of the film that are exposed to the laser pulse rapidly absorb a large amount of energy that results in their local explosive removal. To achieve ablation, it is necessary that the target material has a reasonably large absorption coefficient at the laser wavelength. In general, the LEPs that we have used have had a relatively large absorption coefficient at 248 nm (ranging between $\alpha = 60,000$ and $140,000 \text{ cm}^{-1}$).

A thin film (100 nm) of polyvinyl alcohol [PVA] is then spin-cast from water (step B) onto the laser-patterned surface. The PVA used was supplied by Aldrich Chemicals, and had a molecular weight 10 kDa with 80% hydrolyzation. The purpose of the PVA is to prevent the mutual mixing of different LEP layers that are deposited in the subsequent processing steps. We find that there is negligible penetration of the organic solvent through the PVA layer to the underlying LEP film. Solvent penetration can however occur if there are pinholes in the PVA over-layer. Such pinholes usually arise if there are dust-particles on the substrate surface or within the PVA or LEP layers. By ensuring that the substrate is kept dust-free, and that all polymer solutions are filtered prior to spin-casting, the formation of pin-holes in the PVA can be suppressed.

Control experiments have shown that for most conjugated polymers studied, there is no significant change in the thickness of the underlying LEP film caused by spin-casting a PVA overcoat. Furthermore as we show below, the electronic properties of the LEP are not adversely affected by the deposition (and subsequent removal) of the PVA. The PVA-coated LEP structure is then ablated using the excimer laser to remove every third pixel row (step C). This ablation step defines the location for

the second set of pixels. Even though the LEP is coated with PVA, it can still be ablated as PVA has a negligible absorption coefficient at 248 nm ($\alpha = 400 \text{ cm}^{-1}$). A LEP material is then spin-coated onto the PVA surface (step D). PVA has negligible solubility in toluene and thus a stable multilayer film can be formed. A grid is then ablated into the film to re-define the pixel separators (step E). The substrate is washed in water, which removes the PVA and its top-coat of LEP (step F). Importantly, we have found that the pixel separators permit the water to penetrate into the PVA layer and therefore assist the lift-off process. The surface is again coated with a layer of PVA (step G), followed by ablation to define the location for the third set of LEP pixels (step H). A third LEP material is then spin-coated onto the substrate (step I), which is then followed by a final ablation step to define the pixel separators (step J). The substrate is then given a final wash to remove PVA and unwanted LEP material, resulting in a surface patterned by three different types of LEP pixels (step K).

To demonstrate this process, we have used three proprietary polyfluorene-based co-polymers that emit R, G and B luminescence. Fig. 2(a) shows a fluorescence micrograph of an array of pixels

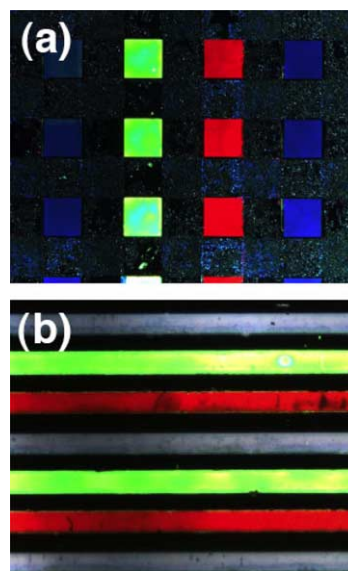


Fig. 2. Fluorescence micrograph of conjugated polymers patterned using the laser-assisted methodology. Part (a) shows fluorescence of $200 \times 200 \mu\text{m}$ pixels consisting of a red, green and a blue-emitting polymer patterned on a silicon substrate. Part (b) shows fluorescence from $10 \mu\text{m}$ wide stripes of the same polymer also patterned on silicon.

patterned on a silicon surface. Here, each individual pixel has a size of $200 \times 200 \mu\text{m}$. Fig. 2(b) shows a fluorescence micrograph of $10 \mu\text{m}$ wide stripes of R, G and B polymers patterned using our process. The stripes are in general well formed and have clean straight edges, demonstrating that limit of resolution of this patterning technique is significantly below $10 \mu\text{m}$. Note, that the background blue emission observed from the regions between the polymer pixels does not result from PL emission from un-removed blue LEP material. Rather, it originates from a small amount of scattering of the excitation radiation from the surface.

Whilst Fig. 2(b) demonstrates the feasibility of high-resolution laser patterning of LEPs, it is important to determine whether the polymers that are deposited retain their optical and electronic functionality. Potential concerns arise as to unwanted photo-oxidation caused by stray laser light and the possible damage occurring to an underlying anode caused by the laser-ablation steps C and H. Furthermore, it is possible that the deposition and subsequent removal of PVA from the surface of a conjugated polymer may cause damage to the surface layer that will be eventually be positioned next to the cathode. However as we demonstrate below each of these processes has a negligible effect on the electronic properties of either the LEPs or the (hole-injecting) anode.

To determine whether the laser-ablation step reduces the PL efficiency of the remaining un-ablated polymers, we performed the following experiments: Firstly we measured the photoluminescence quantum efficiency of freshly cast R, G and B polymer thin films using a technique described previously [29]. We obtained values for the quantum yield of the different LEPs as follows: G = 90%, R = 85%, B = 68%. The polymer films were then coated with a thin film of PVA that was then stripped off using water. Within the accuracy of our measurement technique, we found that this process had no discernable effect on their PL quantum yield. To test the effect of the stray laser light on the polymer pixels, we prepared R, G and B films coated with PVA. A pattern of $100 \mu\text{m}$ stripes on a pitch of $100 \mu\text{m}$ was then ablated into each film. The PVA was stripped from the surface using water and the PL quantum efficiency of the remaining un-ablated LEP measured. Here, it was necessary to compare the quantum efficiency of the patterned films to a control that had experienced a similar processing history. Here films had been stored in the dark, in

air for approximately one month.² Compared to the control, we found that there is no discernable effect on the PL quantum efficiency.

At first sight, this is a somewhat surprising observation considering the large laser flux used to ablate the polymer film. However due to the relatively large absorption coefficients of the different polymers at the laser wavelength, any stray laser light that is scattered or waveguided within the polymer film will only travel a relatively short distance ($\sim 200 \text{ nm}$) into the edge of any un-ablated polymer. As the lateral size of the smallest pixels that we have created is ~ 50 times larger than the width of any photo-oxidised edge region, it is perhaps not unreasonable that the overwhelming majority of the polymer is not damaged by stray laser light. This conclusion was also confirmed using fluorescence microscopy of ablated LEP films, with no change in the intensity of fluorescence at the edge of the pixel being detected. Note that a small amount of radiation induced damage to the edges of the pixels would not present a significant problem in a real display application, as in most cases the size of the LED anode would be significantly smaller than the size of the patterned LEP pixel, making edge-effects largely unimportant.

For display applications, it is also important that the emission spectra of the LEPs are not compromised by the patterning process. Any changes in LEP emission spectra could have a negative impact on the CIE coordinates of the R, G or B pixels within the display and reduce the accessible colour palette. We have therefore explored the effect of the processing procedure on the PL emission spectra of the red, green and blue LEPs. Specifically, thin films of each of the R, G and B LEPs were coated with a PVA film, which was then stripped from the surface by immersion in water for 1 min. Encouragingly, we find that the PL emission spectra of the LEPs are almost completely unaffected by this process; an observation in accord with the relative insensitivity of their PL quantum yield to the patterning process.

To test the effect of the laser-ablation process on the LED anode (i.e. steps C and H), a 70 nm thick

² We found that air storage of spin-cast polymer films can have a significantly detrimental effect on PL quantum efficiency. For air storage periods of 1 month, we found that the PL quantum efficiency of red, green and blue emitting LEPs was reduced to 80%, 40% and 20% of their original value respectively.

poly(3,4-ethylene-dioxythiophene)/poly(styrene-sulphonic acid) (PEDOT:PSS) hole-injecting polymer was coated onto a metallic anode. A 60 nm thick film of a green-emitting LEP was then coated onto the PEDOT:PSS anode. The surface was then ablated with a series of laser pulses, having a fluence between 50 and 300 mJ cm^{-2} (in steps of 25 mJ cm^{-2}). The depth of the ablation region was then measured using a surface profiler. It was found that the entire thickness of the LEP was removed following a single laser pulse having a fluence between 50 and 150 mJ cm^{-2} . However at this pulse fluence, no significant removal of the underlying PEDOT:PSS polymer was observed. Between a laser fluence of 175 and 200 mJ cm^{-2} , mild ablation occurred to the underlying PEDOT:PSS, with significant removal occurring following a laser pulse of fluence $\geq 225 \text{ mJ cm}^{-2}$. This relative insensitivity of PEDOT:PSS to ablation results from its relatively low absorption coefficient at 248 nm ($\alpha = 7500 \text{ cm}^{-1}$).

This structure was washed in toluene to remove the LEP from the surface and a fresh film of the LEP was then spin-coated on to the surface. A thin top layer of calcium was evaporated over the entire substrate to act as an LED cathode. A voltage of 5 V was applied to the cathode and the emission from the entire substrate recorded using a microscope. By comparing the relative intensity of EL from the different ablated regions, we find that the electronic properties of the underlying PEDOT:PSS anode are only damaged following ablation from a single laser pulse having a fluence of 225 mJ cm^{-2} . At ablation fluxes below this threshold, the hole-injecting properties of the PEDOT:PSS anode appear unaffected. Interestingly, the damage threshold that we determine for PEDOT:PSS is above that required for partial ablation, and shows that the PEDOT:PSS anode can withstand limited removal of its surface layer without significant damage to its electronic properties. Importantly, this suggests that pixels in which the anode is never exposed to the laser (corresponding to the blue pixels in Fig. 1), should have similar properties to those from which a LEP has been removed in a previous processing step.

Finally, to test whether the deposition and subsequent stripping of PVA from an LEP damages the electronic properties of the polymer-surface, we have deposited a green-emitting LEP on top of a PEDOT:PSS coated ITO electrode. A 100 nm thick film of PVA was then spin-coated onto the polymer. The PVA film was then stripped from the polymer-surface by rinsing the substrate in cold water for

1 min. We found that it was important to first cross-link the PEDOT:PSS film by adding 5% glycerol (by weight) to the PEDOT:PSS solution. The PEDOT:PSS film was then baked at 180 °C under vacuum for 30 min which rendered it insoluble. In this process, the glycerol cross-links a small fraction of neighbouring PSS molecules via an esterification reaction involving the pendant SO_3^- groups. This cross-linking procedure rendered the PEDOT:PSS polymer largely insoluble and did not apparently compromise its electronic functionality. Without this initial cross-link, small quantities of water can penetrate through the LEP layer and partially dissolve the PEDOT:PSS causing the structure to delaminate. After the PVA film had been stripped, the surface of the conjugated polymer film was dried using a jet of compressed air, and the structure was fabricated into an LED by thermally evaporating an electrode onto the surface composed of 10 nm of calcium backed by 100 nm of aluminum. As a control, an LED was fabricated from otherwise identical thin films of PEDOT:PSS and the green-emitting LEP, however in this case the cathode was directly coated onto the green-emitting LEP without the intermediate PVA coating and stripping steps.

Fig. 3 plots the current–voltage–luminance curves of a representative LED made from a green LEP that had had PVA stripped from the polymer surface (designated as a “processed device”) along with a representative control. In general (apart from a slight increase in leakage current), we find that the electronic properties of the control and the processed

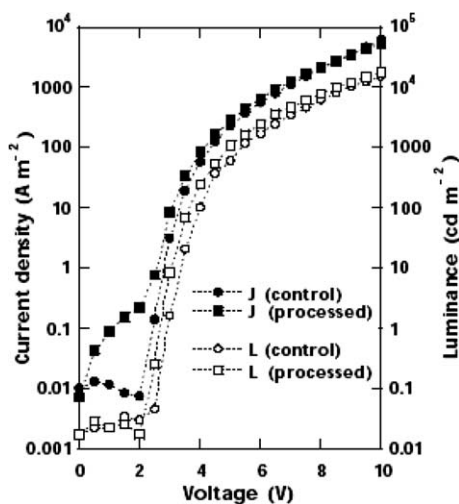


Fig. 3. Typical current–voltage–luminance curves for a control LED and a ‘processed LED’ (see text for details).

devices are similar in terms of efficiency, turn-on voltage and emission brightness, indicating that the electronic properties of the LEP are not significantly compromised by the deposition and subsequent removal of the PVA. We also note that the relative insensitivity of device performance to the processing procedure indicates that very little water remains within the structure after the film has been processed. It therefore appears that any residual water is effectively removed from the structure during the vacuum pump-down that occurs prior to the cathode coating.

X-ray photoelectron spectroscopy (XPS) measurements were performed to study the surface of an LEP film from which PVA has been stripped. XPS measurements were performed using a VG (East Grinstead, UK) CLAM 2 electron energy analyser mounted on an ultra high vacuum chamber equipped with a Mg X-ray anode ($h\nu = 1253$ eV). An 80 nm thick film of a green-emitting LEP was coated onto a silicon wafer, which was then coated with a PVA film. This film was then stripped by immersion in water for 1 min. Control films composed of a pure PVA layer and a pure LEP film were also studied. By detecting the photoelectrons emitted as a function of angle, we can gain approximate information regarding the elemental composition of the film as a function of depth. To probe the depth-dependent distribution of the LEP we determined the relative concentration of sulfur (S) (an element characteristic to many LED-applicable co-polymers [30]) by measuring the relative intensity of the S 2p photoelectrons, which have a characteristic binding energy of ~ 165 eV. To gain simple depth-resolution information, measurements were made at electron take-off angles of 30° , 60° and 90° .

At 30° (where the first ~ 5 nm of the film composition is probed) we did not detect any sulfur. However sulfur was detected at an angle of 60° and 90° (which probes down to a characteristic depth of 8–10 nm). This indicates that the first ≤ 5 nm is principally composed of PVA (i.e. not containing sulfur). The presence of such a surface layer most likely results from the entanglement of polymer chains resulting from the interpenetration of the PVA molecules into the LEP layer. The formation of interface layers having widths very similar to this is a well characterized phenomena in bilayer systems composed of two immiscible polymers [31]. We have performed AFM scans of the surface of unprocessed and stripped LEP films to determine their surface roughness. Encouragingly, it seems that the roughness of films are very similar, both being around



Fig. 4. An image of a simple array of 1 mm^2 polymer pixels emitting either red, green or blue electroluminescence.

~ 1 nm. This indicates that the PVA stripping does not result in significant modification of the LEP surface. Importantly, this surface layer of PVA does not seem to compromise the performance of the LED. Whilst the exact reason for this is not currently understood, we note that experiments have demonstrated that thin (<10 nm) layers of insulating polymers which were deliberately deposited on LEP films, actually improved their EL efficiency. This effect was ascribed to improved electron-injection [32].

To demonstrate that the patterning process could be used to fabricate a display, we have fabricated a simple array of R, G and B LEDs. Fig. 4 shows an image of a device consisting of nine 1 mm^2 pixels emitting either R, G, or B EL. Here, the LED array is fabricated onto a silicon back-plane and utilizes a metallic anode and a common, transparent, calcium cathode, with the devices driven at a voltage of 9 V. Due to the use of a common anode and cathode, it was necessary to prevent a short circuit occurring between the anode and cathode through the regions of the film uncoated with conjugated polymer. This was achieved by first coating a layer of photoresist onto a metallic anode material, which was then photo-patterned using conventional lithography to selectively remove the photoresist from the areas of the anode where the pixels were subsequently patterned. We stress however that in a practical implementation of this technology where pre-pixelated substrates are generally employed (e.g. in an active matrix display), no such lithographic step would be necessary. Whilst we have not yet characterized the current–voltage–luminance of the individually patterned pixels, it can be seen that the different color pixels have approximately equal brightness.³

³ Note that the emission from the green-emitting pixel appears yellow in colour, however this is due to the poor colour-rendering of the camera used to take the image rather than degradation of the polymer film.

Importantly, such prototype devices were still active six months after fabrication, indicating that it is unlikely that significant stability problems arise due to laser-assisted patterning.

We have therefore demonstrated a laser-ablation assisted patterning protocol that can pattern different polymeric thin films on a surface having a characteristic length-scale of 10 μm . We have shown that the electronic properties of such patterned LEPs are not compromised by the patterning process, and have used our methodology to create a simple prototype array of LED pixels emitting either red, green or blue EL. We have not yet determined the minimum feature size than could be achieved using our process, however we have used direct laser-ablation to pattern polymer-films with a resolution of 1 μm . It is clear that our process could be adapted to pattern a range of polymers for a number of different applications; provided the performance of organic field effect transistors (FETs) can be improved to drive PLED pixels at display brightness, it could be used to define, interconnect and integrate fully organic displays and their associated drive electronics. It could also be used to pattern polymers that have a chemical, biochemical or opto-mechanical response [33,34], which could allow the direct integration of electronic and functional polymeric materials together to create new types of miniaturized chemical sensors and micro-machines.

Acknowledgements

We gratefully acknowledge both the UK EPSRC and Department of Trade and Industry (DTI) for the funding of the LINK-OSDA project 'Patterning of PLED materials by laser for microdisplay manufacture (DISPLAY)' (GR/R68276). We also thank Jim O'Brien and Robert Fletcher at The Dow Chemical Company for the provision of the LUMATION⁴ LEPs. We also thank Alex Shard and Patrick Brooks (Sheffield University, Department of Engineering Materials) for the XPS measurements, and Ahmed Iraqi (Sheffield University, Department of Chemistry) for useful comments and suggestions.

References

- [1] S. Holdcroft, *Adv. Mater.* 13 (2001) 1753.
- [2] M. Angelopoulos, *IBM J. Res. Dev.* 45 (2001) 57.
- [3] P.L. Burn, A.B. Holmes, A. Kraft, D.D.C. Bradley, A.R. Brown, R.H. Friend, R.W. Gymer, *Nature* 356 (1992) 47.
- [4] A. Pogantsch, G. Trattnig, G. Langer, W. Kern, U. Scherf, H. Tillmann, H. Hörhold, E. Zojer, *Adv. Mater.* 14 (2002) 1722.
- [5] J.A. DeAro, R. Gupta, A.J. Heeger, S.K. Buratto, *Synth. Met.* 102 (1999) 865.
- [6] W. Schmidt, R. Dankesreiter, J. Gmeiner, Th. Vogtmann, M. Schwoerer, *Acta Polym.* 44 (1993) 208.
- [7] M.L. Renak, G.C. Bazan, D. Roiman, *Adv. Mater.* 9 (1997) 392.
- [8] M. Behl, J. Seekamp, S. Zankovych, C.M.S. Torres, R. Zentel, J. Ahopelto, *Adv. Mater.* 14 (2002) 588.
- [9] R. Riehn, A. Charas, J. Morgado, F. Cacialli, *Appl. Phys. Lett.* 82 (2003) 526.
- [10] R.A.M. Hikmet, R. Thomassen, *Adv. Mater.* 15 (2003) 115.
- [11] C.D. Müller, A. Falcou, N. Reckefuss, M. Rojahn, V. Wiederhirm, P. Rudati, H. Frohne, O. Nuyken, H. Becker, K. Meerholz, *Nature* 42 (2003) 829.
- [12] T. Aernouts, P. Vanlaeke, W. Geens, J. Poortmans, P. Heremans, S. Borghs, R. Mertens, R. Andriessen, L. Leenders, *Thin Solid Films* 451–452 (2004) 23.
- [13] F.C. Krebs, J. Alstrup, H. Spanggaard, K. Larsen, E. Kold, *Sol. Energy Mat. Sol. Cells.* 83 (2004) 293.
- [14] M. Wang, H. Braun, T. Kratzmüller, E. Meyer, *Adv. Mater.* 13 (2001) 1312.
- [15] D.C. Duffy, R.J. Jackman, K.M. Vaeth, K.F. Jensen, G.M. Whitesides, *Adv. Mater.* 11 (2001) 546.
- [16] T.R. Hebner, C.C. Wu, D. Marcy, M.H. Lu, J.C. Sturm, *Appl. Phys. Lett.* 72 (1998) 519.
- [17] H. Kobayashi, S. Sanbe, S. Seki, H. Kigchi, M. Kimura, I. Yudasaka, S. Miyashita, T. Shimoda, C.R. Towns, J.H. Burroughes, R.H. Friend, *Synth. Met.* 111–112 (2000) 125.
- [18] B. de Gans, P. Duineveld, U.S. Schubert, *Adv. Mater.* 16 (2004) 203.
- [19] B. Chen, T. Cui, Y. Liu, K. Varshramyan, *Solid-State Electron.* 47 (2003) 841.
- [20] T. Kawase, H. Siringhaus, R.H. Friend, T. Shimoda, *Adv. Mater.* 13 (2001) 1601.
- [21] Y. Yang, S. Chang, J. Bharathan, J. Liu, *J. Mat. Sci.: Mat. Electron.* 11 (2000) 89.
- [22] J.Z. Wang, Z.H. Zheng, H.W. Li, W.T.S. Huck, H. Siringhaus, *Nature Mater.* 3 (2004) 171.
- [23] M.C. Gower, *Proc. SPIE* 3618 (1999) 251.
- [24] S. Noach, E.Z. Faraggi, G. Cohen, Y. Avny, R. Neumann, D. Davidov, A. Lewis, *Appl. Phys. Lett.* 69 (1996) 3650.
- [25] Y. Tak, C. Kim, M. Kim, K. Kim, M. Lee, S. Kim, *Synth. Met.* 138 (2003) 497.
- [26] See technical information. Available from: <www.exitech.co.uk>.
- [27] G.B. Blanchet, Y.L. Loo, J.A. Rogers, F. Gao, C.R. Fincher, *Appl. Phys. Lett.* 82 (2003) 463.
- [28] J.Y. Lee, S.T. Lee, *Adv. Mater.* 16 (2004) 51.
- [29] N.C. Greenham, I.D.W. Samuel, G.R. Hayes, R.T. Phillips, Y.A.R.R. Kessener, S.C. Morati, A.B. Holmes, R.H. Friend, *Chem. Phys. Lett.* 241 (1995) 89.

⁴ Trademark of The Dow Chemical Company.

- [30] J. Chappell, D.G. Lidzey, P.C. Jukes, A.M. Higgins, R.L. Thompson, S. O'Connor, I. Grizzi, R. Fletcher, J. O'Brien, M. Geoghegan, R.A.L. Jones, *Nature Mater.* 2 (2003) 616.
- [31] L.R. Hutchings, R.W. Richards, R.L. Thompson, A.S. Clough, S. Langridge, *J. Pol. Sci. B.* 39 (2001) 2351.
- [32] J.H. Park, O.O. Park, J.-W. Yu, J.K. Kim, Y.C. Kim, *Appl. Phys. Lett.* 84 (2004) 1783.
- [33] E.W.H. Jager, E. Smela, O. Inganäs, *Science* 290 (1999) 1540.
- [34] Y.L. Yu, M. Nakano, T. Ikeda, *Nature* 425 (2003) 145.

Impact of interfacial barriers on recombination profile in bilayer organic light-emitting diode

B. Mazhari *

Department of Electrical Engineering and Samtel Center for Display Technology, Indian Institute of Technology, Kanpur 208 016, India

Received 23 July 2003; received in revised form 30 June 2004; accepted 8 September 2005

Available online 14 October 2005

Abstract

An analysis of recombination in bilayer organic light-emitting diodes is presented using numerical simulations and analytical model. It is shown using simulations that although recombination occurs close to the organic–organic interface, the recombination peak can lie either in the hole transport layer (HTL) or the electron transport layer (ETL) of the device. An analytical model is presented which provides insight into charge accumulation and transport across the organic interface and explains the shift in recombination peak with changes in interfacial barrier heights. The impact of interfacial barrier heights on electric field at the organic interface is also discussed.

© 2005 Elsevier B.V. All rights reserved.

PACS: 73.61.Ph

Keywords: OLED; Bilayer; Recombination; Analytical model

1. Introduction

Organic light-emitting diode (OLED) displays are being increasingly viewed as the flat panel technology of the future due to their several advantages including wide viewing angle, fast response time, thin size and low cost [1–3]. The simplest OLED structure consisting of a single organic material sandwiched between an anode and a cathode suffers from poor recombination efficiency [4,5]. This is because in most organic materials, the hole mobility is much larger than electron mobility so that carriers

recombine predominantly in a region close to cathode where there is much greater probability of non-radiative recombination. By incorporating an additional suitably chosen organic layer, recombination can be shifted predominantly to a region close to the organic interface. As a result of the shift in recombination peak away from the quenching sites next to the cathode, much higher radiative recombination efficiency can be obtained. Since they were first reported [1], several studies have been conducted to investigate the operating principles of these bilayer devices [6–13]. These studies have led to a greater understanding of the role of interfacial barrier heights in achieving current balance despite large differences in hole and electron mobilities and injection barriers at the contacts. Although

* Tel.: +91 0512 2597924; fax: +91 0512 2590063.

E-mail address: baquer@iitk.ac.in

recombination in bilayer devices takes place predominantly in a region very close to the organic interface, the recombination peak can occur either in HTL or ETL depending on device parameters. The location of recombination peak is important because of its impact on the emission spectrum of the OLED. Although it is recognized that recombination profile depends on interfacial barrier heights, a detailed study of the underlying mechanism has not yet been carried out. We describe in this paper an analysis of carrier recombination in bilayer devices and present a simple analytical model which provides insight into recombination processes close to the organic interface.

2. Recombination profile

A bilayer device consisting of an organic material-1 which serves as a hole transport layer (HTL) and an organic material-2 which serves as an electron transport layer (ETL) is shown in Fig. 1(a). The associated band diagrams are shown in Fig. 1(b). ΔE_C (ΔE_V) is the discontinuity in the LUMO (HOMO) level at the organic–organic interface. The numerical simulations described in this work were carried out using SimWindows device simulation software [14] and assumes trap-free, drift-diffusion transport in the bulk. For simplicity and ease of correlation of numerical results with analytical model, a constant mobility model is taken. Carrier transport at the organic–organic interface is modeled by SimWindows as thermionic emission with backflow similar to that assumed by Crone et al. [9]. For recombination the Langevin

form is assumed. Although both anode and cathode contacts are taken to be Schottky barriers, the barrier height between the anode (cathode) metal and HTL (ETL) is taken to be 0.2 eV or less so that both hole and electron current in the device are bulk-limited. Along with constant mobility model, this assumption simplifies not only development of analytical model but also allows demonstration of effects of changes in interfacial barrier heights in an unambiguous manner. Like in most bilayer devices such as small molecule Alq₃/TPD or polymer PPV/CN-PPV devices, the hole mobility in HTL is assumed to be much larger than electron mobility in ETL. Both the materials are also assumed to have the same dielectric constant. In both numerical simulations and analytical model, material parameters such as mobility, energy gaps, interfacial barrier heights, etc. were chosen to be similar to those used in earlier studies [9].

Fig. 2(a) shows a typical recombination profile within a bilayer OLED. As expected, recombination predominantly occurs close to the organic interface. However, the fraction of carriers that recombine in HTL or ETL depends on the relative magnitudes of interfacial barrier heights. To investigate the role of interfacial barrier heights, consider a situation where for a fixed HOMO energy offset (or hole barrier height), the LUMO energy offset (or electron barrier height) in the device is varied from zero to a value larger than HOMO energy offset. The remaining device parameters and applied voltage are kept constant. Fig. 2(b) shows the recombination rate on the two sides of the organic interface as a function of LUMO energy offset for a constant HOMO energy offset of 0.6 eV. It can be seen that initially, the recombination predominantly takes place within HTL close to the organic interface but when electron barrier height is increased beyond a certain threshold value, the recombination shifts entirely to the ETL side of the interface. For the extreme case of zero electron barrier height, it is easy to understand that recombination rate is high in HTL because the electrons injected from cathode can easily flow into HTL and recombine with the large number of holes therein. Recombination rate in ETL is negligible because the large hole barrier (0.6 eV) suppresses injection of holes into ETL. For the other extreme case of 0.8 eV electron barrier height, it is also understandable that recombination rate in HTL is negligible because the large electron barrier completely blocks injection of electrons into HTL. However, it is not so apparent how most of

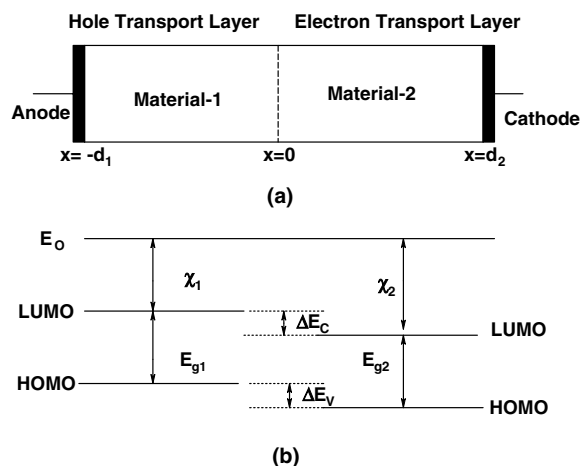


Fig. 1. Schematic diagram of a bilayer organic LED (a) and its associated energy band diagram (b).

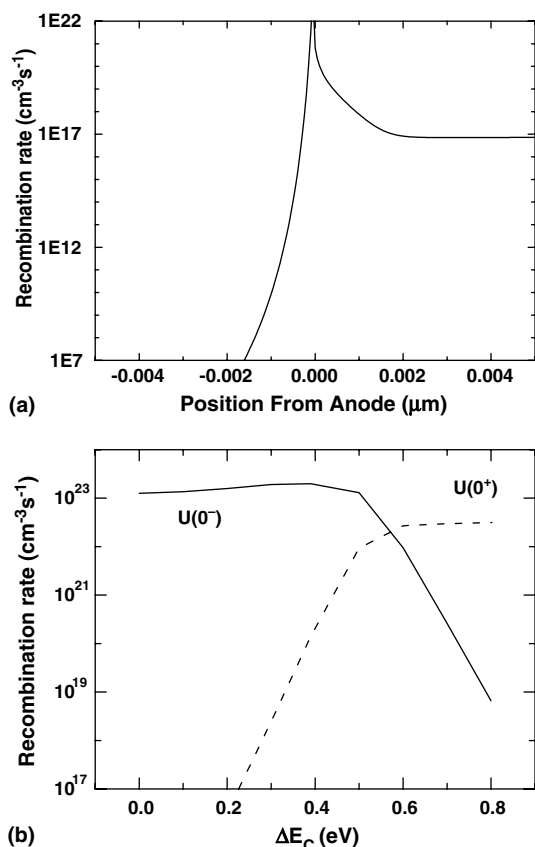


Fig. 2. (a) A typical recombination profile in a bilayer device. Results shown are for a device with $E_{g1} = 2.4$ eV, $E_{g2} = 2.6$ eV, $\chi_1 = 2.9$ eV, $\chi_2 = 3.3$ eV, $\mu_{p1} = \mu_{p2} = 0.5 \times 10^{-6}$ cm²/V s, $\mu_{n1} = \mu_{n2} = 0.5 \times 10^{-8}$ cm²/V s, $d_1 = d_2 = 500$ Å and a constant HOMO energy offset of 0.6 eV. Applied voltage was 5 V. (b) Recombination rate immediately to the left (solid line) and to the right (broken line) of the organic–organic interface as a function of LUMO energy offset.

recombination shifts to ETL side in view of the fact that hole barrier height remains constant at a large value of 0.6 eV. Fig. 2(b) shows that recombination rate in ETL actually increases with increase in electron barrier height. It might appear that this occurs primarily due to increased accumulation of electrons in ETL since bimolecular recombination rate is proportional to product of both electron and hole densities. However, this does not provide the full picture because as will be shown later, current in the device remains relatively constant as LUMO energy offset is increased. This means that all the holes injected from the anode which were earlier recombining in HTL now recombine in ETL. This leads to the implication that hole injection into ETL must increase also with increase in electron

barrier height even though the hole barrier height and applied voltage remain constant. In order to explain the mechanism underlying the dependence of recombination on interfacial barrier heights an analytical model is described in the next section.

3. Analytical model

Consider first a bilayer device in which there is only a HOMO energy offset of a fairly large magnitude of 0.6 eV and zero LUMO energy offset at the organic–organic interface. The choice of 0.6 eV is rather arbitrary and results discussed are applicable in general as long as HOMO energy offset is large enough to ensure that recombination of carriers occur predominantly near the organic interface. When the diode is forward biased, there will be an accumulation of holes in HTL close to the organic interface due to the presence of a barrier to hole current flow. Despite this accumulation of holes, the hole current injected into ETL would however be very small due to the large barrier seen by the holes. The electrons injected from the cathode would drift across the ETL and recombine with the large number of holes in HTL. Because of the large density of holes at the interface, very few electrons will be able to penetrate deeper into the HTL so that the recombination peak is expected to lie in HTL close to the organic interface. Due to the fact that electron mobility in ETL is significantly smaller as compared to hole mobility in HTL, the voltage applied would drop largely across the ETL layer and current in the device would be determined primarily by the arrival of electrons at the interface. This picture of current flow suggests that the bilayer device under these conditions can be modeled effectively as a single layer, single carrier device consisting only of electron transport layer in which current is dominated by electrons injected by the cathode. In this ‘single-layer’ model, the cathode serves as the injecting contact and the accumulated hole density at the organic interface serves the role of second contact by acting as a near perfect sink for the injected electrons. Under trap-free condition, the current can be described by space charge limited flow (SCLC) [11]:

$$J = 9/8 \times \epsilon_0 \epsilon_r \times \mu_{n2} \times \frac{(V - V_{bi})^2}{d_2^3} \quad (1)$$

where V_{bi} is the built-in voltage, μ_{n2} is the mobility of electrons in ETL layer and d_2 is the thickness of ETL layer. Fig. 3(a) shows that results obtained from simulations match quite well with that

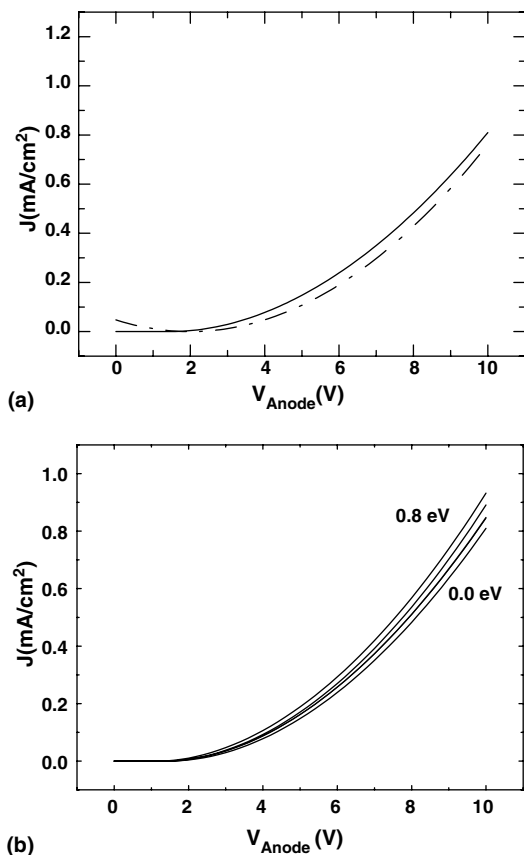


Fig. 3. (a) Current density as a function of voltage obtained from numerical simulations (solid line) and analytical model (dotted line) described by Eq. (1). Results shown are for a device with $E_{g1} = 2.4$ eV, $E_{g2} = 2.6$ eV, $\chi_1 = 2.9$ eV, $\chi_2 = 3.3$ eV, $\mu_{p1} = \mu_{p2} = 0.5 \times 10^{-6}$ cm²/V s, $\mu_{n1} = \mu_{n2} = 0.5 \times 10^{-8}$ cm²/V s, $d_1 = d_2 = 500$ Å and a constant HOMO energy offset of 0.6 eV. (b) Current density as a function of voltage obtained from numerical simulations for different values of LUMO energy offset (0, 0.2, 0.6, 0.8 eV) at the organic–organic interface.

predicted by Eq. (1). Let us next consider the case where for a fixed interfacial hole barrier of 0.6 eV, the LUMO energy offset (or electron barrier height) at the organic interface is gradually increased from 0 to 0.8 eV. Due to the presence of a barrier to electron flow, electrons would now tend to accumulate in ETL close to the interface. The accumulation of electrons at the interface can be understood by noting that as a result of the barrier, the electron density to the right of the interface ($n(0^+)$) will be much larger than electron density to the left of it ($n(0^-)$). The continuity of electric field at the interface means that the drift component of electron current to the right of the interface ($J_N^{\text{drift}}(0^+)$) would be much larger than electron current to the left of the interface ($J_N^{\text{drift}}(0^-)$). The only way in which

continuity of electron current across the interface can then be maintained is if there is a large component of electron diffusion current to the right of the interface which is practically equal and opposite to the electron drift current. As a result, the electrons can be assumed to be in quasi-equilibrium in ETL close to the interface. In this case also the bilayer device can be modeled effectively as a ‘single-layer’ device consisting only of ETL where the cathode serves as the injecting contact and the accumulated electron density in quasi-equilibrium serves as a second ohmic contact. Since I – V characteristics of a single-layer device under these conditions is still described by space charge limited current, Eq. (1) would continue to hold for non-zero LUMO energy offsets as well. Fig. 3(b) shows the I – V characteristics of a bilayer device for a constant HOMO energy offset of 0.6 eV and LUMO offset varying from 0 to 0.8 eV. It can be seen that the I – V characteristics are almost independent of the interfacial electron barrier height. Although the change in I – V characteristics is relatively negligible as the electron barrier height is increased from 0 to 0.8 eV, there is a large impact on carrier density and recombination peak as seen from Fig. 2(b). To understand this behavior consider first the case where electron barrier height is relatively small and recombination peak lies in HTL. In this case the electrons injected by the cathode recombine predominantly in HTL. Assuming that due to the large electric field at the interface, the drift component is predominant, the electron current in HTL at the organic interface can be expressed as:

$$J \cong q\mu_{n1}E(0)n(0^-) \quad (2)$$

where $E(0)$ is the electric field at the organic interface, μ_{n1} the mobility of electrons in HTL and $n(0^-)$ is the density of electrons in HTL at the organic interface. Using the relation $n(0^-) = n(0^+) \exp(-\Delta E_C/kT)$, we can re-write Eq. (2) as:

$$J = q\mu_{n1} \times E(0) \times n(0^+) \times \exp(-\Delta E_C/kT) \quad (3)$$

Since the current remains relatively constant with increase in the magnitude of LUMO energy offset, the product of electric field and electron density at the organic interface must increase proportionately according to Eq. (3). To obtain an analytical estimate of the increase in electric field or electron density separately, a relationship between electron density and electric field next to the interface is required. The results from simulations indicate that carrier density decays rapidly away from the

interface in a complicated manner. To capture the sharp variation in electron density, we assume for simplicity that electron density in ETL decays in an exponential manner away from the organic interface:

$$n(x \geq 0) = n(0^+) \times \exp(-\delta_2 x) \quad (4)$$

Integration of Eq. (4) gives the net accumulated electron density in ETL close to the interface:

$$Q_N^{\text{int.}} = qn(0^+) \times \delta_2^{-1} \quad (5)$$

As discussed earlier, the accumulation of electrons close to the interface also means that electron drift and diffusion currents must be almost equal and in opposition to each other. This assumption of quasi-equilibrium condition together with Eq. (4) can be used to obtain an expression for electric field at the interface :

$$E(0) = kT/q \times \delta_2 \quad (6)$$

Using this expression, Eq. (5) can be re-written as

$$Q_N^{\text{int.}} = n(0^+) \times \frac{kT}{E(0)} \quad (7)$$

Assuming that the accumulation layer in HTL is like a charge-sheet, another expression relating charge and electric field can be obtained through application of Gauss's law at the interface:

$$E(0) = Q_N^{\text{int.}}/\varepsilon + E_{b2} \quad (8)$$

where E_{b2} is electric field in the bulk of ETL close to the interface. Substitution of Eq. (8) in Eq. (7) gives a relationship between electron density and electric field at the organic interface:

$$E(0) = 0.5E_{b2} \times \left\{ 1 + \sqrt{1 + \frac{n(0^+)}{n_2}} \right\} \quad (9)$$

where $n_2 = (\varepsilon E_{b2}^2/4kT)$. Eq. (9) can be rewritten in a form which is more amenable to verification:

$$\left\{ \frac{2E(0) - E_{b2}}{E_{b2}} \right\}^2 = 1 + \frac{n(0^+)}{n_2} \quad (10)$$

In order to verify Eq. (10), numerical simulations were carried out to obtain values of $E(0)$ and $n(0^+)$ for electron barrier height in the range of 0–0.4 eV. The electric field in the bulk of ETL (E_{b2}) was taken to be the electric field at a distance of 50 Å away from the organic interface. Fig. 4(a) shows that a plot of LHS of Eq. (10) as a function of electron density can be fitted with a straight line in agreement with the predictions of the analytical

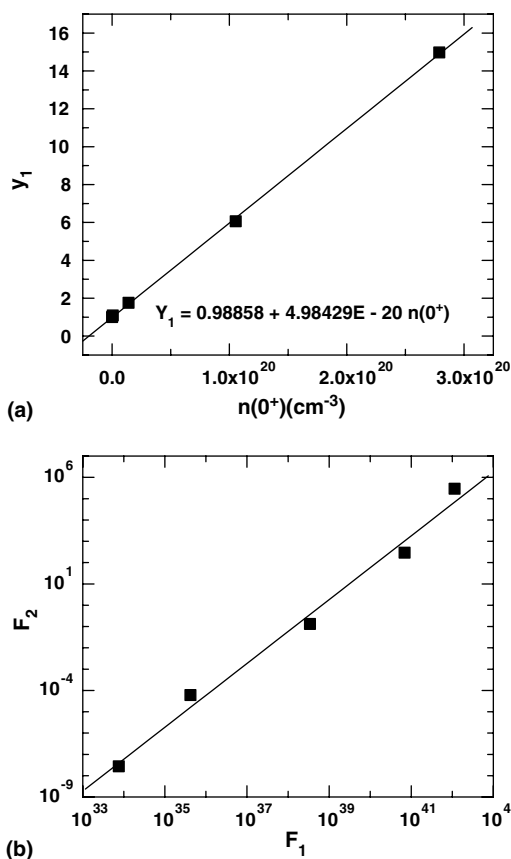


Fig. 4. (a) y_1 (LHS of Eq. (10)) plotted as a function of electron density in ETL at the organic interface. Results shown are for a device with $E_{g1} = 2.4$ eV, $\chi_1 = 2.9$ eV, $\mu_{n1} = \mu_{n2} = 0.5 \times 10^{-8}$ $\text{cm}^2/\text{V s}$, $\mu_{p1} = \mu_{p2} = 0.5 \times 10^{-6}$ $\text{cm}^2/\text{V s}$, $d_1 = d_2 = 500$ Å and a constant HOMO energy offset of 0.6 eV. The LUMO energy offset was varied between 0–0.4 eV and applied voltage was 5 V. (b) F_2 (LHS of Eq. (12)) plotted against F_1 (RHS of Eq. (12)). The solid line shows a linear fit to the simulation results.

expression. Substitution of Eq. (9) in Eq. (3) yields an expression which can be used to determine the impact of increase in LUMO energy offset on electron density at the organic interface:

$$J \cong 0.5q\mu_{n1} \times E_{b2} \times \left\{ 1 + \sqrt{1 + \frac{n(0^+)}{n_2}} \right\} \times n(0^+) \times \exp(-\Delta E_C/kT) \quad (11)$$

Eq. (11) can be re-written as:

$$\left(\frac{J}{\exp(-\Delta E_C/kT)} \right)^2 \propto n(0^+)^2 \times \left(1 + \frac{n(0^+)}{n_2} \right) \quad (12)$$

Fig. 4(b) shows that a plot of left hand side of Eq. (12) (F_2) vs. the right hand side (F_1) obtained from simulations can be fitted with a straight line thereby

indicating that the form of Eq. (11) is also qualitatively correct. It was described earlier that with increase in electron barrier height, the current remains relatively constant. Eq. (11) then implies that an increased accumulation of electrons and hence an increase in electric field must occur so as to maintain a constant current despite increase in electron barrier height. However, the electron density at the organic interface increases in accordance with Eq. (11) only for values of LUMO energy offset below about ~ 0.4 eV. Fig. 5(a) shows that for larger values of interfacial electron barrier height, the electron density saturates to a constant value. To understand this behavior, it is necessary to understand the impact of increase in interfacial electron barrier height on hole density next to the organic interface. As described earlier, an accumulation layer of holes is formed in HTL close to the organic interface due

to the presence of a hole barrier. This accumulated hole density can be modeled in a manner similar to the accumulated electron density in ETL and a set of expressions similar to Eqs. (4)–(8) can be written to obtain the following expression relating the electric field to the hole density in HTL immediately to the left of the interface:

$$E(0) = 0.5E_{b1} \times \left\{ 1 + \sqrt{1 + \frac{p(0^-)}{p_1}} \right\} \quad (13)$$

where $p_1 = (\epsilon E_{b1}^2 / 4kT)$ and E_{b1} is the field in the bulk of HTL close to the organic interface. The hole density injected into ETL ($p(0^+)$) can be written as:

$$\begin{aligned} p(0^+) &= p(0^-) \times \exp(-\Delta E_V / kT) \\ &= 4p_1 \times \left\{ \frac{E(0) - E_{b1}}{E_{b1}^2 / E(0)} \right\} \times \exp(-\Delta E_V / kT) \end{aligned} \quad (14)$$

We have seen earlier that with increase in ΔE_C an increasing accumulation of electrons occurs at the interface so as to maintain a constant current with the consequence that the electric field at the interface also increases. Eqs. (13) and (14) then imply that as a result of this increase in electric field, the accumulated hole density in HTL and injected hole density in ETL should also increase. The results obtained from simulations shown in Fig. 5(b) confirm this increase in injected hole density in ETL with increase in interfacial electron barrier height. To understand the full implications of this very important result, consider the two components of electron current as illustrated in Fig. 6. The components J_{N1} and J_{N2} result from recombination of electrons with holes in HTL and ETL, respectively. The magnitude of J_{N1} (or J_{P1}) is determined primarily by number of electrons that are able to cross over to the HTL because hole density therein is very large. On the other hand, the magnitude of J_{N2} (or J_{P2}) is determined primarily by the number of holes that

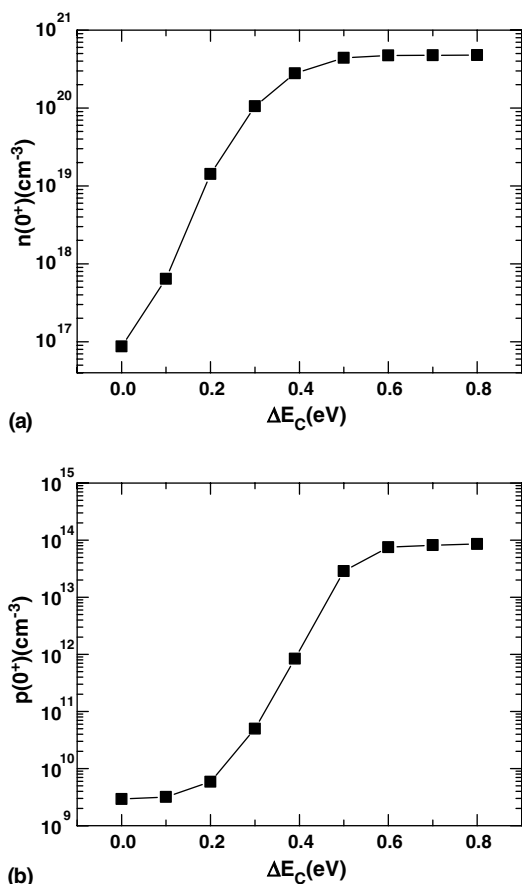


Fig. 5. (a) Electron density in ETL at the organic interface vs. electron barrier height. (b) Hole density in ETL at the organic interface vs. electron barrier height. The simulation conditions were same as in Fig. 4.

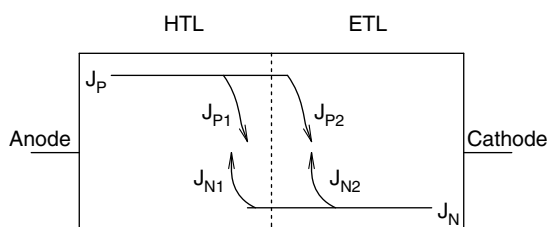


Fig. 6. Schematic diagram of a bilayer device illustrating the components of electron and hole currents.

are able to cross over to ETL. For smaller values of interfacial electron barrier height, the current component J_{N1} is dominant and most of the recombination takes place in HTL. However, as discussed earlier, with increase in the barrier height, the hole injection into ETL also increases so that the fraction of electron current carrier by J_{N2} also increases. In light of the above discussions, the ratio of these two currents can be expressed as:

$$\frac{J_{N2}}{J_{N1}} \propto \frac{p(0^+)}{n(0^-)} \quad (15)$$

The expressions for hole and electron density obtained from Eqs. (14) and (9), respectively can be used to re-write the above expression:

$$\frac{J_{N2}}{J_{N1}} \propto \left(\frac{E(0) - E_{b1}}{E(0) - E_{b2}} \right) \times \exp\left(\frac{\Delta E_C - \Delta E_V}{kT} \right) \quad (16)$$

Since the current components J_{N2} and J_{N1} are also proportional to recombination rates $U(0^+)$ and $U(0^-)$, respectively, an expression relating recombination rates and interfacial barrier heights can be obtained:

$$\frac{U(0^+)}{U(0^-)} \propto \exp\left(\frac{\Delta E_C - \Delta E_V}{kT} \right) \quad (17)$$

In obtaining Eq. (17), the terms involving electric field have been neglected because they have much less impact than the exponential term involving barrier heights. Fig. 7 confirms that the variation of recombination rates with interfacial barrier heights

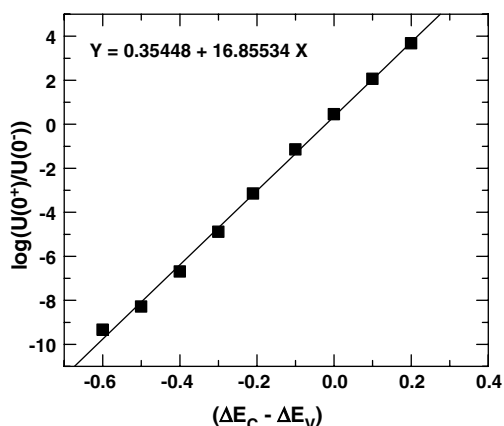


Fig. 7. Variation of the logarithm of the ratio of recombination rates on the two sides of the organic interface as a function of the difference of electron and hole barrier heights. The solid line is the linear fit to the simulation results. Simulation conditions were same as in Fig. 3.

is in qualitative agreement with predictions of Eq. (17).

To summarize the mechanism underlying the shift in recombination from HTL to ETL with increase in electron barrier height, the first important fact is that current in a bilayer device is insensitive to the magnitude of electron barrier height at the interface. Initially, when the electron barrier height is small, it is easier for electrons to crossover to HTL side and recombine with the large density of holes accumulated therein. The holes on the other hand find it difficult to scale the hole barrier height (assumed to be large and constant) and as a result very few recombine with electrons in ETL. As a result, the electron current component J_{N1} is dominant and the recombination peak thus lies in HTL. With increase in electron barrier height, an increased accumulation of electrons occurs at the interface so that despite increase in electron barrier height, enough electrons are able to scale the barrier and recombine with holes so as to maintain a constant current. This raises the electric field at the interface and causes an increased accumulation of holes on the HTL side of the interface. As a result, even though the hole barrier height may be constant, an increased injection of holes into ETL takes place with increase in electron barrier height. The hole current J_{P1} increases in magnitude and more recombination takes place in ETL. Eventually when the electron barrier height becomes sufficiently large (\sim greater than the hole barrier height), recombination shifts entirely to the ETL side of the interface. The current now is determined not by electrons reaching HTL after scaling the interfacial electron barrier but by hole injection into ETL. As a result, the interfacial electron barrier height ceases to have any significant influence on accumulated electron density in ETL which saturates to a constant value as seen in Fig. 5(a). This leads to electric field and hole density injected into ETL also becoming constant leading to a constant recombination rate $U(0^+)$.

As a result of accumulation of electrons and holes, the electric field at the organic–organic interface is significantly higher than elsewhere in the bulk of the bilayer device. Since an excessively large electric field can be detrimental from the point of reliable operation of the device, it is important to understand the factors that determine its strength. Depending on the relative magnitudes of electron and hole barrier heights there can be two situations. For the case $\Delta E_C < \Delta E_V$, recombination as indicated by Eq. (17) occurs largely in HTL. The

magnitude of electron density and thus electric field at the interface is determined by the electron barrier height as shown in Fig. 5(b). Since electric field increases with increase in ΔE_C , an optimal choice of HTL and ETL organic materials would be one in which interfacial electron barrier height is zero. For the case $\Delta E_C > \Delta E_V$, recombination takes place in ETL and both electron density and electric field are independent of the magnitude of electron barrier height and are determined by the magnitude of hole barrier height instead. This can be understood from the observation that electric field increases with ΔE_C and saturates to a constant value when ΔE_C becomes larger than ΔE_V . In this case a smaller hole barrier height is desirable for obtaining smaller charge accumulation and electric field at the organic interface.

4. Conclusion

To summarize, numerical simulations and analytical model developed in this work provide insight into the impact of interfacial barrier heights on the location of recombination peak in bilayer devices. The mechanism by which recombination shifts from HTL side of the organic–organic interface to the ETL side with increase in LUMO energy offset is

described in detail. It is also shown that the magnitude of electric field and charge accumulated at the organic–organic interface is determined by whichever interfacial barrier, electron or hole, is smaller.

References

- [1] C.W. Tang, S.A. Van Slyke, *Appl. Phys. Lett.* 51 (1987) 913.
- [2] J.H. Burroughes, D.D.C. Bradley, A.R. Brown, R.N. Marks, K. Mackey, R.H. Friend, P.L. Burn, A.B. Holmes, *Nature* 347 (1990) 539.
- [3] D. Braun, A.J. Heeger, *Appl. Phys. Lett.* 58 (1991) 1982.
- [4] J.C. Scott, S. Karg, S.A. Carter, *J. Appl. Phys.* 82 (1997) 1454.
- [5] B.K. Crone, I.H. Campbell, P.S. Davids, D.L. Smith, C.J. Neef, J.P. Ferraris, *J. Appl. Phys.* 86 (1999) 5767.
- [6] D.V. Khramtchenkov, V.I. Arkhipov, H. Bassler, *J. Appl. Phys.* 81 (1997) 6954.
- [7] J. Staudigel, M. Stobel, F. Steuber, J. Simmerer, *J. Appl. Phys.* 86 (1999) 3895.
- [8] V. Nikitenko, H. Bassler, *J. Appl. Phys.* 85 (1999) 6515.
- [9] B.K. Crone, P.S. Davids, I.H. Campbell, D.L. Smith, *J. Appl. Phys.* 87 (2000) 1974.
- [10] C.D.J. Blades, A.B. Walker, *Synth. Met.* 111 (2000) 335.
- [11] V. Nikitenko, H. Bassler, *J. Appl. Phys.* 90 (2001) 1823.
- [12] B. Ruhstaller, S.A. Carter, S. Barth, H. Riel, W. Reiss, *J. Appl. Phys.* 89 (2001) 4575.
- [13] V. Nikitenko, O.V. Salata, H. Bassler, *J. Appl. Phys.* 92 (2002) 2359.
- [14] D.W. Winston, R.E. Hayes, *IEEE J. Quantum Electron.* 34 (1998) 707.

Blue polymer light-emitting diodes with organic/inorganic hybrid composite as hole transporting layer

Fushan Li ^a, Zhijian Chen ^{a,*}, Wei Wei ^b, Qihuang Gong ^{a,*}

^a State Key Laboratory for Artificial Microstructures and Mesoscopic Physics and Department of Physics, Peking University, Beijing 100871, People's Republic of China

^b School of Electronics and Information Engineering, Xian jiaotong University, Xian 710049, People's Republic of China

Received 2 November 2004; received in revised form 2 May 2005; accepted 26 August 2005
Available online 14 October 2005

Abstract

Polymer double-layer light-emitting diodes were fabricated with inorganic/organic hybrid composite as hole transporting layer. Two conjugated polymers, poly(9,9-dibutyl)fluorene (PDF) and a dendritic polyfluorene derivative, poly((9,9-dibutyl-2,7-diiodo-9H-fluorene)trisphenylamine) (PDFA) were introduced as light-emitting layer. The former organic double-layer devices showed luminance as high as 833 lm/m², and the power efficiency reached 0.065 lm/W. The latter showed maximum luminance of 1100 lm/m² and the quantum efficiency reached 0.104 lm/W. The values were higher than those single-layer devices without inorganic/organic hybrid hole transporting layer (HHTL). The improvement in the electroluminescent properties of these devices was attributed to that the introduction of HHTL enhanced hole injection and balanced the combination of hole and electron injected from anode (ITO) and cathode (Mg:Ag).

© 2005 Elsevier B.V. All rights reserved.

PACS: 78.55.Kz; 78.60.Fi; 78.66.Qn

Keywords: Electroluminescence; Organic/inorganic hybrid; Hole transporting layer; Polyfluorene

1. Introduction

Organic electroluminescence (EL) possesses extensive applications, such as backlights of liquid-crystal displays, ultra thin flat-displays, and efficient illuminators [1–3]. Since first electroluminescence of conjugated poly(*p*-phenylenevinylene) (PPV) sandwiched between an anode and a cathode with

appropriate work functions was reported in 1990 [4], EL polymers and polymer light-emitting diodes have expanded rapidly. It is well known that most of the polymer organic light-emitting diodes (OLED) are fabricated using spin-coating technique. However, the spin-coating technique is difficult to fabricate multilayer devices (that allows well-balanced double injection for holes and electrons) because the organic solvent would damage the underlying film.

Sol-gel technique provides a very attractive method to prepare organic/inorganic hybrid

* Corresponding authors. Fax: +86 10 62756567.

E-mail addresses: zjchen@pku.edu.cn (Z. Chen), qhong@pku.edu.cn (Q. Gong).

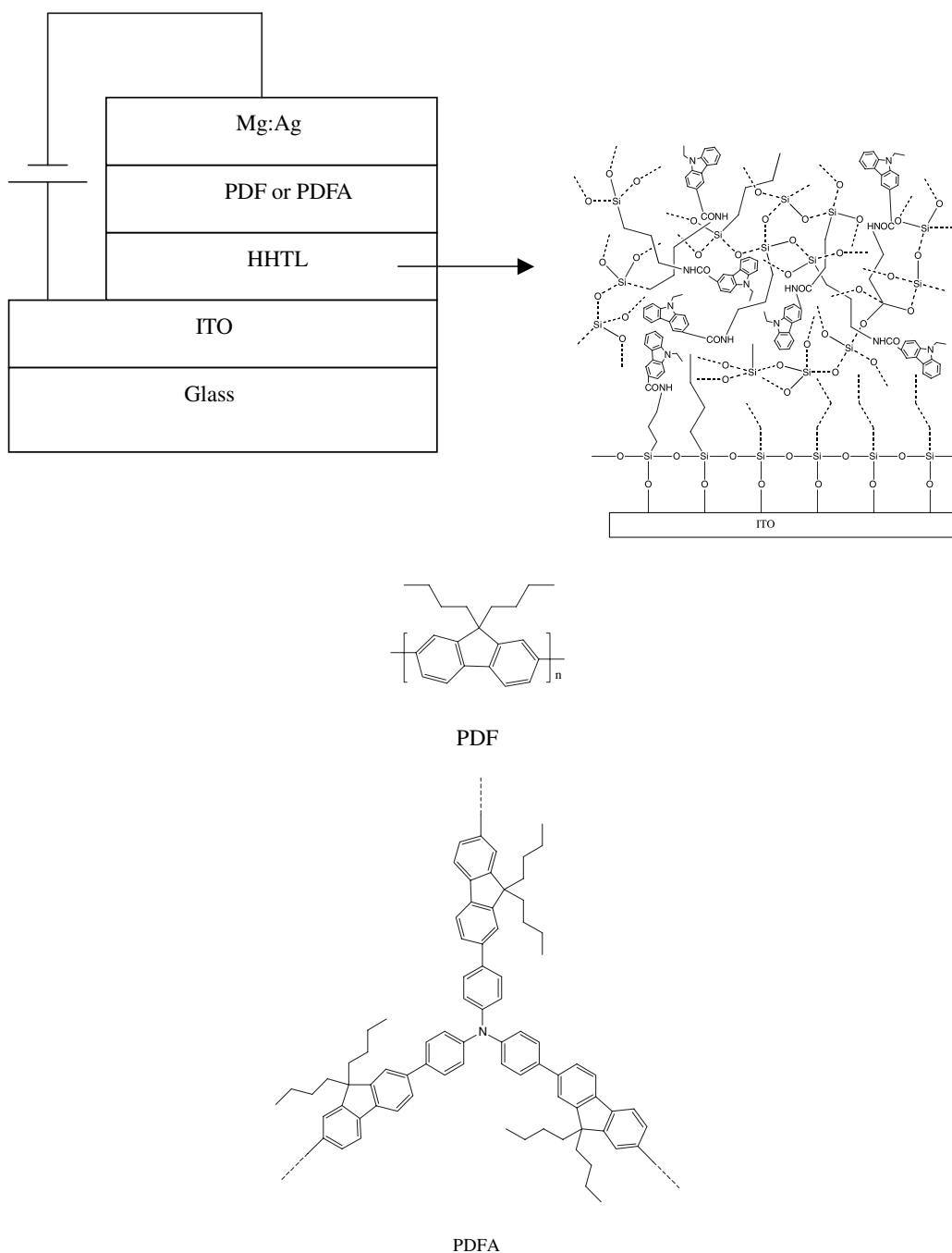


Fig. 1. Structure of OLED device and chemical structure of materials in this study.

composite [5–7]. They exhibit good optical quality and chemical stability. In particular, multilayer device can be readily fabricated because these composites are insoluble in any organic solvent.

In this work, we report a novel blue two-layer polymer light-emitting device with organic/inorganic composite as hole transporting layer (HHTL). Two

polymers, poly(9,9-dibutyl)fluorene (PDF) and a dendritic polyfluorene derivative, poly((9,9-dibutyl-2,7-diiodo-9H-fluorene)trisphenylamine) (PDFA) were synthesized to be used as light-emitting layer. The results showed that the introduction of HHTL can greatly improve the emission intensity and the quantum efficiency of the devices.

2. Experimental

2.1. Synthesis of the polymers

Two polymers, PDF and PDFA were synthesized using NiCl_2 as catalyzer and the chemical structures were shown in Fig. 1. The details about the synthetic process can be found in our previous work [8].

2.2. Preparation of HHTL and light-emitting diodes

The chemical structure of the HHTL can be found in Fig. 1. The active unit of HHTL was achieved from 9-ethyl-3-carboxylic acid-carbazole (ECAC), which was obtained from 9-ethyl-3-carbalde hyde oxidized by hydrogen peroxide. A precursor *N*-ethyl-carboxylic(trimethoxypropylsilane)aminoformate (ECTAF) was prepared from ECAC and aminopropyltrimethoxysilane (APTMS) in toluene at room temperature. ITO electrodes with a sheet resistance of $20 \Omega/\text{sq}$ were pretreated according to a regular chemical cleaning using detergent, deionized water, acetone and anhydrous ethanol in sequence. The precursor was spin-coated onto the cleaned ITO slide to afford the HHTL. Then the slide was heated at 120°C in ambient environment in order to make ECTAF change to acyl amine [9] and sufficiently hydrolyze. The thickness of the HHTL was estimated to be 23 nm on a Jobin Yvon M200 VIS AGMS ellipsometer.

The polymers, PDF and PDFA were dissolved in chloroform and spin-coated onto the ITO substrate with pre-coated HHTL. The thickness of the film was estimated to be ~ 100 nm using ellipsometer. Finally, a 170 nm thick layer of Mg:Ag was deposited onto the substrate as the cathode of the OLED. The EL measurements were carried out in air condition.

3. Results and discussion

3.1. Photophysical properties

The photoluminescence (PL) spectra of ITO slide with hybrid hole transport layer (HHTL) are shown in Fig. 2. HHTL showed absorption maximized at 355 nm, and the PL spectrum peaks at a wavelength of 415 nm. The absorption and photoluminescence mostly are attributed to the active unit (carbazole group) [10]. The PL spectra of PDF and PDFA in spin-coated film were also shown in Fig. 2. The emission of PDFA display an evident blue shift

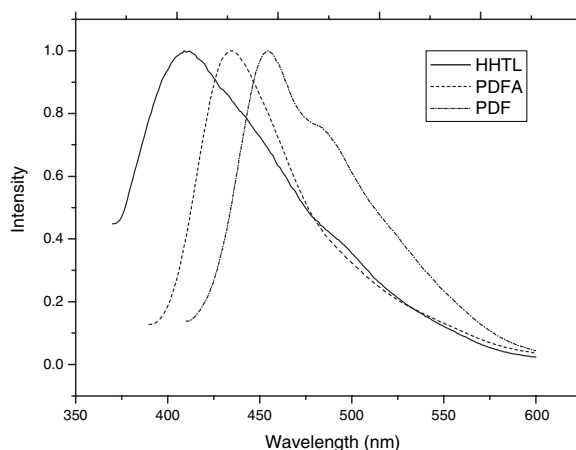


Fig. 2. Photoluminescence spectra of ITO slide coated with HHTL and PDF, PDFA in spin-coated film.

related to PDF, indicating that the aggregation of the molecules was effectively suppressed due to the dendritic structure of PDFA.

3.2. EL characteristics

The EL spectra are depicted in Fig. 3. The EL spectra of double-layer devices are coincident with those of single-layer devices, indicating that the emissions are produced from PDFA and PDF, respectively. The device of ITO/HHTL/PDFA/Mg:Ag showed an emission with maxima at 455 and 489 nm which fell in the blue region with the CIE coordinates of $(x = 0.19, y = 0.22)$. PDF displays a blue-green emission peaked at 520 nm and the CIE coordinates are $(x = 0.26, y = 0.42)$. PDFA

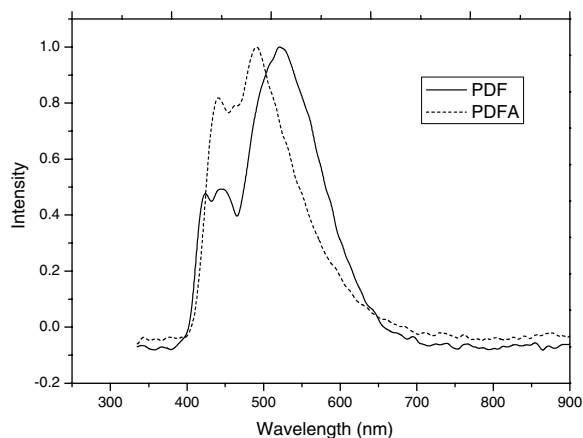


Fig. 3. EL spectra of the devices: ITO/HHTL/PDF/Mg:Ag and ITO/HHTL/PDFA/Mg:Ag.

shows a better light purity than PDF. This might be attributed to the dendritic structure of PDFA which can enhance the steric hindrance of the molecules and effectively prevent the aggregation of the molecules [11–13]. The difference between EL spectra and PL spectra of PDFA and PDF was speculated to be related to the formation of excimers [14,15], the definite mechanics is being under investigation.

Fig. 4 shows the luminance–voltage and current–voltage characteristics of the devices based on PDF and PDFA. For comparison, a device without HHTL was also fabricated. The forward bias current was obtained when the ITO was a positive electrode and Mg:Ag as a negative one. The current and light output increased with the forward bias voltage. In the case of device based on PDF, the device with HHTL exhibits a relatively low turn-on voltage of 8 V, while the turn-on voltage of single-layer device is 12 V. The maximum luminance and quantum efficiency of the double-layer device was about 833

lm/m² and 0.065 lm/W, respectively. For the single-layer device, these values were only 18 lm/m² and 0.008 lm/W. Apparently, the introduction of HHTL to the OLED can greatly improve the electroluminescent property of the light-emitting device. The reason was assumed by that HHTL has high hole injecting and transporting ability, which could enhance hole injection and balances of combination of hole and electron injected from anode (ITO) and cathode (Mg:Ag). Besides, the self-assemble always occurred between APTMS and ITO substrate, as shown in Fig. 1 [16–18]. HHTL can be steadily associated to ITO substrate with strong chemical bonding through the hydrolyzation of APTMS, and the hole injection ability may be greatly improved by these chemical bond [19]. The device based on PDFA exhibited an apparently better light-emitting efficiency than the one based on PDF. This result suggested that the introduction of triphenylamine group in PDFA can effectively improve the charge transfer ability [20].

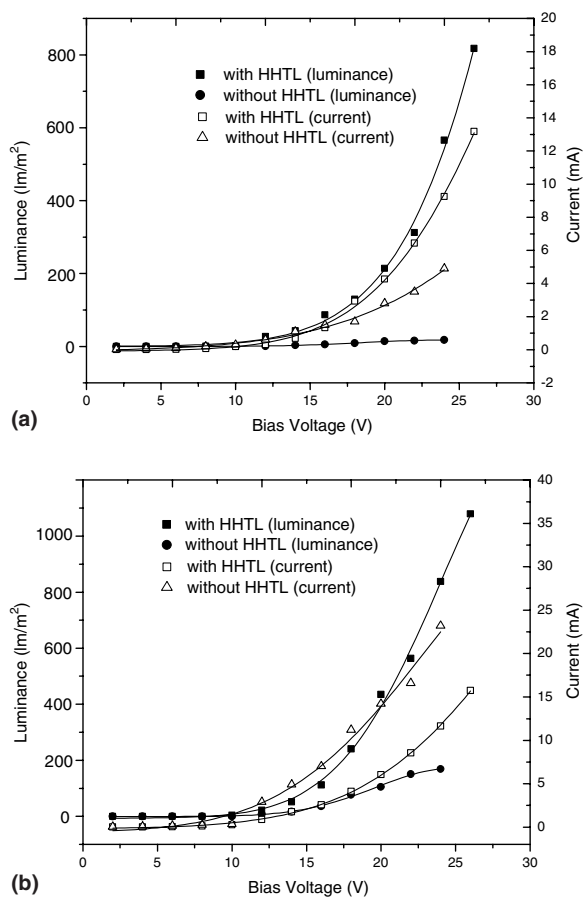


Fig. 4. Brightness–voltage and current–voltage characteristics of the devices based on two polymers: (a) PDF (b) PDFA.

4. Conclusion

Organic/inorganic hybrid composite was introduced into organic light-emitting device as hole transporting layer. Based on this layer, we fabricated organic double-layer light-emitting diodes with two conjugated polymers of PDF and PDFA. The results showed that light output intensity and quantum efficiency can be greatly improved when HHTL was inserted between ITO substrate and light-emitting layer. We expected that, by using HHTL, organic light-emitting devices can be fabricated by spin-coating technique at room temperature and the manufacturing technology will be further simplified consequently.

Acknowledgments

This work supported by the National Key Basic Research Special Foundation (NKBRFSF) under Grant No. TG1999075207, the National Natural Science Foundation of China under Grant Nos. 60407004, 10434020, 60378012, 90206003, 10328407 and 90101027.

References

- [1] C. David Muller, A. Falcou, N. Reckefuss, et al., Nature 421 (2003) 829.
- [2] C.W. Tang, S.A. Vanslyke, Appl. Phys. Lett. 51 (1987) 913.

- [3] K. Ziemelis, *Nature* 399 (1999) 408.
- [4] J.H. Burroughes, D.D.C. Bradley, A.R. Brown, et al., *Nature* 347 (1990) 539.
- [5] I. Zareba-Grodz, W. Mista, W. Strek, et al., *Opt. Mater.* 26 (2004) 199.
- [6] D.A. Loy, K.J. Shea, *Chem. Rev.* 95 (1995) 1431.
- [7] Y. Wei, D.L. Jin, D.J. Brennan, et al., *Chem. Mater.* 10 (1998) 769.
- [8] Fushan Li, Zhijian Chen, Bo. Qu, et al., *J. Phys. D: Appl. Phys.* 38 (2005) 847.
- [9] Qiyi Xing, Ruiqiu Xu, Zheng Zhou, et al., *Basic Organic Chemistry*, Higher Education Press, 2002 (in Chinese).
- [10] Hiroko Yamada, Hiroshi Imahori, Yoshinobu Nishimura, et al., *Adv. Mater.* 14 (2002) 892.
- [11] Jing Li, Zhishan Bo, *Macromolecules* 37 (2004) 2013.
- [12] Hoon-Je Cho, Byung-Jun Jung, Nam Sung Cho, et al., *Macromolecules* 36 (2003) 6704.
- [13] Wei-Jung Lin, Wen-Chang Chen, Wen-chung Wu, et al., *Macromolecules* 37 (2004) 2335.
- [14] Anne Donat-Bouillud, Isabelle Levesque, Ye Tao, et al., *Chem. Mater.* 12 (2000) 1931.
- [15] W. Yu, Y. Cao, J. Pei, et al., *Appl. Phys. Lett.* 75 (1999) 3270.
- [16] E.M. Joshua, G.C.V. Jonathan, E.J. Ghassan, et al., *Chem. Mater.* 14 (2002) 3054.
- [17] Q.L. Huang, J. Cui, J.G.C. Veinot, et al., *Appl. Phys. Lett.* 82 (2003) 331.
- [18] J. Cui, Q.L. Huang, J.G.C. Veinot, et al., *Adv. Mater.* 14 (2002) 565.
- [19] Shuai Wang, Yunqi Liu, Xuebin Huang, et al., *J. Phys. Chem. B* 107 (2003) 12639.
- [20] X. Gong, D. Moses, A.J. Heeger, et al., *Appl. Phys. Lett.* 83 (2003) 183.

Letter

The effects of copper phthalocyanine purity on organic solar cell performance

Rhonda F. Salzman^a, Jiangeng Xue^b, Barry P. Rand^a, Alex Alexander^d,
Mark E. Thompson^c, Stephen R. Forrest^{a,*}

^a Department of Electrical Engineering, Princeton University, Princeton, NJ 08544, United States

^b Global Photonic Energy Corporation, 375 Phillips Blvd, Ewing, NJ 08618, United States

^c Department of Chemistry, University of Southern California, Los Angeles, CA 90089, United States

^d Universal Display Corporation, 375 Phillips Blvd, Ewing, NJ 08618, United States

Received 14 June 2005; received in revised form 13 September 2005; accepted 15 September 2005

Available online 21 October 2005

Abstract

The performance of small-molecular weight organic double heterojunction donor–acceptor bilayer solar cells is studied as a function of the purity of the donor material, copper phthalocyanine (CuPc). We find that the power conversion efficiency under simulated AM1.5G, 1 sun illumination conditions increases from $(0.26 \pm 0.01)\%$ to $(1.4 \pm 0.1)\%$ as the CuPc layer purity increases. Concomitant with the improvements in power conversion efficiency, we find that the hole mobility of the unpurified CuPc is nearly three orders of magnitude lower than for purified source material. Mass spectrometry and Fourier transform infrared spectroscopy are used to identify metal-free phthalocyanine as the primary impurity that degrades both device efficiency and hole mobility.

© 2005 Elsevier B.V. All rights reserved.

Small molecular weight organic semiconductors have been recognized for their potential use in large-area, flexible, and low cost photovoltaic applications since Tang demonstrated the first bilayer heterojunction cell in 1986 [1]. The copper phthalocyanine (CuPc)/3,4,9,10-perylene-tetracarboxylic bis-benzimidazole (PTCBI)/Ag planar heterojunction system has exhibited a peak power conversion efficiency of $(1.1 \pm 0.1)\%$ since its first demonstration [2]. Only recently has this materials system broken the 1% barrier, achieving a power

conversion efficiency of $(2.7 \pm 0.1)\%$ with the use of a bulk heterojunction structure grown via organic vapor phase deposition (OVPD) [3]. Similar devices based on the CuPc/C₆₀ system have resulted in single cell efficiencies up to $(5.0 \pm 0.3)\%$ [4–7]. Previous work investigating the purity dependence of solar cell performance using phthalocyanines as donor materials have shown that diode leakage characteristics [8] and power conversion efficiencies can quadruple with increasing purity of the source material [9]. Here, we find the performance of a CuPc-based thin film cell is strongly impacted by materials purity. Specifically, we find that the cell responsivity and fill factor increase with hole mobility, which is found in turn to depend on material purity as assessed using

* Corresponding author.

E-mail address: forrest@princeton.edu (S.R. Forrest).

mass spectrometry and Fourier transform infrared spectroscopy (FTIR). In particular, double heterojunction cells employing the highly purified CuPc–PTCBI material system show a peak power conversion efficiency of $(1.4 \pm 0.1)\%$ (under simulated AM1.5G 1 sun intensity illumination) compared to less than 0.3% for unpurified CuPc source material. This study provides a clear linkage between organic material purity, charge transport properties, and device performance.

Two different source batches of CuPc were compared: the “unpurified” batch was commercially obtained [10], and was quoted by the manufacturer as 98% pure by mass; whereas the “purified” batch was refined by a single step thermal gradient purification process [11]. Here, the material was heated under a pressure of $\leq 10^{-6}$ Torr for four to six days in a three zone furnace, each zone having a length of 20 cm. The temperature of the first zone was 415 °C, the second was 360 °C, and the third was 320 °C. Purified material was obtained from the second zone. Source materials were loaded into a high vacuum thermal evaporation chamber with a base pressure of 5×10^{-7} Torr, leading to a growth pressure of 1×10^{-6} Torr for purified, and 1×10^{-5} Torr for unpurified material at a deposition rate of 2 Å/s. When not under high vacuum, the sources were stored under a nitrogen atmosphere, with water and oxygen levels below 1 ppm. Purified material was also grown by ultra high vacuum organic molecular beam deposition [11] (OMBD) at a base pressure of 5×10^{-10} Torr, and growth pressure of 1×10^{-9} Torr.

Glass substrates coated with a 1500 Å thick indium tin oxide (ITO) anode having a sheet resistance of 15 Ω/□ were cleaned with detergent in deionized water, followed by a rinse in deionized water, sonication in 2-propanol, 5 min in boiling trichloroethylene performed twice, 5 min sonication in acetone performed twice, 5 min in boiling 2-propanol performed twice, and 5 min exposure to an ultraviolet-ozone surface treatment. The double heterojunction solar cell structure was 200 Å CuPc/250 Å PTCBI/100 Å bathocuproine (BCP)/Ag. Both PTCBI and BCP were purified prior to thermal deposition via a standard thermal gradient sublimation process [11]. A single vacuum break during growth was necessary to attach a shadow mask in the purified nitrogen environment prior to patterned Ag cathode deposition. For space-charge-limited current (SCLC) measurements, CuPc films varying from 1000 Å to 8000 Å thickness were

also grown on similarly prepared ITO-coated glass substrates forming an ITO/CuPc/Au structure. As in the case of the photovoltaic cell film growth, a single vacuum break and exposure to air after CuPc deposition was necessary to attach the shadow mask prior to Au cathode deposition.

The source material in the unpurified boat was not changed throughout this study. Successive film growths, therefore, result in purification of the unpurified material. Solar cell structures and those used for the SCLC measurements were alternately grown to enable measurement at different points in the growth timeline, thereby revealing the characteristics of films with increasing purity. Over the same time period, purified CuPc was also used to grow multiple solar cells and films for SCLC measurements, and these measurements showed consistency, within experimental error.

Current–voltage measurements were obtained at room temperature using a semiconductor parameter analyzer. For comparison with previous work on this “standard” device, and unless otherwise noted, solar cell performance was characterized in the dark and under simulated AM1.5G solar illumination using a 150 W Xenon arc lamp [12]. The cell diameter was 1 mm as defined by the shadow mask openings. In addition, to obtain a more accurate measurement of the absolute power efficiency, in some experiments we included the spectral mismatch of our source and the solar spectrum using a Si reference cell traceable to National Renewable Energy Laboratory standards [13–15]. For SCLC measurements, the device diameter varied from 0.33 mm to 0.5 mm. Materials purity was assessed using X-ray photoelectron spectroscopy (XPS) of 300 Å thick CuPc films deposited under high vacuum on Ag-coated Si substrates. Additionally, mass spectra of the source powders employed a laser desorption ionization time-of-flight Hewlett-Packard G2025A mass spectrometer, and FTIR was carried out on 750 Å thick films deposited on KBr substrates.

Previous investigations into the purity of metallophthalocyanines have found that purity depends on different preparation methods, manufacturers and batches [16]. Principle impurities are typically phthalocyanines other than that which was being studied: i.e. the metal-free phthalocyanine (H_2Pc), or different metal-substituted phthalocyanines mixed with the particular compound of interest [16,17]. Low resolution mass spectra of unpurified and purified source powders are shown in Fig. 1(a). All unlabeled peaks in the figure are

assigned to residue from sinapinic acid used in some runs as a matrix. The unpurified CuPc sample shows several peaks not present in the purified sample. The largest peak at 522 amu is assigned to H₂Pc. The intensity of the H₂Pc peak suggests that it is the most abundant impurity present in the unpurified source material. The mass of metal-free phthalocyanine is 514 amu, which differs somewhat from that measured, possibly due to the low resolution of the spectrometer and complexation of the metal-free Pc. The peak at 562 amu is tentatively assigned to CuPc lacking a single amine group, and that at 648 amu may be a form of CuPc that is coordinated to an extra Cu atom.

Both purified and unpurified CuPc films exhibited nearly indistinguishable FTIR spectra, except in the region between 1515 and 1554 cm⁻¹ where two peaks are detected for the unpurified sample, Fig. 1(b). While a spectrum for CuPc shows no peaks in this region, that for H₂Pc has a small peak near 1540 cm⁻¹ [18], providing further evidence to support the presence of the metal-free phthalocyanine as the principle impurity.

The XPS spectra for both source materials are nearly identical. Five peaks are obtained: a C 1s peak at a binding energy of 285 eV, N 1s at 399 eV, Cu Auger at 571 eV, Cu 2p₃ at 936 eV, and Cu 2p₁ at 956 eV. The relative height of impurity peaks in mass spectra and the low yield of the purification process (<50%) indicate that if the impurities contained elements different from those in CuPc, they would be present in concentrations above the detection limit of XPS. Hence, we conclude that the impurities result from incomplete reactions in the production of CuPc, and are primarily composed of the same elements as CuPc.

To investigate the electrical effects of the impurities, we extracted mobilities for the purified and unpurified materials by fitting the current–voltage characteristics of ITO/CuPc/Au samples to Child's Law: $J = \frac{9}{8} \epsilon_r \epsilon_0 \mu \frac{V^2}{d^3}$, with a field-dependant hole mobility of $\mu = \mu_0 \exp(\gamma E^{1/2})$. Here J is the current density, $\epsilon_r = 3.6$ is the relative permittivity of CuPc [21], ϵ_0 is the permittivity of vacuum, V is the applied voltage, d is the film thickness, μ_0 is the zero-field mobility, and γ is its characteristic field dependence [19,20]. The J – V characteristics were fit in the region where average electric field was <10⁵ V/cm to limit the effects of sample heating and material breakdown. Previous CuPc hole mobility measurements are typically obtained in-plane, and hence normal to the growth direction, whereas the current measurements analyzed here are obtained parallel to the growth direction, consistent with the transport direction in thin film solar cells.

The zero-field mobility, μ_0 , found for purified CuPc films deposited in high vacuum, ranged from 2×10^{-5} to 3×10^{-4} cm²/Vs. Literature values for the hole mobility of CuPc measured via time-of-flight and field-effect methods vary widely [21–24], from 10⁻⁷ to 10⁻² cm²/Vs, indicating a strong dependence on sample preparation conditions [21] and exposure to oxygen [24], among other factors. As shown in Fig. 2, μ_0 obtained for the unpurified material for successive growth runs climbs by three orders of magnitude, from 4.2×10^{-7} cm²/Vs to 1.8×10^{-4} cm²/Vs, the latter value within the range measured for the purified material (shown as dotted lines in Fig. 2). By the 7th evaporation cycle, μ_0 falls off due to the evaporation of less-volatile impurities when the boat temperature is increased to maintain

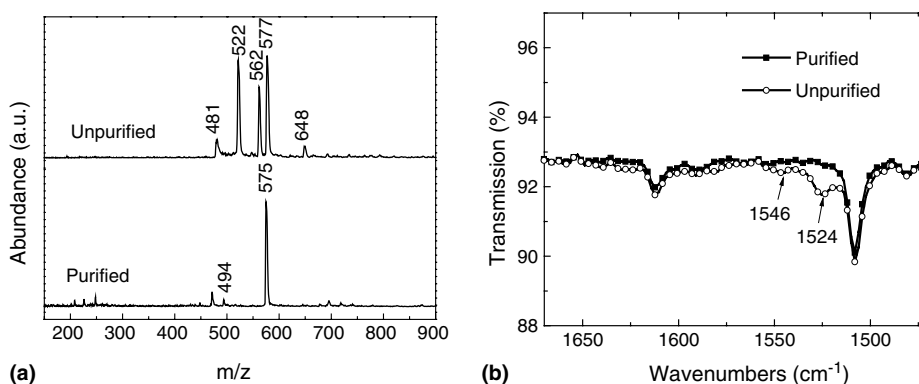


Fig. 1. (a) Mass and (b) Fourier transform infrared (FTIR) spectra for both purified and unpurified copper phthalocyanine (CuPc). The peak at 522 amu in (a), and the differences in the FTIR data in (b) suggest that H₂Pc is the principle impurity in CuPc.

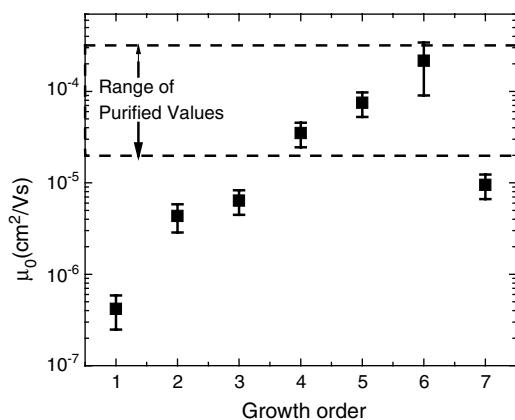


Fig. 2. Zero-field mobility, μ_0 , as a function of order in the growth sequence for originally unpurified copper phthalocyanine (CuPc) source material. Measurements were made for film thicknesses ranging from 1000 Å to 4000 Å, and sandwiched between an indium-tin-oxide anode and Au cathode. The dotted lines delineate the range of values measured for μ_0 of purified CuPc thin films.

a growth rate of 2 Å/s as it empties. From these measurements we conclude that changes in mobility can be directly correlated with material purity, which improves with each evaporation cycle.

The impact of CuPc purity on solar cell performance was measured by comparing the power conversion efficiency and factors that affect efficiency at different points in the growth timeline, shown in Fig. 3. Except for the first unpurified, highly-resistive device, the open circuit voltage showed little variation between different materials and different growths. At 1 sun, the value of the responsivity of the unpurified material increases from 0.020 ± 0.001 A/W to 0.051 ± 0.004 A/W, the latter near that obtained for the purified material deposited in both high and ultra high vacuum (0.050 ± 0.003 A/W). Similarly, the fill factor significantly increases during successive growths of the originally unpurified material. At 1 sun illumination intensity, it progresses from 0.26 ± 0.01 to 0.59 ± 0.03 ; the latter value is comparable to that obtained for the purified material grown in both high and ultra high vacuum (0.59 ± 0.05). At 1 sun, the unpurified power conversion efficiencies increase from $(0.26 \pm 0.01)\%$ to $(1.3 \pm 0.1)\%$ during four successive growth runs. In comparison, the purified material has an average power conversion efficiency of $(1.4 \pm 0.1)\%$ when deposited in high vacuum, and $(1.3 \pm 0.1)\%$ in ultra high vacuum. These values show a significant improvement when compared with past work [1,2] on CuPc/PTCBI cells,

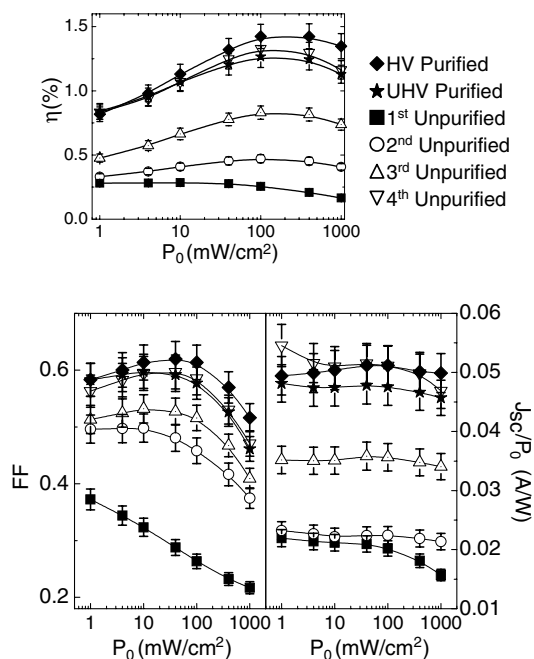


Fig. 3. Comparison of average power conversion efficiency (η), fill factor (FF), and responsivity (J_{sc}/P_0) of four successive growths of solar cells using an originally unpurified copper phthalocyanine (CuPc) source deposited in high vacuum, purified source material deposited in high vacuum, and purified source material deposited in ultra-high vacuum. Filled squares represent the first deposition of the originally unpurified CuPc, open circles the second, open triangles the third run, open upside-down triangles the fourth run, filled diamonds the purified material grown in high vacuum, and filled stars the purified material grown in ultra high vacuum.

whose efficiencies consistently are in the range of $(1.0 \pm 0.1)\%$. When spectral mismatch factor [12,13] corrections are made to compensate for the differences between the solar and simulated spectra, the 1.4% efficiency is decreased to $(1.1 \pm 0.1)\%$. From these data, we conclude that the purity of the source material has a greater impact on device performance than chamber background pressure.

To verify that the CuPc is responsible for the enhancement in power conversion efficiency, the cell external quantum efficiency (η_{EQE}) was measured as shown in Fig. 4. Once again, we see a trend of increasing efficiency as the material is purified: the unpurified material starts with a peak $\eta_{EQE} = 10.5\%$ at a wavelength of $\lambda = 625$ nm, increasing to 18.1% at $\lambda = 625$ nm for the last unpurified run, similar to values measured for the fully purified material. Both high vacuum and ultra high vacuum purified material have $\eta_{EQE} \geq 18\%$. The largest increase in external quantum efficiency occurs between $\lambda = 550$ nm and

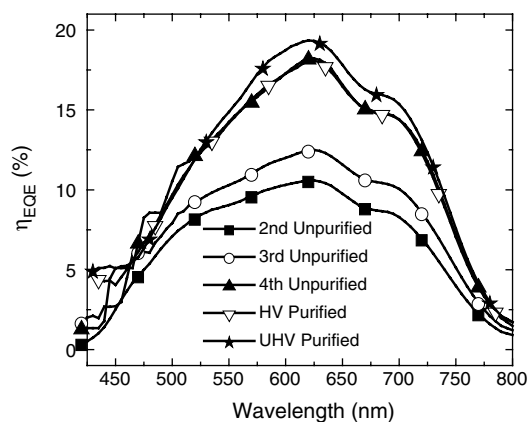


Fig. 4. Comparison of average external quantum efficiency (η_{EQE}) of three successive growths of solar cells using unpurified source material in high vacuum, purified source material in high vacuum, and purified source material in ultra-high vacuum. The key is the same as used for Fig. 3.

750 nm, corresponding to the peak absorption of CuPc [2]. This indicates that the response due to absorption in the CuPc donor material is principally responsible for the increase in cell power conversion efficiency with material purity.

In conclusion, we have found that the purity of the organic small molecular weight material used in the active layers of solar cells strongly impacts the device performance. Mass and FTIR spectra used in conjunction with charge carrier mobility data suggest that impurities such as H_2Pc can significantly influence the electrical characteristics of vacuum deposited organic solar cells employing CuPc as the donor material. We have observed a trend of improving mobility as the source is purified during the growth process, which correspondingly leads to higher photovoltaic cell fill factors, responsivities, and power conversion efficiencies.

Acknowledgements

The authors would like to thank Dorothy Little for mass spectroscopy measurements, and John

Eng for help with FTIR measurements. Support for this work was provided by the Air Force Office of Scientific Research, Global Photonic Energy Corp., and the National Renewable Energy Laboratory (NREL).

References

- [1] C.W. Tang, *Appl. Phys. Lett.* 48 (1986) 183.
- [2] P. Peumans, V. Bulovic, S.R. Forrest, *Appl. Phys. Lett.* 76 (2000) 2650.
- [3] F. Yang, M. Shtein, S.R. Forrest, *Nature Mater.* 4 (2005) 37.
- [4] P. Peumans, S.R. Forrest, *Appl. Phys. Lett.* 79 (2001) 126.
- [5] J. Xue, S. Uchida, B.P. Rand, S.R. Forrest, *Appl. Phys. Lett.* 84 (2004) 3013.
- [6] S. Uchida, J. Xue, B.P. Rand, S.R. Forrest, *Appl. Phys. Lett.* 84 (2004) 4218.
- [7] J. Xue, B.P. Rand, S. Uchida, S.R. Forrest, *Adv. Mater.* 17 (2005) 66.
- [8] J.B. Whitlock, P. Panayotatos, G.D. Sharma, M.D. Cox, R.R. Sauer, G.R. Bird, *Opt. Eng.* 32 (1993) 1921.
- [9] D. Wohrle, L. Kreienhoop, G. Schnurpfeil, J. Elbe, B. Tennigkeit, S. Hiller, D. Schlettwein, *J. Mater. Chem.* 5 (1995) 1819.
- [10] Stock number: 43650, lot number: E17L30. Alfa Aesar 26 Parkridge Rd., Ward Hill, MA 01835, USA.
- [11] S.R. Forrest, *Chem. Rev.* 97 (1997) 1793.
- [12] Oriel Instruments, 150 Long Beach Blvd, Stratford, CT 06615, USA.
- [13] PV Measurements, Inc. 1800 30th Street #216, Boulder, CO 80301, USA.
- [14] ASTM International Standard Test Method E 973-02.
- [15] K. Emery, *IEEE Trans. Electron Devices* 46 (1999) 1928.
- [16] J.A. Thompson, K. Murata, D.C. Miller, J.L. Stanton, W.E. Broderick, B.M. Hoffman, J.A. Ibers, *Inorg. Chem.* 32 (1993) 3546.
- [17] T.G. Abdel-Malik, G.A. Cox, *J. Phys. C* 10 (1977) 63.
- [18] C.J. Pouchert, second ed. *The Aldrich Library of FT-IR Spectra*, Vol. 3, Aldrich, Milwaukee, 1997, pp. 4181–4184.
- [19] W.D. Gill, *J. Appl. Phys.* 43 (1972) 5033.
- [20] D.H. Dunlap, P.E. Parris, V.M. Kenkre, *Phys. Rev. Lett.* 77 (1996) 542.
- [21] R.D. Gould, *J. Phys. D* 19 (1986) 1785.
- [22] K. Xiao, Y.Q. Liu, G. Yu, D.B. Zhu, *Synth. Met.* 137 (2003) 991.
- [23] M. Kitamura, T. Imada, S. Kako, Y. Arakawa, *Jpn. J. Appl. Phys.* 43 (2004) 2326.
- [24] K. Kudo, T. Sumimoto, K. Hiraga, S. Kuniyoshi, K. Tanaka, *Jpn. J. Appl. Phys.* 36 (1997) 6994.

Author index of Volume 6

Abd-El-Rahman, K.F., see El-Nahass, M.M.	6 (2005) 129
Al-Ibrahim, M., H.-K. Roth, M. Schroedner, A. Konkin, U. Zhokhavets, G. Gobsch, P. Scharff and S. Sensfuss, The influence of the optoelectronic properties of poly(3-alkylthiophenes) on the device parameters in flexible polymer solar cells	6 (2005) 65
Alexander, A., see Salzman, R.F.	6 (2005) 242
Allott, R., see Lidzey, D.G.	6 (2005) 221
Amy, F., C. Chan and A. Kahn, Polarization at the gold/pentacene interface	6 (2005) 85
Amy, F., see Wan, A.	6 (2005) 47
Andersson, T.G., see Andreasson, M.	6 (2005) 175
Andreasson, M., M. Tengelin-Nilsson, T.G. Andersson, L. Ilver and J. Kanski, Importance of ITO surface conditions for the interaction with thin CuPc layers	6 (2005) 175
Andreev, A., see Singh, Th.B.	6 (2005) 105
Asano, T., see Chutinan, A.	6 (2005) 3
Bäcklund, T.G., see Sandberg, H.G.O.	6 (2005) 142
Baik, H.K., see Jeong, S.M.	6 (2005) 149
Baral, J.K., see Majumdar, H.S.	6 (2005) 188
Bauer, S., see Singh, Th.B.	6 (2005) 105
Böhlen, K., see Lidzey, D.G.	6 (2005) 221
Bradley, D., S. Forrest, J. Salbeck and K. Seki, Announcing: Organic Electronics Letters	6 (2005) 1
Buckley, A., see Lidzey, D.G.	6 (2005) 221
Bulović, V., see Mascaro, D.J.	6 (2005) 211
Cadby, A., see Voigt, M.	6 (2005) 35
Cao, Y., see Wu, H.	6 (2005) 118
Chan, C., see Amy, F.	6 (2005) 85
Chang, W.R., see Chen, S.F.	6 (2005) 92
Chappell, J., see Voigt, M.	6 (2005) 35
Chen, S., Z. Wu, Y. Zhao, C. Li, J. Hou and S. Liu, Efficient organic light-emitting device from exciplex emission between 4,4',4''-tris[3-methylphenyl(phenyl)amino]triphenylamine and 2,2',2''-(1,3,5-benzenetriyl)tris-[1-phenyl-1H-benzimidazole]	6 (2005) 111
Chen, S.F., Y.K. Fang, S.C. Hou, C.Y. Lin, C.S. Lin, W.R. Chang and T.H. Chou, The effect of doping iodine on organic light-emitting diode	6 (2005) 92
Chen, Z., see Li, F.	6 (2005) 237
Choi, S.H., see Jeong, S.M.	6 (2005) 149
Chou, T.H., see Chen, S.F.	6 (2005) 92
Chutinan, A., K. Ishihara, T. Asano, M. Fujita and S. Noda, Theoretical analysis on light-extraction efficiency of organic light-emitting diodes using FDTD and mode-expansion methods	6 (2005) 3
Crispin, A., see Tengstedt, C.	6 (2005) 21
D'Andrade, B.W., S. Datta, S.R. Forrest, P. Djurovich, E. Polikarpov and M.E. Thompson, Relationship between the ionization and oxidation potentials of molecular organic semiconductors	6 (2005) 11
Darwish, A.A.A., see El-Nahass, M.M.	6 (2005) 129
Datta, S., see D'Andrade, B.W.	6 (2005) 11
de Kok, M.M., see Weijtens, C.H.L.	6 (2005) 97
de Winter, S.H.P.M., see Weijtens, C.H.L.	6 (2005) 97
Deman, A.-L. and J. Tardy, PMMA-Ta ₂ O ₅ bilayer gate dielectric for low operating voltage organic FETs	6 (2005) 78

Djurovich, P., see D'Andrade, B.W.	6 (2005) 11
Domercq, B., see Haddock, J.N.	6 (2005) 182
El-Nahass, M.M., K.F. Abd-El-Rahman, A.A.M. Farag and A.A.A. Darwish, Photovoltaic properties of NiPc/p-Si (organic/ inorganic) heterojunctions	6 (2005) 129
Fahlman, M., see Tengstedt, C.	6 (2005) 21
Fang, Y.K., see Chen, S.F.	6 (2005) 92
Farag, A.A.M., see El-Nahass, M.M.	6 (2005) 129
Fieret, J., see Lidzey, D.G.	6 (2005) 221
Forrest, S., see Bradley, D.	6 (2005) 1
Forrest, S.R., see D'Andrade, B.W.	6 (2005) 11
Forrest, S.R., see Salzman, R.F.	6 (2005) 242
Fujita, M., see Chutinan, A.	6 (2005) 3
Geoghegan, M., see Voigt, M.	6 (2005) 35
Giebeler, C., see Lidzey, D.G.	6 (2005) 221
Gobsch, G., see Al-Ibrahim, M.	6 (2005) 65
Godlewski, J., see Kotowski, D.	6 (2005) 193
Gomes, H.L., see Stallinga, P.	6 (2005) 137
Gong, Q., see Li, F.	6 (2005) 237
Gorgoi, M. and D.R.T. Zahn, "Band bending" in copper phthalocyanine on hydrogen-passivated Si(1 1 1)	6 (2005) 168
Günes, S., see Singh, Th.B.	6 (2005) 105
Haddock, J.N., X. Zhang, B. Domercq and B. Kippelen, Fullerene based n-type organic thin-film transistors	6 (2005) 182
Hou, J., see Chen, S.	6 (2005) 111
Hou, S.C., see Chen, S.F.	6 (2005) 92
Hsu, C.-H., see Tengstedt, C.	6 (2005) 21
Huang, F., see Wu, H.	6 (2005) 118
Hwang, J., see Wan, A.	6 (2005) 47
Ikkala, O., see Majumdar, H.S.	6 (2005) 188
Ilver, L., see Andreasson, M.	6 (2005) 175
Ishihara, K., see Chutinan, A.	6 (2005) 3
Jeong, S.M., W.H. Koo, S.H. Choi and H.K. Baik, Properties of organic light-emitting diodes by aluminum cathodes modification using Ar ⁺ ion beam	6 (2005) 149
Jones, R.A.L., see Voigt, M.	6 (2005) 35
Kahn, A., see Amy, F.	6 (2005) 85
Kahn, A., see Wan, A.	6 (2005) 47
Kanski, J., see Andreasson, M.	6 (2005) 175
Kim, Y.-G., see Snook, J.H.	6 (2005) 55
Kippelen, B., see Haddock, J.N.	6 (2005) 182
Konkin, A., see Al-Ibrahim, M.	6 (2005) 65
Koo, W.H., see Jeong, S.M.	6 (2005) 149
Kotowski, D., B. Kutrzeba-Kotowska, M. Obarowska, R. Signerski and J. Godlewski, Surface photocurrents in tetracene layers	6 (2005) 193
Kumar, J., see Snook, J.H.	6 (2005) 55
Kutrzeba-Kotowska, B., see Kotowski, D.	6 (2005) 193
Li, C., see Chen, S.	6 (2005) 111
Li, F., Z. Chen, W. Wei and Q. Gong, Blue polymer light-emitting diodes with organic/inorganic hybrid composite as hole transporting layer	6 (2005) 237
Lidzey, D.G., see Voigt, M.	6 (2005) 35
Lidzey, D.G., M. Voigt, C. Giebeler, A. Buckley, J. Wright, K. Böhlen, J. Fieret and R. Allott, Laser-assisted patterning of conjugated polymer light emitting diodes	6 (2005) 221
Lin, C.S., see Chen, S.F.	6 (2005) 92
Lin, C.Y., see Chen, S.F.	6 (2005) 92
Liu, S., see Chen, S.	6 (2005) 111
Majumdar, H.S., J.K. Baral, R. Österbacka, O. Ikkala and H. Stubb, Fullerene-based bistable devices and associated negative differential resistance effect	6 (2005) 188
Marjanović, N., see Singh, Th.B.	6 (2005) 105

Mascaro, D.J., M.E. Thompson, H.I. Smith and V. Bulović, Forming oriented organic crystals from amorphous thin films on patterned substrates via solvent-vapor annealing	6 (2005) 211
Matt, G.J., see Singh, Th.B.	6 (2005) 105
Mazhari, B., Impact of interfacial barriers on recombination profile in bilayer organic light-emitting diode	6 (2005) 229
McCulloch, I., see Sandberg, H.G.O.	6 (2005) 142
Montaigne Ramil, A., see Singh, Th.B.	6 (2005) 105
Noda, S., see Chutinan, A.	6 (2005) 3
Obarowska, M., see Kotowski, D.	6 (2005) 193
Österbacka, R., see Majumdar, H.S.	6 (2005) 188
Österbacka, R., see Sandberg, H.G.O.	6 (2005) 142
Parker, I.D., see Tengstedt, C.	6 (2005) 21
Peng, J., see Wu, H.	6 (2005) 118
Polikarpov, E., see D'Andrade, B.W.	6 (2005) 11
Rand, B.P., see Salzman, R.F.	6 (2005) 242
Roichman, Y., see Tessler, N.	6 (2005) 200
Roth, H.-K., see Al-Ibrahim, M.	6 (2005) 65
Roth, H.-K., see Schrödner, M.	6 (2005) 161
Rowson, T., see Voigt, M.	6 (2005) 35
Salaneck, W.R., see Tengstedt, C.	6 (2005) 21
Salbeck, J., see Bradley, D.	6 (2005) 1
Salzman, R.F., J. Xue, B.P. Rand, A. Alexander, M.E. Thompson and S.R. Forrest, The effects of copper phthalocyanine purity on organic solar cell performance	6 (2005) 242
Samuelson, L.A., see Snook, J.H.	6 (2005) 55
Sandberg, H.G.O., T.G. Bäcklund, R. Österbacka, M. Shkunov, D. Sparrowe, I. McCulloch and H. Stubb, Insulators and device geometry in polymer field effect transistors	6 (2005) 142
Sariciftci, N.S., see Singh, Th.B.	6 (2005) 105
Scharff, P., see Al-Ibrahim, M.	6 (2005) 65
Schrödner, M., R.-I. Stohn, K. Schultheis, S. Sensfuss and H.-K. Roth, Polymer field effect transistors made by laser patterning	6 (2005) 161
Schroedner, M., see Al-Ibrahim, M.	6 (2005) 65
Schultheis, K., see Schrödner, M.	6 (2005) 161
Schwödiauer, R., see Singh, Th.B.	6 (2005) 105
Seki, K., see Bradley, D.	6 (2005) 1
Sensfuss, S., see Al-Ibrahim, M.	6 (2005) 65
Sensfuss, S., see Schrödner, M.	6 (2005) 161
Shkunov, M., see Sandberg, H.G.O.	6 (2005) 142
Signerski, R., see Kotowski, D.	6 (2005) 193
Singh, Th.B., N. Marjanović, G.J. Matt, S. Günes, N.S. Sariciftci, A. Montaigne Ramil, A. Andreev, H. Sitter, R. Schwödiauer and S. Bauer, High-mobility <i>n</i> -channel organic field-effect transistors based on epitaxially grown C ₆₀ films	6 (2005) 105
Sitter, H., see Singh, Th.B.	6 (2005) 105
Smith, H.I., see Mascaro, D.J.	6 (2005) 211
Snook, J.H., L.A. Samuelson, J. Kumar, Y.-G. Kim and J.E. Whitten, Ultraviolet photoelectron spectroscopy of nanocrystalline TiO ₂ films sensitized with (2,2'-bipyridyl)ruthenium(II) dyes for photovoltaic applications	6 (2005) 55
Sparrowe, D., see Sandberg, H.G.O.	6 (2005) 142
Stallinga, P. and H.L. Gomes, Trap states as an explanation for the Meyer–Neldel rule in semiconductors	6 (2005) 137
Stohn, R.-I., see Schrödner, M.	6 (2005) 161
Stubb, H., see Majumdar, H.S.	6 (2005) 188
Stubb, H., see Sandberg, H.G.O.	6 (2005) 142
Tardy, J., see Deman, A.-L.	6 (2005) 78
Tengelin-Nilsson, M., see Andreasson, M.	6 (2005) 175
Tengstedt, C., A. Crispin, C.-H. Hsu, C. Zhang, I.D. Parker, W.R. Salaneck and M. Fahlman, Study and comparison of conducting polymer hole injection layers in light emitting devices	6 (2005) 21
Tessler, N. and Y. Roichman, Amorphous organic molecule/polymer diodes and transistors—Comparison between predictions based on Gaussian or exponential density of states	6 (2005) 200
Thompson, M.E., see D'Andrade, B.W.	6 (2005) 11

Thompson, M.E., see Mascaro, D.J.	6 (2005) 211
Thompson, M.E., see Salzman, R.F.	6 (2005) 242
van Elsbergen, V., see Weijtens, C.H.L.	6 (2005) 97
Voigt, M., see Lidzey, D.G.	6 (2005) 221
Voigt, M., J. Chappell, T. Rowson, A. Cadby, M. Geoghegan, R.A.L. Jones and D.G. Lidzey, The interplay between the optical and electronic properties of light-emitting-diode applicable conjugated polymer blends and their phase-separated morphology	6 (2005) 35
Wan, A., J. Hwang, F. Amy and A. Kahn, Impact of electrode contamination on the α -NPD/Au hole injection barrier	6 (2005) 47
Wei, W., see Li, F.	6 (2005) 237
Weijtens, C.H.L., V. van Elsbergen, M.M. de Kok and S.H.P.M. de Winter, Effect of the alkali metal content on the electronic properties of PEDOT:PSS.	6 (2005) 97
Whitten, J.E., see Snook, J.H.	6 (2005) 55
Wright, J., see Lidzey, D.G.	6 (2005) 221
Wu, H., F. Huang, J. Peng and Y. Cao, High-efficiency electron injection cathode of Au for polymer light-emitting devices.	6 (2005) 118
Wu, Z., see Chen, S.	6 (2005) 111
Xue, J., see Salzman, R.F.	6 (2005) 242
Zahn, D.R.T., see Gorgoi, M.	6 (2005) 168
Zhang, C., see Tengstedt, C.	6 (2005) 21
Zhang, X., see Haddock, J.N.	6 (2005) 182
Zhao, Y., see Chen, S.	6 (2005) 111
Zhokhavets, U., see Al-Ibrahim, M.	6 (2005) 65